

AJNR

AMERICAN JOURNAL OF NEURORADIOLOGY

Official Journal ASNR • ASFNR • ASHNR • ASPNR • ASSR

MAY 2024 | VOLUME 45 | NUMBER 5 | WWW.AJNR.ORG

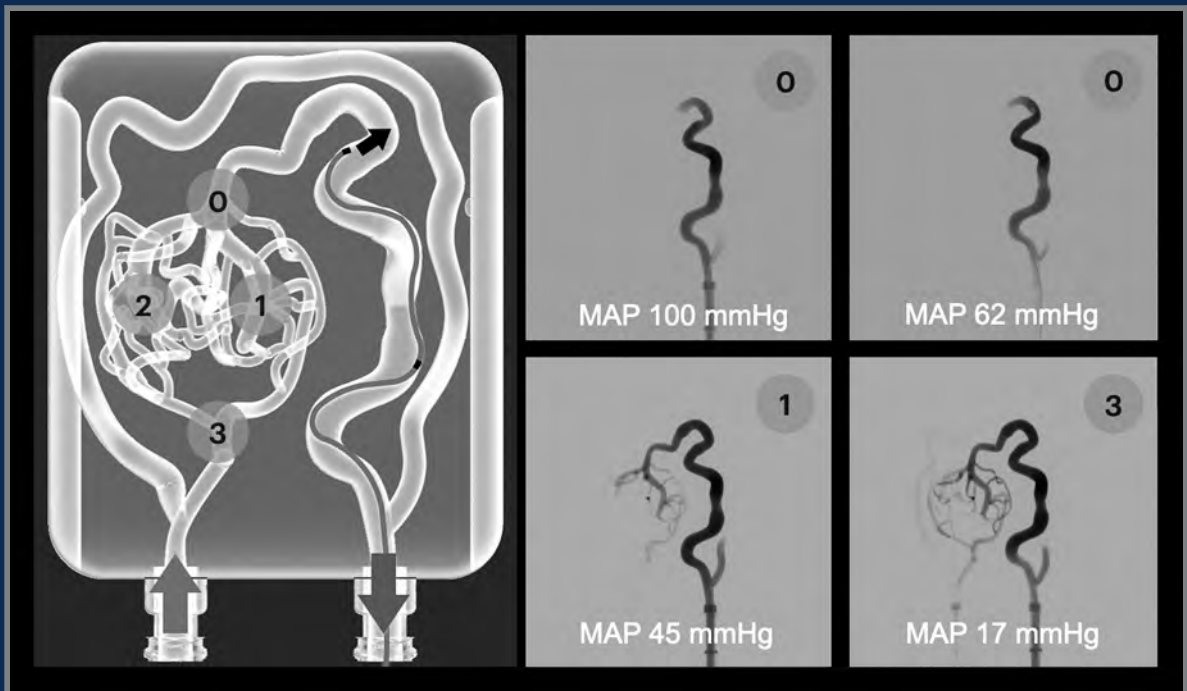
THE JOURNAL OF DIAGNOSTIC AND INTERVENTIONAL NEURORADIOLOGY

Clinical value of DWI-FLAIR mismatch in patients with acute ischemic stroke

Recanalization of coiled intracranial aneurysms with wall enhancement

Optic nerve sheath measurements in patients with orthostatic headaches predicts underlying CSF-venous fistula

ASL screening for typical and atypical neurodegenerative disease

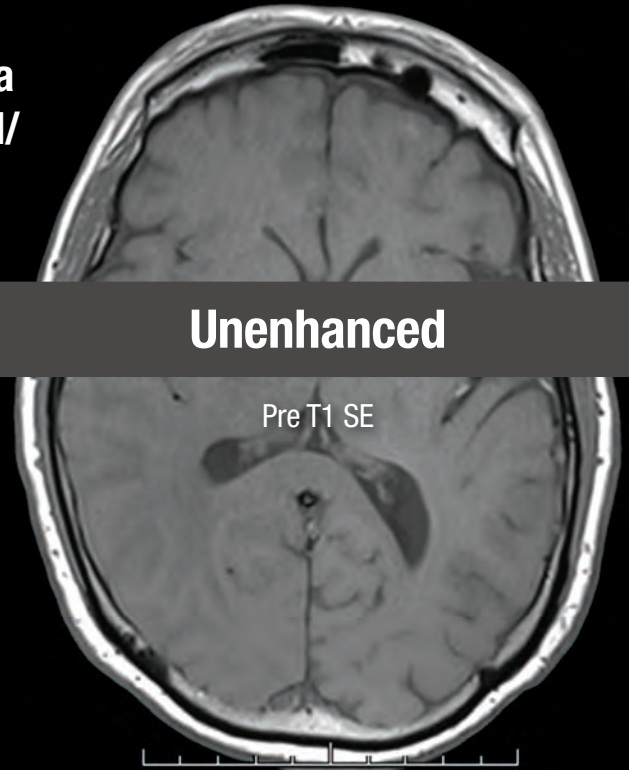


THIS IS HALF Gd*

***Effective contrast enhancement at half the gadolinium dose (0.05 mmol/kg) vs a macrocyclic GBCA at a dose of 0.1 mmol/kg in approved indications in the U.S.^{1-6†}**


Vueway[®]
[gadopiclenol] injection
485.1 mg/mL

**NO COMPROMISE IN MRI FROM BRACCO,
YOUR TRUSTED PARTNER**



[†]Phase III CNS Study Design (Study GDX-44-010): Intra-individual, crossover comparison of 0.05 mmol/kg VUEWAY (gadopiclenol) injection vs. 0.1 mmol/kg Gadavist[®] in MRI of the CNS. Patients with known or suspected CNS lesions. Three primary visualization endpoints (lesion border delineation, lesion internal morphology, degree of contrast enhancement). The CNS study included 256 patients with known or highly suspected CNS lesion(s) with a mean age of 57 years (range: 18-84 years), and 53% female patients.

Please see Brief Summary of Prescribing Information including Boxed Warning on adjacent page.

VUEWAY[®] (gadopiclenol) solution for injection

Indications

VUEWAY injection is indicated in adults and children aged 2 years and older for use with magnetic resonance imaging (MRI) to detect and visualize lesions with abnormal vascularity in:

- the central nervous system (brain, spine and surrounding tissues),
- the body (head and neck, thorax, abdomen, pelvis, and musculoskeletal system).

IMPORTANT SAFETY INFORMATION

WARNING: RISK ASSOCIATED WITH INTRATHECAL USE and NEPHROGENIC SYSTEMIC FIBROSIS

Risk Associated with Intrathecal Use

Intrathecal administration of gadolinium-based contrast agents (GBCAs) can cause serious adverse reactions including death, coma, encephalopathy, and seizures. VUEWAY is not approved for intrathecal use.

NEPHROGENIC SYSTEMIC FIBROSIS

Gadolinium-based contrast agents (GBCAs) increase the risk for NSF among patients with impaired elimination of the drugs. Avoid use of GBCAs in these patients unless the diagnostic information is essential and not available with non-contrasted MRI or other modalities. NSF may result in fatal or debilitating fibrosis affecting the skin, muscle and internal organs.

- The risk for NSF appears highest among patients with:

- **Chronic, severe kidney disease (GFR < 30 mL/min/1.73 m²), or**
- **Acute kidney injury.**
- **Screen patients for acute kidney injury and other conditions that may reduce renal function. For patients at risk for chronically reduced renal function (e.g. age > 60 years, hypertension, diabetes), estimate the glomerular filtration rate (GFR) through laboratory testing.**
- **For patients at highest risk for NSF, do not exceed the recommended VUEWAY dose and allow a sufficient period of time for elimination of the drug from the body prior to any re-administration.**

Contraindications

VUEWAY injection is contraindicated in patients with history of hypersensitivity reactions to VUEWAY.

Warnings and Precautions

There are **risks associated with intrathecal use** of GBCAs that can cause serious adverse reactions including death, coma, encephalopathy, and seizures. The safety and effectiveness of VUEWAY have not been established with intrathecal use and VUEWAY is not approved for intrathecal use.

Risk of **nephrogenic systemic fibrosis** is increased in patients using GBCA agents that have impaired elimination of the drugs, with the highest risk in patients with chronic, severe kidney disease as well as patients with acute kidney injury. Avoid use of GBCAs among these patients unless the diagnostic information is essential and not available with non-contrast MRI or other modalities.

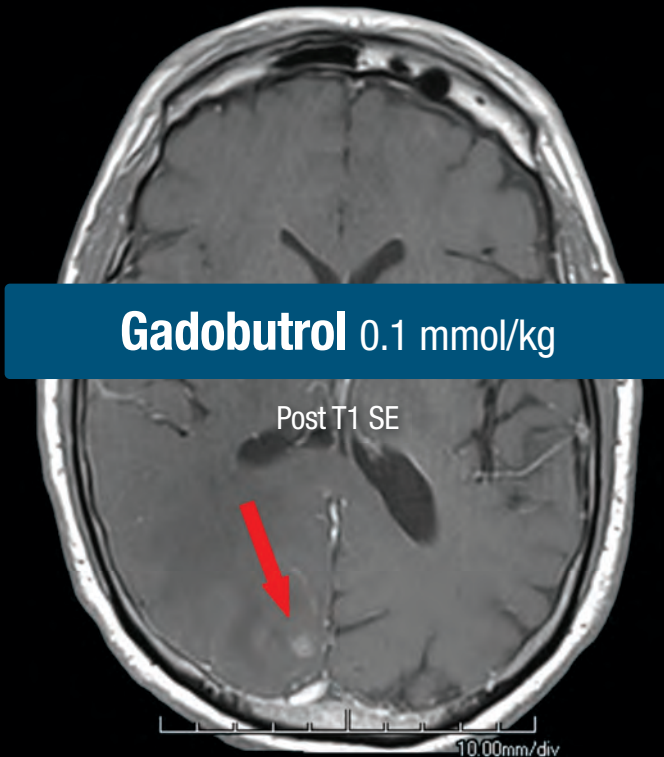
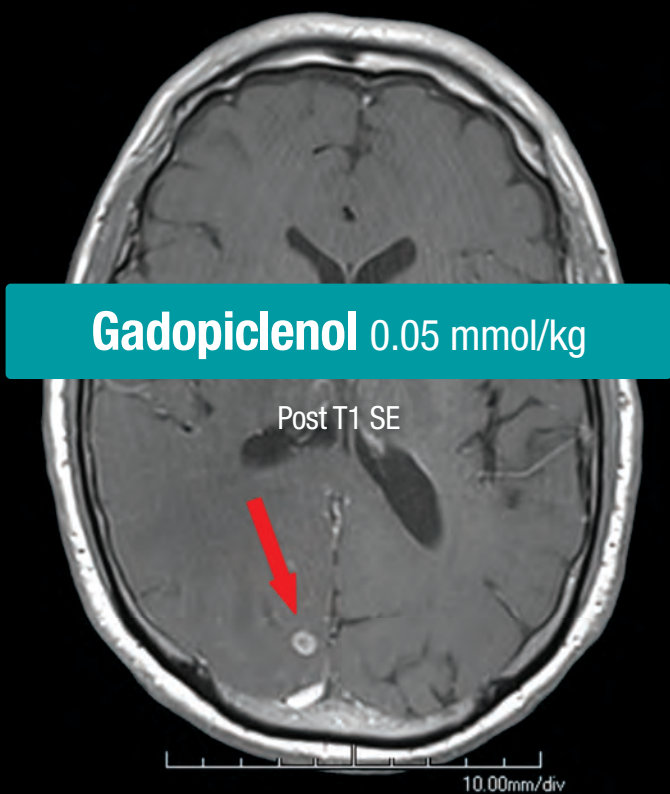
Hypersensitivity reactions, including serious hypersensitivity reactions, could occur during use or shortly following VUEWAY administration. Assess all patients for any



LIFE FROM INSIDE

65-year-old man – 3.0 T Siemens
Brain metastasis from lung adenocarcinoma⁷

SE = Spin Echo. These are representative images from reference studies; individual results may vary.



history of a reaction to contrast media, bronchial asthma and/or allergic disorders, administer VUEWAY only in situations where trained personnel and therapies are promptly available for the treatment of hypersensitivity reactions, and observe patients for signs and symptoms of hypersensitivity reactions after administration.

Gadolinium retention can be for months or years in several organs after administration. The highest concentrations (nanomoles per gram of tissue) have been identified in the bone, followed by other organs (brain, skin, kidney, liver and spleen). Minimize repetitive GBCA imaging studies, particularly closely spaced studies, when possible.

Acute kidney injury requiring dialysis has occurred with the use of GBCAs in patients with chronically reduced renal function. The risk of acute kidney injury may increase with increasing dose of the contrast agent.

Extravasation and injection site reactions can occur with administration of VUEWAY. Ensure catheter and venous patency before the injection of VUEWAY.

VUEWAY may **impair the visualization of lesions** seen on non-contrast MRI. Therefore, caution should be exercised when VUEWAY MRI scans are interpreted without a companion non-contrast MRI scan.

The most common adverse reactions (incidence \geq 0.5%) are injection site pain (0.7%), and headache (0.7%).

You are encouraged to report negative side effects of prescription drugs to the FDA. Visit www.fda.gov/medwatch or call 1-800-FDA-1088.

Please see BRIEF SUMMARY of Prescribing Information for VUEWAY

(gadopiclenol) solution for injection including BOXED WARNING on Nephrogenic Systemic Fibrosis.

Manufactured for Bracco Diagnostics Inc. by Liebel-Flarsheim Company LLC - Raleigh, NC, USA 27616.

VUEWAY is a trademark of Bracco Imaging S.p.A.

All other trademarks and registered trademarks are the property of their respective owners.

References: **1.** VUEWAY[®] (gadopiclenol) solution for injection, 485.1 mg/mL Full Prescribing Information and Patient Medication Guide. Monroe Twp., NJ: Bracco Diagnostics Inc.; January 2024. **2.** Robic C, Port M, Rousseaux O, et al. Physicochemical and pharmacokinetic profiles of gadopiclenol: a new macrocyclic gadolinium chelate with high T1 relaxivity. *Invest Radiol.* 2019 Aug;54:475-484. **3.** GADAVIST[®] (gadobutrol) Injection. Full Prescribing Information. Bayer HealthCare Pharmaceuticals Inc. Whippany, NJ; April 2022. **4.** DOTAREM[®] (gadoterate meglumine) Injection. Full Prescribing Information. Guerbet LLC. Princeton, NJ; April 2022. **5.** CLARISCAN[™] (gadoterate meglumine) injection for intravenous use. Full Prescribing Information. GE Healthcare. Chicago, IL; February 2020. **6.** ProHance[®] (Gadoteridol) Injection, 279.3 mg/mL Full Prescribing Information and Patient Medication Guide. Monroe Twp., NJ: Bracco Diagnostics Inc.; January 2024. **7.** Loevner LA, Kolumban B, Hutóczy G, et al. Efficacy and safety of gadopiclenol for contrast-enhanced MRI of the central nervous system: the PICTURE randomized clinical trial. *Invest Radiol.* 2023 May;58(5):307-313.

Bracco Diagnostics Inc.
259 Prospect Plains Road, Building H
Monroe Township, NJ 08831 USA
Phone: 609-514-2200
Toll-Free: 1-877-272-2269 (U.S. only)
Fax: 609-514-2446

© 2024 Bracco Diagnostics Inc.
All Rights Reserved. US-VW-2300022 02/24



VISIT
VUEWAY.COM
FOR MORE
INFORMATION

VUEWAY®

(gadopiclenol) injection, for intravenous use

BRIEF SUMMARY: Please see package insert of full prescribing information.

WARNING: RISK ASSOCIATED WITH INTRATHECAL USE and NEPHROGENIC SYSTEMIC FIBROSIS

Risk Associated with Intrathecal Use
Intrathecal administration of gadolinium-based contrast agents (GBCAs) can cause serious adverse reactions including death, coma, encephalopathy, and seizures. VUEWAY is not approved for intrathecal use [see Warnings and Precautions (5.1) in the full Prescribing Information].

Nephrogenic Systemic Fibrosis
Gadolinium-based contrast agents (GBCAs) increase the risk for NSF among patients with impaired elimination of the drugs. Avoid use of GBCAs in these patients unless the diagnostic information is essential and not available with non-contrast MRI or other modalities. NSF may result in fatal or debilitating fibrosis affecting the skin, muscle and internal organs.

- The risk for NSF appears highest among patients with:
 - Chronic, severe kidney disease (GFR <30 mL/min/1.73 m²), or
 - Acute kidney injury.
- Screen patients for acute kidney injury and other conditions that may reduce renal function. For patients at risk for chronically reduced renal function (e.g. age >60 years, hypertension, diabetes), estimate the glomerular filtration rate (GFR) through laboratory testing.
- For patients at highest risk for NSF, do not exceed the recommended VUEWAY dose and allow a sufficient period of time for elimination of the drug from the body prior to any re-administration [see Warnings and Precautions (5.2) in the full Prescribing Information].

INDICATIONS AND USAGE

VUEWAY® (gadopiclenol) is a gadolinium-based contrast agent indicated in adult and pediatric patients aged 2 years and older for use with magnetic resonance imaging (MRI) to detect and visualize lesions with abnormal vascularity in:

- the central nervous system (brain, spine, and associated tissues),
- the body (head and neck, thorax, abdomen, pelvis, and musculoskeletal system).

CONTRAINDICATIONS

VUEWAY is contraindicated in patients with history of hypersensitivity reactions to gadopidolol.

WARNINGS AND PRECAUTIONS

Risk Associated with Intrathecal Use Intrathecal administration of GBCAs can cause serious adverse reactions including death, coma, encephalopathy, and seizures. The safety and effectiveness of VUEWAY have not been established with intrathecal use. VUEWAY is not approved for intrathecal use [see Dosage and Administration (2.1) in the full Prescribing Information].

Nephrogenic Systemic Fibrosis Gadolinium-based contrast agents (GBCAs) increase the risk for nephrogenic systemic fibrosis (NSF) among patients with impaired elimination of the drugs. Avoid use of GBCAs among these patients unless the diagnostic information is essential and not available with non-contrast MRI or other modalities. The GBCA-associated NSF risk appears highest for patients with chronic, severe kidney disease (GFR <30 mL/min/1.73 m²) as well as patients with acute kidney injury. The risk appears lower for patients with chronic, moderate kidney disease (GFR 30-59 mL/min/1.73 m²) and little, if any, for patients with chronic, mild kidney disease (GFR 60-89 mL/min/1.73 m²). NSF may result in fatal or debilitating fibrosis affecting the skin, muscle, and internal organs. Report any diagnosis of NSF following VUEWAY administration to Bracco Diagnostics Inc. (1-800-257-5181) or FDA (1-800-FDA-1088 or www.fda.gov/medwatch).

Screen patients for acute kidney injury and other conditions that may reduce renal function. Features of acute kidney injury consist of rapid (over hours to days) and usually reversible decrease in kidney function, commonly in the setting of surgery, severe infection, injury or drug-induced kidney toxicity. Serum creatinine levels and estimated GFR may not reliably assess renal function in the setting of acute kidney injury. For patients at risk for chronically reduced renal function (e.g., age >60 years, diabetes mellitus or chronic hypertension), estimate the GFR through laboratory testing.

Among the factors that may increase the risk for NSF are repeated or higher than recommended doses of a GBCA and the degree of renal impairment at the time of exposure. Record the specific GBCA and the dose administered to a patient. For patients at highest risk for NSF, do not exceed the recommended VUEWAY dose and allow a sufficient period of time for elimination of the drug prior to re-administration. For patients receiving hemodialysis, physicians may consider the prompt initiation of hemodialysis following the administration of a GBCA in order to enhance the contrast agent's elimination [see Use in Specific Populations (8.6) and Clinical Pharmacology (12.3) in the full Prescribing Information]. The usefulness of hemodialysis in the prevention of NSF is unknown.

Hypersensitivity Reactions With GBCAs, serious hypersensitivity reactions have occurred. In most cases, initial symptoms occurred within minutes of GBCA administration and resolved with prompt emergency treatment.

- Before VUEWAY administration, assess all patients for any history of a reaction to contrast media, bronchial asthma and/or allergic disorders. These patients may have an increased risk for a hypersensitivity reaction to VUEWAY.
- VUEWAY is contraindicated in patients with history of hypersensitivity reactions to VUEWAY [see Contraindications (4) in the full Prescribing Information].
- Administer VUEWAY only in situations where trained personnel and therapies are promptly available for the treatment of hypersensitivity reactions, including personnel trained in resuscitation.

- During and following VUEWAY administration, observe patients for signs and symptoms of hypersensitivity reactions.

Gadolinium Retention Gadolinium is retained for months or years in several organs. The highest concentrations (nanomoles per gram of tissue) have been identified in the bone, followed by other organs (e.g. brain, skin, kidney, liver, and spleen). The duration of retention also varies by tissue and is longest in bone. Linear GBCAs cause more retention than macrocyclic GBCAs. At equivalent doses, gadolinium retention varies among the linear agents with gadodiamide causing greater retention than other linear agents such as gadoxetate disodium, and gadobenate dimeglumine. Retention is lowest and similar among the macrocyclic GBCAs such as gadoterate meglumine, gadobutrol, gadoteridol, and gadopidolol. Consequences of gadolinium retention in the brain have not been established. Pathologic and clinical consequences of GBCA administration and retention in skin and other organs have been established in patients with impaired renal function [see Warnings and Precautions (5.2) in the full Prescribing Information]. There are rare reports of pathologic skin changes in patients with normal renal function. Adverse events involving multiple organ systems have been reported in patients with normal renal function without an established causal link to gadolinium.

While clinical consequences of gadolinium retention have not been established in patients with normal renal function, certain patients might be at higher risk. These include patients requiring multiple lifetime doses, pregnant and pediatric patients, and patients with inflammatory conditions. Consider the retention characteristics of the agent when choosing a GBCA for these patients. Minimize repetitive GBCA imaging studies, particularly closely spaced studies, when possible.

Acute Kidney Injury In patients with chronically reduced renal function, acute kidney injury requiring dialysis has occurred with the use of GBCAs. The risk of acute kidney injury may increase with increasing dose of the contrast agent. Do not exceed the recommended dose.

Extravasation and Injection Site Reactions Injection site reactions such as injection site pain have been reported in the clinical studies with VUEWAY [see Adverse Reactions (6.1) in the full Prescribing Information]. Extravasation during VUEWAY administration may result in tissue irritation [see Nonclinical Toxicology (13.2) in the full Prescribing Information]. Ensure catheter and venous patency before the injection of VUEWAY.

Interference with Visualization of Lesions Visible with Non-Contrast MRI As with any GBCA, VUEWAY may impair the visualization of lesions seen on non-contrast MRI. Therefore, caution should be exercised when VUEWAY MRI scans are interpreted without a companion non-contrast MRI scan.

ADVERSE REACTIONS

The following serious adverse reactions are discussed elsewhere in labeling:

- Nephrogenic Systemic Fibrosis [see Warnings and Precautions (5.2) in the full Prescribing Information]
- Hypersensitivity Reactions [see Contraindications (4) and Warnings and Precautions (5.3) in the full Prescribing Information]

Clinical Trials Experience Because clinical trials are conducted under widely varying conditions, adverse reaction rates observed in the clinical trials of a drug cannot be directly compared to rates in the clinical trials of another drug and may not reflect the rates observed in clinical practice.

The safety of VUEWAY was evaluated in 1,047 patients who received VUEWAY at doses ranging from 0.025 mmol/kg (one half the recommended dose) to 0.3 mmol/kg (six times the recommended dose). A total of 708 patients received the recommended dose of 0.05 mmol/kg. Among patients who received the recommended dose, the average age was 51 years (range 2 years to 88 years) and 56% were female. The ethnic distribution was 79% White, 10% Asian, 7% American Indian or Alaska native, 2% Black, and 2% patients of other or unspecified ethnic groups.

Overall, approximately 4.7% of subjects receiving the labeled dose reported one or more adverse reactions.

Table 1 lists adverse reactions that occurred in >0.2% of patients who received 0.05 mmol/kg VUEWAY.

TABLE 1. ADVERSE REACTIONS REPORTED IN >0.2% OF PATIENTS RECEIVING VUEWAY IN CLINICAL TRIALS	
Adverse Reaction	VUEWAY 0.05 mmol/kg (n=708) (%)
Injection site pain	0.7
Headache	0.7
Nausea	0.4
Injection site warmth	0.4
Injection site coldness	0.3
Dizziness	0.3
Local swelling	0.3

Adverse reactions that occurred with a frequency ≤ 0.2% in patients who received 0.05 mmol/kg VUEWAY included: maculopapular rash, vomiting, worsened renal impairment, feeling hot, pyrexia, oral paresthesia, dysgeusia, diarrhea, pruritus, allergic dermatitis, erythema, injection site paresthesia, Cystatin C increase, and blood creatinine increase.

Adverse Reactions in Pediatric Patients

One study with a single dose of VUEWAY (0.05 mmol/kg) was conducted in 80 pediatric patients aged 2 years to 17 years, including 60 patients who underwent a central nervous system (CNS) MRI and 20 patients who underwent a body MRI. One adverse reaction (maculopapular rash of moderate severity) in one patient (1.3%) was reported in the CNS cohort.

USE IN SPECIFIC POPULATIONS

Pregnancy Risk Summary There are no available data on VUEWAY use in pregnant women to evaluate for a drug-associated risk of major birth defects, miscarriage or other adverse maternal or fetal outcomes. GBCAs cross the human placenta and result in fetal exposure and gadolinium retention. The available human data on GBCA exposure during pregnancy and adverse fetal outcomes are limited and inconclusive [see Data]. In animal reproduction studies, there were no adverse developmental effects observed in rats or rabbits with intravenous administration of VUEWAY during organogenesis [see Data]. Because of the potential risks of gadolinium to the fetus, use VUEWAY only if imaging is essential during pregnancy and cannot be delayed. The estimated background risk of major birth defects and miscarriage for the indicated population(s) are unknown. All pregnancies have a background risk of birth defect, loss, or other adverse outcomes. In the U.S. general population, the estimated background risk of major birth defects and miscarriage in clinically recognized pregnancies is 2% to 4% and 15% to 20% respectively. **Data Human Data Contrast enhancement** is visualized in the placenta and fetal tissues after maternal GBCA administration. Cohort studies and case reports on exposure to GBCAs during pregnancy have not reported a clear association between GBCAs and adverse

effects in the exposed neonates. However, a retrospective cohort study comparing pregnant women who had a GBCA MRI to pregnant women who did not have an MRI reported a higher occurrence of stillbirths and neonatal deaths in the group receiving GBCA MRI. Limitations of this study include a lack of comparison with non-contrast MRI and lack of information about the maternal indication for MRI. Overall, these data preclude a reliable evaluation of the potential risk of adverse fetal outcomes with the use of GBCAs in pregnancy.

Animal Data Gadolinium Retention: GBCAs administered to pregnant non-human primates (0.1 mmol/kg on gestational days 85 and 135) result in measurable gadolinium concentration in the offspring in bone, brain, skin, liver, kidney, and spleen for at least 7 months. GBCAs administered to pregnant mice (2 mmol/kg daily on gestational days 16 through 19) result in measurable gadolinium concentrations in the pups in bone, brain, kidney, liver, blood, muscle, and spleen at one-month postnatal age.

Reproductive Toxicology: Animal reproduction studies conducted with gadopidolol showed some signs of maternal toxicity in rats at 10 mmol/kg and rabbits at 5 mmol/kg (corresponding to 52 times and 57 times the recommended human dose, respectively). This maternal toxicity was characterized in both species by swelling, decreased activity, and lower gestation weight gain and food consumption.

No effect on embryo-fetal development was observed in rats at 10 mmol/kg (corresponding to 52 times the recommended human dose). In rabbits, a lower mean fetal body weight was observed at 5 mmol/kg (corresponding to 57 times the recommended human dose) and this was attributed as a consequence of the lower gestation weight gain.

Lactation Risk Summary There are no data on the presence of gadopidolol in human milk, the effects on the breastfed infant, or the effects on milk production. However, published lactation data on other GBCAs indicate that 0.01% to 0.04% of the maternal gadolinium dose is excreted in breast milk. Additionally, there is limited GBCA gastrointestinal absorption in the breast-fed infant. Gadopidolol is present in rat milk. When a drug is present in animal milk, it is likely that the drug will be present in human milk [see Data]. The developmental and health benefits of breastfeeding should be considered along with the mother's clinical need for VUEWAY and any potential adverse effects on the breastfed infant from VUEWAY or from the underlying maternal condition. **Data** In lactating rats receiving single intravenous injection of [¹⁵²Gd]-gadopiclenol, 0.3% and 0.2% of the total administered radioactivity was transferred to the pups via maternal milk at 6 hours and 24 hours after administration, respectively. Furthermore, in nursing rat pups, oral absorption of gadopidolol was 3.6%.

Pediatric Use The safety and effectiveness of VUEWAY for use with MRI to detect and visualize lesions with abnormal vascularity in the CNS (brain, spine, and associated tissues), and the body (head and neck, thorax, abdomen, pelvis, and musculoskeletal system) have been established in pediatric patients aged 2 years and older.

Use of VUEWAY in this age group is supported by evidence from adequate and well-controlled studies in adults with additional pharmacokinetic and safety data from an open-label, uncontrolled, multicenter, single dose study of VUEWAY (0.05 mmol/kg) in 80 pediatric patients aged 2 to 17 years. The 80 patients consisted of 60 patients who underwent a CNS MRI and 20 patients who underwent a body MRI [see Adverse Reactions (6.1) and Clinical Pharmacology (12.3) in the full Prescribing Information].

The safety and effectiveness of VUEWAY have not been established in pediatric patients younger than 2 years of age.

Geriatric Use Of the total number of VUEWAY-treated patients in clinical studies, 270 (26%) patients were 65 years of age and over, while 62 (6%) patients were 75 years of age and over. No overall differences in safety or efficacy were observed between these subjects and younger subjects.

This drug is known to be substantially excreted by the kidney, and the risk of adverse reactions to this drug may be greater in patients with impaired renal function. Because elderly patients are more likely to have decreased renal function, it may be useful to monitor renal function.

Renal Impairment In patients with renal impairment, the exposure of gadopidolol is increased compared to patients with normal renal function. This may increase the risk of adverse reactions such as nephrogenic systemic fibrosis (NSF). Avoid use of GBCAs among these patients unless the diagnostic information is essential and not available with non-contrast MRI or other modalities. No dose adjustment of VUEWAY is recommended for patients with renal impairment. VUEWAY can be removed from the body by hemodialysis [see Warnings and Precautions (5.2, 5.4, 5.5) and Clinical Pharmacology (12.3) in the full Prescribing Information].

OVERDOSAGE

Among subjects who received a single 0.3 mmol/kg intravenous dose of gadopidolol (6 times the recommended dose of VUEWAY), headache and nausea were the most frequently reported adverse reactions. Gadopidolol can be removed from the body by hemodialysis [see Clinical Pharmacology (12.3) in the full Prescribing Information].

PATIENT COUNSELING INFORMATION Advise the patient to read the FDA-approved patient labeling (Medication Guide).

Nephrogenic Systemic Fibrosis Inform the patient that VUEWAY may increase the risk for NSF among patients with impaired elimination of the drugs and that NSF may result in fatal or debilitating fibrosis affecting the skin, muscle and internal organs.

Instruct the patients to contact their physician if they develop signs or symptoms of NSF following VUEWAY administration, such as burning, itching, swelling, scaling, hardening and tightening of the skin; red or dark patches on the skin; stiffness in joints with trouble moving, bending or straightening the arms, hands, legs or feet; pain in the hip bones or ribs; or muscle weakness [see Warnings and Precautions (5.2) in the full Prescribing Information].

Gadolinium Retention Advise patients that gadolinium is retained for months or years in brain, bone, skin, and other organs following VUEWAY administration even in patients with normal renal function. The clinical consequences of retention are unknown. Retention depends on multiple factors and is greater following administration of linear GBCAs than following administration of macrocyclic GBCAs [see Warnings and Precautions (5.4) in the full Prescribing Information].

Injection Site Reactions Inform the patient that VUEWAY may cause reactions along the venous injection site, such as mild and transient burning or pain or feeling of warmth or coldness at the injection site [see Warnings and Precautions (5.6) in the full Prescribing Information].

Pregnancy Advise pregnant women of the potential risk of fetal exposure to VUEWAY [see Use in Specific Populations (8.1) in the full Prescribing Information].

Rx only

US Patent No. 10,973,934
Manufactured for Bracco Diagnostics Inc. by Liebel-Flarsheim Company LLC - Raleigh, NC, USA 27616.
Toll-Free: 1-877-272-2269 (U.S. only)
Revised February 2024

AJNR

AMERICAN JOURNAL OF NEURORADIOLOGY

MAY 2024
VOLUME 45
NUMBER 5
WWW.AJNR.ORG

Publication Preview at www.ajnr.org features articles released in advance of print.
Visit www.ajnrblog.org to comment on AJNR content and chat with colleagues.

EDITORIALS

- 533 **From pAJNR to eAJNR** *Mauricio Castillo*
- 535 **Introducing the American Society of Neuroradiology PET-Guided Diagnosis and Management in Neuro-Oncology Study Group**
A. Nabavizadeh, et al.

REVIEW ARTICLE

-   537 **Imaging Genomics of Glioma Revisited: Analytic Methods to Understand Spatial and Temporal Heterogeneity** *Cymon N. Kersch, et al.*

**BRAIN TUMOR
IMAGING**

STATE OF PRACTICE

-  549 **Artificial Intelligence in the Future Landscape of Pediatric Neuroradiology: Opportunities and Challenges** *Aashim Bhatia, et al.*

**PEDIATRIC
NEUROIMAGING**

GENERAL CONTENTS

-   554 **Implementation of a Clinical Vessel Wall MR Imaging Program at an Academic Medical Center** *Jae W. Song, et al.*
- 562 **Automated Assessment of the DWI-FLAIR Mismatch in Patients with Acute Ischemic Stroke: Added Value to Routine Clinical Practice**
E. Tavakkol, et al.
-  568 **Lesion Indexes Predict Early Neurologic Deterioration in Lenticulostriate Single Small Subcortical Infarction** *Yuan Gao, et al.*
- 574 **Association of Carotid Artery Disease with Collateralization and Infarct Growth in Patients with Acute Middle Cerebral Artery Occlusion**
Resul Güneş, et al.
- 581 **IV Flat Detector CT Angiography in Flat Detector CT Image-Guided Minimally Invasive Surgery for the Treatment of Intracerebral Hypertensive Hemorrhage** *Zhang Shu, et al.*
-  588 **Mechanical Thrombectomy for Pediatric Arterial Ischemic Stroke from Acute M2 Occlusion** *Kartik D. Bhatia, et al.*
-  592 **Prasugrel Single Antiplatelet Therapy versus Aspirin and Clopidogrel Dual Antiplatelet Therapy for Flow Diverter Treatment for Cerebral Aneurysms: A Retrospective Multicenter Study** *Sophia Hohenstatt, et al.*

**NEUROVASCULAR/
STROKE IMAGING**

NEUROINTERVENTION

NEUROINTERVENTION

AJNR (Am J Neuroradiol ISSN 0195–6108) is a journal published monthly, owned and published by the American Society of Neuroradiology (ASNR), 820 Jorie Boulevard, Oak Brook, IL 60523. Annual dues for the ASNR include approximately 19% for a journal subscription. The journal is printed by Intellicor Communications, 330 Eden Road, Lancaster, PA 17601; Periodicals postage paid at Oak Brook, IL and additional mailing offices. Printed in the U.S.A. POSTMASTER: Please send address changes to American Journal of Neuroradiology, P.O. Box 3000, Denville, NJ 07834, U.S.A. Subscription rates: nonmember \$475 (\$560 foreign) print and online, \$320 online only; institutions \$550 (\$625 foreign) print and basic online, \$1080 (\$1160 foreign) print and extended online, \$380 online only (basic), \$825 online only (extended); single copies are \$35 each (\$40 foreign). Indexed by PubMed/MEDLINE, BIOSIS Previews, Current Contents (Clinical Medicine and Life Sciences), EMBASE, Google Scholar, HighWire Press, Q-Sensei, RefSeek, Science Citation Index, SCI Expanded, ReadCube, and Semantic Scholar. Copyright © American Society of Neuroradiology.

- 599   **Wall Enhancement of Coiled Intracranial Aneurysms Is Associated with Aneurysm Recanalization: A Cross-Sectional Study** *Stefan L. Leber, et al.*
- 605  **Large Single-Center Experience with Short-Term Follow-up of Neqstent-Assisted Coiling** *Fathallah Ismail Islim, et al.*
- 612 **Brain Arteriovenous Malformation In Vitro Model for Transvenous Embolization Using 3D Printing and Real Patient Data**
Rodrigo Rivera, et al.
- 618  **Tumor Embolization via the Meningohypophyseal and Inferolateral Trunk in Patients with Skull Base Tumors Using the Distal Balloon Protection Technique** *Kei Yamashiro, et al.*
- 626  **Imaging Features of Primary Intracranial Sarcoma with *DICER1* Mutation: A Multicenter Case Series** *Rami W. Eldaya, et al.*
- 632   **Clinical Arterial Spin-Labeling MR Imaging to Screen for Typical and Atypical Neurodegenerative Disease in the New Era of Alzheimer Treatment** *Kevin Lee, et al.*
- 637   **A Comprehensive and Broad Approach to Resting-State Functional Connectivity in Adult Patients with Mild Traumatic Brain Injury**
Soroush Arabshahi, et al.
- 647   **Reduced Cortical Thickness Correlates of Cognitive Dysfunction in Post-COVID-19 Condition: Insights from a Long-Term Follow-up**
Rosalia Dacosta-Aguayo, et al.
- 655   **Optic Nerve Sheath MR Imaging Measurements in Patients with Orthostatic Headaches and Normal Findings on Conventional Imaging Predict the Presence of an Underlying CSF-Venous Fistula**
Wouter I. Schievink, et al.
- 662   **Evaluation of MR Elastography as a Noninvasive Diagnostic Test for Spontaneous Intracranial Hypotension** *Ian T. Mark, et al.*
- 668  **Benefits of Photon-Counting CT Myelography for Localization of Dural Tears in Spontaneous Intracranial Hypotension** *Ajay A. Madhavan, et al.*

NEUROINTERVENTION

NEUROINTERVENTION

NEUROINTERVENTION

NEUROINTERVENTION

BRAIN TUMOR
IMAGING

NEURODEGENERATIVE
DISORDER IMAGING

NEUROIMAGING
PHYSICS/FUNCTIONAL
NEUROIMAGING/CT
AND MRI TECHNOLOGY

NEUROIMAGING
PHYSICS/FUNCTIONAL
NEUROIMAGING/CT
AND MRI TECHNOLOGY

SPINE IMAGING AND
SPINE IMAGE-GUIDED
INTERVENTIONS

SPINE IMAGING AND
SPINE IMAGE-GUIDED
INTERVENTIONS

SPINE IMAGING AND
SPINE IMAGE-GUIDED
INTERVENTIONS

ONLINE FEATURES

MEMORIAL

- E3 **Anton N. Hasso** *Daniel Chow*

LETTERS

- E4 **Spaceflight-Associated Neuro-Ocular Syndrome and Idiopathic Intracranial Hypertension: Can Anemia and Hyperemia Underlie Both?** *Grant A. Bateman, et al.*
- E5 **Reply** *Donna R. Roberts, et al.*
- E6 **Enlargement of Perivascular Spaces as a Downstream Consequence of Spaceflight Analog-Induced Alterations in Cerebral Venous Hemodynamics** *Peter Wostyn, et al.*
- E7 **Reply** *Donna R. Roberts, et al.*

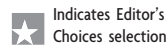
BOOK REVIEWS

R.M. Quencer, Section Editor

Please visit www.ajnr.org to read and comment on Book Reviews.



Transvenous embolization is a novel technique for treating selected brain AVMs with high reported occlusion rates. Rivera et al, developed a novel, patient-specific brain AVM in vitro model for transvenous embolization using 3D printing technology. They tested the effect of mean arterial pressure in a closed pulsed circuit to fill the AVM and found that retrograde contrast flow into the nidus was directly related to lower mean arterial pressure.



Indicates article with supplemental online video



Indicates Fellows' Journal Club selection



Indicates open access to non-subscribers at www.ajnr.org



Indicates article with supplemental online data



Indicates article with supplemental online video



Evidence-Based Medicine Level 1



Evidence-Based Medicine Level 2

Official Journal:

American Society of Neuroradiology
American Society of Functional Neuroradiology
American Society of Head and Neck Radiology
American Society of Pediatric Neuroradiology
American Society of Spine Radiology

MAY 2024 • VOLUME 45 • NUMBER 5 • WWW.AJNR.ORG

EDITOR-IN-CHIEF

Max Wintermark, MD, MAS, FASFN, FICIS

*Frank T. McGraw Memorial Chair in the Study of Cancer
Professor and Chair of Neuroradiology
The University of Texas MD Anderson Center*

DEPUTY EDITOR

Lubdha M. Shah, MD, MS

Professor of Radiology and Director of Spine Imaging
Department of Radiology and Imaging Sciences
University of Utah

SPECIAL ADVISORS TO THE EDITOR-IN-CHIEF

Mauricio Castillo, MD, FACR

MA Mauro Distinguished Professor of Radiology
University of North Carolina-Chapel Hill

Robert Quencer, MD

Professor Emeritus
Department of Radiology
University of Miami

ARTIFICIAL INTELLIGENCE

Senior Editor

Reza Forghani, MD, PhD

Professor of Radiology & Artificial Intelligence
Vice Chair of AI
Director, Radiomics & Augmented Intelligence Laboratory (RAIL)
Department of Radiology
University of Florida College of Medicine

Associate Editors

Andreas Rauschecker, MD, PhD

Assistant Professor-in-Residence
Co-Executive Director and Clinical Director,
Center for Intelligent Imaging (ci²)
Department of Radiology & Biomedical Imaging
University of California, San Francisco

Sam (Seyedmehdi) Payabvash, MD

Assistant Professor of Radiology
Yale School of Medicine
Connecticut

BRAIN TUMOR IMAGING

Senior Editor

Ben Ellingson, PhD

Professor and Director of MRI Research
Director, UCLA Brain Tumor Imaging Laboratory
Department of Radiological Sciences
David Geffen School of Medicine
University of California, Los Angeles

Associate Editors

Ali Nabavizadeh, MD

Assistant Professor of Radiology
Division of Neuroradiology
University of Pennsylvania

Mark S. Shiroishi, MD, MS, FASFN

Assistant Professor, Division of Neuroradiology,
Department of Radiology
Director of Neuro-Oncology Imaging - USC Brain
Tumor Center
Chief of Pediatric Neuroradiology – Los Angeles
General Medical Center
Affiliated Faculty - USC Imaging Genetics Center
Mark and Mary Stevens Neuroimaging and
Informatics Institute
Keck School of Medicine of USC
University of Southern California

EMERGENCY NEURORADIOLOGY

Senior Editor

Karen Buch, MD

Assistant Professor of Radiology
Massachusetts General Hospital

Associate Editors

Melissa A. Davis, MD, MBA

Vice Chair of Medical Informatics
Associate Professor
Department of Radiology and Biomedical
Imaging
Yale School of Medicine
Connecticut

Jason Talbott, MD, PhD

Associate Professor, Neuroradiology Section
Department of Radiology and Biomedical
Imaging
University of California, San Francisco and
Zuckerberg San Francisco General Hospital

HEAD AND NECK IMAGING

Senior Editor

Amy Juliano, MD

Associate Professor of Radiology
Massachusetts Eye and Ear
Harvard Medical School

Associate Editors

Burce Ozgen, MD

Clinical Professor of Radiology
University of Illinois at Chicago

David Zander, MD

Assistant Professor, Radiology
University of Colorado School of Medicine

HEALTH POLICIES/QUALITY IMPROVEMENT/ EVIDENCE-BASED NEUROIMAGING

Senior Editor

Nadja Kadom, MD, FACR, FAAP

Professor, Department of Radiology and Imaging
Sciences
Emory University School of Medicine
Pediatric Neuroradiologist, Department of
Radiology
Children's Healthcare of Atlanta

Associate Editors

Melissa M. Chen, MD

Associate Professor,
Department of Neuroradiology, Division of
Diagnostic Imaging
The University of Texas MD Anderson Center

Ajay Malhotra, MBBS, MD, MMM

Professor of Radiology and Biomedical
Imaging and Neurosurgery
Yale School of Medicine
Connecticut

MOLECULAR NEUROIMAGING/NUCLEAR MEDICINE

Senior Editor

Ana M. Franceschi, MD, PhD

Associate Professor of Radiology
Donald and Barbara Zucker School of Medicine
at Hofstra/Northwell
The Feinstein Institutes for Medical Research
Neuro-PET Imaging
Lenox Hill Hospital
New York

Associate Editors

Nadya Pyatigorskaya, MD, PhD

Neuroradiology Department, Pitié-Salpêtrière
Hospital
Researcher, Brain Institute (ICM)
France

Marc Daniel Benayoun, PhD, MD

Assistant Professor of Radiology
Co-Section Head of Nuclear Medicine
Medical Director of Nuclear Medicine and PET
Vice Chair of Radiation Drug Research
Committee
Atrium Wake Forest Health
North Carolina

NEURODEGENERATIVE DISORDER IMAGING

Senior Editor

Gloria Chiang, MD

Associate Professor, Co-Director of the Brain
Health Imaging Institute
Department of Radiology
Weill Cornell Medicine/NewYork-Presbyterian
Hospital

Associate Editors

Fang Frank Yu, MD

Assistant Professor of Radiology
Division of Neuroradiology, Department of
Radiology
Advanced Imaging Research Center
University of Texas Southwestern Medical
Center

Priya Rajagopalan, MBBS, MPH

Assistant Professor of Radiology, Division of Neuroradiology
Associate Program Director, Neuroradiology Fellowship
Medical Director, Center for Image Acquisition Mark and Mary Stevens Neuroimaging and Informatics Institute
Keck School of Medicine, University of Southern California

NEUROIMAGING PHYSICS/FUNCTIONAL NEUROIMAGING/CT AND MRI TECHNOLOGY**Senior Editor****Hongyu An, DSc**

Professor, Mallinckrodt Institute of Radiology Neurology, Biomedical Engineering, Electrical and Systems Engineering, Division of Biology and Biomedical Sciences
Director, Biomedical Magnetic Resonance Center
Associate Director, Center for Clinical Imaging Research
Washington University in St. Louis

Associate Editors**Timothy J. Carroll, PhD**

Professor, Department of Radiology
University of Chicago

Hugo de Jong, PhD

Professor of Medical Physics Radiology and Nuclear Medicine
UMC Utrecht
the Netherlands

NEUROINTERVENTION**Senior Editor****Steven Hetts, MD, FACP**

Co-Chief, NeuroEndovascular Surgery Service Line
Chief of Interventional Neuroradiology, Mission Bay Hospitals
Professor of Radiology, Biomedical Imaging, and Neurological Surgery
University of California, San Francisco

Associate Editors**Kristine Blackham, MD**

Associate Professor
Diagnostic and Interventional Neuroradiology
Clinic for Radiology and Nuclear Medicine
University Hospital of Basel

Maksim Shapiro, MD

Clinical Associate Professor
Departments of Radiology, Neurosurgery, and Neurology
Division of Neurointerventional Radiology
NYU Langone Health and Bellevue NYCH + Hospitals
New York

NEUROPSYCHIATRIC IMAGING**Senior Editor****Jody Tanabe, MD**

Professor
Chief of Neuroradiology
University of Colorado-Anschutz Medical Campus

Associate Editors**John-Paul J. Yu, MD, PhD**

Assistant Professor of Radiology, Psychiatry, and Biomedical Engineering
University of Wisconsin School of Medicine and Public Health

J. Eric Schmitt, MD, PhD

Assistant Professor of Radiology and Psychiatry
Division of Neuroradiology
Perelman School of Medicine, University of Pennsylvania

NEUROVASCULAR/STROKE IMAGING**Senior Editor****Ajay Gupta, MD, MS**

Professor and Chair, Department of Radiology
Columbia University
New York

Associate Editors**Shalini Amukotuwa, MB BS, PhD, FRANZCR**

Head of Neuroradiology and Director of MRI, Monash Health
Associate Professor of Radiology, Monash University
Australia

Mahmud Mossa-Basha, MD

Professor of Radiology, Neurology and Electrical Engineering
Vice Chair of Clinical Research and Clinical Transformation
Co-Director of the Research Vascular Imaging Lab
University of Washington School of Medicine

PEDIATRIC NEUROIMAGING**Senior Editor****Caroline D. Robson, MBChB**

Division Chief & Endowed Chair, Neuroradiology
Director, Head & Neck Imaging
Department of Radiology
Department of Otolaryngology
Boston Children's Hospital
Harvard Medical School

Associate Editors**Anna Trofimova, MD, PhD**

Assistant Professor, Radiology and Imaging Sciences, Emory University
Pediatric Neuroradiologist, Children's Healthcare of Atlanta

Matthew Whitehead, MD

Department of Radiology, Division of Neuroradiology
Children's Hospital of Philadelphia
Associate Professor of Radiology
Perelman School of Medicine, University of Pennsylvania

SPINE IMAGING AND SPINE IMAGE-GUIDED INTERVENTIONS**Senior Editor****J. Levi Chazen, MD**

Associate Professor, Neuroradiology
Director, Spine Imaging
Hospital for Special Surgery
Weill Cornell Medicine
New York

Associate Editors**Jennifer McCarty, MD**

UTHealth Houston

Vinil Shah, MD

Associate Professor of Radiology Neuroradiology
Division Chief
University of California, San Francisco

ULTRA-HIGH-FIELD MRI/IMAGING OF EPILEPSY/DEMYELINATING DISEASES/INFLAMMATION/INFECTION**Senior Editor****Erik Middlebrooks, MD**

Professor of Radiology
Mayo Clinic Florida

Associate Editors**Susie Y. Huang, MD, PhD**

Associate Professor of Radiology, Harvard Medical School
Associate Chair, Faculty Affairs, Department of Radiology
Director of Translational Neuro MR Imaging & Connectomics, Athinoula A. Martinos Center for Biomedical Imaging
Massachusetts General Hospital

Girish Bathla, MD, FRCR

Associate Professor, Neuroradiology
Mayo Clinic
Minnesota

OUTREACH AND EDUCATION**Senior Editor****Lea Alhilali, MD**

Radiology Partners, HonorHealth Research Institute
Arizona

DIGITAL MEDIA AND ENGAGEMENT**Senior Editor****Kevin Hsu, MD**

Clinical Assistant Professor
Department of Radiology
NYU Grossman School of Medicine
New York

Case Collection Editors**Matylda Machnowska, BMedSc, MD, FRCSC, ABR**

Assistant Professor of Radiology, University of Toronto
Neuroradiologist, Sunnybrook Health Sciences Centre

Anvita Pauranik, MD

Clinical Assistant Professor of Radiology
BC Children's Hospital
University of British Columbia

Sandy Cheng-Yu Chen, MD

Chair, Translational Imaging Research Center
Taipei Medical University Hospital
Vice President of Taipei Medical University

Social Media Editor**Kimberly Seifert, MD, MS**

Stanford University
California

Assistant Social Media Editors**Ani Hoxha, MD**

Mother Theresa UHC
Albania

Maxwell Opoku, MD

Novosibirsk State Research University
Russia

Podcast Editor

Kevin Hiatt, MD

Assistant Professor, Radiology
Wake Forest University School of Medicine
North Carolina

Deputy Podcast Editor

George K. Vilanilam, MD

PGY5 Resident Physician, Department of Radiology
University of Arkansas for Medical Sciences

STATISTICS

Senior Editor

Bryan A. Comstock, MS

Senior Biostatistician, Department of Biostatistics
University of Washington

EDITORIAL FELLOWS

Alexandre Boutet, MD, PhD

Neuroradiologist
Joint Department of Medical Imaging
University of Toronto

Nicholas S. Cho, MD/PhD Candidate

University of California, Los Angeles

Burak Berksu Ozkara, MD

Research Fellow
Department of Neuroradiology
The University of Texas MD Anderson Center

BOOK REVIEW EDITOR

Robert Quencer, MD

Professor Emeritus
Department of Radiology
University of Miami

Founding Editor

Juan M. Taveras

Editors Emeriti

Mauricio Castillo, Robert I. Grossman,
Michael S. Huckman, Robert M. Quencer,
Jeffrey S. Ross

Managing Editor

Karen Halm

Assistant Managing Editor

Laura Wilhelm

Executive Director, ASNR

Mary Beth Hepp

Scientific Editor

Theresa S. Richards, PhD

Digital Publications Senior Manager

Gwen Travis



The ASNR Career Center

The Go-To Job Site for Neuroradiology Employers and Job Seekers

For Job Seekers

- Access to an expanded network of jobs via the National Healthcare Career Network
- Confidential resume posting
- Professional online profile

For Employers

- Employer resources to help you recruit top talent
- Multiple pricing options, including free Fellowship listings
- Resume search

Start here: careers.asnr.org

From *pAJNR* to *eAJNR*

Mauricio Castillo

Eighteen years ago, when I became Editor of the *American Journal of Neuroradiology (AJNR)*, the editorial team wanted the journal to go paperless. We surveyed the readership and found that about 50% still preferred their journal in a printed format. Four years later, we sent out the same survey again only to find that reader preferences had not changed. Thus, we decided to implement a “Go Green” initiative so that our readers could voluntarily give up their printed journals and go paperless. You may recall that this idea was successful and thus paved the way for a paperless publication.

Let’s begin by thinking of the advantages of a paperless journal. Things that immediately come to mind are efficiency, reduced costs, easier access through a variety of electronic devices, safeguarding contents by automatic backups (durability), streamlining publication processes, readability, improved searches, multimedia inclusion, and, finally, portability that goes with user convenience and comfort. Of course, helping the environment is also a benefit that is important to us all but especially to the younger generations of readers. Although *AJNR* has a circulation of only a few thousand, is printed on paper certified by the Forest Stewardship Council, and is packed in eco-friendly bags, any contribution to better our environment should be taken seriously.

In this era of spiraling costs, how does a paperless journal reduce expenses? Lower stationary costs, no ink printing, no pagination, no binding, no bag or wrapper, no mailing labels (which also need to be printed and attached), and no postage all help manage expenses. Replacement of journals lost in the mail, something that commonly happens with sending *AJNR* internationally, is also avoided. Studies have shown that employees spend an average of 86 hours/year in activities related to paper-based file retrieval and that this time could be used in other more beneficial activities, especially at *AJNR* where the office consists of only 3 individuals. Companies offering paperless solutions also cite a savings in office space, something that is becoming more important as we migrate to hybrid working environments and spend more time doing our jobs from home.

Thus, there are significant advantages to going paperless and that is why I was delighted when Dr Wintermark, *AJNR* Editor-in-Chief, told me that the decision to cease printing the journal was recently made. Worried that my reaction would not be enthusiastically shared by others, I asked all surviving Editors of *AJNR* (in chronological order) to give me their opinions regarding this decision, and this is what they had to say:

Robert M. Quencer: “The decision to evolve the *American Journal of Neuroradiology* to a paperless format makes sense on many levels. For those who already receive medical and scientific journals in digital formats, it is recognized that there are myriad advantages to such transmission of information. The easy accessibility on smartphones, tablets, and desktop computers is obvious,

but it goes beyond this ease of use and portability. Making the text size proper for reading, saving/filing articles, importing images to files for future reference, and ready accessibility to articles are immediately recognized values of an electronic format. Conversion to a paperless environment is in keeping with the way medicine is practiced today as seen with electronic medical records, consultations, and acquisition of crucial patient information, and there is no reason a medical journal should view educational and new scientific information any differently. There are more benefits to this change, including but not limited to costs but also to more subtle ones such as demonstrating a commitment to lessening the environmental impact of printed publications. Finally, although I am somewhat reticent to speak for others particularly when they cannot have a say in this issue, I wish to add that I believe that both Drs Juan Taveras and Michael Huckman as past Editors of *AJNR* would have enthusiastically endorsed the change to an entirely paperless journal. They both were forward-looking and would recognize this new format as an important step forward. This is the proper time for the *AJNR* to make this change.”

Robert I. Grossman: “It is interesting to me that I had this discussion with neuroradiology colleagues more than 25 years ago. Yes, it is the right time to stop destroying forests and have the journal at any place and at any time desired. It will get read more as access is available on your smartphone, even as you are sitting in a waiting room! Paper journals gather a lot of dust because they often go unread. How wonderful not to have to tear, print, and file any pertinent articles. This is an idea whose time has more than come. It will improve the quality of images and save postage and print costs. Let’s face it, depending on the postal service is not always a good thing. Anyone who desires to read the journal on paper can always print what they want, hopefully on 2 sides of the paper. For the Luddites still lamenting the loss of hard copies and the arrival of the electronic age, the passing of direct carotid angiography, pneumoencephalography, and myelography, may I suggest that any time saved can be spent in search of the dodo! Younger neuroradiologists may enjoy reading *AJNR* with their Apple Vision Pro devices, and I am sure that soon this type of device will proliferate. Congratulations to Max Wintermark and *AJNR*.”

Let me expand a bit on the last comment from Dr Grossman. Imagine embedding 3D files in articles that can be printed as such. Brain models would facilitate the understanding of anatomy while printing devices would help us to understand how they work. Visualizing lesions and procedures in 3D on virtual or augmented reality goggles from files found in articles would be fantastic for educational purposes and patient care while maintaining privacy. Many articles already offer accompanying videos, but to be able to interact with them is something that only electronic media can offer.

Jeffrey Ross: “I started my tenure with a ‘don’t fix what isn’t broken’ attitude, given that a relatively large contingency of polled subscribers at that time were still in favor of maintaining the print issue. This percentage decreased significantly during my 8 years as Editor, and over the past 2 years, the possibility of

converting to solely an online publication was very much an option. It then became more of a philosophical question: Do we transition now or allow a new Editor to make that transition? I believe in giving this opportunity to the new Editor and to determine its timing. The reasons for online-only are many, but since I like alliterations, let's go with S's... Speed, Space, Search, Specie, and acceSSibility. Speed: articles do not need to be embargoed by waiting for discrete issues of the journal to be published but should be available in real-time as manuscripts are accepted and formatted. Space: space is larger for electronic publications and always more limited for print. The decision to move images and tables to online-only became a frequent choice toward the end of my tenure. The downside of infinite online space is the author's responsibility to maintain readability and tight prose construction and not present the reader with an unfocused and rambling montage of words and images. I think the quotation (variously attributed to Mark Twain and Winston Churchill) 'I would have written a shorter letter if I had more time' is appropriate for all scientific publications. Search: an obvious advantage of electronic publications is the ability to search easily within documents and to link out to references and other materials. Specie: the cost of the print component to the budget of the journal is significant and that money is better spent on providing other services. This positive aspect must be balanced with the loss of revenue from advertising, which is greater for hard copy publications than for those online, but *AJNR*'s advertisement revenue is not critical. Accessibility: we all have smartphones, so we all have the journal with us 24/7. Download the PDF before a flight (though many airlines now offer Wi-Fi) and keep up with the latest research. Online materials also provide greater flexibility in formatting and displaying text/images, which is not possible with hard copies. Dynamic scrolling with viewing of image stacks or angiographic runs is only possible with electronic publications. The future of a paperless *AJNR* is bright, and I look forward to seeing the innovative changes that are made to improve and make more efficient the dissemination of research and educational materials to our readers."

Because a paperless *AJNR* makes sense, I was not surprised to find out that my colleagues and past Editors agree with me,

and I think that the readership should share our excitement. Despite all the above advantages, many of our readers may still ask about other benefits they can expect from a paperless *AJNR*. For this, I asked Dr Wintermark to briefly give us an idea about new activities, contents, and benefits that *eAJNR* will bring to us, and this is his response.

Max Wintermark: "I am truly humbled by reading the words of those who came before me. Previous *AJNR* Editors-in-Chief have highlighted the numerous advantages inherent in a modern electronic journal. Our strategic roadmap includes exciting features that empower readers to personalize their preferred content. These entail both primary, indexed content (streams of articles sorted on the basis of an individualized reader's interest) and secondary content (including cases, educational materials for trainees, technical updates, medicolegal insights, and technical tidbits). A new *AJNR* Web site will allow readers to seamlessly navigate through stacks of images, mirroring the routine practice of radiologists. This navigation will significantly elevate the quality and value of our articles, enhancing the learning potential derived from reviewing these images. Articles related to artificial intelligence will provide direct access to algorithm codes shared by the authors. The search functionality of the Web site will undergo substantial enhancement, transforming the journal into an extensive teaching file repository, readily accessible. The roadmap also includes automated translation of our articles into languages other than English, broadening the global reach of our journal. These are a few examples of the innovative features we intend to introduce in the upcoming months. We invite input and suggestions from our readers. Please feel free to reach out directly to me at mw.ajnr.eic@gmail.com."

My hope with this short editorial was to explain why *AJNR* must go paperless and why our contributors and readers, regardless of age, should embrace and support the change. To continue being the pre-eminent publication in neuroradiology, we must grow, change, and evolve. Because our professional organization owns the journal, because we are all colleagues with the same interests in mind, and because our size allows us to be nimble, we welcome this new era for *AJNR*.

Introducing the American Society of Neuroradiology PET-Guided Diagnosis and Management in Neuro-Oncology Study Group

A. Nabavizadeh, N. Galdiks, M. Veronesi, P. Lohmann, J.E. McConathy, D.R. Johnson, M.S. Aboian, R.F. Barajas Jr, and J. Ivanidze

The American Society of Neuroradiology (ASNR) is pleased to introduce its latest initiative: the PET-Guided Diagnosis and Management in Neuro-Oncology Study Group. This group will focus on leveraging molecular imaging and theranostics to enhance the care of adult and pediatric patients with primary and metastatic brain tumors, driving progress through collaborative research, consensus recommendations, and advocacy efforts.

The rapid clinical translation of PET and theranostics in recent years has expanded our understanding of brain tumor metabolism and is opening new pathways for personalized medicine. However, the rapid pace of these advancements has also introduced challenges, including standardization of clinical practices, health care economics, and the need for a coordinated approach that aligns with the interests of all stakeholders. The new Study Group embodies a multidisciplinary effort to empower clinical neuroradiologists and other health care professionals and to bridge the gap between cutting-edge technology and everyday clinical practice by uniting experts from neuroradiology, nuclear medicine, clinical neuro-oncology, and translational sciences.

The objectives are multifaceted. The primary goal is to disseminate the latest evidence regarding the clinical utility of validated radiotracers in adult and pediatric CNS tumors. This knowledge empowers clinicians to make informed decisions regarding the delineation of brain tumor extent, treatment planning, and response assessment. In the near-term, the focus will be on amino acid PET in gliomas¹⁻⁴ and brain metastases⁵ as well as somatostatin receptor (SSTR) targeted PET in meningiomas and other SSTR-positive brain tumors.^{6,7} For example, gallium 68 DOTA-Phe1-Tyr3-octreotate (⁶⁸Ga DOTATATE PET) has shown utility and is increasingly used in the clinical setting in meningioma and paraganglioma diagnosis and radiation therapy planning. Numerous prospective studies have shown added clinical value of fluorine 18 [¹⁸F] labeled amino acids in combination with MR imaging for brain tumor management, including O-(2-[¹⁸F] fluoroethyl)-L-tyrosine¹ (¹⁸F-FET), anti-1-amino-3-[¹⁸F]fluorocyclobutane-1-carboxylic acid² (¹⁸F Fluciclovine), and 3,4-dihydroxy-6-[¹⁸F]-fluorophenylalanine⁸ (¹⁸F-FDOPA), with ongoing effort toward US FDA approval for amino acid PET currently underway. In addition, unique applications of PET/MR imaging and theranostics to pediatric CNS tumors will be highlighted.

The Study Group also acknowledges the current limitations of companion diagnostics in neuro-oncology due to lack of validated

imaging probes, as well as the heterogeneity of patient management contributing to therapeutic clinical trials with negative outcomes.⁹ To address these limitations, the Study Group advocates biomarker-driven patient selection, akin to the successful application of prostate-specific membrane antigen (PSMA) PET in prostate cancer, and [¹⁸F] fluoroestradiol PET in breast cancer.¹⁰ Tailoring treatments based on specific biomarkers can optimize therapeutic efficacy and improve patient outcomes.¹¹ In addition to amino acid metabolism and SSTR overexpression, which were discussed above, emerging targets for primary and metastatic brain tumors can include imaging probes for cell proliferation and cell membrane biosynthesis, epidermal growth factor receptor expression, chemokine receptor expression, the 18 kDa translocator protein (TSPO), PSMA, integrins, hypoxia, and finally the immune system.^{12,13} Additionally, targeted PET agents for primary neoplasms outside the CNS can be applied to improve the detection and biologic characterization of brain metastases.¹¹

Short-term goals are focused on the ASNR 2024 Annual Meeting, where 2 sessions will be offered to introduce the critical topics in molecular neuro-oncology and discuss the clinical use of state-of-the-art PET and theranostics. After the ASNR meeting, the Study Group plans to publish a state-of-practice article, summarizing the evidence presented in the 2 sessions.

In the longer term, we aim to accelerate translational research by leveraging the collective expertise of physicians and scientists working in the field of neuro-oncology. Collaboration will be the key to advancing the development of novel radiotracers, which is essential for enhancing diagnostic accuracy and therapeutic efficacy in neuro-oncology. In collaboration with the Society of Nuclear Medicine and Molecular Imaging and the Society for Neuro-Oncology, the ASNR Study Group will work to establish research priorities and consensus recommendations and develop evidence to support reimbursement for neuro-oncologic PET through cost-effectiveness studies as well as educational sessions during national meetings and webinars. These efforts will provide clarity and direction regarding the optimal applications of PET in neuro-oncology, ensuring consistency and quality of care across institutions.

We invite our colleagues from seasoned experts to early-career professionals to engage with the Study Group, whether through active participation in meetings, contribution to collaborative research, or dissemination of knowledge within their networks. Together, we can overcome the challenges that lie ahead, ensuring that neuroradiologists have a seat at the table in this multidisciplinary effort to improve patient outcomes.

In conclusion, we hope that the establishment of the PET-Guided Diagnosis and Management in Neuro-Oncology Study Group will facilitate continued progress in neuro-oncologic imaging. Through collaborative research, consensus recommendations, and advocacy efforts, the Study Group aims to address challenges and drive progress in the field. When neuroradiologists join forces with nuclear medicine physicians, neuro-oncologists, neurologic surgeons, radiation oncologists, and other physicians and members of the multidisciplinary care team, along with physicists and

other imaging scientists and advocates, we can work toward a brighter future for patients battling CNS tumors.

REFERENCES

1. Smith NJ, Deaton TK, Territo W, et al. **Hybrid (18)F-fluoroethyltyrosine PET and MRI with perfusion to distinguish disease progression from treatment-related change in malignant brain tumors: the quest to beat the toughest cases.** *J Nucl Med* 2023;64:1087–92 CrossRef Medline
2. Nabavizadeh A, Bagley SJ, Doot RK, et al. **Distinguishing progression from pseudoprogression in glioblastoma using (18)F-Fluciclovine PET.** *J Nucl Med* 2023;64:852–58 CrossRef Medline
3. Law I, Albert NL, Arbizu J, et al. **Joint EANM/EANO/RANO practice guidelines/SNMMI procedure standards for imaging of gliomas using PET with radiolabelled amino acids and [¹⁸F] FDG: version 1.0.** *Eur J Nucl Med Mol Imaging* 2019;46:540–57 CrossRef Medline
4. Albert NL, Weller M, Suchorska B, et al. **Response Assessment in Neuro-Oncology Working Group and European Association for Neuro-Oncology recommendations for the clinical use of PET imaging in gliomas.** *Neuro Oncol* 2016;18:1199–208 CrossRef Medline
5. Galldiks N, Lohmann P, Fink GR, et al. **Amino acid PET in neuro-oncology.** *J Nucl Med* 2023;64:693–700 CrossRef Medline
6. Galldiks N, Albert NL, Sommerauer M, et al. **PET imaging in patients with meningioma-report of the RANO/PET Group.** *Neuro Oncol* 2017;19:1576–87 CrossRef Medline
7. Ivanidze J, Roytman M, Skafida M, et al. **Dynamic (68)Ga-DOTATATE PET/MRI in the diagnosis and management of intracranial meningiomas.** *Radiol Imaging Cancer* 2022;4:e210067 CrossRef Medline
8. Darcourt J, Chardin D, Bourg V, et al. **Added value of [¹⁸F]FDOPA PET to the management of high-grade glioma patients after their initial treatment: a prospective multicentre study.** *Eur J Nucl Med Mol Imaging* 2023;50:2727–35 CrossRef Medline
9. Mankoff DA, Edmonds CE, Farwell MD, et al. **Development of companion diagnostics.** *Semin Nucl Med* 2016;46:47–56 CrossRef Medline
10. Ivanidze J, Subramanian K, Youn T, et al. **Utility of [¹⁸F]-fluoroestradiol (FES) PET/CT with dedicated brain acquisition in differentiating brain metastases from posttreatment change in estrogen receptor-positive breast cancer.** *Neurooncol Adv* 2021;3:vdab178 CrossRef Medline
11. Burkett BJ, Bartlett DJ, McGarrah PW, et al. **A review of theranostics: perspectives on emerging approaches and clinical advancements.** *Radiol Imaging Cancer* 2023;5:e220157 CrossRef Medline
12. Kersch CN, Ambady P, Hamilton BE, et al. **MRI and PET of brain tumor neuroinflammation in the era of immunotherapy, from the AJR Special Series on Inflammation.** *AJR Am J Roentgenol* 2022;218:582–96 CrossRef Medline
13. Galldiks N, Langen KJ, Albert NL, et al. **Investigational PET tracers in neuro-oncology: what's on the horizon? A report of the PET/RANO group.** *Neuro Oncol* 2022;24:1815–26 CrossRef Medline

Imaging Genomics of Glioma Revisited: Analytic Methods to Understand Spatial and Temporal Heterogeneity

 Cymon N. Kersch,  Minjae Kim,  Jared Stoller,  Ramon F. Barajas Jr., and  Ji Eun Park



ABSTRACT

SUMMARY: An improved understanding of the cellular and molecular biologic processes responsible for brain tumor development, growth, and resistance to therapy is fundamental to improving clinical outcomes. Imaging genomics is the study of the relationships between microscopic, genetic, and molecular biologic features and macroscopic imaging features. Imaging genomics is beginning to shift clinical paradigms for diagnosing and treating brain tumors. This article provides an overview of imaging genomics in gliomas, in which imaging data including hallmarks such as *IDH*-mutation, *MGMT* methylation, and *EGFR*-mutation status can provide critical insights into the pretreatment and posttreatment stages. This article will accomplish the following: 1) review the methods used in imaging genomics, including visual analysis, quantitative analysis, and radiomics analysis; 2) recommend suitable analytic methods for imaging genomics according to biologic characteristics; 3) discuss the clinical applicability of imaging genomics; and 4) introduce subregional tumor habitat analysis with the goal of guiding future radiogenetics research endeavors toward translation into critically needed clinical applications.

ABBREVIATIONS: AI = artificial intelligence; CE = contrast-enhanced; DCE = dynamic contrast-enhancement; DMG = diffuse midline glioma; H3K27-DMG = histone H3 lysine 27-altered diffuse midline glioma; H3K27me3 = H3 lysine 27 trimethylation; IVIM = intravoxel incoherent motion; LASSO = least absolute shrinkage and selection operator; PCA = principal component analysis; rCBV = relative CBV; *TERT* = telomerase reverse transcriptase; TME = tumor microenvironment; WHO = World Health Organization

Imaging genomics is the study of the relationships between microscopic, genetic, and molecular biologic features and macroscopic imaging features. Imaging genomics is important in CNS pathologies because tissue sampling faces challenges, including invasiveness in a critically functioning organ, the feasibility of intraoperative imaging, technical difficulties in site-specific tissue sampling, and requirements for study team coordination among neurosurgeons, radiologists, and pathologists. Through the use of

imaging genomics, we seek to improve the clinical care of patients by predicting risk and patient outcomes with identification of noninvasive imaging biomarkers.¹ Imaging features can be divided into 2 categories: first, low-dimensional imaging features that include semantic or qualitative features comprising a standardized lexicon for the description of tumors (Visually AcceSable Rembrandt Images [VASARI]; <https://radiopaedia.org/articles/vasari-mri-feature-set>) or a description of tumor morphology (ie, T2-FLAIR mismatch sign). Second, radiomics features include high-throughput data that completely cover the range of quantitative features that can be extracted from images such as texture, shape, and margin gradient.² Radiomics can be derived from either handcrafted or deep learning techniques.³ Radiogenomics is a subcategory of imaging genomics that is based on radiomics.^{1,2} In radiogenomics, imaging features are extracted automatically and with high throughput, and radiogenomics often requires the use of a machine learning algorithm for model development.^{2,4}

Imaging genomics is technology-heavy and incorporates some combination of clinical imaging, “-omic” tissue analyses with “big data” bioinformatics, and artificial intelligence (AI) through machine learning algorithms. Imaging genomics has different methodologic approaches and uses low-dimensional semantic features and high-dimensional radiomics features. During cancer development, a few genes undergo distinct

Received July 28, 2023; accepted after revision November 9.

From the Department of Radiation Medicine (C.N.K.), Department of Diagnostic Radiology (J.S., R.F.B.), Knight Cancer Institute (R.F.B.), and Advanced Imaging Research Center (R.F.B.), Oregon Health and Science University, Portland, Oregon; and Department of Radiology and Research Institute of Radiology (M.K., J.E.P.), Asan Medical Center, University of Ulsan College of Medicine, Seoul, Korea.

C.N. Kersch and M. Kim are co-first authors.

Ji Eun Park was supported by the National Research Foundation of Korea grant funded by the Korean government [grant No.: RS-2023-00305153] and Korea Health Technology R&D Project through the Korea Health Industry Development Institute, funded by the Ministry of Health & Welfare: HI22C0471. Ramon F. Barajas, Jr was supported by the National Institutes of Health, National Cancer Institute K08CA237809, KL2TR002370, and L30CA220897 and Jonathan D + Mark C. Lewis Foundation.

Please address correspondence to Ji Eun Park, MD, PhD, Department of Radiology and Research Institute of Radiology, Asan Medical Center, University of Ulsan College of Medicine, 88 Olympic-ro 43-gil, Songpa-gu, Seoul 05505, Korea; e-mail: jieunp@gmail.com



Indicates article with online supplemental data.

<http://dx.doi.org/10.3174/ajnr.A8148>

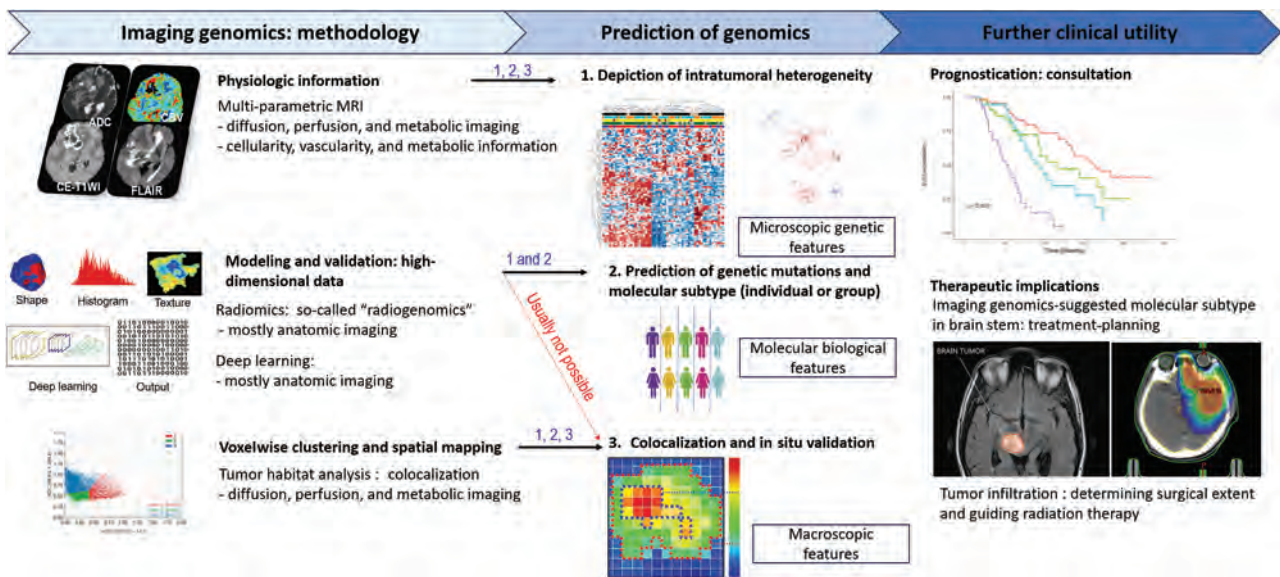


FIG 1. Sample workflow for imaging genomics studies to integrate glioma imaging phenotypes with molecular features. In imaging genomics studies of glioma, pretreatment MR imaging sequences are typically obtained. Next, tumor tissue is collected, sometimes under image guidance in relation to specific imaging features, and then subjected to various types of genomics, transcriptomics, and proteomics analyses. Both the imaging and molecular data require preprocessing and normalization steps before they are integrated to assess the associations between imaging phenotypes and genomic and molecular features. Finally, these associations are interpreted in the context of the clinical disease and known complex biologic processes and pathways.

changes in specific locations,⁵ and identifying these with imaging biomarkers requires distinct radiomics techniques. For instance, an *IDH* mutation is an ideal tumor-specific neoantigen that can be assessed with low-dimensional imaging features because it is uniform in a given tumor and does not change with time.⁶ On the other hand, epidermal growth factor receptor (*EGFR*) amplification and *MGMT* promoter methylation status are distributed heterogeneously within a given tumor, and loss of *EGFR* amplification⁷ and alterations of the *MGMT* promoter methylation status occur during treatment.⁸ These results necessitate using high-dimensional imaging features including radiomics and deep learning-based features to spatially discern these heterogeneous biologic expression patterns. AI is particularly helpful to handle high-dimensional imaging features as well as large-scale transcriptomics and genomics data.

Imaging genomics can be applicable to many clinical scenarios from diagnosis to treatment-planning and evaluating the treatment response. For example, it may be applied when tumor diagnostics are incomplete due to challenges with tissue sampling or when noninvasively subtyping gliomas on the basis of known gene expression or mutation patterns, including those associated with *IDH*, *MGMT*, *EGFR*, and others.⁹⁻¹¹ Moreover, imaging genomics and radiomics have applicability in prognostication, which can support decision-making of patients and clinicians. Its applications also extend into evaluating the tumor microenvironment and determining how this microenvironment changes with time in response to treatment. Finally, imaging genomics and especially radiomics may provide novel tools to evaluate the response to these therapies when it is challenging to distinguish posttreatment changes such as pseudoprogression, tumor progression, and treatment complications such as radionecrosis.

This article will achieve the following: 1) review the methods used in imaging genomics including visual analysis, quantitative analysis, and radiomics analysis; 2) recommend suitable analytic methods for imaging genomics according to biologic characteristics; 3) discuss the clinical applicability of imaging genomics; and 4) introduce subregional tumor habitat analysis with the goal of guiding future radiogenetics research endeavors toward translation into critically needed clinical applications.

PART 1: METHODOLOGY OVERVIEW

An overview of the methodology and clinical utility of imaging genomics is shown in Fig 1. Imaging genomics studies are usually based on 3 main methodologies: First, physiologic information from multiparametric MR imaging, usually based on low-dimensional features, can be used. Second, modeling and validation using high-dimensional data including radiomics and deep learning can be performed. Third, voxelwise spatial mapping and clustering using voxels from multiparametric MR imaging can be used. The main role of imaging genomics is prediction of genomics, including depiction of intratumoral heterogeneity, prediction of molecular subtypes, or colocalization and in situ validation. Depiction of intratumoral heterogeneity, which is often achieved with radiomics, facilitates understanding of microscopic genetic features. Prediction of molecular and genetic mutations in individuals or groups facilitates understanding of molecular and biologic features. Colocalization and in situ validation, which are often achieved with voxel-wise clustering and spatial mapping, facilitate understanding of macroscopic features to predict tumor aggressiveness, tumor infiltration, and vascularity. Further clinical utilities for imaging genomics include prognostication for patient consultation and determination of the

therapeutic implications of treatment-planning for chemotherapy and radiation therapy. A detailed process of structuring an imaging genomics study is summarized as follows.

Data Collection

Imaging data are collected through standard and specialized protocols that provide detailed information about the size, shape, location, and other imaging characteristics of the tumor, while biologic data collected from tissue samples reveal the genomic/transcriptomic profile of the tumor. Imaging data variability must be considered and harmonized across different imaging vendors and institutions because it greatly affects the reproducibility of imaging features. Imaging-acquisition protocols need to be unified across multiple centers to conduct a prospective study. For retrospective analysis, a phantom study, test-retest analysis, quantitative maps, or value normalization can be used. The detailed methodology is explained elsewhere.¹² For tumor characteristics that are binary (such as the presence or absence of an *IDH* mutation) and that do not change across a tumor, tumor tissue samples do not need to be spatially colocalized with the specific imaging features with which they are being correlated. Publicly available databases of genomics and transcriptomic data and their correlated clinical radiographs have resulted in some of the first large number of cohort studies in this field, for instance, the National Cancer Institute's large The Cancer Genomic Atlas was expanded to include a companion imaging database, The Cancer Imaging Archive, which has led to hundreds of publications in oncology exploring radiogenomics (<https://www.cancerimagingarchive.net>). However, for biologic features that vary over regions of a single tumor, spatially colocalized data (imaging and biologic) need to be collected from brain tumors. Precise colocalization of the tissue and imaging data is critical to permit these correlates, and this can be achieved through intraoperative stereotactic tissue sampling.^{13,14}

Imaging Data Preprocessing

Once the data are collected, they undergo preprocessing steps to ensure their quality and suitability for postprocessing. These may involve tasks such as resizing the images to a consistent resolution, normalizing the intensity values, removing artifacts or noise, and aligning the images in a standardized orientation.

ROI Segmentation

Once the images are acquired, an ROI is defined. The ROI is typically used as a bounding method (manual or automated segmentation) that prevents analytic extension into normal brain structures. This step ensures that subsequent analyses are specifically conducted on the tumor region.

Image Processing and Feature Extraction (especially, radiomics)

Once the imaging data are collected, they can undergo any number of image-processing steps to extract relevant features from the precise location of the colocalized tissue sample. Imaging features can be obtained from anatomic images (T1, T2-weighted, FLAIR), diffusion-weighted images, perfusion-weighted images, and metabolic images. Relevant imaging features according to genetic/molecular features are demonstrated in Part 2. In

radiomics, these include intensity-based features (voxel intensities), shape-based features (geometric properties), texture-based features (spatial patterns), and spatial-based features (relationships between different regions).

Biologic Analysis

The tissue data are simultaneously processed and analyzed to identify genetic mutations, gene-expression patterns, methylation patterns, and other biologic alterations. This direct tissue analysis provides information about the molecular characteristics and nuanced tumor biology, which can include potential therapeutic targets. Further subanalyses of the gene-expression profile can provide additional tissue features such as an estimation of the abundance of member cell types in a mixed cell population with cellular deconvolution techniques.

Data Integration and Analysis

The extracted imaging features and biologic data are then integrated and analyzed together to define biologic processes that are correlated with imaging features or phenotypes. The detailed integration analysis is explained in Part 2 regarding molecular features. Supervised learning including modeling is the most common method to predict 1 or 2 genomic mutations and molecular features. In radiomics, statistical and machine learning techniques including dimensionality reduction methods, feature selection techniques, or modeling approaches are used. When one uses AI, the choice of model depends on the specific task and available data. For example, convolutional neural networks can achieve image-analysis tasks by learning patterns and features from the input training images. The training process adjusts the internal parameters of the model to minimize the differences between the predicted and ground truth tumor annotations. After training, the model is evaluated using a separate validation data set. This step assesses the performance and generalizability of the model and may involve adjusting hyperparameters (eg, learning rate, regularization), exploring different model architectures, or augmenting the training data with transformations or variations. For validation, external validation is highly recommended to achieve the generalizability of the model. The detailed radiologic and statistical perspectives are summarized elsewhere.¹² Other analytic methods are as follows: Correlation plots or unsupervised learning methods including clustering are adopted to demonstrate heterogeneity to demonstrate correlation among multiple different genomic mutations and molecular features. To perform a prognostication or outcome study using imaging genomics, one can perform time-to-event analysis.

PART 2: ANALYTIC METHODOLOGY FOR DIFFERENT MOLECULAR FEATURES OF GLIOMAS

The spatial distribution of tumor molecular features has a substantial influence on the choice of analytic methodology (Fig 2). The biologic background of the molecular features of gliomas is summarized with a review of current analytic methodologies (Online Supplemental Data).^{4,15,16} The analytic approaches that best reflect the spatial distribution of given molecular features are proposed. Ubiquitously expressed biologic features such as *IDH* mutations may be assessed using low-dimensional, lesion-wide analysis.

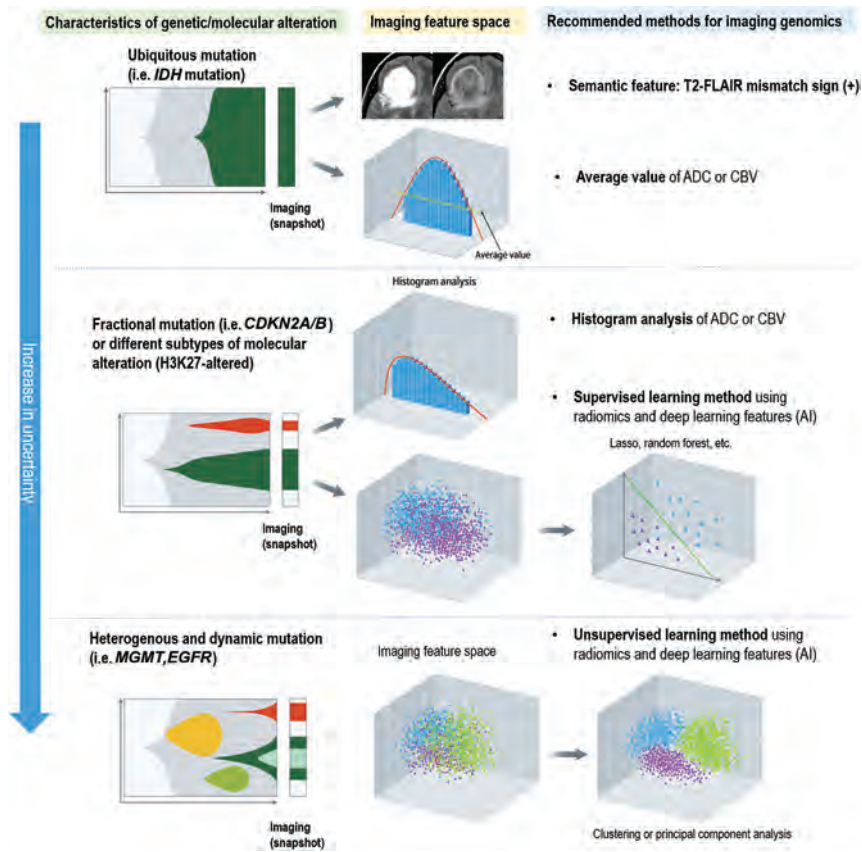


FIG 2. Differences in the biologic distribution of genes and molecular subtypes in glioma and suggested analytic methods of imaging genomics. For genes and molecular subtypes that are stable and ubiquitous, imaging genomics using averaged values or a simple imaging phenotype such as T2-FLAIR mismatch sign is applicable. For genes and molecular subtypes with a skewed distribution or those that include different subtypes, a histogram analysis or supervised learning using AI or radiomics is applicable. For genes and molecular subtypes that are dynamic and heterogeneous, pattern-wise analysis using unsupervised learning or subregional analysis to explain intratumoral heterogeneity needs to be applied.

Conversely, for molecular features with fractional mutation (ie, CDKN2A/B) or different subtypes of molecular alterations (ie, H3K27-altered), a histogram analysis or high-dimensional analysis using imaging-based computational techniques such as radiomics and deep learning with a supervised approach may be the most appropriate. For heterogeneous and dynamic molecular features (ie, MGMT promoter methylation, EGFR amplification), radiomics and deep learning with an unsupervised approach may best reflect spatial and temporal heterogeneity.

Imaging Genomics for Ubiquitously Expressed Biologic Features

Biologic Features of IDH Mutations. IDH mutation in glioma is ubiquitously expressed in all tumor cells in the IDH-mutant type.¹⁶ In the World Health Organization (WHO) CNS5 edition published in 2021, secondary glioblastoma or IDH-mutant glioblastoma is no longer listed.¹⁶ Regardless of the histologic grade, tumors with IDH wild-type are now assigned as “(molecular) glioblastoma, IDH-wild-type, CNS grade grade 4.” Thus, distinguishing IDH-mutational status becomes more important because it is a strong prognostic factor for survival.¹⁷

Review of Current Analytic Methodologies.

Visual analysis of various imaging features has been shown to differ according to IDH1-mutation status as characterized by standardized imaging lexicons such as VASARI.¹⁸ In addition, the T2-FLAIR mismatch sign is a validated imaging sign for IDH-mutant status in patients with diffuse adult-type glioma, specifically in diffuse astrocytoma, IDH-mutant type without the 1p/19q codeletion. The T2-FLAIR mismatch sign is expressed in the entire tumor, which shows entirely homogeneous high signal intensity on T2-weighted images and low signal intensity in the internal portion on FLAIR images. The T2-FLAIR mismatch sign has been previously described in detail.^{19–21} Imaging genomics clinicopathologic analysis suggests that the presence of tumor microcystic change is a causative etiology of FLAIR suppression.²² The positive predictive value of the T2-FLAIR mismatch sign for IDH-mutation status was 100% in retrospective cohort studies of diffuse adult-type gliomas.^{19,20}

There are false-positives for the T2-FLAIR mismatch sign when it is observed in other tumors such as dysplastic embryogenic tumors²³ and pilocytic astrocytoma.²⁴ When a study design includes all gliomas, both the positive predictive value and specificity of the T2-FLAIR mismatch sign for IDH-mutation may decrease.

Advanced physiologic imaging has also been shown to predict IDH-mutation status such as DSC,²⁵ dynamic contrast-enhancement (DCE),²⁶ intravoxel incoherent motion (IVIM),²⁶ and metabolic imaging such as amide proton transfer-weighted imaging.²⁷ While CBF is not useful in distinguishing IDH-mutation status, the medians of the parameters derived from DSC and IVIM such as the CBV, microcirculation perfusion coefficient, and simplified perfusion fraction were lower in IDH-mutant gliomas.²⁵ In addition, the median lower fractional volume of intravascular space using a distributed parameter model showed the highest diagnostic performance among DCE-derived parameters, including those based on the Tofts model.²⁶ Such findings may support the lower vascularity, permeability, and flow in the tumor microenvironment of IDH-mutant gliomas due to resistance to neoangiogenesis by regulation of hypoxia-inducible factor α .²⁸ In terms of chemical exchange saturation transfer (CEST) imaging metrics, the median amide/amine signal ratio and levels of amine signal differentiated IDH wild-type from the pooled IDH-mutant gliomas, supporting the relevance of tumor acidity in differentiating gliomas.²⁷

Supervised learning approaches with radiomics features and deep learning features have been used to predict IDH-mutation

status with multiparametric MR imaging.²⁹ This approach often requires large, highly curated data sets. On the basis of the glioma The Cancer Genomic Atlas cohort, a prediction model of *IDH*-mutation status using multiple machine learning classifiers exhibited a preoperative accuracy of up to 88.9%.³⁰ In terms of AI, use of convolutional neural networks has demonstrated an accuracy of 94% for *IDH*-1 mutation status and 92% for 1p/19q codeletion status.³¹

Proposed Analytic Methodology. For ubiquitously expressed biologic features such as *IDH* mutations, a lesion-wide visual analytic approach that captures the whole tumor and provides direct and intuitive information is proposed. The ubiquitous expression of *IDH* mutations in all tumor cells negates the need to reflect intratumoral heterogeneity, making histogram or radiomics approaches excessive.

The T2-FLAIR mismatch sign, when applied appropriately, is a representative visual analytic approach that is simple to use and has been extensively validated in real-world clinical settings. For physiologic imaging, the median or mean values from physiologic imaging modalities including DSC, DCE, IVIM, and amide proton transfer-weighted imaging from the entire tumor ROI are suitable for analyzing this ubiquitous expression of genetic mutation. Supervised learning using high-dimensional imaging features to classify *IDH*-mutant tumors is feasible, but future research should be directed to proposing and validating a simple, visual, or statistical analytic approach that enables lesion-wide reflection of ubiquitously expressed biologic features.

Imaging Genomics for Subtypes with a Skewed Distribution
Intratumoral Heterogeneity of *CDKN2A/B*. Certain molecular features of gliomas are characterized by fractional mutations or different subtypes of molecular alterations. *CDKN2A/B* is a tumor-suppressor gene that, when homozygously deleted, promotes biologic aggressiveness in *IDH*-mutant gliomas.³² In the WHO CNS classification published in 2021, a *CDKN2A/B* homozygous deletion results in a CNS WHO grade of 4 for *IDH*-mutant tumors, even without microvascular proliferation or necrosis.¹⁶ Thus, grading is no longer entirely histologic, and *CDKN2A/B* status becomes important. The percentage of cells with homozygous deletion across all *IDH*-mutant tumors is bimodal, with a median value of <10%.³³ However, this distribution is skewed toward histologically high-grade tumors having >50% deletion.

Intratumoral Heterogeneity of Histone H3 Lysine 27-Altered Diffuse Midline Glioma. Histone H3 lysine 27-altered diffuse midline glioma (H3K27-DMG) is a unique molecular subgroup that includes subtypes with an alternative mechanism for the loss of H3K27 trimethylation, such as additional somatic genetic alterations of receptor tyrosine kinases, cell cycle regulators, mediators of DNA repair, and/or phosphoinositide 3-kinase/protein kinase B/mammalian target of rapamycin signaling.³⁴ The 2021 WHO classification adopted the revised designation “diffuse midline glioma, H3K27-altered” to include subtypes of diffuse midline glioma (DMG) with an alternative mechanism for the loss of H3K27 trimethylation. These include 4 subtypes of DMGs: 1) H3.3 p.K28M (*K27M*)-mutant, 2) H3.1 or 3.2 p.K28M (*K27M*)-mutant,

3) H3-wild-type with *EZH1* overexpression, and 4) *EGFR*-mutant, which mainly includes bithalamic diffuse gliomas that present H3K27M or *EZH1* overexpression together with strong enrichment in *EGFR* alterations. The H3K27-altered type is characterized by low intratumoral heterogeneity because the *K27M*-mutant variant causes a global reduction in levels of H3 lysine 27 trimethylation (H3K27me3).³⁵ In addition, *EZH1* overexpression results in H3K27me3 global reduction.³⁶

Review of Current Analytic Methodologies. There are a limited number of studies predicting *CDKN2A/B* status, and most have used supervised learning approaches.^{37,38} A recent study of imaging genomics for *CDKN2A/B* showed a trend toward an infiltrative pattern, a larger maximal diameter, and a higher value of the 95th percentile of normalized CBV being independent predictors of *CDKN2A/B*.³⁹ Imaging features of *CDKN2A/B* deletion may overlap with those implying tumor aggressiveness.

For H3K27M-DMG, imaging features have been characterized by comparing the mean values or histogram parameters of ADC or relative CBV (rCBV).^{40,41} Imaging features of H3K27-altered tumors have various presentations (high intertumoral heterogeneity), but most tumors show relatively uniform signals (low intratumoral heterogeneity).⁴² Metabolic imaging with MRS has demonstrated significantly higher citrate and glutamine levels in H3K27-DMG tumors.⁴³

Proposed Analytic Methodology. For fractional mutation of *CDKN2A/B*, the proposed analytic methodology is histogram analysis. To depict intratumoral heterogeneity of *CDKN2A/B*, histogram parameters of skewness, kurtosis, and percentile values are useful. By means of radiomics, intratumoral heterogeneity can be captured, and *CDKN2A/B* can be diagnosed using supervised learning. Using the median or mean value derived from histograms of physiologic imaging biomarkers, imaging prediction of *CDKN2A/B* may be difficult because there is no clear technical cutoff, and *IDH*-mutant tumors evolve toward homozygous deletion across time.

For H3K27-altered DMG, the imaging features have various presentations (high intertumoral heterogeneity), but most tumors show relatively uniform signals (low intratumoral heterogeneity).⁴² Pattern-wise diagnosis is helpful to depict intertumoral heterogeneity of H3K27-altered DMG. Metabolic imaging with MRS has demonstrated significantly higher citrate and glutamine levels in H3K27-DMG tumors.⁴³ On the basis of the low intratumoral heterogeneity of metabolic/cell signaling alterations, non-invasive metabolic imaging may provide a method for improved preoperative diagnosis of tumors with H3K27 alterations.

Imaging Genomics for Subtypes with Dynamic and Heterogeneous Biologic Features

Biologic Background of *MGMT* Methylation and *EGFR*-Mutation Status. Some molecular features of gliomas have spatial and temporal heterogeneity with evolution of the mutational status with treatment. DNA promoter methylation of the *MGMT* gene is a clinically important feature that is predictive of temozolomide sensitivity, which is the standard-of-care chemotherapeutic agent used in the treatment of glioblastoma. Prior investigations have demonstrated *MGMT* methylation to be heterogeneous, with

heterogeneity of methylation patterns across the *MGMT* 5' CpG island, and capable of changing through the course of therapy.

EGFR amplification and *EGFR variant III (EGFRvIII)* mutations have both temporal and spatial heterogeneity. *EGFRvIII* mutations were detectable only in subclones of the tumor in *EGFR* amplification samples of individual patients, which suggested that *EGFRvIII* mutations are late events in tumor development.⁴⁴ Heterogeneity of *EGFRvIII* has also been observed at the protein level. In contrast, wild-type *EGFR* expression is much more abundant and lacks the profound heterogeneity observed with *EGFRvIII*. This finding indicates that both the occurrence and disappearance of *EGFR* mutations are frequent processes that significantly contribute to tumor heterogeneity.

Review of Current Analytic Methodologies. Radiomics and deep learning-based approaches involve the extraction of hundreds of quantitative features from images.⁴ Typically, machine-learning techniques are subsequently applied to the extracted radiomics features. These techniques use 2 main methods:⁴⁵ 1) dimensionality reduction and feature selection via unsupervised approaches, and 2) association analysis with ≥ 1 specific outcome via supervised approaches.

***MGMT* Promoter Methylation Status.** Using supervised learning methods, numerous studies have assessed the correlation of conventional MR imaging features from T1-weighted, T2-weighted, FLAIR, and T1-weighted gadolinium contrast-enhanced (CE-T1WI) images with *MGMT* methylation status. Published studies have reported a wide range of predictive accuracy ranging from 60% to $>80\%$.⁴⁶⁻⁴⁹ For dimensionality reduction and feature selection, algorithms such as maximum redundancy and maximum relevance⁴⁶ or least absolute shrinkage and selection operator (LASSO) have been used. Fusion radiomics signatures determined by logistic regression modeling of single radiomics signatures selected from each sequence and habitat have been shown to predict survival.⁴⁶ In particular, convolutional neural networks-based architectures have been validated or further developed with transfer learning to determine *MGMT* promoter methylation status.^{48,49}

***EGFR* Amplification Status.** Histogram analysis and supervised learning approaches (machine learning) with radiomics have been used to predict *EGFR* amplification in glioblastomas and have achieved a diagnostic accuracy of up to 78%.⁵⁰⁻⁵³ Measures such as the maximum rCBV, relative peak height, and percentage signal recovery from DSC have been correlated with *EGFR* mutation status.⁵³ Logistic regression models with or without dimensionality reduction and feature selection via LASSO using conventional images such as T2WI, CE-T1WI, FLAIR, and DWI have been most commonly used.^{51,52}

Proposed Analytic Methodology. For genes exhibiting both spatial and temporal heterogeneity, unsupervised approaches to dimensionality reduction and feature selection are more beneficial than supervised approaches. The 2 most commonly used unsupervised approaches are cluster analysis and principal component analysis (PCA).² Genomics data are often multidimensional.

Cluster analysis is a method that sorts through genomics data and allows better visualization through heatmaps.⁵⁴ A heatmap can readily display trends in data by simultaneously accounting for each dimension of the genomic data fed into the computational pipeline. PCA also explores multidimensional genomics data and determines the impact a specific dimension of the data has on variation in the data set as a whole. This process shows the likelihood of contribution from a specific attribute compared with the contributions of other dimensions in the data.⁵⁵ Both cluster analysis and PCA allow the analysis of contributions from individual vectors within an extensive basis of vectors.

One good example of unsupervised learning for *MGMT* promoter methylation status is a study that used dimensionality reduction with unsupervised learning to account for the intra- and intertumor heterogeneity of *MGMT*. By means of anatomic FLAIR and CE-T1WI features, K-means clustering of radiomics features obtained 3 distinct and reproducible imaging subtypes of glioblastoma with molecular characteristics, including *MGMT* promoter methylation status.⁴⁷

For *EGFR* amplification status, unsupervised learning using regional information has been studied. Intratumoral heterogeneity can be depicted by conducting separate regional-based analyses of imaging biomarkers, including enhancing tumors, nonenhancing tumors, necrosis, and edema. In a multiparametric MR imaging and multisegmentation study, the spatial tumor pattern (location) and intensity distribution obtained from histograms of T2-FLAIR, ADC, and rCBV values were compared between *EGFR variant III*-positive (*EGFRvIII+*) versus *EGFR variant III*-negative (*EGFRvIII-*) tumors. *EGFRvIII+* tumors displayed a higher rCBV, lower ADC, higher fractional anisotropy, lower T2-FLAIR, and a distinctive spatial pattern (Fig 3).⁵⁶ *EGFRvIII+* tumors had a more isotropic distribution of rCBV in enhancing and nonenhancing tumors and a low rCBV in perinecrotic tissue. This finding was observed with PCA of complex time-signal-intensity curves from DSC imaging of the peritumoral region.⁵⁷ This unsupervised learning approach showed that *EGFRvIII+* tumors had more homogeneity in time-signal-intensity curve-based features between immediate and distant peritumoral ROIs, while greater heterogeneity was observed in *EGFRvIII* tumors.

PART 3: ADVANCING PERSONALIZED MEDICINE USING IMAGING GENOMICS AND RADIOMICS

The standard-of-care treatment for glioblastoma includes upfront maximal safe resection followed by concurrent radiation therapy and temozolomide and then adjuvant temozolomide.⁵⁸ For patients with a good performance status, their treatment often includes the use of tumor-treating fields after concurrent chemoradiation. With this treatment paradigm, patients with glioblastoma have a median survival of 20.9 months.⁵⁹ However, there is substantial variation in individual outcomes, with survival ranging from a few weeks to many years. Imaging genomics has demonstrated clinical feasibility in selecting subgroups of patients who are likely to benefit from specific therapies, including immunotherapies and targeted molecular therapies, and in improving our ability to assess treatment responses.

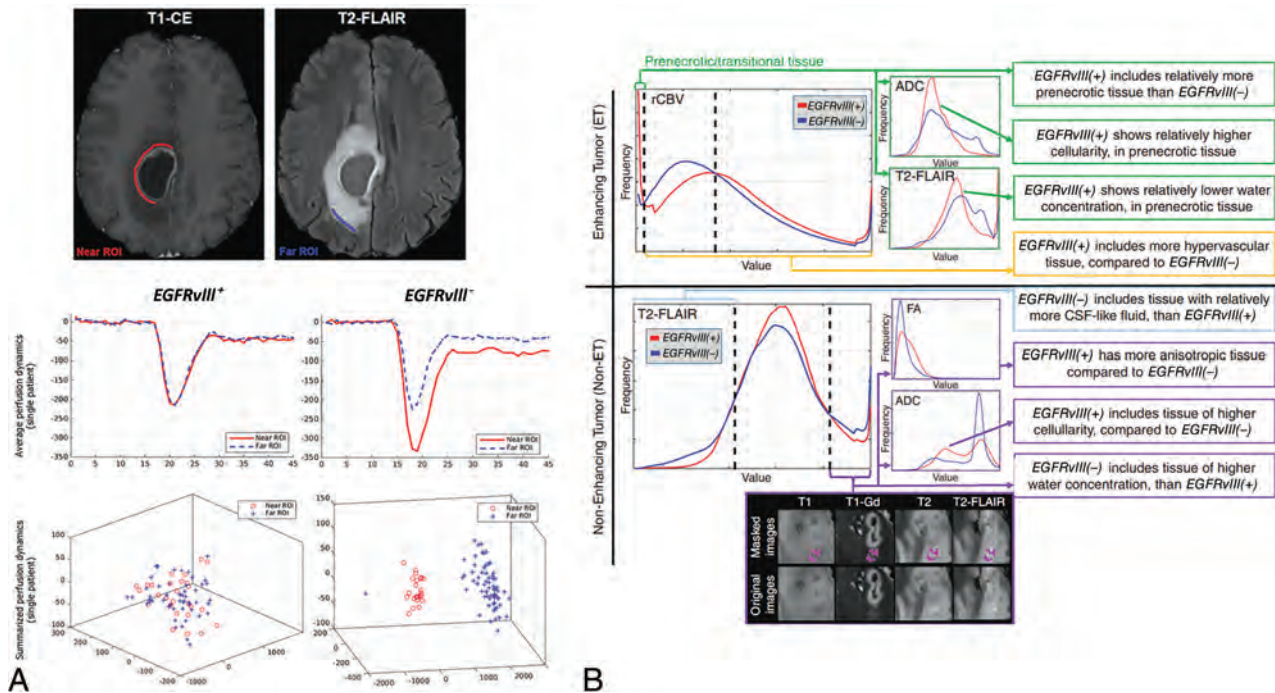


FIG 3. Illustration of the use of an unsupervised learning method and a subregional analysis to account for an *EGFRvIII* mutation. **A**, Histogram analysis of multiparametric MR imaging enables depiction of the differences between the *EGFRvIII*-mutant and wild group (reproduced with permission from Bakas et al⁵⁷). **B**, For *EGFRvIII*-mutant tumors, there is no heterogeneity in the perfusion pattern distribution between the far and near ROIs, while there is considerable heterogeneity between the far and near ROIs for patients who have *EGFRvIII*- tumors (reproduced with permission from Akbari et al⁵⁶).

Surgery

Maximal safe surgical cytoreduction is unequivocally linked to improved clinical outcomes for patients with glioblastoma. However, the highly infiltrative growth pattern often leads to involvement of eloquent brain regions and challenges discerning areas with the highest risk of tumor recurrence. This feature makes achieving “negative” surgical margins difficult, if not impossible. Assessing tumor infiltration by using imaging genomics is an important issue and needs to be validated with spatial mapping. A colocalization study demonstrated imaging correlates of tumor infiltration using anatomic, perfusion, diffusion images and O-(2-[18F]-fluoroethyl)-L-tyrosine ([¹⁸F] FET) PET and subsequent multiregion stereotactic biopsies.¹⁴ In nonenhancing gliomas, FLAIR had the highest diagnostic accuracy. Recently, an optical imaging technique and fiber laser-based stimulated Raman histology showed the potential to noninvasively predict residual infiltrative glioma.⁶⁰ This finding has the potential to assist in personalizing resection plans on the basis of the individual risk of local recurrence, while concurrently minimizing the risk of neurologic deficits and preserving function status. Although radiomics has begun to explore imaging correlates of tumor cellularity⁶¹ and the extent of infiltration,⁶² spatial mapping and colocalization are difficult to achieve for radiomics because this technique demonstrates heterogeneity and complexity, and spatial information is lost.

Temozolomide

Temozolomide is used in glioblastoma treatment alongside radiation therapy. However, response to this agent varies among patients and depends on individual tumor biology. Patients with methylated

MGMT promoters show an enhanced response to temozolomide.^{9,10} Therefore, noninvasive determination of *MGMT* methylation status using imaging genomic applications can predict temozolomide sensitivity. Imaging genomics methodologies to assess *MGMT* promoter methylation have been previously discussed herein. Similarly, the gene telomerase reverse transcriptase (*TERT*), which is sometimes mutated in glioblastoma, impacts temozolomide and radiation sensitivity. A recent study created an optimized radiomics score using a LASSO regression model and multivariate analysis to predict *TERT* promoter mutations.⁶³ This model, which combines the radscore with patient characteristics, demonstrated high prediction accuracy.

Radiation Therapy

Radiation, a standard treatment for glioblastoma and many gliomas, may be optimized through radiomics. A recent review article⁶⁴ demonstrated that a radiomics-guided radiation therapy approach may aid radiation therapy planning by using radiomics volumetric signature maps and radiomics subvolumes. This approach would further enable personalization of radiation treatment plans based on patient-specific anatomic and tumor characteristics using radiomics. Radiomics and imaging genomics could offer novel biomarkers for variable inter- and intratumoral radiation sensitivity, guiding individualized dose/fractionation plans and dose painting across a tumor.

Immunotherapy

Immunotherapies, primarily targeting programmed cell death protein 1/programmed death-ligand 1, or anti-cytotoxic T-

lymphocyte-associated protein 4, use the adaptive immune system against tumor cells. Unfortunately, these therapies have shown little benefit in improving survival of patients with glioblastoma to date. Two recently published international randomized Phase III trials evaluating the efficacy of adding nivolumab to the treatment of newly diagnosed glioblastoma with and without *MGMT* promoter methylation showed no benefit over the standard-of-care treatment.^{65,66} The ineffectiveness of immune checkpoint blockade in glioblastoma could be due to decreased CNS immune surveillance, low tumor mutation burden, poor BBB penetration, or insufficient immunologic response to glioblastomas. However, some glioblastoma subtypes may respond better to immune-modulating therapeutics. One randomized control study showed that patients who received neoadjuvant and/or adjuvant therapy with pembrolizumab had significantly extended overall survival among patients with recurrent glioblastoma.⁶⁷ Imaging genomics and radiomics may provide insight into more immunogenic glioblastomas that could have heightened sensitivity to immune-modulating therapies. One imaging study used radiomics to characterize tumor macrophage infiltration within the tissue microenvironment, which plays a critical role in the tumor-immune interface.⁶⁸ A recent review elaborated on how radiomics and imaging phenotypes correlate with the immune microenvironment of gliomas, their applications in immunotherapy era, and ongoing challenges in the field.⁶⁹

PART 4: POTENTIAL POWERFUL IMAGING GENOMICS TOOL FOR ENABLING BOTH SPATIAL MAPPING AND DEPICTING HETEROGENEITY—TUMOR HABITAT ANALYSIS

When assessing the translational utility of imaging genomics to the previously discussed clinical diagnostic and treatment pathways, it is critically important at the methodologic level to account for the vast intratumoral heterogeneity that these tumors exhibit. Imaging analyses that use supervised learning with radiomics or deep learning features are limited for biologic validation for 3 reasons: First, the end point of the classifier is singular for radiomics using supervised learning, which does not consider any heterogeneity. Second, there is a danger of overfitting or overinterpreting the derived models for supervised learning.⁷⁰ Third, radiomics depicts heterogeneity and complexity within a given ROI, in which any spatial information is lost. Pattern-wise analysis using unsupervised learning may reduce dimensionality and the risks of overfitting, but regional biologic validation is ultimately needed.⁷⁰

Tumor habitat analysis uses spatially oriented “voxels.” Grouping “similar” voxels together (parcellation) may define multiple subregions with a common biology that respond differentially to therapy or drive progression.⁷¹ Parcellation methods include either an a priori assumption of a binary threshold, a geographic assumption, or a data-driven analysis using a clustering method. Tumor habitat analysis is in line with existing methods of imaging genomics, including subregions or subvolumes of a tumor or signature map. This method enables depiction of intratumoral heterogeneity similar to that of radiomics as well as spatial mapping and colocalization for further biologic validation. By means of subregions or subvolumes, tumor habitat

analysis may guide imaging-guided treatment-planning and predict localization of tumor recurrence site. Below is a description of studies demonstrating use cases (specific situations or scenarios) of tumor habitat analysis are utilized.

Depiction of the Tumor Microenvironment Using Tumor Habitat Analysis

A data-driven analysis of clustering demonstrated tumor subregions with distinct biology and pathologic correlations with the tumor microenvironment (TME).⁷¹ Figure 4 explains the difference between radiomics-based supervised learning methods and voxelwise unsupervised learning (clustering) methods for tumor habitat analysis. These data-driven approaches have successfully distinguished viable tumors from nonviable tumors using multiparametric MR imaging and validated the method against H&E histology.^{72,73}

In glioblastoma, tumor habitat analysis using multiparametric MR imaging with diffusion-weighted and perfusion-weighted imaging has been conducted with a voxel-based clustering method.⁷⁴ The process is assisted by deep learning-based segmentation, which enables reproducible tumor delineation, and the voxels containing physiologic information—the ADC reflecting cellularity and the rCBV reflecting vascular density—can be extracted within the ROI.

Potential Utility of Tumor Habitat Analysis

Virtual Biopsy and Radiogenomics. Voxelwise clustering and tumor habitat analysis enable the establishment of distinct functional regions with spatial information and the spatial coregistration of the images and corresponding histologic findings.⁷⁰ In breast cancer, multiparametric MR imaging habitat analysis and coregistered histology identified biologically validated subregions of hypoxia, necrosis, and other conditions.⁷⁵ This result suggests the possibility that virtual biopsies can depict the most aggressive tumor portion of the glioma as well as help to predict genetic mutations under different TMEs. In terms of radiogenomics, tumor heterogeneity is shaped by both genetic differences and the local microenvironment.⁷⁶ Due to differences in the tissue architecture and nutrient and oxygen levels, regional differences in the TME lead to different selection of subpopulation of tumor cells (clonal selection). For example, late development of *EGFRvIII* is correlated with a TME promoting anabolic metabolism in glioblastoma cells, leading to alterations in the levels of *EGFRvIII* expression.⁷⁶ Depiction of tumor habitats based on hypoxic regions enables investigation of genetic/molecular alterations per subregion that may enhance the prediction of certain mutations.

Treatment Monitoring. The most promising clinical application of tumor habitat analysis is assessing the treatment response.⁷⁰ Temporal changes in the tumor habitat, the “spatiotemporal habitat,” occur during and after treatment with both spatial and temporal variation. Following treatment, outcomes can include tumor response, tumor progression, pseudoprogression, and radiation necrosis or other adverse effects of the anticancer therapies, all of which could be evaluated with habitat analysis.

Pseudoprogression. Pseudoprogression is thought to represent an inflammatory response to treatment but radiographically mimics

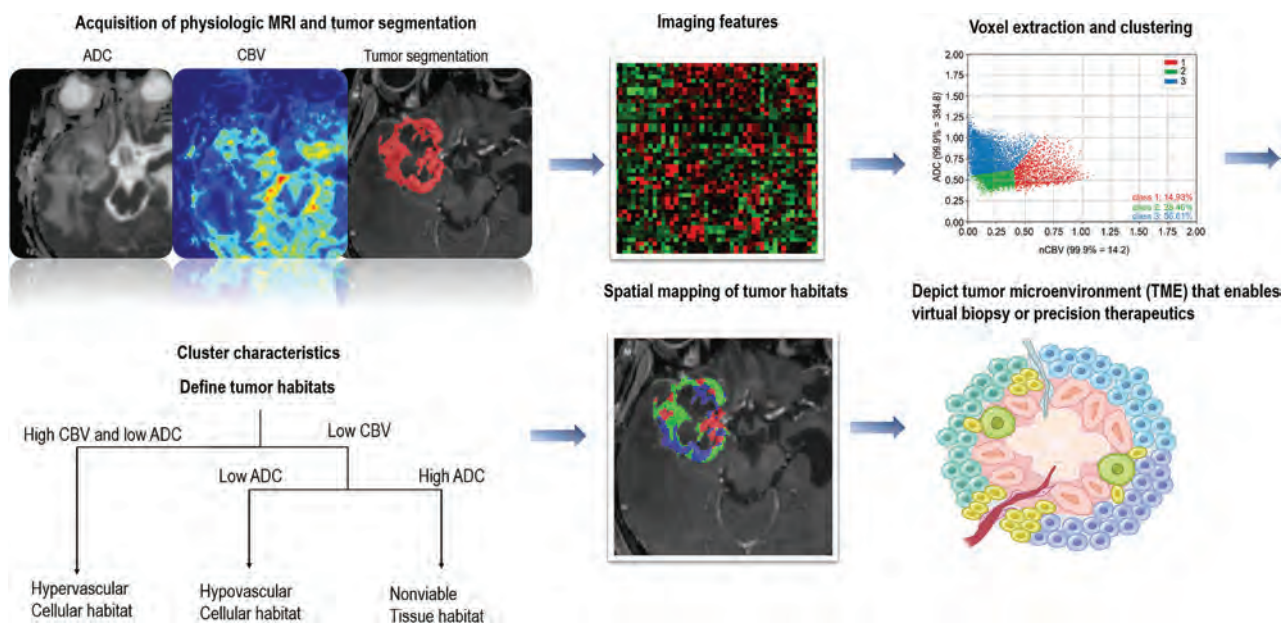


FIG 4. Limitations of radiomics with supervised learning for explaining intratumoral heterogeneity. The TME interacts with genes, and subregions evolve and develop certain genomic mutations. Tumor habitat (subregional) analysis is an analytic method using voxelwise clustering of multiparametric MR imaging data that maintains the spatial information.

tumor growth and thus poses a dilemma for the clinician when considering a treatment change or pursuing close surveillance. The feasibility of subregional analysis was shown in differentiating pseudoprogression on the basis of a voxelwise clustering method that exhibited better performance than the single parameters of the ADC or CBV.⁷⁴ By means of spatiotemporal habitat analysis on the ADC and CBV, 3 spatial habitats of a hypervascular cellular (high CBV and low ADC), a hypovascular cellular (low CBV and low ADC), and a nonviable tissue habitat (low CBV and high ADC) were identified, and an increase in the hypervascular cellular (OR, 4.55, $P = .002$) and hypovascular cellular (OR, 1.22, $P < .001$) habitats was predictive of tumor progression.⁷⁷

Prediction of Treatment Response. Spatiotemporal habitats also assist in monitoring treatment responses in patients with glioblastoma.⁷⁷ On the basis of a spatiotemporal habitat analysis of the ADC and CBV, a short-term increase in the hypervascular cellular habitat (hazard ratio, 40.0; $P = .001$) and hypovascular cellular habitat was significantly associated with shorter progression-free survival (hazard ratio, 3.78; $P < .001$) after concurrent chemoradiation therapy. Validation using a prospective cohort showed that an immediate increase in hypovascular cellular tumors after concurrent chemoradiation therapy was strongly associated with shorter progression-free survival.⁷⁷

Comparative Assessment with Current Methodology. By means of spatially oriented voxels and learning methods, tumor habitat analysis has the potential to become a powerful tool for imaging genomics. While traditional radiomics methods offer valuable insights into tumor heterogeneity, they often fail to account for spatial information, an area in which habitat analysis excels. Therefore, tumor habitat analysis is likely to be most beneficial for accurately distinguishing various intratumoral regions,

thereby enhancing our ability to differentiate between viable and nonviable tumor areas as well as to discern treatment-induced changes such as pseudoprogression. However, comparisons with traditional radiomics methods indicate the need for further studies to establish the role of habitat analysis, because the specificity and sensitivity of the latter can be influenced by factors such as the choice of clustering methods, the quality of input imaging data, and the presence of overlapping imaging features. Despite these hurdles, its potential for improving therapeutic decision-making, predicting prognosis, and monitoring treatment response makes tumor habitat analysis a promising avenue in neuro-oncology.

PART 5. LIMITATIONS, CHALLENGES TO BE ADDRESSED, AND FUTURE OPPORTUNITIES

Imaging genomics is not aimed at replacing actual genomics. There are features that are only attainable through direct tissue analysis of genetic data and molecular characteristics that lack specific imaging features. Furthermore, imaging features overlap among high-grade gliomas with increased cellularity showing a low ADC and increased vascularity exhibiting a high rCBV. Nonetheless, imaging genomics is useful in patients with brainstem glioma or deep-located tumors in the pretreatment stage. With spatial mapping, imaging genomics can become a powerful noninvasive tool for guiding treatment and treatment monitoring. Surgery and radiation therapy can be guided by demonstrating an infiltrative tumor component. Timely and noninvasive diagnosis is possible for the posttreatment stage by enabling localization of viable tumor or tumor progression that requires subsequent treatment.

For future studies, different analytic approaches for biologic features that are ubiquitously expressed, demonstrate skewed distribution, or display temporal or spatial heterogeneity are

proposed. Biologic validation, when possible and appropriate, should be encouraged, and analytic techniques such as molecular imaging and tumor habitat analysis that enable colocalization will prove promising.

CONCLUSIONS

Imaging genomics not only identifies genomic and molecular alterations noninvasively but also can help with prognostication, assessing and predicting tumor progression, and guiding therapy by spatial mapping and localization. In the pretreatment and diagnostic stage, different analytic approaches should be applied for imaging genomics. For ubiquitously expressed genomics features such as *IDH*-mutation status, a simple visual evaluation is sufficient. For skewed distribution or intra-/intertumoral heterogeneity including *CDKN2A/B* homozygous deletion or H3K27-altered status, histogram analysis of physiologic imaging biomarkers or radiomics with supervised learning methods are suitable. For dynamic alterations of *MGMT* promoter methylation or *EGFR*-mutation status, unsupervised learning of high-dimensional data is suitable. In the posttreatment stage, spatial mapping of imaging genomics has greater clinical implications through tumor habitat analysis to localize and predict tumor progression and guide therapy. Ultimately, colocalization of imaging genomics and actual pathology will improve this technique and broaden its utility in patients with glioma.

ACKNOWLEDGMENTS

We thank Bethany Barajas, MSN, for her helpful comments regarding this article and the many wonderful patients who selflessly contribute their time to undergo research medical imaging while confronting a deadly disease.

Disclosure forms provided by the authors are available with the full text and PDF of this article at www.ajnr.org.

REFERENCES

- Diehn M, Nardini C, Wang DS, et al. **Identification of noninvasive imaging surrogates for brain tumor gene-expression modules.** *Proc Natl Acad Sci U S A* 2008;105:5213–18 CrossRef Medline
- Kumar V, Gu Y, Basu S, et al. **Radiomics: the process and the challenges.** *Magn Reson Imaging* 2012;30:1234–48 CrossRef Medline
- Hosny A, Parmar C, Quackenbush J, et al. **Artificial intelligence in radiology.** *Nat Rev Cancer* 2018;18:500–10 CrossRef Medline
- Gillies RJ, Kinahan PE, Hricak H. **Radiomics: images are more than pictures, they are data.** *Radiology* 2016;278:563–77 CrossRef Medline
- Hiley C, de Bruin EC, McGranahan N, et al. **Deciphering intratumor heterogeneity and temporal acquisition of driver events to refine precision medicine.** *Genome Biol* 2014;15:453 CrossRef Medline
- Waitkus MS, Diplas BH, Yan H. **Isocitrate dehydrogenase mutations in gliomas.** *Neuro Oncol* 2015;18:16–26 CrossRef Medline
- van den Bent MJ, Gao Y, Kerkhof M, et al. **Changes in the EGFR amplification and EGFRvIII expression between paired primary and recurrent glioblastomas.** *Neuro Oncol* 2015;17:935–41 CrossRef Medline
- Brandes AA, Franceschi E, Tosoni A, et al. **O(6)-methylguanine DNA-methyltransferase methylation status can change between first surgery for newly diagnosed glioblastoma and second surgery for recurrence: clinical implications.** *Neuro Oncol* 2010;12:283–88 CrossRef Medline

- Esteller M, Garcia-Foncillas J, Andion E, et al. **Inactivation of the DNA-repair gene MGMT and the clinical response of gliomas to alkylating agents.** *N Engl J Med* 2000;343:1350–54 CrossRef Medline
- Hegi ME, Diserens AC, Gorlia T, et al. **MGMT gene silencing and benefit from temozolomide in glioblastoma.** *N Engl J Med* 2005;352:997–1003 CrossRef Medline
- Yan H, Parsons DW, Jin G, et al. **IDH1 and IDH2 mutations in gliomas.** *N Engl J Med* 2009;360:765–73 CrossRef Medline
- Park JE, Park SY, Kim HJ, et al. **Reproducibility and generalizability in radiomics modeling: possible strategies in radiologic and statistical perspectives.** *Korean J Radiol* 2019;20:1124–37 CrossRef Medline
- Jiang S, Eberhart CG, Zhang Y, et al. **Amide proton transfer-weighted magnetic resonance image-guided stereotactic biopsy in patients with newly diagnosed gliomas.** *Eur J Cancer* 2017;83:9–18 CrossRef Medline
- Verburg N, Koopman T, Yaqub MM, et al. **Improved detection of diffuse glioma infiltration with imaging combinations: a diagnostic accuracy study.** *Neuro Oncol* 2020;22:412–22 CrossRef Medline
- Park JE, Kickingreder P, Kim HS. **Radiomics and deep learning from research to clinical workflow: neuro-oncologic imaging.** *Korean J Radiol* 2020;21:1126–37 CrossRef Medline
- Louis DN, Perry A, Wesseling P, et al. **The 2021 WHO Classification of Tumors of the Central Nervous System: a summary.** *Neuro Oncol* 2021;23:1231–51 CrossRef Medline
- Ramos-Fresnedo A, Pullen MW, Perez-Vega C, et al. **The survival outcomes of molecular glioblastoma IDH-wildtype: a multicenter study.** *J Neurooncol* 2022;157:177–85 CrossRef Medline
- Park YW, Han K, Ahn SS, et al. **Prediction of IDH1-mutation and 1p/19q-codeletion status using preoperative MR imaging phenotypes in lower grade gliomas.** *AJNR Am J Neuroradiol* 2018;39:37–42 CrossRef Medline
- Patel SH, Poisson LM, Brat DJ, et al. **T2-FLAIR mismatch, an imaging biomarker for IDH and 1p/19q status in lower-grade gliomas: a TCGA/TCIA project.** *Clin Cancer Res* 2017;23:6078–85 CrossRef Medline
- Broen MP, Smits M, Wijnenga MM, et al. **The T2-FLAIR mismatch sign as an imaging marker for non-enhancing IDH-mutant, 1p/19q-intact lower-grade glioma: a validation study.** *Neuro Oncol* 2018;20:1393–99 CrossRef Medline
- Jain R, Johnson DR, Patel SH, et al. **“Real world” use of a highly reliable imaging sign: “T2-FLAIR mismatch” for identification of IDH mutant astrocytomas.** *Neuro Oncol* 2020;22:936–43 CrossRef Medline
- Deguchi S, Oishi T, Mitsuya K, et al. **Clinicopathological analysis of T2-FLAIR mismatch sign in lower-grade gliomas.** *Sci Rep* 2020;10:10113 CrossRef Medline
- Onishi S, Amatya VJ, Kolakshyapati M, et al. **T2-FLAIR mismatch sign in dysembryoplasticneuroepithelial tumor.** *Eur J Radiol* 2020;126:108924 CrossRef Medline
- Johnson DR, Kaufmann TJ, Patel SH, et al. **There is an exception to every rule-T2-FLAIR mismatch sign in gliomas.** *Neuroradiology* 2019;61:225–27 CrossRef Medline
- Lu J, Li X, Li H. **Perfusion parameters derived from MRI for preoperative prediction of IDH mutation and MGMT promoter methylation status in glioblastomas.** *Magn Reson Imaging* 2021;83:189–95 CrossRef Medline
- Li Z, Zhao W, He B, et al. **Application of distributed parameter model to assessment of glioma IDH mutation status by dynamic contrast-enhanced magnetic resonance imaging.** *Contrast Media Mol Imaging* 2020;2020:8843084 CrossRef Medline
- Mancini L, Casagrande S, Gautier G, et al. **CEST MRI provides amide/amine surrogate biomarkers for treatment-naïve glioma sub-typing.** *Eur J Nucl Med Mol Imaging* 2022;49:2377–91 CrossRef Medline
- Rohwer N, Zasada C, Kempa S, et al. **The growing complexity of HIF-1 α 's role in tumorigenesis: DNA repair and beyond.** *Oncogene* 2013;32:3569–76 CrossRef Medline

29. Choi YS, Bae S, Chang JH, et al. **Fully automated hybrid approach to predict the IDH mutation status of gliomas via deep learning and radiomics.** *Neuro Oncol* 2021;23:304–13 CrossRef Medline
30. Lu CF, Hsu FT, Hsieh KL, et al. **Machine learning–based radiomics for molecular subtyping of gliomas.** *Clin Cancer Res* 2018;24:4429–36 CrossRef Medline
31. Chang P, Grinband J, Weinberg BD, et al. **Deep-learning convolutional neural networks accurately classify genetic mutations in gliomas.** *AJNR Am J Neuroradiol* 2018;39:1201–07 CrossRef Medline
32. Huang LE. **Impact of CDKN2A/B homozygous deletion on the prognosis and biology of IDH-mutant glioma.** *Biomedicines* 2022;10:246 CrossRef Medline
33. Marker DF, Pearce TM. **Homozygous deletion of CDKN2A by fluorescence in situ hybridization is prognostic in grade 4, but not grade 2 or 3 IDH-mutant astrocytomas.** *Acta Neuropathol Commun* 2020;8:169 CrossRef Medline
34. Paugh BS, Broniscer A, Qu C, et al. **Genome-wide analyses identify recurrent amplifications of receptor tyrosine kinases and cell-cycle regulatory genes in diffuse intrinsic pontine glioma.** *J Clin Oncol* 2011;29:3999–4006 CrossRef Medline
35. Chan KM, Fang D, Gan H, et al. **The histone H3.3K27M mutation in pediatric glioma reprograms H3K27 methylation and gene expression.** *Genes Dev* 2013;27:985–90 CrossRef Medline
36. Vallero SG, Bertero L, Morana G, et al. **Pediatric diffuse midline glioma H3K27- altered: a complex clinical and biological landscape behind a neatly defined tumor type.** *Front Oncol* 2022;12:1082062 CrossRef Medline
37. Zhang L, Wang R, Gao J, et al. **A novel MRI-based deep learning networks combined with attention mechanism for predicting CDKN2A/B homozygous deletion status in IDH-mutant astrocytoma.** *Eur Radiol* 2023;34:391–99 CrossRef Medline
38. Gao J, Liu Z, Pan H, et al. **Preoperative discrimination of CDKN2A/B homozygous deletion status in isocitrate dehydrogenase-mutant astrocytoma: a deep learning-based radiomics model using MRI.** *J Magn Reson Imaging* 2023 Aug 9. [Epub ahead of print] CrossRef Medline
39. Park YW, Park KS, Park JE, et al. **Qualitative and quantitative magnetic resonance imaging phenotypes may predict CDKN2A/B homozygous deletion status in isocitrate dehydrogenase-mutant astrocytomas: a multicenter study.** *Korean J Radiol* 2023;24:133–44 CrossRef Medline
40. Zhao JP, Liu XJ, Lin HZ, et al. **MRI comparative study of diffuse midline glioma, H3 K27-altered and glioma in the midline without H3 K27-altered.** *BMC Neurol* 2022;22:498 CrossRef Medline
41. Kurokawa R, Kurokawa M, Baba A, et al. **Dynamic susceptibility contrast-MRI parameters, ADC values, and the T2-FLAIR mismatch sign are useful to differentiate between H3-mutant and H3-wild-type high-grade midline glioma.** *Eur Radiol* 2022;32:3672–82 CrossRef Medline
42. Aboian MS, Solomon DA, Felton E, et al. **Imaging characteristics of pediatric diffuse midline gliomas with histone H3 K27M mutation.** *AJNR Am J Neuroradiol* 2017;38:795–800 CrossRef Medline
43. Chung C, Sweha SR, Pratt D, et al. **Integrated metabolic and epigenomic reprogramming by H3K27M mutations in diffuse intrinsic pontine gliomas.** *Cancer Cell* 2020;38:334–49.e9 CrossRef Medline
44. Eskilsson E, Rösland GV, Solecki G, et al. **EGFR heterogeneity and implications for therapeutic intervention in glioblastoma.** *Neuro Oncol* 2018;20:743–52 CrossRef Medline
45. Rizzo S, Botta F, Raimondi S, et al. **Radiomics: the facts and the challenges of image analysis.** *Eur Radiol Exp* 2018;2:36 CrossRef Medline
46. Wei J, Yang G, Hao X, et al. **A multi-sequence and habitat-based MRI radiomics signature for preoperative prediction of MGMT promoter methylation in astrocytomas with prognostic implication.** *Eur Radiol* 2019;29:877–88 CrossRef Medline
47. Rathore S, Akbari H, Rozycki M, et al. **Radiomic MRI signature reveals three distinct subtypes of glioblastoma with different clinical and molecular characteristics, offering prognostic value beyond IDH1.** *Sci Rep* 2018;8:5087 CrossRef Medline
48. Yogananda CG, Shah BR, Nalawade SS, et al. **MRI-based deep-learning method for determining glioma MGMT promoter methylation status.** *AJNR Am J Neuroradiol* 2021;42:845–52 CrossRef Medline
49. Kim BH, Lee H, Choi KS, et al. **Validation of MRI-based models to predict MGMT promoter methylation in gliomas: BraTS 2021 radiogenomics challenge.** *Cancers (Basel)* 2022;14:14 CrossRef Medline
50. Hu LS, Wang L, Hawkins-Daarud A, et al. **Uncertainty quantification in the radiogenomics modeling of EGFR amplification in glioblastoma.** *Sci Rep* 2021;11:3932 CrossRef Medline
51. Li Y, Liu X, Xu K, et al. **MRI features can predict EGFR expression in lower grade gliomas: a voxel-based radiomic analysis.** *Eur Radiol* 2018;28:356–62 CrossRef Medline
52. Kihira S, Tsankova NM, Bauer A, et al. **Multiparametric MRI texture analysis in prediction of glioma biomarker status: added value of MR diffusion.** *Neurooncol Adv* 2021;3:vda051 CrossRef Medline
53. Gupta A, Young RJ, Shah AD, et al. **Pretreatment dynamic susceptibility contrast MRI perfusion in glioblastoma: prediction of EGFR gene amplification.** *Clin Neuroradiol* 2015;25:143–50 CrossRef Medline
54. Gu Z, Eils R, Schlesner M. **Complex heatmaps reveal patterns and correlations in multidimensional genomic data.** *Bioinformatics* 2016;32:2847–49 CrossRef Medline
55. Ringnér M. **What is principal component analysis?** *Nat Biotechnol* 2008;26:303–04 CrossRef Medline
56. Akbari H, Bakas S, Pisapia JM, et al. **In vivo evaluation of EGFRvIII mutation in primary glioblastoma patients via complex multiparametric MRI signature.** *Neuro Oncol* 2018;20:1068–79 CrossRef Medline
57. Bakas S, Akbari H, Pisapia J, et al. **In vivo detection of EGFRvIII in glioblastoma via perfusion magnetic resonance imaging signature consistent with deep peritumoral infiltration: the φ -index.** *Clin Cancer Res* 2017;23:4724–34 CrossRef Medline
58. Nabors LB, Portnow J, Ahluwalia M, et al. **Central nervous system cancers, Version 3.2020, NCCN Clinical Practice Guidelines in Oncology.** *J Natl Compr Canc Netw* 2020;18:1537–70 CrossRef Medline
59. Stupp R, Taillibert S, Kanner A, et al. **Effect of tumor-treating fields plus maintenance temozolomide vs maintenance temozolomide alone on survival in patients with glioblastoma: a randomized clinical trial.** *JAMA* 2017;318:2306–16 CrossRef Medline
60. Pekmezci M, Morshed RA, Chunduru P, et al. **Detection of glioma infiltration at the tumor margin using quantitative stimulated Raman scattering histology.** *Sci Rep* 2021;11:12162 CrossRef Medline
61. Chang PD, Malone HR, Bowden SG, et al. **A multiparametric model for mapping cellularity in glioblastoma using radiographically localized biopsies.** *AJNR Am J Neuroradiol* 2017;38:890–98 CrossRef Medline
62. Akbari H, Macyszyn L, Da X, et al. **Imaging surrogates of infiltration obtained via multiparametric imaging pattern analysis predict subsequent location of recurrence of glioblastoma.** *Neurosurgery* 2016;78:572–80 CrossRef Medline
63. Tian H, Wu H, Wu G, et al. **Noninvasive prediction of TERT promoter mutations in high-grade glioma by radiomics analysis based on multiparameter MRI.** *Biomed Res Int* 2020;2020:3872314 CrossRef Medline
64. Abdollahi H, Chin E, Clark H, et al. **Radiomics-guided radiation therapy: opportunities and challenges.** *Phys Med Biol* 2022;67 CrossRef Medline
65. Lim M, Weller M, Idbaih A, et al. **Phase III trial of chemoradiotherapy with temozolomide plus nivolumab or placebo for newly diagnosed glioblastoma with methylated MGMT promoter.** *Neuro Oncol* 2022;24:1935–49 CrossRef Medline
66. Omuro A, Brandes AA, Carpentier AF, et al. **Radiotherapy combined with nivolumab or temozolomide for newly diagnosed glioblastoma with unmethylated MGMT promoter: an international randomized phase III trial.** *Neuro Oncol* 2023;25:123–34 CrossRef Medline
67. Cloughesy TF, Mochizuki AY, Orpilla JR, et al. **Neoadjuvant anti-PD-1 immunotherapy promotes a survival benefit with intratumoral**

- and systemic immune responses in recurrent glioblastoma. *Nat Med* 2019;25:477–86 CrossRef Medline
68. George E, Flagg E, Chang K, et al. **Radiomics-based machine learning for outcome prediction in a multicenter Phase II study of programmed death-ligand 1 inhibition immunotherapy for glioblastoma.** *AJNR Am J Neuroradiol* 2022;43:675–81 CrossRef Medline
69. Khalili N, Kazerooni AF, Familiar A, et al. **Radiomics for characterization of the glioma immune microenvironment.** *NPJ Precis Oncol* 2023;7:59 CrossRef Medline
70. Tomaszewski MR, Gillies RJ. **The biological meaning of radiomic features.** *Radiology* 2021;298:505–16 CrossRef Medline
71. O'Connor JP, Rose CJ, Waterton JC, et al. **Imaging intratumor heterogeneity: role in therapy response, resistance, and clinical outcome.** *Clin Cancer Res* 2015;21:249–57 CrossRef Medline
72. Henning EC, Azuma C, Sotak CH, et al. **Multispectral quantification of tissue types in a RIF-1 tumor model with histological validation: Part I.** *Magn Reson Med* 2007;57:501–12 CrossRef Medline
73. Carano RA, Ross AL, Ross J, et al. **Quantification of tumor tissue populations by multispectral analysis.** *Magn Reson Med* 2004;51:542–51 CrossRef Medline
74. Park JE, Kim HS, Goh MJ, et al. **Pseudoprogression in patients with glioblastoma: assessment by using volume-weighted voxel-based multiparametric clustering of MR imaging data in an independent test set.** *Radiology* 2015;275:792–802 CrossRef Medline
75. Jardim-Perassi BV, Huang S, Dominguez-Viqueira W, et al. **Multiparametric MRI and coregistered histology identify tumor habitats in breast cancer mouse models.** *Cancer Res* 2019;79:3952–64 CrossRef Medline
76. Furnari FB, Cloughesy TF, Cavenee WK, et al. **Heterogeneity of epidermal growth factor receptor signalling networks in glioblastoma.** *Nat Rev Cancer* 2015;15:302–10 CrossRef Medline
77. Kim M, Park JE, Kim HS, et al. **Spatiotemporal habitats from multiparametric physiologic MRI distinguish tumor progression from treatment-related change in post-treatment glioblastoma.** *Eur Radiol* 2021;31:6374–83 CrossRef Medline

Artificial Intelligence in the Future Landscape of Pediatric Neuroradiology: Opportunities and Challenges

 Aashim Bhatia,  Farzad Khalvati, and  Birgit Betina Ertl-Wagner



ABSTRACT

SUMMARY: This paper will review how artificial intelligence (AI) will play an increasingly important role in pediatric neuroradiology in the future. A safe, transparent, and human-centric AI is needed to tackle the quadruple aim of improved health outcomes, enhanced patient and family experience, reduced costs, and improved well-being of the healthcare team in pediatric neuroradiology. Equity, diversity and inclusion, data safety, and access to care will need to always be considered. In the next decade, AI algorithms are expected to play an increasingly important role in access to care, workflow management, abnormality detection, classification, response prediction, prognostication, report generation, as well as in the patient and family experience in pediatric neuroradiology. Also, AI algorithms will likely play a role in recognizing and flagging rare diseases and in pattern recognition to identify previously unknown disorders. While AI algorithms will play an important role, humans will not only need to be in the loop, but in the center of pediatric neuroimaging. AI development and deployment will need to be closely watched and monitored by experts in the field. Patient and data safety need to be at the forefront, and the risks of a dependency on technology will need to be contained. The applications and implications of AI in pediatric neuroradiology will differ from adult neuroradiology.

ABBREVIATIONS: AI = artificial intelligence; LLM = large language models

“It is difficult to make predictions, especially about the future.” This quote has been attributed to many different people, most popularly to Mark Twain and Yogi Berra. There have been methodologic leaps in the evolution of artificial intelligence (AI) that have not been foreseen, even by experts in the field.¹ One of the most recent examples is the rapid development and unprecedented impact of ChatGPT and other large language models (LLMs), the success of which had not been foreseen, at least not at that time and to that extent. A search with the key word “ChatGPT” on PubMed on August 18, 2023, rendered 4 publications in 2022 and 1046 publications in 2023 to date.² LLMs are currently causing major discussions on the future of medical scientific publishing.³ Of note, this article has not been written with the help of LLMs, such as ChatGPT.

ChatGPT produces references that are fake and may initially appear legitimate. A significant amount of time can be spent to search for these falsified articles.⁴ This provides an opportunity to

teach LLM what is a true reference and an example of continued learning of the LLM, which requires human intervention. An author of this paper had a similar experience with ChatGPT3; it needs to be noted that ChatGPT4 has been released and is more advanced with fewer errors.

There is general agreement that AI will positively influence the field of radiology. This has evolved from an initial fear that radiologists would be replaced by AI to a more nuanced understanding and embracing of the methodology.⁵ The influence of AI on the field of pediatric neuroradiology will be different from its impact on general radiology and even different from its impact on adult neuroradiology, where advances are being made especially in disorders with a high disease prevalence such as stroke.^{6,7} There are several reasons for this, included in the Table.

Currently, only a relatively small percentage of neuroradiologists spend 100% of their clinical time on pediatric neuroradiology. The impact of AI software customized to pediatric neuroradiology will affect a smaller pool of neuroradiologists compared with software focused on adult pathologies, such as neurodegenerative diseases, and there is less commercial interest from companies to develop software dedicated to pediatric neuroradiology. However, the impact on healthcare outcomes can be highly relevant, especially in settings in which there is only limited pediatric neuroradiology expertise.

Received August 22, 2023; accepted after revision October 17.

From the Children’s Hospital of Philadelphia (A.B.), Philadelphia, Pennsylvania; and Hospital for Sick Children (F.K., B.B.E.-W.), Toronto, Ontario, Canada.

Please address correspondence to Aashim Bhatia, MD, Children’s Hospital of Philadelphia, Department of Radiology, Division of Neuroradiology, 3500 Civic Center Blvd, Office 2592, Philadelphia, PA 19104; e-mail: aashimhatia@gmail.com

 Indicates article with online supplemental data.

<http://dx.doi.org/10.3174/ajnr.A8086>

Reasons for a differing impact of artificial intelligence on pediatric neuroradiology compared with adult neuroradiology

- Lower number of pediatric neuroradiologists
- High degree of subspecialization
- Rapid evolution of the field with an evolving understanding of the molecular and genetic underpinnings of disorders
- Wide spectrum of neurologic disorders in the pediatric age range
- Differing neuroimaging manifestations of disorders depending on age
- Small sample sizes of rare neuropediatric disorders, especially when considering subcategories/molecular subtypes
- More rare and orphan diseases in the pediatric age range
- Rapid evolution of targeted therapeutic approaches for precision child health

We strongly believe that AI in pediatric neuroradiology not only requires a “human in the loop,” but humans in the center.⁸ AI in pediatric neuroradiology needs to be patient-centered, family-centered, and physician/pediatric neuroradiologist-centered. AI in pediatric neuroradiology needs to be centered around the quadruple aim in health care, which encompasses⁹:

- improvement of health outcomes
- enhancement of the patient and family experience
- reduction of costs
- improvement of well-being of the health care team.

All these aims need to be based on the principles of equity, diversity, and inclusivity, and access to care needs to be a global consideration. The American College of Radiology has published on the safe, reliable, and effective use of AI in children.¹⁰

AI can and will help to achieve the quadruple aim in pediatric neuroradiology, but the development and deployment of its algorithms will need to be closely watched and monitored by experts in the field. Patient and data safety need to be at the forefront of all endeavors, and it will need to be ascertained that the risks of a dependency on technology will be contained.

AI algorithms will play an increasingly important role in access to care, workflow management, abnormality detection, classification, response prediction, prognostication, and report generation, as well as in the patient and family experience in pediatric neuroradiology in the years to come. The human aspect of pediatric neuroradiology will remain central, with a pediatric neuroradiologist being key to imaging interpretation. Pediatric patients currently require imaging at record high numbers due to improved imaging capabilities for diagnosis, and assessing and predicting treatment responses and this is likely to further increase in the future. More advanced imaging techniques, such as 7T MR imaging, chemical exchange saturation transfer, sodium MR imaging, and PET, will likely play an increasing role in the future, warranting the development of algorithms tailored to pediatric patients. Decreasing image acquisition times will allow for higher number of patients being examined. At the same time, the current shortage of radiologists qualified to interpret pediatric neuroradiology is not likely to reverse anytime soon and the strain on already challenged pediatric neuroradiology divisions is bound to increase (Online Supplemental Data).

Access to Pediatric Neuroimaging Care

On a global level, access to pediatric neuroimaging care is limited and we will need to increase our efforts to improve equitable

access. Reasons for these limitations in access are manifold and opportunities for AI to support are centered along various lines (Online Supplemental Data).

Workflow Management

Workflow management in pediatric neuroradiology is very complex as it requires a balancing of priorities in an often resource-restricted environment, a judicious use of various imaging modalities and image-guided treat-

ment approaches, and differing needs for emergency patients, inpatients, and outpatients. In addition, the requirement for sedation depending on the age and developmental stage of the patient and type of imaging examination or intervention adds a further layer of complexity as it requires coordination between various services, including anesthesiology, nursing, and pediatric neuroradiology, and risk levels need to be considered.¹¹ Often, several imaging examinations are combined under a single sedation. Traditionally, workflow management, including scheduling and rostering in pediatric neuroradiology, is largely dependent on humans often in interaction with dedicated software systems. AI algorithms can help facilitate workflow management in pediatric neuroradiology from various perspectives:

- Clinical decision support: AI-based clinical decision support systems can be trained on available demographic information and clinical data, to help in deciding whether imaging should be performed at all, in which timeframe it should be performed, and which imaging modality is best suited for the clinical indication in pediatric neuroradiology.
- Prioritization of examinations: AI algorithms can aid in prioritizing pediatric neuroimaging examinations according to urgency. This is especially important for situations in which there are long waitlists for imaging examinations and in which more urgent examination requests need to be scheduled for imaging, for example, based on ordering request details such as stat priority, history, neurologic status, and/or electronic medical record.
- Scanner and protocol selection: Based on the ordering comments and/or information from the electronic medical record, AI algorithms can help select the optimal scanner and imaging protocol for the individual patient’s indication.
- Scheduling: AI algorithms can help to optimally schedule patient examinations based on various criteria, including availability of a specific imaging modality and pediatric neuroradiologist, child life services, and/or pediatric anesthesiologist, as well as patient and family preferences.¹² They can help to ascertain that imaging examinations are optimally combined, which is especially important when sedation is needed.¹³ AI-assisted scheduling can also help in ensuring equitable access. It has been shown that the rate of no-shows and long waiting room times is not the same for all patients, and there are associations between these negative experiences and patient demographics.¹⁴ AI-assisted scheduling can make access to

pediatric (neuro)radiology more equitable, regardless of the socioeconomic status of patients.¹⁵

- **Prioritization of reporting:** Once images are acquired, AI algorithms can check for various urgent imaging findings which necessitate urgent or emergent reporting, such as hemorrhage, hydrocephalus, or impending herniation. If such an urgent or emergent imaging finding is present, the examinations can be flagged and the reporting pediatric neuroradiologist can be automatically alerted. In the future, AI algorithms may also be trained to flag the need for subspecialty reporting, in addition to indicating the degree of urgency.
- **Communication of urgent, emergent, or unexpected findings:** When urgent, emergent, or unexpected findings are found on pediatric neuroimaging, they need to be communicated to the referring provider. AI algorithms using natural language processing can screen radiological reports for indicators of urgent, emergent, or unexpected findings and either alert the reporting pediatric neuroradiologist to the necessity to communicate these or even prepare the communication, similarly to a reading room assistant.

Abnormality Detection

AI-based abnormality detection in pediatric neuroradiology is inherently different from adult neuroradiology as it will need to take the age and physiologic developmental stage of the child into account. Normal brain imaging in a neonate differs vastly from normal brain imaging in an adolescent, which makes the AI-based detection of a deviation from a typical developmental pattern more challenging. AI-based detection algorithms in pediatric neuroradiology will therefore need to rely on typical developmental trajectories for various imaging features and parameters. These may, among others, include myelination patterns and myelin volumes, global or focal brain parenchymal volumes, cortical thickness, CSF volumes, and sulcation patterns. One must also factor in brain development in premature neonates, which can be delayed for years after birth compared with term neonates.

In addition, AI-based abnormality detection can play an important role in identifying (and subsequently flagging) urgent and emergent imaging findings that require immediate attention, such as hemorrhage, acute ischemia, mass effect, or impending herniation. These detection algorithms can be more similar to AI algorithms in adult neuroradiology, but they nevertheless require consideration of the age and development of the child, which makes them more complex. A relatively large set of normal cases is usually required to train an abnormality-detection AI model, which learns the distribution of normal images. The deviation of a given image from the learned distribution of normal cases determines whether there is an abnormality in the image. This represents a semi-supervised AI algorithm where only normal cases are needed for training. Generative adversarial networks, and diffusion models have recently been used for abnormality detection for different disease, including brain tumors in adults.^{16,17}

AI-based anomaly detection algorithms can also be helpful in pattern recognition of previously unrecognized disorders. When a similar imaging pattern is detected in a large data base, clinical and genetic similarities can then be investigated.

Classification

AI-based classification tasks already play a role in pediatric neuro-radiology, and this is expected to grow in importance in the years to come. The classification of neuropediatric disorders has become markedly more complex in the last decade. One example for this is the classification of pediatric brain tumors, with the recent 5th edition of the WHO classification of CNS tumors being reflective of these molecular-driven changes.^{18,19} What used to be one tumor category (eg, “medulloblastoma”), is now divided into groups and subgroups based on molecular markers. AI algorithms must reflect this increasing complexity. They are expected to evolve along with the evolution of the molecular-based tumor classification, and AI researchers need to be well versed in these evolving classifications to remain clinically relevant. Molecular-based tumor classification can lead to individualized treatment planning, significantly improving patient outcome. Currently, the molecular landscape of brain tumors is more complex and heterogeneous in the pediatric age range compared with adults. At the same time, these tumors are less common and sample sizes are typically smaller, which is a challenge for AI algorithm development. AI-based classification algorithms are usually trained in a fully supervised manner where large enough sample sizes are needed for each of the classes (eg, tumor types). To overcome the small sample sizes in pediatric neuro-radiology, transfer learning may be considered. However, it has been shown that differences in MR imaging signal characteristics between pediatric and adult brain tumors pose a challenge for using transfer learning methods.²⁰ Therefore, more advanced generative adversarial network and transformer-based data augmentation methods may be needed to tackle this problem.^{21,22}

AI-based classification tasks are also important for other parts of pediatric neuroradiology, beyond tumor imaging. Examples include neuroinflammatory disorders, such as multiple sclerosis, neuromyelitis optica spectrum disorder, anti-MOG associated disease and autoimmune encephalitis, and metabolic disorders such as leukodystrophies. The classification of these disorders has also become more complex in the last decade, and AI algorithms will likely play an increasing role in their imaging-based classification.²³⁻²⁶

Prognostication

Deriving a prognosis based on imaging features is important for counseling and therapeutic decision making. AI-based algorithms can be trained to estimate molecular information, which in turn contains prognostic information.²⁷ On the other hand, AI can also directly predict prognostic information (eg, on overall survival, progression-free survival, or neurodevelopmental outcome), depending on the data with which the algorithms were trained.²⁸ Imaging-based prognostication with AI algorithms will likely become more important in pediatric neuroradiology in the next decade, especially in neuro-oncological imaging and neonatal imaging. The ability to predict prognosis of a neonate can help deliver earlier and more accurate treatment options, which can improve outcomes.

Treatment–Response Prediction

Treatment–response prediction at the earliest possible time point is of utmost importance for precision child health, and ultimately

for health outcomes. The earlier we know whether a neuropediatric disorder (eg, a brain tumor, a neuroinflammatory disease, or an epileptogenic lesion) responds to a given therapy or not, the earlier the treatment can be adapted. Ideally, treatment response could be predicted on pretherapeutic imaging, and the most effective therapy can be chosen beforehand.²⁹ Alternatively, AI-based response prediction can be performed on post treatment imaging. For the best efficacy, it will be important to know the optimal time window between initiation of therapy and treatment–response prediction, which will be different for different tumor types or disease entities — and possibly also will be different for different age groups. Follow-up imaging schedules as well as therapeutic regimens could then be individualized leading to a more precise and personalized treatment scheme, which will eventually help in containing healthcare costs.

Image-to-Image Translation

AI-based image-to-image translation algorithms have recently been shown to enable the creation of images of a different contrast or technique based on acquired images. These algorithms are trained on imaging examinations where both types of acquisitions or modalities were present. Examples are the generation of PET images from MR imaging examinations or of perfusion-weighted images from standard MR imaging sequences; both studies were in adults.^{30,31} These image-to-image translation techniques have been mostly studied in adult neuroradiology, but it is likely that they will play a bigger role in pediatric neuroradiology in the years to come. AI-based augmentation of data sets is another potential application for image-to-image translation. Given that pediatric neuroimaging generally lacks large data sets, and considering the prevalence of rare diseases or rare molecular subtypes, image-to-image-translation can be used to artificially increase the size of training sets for classification models.

Rare Diseases

AI applications for rare diseases are a challenge in pediatric neuroradiology as case numbers are low and often not sufficient for training, validating, and testing complex AI algorithms. Transfer learning and artificial augmentation of data sets may be helpful in this setting. In addition, AI algorithms can be helpful in identifying rare diseases among more common disorders and flag these for subspecialty consultation. An example would be the identification of a rare tumor type among more common tumors, for example, an embryonal tumor with multilayered rosettes among other pediatric embryonal brain tumors. Our understanding of the pathophysiology, imaging findings, and response patterns of these rare disorders are usually still quite limited, which is a challenge for developing AI algorithms.

In rare diseases that have yet to be discovered, imaging patterns may be flagged by AI algorithms that point pediatric neuro-radiologists to new disease entities, such as a metabolic disorder or leukodystrophy. This pattern-based approach can be based on institutional or multicentric databases or registries or may rely on publicly available imaging databases.^{32,33} This may not only allow the detection of new disease entities, but may also spark development of new therapeutic approaches.

AI Reliability in Pediatric Neuroradiology

To date, there is a large translational gap between the development of AI algorithms and actual clinical reality in radiology in general, but specifically in pediatric neuroradiology. One of the most important reasons for this disconnect is the elusive “black-box” nature of AI algorithms.³⁴ This translates into the absence of explainability in AI algorithms, which may lead to the lack of trust by pediatric neuroradiologists in AI algorithms. A human-centered AI workflow is required where 1) the results of AI algorithms are accurate, repeatable, and generalizable; 2) the AI results are adequately explainable and understandable by radiologists; 3) the radiologists can make a change to the AI algorithm (eg, changing the weight of loss function depending on the importance of input) or the input data (eg, changing the ROI), retrain the model, and monitor the results; and finally, 4) the radiologist’s feedback is taken into consideration by the AI algorithm to ensure perpetual improvement of the algorithm.

Integrating AI into a PACS

Currently, PACS systems do not provide a plugin mechanism for AI algorithms; thus, AI vendors must develop special interfaces for communication with PACS. This leads to stand-alone AI algorithms, which are not properly integrated with PACS systems, making their usability a challenge. Integration of AI algorithms into clinical practice requires a seamless integration into the hospital’s PACS systems, which requires a more AI-friendly interface for PACS systems.

CONCLUSIONS

AI will play an important role in pediatric neuroradiology in the next decade. Its impact will be different from adult neuroradiology, due to the high degree of subspecialization, lower number of pediatric neuroradiologists, wide spectrum of neuropediatric disorders with often relatively low case numbers, and age-dependent variation in imaging patterns. While AI algorithms will play an important role, humans will not only need to be in the loop, but in the center of pediatric neuroimaging.

Disclosure forms provided by the authors are available with the full text and PDF of this article at www.ajnr.org.

REFERENCES

1. Saboury B, Morris M, Siegel E. **Future directions in artificial intelligence.** *Radiol Clin North Am* 2021;59:1085–95 CrossRef Medline
2. Ray PP. **Re-evaluating the role of AI in scientific writing: a critical analysis on ChatGPT.** *Skeletal Radiol* 2023;52:2487–88 CrossRef Medline
3. Shen Y, Heacock L, Elias J, et al. **ChatGPT and other large language models are double-edged swords.** *Radiology* 2023;307:e230163 CrossRef Medline
4. Branum C, Schiavenato M. **Can ChatGPT accurately answer a PICOT question? Assessing AI response to a clinical question.** *Nurse Educ* 2023;48:231–33 CrossRef Medline
5. Rajpurkar P, Lungren MP. **The current and future state of AI interpretation of medical images.** *N Engl J Med* 2023;388:1981–90 CrossRef Medline
6. Yedavalli VS, Tong E, Martin D, et al. **Artificial intelligence in stroke imaging: current and future perspectives.** *Clin Imaging* 2021;69:246–54 CrossRef Medline

7. Soun JE, Chow DS, Nagamine M, et al. **Artificial intelligence and acute stroke imaging.** *AJNR Am J Neuroradiol* 2021;42:2–11 CrossRef Medline
8. Wagner MW, Namdar K, Biswas A, et al. **Radiomics, machine learning, and artificial intelligence: what the neuroradiologist needs to know.** *Neuroradiology* 2021;63:1957–67 CrossRef Medline
9. Valaitis RK, Wong ST, MacDonald M, et al. **Addressing quadruple aims through primary care and public health collaboration: ten Canadian case studies.** *BMC Public Health* 2020;20:507 CrossRef Medline
10. Sammer MB, Akbari YS, Barth RA, et al. **Use of artificial intelligence in radiology: impact on pediatric patients, a white paper from the ACR pediatric AI workgroup.** *J Am Coll Radiol* 2023;20:730–37 CrossRef Medline
11. Arlachov Y, Ganatra RH. **Sedation/anaesthesia in paediatric radiology.** *Br J Radiol* 2012;85:e1018–e1031 CrossRef Medline
12. Rajkomar A, Oren E, Chen K, et al. **Scalable and accurate deep learning with electronic health records.** *NPJ Digit Med* 2018;1:18 CrossRef Medline
13. Bush J. **How AI is taking the scut work out of health care.** *Harvard Business Rev* <https://hbr.org/2018/03/how-ai-is-taking-the-scut-work-out-of-health-care>
14. Taheri-Shirazi M, Namdar K, Ling K, et al. **Exploring potential barriers in equitable access to pediatric diagnostic imaging using machine learning.** *Front Public Health* 2023;11:968319 CrossRef Medline
15. Davenport T, Kalakota R. **The potential for artificial intelligence in healthcare.** *Future Healthc J* 2019;6:94–98 CrossRef Medline
16. Pinaya WH, Graham MS, Gray R, et al. **Fast unsupervised brain anomaly detection and segmentation with diffusion models.** *arXiv* 2022 CrossRef
17. Motamed S, Rogalla P, Khalvati F. **RANDGAN: randomized generative adversarial network for detection of COVID-19 in chest X-ray.** *Sci Rep* 2021;11:8602 CrossRef Medline
18. Kurokawa R, Kurokawa M, Baba A, et al. **Major changes in 2021 World Health Organization Classification of Central Nervous System Tumors.** *Radiographics* 2022;42:1474–93 CrossRef Medline
19. Bale TA, Rosenblum MK. **The 2021 WHO Classification of Tumors of the Central Nervous System: an update on pediatric low-grade gliomas and glioneuronal tumors.** *Brain Pathol* 2022;32:e13060 CrossRef Medline
20. Vafaekia P, Wagner MW, Hawkins C, et al. **MRI-based end-to-end pediatric low-grade glioma segmentation and classification.** *Can Assoc Radiol J* 2023;8465371231184780 CrossRef Medline
21. Esser P, Rombach R, Ommer B. **Taming transformers for high-resolution image synthesis.** *arXiv* 2020 CrossRef
22. Motamed S, Rogalla P, Khalvati F. **Data augmentation using Generative Adversarial Networks (GANs) for GAN-based detection of Pneumonia and COVID-19 in chest X-ray images.** *Inform Med Unlocked* 2021;27:100779 CrossRef Medline
23. Lin L, Dou Q, Jin YM, et al. **Deep learning for automated contouring of primary tumor volumes by MRI for nasopharyngeal carcinoma.** *Radiology* 2019;291:677–86 CrossRef Medline
24. Colen RR, Hassan I, Elshafeey N, et al. **Shedding light on the 2016 World Health Organization Classification of Tumors of the Central Nervous System in the Era of Radiomics and Radiogenomics.** *Magn Reson Imaging Clin North Am* 2016;24:741–49 CrossRef Medline
25. Forghani R. **Precision digital oncology: emerging role of radiomics-based biomarkers and artificial intelligence for advanced imaging and characterization of brain tumors.** *Radiol Imaging Cancer* 2020;2:e190047 CrossRef Medline
26. Kniep HC, Madesta F, Schneider T, et al. **Radiomics of brain MRI: utility in prediction of metastatic tumor type.** *Radiology* 2019;290:479–87 CrossRef Medline
27. Wagner MW, Hainc N, Khalvati F, et al. **Radiomics of pediatric low-grade gliomas: toward a pretherapeutic differentiation of BRAF-mutated and BRAF-fused tumors.** *AJNR Am J Neuroradiol* 2021;42:759–65 CrossRef Medline
28. Wagner MW, Namdar K, Napoleone M, et al. **Radiomic features based on MRI predict progression-free survival in pediatric diffuse midline glioma/diffuse intrinsic pontine glioma.** *Can Assoc Radiol J* 2023;74:119–26 CrossRef Medline
29. Hu Z, Jiang D, Zhao X, et al. **Predicting drug treatment outcomes in children with tuberous sclerosis complex-related epilepsy: a clinical radiomics study.** *AJNR Am J Neuroradiol* 2023;44:853–60 CrossRef Medline
30. Kao CH, Chen YS, Chen LF, et al. **Demystifying T1-MRI to FDG [18]-PET image translation via representational similarity.** In: de Bruijne M, Cattin PC, Cotin S, et al. eds. *Medical Image Computing and Computer Assisted Intervention: MICCAI 2021: 24th International Conference, Strasbourg, France, September 27–October 1, 2021, Proceedings, Part III*. Vol 12903. Lecture notes in computer science. Berlin: Springer-Verlag 2021;402–412 CrossRef
31. Takita H, Matsumoto T, Tatekawa H, et al. **AI-based virtual synthesis of methionine PET from contrast-enhanced MRI: development and external validation study.** *Radiology* 2023;308:e223016 CrossRef Medline
32. Nabavizadeh A, Barkovich MJ, Mian A, et al. **Current state of pediatric neuro-oncology imaging, challenges and future directions.** *Neoplasia* 2023;37:100886 CrossRef Medline
33. Kazerooni AF, Arif S, Madhogarhia R, et al. **Automated tumor segmentation and brain tissue extraction from multiparametric MRI of pediatric brain tumors: a multi-institutional study.** *medRxiv* 2023 CrossRef
34. Reyes M, Meier R, Pereira S, et al. **On the interpretability of artificial intelligence in radiology: challenges and opportunities.** *Radiol Artif Intell* 2020;2:e190043 CrossRef Medline

Implementation of a Clinical Vessel Wall MR Imaging Program at an Academic Medical Center

 Jae W. Song, Megan Y. Frame, Rob T. Sellers, Connie Klahn, Kevin Fitzgerald, Bridget Pomponio, Mitchell D. Schnall,  Scott E. Kasner, and Laurie A. Loevner



ABSTRACT

BACKGROUND AND PURPOSE: The slow adoption of new advanced imaging techniques into clinical practice has been a long-standing challenge. Principles of implementation science and the reach, effectiveness, adoption, implementation, maintenance (RE-AIM) framework were used to build a clinical vessel wall imaging program at an academic medical center.

MATERIALS AND METHODS: Six phases for implementing a clinical vessel wall MR imaging program were contextualized to the RE-AIM framework. Surveys were designed and distributed to MR imaging technologists and clinicians. Effectiveness was measured by surveying the perceived diagnostic value of vessel wall imaging among MR imaging technologists and clinicians, trends in case volumes in the clinical vessel wall imaging examination, and the number of coauthored vessel wall imaging–focused publications and abstracts. Adoption and implementation were measured by surveying stakeholders about workflow. Maintenance was measured by surveying MR imaging technologists on the value of teaching materials and online tip sheets. The Integration dimension was measured by the number of submitted research grants incorporating vessel wall imaging protocols. Feedback during the implementation phases and solicited through the survey is qualitatively summarized. Quantitative results are reported using descriptive statistics.

RESULTS: Six phases of the RE-AIM framework focused on the following: 1) determining patient and disease representation, 2) matching resource availability and patient access, 3) establishing vessel MR wall imaging (VWI) expertise, 4) forming interdisciplinary teams, 5) iteratively refining workflow, and 6) integrating for maintenance and scale. Survey response rates were 48.3% (MR imaging technologists) and 71.4% (clinicians). Survey results showed that 90% of the MR imaging technologists agreed that they understood how vessel wall MR imaging adds diagnostic value to patient care. Most clinicians (91.3%) reported that vessel wall MR imaging results changed their diagnostic confidence or patient management. Case volumes of clinical vessel wall MR imaging performed from 2019 to 2022 rose from 22 to 205 examinations. Workflow challenges reported by MR imaging technologists included protocoling examinations and scan length. Feedback from ordering clinicians included the need for education about VWI indications, limitations, and availability. During the 3-year implementation period of the program, the interdisciplinary teams coauthored 27 publications and abstracts and submitted 13 research grants.

CONCLUSIONS: Implementation of a clinical imaging program can be successful using the principles of the RE-AIM framework. Through iterative processes and the support of interdisciplinary teams, a vessel wall MR imaging program can be integrated through a dedicated clinical pipeline, add diagnostic value, support educational and research missions at an academic medical center, and become a center for excellence.

ABBREVIATIONS: RE-AIM = reach, effectiveness, adoption, implementation, maintenance; VWI = vessel wall MR imaging

Vessel wall MR imaging (VWI) is an emerging technique for vasculopathy assessment. The primary clinical application is to differentiate among vasculopathies that cause stroke such as atherosclerosis, vasculitis, and arterial dissections.^{1,2} VWI was

first introduced in the mid-1990s.^{3,4} However, even after nearly 30 years, a recent American Society of Neuroradiology (ASNR) Vessel Wall MR Imaging Study Group survey querying the clinical adoption of this technique across an international group of neuroradiologists showed that only 52% of survey respondents

Received November 22, 2023; accepted after revision January 12, 2024.

From the Departments of Radiology (J.W.S., M.Y.F., R.T.S., B.P., M.D.S., L.A.L.), and Neurology (S.E.K.), Hospital of the University of Pennsylvania, Philadelphia, Pennsylvania; Department of Radiology (C.K.), Penn Presbyterian Hospital, Philadelphia, Pennsylvania; and Department of Radiology (K.F.), Penn Radnor, Philadelphia, Pennsylvania.

J.W. Song is supported by the American Heart Association (938082).

Please address correspondence to Jae W. Song, MD, MS, Hospital of the University of Pennsylvania, 3400 Spruce St, Philadelphia, PA 19104; e-mail: jae.song@penncmedicine.upenn.edu; @jsongmd

 Indicates article with online supplemental data.

<http://dx.doi.org/10.3174/ajnr.A8191>

Six phases contextualized to the RE-AIM framework

Domain	Goals	Measures
Phase 1: Reach domain Phase 2: Reach domain Phase 3: Effectiveness domain Phase 4: Effectiveness domain	Patient and disease representativeness Patient access and facility resources Establishing radiology VWI expertise Interdisciplinary teams focused on patient care and education	Systematic reviews of the literature Survey: VWI adds diagnostic value for patient care (clinicians and MR imaging technologists) Clinical volume: annual trends in clinical VWI examinations Academic-education metrics: coauthored publications and abstracts
Phase 5: Adoption and Implementation domains	Establishing workflow, effective communication, and best practices	Survey: ease of ordering a clinical VWI (clinicians) Survey: ease of selecting a specific VWI protocol and ease of scanning a patient for VWI (MR imaging technologists)
Phase 6: Maintenance domain	Integration and Scale	Survey: value of online tip sheets and training materials (MR imaging technologists) Academic-research metrics: grants submitted

reported that their institution performed clinical VWI.⁵ The survey identified a need for educational and technical expertise and support to overcome the slow rate of clinical adoption. Understanding strategies to enhance the adoption process of new techniques and applications is needed, particularly as the next wave of innovative imaging and artificial intelligence–aided applications is fused into clinical practice.

The failure rates for implementing innovations in medicine range from 30% to 90%.^{6–8} The translation of scientific discoveries and innovations has been called attempts to bridge over the “valley of death”⁹ and the implementation effort as a “failure to launch.”¹⁰ The cost in resources, time, and loss of potential benefit to patients is enormous. Recognizing a need to support translational bridges, the National Institutes of Health funded the Clinical and Translational Award Program in 2006 with >60 participating institutions by 2012. Frameworks were also designed to speed the translation of research discovery and promote the effective adoption of evidence-based interventions to improve patient care and health. Reach, effectiveness, adoption, implementation, and maintenance (RE-AIM; <https://re-aim.org/>) is one such framework.¹¹ We applied the RE-AIM framework to plan and evaluate a new clinical vessel wall MR imaging program at an academic medical center. Effectiveness, adoption and implementation of the VWI program were measured through quality-improvement surveys among key stakeholders. We report best practices and how interdisciplinary teams were established leading to the successful scaling of this imaging program.

MATERIALS AND METHODS

The RE-AIM framework served as the implementation science framework for this initiative.¹² This project was conducted between 2019 and March 30, 2023, and was reviewed and qualified as quality improvement by the University of Pennsylvania institutional review board. The Standards for Quality Improvement Reporting Excellence 2.0 guidelines were reviewed to report this practice improvement.¹³

Processes and pitfalls for six phases based on the RE-AIM framework are detailed in the Table. These six phases comprise of assessing patient and disease representativeness, patient access and

facility resources (Reach domain), establishing radiology VWI expertise and interdisciplinary teams focused on patient care and education (Effectiveness domain), establishing workflows, effective communication, and best practices (Adoption and Implementation domains), and integrating and scaling the program (Maintenance domain). Contextual elements that contributed to the success, failure, pitfalls, and efficiency are qualitatively summarized based on feedback from the users and stakeholders of the program.

Study Setting and Intervention

The clinical VWI exam was the intervention and was implemented at 3 acute-care hospitals and 3 outpatient imaging centers, all of which are part of the health system of the academic medical center. Within these 6 sites, the VWI protocols were built on seven 3T (Skyra, Skyra Fit, 3 Vida, 2 PRISMA Fit) and two 1.5T (Avanto Fit and Aera) Siemens MR imaging scanners. The VWI imaging protocols built on each MR imaging scanner included protocols optimized for intracranial, scalp, and cervical carotid and vertebral artery imaging to assess intracranial vasculopathies, giant cell arteritis, and cervical carotid plaque or dissections in the neck, respectively.

Domain Outcomes and Data Analysis

Assessment of the Reach and Effectiveness domains to establish patient and disease representativeness and radiologic expertise was based on systematic reviews of the literature by the interdisciplinary team as part of a planning stage. Two surveys were also designed and distributed to the ordering clinicians and MR imaging technologists to obtain data on the Effectiveness, Adoption and Implementation, and Maintenance domains (Table). On March 30, 2023, e-mail groups and Listservs were used to distribute the surveys on a Qualtrics platform (<https://www.qualtrics.com/platform/>) (Online Supplemental Data) followed by 2 e-mail reminders sent 1 and 4 weeks from the initial survey distribution. The effectiveness of diagnostic value added was measured by survey results reporting the perception of the value of VWI for patient care among the ordering clinicians and the MR technologists. We also measured VWI case-volume trends between 2019 and 2022 by tallying the number of VWI fit-for-purpose examination codes. The effectiveness of educational value added was

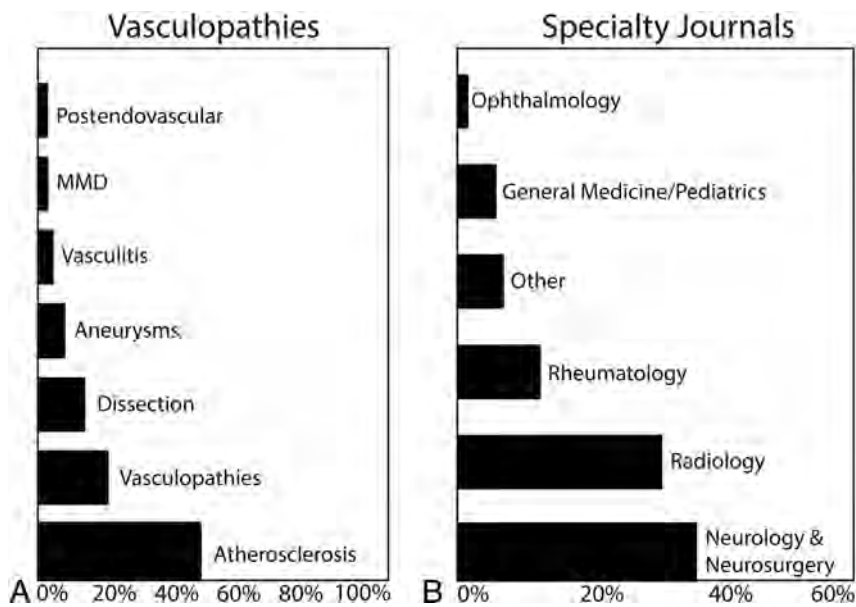


FIG 1. Reach domain: vasculopathy types and specialty journals. *A*, VWI and the types of vasculopathies for clinical and research applications. “Vasculopathies” include reversible cerebral vasoconstriction syndrome, vessel lesions, non-perimesencephalic hemorrhage, and radiation vasculopathy. MMD indicates Moyamoya disease/syndrome. *B*, Specialty journals that report on vasculopathies and vessel wall imaging findings. “Other” includes otolaryngology, infectious diseases, cardiology, oncology, and nephrology.

measured by trends in coauthored VWI-focused publications by the institutional interdisciplinary teams. Adoption and Implementation domains were measured by survey results among clinicians reporting the ease of ordering clinical VWI and the ease of selecting specific VWI protocols on MR imaging consoles and scanning a patient for VWI among MR imaging technologists. The Maintenance domain was measured by survey results about the value of the online tips sheets and training materials among MR imaging technologists to support scaling the program, and Integration was measured by the number of submitted research grants incorporating VWI by the interdisciplinary team. Qualitative results based on feedback from the clinicians and MR imaging technologists from the survey are summarized and provided insight into the implementation barriers. Quantitative results are reported in counts, percentages, and means.

RESULTS

Phase 1: Reach Domain—Patient and Disease Representativeness

We first identified the target patient populations and the clinical specialists who care for these patients. Two systematic reviews of the literature were conducted to identify the types of vasculopathies commonly imaged using VWI and specialty journals publishing cases imaged by VWI to identify interested specialists.^{14,15} The results indicated that atherosclerosis was the most commonly studied vasculopathy (Fig 1A);¹⁴ neurology and neurosurgery had the most published VWI studies (Fig 1B).¹⁵ Next, to identify institutional priorities, we evaluated our local patient population and specialties with VWI interests, which included vascular neurology, neurointerventional, neuro-ophthalmology, and rheumatology. This planning phase established our needs and goals.

Pitfalls. It was important to recognize a distinction between the use of VWI for clinical applications versus research. Tailored and efficient clinical MR imaging protocols were necessary to ensure diagnostic interpretations within a clinical MR imaging time slot. VWI protocols were not one-size-fits-all. Each protocol was designed with intention.¹⁶ Second, clinical subspecialists such as those in vascular neurology or neuro-ophthalmology often served as consultants who provided recommendations to internal medicine or emergency medicine care teams. Thus, there was a broader user base than anticipated, requiring communication and education across specialties.

Phase 2: Reach Domain—Patient Access and Facility Resources

Ensuring that VWI examinations are accessible to the target patient population was an important dimension of the Reach domain. Consistent with the principles of implementation science,

we assessed available hospital and outpatient imaging facility resources to meet patient and provider needs. This assessment required careful planning and support from our MR imaging technologists and department, because we had to assess scanner availability, patient scheduling and throughput, examination volume, and the bandwidth of the MR imaging technologists. For example, acute stroke care required the VWI protocols to be available on emergency and inpatient MR imaging scanners. However, outpatient VWI requests for follow-up examinations and rheumatologic work-ups required outpatient centers to have VWI protocols to accommodate requests.

Pitfalls. Due to the need for high-spatial-resolution imaging, 3T MR imaging scanners provide optimal quality to image the vessel walls. However, with the increasing recognition of the diagnostic value of VWI, there were requests for VWI for patients with pacemakers and discussions about hospital transfers solely to acquire VWI. The VWI protocols were thus built on 2 additional 1.5T MR imaging scanners to address this need.

Phase 3: Effectiveness—Establishing Radiology VWI Expertise

Establishing expertise as a neuroradiologist focused on 3 areas: imaging technique,¹⁶ disease and vasculopathy,^{14,15} and interpretation.^{15,17,18} Technical expertise required knowledge of VWI pulse sequences, protocols, and its limitations and optimizations.¹⁶ This expertise was acquired through the scientific literature and collaborations with MR imaging physicists. An optimized vessel wall imaging pulse sequence was used for the protocols. Disease expertise on the vasculopathy spectrum, clinical presentations, and imaging appearances was acquired through multidisciplinary collaborations, participation in multidisciplinary

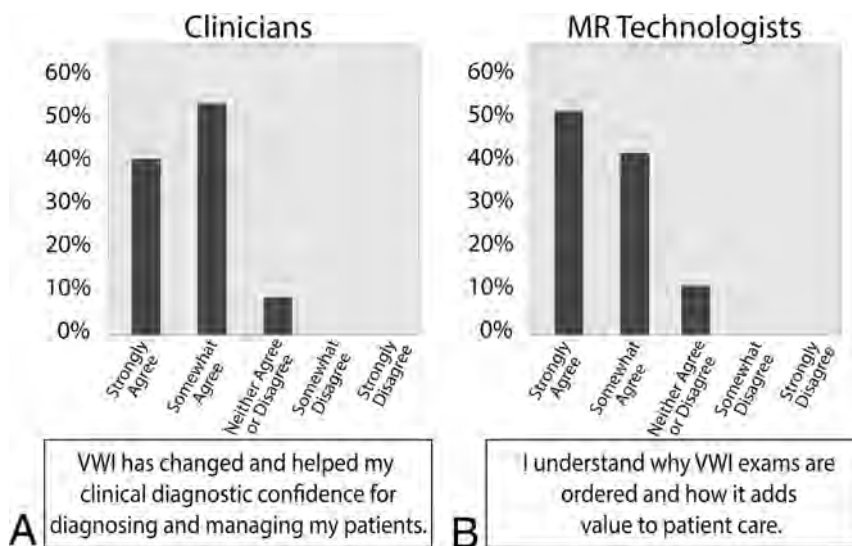


FIG 2. Effectiveness domain: perceived diagnostic value among MR technologists and clinicians. A, The reported perception of the understanding of the diagnostic value of VWI for patients among clinicians. B, The reported perception of the diagnostic value of vessel wall MR imaging for patient care among MR technologists.

clinical conferences and educational initiatives, and experience. Interpretive expertise was developed through the scientific literature,^{15,17,18} accruing experience by interpreting VWI cases, and participating in the ASNR Vessel Wall Imaging Study Group Webinars to learn from the collective experience of VWI experts.¹

Pitfalls. First, building the VWI protocols on the different scanners was an iterative and time-consuming process, given that many of the scanners differed in model, software, and magnet strength. This step was facilitated by all MR imaging scanners being Siemens products at our institution. Quality checks were still required and performed in an iterative fashion to ensure interpretable image quality on each scanner. MR imaging technologists and the Siemens Collaboration Manager were critical for these checks. Second, imaging patients with stroke and neurologic conditions often resulted in motion-degraded VWI. However, the ability to provide valuable and diagnostic image interpretations did not necessarily rely on perfect image quality. Rather, expertise about the disease and the evolution of imaging findings and post-treatment appearance was key. The initial focus on trying to achieve perfect image quality was, in retrospect, not as crucial for clinical applications. Nevertheless, this initiative had to be balanced with a need to conduct reproducible quantitative measurements for parallel research investigations.

Phase 4: Effectiveness—Multidisciplinary Teams Focused on Patient Care and Education

Identifying leaders and champions for the VWI program among the different stakeholder groups was imperative. Among the MR imaging technologists, an MR imaging educator and a Siemens MR Collaborations Manager led support for promoting the VWI program and addressed technical challenges. Lead technologists at each site also supported and promoted the program. Among the clinicians, VWI promoters emerged through

multidisciplinary engagement at case conferences and discussions included education about the utility of incorporating VWI. With challenging clinical cases, discussions about patient care naturally led to developing research questions together. Proactive engagement was through publications, preparation of research grants, lectures and case presentations to radiology, neurology, and internal medicine trainees, and grand rounds to the Department of Neurology.

Measures of Effectiveness

Response rates from the surveys from ordering clinicians were 71.4% ($n = 30$ of 42) and 48.3% ($n = 14$ of 29) from MR imaging technologists. Among the clinicians, 89.3% had previously ordered a VWI examination. Among clinicians who ordered VWI, 39.1% responded “Strongly Agree,” and 52.2%

responded “Somewhat Agree” to the statement, “Vessel wall MR imaging has changed and helped my clinical diagnostic confidence of diagnosing and managing my patients” (Fig 2A). Among the MR imaging technologists, 100% reported that they had scanned a patient for a VWI examination and 50% responded “Strongly Agree” and 40% responded “Somewhat Agree” to the statement, “I understand why vessel wall MR imaging examinations are ordered and how it adds value to patient care” (Fig 2B).

The number of clinical VWI examinations ordered and performed from January 1, 2019, to December 31, 2022, revealed increasing annual volumes rising from 22 to 205 examinations since the establishment of the program in 2019 (Fig 3).

The number of coauthored VWI publications and accepted abstracts by the local multidisciplinary teams trended from 2 (2019), 5 (2020), 8 (2021), to 12 (2022). This effort further promoted education about VWI and engaged the teams.

Pitfalls. As enthusiasm grew, VWI became incorporated into clinical practice algorithms. The incorporation of VWI demonstrated its value but required discussions about the appropriate use and limitations of resource-intensive MR imaging requests. These discussions highlighted a need for rigorous evidence-based effectiveness studies. A timely effort from the American College of Radiology is the formation of a committee to write a Vessel Wall Imaging Practice Parameters and Technical Standards white paper, which is currently in preparation.

Phase 5: Adoption and Implementation—Easy Workflows, Communication, and Best Practices

Adoption and Implementation strategies are facilitated when processes and communication are streamlined, and workflow disruptions are minimized.¹¹ Adoption strategies were iteratively reviewed with VWI program promoters. Informal and formal

feedback was proactively solicited for quality improvement to identify and address problems. Low-complexity processes, education, and engagement bring greater consistency in the delivery of a program and were our goal.¹⁹ Feedback from the survey results from clinicians indicated challenges with ordering examinations. Initially, VWI examinations were ordered as special requests after a 1:1 discussion between a clinician and a radiologist. Examinations were protocolled with typed-in instructions to the MR imaging technologists. With increasing requests, VWI fit-for-purpose examination codes were created for clinicians to order indication-specific VWI examinations. Ordering interfaces were designed with an order set to request vessel wall MR imaging and MRA examinations together. The fit-for-purpose codes facilitated communication. The clinical indication was evident in the examination name, which could be matched to the intended protocoling interface for the neuroradiologist and VWI protocol folders on the MR imaging consoles (Fig 4). This workflow improved communication and reduced phone calls for order clarifications

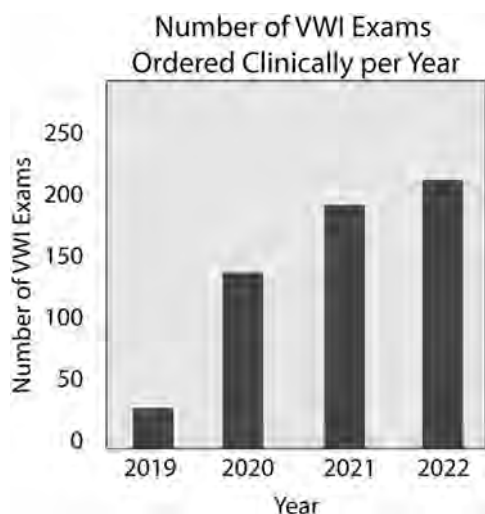


FIG 3. Effectiveness domain: annual number of VWI examinations (2019–2022). The annual number of vessel wall MR imaging examinations clinically ordered and performed from 2019 to 2022 increased from 22 (2019) to 205 (2022) VWI examinations.

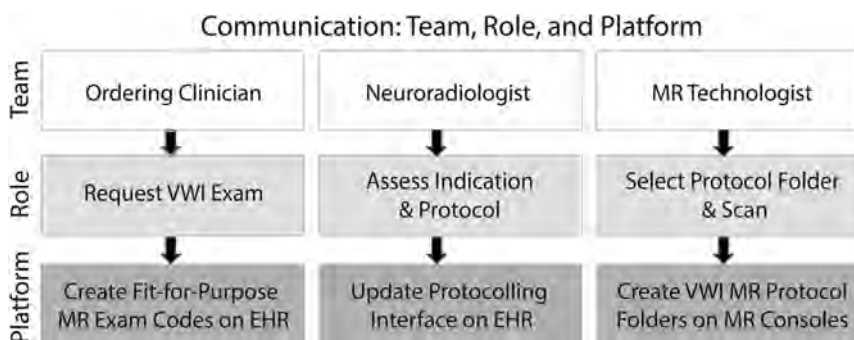


FIG 4. Communication: team, role, and platform. We identified the primary role of each team member (ordering clinician, neuroradiologist, and MR technologist) in the workflow and established a low-complexity platform for the team member to accomplish his or her task. This workflow improved communication between clinicians and radiologists and MR technologist and radiologists. EHR indicates electronic health record.

between ordering clinicians and radiologists and MR technologists and radiologists.

Educating and engaging the MR imaging technologists who performed the scanning and initial image quality control were paramount. A series of short educational lectures were given during staff meetings to explain VWI clinical indications and how to assess diagnostic image quality. During the initial stages of the program, the neuroradiologist was frequently called to check images. For all cases that were monitored by the neuroradiologist, personalized feedback was provided to the MR imaging technologist. Additionally, when possible, key annotated images and diagnoses were shared with both the clinician and scanning MR technologist. This process highlighted a patient care team for the imaging workflow, which comprised the clinician, the MR imaging technologist who had direct interaction with the patient, and the radiologist.

Measures of Adoption and Implementation: Ease of Workflow

Clinicians were surveyed about the ease of ordering VWI (Fig 5A), among whom 75% responded “Yes”. The survey feedback showed that clinicians wanted more education about VWI diagnostic indications, the limitations of the examinations, and a list of available sites that perform VWI.

MR imaging technologists were surveyed about the ease of VWI protocol selection on MR imaging consoles and scanning VWI examinations (Fig 5B). One hundred percent responded that it was easy to identify the VWI protocol folders on the MR imaging consoles. Two respondents reported that scanning VWI was challenging due to remembering coverage and field-of-views for some VWI pulse sequences. Feedback from the survey indicated that MR imaging technologists were concerned about challenges with long scan times and posed a request to protocol examinations in advance.

Pitfalls. As everyone gained more experience with VWI applications and indications were refined, VWI protocols were revised. As a result, a second iteration of the VWI fit-for-purpose examination codes was presented and approved. Initial examination codes were called “vessel wall,” which were subsequently revised to specify the clinical indications (eg, vessel wall vasculopathy, giant cell arteritis, or vessel wall dissection). Additionally, to accommodate new, rotating, and expanding work forces, an online website was created for instructions on ordering VWI by indication for clinicians and training materials on performing VWI scanning for MR imaging technologists.

Phase 6: Maintenance—Integration and Scale

The key to the sustainability of a program starts with recognizing that the new program addresses a clinical need, has purpose, and identifies knowledge gaps. Research questions were identified through ongoing discussions, especially

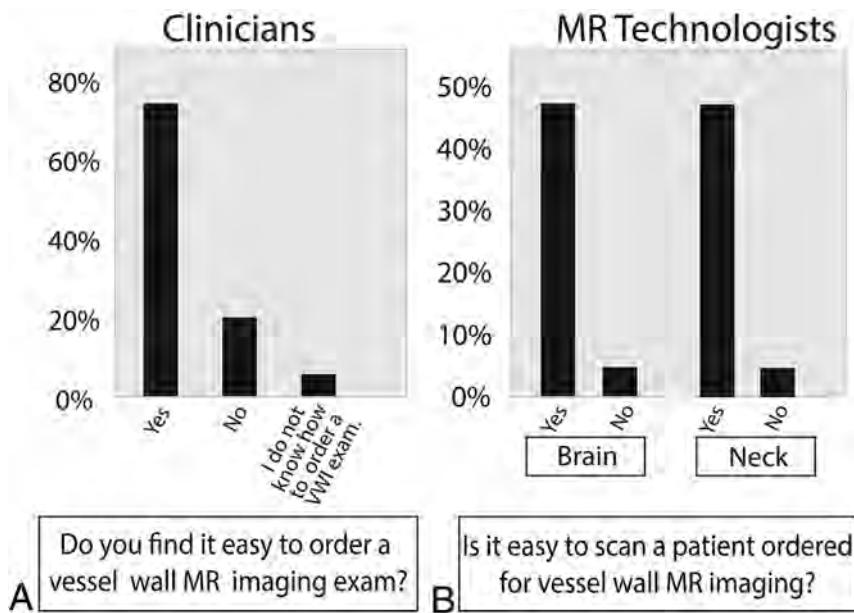


FIG 5. Adoption domain: ease of ordering VWI by clinicians and scanning by MR technologists. *A*, The reported perception of the ease of clinically ordering VWI among clinicians. *B*, The reported perception of the ease of scanning a VWI examination among MR technologists.

with challenging clinical cases. Between 2019 and 2022, thirteen research grants incorporating VWI protocols were submitted for institutional, foundational, or National Institutes of Health funding. This metric is an outcome measure reflecting the integration dimension of the VWI program into an academic mission.

Second, because the clinicians valued the vessel wall imaging program, after the infrastructure was built, needs continued to increase. Processes to scale the program were started to address this need. With a changing work force of MR imaging technologists, ongoing education for the technologists was important. Survey results from the MR imaging technologists indicated that 100% found the online VWI imaging protocol tip sheets and instructions helpful, given their accessibility. Additionally, a group of 7 neuroradiologists within the neuroradiology division with cerebrovascular and advanced imaging interests were identified to become VWI superusers and accrue experience. Reporting templates, case conferences, interpretation tip sheets, and a dedicated chat group were created to share cases, for questions, and to create a forum for dialogue. Enhancing comfort levels with protocoling and assessing appropriate use, evaluating image quality, and VWI interpretations were prioritized. At the onset of the rollout initiative among neuroradiologists, all were encouraged to share input and suggestions and foster discussion.

Pitfalls. Recognizing a neuroradiologist with expertise as a resource was important. Balancing the need to establish expertise by accruing experience through case volume and not diluting the experience were limitations to scaling. Conversely, consistency in image interpretation and minimizing long differential diagnoses and descriptive reports were also important for clinical adoption among clinicians at the beginning of the program. Interpretation tip sheets were created and VWI-focused case conferences were held to address this challenge. Another challenge was the clinical

application of VWI for stroke assessment. Stroke care is emergent. During the establishment of the clinical program, nearly all cases and queries were directed to 1 neuroradiologist to ensure consistency in reporting quality and instructions to clinicians and MR imaging technologists. Creation of accessible training materials and an instructional website and expanding the program with a group of superuser neuroradiologists reduced this need to be continuously available for all cases at all times.

DISCUSSION

The successful implementation of a clinical VWI program was driven by aligning initiatives in parallel across multiple stakeholders. First, we assessed clinical care needs, teams, and resources. Second, we built optimized VWI protocols and evidence-based content to deliver tailored images and diagnostic interpretations, respectively.

Third, we implemented the program through a low-complexity workflow, education, and continued engagement. High effectiveness was measured by most surveyed stakeholders reporting that VWI added diagnostic value to their patient care and manifested by the rising trends in VWI case volumes. Finally, we sustained the program by continuously refining our approach to create educational materials, evaluate outcomes, and expand the team of neuroradiologists to meet needs. The stages reflect the RE-AIM framework.

Several key strategies were identified during implementation. First, communication was key. Communication was written, verbal, and in person (eg, MR imaging technologist staff meetings and multidisciplinary conferences with clinicians). With the MR imaging technologists, personalized communication while providing oversight during real-time patient scanning was supplemented with face-to-face communication and short didactic lectures at staff meetings. These steps promoted connection. The survey showed that 90% of MR imaging technologists agreed that they understood how VWI added value to patient care. The teaching and communication during scanning and staff meetings most likely contributed to this understanding. Studies show that engagement and adherence to protocols are higher when one understands the purpose.²⁰ A sense of community, support, engagement, and adding value to patient care also serve to improve retention.²¹

Second, a low-complexity workflow was critical. Iterative improvements were made to facilitate clinical workflows for clinical teams and the MR imaging technologists. For example, specific VWI indications required tailored MR imaging protocols. As a result, VWI examination codes were renamed to match the indications, such as dissection, vasculopathy, or giant cell arteritis. Refining fit-for-purpose examination codes resulted in an easier workflow. For the MR imaging technologists,

an interface with protocol selection strategies was designed on the MR imaging console to facilitate VWI protocol identification. These steps likely explain why 100% of the MR imaging technologists reported that it was easy to identify named VWI protocol folders on the MR imaging consoles. Auto-protocolling these cases could be a consideration in the future to further reduce protocolling burden. Studies show that a barrier to implementation is a complex workflow or insisting on change when existing workflow is perceived sufficient.^{22,23} However, with new imaging programs and new tools, once the value is recognized, this perception of change as a barrier is altered and adoption is facilitated with streamlined workflows.

A barrier identified in the ASNR vessel wall imaging survey included the need for technical and vendor support for protocol development.⁵ An optimized intracranial VWI pulse sequence from a cerebrovascular MR imaging physicist collaborator was acquired,²⁴ and multiple protocol revisions on the clinical MR imaging scanners across the health system were supported by a clinical MR imaging educator, a Siemens applications specialist, and site-based lead MR imaging technologists. Diversifying and partnering with these teams were critical to the success of the imaging program.

The successful adoption and maintenance of the VWI program hinged on interpretations of the clinical report. Descriptions of vessel wall findings alone were inadequate because they provided little clinical context. Providing diagnostic interpretations relied on experience and expertise. Systematic reviews of the literature supplemented the experiential expertise. Understanding the disease process and imaging manifestations was a critical component of VWI interpretation and staying relevant. The VWI interpretations are the most likely reason that 91.3% of clinician survey respondents agreed to the statement, "Vessel wall MR imaging has changed and helped my clinical diagnostic confidence of diagnosing and managing my patients."

Several limitations of the implementation strategies of this program were based on the team experiences and survey feedback. Scope creep of an MR imaging protocol can lengthen the protocol time. We balanced innovation with clinically achievable strategies for diagnostic quality. Iterative protocol optimizations included trimming the number of pulse sequences as more diagnostic expertise was gained. A second limitation was resource allocation. The availability of neuroradiologists with expertise in VWI interpretation should be balanced with inpatients and emergency patients needing VWI 24–7. As the coronavirus 2019 (COVID-19) pandemic ended, awareness for changing management to effectively navigate resources was needed. Another consequence of the pandemic was a turnover of both clinicians and MR imaging technologists. This changing workforce required adaptability in the program. Creation and dissemination of training materials and resources were an efficient strategy. Finally, the low response rate to the surveys may be related to new staff unfamiliar with the program and prior years of iterative process changes. Nevertheless, 48% and 71% response rates among MR imaging technologists and clinicians are comparable and higher, respectively, than those in most physician surveys.^{25,26} The response rates also reflect the relatively small number of respondents due to the study being a single-center institutional experience.

CONCLUSIONS

We describe how to establish a new imaging program using the RE-AIM framework. The framework guided processes for implementation and highlights the importance of planning and iteratively refining processes while engaging all stakeholders. Survey results show that both clinicians and MR imaging technologists understood the diagnostic value of the VWI program. Engagement and understanding are associated with the Adoption and Implementation and Maintenance domains. Because the imaging program represents centralized knowledge and expertise, it can also drive innovation, efficiency, and excellence by addressing the patient care, education, and research missions of an academic medical center.

Disclosure forms provided by the authors are available with the full text and PDF of this article at www.ajnr.org.

REFERENCES

1. Mandell DM, Mossa-Basha M, Qiao Y, et al; Vessel Wall Imaging Study Group of the American Society of Neuroradiology. **Intracranial vessel wall MRI: principles and expert consensus recommendations of the American Society of Neuroradiology.** *AJNR Am J Neuroradiol* 2017;38:218–29 CrossRef Medline
2. Lindenholz A, van der Kolk AG, Zwanenburg JJM, et al. **The use and pitfalls of intracranial vessel wall imaging: how we do it.** *Radiology* 2018;286:12–28 CrossRef Medline
3. Kitanaka C, Tanaka J, Kuwahara M, et al. **Magnetic resonance imaging study of intracranial vertebral artery dissections.** *Stroke* 1994;25:571–75 CrossRef Medline
4. Aoki S, Shirouzu I, Sasaki Y, et al. **Enhancement of the intracranial arterial wall at MR imaging: relationship to cerebral atherosclerosis.** *Radiology* 1995;194:477–81 CrossRef Medline
5. Mossa-Basha M, Zhu C, Yuan C, et al. **Survey of the American Society of Neuroradiology Membership on the Use and Value of Intracranial Vessel Wall MRI.** *AJNR Am J Neuroradiol* 2022;43:951–57 CrossRef Medline
6. Alexander JA, Weiner BJ, Shortell SM, et al. **The role of organizational infrastructure in implementation of hospitals' quality improvement.** *Hosp Top* 2006;84:11–20 CrossRef Medline
7. Alexander JA, Hearld LR. **The science of quality improvement implementation: developing capacity to make a difference.** *Med Care* 2011;49(Suppl):S6–20 CrossRef Medline
8. Jacobs SR, Weiner BJ, Reeve BB, et al. **Determining the predictors of innovation implementation in healthcare: a quantitative analysis of implementation effectiveness.** *BMC Health Serv Res* 2015;15:6 CrossRef Medline
9. Butler D. **Translational research: crossing the valley of death.** *Nature* 2008;453:840–42 CrossRef Medline
10. Bottomley PA. **Barriers to technology translation in magnetic resonance to medicine.** *MAGMA* 2021;34:643–47 CrossRef Medline
11. Glasgow RE, Harden SM, Gaglio B, et al. **RE-AIM planning and evaluation framework: adapting to new science and practice with a 20-year review.** *Front Public Health* 2019;7:64 CrossRef Medline
12. Kwan BM, McGinnes HL, Ory MG, et al. **RE-AIM in the real world: use of the RE-AIM framework for program planning and evaluation in clinical and community settings.** *Front Public Health* 2019;7:345 CrossRef Medline
13. Ogrinc G, Davies L, Goodman D, et al. **SQUIRE 2.0 (Standards for Quality Improvement Reporting Excellence): revised publication guidelines from a detailed consensus process.** *Am J Med Qual* 2015;30:543–49 CrossRef Medline
14. Song JW, Guiry SC, Shou H, et al. **Qualitative assessment and reporting quality of intracranial vessel wall MR imaging studies: a systematic review.** *AJNR Am J Neuroradiol* 2019;40:2025–32 CrossRef Medline

15. Arnett N, Pavlou A, Burke MP, et al. **Vessel wall MR imaging of central nervous system vasculitis: a systematic review.** *Neuroradiology* 2021;64:43–58 CrossRef Medline
16. Song JW, Moon BF, Burke MP, et al. **MR intracranial vessel wall imaging: a systematic review.** *J Neuroimaging* 2020;30:428–42 CrossRef Medline
17. Song JW, Pavlou A, Xiao J, et al. **Vessel wall magnetic resonance imaging biomarkers of symptomatic intracranial atherosclerosis: a meta-analysis.** *Stroke* 2021;52:193–202 CrossRef Medline
18. Song JW, Pavlou A, Burke MP, et al. **Imaging endpoints of intracranial atherosclerosis using vessel wall MR imaging: a systematic review.** *Neuroradiology* 2021;63:847–56 CrossRef Medline
19. Foster D. **Strategies to Effectively Engage Learners Across the Enterprise.** [harvardbusiness.org](https://www.harvardbusiness.org/strategies-to-effectively-engage-learners-across-the-enterprise/). <https://www.harvardbusiness.org/strategies-to-effectively-engage-learners-across-the-enterprise/>. Accessed September 16, 2023
20. Santos S. **Employee Engagement: Our Favorite Reads.** [harvardbusiness.org](https://www.harvardbusiness.org/employee-engagement-our-favorite-reads/). <https://www.harvardbusiness.org/employee-engagement-our-favorite-reads/>. Accessed September 16, 2023
21. Tupper H, Ellis S. **It's Time to Reimagine Employee Retention.** [hbr.org](https://hbr.org/2022/07/its-time-to-reimagine-employee-retention). <https://hbr.org/2022/07/its-time-to-reimagine-employee-retention>. Accessed September 16, 2023
22. Spallek H, Song M, Polk DE, et al. **Barriers to implementing evidence-based clinical guidelines: a survey of early adopters.** *J Evid Based Dent Pract* 2010;10:195–206 CrossRef Medline
23. Fischer F, Lange K, Klose K, et al. **Barriers and strategies in guideline implementation: a scoping review.** *Healthcare (Basel)* 2016;4:36 CrossRef
24. Fan Z, Yang Q, Deng Z, et al. **Whole-brain intracranial vessel wall imaging at 3 Tesla using cerebrospinal fluid-attenuated T1-weighted 3D turbo spin-echo.** *Magn Reson Med* 2017;77:1142–50 CrossRef Medline
25. Cunningham CT, Quan H, Hemmelgarn B, et al. **Exploring physician specialist response rates to web-based surveys.** *BMC Med Res Methodol* 2015;15:32 CrossRef Medline
26. Cummings SM, Savitz LA, Konrad TR. **Reported response rates to mailed physician questionnaires.** *Health Serv Res* 2001;35:1347–55 Medline

Automated Assessment of the DWI-FLAIR Mismatch in Patients with Acute Ischemic Stroke: Added Value to Routine Clinical Practice

E. Tavakkol, S. Kihira, M. McArthur, J. Polson, H. Zhang, C. W. Arnold, B. Yoo, M. Linetsky, B. Salehi, L. Ledbetter, C. Kim, R. Jahan, G. Duckwiler, J. L. Saver, D. S. Liebeskind, and K. Nael

ABSTRACT

BACKGROUND AND PURPOSE: The DWI-FLAIR mismatch is used to determine thrombolytic eligibility in patients with acute ischemic stroke when the time since stroke onset is unknown. Commercial software packages have been developed for automated DWI-FLAIR classification. We aimed to use e-Stroke software for automated classification of the DWI-FLAIR mismatch in a cohort of patients with acute ischemic stroke and in a comparative analysis with 2 expert neuroradiologists.

MATERIALS AND METHODS: In this retrospective study, patients with acute ischemic stroke who had MR imaging and known time since stroke onset were included. The DWI-FLAIR mismatch was evaluated by 2 neuroradiologists blinded to the time since stroke onset and automatically by the e-Stroke software. After 4 weeks, the neuroradiologists re-evaluated the MR images, this time equipped with automated predicted e-Stroke results as a computer-assisted tool. Diagnostic performances of e-Stroke software and the neuroradiologists were evaluated for prediction of DWI-FLAIR mismatch status.

RESULTS: A total of 157 patients met the inclusion criteria. A total of 82 patients (52%) had a time since stroke onset of ≤ 4.5 hours. By means of consensus reads, 81 patients (51.5%) had a DWI-FLAIR mismatch. The diagnostic accuracy (area under the curve/sensitivity/specificity) of e-Stroke software for the determination of the DWI-FLAIR mismatch was 0.72/90.0/53.9. The diagnostic accuracy (area under the curve/sensitivity/specificity) for neuroradiologists 1 and 2 was 0.76/69.1/84.2 and 0.82/91.4/73.7, respectively; both significantly ($P < .05$) improved to 0.83/79.0/86.8 and 0.89/92.6/85.5, respectively, following the use of e-Stroke predictions as a computer-assisted tool. The interrater agreement (κ) for determination of DWI-FLAIR status was improved from 0.49 to 0.57 following the use of the computer-assisted tool.

CONCLUSIONS: This automated quantitative approach for DWI-FLAIR mismatch provides results comparable with those of human experts and can improve the diagnostic accuracies of expert neuroradiologists in the determination of DWI-FLAIR status.

ABBREVIATIONS: AIS = acute ischemic stroke; AUC = area under the curve; CAT = computer-assisted tool; ROC = receiver operating characteristic; rSIR = relative signal intensity ratio; TSS = time since stroke onset

In patients with acute ischemic stroke (AIS), the time since stroke onset (TSS) of < 4.5 hours has been used as a criterion for thrombolytic eligibility.¹ Recently, advanced imaging has played a critical role in showing that a greater number of patients may benefit from thrombolytic therapy when using a “tissue clock” concept rather than considering the TSS alone. For example, in the Extending the Time for Thrombolysis in Emergency Neurological Deficits (EXTEND) trial,² perfusion imaging was successfully used to extend the thrombolytic

window up to 9 hours in patients who had salvageable brain tissue.

The DWI-FLAIR mismatch has been used as a tissue clock imaging biomarker that may better guide the appropriate use of thrombolytic therapy than the TSS alone.^{1,3} Generally, stroke lesions become more visible on FLAIR images as time passes from stroke onset. This concept was used in the design of the Efficacy and Safety of MRI-based Thrombolysis in Wake-up Stroke: a Randomised, Double-blind, Placebo-controlled Trial (WAKE-UP),³ which showed the benefit of thrombolytic treatment in patients with AIS with unknown onset or wake-up stroke as long as they had a DWI-FLAIR mismatch. However, the DWI-FLAIR mismatch has some limitations. These include its subjective nature, which introduces variability among human interpreters, which may, in part, depend on the level of expertise. A binary reporting standard of negative or positive is also

Received September 14, 2023; accepted after revision January 12, 2024.

From the Departments of Radiological Sciences (E.T., S.K., M.M.J.P., H.Z., C.W.A., B.Y., M.L., B.S., L.L., C.K., R.J., G.D., K.N.) and Neurology (J.L.S., D.S.L.), University of California, Los Angeles, Los Angeles, California.

Please address correspondence to Kambiz Nael, MD, Department of Radiological Sciences, David Geffen School of Medicine at UCLA, 757 Westwood Plaza, Suite 1621, Los Angeles, CA, 90095-7532; e-mail: kambiznael@gmail.com; @kambiznael
<http://dx.doi.org/10.3174/ajnr.A8170>

limiting because the signal intensity difference between DWI and FLAIR often has a range and may be weakly positive or weakly negative rather than absolute. These limitations have resulted in modest interobserver agreement and diagnostic accuracies.^{4,5}

Advances in image segmentation and machine learning techniques have shown promising results in an automated analysis of MR images to determine the DWI-FLAIR status.⁶⁻⁸ In this study, we aimed to use an automated image-segmentation algorithm that is now commercially available (e-Stroke software; Brainomix) to automatically classify the DWI-FLAIR mismatch in a cohort of patients with AIS and to perform a comparative analysis with expert neuroradiologists. Specifically, we performed the following: 1) comparison of the diagnostic accuracy of e-stroke DWI-FLAIR mismatch output with that of expert neuroradiologists in the determination of the TSS; 2) assessment of the diagnostic accuracy of e-stroke DWI-FLAIR mismatch output in the prediction of the tissue clock as determined by consensus reads of 2 expert neuroradiologists; and 3) evaluation of the added value of e-Stroke DWI-FLAIR mismatch output when used as computer-assisted tool (CAT) to the diagnostic performance of expert neuroradiologists.

MATERIALS AND METHODS

Study Design and Patient Selection

In this retrospective study, consecutive patients with AIS who had pretreatment MR imaging and known TSS were included between September 2011 to August 2021. Institutional review board approval was obtained. The clinical characteristics such as age, sex, NIHSS, TSS, and location of the arterial occlusion if known were documented. Patients were excluded if they had an unknown or questionable TSS and poor MR image quality that impaired diagnostic evaluation by neuroradiologists.

Image Acquisition

MR imaging was performed on either a 1.5T MR imaging scanner (Avanto; Siemens) or a 3T MR imaging scanner (Magnetom Trio; Siemens) in our hospital. DWI was acquired using a single-shot spin-echo EPI sequence (TR/TE = 4900/98 ms [1.5T] or 4100/95 ms [3T]; FOV = 220 × 220 mm; matrix = 128 × 128 mm; slices = 30 × 5 mm). Diffusion gradients were applied along 3 orthogonal directions with $b=0$ and 1000 s/mm². The FLAIR images were acquired using a TR/TE = 9000/89 ms at 1.5T and 9000/122 ms at 3T; matrix = 256 × 256 mm; slices = 30 × 5 mm. The TI was 2504 ms at 1.5T and 2500 ms at 3T.

Image Analysis

For automated image analysis, MR diffusion and FLAIR images were uploaded to e-Stroke software (e-MRI module, Version 11.1; Brainomix) for automated image-processing and quantitative analysis. The software used an ADC threshold of 620 × 10⁻⁶ mm²/s to guide segmentation and generated a volume of interest that was used as an infarction mask.⁹ The FLAIR images were spatially realigned in 3D with the B₀ image from the DWI data set. The process of realignment used a standard 3D rigid registration to determine the image transformation function with 6 *df* consisting of 3 rotations and 3 translations.^{10,11} Then, the coregistered flipped FLAIR

images were used to compute the voxelwise relative FLAIR maps. The coregistered flipped FLAIR images were first smoothed with a 3D median filter (size: 7, 7, and 1 mm in x, y, z dimension). Tissue masks were generated by thresholding the B₀ image to remove the CSF. The threshold was obtained by a K-means algorithm to group the voxels within the brain mask region to 2 clusters (CSF range and tissue range).¹² For each voxel within the brain, the voxel value from the intensity-normalized FLAIR image was divided by the corresponding intensity value in its contralateral voxel and resulted in a relative FLAIR map. Voxel-based relative signal intensity ratios (rSIRs) from the infarction mask were computed and the values were reported as median and interquartile range within the infarction mask. Following calculation of rSIRs, the software automatically assigned each case as a match or mismatch using a median rSIR cutoff of ≥ 1.15 for a match.¹³

Two board-certified neuroradiologists (with 10 and 18 years of experience) blinded to the TSS and the results of automated analysis independently assessed the MR imaging studies to classify the DWI-FLAIR mismatch status for each patient. Mismatch was assigned when there was reduced diffusion on DWI with no signal on FLAIR, and match assignment was for cases in which there was corresponding FLAIR signal along the infarction territory. All disagreements were subsequently resolved by consensus between the 2 neuroradiologists.

In a subsequent follow-up analysis approximately 4 weeks after the initial readout session, the neuroradiologists were instructed to reclassify the DWI-FLAIR mismatch status while using e-Stroke predicted results as a CAT.

The final consensus reads of 2 neuroradiologists were used as the reference standard for final assignment of DWI-FLAIR mismatch status.

Statistical Analysis

Data were presented as mean (SD) for continuous data and median and interquartile range with relative frequencies (percentages) for categorical data. Receiver operating characteristic (ROC) analysis was performed, and the area under the curve (AUC) was calculated for the prediction of the TSS and tissue clock with accuracy measures including sensitivity and specificity. Interobserver agreement between readers was evaluated using a weighted κ test. For prediction of the TSS, the accuracy of the DWI-FLAIR mismatch status was compared against a dichotomized stroke-onset time using a TSS ≤ 4.5 or > 4.5 hours. For prediction of the tissue clock, the consensus reads of the 2 neuroradiologists were used as the reference standard. The diagnostic performance of the e-Stroke software and each neuroradiologist before and after using e-Stroke as the CAT was then analyzed against the consensus reads. The added value of e-Stroke predictions to the accuracy of each neuroradiologist was evaluated using comparative ROC analysis and tested by the Delong test. The significance level was defined as $P < .05$. Statistical analyses were performed with MedCalc for Windows (Version 20.008; MedCalc Software).

RESULTS

Clinical Characteristics of the Patient Population

A total of 157 patients met our inclusion criteria. The average age was a mean of 68.7 (SD, 16.3) years, and a total of 79 (50.3%)

The breakdown of correctly identified matched and mismatched DWI-FLAIR status in addition to diagnostic performances for e-Stroke software, for each neuroradiologist alone and in conjunction with CAT

	Consensus Interpretation		AUC/Sensitivity/Specificity	P Value ^b
	Matched (n = 76) ^a	Mismatched (n = 81) ^a		
e-Stroke	41 (54.0%)	73 (90.1%)	0.72/90.0/53.9	<.001
R1	64 (84.2%)	56 (69.1%)	0.76/69.1/84.2	<.001
R1-CAT	66 (86.8%)	64 (79.0%)	0.83/79.0/86.8	<.001
R2	56 (73.7%)	74 (91.3%)	0.82/91.4/73.7	<.001
R2-CAT	65 (85.5%)	75 (92.5%)	0.89/92.6/85.5	<.001

^aData are numbers and percentages of correctly identified patients as DWI-FLAIR matched or mismatched against final consensus read.

^bSignificance of diagnostic performance against the consensus interpretation of 2 neuroradiologists using ROC analysis.

patients were women. The severity of stroke determined by the NIHSS was a median of 10 (interquartile range, 5–16). A total of 151 (96%) patients had an identifiable intracranial arterial occlusion, including of the ICA (n = 18, 11.5%), M1 (n = 100, 63.7%), M2 (n = 19, 12%), anterior cerebral artery (n = 2, 1.2%), or posterior cerebral artery (n = 12, 7.6%). Three (2%) patients had lacunar infarction, and the other 3 (2%) patients had multiple small foci of infarctions in >2 vascular territories, likely related to an embolic shower. The infarct volume was a mean of 18.0 (SD, 25.6) mL. The TSS was a mean of 267.4 (SD, 269.2) minutes. By means of 4.5 hours as a threshold for thrombolytic treatment eligibility, a total of 75 (48%) patients had a TSS of >4.5 hours, while 82 (52%) patients had a TSS of ≤4.5 hours.

Determination of DWI-FLAIR Status

Automated image analysis by e-Stroke software using the FLAIR rSIR showed matched DWI-FLAIR in 49 patients and mismatch in 108 patients. Neuroradiologist 1 assigned 89 patients as matched and 68 patients as mismatched, while neuroradiologist 2 identified 63 as matched and 94 as mismatched for DWI-FLAIR status. The interobserver agreement for the determination of the DWI-FLAIR mismatch status was moderate ($\kappa = 0.49$; 95% CI, 0.36–0.62).

Following consensus reads between the 2 readers, a total of 76 patients were assigned as matched; and 81 patients as mismatched.

Diagnostic accuracy (AUC/sensitivity/specificity) of e-Stroke software for the determination of the DWI-FLAIR mismatch against consensus reads was 0.72/90.0/53.9 ($P < .001$) (Table).

For neuroradiologist 1, the diagnostic performance (AUC/sensitivity/specificity) of the initial interpretation was 0.76/69.1/84.2, which was significantly ($P = .003$) improved to 0.83/79.0/86.8 in the second interpretation following the use of e-Stroke predictions as a CAT (Table and Fig 1).

For neuroradiologist 2, the diagnostic performance (AUC/sensitivity/specificity) of the initial interpretation was 0.82/91.4/73.7, which was significantly ($P = .005$) improved to 0.89/92.6/85.5 after using e-Stroke predictions as a CAT (Table and Fig 1).

The interrater agreement for determination of the DWI-FLAIR status following the use of the CAT was also modestly improved to $\kappa = 0.57$ (95% CI, 0.44–0.72). In a sub-analysis to assess the diagnostic performance in determination of TSS (≤ or > 4.5 hours), the AUC/sensitivity/specificity were 0.63/81.7/45.3 ($P < .001$) for e-Stroke software, 0.67/57.3/76.0 for neuroradiologist 1 ($P < .001$) and 0.70/69.5/70.7 for neuroradiologist 2 ($P < .001$). There was no statistically significant difference between the neuroradiologists and e-Stroke software in prediction of TSS.

Delong test showed P -values of 0.51 for e-Stroke software versus neuroradiologist 1, 0.13 for e-Stroke software versus neuroradiologist 2, and 0.38 between the two neuroradiologists.

The Figure 2 shows an example of a patient with TSS < 4.5 hours who was correctly classified by both neuroradiologists as DWI-FLAIR mismatch and automatically assigned as mismatch by e-Stroke software. The Figure 3 shows an example in a patient who had weak FLAIR signal associated with infarct region resulting in discrepant interpretation of DWI-FLAIR status between two neuroradiologists during the initial assessment. This case was subsequently corrected after using e-Stroke prediction as CAT to match the consensus reads.

DISCUSSION

Our results showed that automated image analysis afforded by advanced and streamlined image-segmentation techniques that are now commercially available can provide results similar to those of human experts in the determination of the DWI-FLAIR mismatch as a biomarker for the tissue clock. We would like to highlight 2 major findings in our results.

Our first finding is that e-Stroke software provided improved diagnostic accuracy and interrater agreement for determination of the tissue clock when used in conjunction with human interpreters. Assessment of the DWI-FLAIR mismatch is a difficult task that requires extensive training. Due to the binary reporting nature (negative or positive) of the DWI-FLAIR mismatch, current human assessment does not consider the wide range of signal intensities on FLAIR images. The heterogeneity of FLAIR signal intensity change across the infarction bed is one of the major contributing factors resulting in inconsistency and possible disagreements in interpretation of the DWI-FLAIR mismatch status.^{4,5} This limitation is reflected in modest interobserver agreement ($\kappa = 0.49$), similar to previously reported values ranging from 0.4 to 0.6 by human observers.^{4,5} However, after using the e-Stroke prediction as a CAT, the interrater agreement improved to $\kappa = 0.57$. Furthermore, the use of e-Stroke prediction as a CAT resulted in significantly improved diagnostic accuracy of the DWI-FLAIR mismatch (tissue clock) assignment, with approximately 10% increased sensitivity for one neuroradiologist and 11% increased specificity for the other.

Comparable diagnostic accuracies for e-Stroke software in the determination of the tissue clock (DWI-FLAIR mismatch) with the consensus reads of 2 expert neuroradiologists highlight the potential for this solution to aid thrombolytic decision-making,

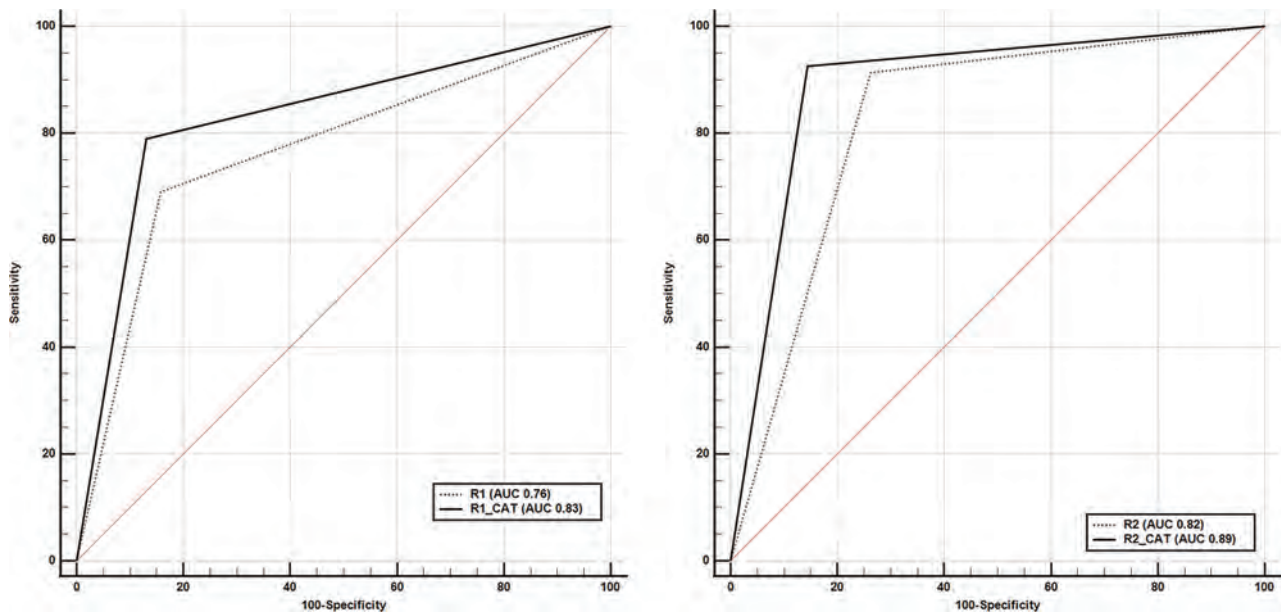


FIG 1. Comparative analysis of ROC curves for diagnostic performance of each neuroradiologist alone (R1, R2) and in conjunction with predicted results of e-Stroke software used as a CAT (R1-CAT, R2-CAT). The diagnostic performance of both neuroradiologists in determination of the DWI-FLAIR status was significantly improved compared with the consensus interpretations.

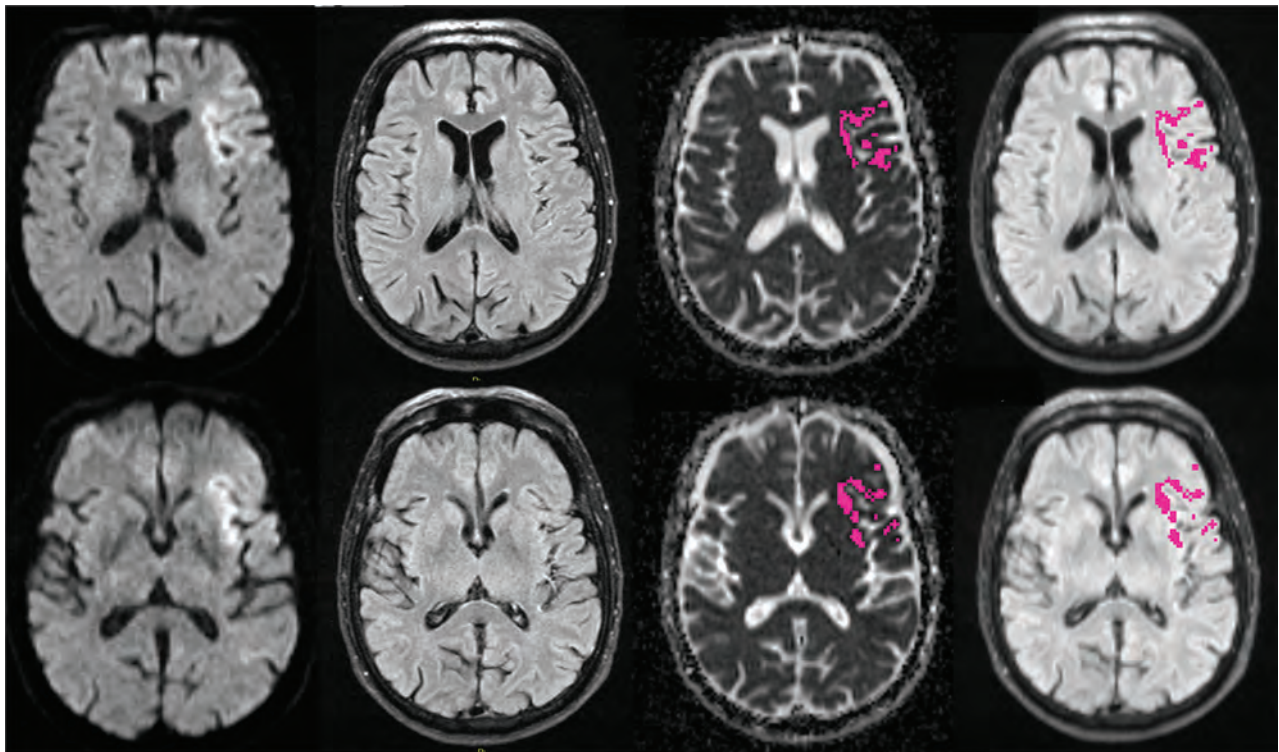


FIG 2. A 73-year-old man with a left MCA-MI occlusion who presented within 117 minutes from stroke onset. There is infarction involving the left frontal lobe, opercular region, and insula with reduced diffusion that is negative on FLAIR (ie, DWI-FLAIR mismatch). The infarction was automatically segmented by e-Stroke software (*highlighted in purple*), and the relative signal intensity of the infarction bed was calculated from corresponding FLAIR images at 1.03, rendering the DWI-FLAIR mismatch classification concordant with both neuroradiologists and TSS.

to supplant human interpretation when used as a decision support tool. By means of leveraging automated analysis tools in e-Stroke, the potential benefit may be even more relevant in settings where there is lack of neuroimaging expertise to ensure that

efficient and consistent assessment can be obtained for treatment decisions equally in all patients.

Our second finding is that e-Stroke software provided results comparable with those of expert neuroradiologists in

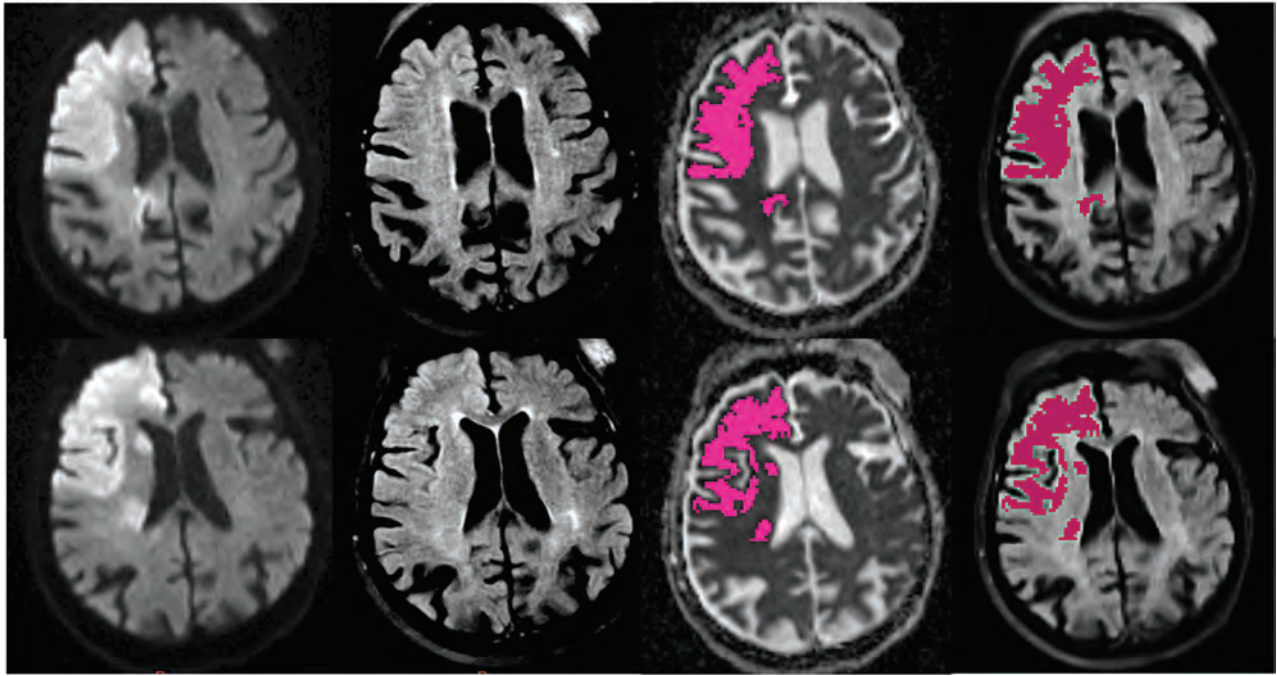


FIG 3. A 90-year-old woman with right internal carotid occlusion presented 190 minutes from stroke onset. The infarction was automatically segmented by e-Stroke software (*highlighted in purple*). The signal intensity ratio calculated automatically by e-Stroke software at 1.14, rendered the correct assignment of the DWI-FLAIR mismatch. The weak FLAIR signal associated with the infarct region resulted in a discrepant interpretation between 2 neuroradiologists. However, the neuroradiologist who initially classified this case as a match changed his interpretation to mismatch after using the e-Stroke software as a CAT, which was concordant with the consensus read.

the prediction of the TSS using a cutoff value of 4.5 hours. Prior reports have shown that approximately 27%–50% of patients with stroke have positive FLAIR findings within 3 hours and 93% at >6 hours.^{14–16} Our results are concordant with the results of prior reports showing only modest sensitivity in the range of 60% for TSS prediction by human observers.^{15,17,18} While the diagnostic performance of e-Stroke software in the prediction of the TSS was comparable with that of expert neuroradiologists, the automated TSS prediction provided by e-Stroke resulted in higher sensitivity (81.7%) in comparison with the modest sensitivity of human experts but at a cost of lower specificity.

Although the 4.5-hour cutoff for the TSS remains a thrombolytic eligibility criterion, there is now a transition toward accepting tissue status rather than the TSS alone for thrombolytic decision-making, at least for patients with an unknown TSS or wake-up strokes.³ In addition, there are some patients with stroke who may become FLAIR-positive in <4.5 hours and others who could remain FLAIR-negative even after 6 hours. Therefore, the classification of the TSS based on a 4.5 hour cutoff is imperfect¹⁹ and a waning cause.

Application of advanced image-processing techniques and artificial intelligence has shown promising potential to provide more consistent results for the prediction of the TSS and DWI-FLAIR status while mitigating the variability issues related to human observers.^{6–8} However, these algorithms are yet to become commercially available for broad clinical use. Automated image-processing and segmentation by the e-Stroke solution that is now commercially available provides an opportunity for routine use

to support treatment decisions if its potential is realized in a broader clinical setting.

Our study has several limitations. First, it was a retrospective study, which may introduce unknown bias. Second, this was a single-institution study with MR images included from a limited number of scanners. Including data from multicenter studies with greater variability in image-acquisition parameters and MR imaging scanners will be required to further generalize our results. Third, we were unable to test how e-Stroke software could affect treatment decisions in our retrospective design. In our cohort, the decision for thrombolysis was based solely on the TSS, which was determined at the time of patient presentation. We did not screen for patients with extensive white matter disease, and it is plausible that underlying leukoaraiosis could confound quantitative assessment of signal intensity ratios in a subset of our patients. Although the software algorithm considers the presence of non-normal voxels such as CSF and older white matter lesions, this potential mitigating effect of the software was not tested systematically for the presence of substantial white matter disease. Last, the criterion standard for ischemic brain tissue status was consensus reads of the DWI-FLAIR mismatch by 2 neuroradiologists. This is less than ideal but the best practical reference standard that could be adopted for our study because the DWI-FLAIR mismatch has been used as a surrogate for tissue clock.

CONCLUSIONS

Our study demonstrates the potential diagnostic utility of a fully automated quantitative approach provided by e-Stroke software to assess the DWI-FLAIR mismatch in patients with AIS. We

showed that the automated software provides diagnostic accuracies comparable with those of expert neuroradiologists. Most important, when used by neuroradiologists as a CAT, the automated software significantly improved the diagnostic performance of neuroradiologists for more accurate classification of the DWI-FLAIR mismatch as a surrogate for tissue clock.

Disclosure forms provided by the authors are available with the full text and PDF of this article at www.ajnr.org.

REFERENCES

1. Powers WJ, Rabinstein AA, Ackerson T, et al. **Guidelines for the Early Management of Patients with Acute Ischemic Stroke: 2019 Update to the 2018 Guidelines for the Early Management of Acute Ischemic Stroke: A Guideline for Healthcare Professionals from the American Heart Association/American Stroke Association.** *Stroke* 2019;50:e344–418 CrossRef Medline
2. Ma H, Campbell BCV, Parsons MW, et al; EXTEND Investigators. **Thrombolysis guided by perfusion imaging up to 9 hours after onset of stroke.** *N Engl J Med* 2019;380:1795–803 CrossRef Medline
3. Thomalla G, Simonsen CZ, Boutitie F, et al; WAKE-UP Investigators. **MRI-guided thrombolysis for stroke with unknown time of onset.** *N Engl J Med* 2018;379:611–22 CrossRef Medline
4. Ziegler A, Ebinger M, Fiebach JB, et al. **Judgment of FLAIR signal change in DWI-FLAIR mismatch determination is a challenge to clinicians.** *J Neurol* 2012;259:971–73 CrossRef Medline
5. Galinovic I, Puig J, Neeb L, et al. **Visual and region of interest-based inter-rater agreement in the assessment of the diffusion-weighted imaging-fluid-attenuated inversion recovery mismatch.** *Stroke* 2014;45:1170–72 CrossRef Medline
6. Lee H, Lee EJ, Ham S, et al. **Machine learning approach to identify stroke within 4.5 hours.** *Stroke* 2020;51:860–66 CrossRef Medline
7. Ho KC, Speier W, Zhang H, et al. **A machine learning approach for classifying ischemic stroke onset time from imaging.** *IEEE Trans Med Imaging* 2019;38:1666–76 CrossRef Medline
8. Zhu H, Jiang L, Zhang H, et al. **An automatic machine learning approach for ischemic stroke onset time identification based on DWI and FLAIR imaging.** *Neuroimage Clin* 2021;31:102744 CrossRef Medline
9. Purushotham A, Campbell BC, Straka M, et al. **Apparent diffusion coefficient threshold for delineation of ischemic core.** *Int J Stroke* 2013;10:348–53 CrossRef Medline
10. Wyawahare M, Patil PM, Abhyankar HK. **Image Registration Techniques: An overview.** Vol. 2, No.3, September 2009. <https://www.semanticscholar.org/paper/Image-Registration-Techniques%3A-An-overview-Wyawahare-Patil/78b84eca4cc00c8b09b1d8082b41251c43f2dd7f>.
11. Maintz JB, Viergever MA. **A survey of medical image registration.** *Med Image Anal* 1998;2:1–36 CrossRef Medline
12. Ikotun AM, Ezugwu AE, Abualigah L, et al. **K-means clustering algorithms: a comprehensive review, variants analysis, and advances in the era of big data.** *Inform Sciences* 2023;622:178–210 CrossRef
13. Song SS, Latour LL, Ritter CH, et al. **A pragmatic approach using magnetic resonance imaging to treat ischemic strokes of unknown onset time in a thrombolytic trial.** *Stroke* 2012;43:2331–35 CrossRef Medline
14. Geraldo AF, Berner L-P, Haesebaert J, et al. **Negative fluid-attenuated inversion recovery imaging identifies acute ischemic stroke at 3 hours or less.** *Annals Neurol* 2009;47:877–81 CrossRef Medline
15. Thomalla G, Cheng B, Ebinger M, et al; STIR and VISTA Imaging Investigators. **DWI-FLAIR mismatch for the identification of patients with acute ischaemic stroke within 4.5 h of symptom onset (PRE-FLAIR): a multicentre observational study.** *Lancet Neurol* 2011;10:978–86 CrossRef Medline
16. Petkova M, Rodrigo S, Lamy C, et al. **MR imaging helps predict time from symptom onset in patients with acute stroke: implications for patients with unknown onset time.** *Radiology* 2010;257:782–92 CrossRef Medline
17. Ebinger M, Galinovic I, Rozanski M, et al. **Fluid-attenuated inversion recovery evolution within 12 hours from stroke onset: a reliable tissue clock?** *Stroke* 2010;41:250–55 CrossRef Medline
18. Emeriau S, Serre I, Toubas O, et al. **Can diffusion-weighted imaging-fluid-attenuated inversion recovery mismatch (positive diffusion-weighted imaging/negative fluid-attenuated inversion recovery) at 3 Tesla identify patients with stroke at <4.5 hours?** *Stroke* 2013;44:1647–51 CrossRef
19. Odland A, Særvoll P, Advani R, et al. **Are the current MRI criteria using the DWI-FLAIR mismatch concept for selection of patients with wake-up stroke to thrombolysis excluding too many patients?** *Scand J Trauma Resusc Emerg Med* 2015;23:22 CrossRef Medline

Lesion Indexes Predict Early Neurologic Deterioration in Lenticulostriate Single Small Subcortical Infarction

Yuan Gao, Ke Zhang, Hongbing Liu, Ce Zong, Hongxun Yang, Ying Yao, and Yuming Xu



ABSTRACT

BACKGROUND AND PURPOSE: Early neurologic deterioration (END) often occurs during hospitalization in single small subcortical infarction (SSSI). The objective was to identify imaging predictors of END.

MATERIALS AND METHODS: SSSIs in the lenticulostriate artery within 72 hours of stroke onset from January 2015 to June 2021 were consecutively enrolled. The posteriority and laterality indexes were assessed on the second section from the top of the corona radiata section showing the lateral ventricle on DWI. A multivariate logistic analysis was used to explore the predictors of END.

RESULTS: A total of 402 patients were included in this study, among whom 93 (23.1%) experienced END. The optimal cutoff points of the posteriority and laterality indexes for predicting END were given by a receiver operating characteristic curve. A multivariate logistic analysis showed that the posteriority index of ≥ 0.669 (OR: 2.53; 95% CI: 1.41–4.56; $P = .002$) and the laterality index of ≥ 0.950 (OR: 2.03; 95% CI: 1.03–4.00; $P = .042$) were independently associated with the risk of END. Accordingly, the SSSIs were further divided into 4 types: anterior lateral type (AL-type), anterior medial type (AM-type), posterior lateral type (PL-type), and posterior medial type (PM-type). After the multivariate analysis, in comparison with the AL-type, the AM-type (OR: 3.26; 95% CI: 1.10–9.65), PL-type (OR: 4.68; 95% CI: 1.41–15.56), and PM-type (OR: 6.77; 95% CI: 2.53–18.04) carried significantly elevated risks of END. The PM-type was associated with the highest risk of END.

CONCLUSIONS: The PM-type was found to be associated with the highest risk of END.

ABBREVIATIONS: AL = anterior lateral; AM = anterior medial; CR = corona radiata; CST = corticospinal tract; END = early neurologic deterioration; LSA = lenticulostriate artery; ISSSI = large SSSI; LV = lateral ventricle; MAD = maximum axial diameter; PAD = parent artery disease; PL = posterior lateral; PM = posteriormedial type; pSSSI = proximal SSSI; SSSI = single small subcortical infarction

Single small subcortical infarctions (SSSIs) are defined as isolated deep infarctions in the territory of the perforating artery with a maximum axial diameter (MAD) of ≤ 20 mm on DWI.¹ Approximately 13.5% to 43%^{2–7} of patients with SSSI experience early neurologic deterioration (END)⁸ in the acute

phase, which is generally associated with a relatively unfavorable prognosis. The location of SSSI lesions within the lenticulostriate artery (LSA) territory, such as proximal SSSI (pSSSI), large SSSI (ISSSI), and posterior-type SSSI, has been found to be correlated with the occurrence of END. The proximity of the lesion to the corticospinal tract (CST) appears to be an underlying mechanism.^{3,5,9–15} MR tractography studies revealed that the CST crossed the LSA territory exclusively in the posterosuperior quadrant, which corresponds to the posterior part of the corona radiata (CR) area adjacent to the lateral ventricle.^{16–18} One previous study reported that the posterior-type SSSI, defined as a lesion with more than one-half of its extent in the posterior half of the CR on DWI, were identified as a predictor for the progression of motor deficits after admission in patients with SSSI in the LSA territory.⁵ However, the definition of the division was primarily derived from subjective estimations without a robust and scientifically validated approach. The purpose of this study was to identify more specific imaging markers for the occurrence of END by analyzing quantitative indexes that reflect lesion location information.

Received July 2, 2023; accepted after revision January 8, 2024.

From the Department of Neurology (Y.G., K.Z., H.L., C.Z., H.Y., Y.Y., Y.X.), The First Affiliated Hospital of Zhengzhou University, Zhengzhou, Henan Province, China; NHC Key Laboratory of Prevention and Treatment of Cerebrovascular Disease (Y.X.); and Henan Key Laboratory of Cerebrovascular Diseases (Zhengzhou University), (Y.X.), Zhengzhou, Henan Province, China.

Yuan Gao and Ke Zhang contributed equally to this article.

This research has been supported by the China National Key R&D Program during the 13th Five-year Plan Period (Grant No. 2018YFC1311303) and Major Science and Technology Projects of Henan Province in 2020 (Grant No. 201300310300).

Please address correspondence to Yuming Xu, Neurology, The First Affiliated Hospital of Zhengzhou University, No.1 Eastern Jianshe Road, Erqi District, Zhengzhou, Henan Province, Zhengzhou 450052, China; e-mail: xuyuming@zzu.edu.cn



Indicates article with online supplemental data.

<http://dx.doi.org/10.3174/ajnr.A8176>

MATERIALS AND METHODS

Patient Selection

Patients were enrolled consecutively from a hospital-based prospective registry of SSSIs at The First Affiliated Hospital of Zhengzhou University between January 2015 and June 2021. The inclusion criteria were as follows: 1) age ≥ 18 years; 2) SSSI within the LSA territory with MAD ≤ 20 mm on DWI; and 3) at least 1 vascular examination, including MRA, CTA, or DSA. The exclusion criteria were as follows: 1) stroke onset time beyond 72 hours; 2) occurrence of END beyond 7 days after admission; 3) interval from admission to the first MR imaging after admission beyond 72 hours; 4) END occurring before the first brain MR imaging was performed after admission; 5) suspected cardioaortic embolism or ipsilateral carotid artery stenosis of $\geq 50\%$; 6) suspected anterior choroidal artery infarction involving the posterior limb of the internal capsule or paraventricular area; 7) lesions without involvement of the CR level showing the lateral ventricle on DWI in the standard axial image template in the LSA territory; 8) unclear MR imaging or cerebrovascular imaging examination affecting the evaluation of the results; or 9) refusal to participate in the study. A flowchart outlining the patient selection process is depicted in Fig 1. A total of 402 patients were included in this study, which received approval from the Ethics Committee of The First Affiliated Hospital of Zhengzhou University. Informed consent was obtained from all participating patients.

Clinical Parameters

The following clinical and laboratory parameters were collected on admission: age, sex, hypertension (documentation of 2 or more blood pressure measures of $\geq 140/90$ mmHg or the use of

antihypertensive medications), diabetes mellitus (serum glucose level of more than 11.1 mmol/L in a 2-hour oral glucose tolerance test or the use of insulin or oral hypoglycemic agents), hyperlipidemia (total cholesterol level of 5.2 mmol/L or higher, triglyceride level of 1.7 mmol/L or higher, or the use of cholesterol-reducing agents), current smoking, systolic blood pressure, diastolic blood pressure, NIHSS score on admission, stroke history, onset to admission time, glycosylated hemoglobin, hemoglobin, creatinine levels, and glomerular filtration rate. Thrombolysis and dual antiplatelet therapy were also recorded. END was defined as a worsening of ≥ 2 points in the total NIHSS score or ≥ 1 point in the motor items of the NIHSS score.

Imaging Assessment

This study was performed by using a previously reported standard axial image template with 6 standard layers in the LSA territory. In this template, the first layer represents the lowest part of the basal ganglia region closest to the opening of the perforating branch of the middle cerebral artery, and the sixth layer represents the farthest level of the perforating artery. The anteroposterior and mediolateral localization of the lesion were assessed at the level of the second section from the top of the CR section showing the lateral ventricle on DWI. Two parallel tangents were drawn along both sides of the anterior and posterior horns of the lateral ventricles. As shown in Fig 2, we measured the longitudinal distance between the tangents (d_1), the distance from the inferior edge of the lesion to the tangent of the superior horn of the lateral ventricle (d_2), the horizontal distance from the lateral ventricle to the ipsilateral cerebral parenchyma passing through the innermost margin of the lesion (d_3), and the horizontal distance

from the innermost margin of the lesion to the edge of the ipsilateral cerebral parenchyma (d_4). The posteriority index was defined as the d_2/d_1 ratio, and it indicated the anteroposterior localization of the lesions. The laterality index was defined as the d_4/d_3 ratio, and it indicated the mediolateral localization of the lesions (Fig 2). The lowest section and number of slices were also evaluated. On the basis of the lowest section and number of slices, SSSIs were categorized as pSSSI (lowest section ≤ 2), distal SSSI (lowest section > 2), small SSSI (number of slices < 3), and lSSSI (number of slices ≥ 3). Any degree of abnormality seen on an imaging assessment of the M1 segment of the MCA ipsilateral to the lesion was classified as parent artery disease (PAD)^{19,20} and cases that did not show such abnormalities were categorized as non-PAD. The Fazekas score was used to evaluate paraventricular and deep white matter hyperintensities. Severe white matter hyperintensity was defined if either score was ≥ 2 .²¹ All

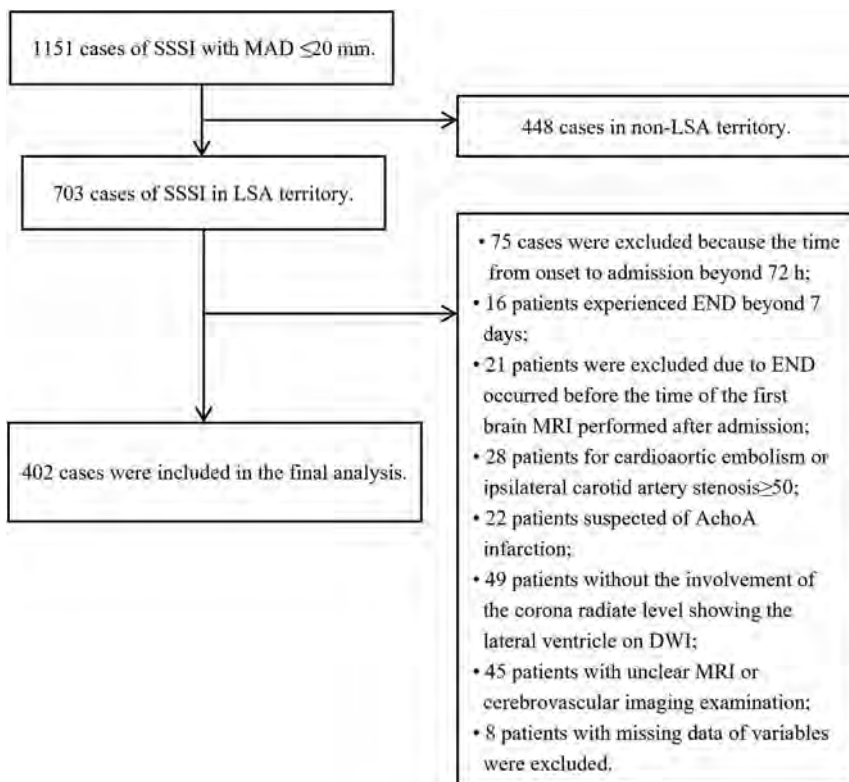


FIG 1. Flowchart of patient selection. AchoA indicates anterior choroidal artery.

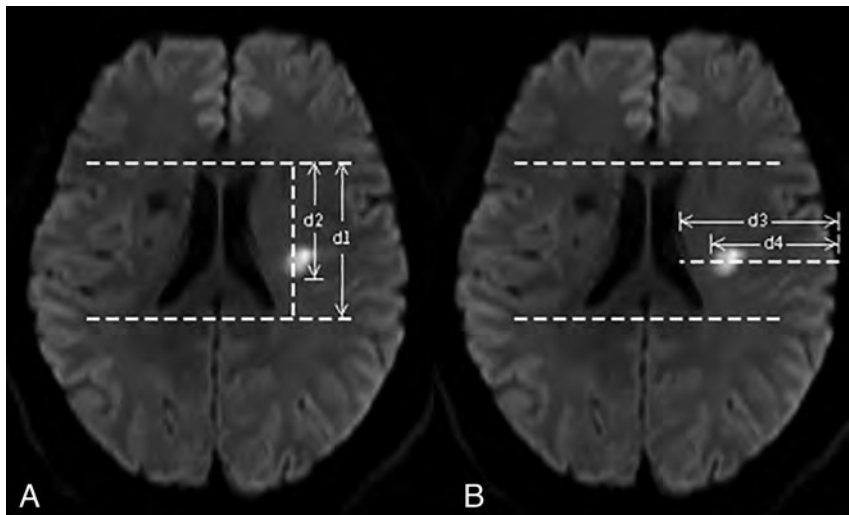


FIG 2. The longitudinal distance between the tangents (d1) and the distance from the inferior edge of the lesion to the tangent of the superior horn of the lateral ventricle (d2) (A). The horizontal distance from the lateral ventricle to the ipsilateral cerebral parenchyma passing through the innermost margin of the lesion (d3) and the horizontal distance from the innermost margin of the lesion to the edge of the ipsilateral cerebral parenchyma (d4) (B).

images were reviewed independently by 2 physicians who were blinded to the clinical data. In cases where discrepancies arose, a final decision was reached by remeasuring.

Statistical Analysis

The SPSS Statistics software package (IBM; version 25.0) was used for all statistical analyses. Before analysis, the Kolmogorov-Smirnov test was performed to assess normality. The association between the variables and END was analyzed by using univariate and multivariate analyses. In the univariate analyses, the Student *t* test was used for continuous variables, and the χ^2 test was used for categorical variables. To determine the predictors of END, all associated variables ($P < .1$) in the univariate analysis were included in the multivariate logistic regression analysis and were removed via Wald selection. All statistical tests were 2-sided with a significance level of $P < .05$. Restricted cubic spline analyses and curves were performed by using the RStudio software package to depict the relationship between lesion location indexes and the risk of END. The discriminative power of the lesion location indexes in predicting END was assessed via receiver operating characteristic curve analyses conducted using the MedCalc statistical software package. In addition, the area under the receiver operating characteristic curve and the optimal cutoff point were calculated. Based on these optimal cutoff points, the posteriority and laterality indexes were dichotomized (\geq the optimal cutoff point or \leq the optimal cutoff point). The lesion locations were then categorized into 4 different types based on the 2 optimal cutoff points. All images were independently reviewed by 2 physicians who were blinded to the clinical data. In cases where discrepancies arose, a consensus decision was reached.

RESULTS

Baseline

A total of 402 patients were included in the final analyses, 93 (23.1%) of whom experienced END. The average age of the

patients was 58.7 ± 12.5 years. Out of the total, 117 (29.1%) patients were female. The prevalence of risk factors among the patients was as follows: 238 (59.2%) had a history of hypertension, 90 (22.4%) had diabetes mellitus, 137 (34.1%) were smokers, 116 (28.9%) were regular alcohol drinkers, 163 (40.5%) had hyperlipidemia, and 94 (23.4%) had experienced previous strokes. The median NIHSS score on admission was 2 (IQR: 1–4). The mean onset to admission time and onset to MR imaging time were 25.7 ± 22.7 hours and 36.9 ± 30.4 hours, respectively. The numbers of patients with pSSSI, lSSSI, PAD, posteriority index ≥ 0.669 , and laterality index ≥ 0.950 were 184 (45.8%), 241 (60%), 120 (29.9%), 221 (55.0%), and 259 (64.4%), respectively. Other baseline characteristics are presented in Table.

Factors Associated with END

In the univariate analysis, smoking, initial NIHSS score, onset to admission time, creatinine level, MAD, PAD, posteriority index ≥ 0.669 , laterality index ≥ 0.950 , thrombolysis, and dual antiplatelet therapy were selected for further analysis (Table). A multivariate logistic analysis showed that smoking (odds ratio [OR]: 1.94; 95% confidence interval [CI]: 1.14–3.32; $P = .015$), initial NIHSS score (OR: 1.10; 95% CI: 1.01–1.19; $P = .033$), MAD (OR: 1.07; 95% CI: 1.00–1.14; $P = .049$), PAD (OR: 2.80; 95% CI: 1.64–4.75; $P < .001$), posteriority index ≥ 0.669 (OR: 2.53; 95% CI: 1.41–4.56; $P = .002$) and laterality index ≥ 0.950 (OR: 2.03; 95% CI: 1.03–4.00; $P = .042$) were independently associated with the risk of END, as shown in Fig 3.

Lesion Location and Risk of END

The restricted cubic spline curve showed that the risk of END increased with an increase in the posteriority and laterality indexes (Fig 4). After the receiver operating characteristic curve analysis, the optimal cutoff points of the posteriority and laterality indexes for predicting END were determined (0.669, 0.950), and these cutoff values were used to divide the lenticulostriate SSSIs into 4 types: anterior lateral type (AL-type), anterior medial type (AM-type), posterior lateral type (PL-type), and posterior medial type (PM-type) (Fig 5). After the multivariate analysis, in comparison with the AL-type, the AM-type (OR: 3.26; 95% CI: 1.10–9.65), PL-type (OR: 4.68; 95% CI: 1.41–15.56), and PM-type (OR: 6.77; 95% CI: 2.53–18.04) showed significantly elevated risks of END. The PM-type had the highest risk of END (Fig 6).

DISCUSSION

Our study found that the posteriority and laterality indexes were both associated with the risk of END in patients with lenticulostriate SSSI. Patients with PM-type lenticulostriate SSSIs were at the highest risk of END.

Univariate logistic analysis of the risk factors for END

	Univariable Analysis			
	Total (n = 418)	Non-END (n = 309)	END (n = 93)	P Value
Demographic variables				
Age, year (mean ± SD)	58.7 ± 12.5	59.0 ± 12.5	57.5 ± 12.3	.301
Female, n (%)	117 (29.1)	91 (29.4)	26 (28.0)	.781
Hypertension, n (%)	238 (59.2)	185 (59.9)	53 (57.0)	.620
DM, n (%)	90 (22.4)	72 (23.3)	18 (19.4)	.424
HHcy, n (%)	324 (80.6)	249 (87.4)	75 (87.2)	.969
Hyperlipidemia, n (%)	163 (40.5)	129 (42.3)	34 (36.6)	.325
CHD, n (%)	34 (8.5)	29 (9.4)	5 (5.4)	.229
Stroke history, n (%)	94 (23.4)	68 (22.0)	26 (28.0)	.236
Smoking, n (%)	137 (34.1)	98 (31.7)	39 (41.9)	.069
Drinking, n (%)	116 (28.9)	83 (26.9)	33 (35.5)	.159
SBP, mmHg (mean ± SD)	146.7 ± 20.1	146.0 ± 20.1	148.9 ± 20.2	.220
DBP, mmHg (mean ± SD)	88.2 ± 13.2	87.4 ± 12.8	90.7 ± 14.1	.215
Initial NIHSS, median (IQR)	2 (1,4)	2 (1,4)	4 (2,6)	<.001
Onset to admission time, h, (mean ± SD)	25.7 ± 22.7	27.0 ± 23.0	21.6 ± 21.3	.047
Laboratory parameters				
TC, mmol/L (mean ± SD)	4.3 ± 1.1	4.2 ± 1.1	4.4 ± 1.4	.413
TG, mmol/L (mean ± SD)	1.6 ± 1.3	1.6 ± 1.1	1.7 ± 1.7	.454
HDL-C, mmol/L (mean ± SD)	1.1 ± 0.3	1.1 ± 0.3	1.1 ± 0.3	.710
LDL-C, mmol/L (mean ± SD)	2.7 ± 0.9	2.7 ± 0.9	2.6 ± 0.8	.399
HbA1c, %, median (IQR)	6 (5.6,6.6)	6.0 (5.6,6.5)	5.9 (5.4,6.9)	.607
Hemoglobin, g/L (mean ± SD)	138.8 ± 17.6	138.0 ± 18.4	141.3 ± 14.3	.119
Cr, μmol/L, (Mean ± SD)	72.2 ± 30.5	73.8 ± 33.4	67.1 ± 16.6	.065
eGFR, mL/min/1.73m2 (mean ± SD)	93.8 ± 17.7	93.0 ± 18.0	96.4 ± 16.7	.181
Imaging parameters				
Onset to MRI time, h (mean ± SD)	36.9 ± 30.4	37.3 ± 29.3	35.2 ± 33.6	.550
MAD, mm (mean ± SD)	12.9 ± 4.2	12.4 ± 4.1	14.5 ± 4.2	<.001
pSSSI, n (%)	184 (45.8)	143 (46.3)	41 (44.1)	.710
lSSSI, n (%)	241 (60)	183 (59.2)	58 (62.4)	.588
sWMH, n (%)	158 (39.3)	123 (39.8)	35 (37.6)	.707
PAD, n (%)	120 (29.9)	73 (23.6)	47 (50.5)	.001
Posteriority index ≥ 0.669	221 (55.0)	149 (48.2)	72 (77.4)	<.001
Laterality index ≥ 0.950	259 (64.4)	181 (58.6)	78 (83.9)	<.001
Treatment				
Thrombolysis, n (%)	40 (10.0)	25 (8.1)	15 (16.1)	.026
DAPT, n (%)	208 (51.7)	208 (67.3)	72 (77.4)	.060

Note:—DM indicates diabetes mellitus; HHcy, hyperhomocysteinemia; CHD, coronary heart disease; SBP, systolic blood pressure; DBP, diastolic blood pressure; TC, total cholesterol; TG, triglycerides; HDL, high-density lipoprotein; LDL, low-density lipoprotein; HbA1c, glycosylated hemoglobin; Cr, creatinine; eGFR, glomerular filtration rate; sWMH, severe white matter hyperintensity; DAPT, dual antiplatelet therapy.

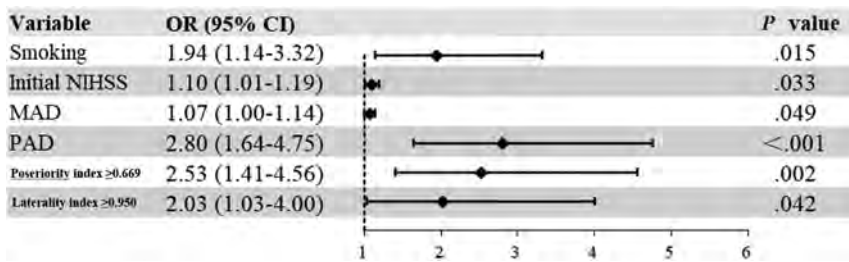


FIG 3. Multivariate logistic analysis for the risk factors of END.

The aggravation of motor function is commonly defined as END in clinical practice and is closely related to the impairment of motor fibers in the CST. The expansion of the lesion volume on DWI has been recognized as a common feature of ENDs.²²⁻²⁴ Therefore, to some extent, the proximity of the lesion to the CST has a notable effect on the risk of END. Previous studies using MR tractography have revealed that the CST crosses the LSA territory exclusively at the posterosuperior quadrant, which corresponds to the posterior part of the CR area adjacent to the lateral ventricle;¹⁸

therefore, if the SSSI lesion is located adjacent to or overlaps the CST, a higher risk of progression is reasonable. Our results could be explained on the basis of these anatomic characteristics. In our study, the more posterior and medial the lesion, the greater the risk of END within the CR area. We found that the best cut-off points of the posteriority index and laterality index were located near the location where the CST passes through,

which could be verified by the results of previous studies that focused on the location of the CST in the LSA area.²⁵ Therefore, the highest risk of END in the PM-type can easily be explained.

A previous study reported that DWI findings showing the “posterior-type” of SSSI were an independent predictor for the progression of motor deficits after admission in patients with lacunar infarction in the LSA territory. The “posterior-type” was defined by the presence of more than one-half of the lesion in the posterior half of the CR.⁵ The explanation for this division was not

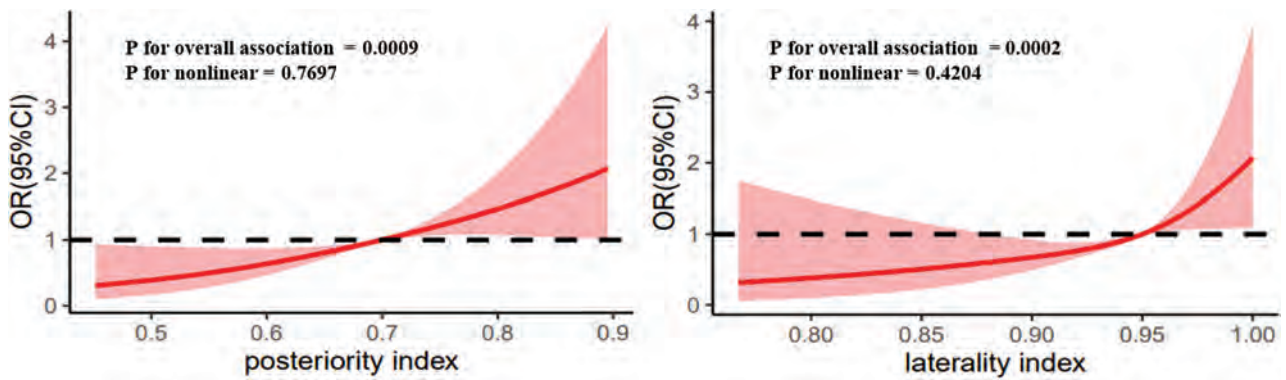


FIG 4. Restricted cubic spline curve for the association of the posteriority and laterality indexes with the risk of END. The risk of END increased with increases the in posteriority and laterality indexes.

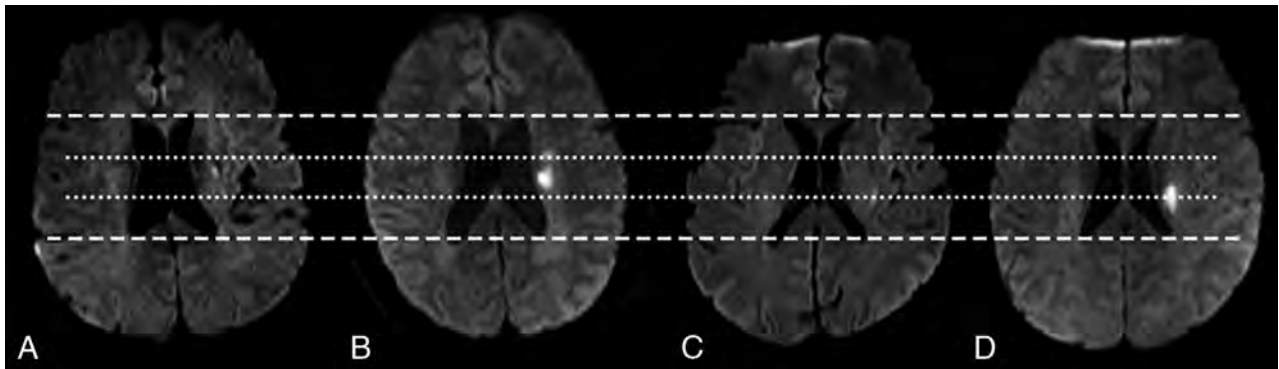


FIG 5. Lesion location types (A) anterior lateral type (AL-type, posteriority index <0.669 and laterality index <0.950); (B) anterior medial type (AM-type, posteriority index <0.669 and laterality index ≥ 0.950); (C) posterior lateral type (PL-type, posteriority index ≥ 0.669 and laterality index <0.950); (D) posterior medial type (PM-type, posteriority index ≥ 0.669 and laterality index ≥ 0.950).

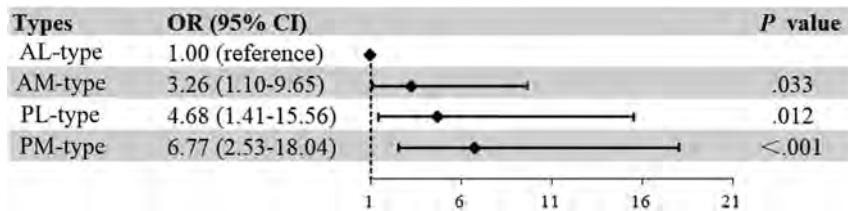


FIG 6. Multivariate analysis of the 4 lesion types for END in patients with SSSI. Adjusted for smoking, initial NIHSS score, MAD, and PAD.

clearly described and may reflect a rough estimate according to the distribution of CST. The novelty of our study is that it is the first study to characterize a credible imaging predictor obtained via data analyses based on the best cutoff points of lesion location parameters in a cohort study with the largest sample, to our knowledge. The division line defined by our optimal cutoff points was more adjacent to the CST.

Our results have several notable clinical implications. Our study provides a novel and reliable imaging marker for predicting END in patients with lenticulostriate SSSIs. Physicians should pay more attention to patients with PM-type lesions, which carry the highest risk for END. For clinical user convenience, PM-type lesions can be considered as lesions located at the posterior one-third of d1 and adjacent to the lateral ventricle,

as shown in Fig 5. Once high-risk patients are identified, earlier doctor-patient communication may prevent potential medical disputes. More aggressive treatment strategies should be considered to eliminate upcoming progress.

This study had some limitations. First, the definition of END varied in previously published studies; a more liberal or strict definition may lead to

different results. Second, some asymptomatic patients with SSSI may not have consulted a doctor, which might have led to an overestimation of the occurrence of END. Third, given that our study was a single-center study, further prospective and larger-sample studies are needed to confirm these results.

CONCLUSIONS

Lesion location indexes of posteriority and laterality at the level of the CR showing the lateral ventricle on DWI were associated with the risk of END occurrence in patients with lenticulostriate SSSI. The PM-type was found to be associated with the highest risk of END. These findings may be helpful for clinicians preparing appropriate clinical interventions to address the future risks of END.

ACKNOWLEDGMENTS

The authors declare that the research was conducted in the absence of any commercial or financial relationships that could be construed as a potential conflict of interest. Project development: Dr. Yuming Xu and Dr. Yuan Gao; Writing (original draft preparation): Dr. Yuan Gao and Dr. Ke Zhang; Data collection: Dr. Hongbing Liu; Data analysis: Ce Zong; Figures and tables: Hongxun Yang and Ying Yao. All authors approved the final article.

Disclosure forms provided by the authors are available with the full text and PDF of this article at www.ajnr.org.

REFERENCES

1. Kim JS, Yoon Y. **Single subcortical infarction associated with parental arterial disease: important yet neglected sub-type of atherothrombotic stroke.** *Int J Stroke* 2013;8:197–203 CrossRef Medline
2. Castellanos M, Castillo J, García MM, et al. **Inflammation-mediated damage in progressing lacunar infarctions: a potential therapeutic target.** *Stroke* 2002;33:982–87 CrossRef Medline
3. Jeong HG, Kim BJ, Yang MH, et al. **Neuroimaging markers for early neurologic deterioration in single small subcortical infarction.** *Stroke* 2015;46:687–91 CrossRef Medline
4. Kitanaka C, Teraoka A. **Clinical features of progressive lacunar infarction—retrospective analysis of patients with motor syndromes.** *Neurol Med Chir (Tokyo)* 1995;35:663–66 CrossRef Medline
5. Ohara T, Yamamoto Y, Tamura A, et al. **The infarct location predicts progressive motor deficits in patients with acute lacunar infarction in the lenticulostriate artery territory.** *J Neurol Sci* 2010; 293:87–91 CrossRef Medline
6. Saji N, Kimura K, Kawarai T, et al. **Arterial stiffness and progressive neurological deficit in patients with acute deep subcortical infarction.** *Stroke* 2012;43:3088–90 CrossRef Medline
7. Zong C, Liu H, Zhang K, et al. **Prediction of symptoms on admission with early neurological deterioration in single small subcortical infarct.** *Curr Neurovasc Res* 2022;19:232–39 CrossRef Medline
8. Siegler JE, Martin-Schild S. **Early neurological deterioration (END) after stroke: the END depends on the definition.** *Int J Stroke* 2011;6:211–12 CrossRef Medline
9. Duan Z, Fu C, Chen B, et al. **Lesion patterns of single small subcortical infarct and its association with early neurological deterioration.** *Neurol Sci* 2015;36:1851–57 CrossRef Medline
10. Gao Y, Song B, Yong Q, et al. **Pathogenic heterogeneity of distal single small subcortical lenticulostriate infarctions based on lesion size.** *J Stroke Cerebrovasc Dis* 2016;25:7–14 CrossRef Medline
11. Sudlow CL, Warlow CP. **Comparable studies of the incidence of stroke and its pathological types: results from an international collaboration.** *International stroke incidence collaboration.* *Stroke* 1997;28:491–99 CrossRef Medline
12. Duan Z, Sun W, Liu W, et al. **Acute diffusion-weighted imaging lesion patterns predict progressive small subcortical infarct in the perforator territory of the middle cerebral artery.** *Int J Stroke* 2015;10:207–12 CrossRef Medline
13. Gao Y, Song B, Zhao L, et al. **Vascular lesion thickness in the lenticulostriate artery region serves as a biomarker for early neurological deterioration.** *Curr Neurovasc Res* 2017;14:215–21 CrossRef Medline
14. Yamamoto Y, Nagakane Y, Tomii Y, et al. **The relationship between progressive motor deficits and lesion location in patients with single infarction in the lenticulostriate artery territory.** *J Neurol* 2017;264:1381–87 CrossRef Medline
15. Kim SK, Song P, Hong JM, et al. **Prediction of progressive motor deficits in patients with deep subcortical infarction.** *Cerebrovasc Dis* 2008;25:297–303 CrossRef Medline
16. Yamada K, Ito H, Nakamura H, et al. **Stroke patients' evolving symptoms assessed by tractography.** *J Magn Reson Imaging* 2004;20:923–29 CrossRef Medline
17. Lai C, Zhang SZ, Liu HM, et al. **White matter tractography by diffusion tensor imaging plays an important role in prognosis estimation of acute lacunar infarctions.** *Br J Radiology* 2007;80:782–89 CrossRef Medline
18. Konishi J, Yamada K, Kizu O, et al. **MR tractography for the evaluation of functional recovery from lenticulostriate infarcts.** *Neurology* 2005;64:108–13 CrossRef Medline
19. Fisher CM. **Capsular infarcts: the underlying vascular lesions.** *Arch Neurol* 1979;36:65–73 CrossRef Medline
20. Caplan LR. **Intracranial branch atheromatous disease: a neglected, understudied, and underused concept.** *Neurology* 1989;39:1246–50 CrossRef Medline
21. Kapeller P, Barber R, Vermeulen RJ, et al. **Visual rating of age-related white matter changes on magnetic resonance imaging: scale comparison, interrater agreement, and correlations with quantitative measurements.** *Stroke* 2003;34:441–45 CrossRef Medline
22. Takase K, Murai H, Tasaki R, et al. **Initial MRI findings predict progressive lacunar infarction in the territory of the lenticulostriate artery.** *Eur Neurol* 2011;65:355–60 CrossRef Medline
23. Kim BJ, Lee DH, Kang DW, et al. **Branching patterns determine the size of single subcortical infarctions.** *Stroke* 2014;45:1485–87 CrossRef Medline
24. Cho KH, Kang DW, Kwon SU, et al. **Lesion volume increase is related to neurologic progression in patients with subcortical infarction.** *J Neurol Sci* 2009;284:163–67 CrossRef Medline
25. Jang SH. **A review of corticospinal tract location at corona radiata and posterior limb of the internal capsule in human brain.** *Neuro Rehabilitation* 2009;24:279–83 CrossRef Medline

Association of Carotid Artery Disease with Collateralization and Infarct Growth in Patients with Acute Middle Cerebral Artery Occlusion

Resul Güney, Arne Potreck, Ulf Neuberger, Niclas Schmitt, Jan Purrucker, Markus A. Möhlenbruch, Martin Bendszus, and Fatih Seker

ABSTRACT

BACKGROUND AND PURPOSE: Collaterals are important in large vessel occlusions (LVO), but the role of carotid artery disease (CAD) in this context remains unclear. This study aimed to investigate the impact of CAD on intracranial collateralization and infarct growth after thrombectomy in LVO.

MATERIALS AND METHODS: All patients who underwent thrombectomy due to M1 segment occlusion from 01/2015 to 12/2021 were retrospectively included. Internal carotid artery stenosis according to NASCET was assessed on the affected and nonaffected sides. Collaterals were assessed according to the Tan score. Infarct growth was quantified by comparing ASPECTS on follow-up imaging with baseline ASPECTS.

RESULTS: In total, 709 patients were included, 118 (16.6%) of whom presented with CAD (defined as severe stenosis $\geq 70\%$ or occlusion ipsilaterally), with 42 cases (5.9%) being contralateral. Good collateralization (Tan 3) was present in 56.5% of the patients with ipsilateral CAD and 69.1% of the patients with contralateral CAD. The ipsilateral stenosis grade was an independent predictor of good collateral supply (adjusted OR: 1.01; NASCET point, 95% CI: 1.00–1.01; $P = .009$), whereas the contralateral stenosis grade was not ($P = .34$). Patients with ipsilateral stenosis of $\geq 70\%$ showed less infarct growth (median ASPECTS decay: 1; IQR: 0–2) compared with patients with 0%–69% stenosis (median: 2; IQR: 1–3) ($P = .005$). However, baseline ASPECTS was significantly lower in patients with stenosis of 70%–100% ($P < .001$). The results of a multivariate analysis revealed that increasing ipsilateral stenosis grade (adjusted OR: 1.0; 95% CI: 0.99–1.00; $P = .004$) and good collateralization (adjusted OR: 0.5; 95% CI: 0.4–0.62; $P < .001$) were associated with less infarct growth.

CONCLUSIONS: CAD of the ipsilateral ICA is an independent predictor of good collateral supply. Patients with CAD tend to have larger baseline infarct size but less infarct growth.

ABBREVIATIONS: CAD = carotid artery disease; LVO = large vessel occlusion

In acute ischemic stroke due to large vessel occlusion (LVO), collateral pathways play a decisive role in preventing extensive infarction.^{1,2} Primary collaterals (circle of Willis) and/or secondary collaterals (eg, ophthalmic or leptomeningeal arteries) are activated to ensure that the cerebral oxygen demands are met.^{3–6} However, the extent of collateralization is highly variable.

Numerous factors, such as age, diabetes, small vessel disease, arterial hypertension, and metabolic syndrome have been identified to impact collateral status.^{7–10} However, there are heterogeneous study results regarding the correlation of ICA stenosis and collateralization. Several of these studies indicate that pre-existing carotid artery disease (CAD) might promote collateral formation in patients

with subsequent ischemic stroke.^{11–16} The physiologic rationale for this is that chronic hypoxia stimulates blood vessel formation.^{17–20}

However, the inclusion criteria were heterogeneous. Some studies included terminal ICA occlusions, potentially compromising collateral recruitment through the circle of Willis. In addition, some included M2 segment occlusions, which might also lead to a bias.^{11–15}

In addition, the pathophysiological relationship between CAD, collaterals, and infarct growth remains unclear, as none of these studies examined infarct progression. Furthermore, they did not evaluate the contralateral ICA in terms of stenosis degree, neglecting its possible impact on collateralization.^{11–15}

Understanding the relationship of CAD, collateralization, and infarct growth is of not only pathophysiological interest but also clinical interest, as it is still not clear whether patients with stroke with tandem occlusion and large ischemic core benefit from endovascular treatment.

Therefore, the aim of this study is to investigate the impact of ipsilateral and contralateral carotid artery stenosis on intracranial

Received October 9, 2023; accepted after revision January 11, 2024.

From the Departments of Neuroradiology (R.G., A.P., U.N., N.S., M.A.M., M.B., F.S.) and Neurology (J.P.), Heidelberg University Hospital, Heidelberg, Germany.

Please address correspondence to Resul Güney, Im Neuenheimer Feld 400, 69120 Heidelberg, Germany; e-mail: resul.guene@med.uni-heidelberg.de

<http://dx.doi.org/10.3174/ajnr.A8180>

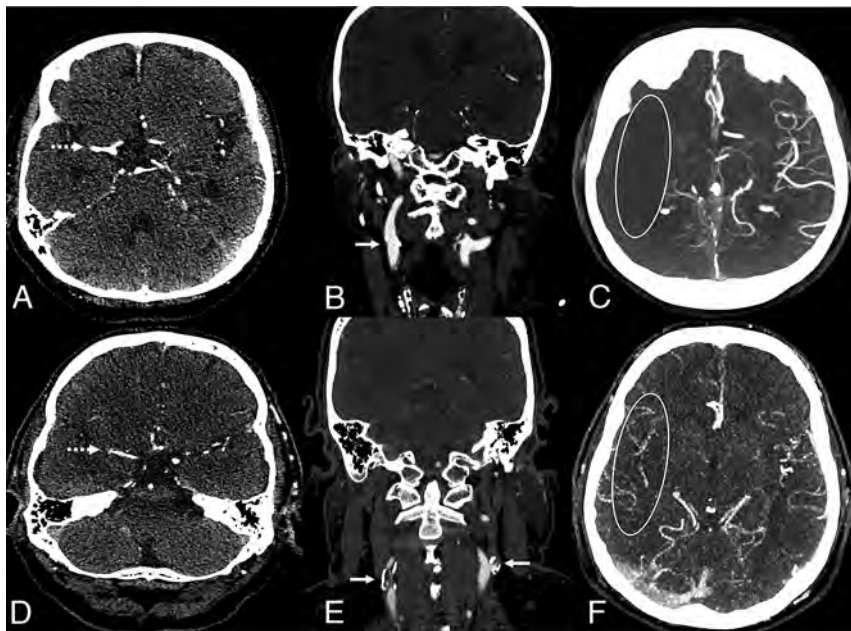


FIG 1. Two exemplary cases of good and poor collaterals in patients with acute right side M1 occlusion of the middle cerebral artery (A and D, dotted arrow). Patient 1 shows no ipsilateral or contralateral stenosis of the extracranial ICA (B, straight arrow) and poor intracranial collaterals, Tan score 0 (C). Patient 2 demonstrates an ipsilateral and contralateral carotid artery disease marked with an arrow (E) with good intracranial collateralization, Tan score 3 (F).

collateralization, initial infarct size, and infarct growth after thrombectomy. We hypothesize that CAD reduces infarct growth in LVO by promoting better intracranial collateralization.

MATERIALS AND METHODS

Study Design

This is a retrospective, observational single-center study. Approval was obtained from the Ethics Committee of the Medical Faculty of Heidelberg University, Heidelberg, Germany. The need for informed consent was waived by the local ethics committee in view of the retrospective nature of the study, and all of the procedures being performed were part of routine care.

All patients undergoing endovascular stroke treatment are prospectively recorded in our institutional thrombectomy registry. This registry was screened for all patients from January 2015 to December 2021. Clinical information was retrospectively collected from medical reports.

The inclusion criteria were: 1) availability of nonenhanced CT and CTA before thrombectomy, and 2) an acute occlusion of the M1 segment of the middle cerebral artery on preinterventional CTA. The M1 segment was defined as the horizontal segment of the middle cerebral artery from the internal carotid bifurcation to the distal genu of the middle cerebral artery, as described by Fischer in his anatomic studies in 1938.^{21,22}

Patients were excluded if a dissection of the carotid artery was present or if the stenosis grade, infarct size, and collateralization were not assessable on CT or CTA. In addition, patients with concomitant occlusion of the intracranial carotid terminus (carotid T or L occlusions) were excluded due to the potential impact on the circle of Willis and infarct progression.^{23,24} Furthermore, assessing carotid stenosis on CTA can be difficult or even impossible in patients

with carotid terminus occlusion due to the common occurrence of pseudoocclusion. Patients with \geq M2 occlusions were also excluded because the extent of leptomeningeal collateral recruitment may have been affected and could not be accurately assessed.

All patients were treated according to national guidelines and in-house standards. This article was written according to the Strengthening the Reporting of Observational Studies in Epidemiology reporting guidelines.

Image Acquisition

Nonenhanced CT and CTA images were acquired at various CT machines within our regional stroke network. Although the technical CT parameters may vary, the image quality was similar, overall. Follow-up imaging (CT or MR imaging) was usually done 1 day after the thrombectomy.

Image Evaluation

The degree of stenosis was assessed on CTA for the ipsilateral and contralateral

ICA, according to the North American Symptomatic Carotid Endarterectomy Trial (NASCET).²⁵ NASCET grading was originally based on conventional angiography but has been reported to show comparable results to those obtained via CTA.²⁶⁻²⁹ In the present study, stenosis grading was evaluated on CTA, analogously to the work of Randoux et al²⁸; briefly, the degree of stenosis was determined on the plane that projected the most severe stenosis. Carotid artery disease was defined as a severe stenosis (\geq 70%) or occlusion of the proximal ICA.

Collaterals were assessed according to the Tan collateral score on the same single-phase CT angiography images. Briefly, the collateral status of the affected hemisphere was compared with that of the nonaffected hemisphere. The score reaches from 0 to 3, with 0 indicating no collaterals, 1 indicating the collateralization of 1%–50% of the occluded MCA territory, 2 indicating the collateralization 51%–99% of the occluded MCA territory, and 3 indicating 100% collateralization.³⁰ Good collateralization was defined as a Tan score of 3, as Tan score 2 covers too broad of a spectrum; for example, 52% is considered equivalent to 95% (Fig 1).

The assessments of the NASCET and Tan scores were conducted by a neuroradiologist and double checked in multiple complicated cases by a second neuroradiologist.

The Alberta Stroke Program Early CT Score (ASPECTS) was initially prospectively assessed on preinterventional and follow-up imaging, and the ratings were checked again for this study. Infarct growth was defined as a decrease of more than 1 ASPECTS point on follow-up imaging compared with the baseline ASPECTS.

Statistics

The statistical analysis was performed using R version 4.2.3 and RStudio. After calculating the descriptive statistics of the data, the

correlation between the stenosis grade and collateral grade was analyzed using the Spearman rank correlation. ASPECTS and infarct growth were compared between patients with and without CAD via the Mann-Whitney U test for continuous data. Univariate regression analyses were performed to identify predictors of good collateralization (Tan score 3) and infarct growth (ASPECTS decay of more than 1 point). Variables with a *P* value of <.05 were used in a multivariate analysis. A *P* value of <.05 was considered to be indicative of a statistically significant result.

RESULTS

Baseline Characteristics

Between 2015 and 2021, 876 patients with an occlusion of the M1 segment of the MCA were treated and recorded in our institutional registry. Fifty-five patients were excluded because preinterventional CTA was not available. Four patients were excluded due to a dissection of the internal carotid artery on preinterventional imaging. Furthermore, an additional 108 patients had to be excluded due to motion or dental implant artifacts or due to insufficient contrast enhancement on CTA. Thus, a total of 709 patients were included in this study. Retrospectively collected demographic data and clinical information from medical reports are presented in Table 1.

Association of Stenosis Degree and Collaterals

Of the eligible 709 patients, 421 (59.4%) showed no carotid stenosis (NASCET 0%) ipsilaterally, and 456 patients (65.3%) presented no carotid stenosis contralaterally. There were 118 patients (16.6%) who had ipsilateral CAD, ie, either a severe stenosis ($\geq 70\%$) or

occlusion ipsilaterally. In 42 cases (5.9%), the contralateral ICA had a severe stenosis or occlusion.

Average Tan score points were slightly increasing with each stenosis grade (Table 2). For patients with ipsilateral CAD, 56.5% presented with good collaterals (Tan score 3), whereas this value was 69.1% for patients with contralateral CAD (Fig 2). In cases with bilateral CAD (*n* = 22), 66.7% presented with good collaterals.

There was no rank correlation between the Tan collateral score and ipsilateral ($\rho = 0.11$) or contralateral carotid stenosis degree ($\rho = 0.09$). Still, the ipsilateral stenosis degree was an independent predictor of good collateral supply in a multivariate analysis (adjusted OR: 1.01 per NASCET point; 95% CI: 1.0–1.01; *P* = .009), whereas the contralateral stenosis degree was not (*P* = .34) (Table 3). Ipsilateral CAD was associated with better collateralization (unadjusted OR: 2.16; 95% CI: 1.40–3.40; *P* < .001).

Infarct Growth

Patients with CAD of the ipsilateral ICA showed less infarct growth (median: 1; IQR: 0–2) compared with patients without CAD (median: 2; IQR: 1–3) (*P* = .005). However, baseline ASPECTS was lower in patients with CAD compared with patients without CAD (*P* < .001). Follow-up ASPECTS was similar in both groups (*P* = .337). Contralateral CAD did not show an association with infarct size or growth (Table 4). A multivariate analysis revealed that an increasing ipsilateral carotid stenosis degree (adjusted OR: 1.0; 95% CI: 0.99–1.0; *P* = .004) and good collateralization (adjusted OR: 0.5; 95% CI: 0.4–0.62, *P* < .001) were associated with less infarct growth (Table 5).

DISCUSSION

Because collaterals are considered an important prognostic factor in large vessel occlusion, factors influencing the collateral status are of high interest.^{1,2} There are heterogeneous data on the correlation of CAD with the intracranial collateral supply.^{11–16} Until now, the pathophysiological role of CAD in collateralization was unclear. According to our results, ipsilateral CAD is associated with good collateralization. However, there is no rank correlation of the stenosis degree with the collateral grading, ie, patients with stroke with a concomitant 20% ICA stenosis do not necessarily have better collaterals compared with patients with a 10% stenosis.

Furthermore, we could demonstrate a positive association of ipsilateral CAD with infarct growth independent of collateralization. This means that patients with CAD and poor collaterals show less infarct progression than do patients without CAD.

Hence, our data, with the largest cohort (*n* = 709), confirms the study results of Rebello et al¹⁴ (*n* = 122), Pienimäki et al¹¹ (*n* = 247), Hassler et al¹² (*n* = 281), and Guglielmi et al¹³ (*n* = 666), all of whom reported an association between good collateral status and carotid stenosis in their studies.

However, the study designs including patient inclusion criteria have noteworthy differences and potential bias. All 4 studies supporting our results included terminal ICA occlusions, consequently impacting the circle of Willis flow by

Table 1: Demographics

Characteristic	Value
Age, mean \pm SD (years)	73.9 \pm 12.6
Female, <i>n</i> (%)	404 (56.9)
Risk factors, <i>n</i> (%)	
Hypertension	526 (74.2)
Diabetes	161 (22.7)
Atrial fibrillation	267 (37.7)
Time from onset to imaging, min (mean, IQR)	357 (94–390)
Baseline NIHSS, median (IQR)	15 (10–20)
Premorbid mRS, median (IQR)	1 (0–2)
Baseline ASPECTS, median (IQR)	8 (7–10)
Ipsilateral carotid stenosis grade according to NASCET, mean, median (IQR)	24.0, 0 (0–38)
Contralateral carotid stenosis grade according to NASCET, mean, median (IQR)	16.3, 0 (0–30)
Tan collateral score, <i>n</i> (%)	
0	17 (2.4)
1	85 (12.0)
2	186 (26.2)
3	421 (59.4)

Table 2: Distribution of stenosis grading (NASCET)

Tan Score	Ipsilateral Stenosis Grade (%)			Contralateral Stenosis Grade (%)		
	Mean	Median	IQR	Mean	Median	IQR
0	12.8	0	0–8	11.3	0	0–20
1	18.4	0	0–25	11.3	0	0–0
2	19.0	0	0–29	14.7	0	0–26
3	22.8	0	0–52	18.3	0	0–35

obstructing a potential blood pathway from the posterior communicating artery to the A1 segment of the anterior cerebral artery or vice versa. Depending on anatomic variation of the circle of Willis, this could have a relevant impact.²³ In the cases of Pienimäki et al¹¹ and Guglielmi et al¹³, it is also unclear how the stenosis degree in these particular patient groups was assessed on CTA, as the pseudo-occlusion of the ICA are frequently observed in patients with terminal ICA occlusions. Rebello et al¹⁴ solved this issue by using DSA, and Hassler et al¹² also mention that they validated their results with DSA.

Furthermore, Hassler et al¹² and Guglielmi et al¹³ included M2 occlusions, while also using the Tan score for collateral status

evaluation. This potentially increased the number of patients with good collateral supply, as they considered Tan 2 as good collateral status. Rebello et al¹⁴ also included M2 occlusions while using the Souza score, which is a modified version of the Tan score. Nevertheless, there was also a potential increase of patients with better collaterals, as dichotomized between a Souza score of 0–1 (absent/poor collaterals) and a Souza score of ≥ 2 (moderate/good collaterals).

We tried to homogenize our cohort by solely including intracranial M1 occlusions and only considering Tan 3 as good collaterals, similarly to Pienimäki et al¹¹, who considered Souza 3 and 4 as very good collaterals and statistically conjoined them due to a small number of patients having a Souza score of 4.^{11–14,31}

Contrary results were reported by Dankbaar et al¹⁵ and Sobczyk et al.¹⁶ Dankbaar et al¹⁵ analyzed 188 patients with M1 occlusion from the prospective Dutch Acute Stroke Trial and found no correlation between stenosis degree and collateralization. However, only 18 patients had a stenosis of $\geq 70\%$. As pointed out by Pienimäki et al¹¹, this is a relatively small number of patients compared with their study of 51 patients (approximately 20%) with $\geq 75\%$ stenosis. In our cohort, 118 patients (approximately 17%) presented with carotid stenosis of $\geq 70\%$. Therefore, there is a higher likelihood of bias in the data of Dankbaar et al.^{11,15} This correlation is also supported by the results of Guglielmi et al¹³, who report a slightly better collateralization in patients with severe carotid stenosis ($>70\%$) compared with moderate stenosis (51%–70%).

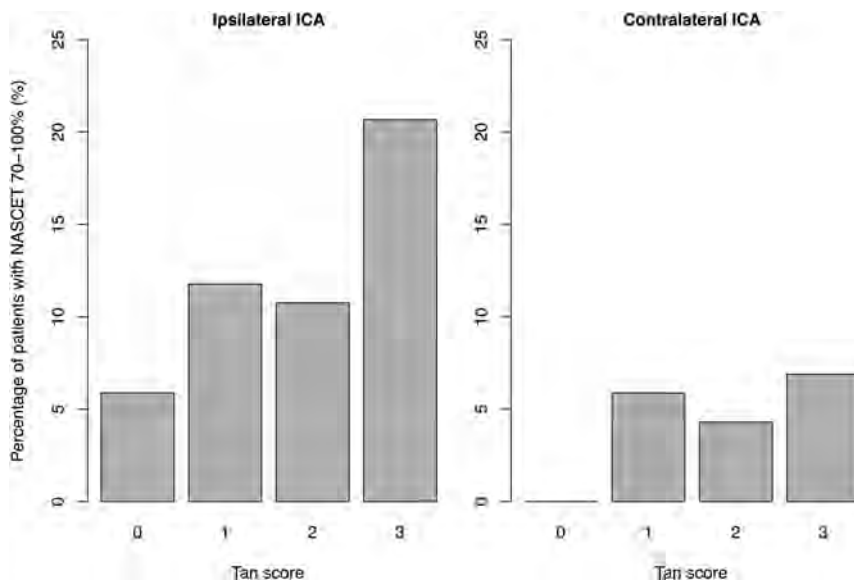


FIG 2. Tan collateral score distribution in patients with ipsilateral and contralateral carotid artery disease.

Table 3: Univariate and multivariate analysis regarding the prediction of good collaterals (Tan 3)

	Unadjusted OR (95% CI)	P Value	Adjusted OR (95% CI)	P Value
Age (per year)	1.0 (0.99–1.01)	.684		
Female	0.98 (0.72–1.32)	.89		
Hypertension	1.07 (0.76–1.52)	.686		
Diabetes	1.08 (0.76–1.56)	.659		
Atrial fibrillation	1.07 (0.78–1.46)	.692		
Premorbid mRS	0.96 (0.85–1.07)	.437		
Ipsilateral stenosis grade (per NASCET point)	1.01 (1.0–1.01)	< .001*	1.01 (1.0–1.01)	.009*
Contralateral stenosis grade (per NASCET point)	1.01 (1.0–1.01)	.019*	1.0 (1.0–1.01)	.34

Note:—An asterisk indicates a statistically significant *P* value.

Table 4: Distribution of ASPECTS and infarct growth

	Ipsilateral Stenosis Grade 0%–69%	Ipsilateral Stenosis Grade 70%–100%	P Value	Contralateral Stenosis Grade 0%–69%	Contralateral Stenosis Grade 70%–100%	P Value
Baseline ASPECTS, median (IQR)	9 (7–10)	8 (7–9)	< .001	8 (7–10)	8 (7–9)	.077
Follow-up ASPECTS, median (IQR)	7 (4–8)	6 (5–8)	.377	7 (5–8)	6 (4–8)	.131
Infarct growth, median (IQR)	2 (1–3)	1 (0–2)	.005	2 (1–3)	1 (1–4)	.786

Table 5: Univariate and multivariate analysis regarding the prediction of infarct growth

	Unadjusted OR (95% CI)	P Value	Adjusted OR (95% CI)	P Value
Age (per year)	1.01 (0.99–1.02)	.334		
Female	1.04 (0.77–1.4)	.795		
Hypertension	0.98 (0.69–1.38)	.895		
Diabetes	1.03 (0.72–1.47)	.868		
Atrial fibrillation	0.93 (0.69–1.27)	.653		
Premorbid mRS	0.96 (0.86–1.07)	.453		
Ipsilateral stenosis grade (per NASCET point)	0.99 (0.99–0.99)	< .001*	0.99 (0.99–1.0)	.004*
Contralateral stenosis (per NASCET point)	0.99 (0.99–1.00)	.003*	1.0 (0.99–1.0)	.355
Tan collateral score 3	0.48 (0.39–0.59)	< .001*	0.5 (0.4–0.62)	< .001*

Note:—An asterisk indicates a statistically significant *P* value.

However, Sobczyk et al¹⁶ had a completely different study design and did not investigate patients with LVO. They included 58 patients with different stenosis degrees from their database and primarily investigated cerebrovascular reactivity. They concluded that collateralization varies greatly and cannot be predicted solely based on the degree of carotid stenosis.

As pointed out initially, we could demonstrate a positive association of ipsilateral CAD with infarct growth independent of collateralization. Patients with CAD and poor collaterals still had a lower rate of infarct progression than did patients without CAD. To our knowledge, this is the first report of a correlation between CAD and infarct growth.

Interestingly, while patients with ipsilateral CAD had a greater baseline infarct size, infarct growth was smaller compared with patients without ipsilateral CAD. In the end, follow-up ASPECTS was similar in patients with and without CAD in our cohort. To our knowledge, this particular finding has not been reported previously, and it stands in contrast to the study results by Deng et al³², who, in their retrospective study of 158 patients who underwent thrombectomy, demonstrated that greater baseline ASPECTS was associated with less infarct growth. However, they did not differentiate between patients with CAD.

The pathophysiological correlation between CAD and collateralization/infarct growth is not yet fully understood. One possible explanation for the lower baseline ASPECTS could be that patients with initially activated collaterals due to CAD have impaired reserve capacities.^{5,16} However, in theory, the chronic hypoxic state caused by CAD may have preconditioned neurons to hypoxia, which ultimately prolonged their resilience in the event of an acute intracranial large vessel occlusion.³³ This hypothesis is supported by an animal experiment by Choi et al³⁴, who experimented on rats with either bilateral common carotid artery ligation or sham operation that were exposed to MCA occlusion and reperfusion. Conclusively, rats with bilateral common carotid artery ligation had smaller infarcts, less DNA-damaged cells, increased cellular defense mechanisms, and evidence of extracellular matrix remodeling. Another possible explanation for the association of CAD and collateralization is that a chronic cerebral hypoxic state stimulates arteriogenesis and angiogenesis, as suggested by Busch et al¹⁸ and Kahn et al¹⁷, based on animal experimental studies. Similar results were reported by Ohtaki et al¹⁹ and Hai et al²⁰, who observed angiogenesis in chronic cerebral hypoperfusion due to an upregulation of vascular endothelial growth factor in rat models.

Therefore, in view of clinical practice, our retrospective data suggest that patients with large ischemic core and tandem lesions

should not be excluded from endovascular treatments, as infarct growth seems to be less present in patients with CAD. This is notable, considering that patients with tandem occlusions are typically more technically challenging and take longer to recanalize than do those with isolated MCA occlusions.³⁵

This finding is of particular interest, as the 6 randomized controlled trials on thrombectomy in patients with large ischemic core were in favor of thrombectomy. Only 3 of the 6 large core trials included cervical tandem occlusions.^{36–41} Further studies and post hoc analyses are necessary to understand the relevance of tandem lesions.

In contrast to other studies, we also analyzed the contralateral ICA for the presence of CAD and its relationship with collateral status and infarct growth. According to our results, contralateral CAD is associated with infarct growth, but it is not an independent predictor when taken together with ipsilateral CAD. Regarding this topic, Maus et al⁴² retrospectively analyzed 197 patients with tandem occlusion who were undergoing endovascular therapy. Even though they did not explicitly investigate infarct progression, their results suggest an adverse effect of contralateral stenosis on clinical outcome. They reported that the presence of a contralateral carotid stenosis of >50% was associated with a worse clinical outcome.⁴² However, further studies are necessary.

The strengths of our study are its large cohort size with 709 patients and its assessment of not only ipsilateral but also contralateral ICA regarding CAD. In addition, to our knowledge, this is the first report of a correlation between CAD and infarct growth. We potentially avoided multiple pitfalls by only focusing on intracranial M1 occlusions. By excluding terminal ICA occlusions, we prevented the potential impairment of collateral recruitment through the circle of Willis and avoided issues with stenosis assessment with pseudo-occlusion. By excluding M2 and distal occlusions, we made the assessment of collateral more distinct.

However, this study has some limitations. The retrospective design of our study may have led to selection bias. Our study was limited to patients with M1 segment occlusions and therefore may not be applied to other occlusion locations. Another bias may have resulted from the use of conventional (single phase) CTA for the collateral assessment, as it is static and only displays a single momentum in the arterial phase. However, multiphase or dynamic CTA was not available for every patient. Excluding patients without multiphase or dynamic CTA would have led to a selection bias. Moreover, nonenhanced CT and CTA images were acquired using various CT machines within our regional stroke network. Even though the image quality was similar

overall, it may have resulted in a bias. In addition, CT or MR imaging was used for follow-up imaging, which may have led to a bias in ASPECTS interpretation.⁴³ Moreover, we did not distinguish between different onset times to imaging. As such, this may have an impact, especially on the initial ASPECTS, as reported by Potreck et al.⁴⁴ Similarly, the exact time of follow-up imaging was not recorded in our institutional thrombectomy registry. It is usually done 1 day after thrombectomy, but this time interval might have an impact on the assessment of the postinterventional infarct size.

CONCLUSIONS

CAD of the ipsilateral ICA, but not the contralateral ICA, is an independent predictor of good collateral supply. Patients with ipsilateral CAD tend to have larger baseline infarct sizes but less infarct growth. Ultimately, follow-up infarct size is similar overall in patients with and without CAD. Our results suggest that CAD has an influence on infarct growth. Hence, patients with CAD should not be excluded from endovascular treatments, despite large infarct sizes on admission.

Disclosure forms provided by the authors are available with the full text and PDF of this article at www.ajnr.org.

REFERENCES

- Jiang B, Ball RL, Michel P, et al. **Factors influencing infarct growth including collateral status assessed using computed tomography in acute stroke patients with large artery occlusion.** *Int J Stroke* 2019;14:603–12 CrossRef Medline
- Liebeskind DS, Saber H, Xiang B, et al. **Collateral circulation in thrombectomy for stroke after 6 to 24 hours in the DAWN trial.** *Stroke* 2022;53:742–48 CrossRef Medline
- Liebeskind DS. **Collateral circulation.** *Stroke* 2003;34:2279–84 CrossRef Medline
- Seböck M, Niftrik C, Lohaus N, et al. **Leptomeningeal collateral activation indicates severely impaired cerebrovascular reserve capacity in patients with symptomatic unilateral carotid artery occlusion.** *J Cereb Blood Flow Metab* 2021;41:3039–51 CrossRef Medline
- Hartkamp NS, Petersen ET, Chappell MA, et al. **Relationship between haemodynamic impairment and collateral blood flow in carotid artery disease.** *J Cereb Blood Flow Metab* 2018;38:2021–32 CrossRef Medline
- Hofmeijer J, Klijn CJM, Kappelle LJ, et al. **Collateral circulation via the ophthalmic artery or leptomeningeal vessels is associated with impaired cerebral vasoreactivity in patients with symptomatic carotid artery occlusion.** *Cerebrovasc Dis* 2002;14:22–26 CrossRef Medline
- Menon BK, Smith EE, Coutts SB, et al. **Leptomeningeal collaterals are associated with modifiable metabolic risk factors.** *Ann Neurol* 2013;74:241–48 CrossRef Medline
- Forestier G, Agbonon R, Bricout N, et al. **Small vessel disease and collaterals in ischemic stroke patients treated with thrombectomy.** *J Neurol* 2022;269:4708–16 CrossRef Medline
- Cipolla MJ, Liebeskind DS, Chan SL. **The importance of comorbidities in ischemic stroke: Impact of hypertension on the cerebral circulation.** *J Cereb Blood Flow Metab* 2018;38:2129–49 CrossRef Medline
- Arsava EM, Vural A, Akpınar E, et al. **The detrimental effect of aging on leptomeningeal collaterals in ischemic stroke.** *J Stroke Cerebrovasc Dis* 2014;23:421–26 CrossRef Medline
- Pienimäki JP, Sillanpää N, Jolma P, et al. **Carotid artery stenosis is associated with better intracranial collateral circulation in stroke patients.** *Cerebrovasc Dis* 2020;49:200–5 CrossRef Medline
- Hassler E, Kneihsl M, Deutschmann H, et al. **Relationship between stroke etiology and collateral status in anterior circulation large vessel occlusion.** *J Neurol* 2020;267:3362–70 CrossRef Medline
- Guglielmi V, LeCouffe NE, Zinkstok SM, et al. **Collateral circulation and outcome in atherosclerotic versus cardioembolic cerebral large vessel occlusion.** *Stroke* 2019;50:3360–68 CrossRef Medline
- Rebello LC, Bouslama M, Haussen DC, et al. **Stroke etiology and collaterals: atheroembolic strokes have greater collateral recruitment than cardioembolic strokes.** *Eur J Neurol* 2017;24:762–67 CrossRef Medline
- Dankbaar JW, Kerckhoffs KGP, Horsch AD, et al. **Internal carotid artery stenosis and collateral recruitment in stroke patients.** *Clin Neuroradiol* 2018;28:339–44 CrossRef Medline
- Sobczyk O, Sam K, Mandell DM, et al. **Cerebrovascular reactivity assays collateral function in carotid stenosis.** *Front Physiol* 2020;11:1031 CrossRef Medline
- Khan MB, Hafez S, Hoda MN, et al. **Chronic remote ischemic conditioning is cerebroprotective and induces vascular remodeling in a VCID model.** *Transl Stroke Res* 2018;9:51–63 CrossRef Medline
- Busch HJ, Buschmann IR, Mies G, et al. **Arteriogenesis in hypoperfused rat brain.** *J Cereb Blood Flow Metab* 2003;23:621–28 CrossRef Medline
- Ohtaki H, Fujimoto T, Sato T, et al. **Progressive expression of vascular endothelial growth factor (VEGF) and angiogenesis after chronic ischemic hypoperfusion in rat.** *Acta Neurochir Suppl* 2006;96:283–87 CrossRef Medline
- Hai J, Li ST, Lin Q, et al. **Vascular endothelial growth factor expression and angiogenesis induced by chronic cerebral hypoperfusion in rat brain.** *Neurosurgery* 2003;53:963–72 CrossRef Medline
- Fischer E. **Die Lageabweichungen der vorderen Hirnarterie im Gefäßbild.** *Zentralbl Neurochir* 1938;3:300–13
- Capocci R, Shotar E, Sourour NA, et al. **Caution; confusion ahead.** *AJNR Am J Neuroradiol* 2017;38:E40–E43 CrossRef Medline
- Ospel JM, Hill MD, Kappelle M, et al. **Which acute ischemic stroke patients are fast progressors?: Results from the ESCAPE trial control arm.** *Stroke* 2021;52:1847–50 CrossRef Medline
- Liebeskind DS, Flint AC, Budzik RF, et al. **Carotid I's, L's and T's: collaterals shape the outcome of intracranial carotid occlusion in acute ischemic stroke.** *J Neurointerv Surg* 2015;7:402–7 CrossRef Medline
- Collaborators. **NASCET. Beneficial effect of carotid endarterectomy in symptomatic patients with high grade stenosis.** *N Engl J Med* 1991;325:445–53
- Saba L, Mallarini G. **A comparison between NASCET and ECST methods in the study of carotids: evaluation using Multi-Detector-Row CT angiography.** *Eur J Radiology* 2010;76:7
- Saba L, Mallarini G. **Comparison between quantification methods of carotid artery stenosis and computed tomographic angiography.** *J Comput Assist Tomogr* 2010;34:421–30 CrossRef Medline
- Randoux B, Marro B, Koskas F, et al. **Carotid artery stenosis: prospective comparison of CT, three-dimensional gadolinium-enhanced MR, and conventional angiography.** *Radiology* 2001;220:179–85 CrossRef Medline
- Bartlett E, Walters T, Symons S, et al. **Quantification of carotid stenosis on CT angiography.** *AJNR Am J Neuroradiol* 2006;27:13–19
- Tan IY, Demchuk AM, Hopyan J, et al. **CT angiography clot burden score and collateral score: correlation with clinical and radiologic outcomes in acute middle cerebral artery infarct.** *AJNR Am J Neuroradiol* 2009;30:525–31 CrossRef Medline
- Souza LC, Yoo AJ, Chaudhry ZA, et al. **Malignant CTA collateral profile is highly specific for large admission DWI infarct core and poor outcome in acute stroke.** *AJNR Am J Neuroradiol* 2012;33:1331–36. 20120301. CrossRef Medline
- Deng W, Teng J, Liebeskind D, et al. **Predictors of infarct growth measured by apparent diffusion coefficient quantification in patients with acute ischemic stroke.** *World Neurosurg* 2019;123:e797–e802 CrossRef Medline

33. Dirnagl U, Becker K, Meisel A. **Preconditioning and tolerance against cerebral ischaemia: from experimental strategies to clinical use.** *Lancet Neurol* 2009;8:398–412 CrossRef Medline
34. Choi SA, Kim EH, Lee JY, et al. **Preconditioning with chronic cerebral hypoperfusion reduces a focal cerebral ischemic injury and increases apurinic/apyrimidinic endonuclease/redox factor-1 and matrix metalloproteinase-2 expression.** *Curr Neurovasc Res* 2007;4:89–97 CrossRef Medline
35. Kim YS, Garami Z, Mikulik R, et al. **Early recanalization rates and clinical outcomes in patients with tandem internal carotid artery/middle cerebral artery occlusion and isolated middle cerebral artery occlusion.** *Stroke* 2005;36:869–71 CrossRef Medline
36. Zaidat OO, Kasab SA, Sheth S, et al. **TESLA trial: Rationale, protocol, and design.** *SVIN* 2023;3:e000787 CrossRef
37. Yoshimura S, Sakai N, Yamagami H, et al. **Endovascular therapy for acute stroke with a large ischemic region.** *N Engl J Med* 2022;386:1303–13 CrossRef Medline
38. Sarraj A, Hassan AE, Abraham MG, et al. **Trial of endovascular thrombectomy for large ischemic strokes.** *N Engl J Med* 2023;388:1259–71 CrossRef Medline
39. Huo X, Ma G, Tong X, et al. **Trial of endovascular therapy for acute ischemic stroke with large infarct.** *N Engl J Med* 2023;388:1272–83 CrossRef Medline
40. Costalat V, Lapergue B, Albucher J, et al. **Evaluation of acute mechanical revascularization in large stroke (ASPECTS \leq 5) and large vessel occlusion within 7h of last-seen-well: The LASTE multicenter, randomized, clinical trial protocol.** *Int J Stroke* 2023;19:114–19 CrossRef Medline
41. Bendszus M, Fiehler J, Subtil F, et al. **Endovascular thrombectomy for acute ischaemic stroke with established large infarct: multicentre, open-label, randomised trial.** *Lancet* 2023;402:1753–63 CrossRef Medline
42. Maus V, Behme D, Borggrefe J, et al. **Carotid artery stenosis contralateral to acute tandem occlusion: an independent predictor of poor clinical outcome after mechanical thrombectomy with concomitant carotid artery stenting.** *Cerebrovasc Dis* 2018;45:10–17 CrossRef Medline
43. McTaggart RA, Jovin TG, Lansberg MG, et al. **Alberta stroke program early computed tomographic scoring performance in a series of patients undergoing computed tomography and MRI: reader agreement, modality agreement, and outcome prediction.** *Stroke* 2015;46:407–12 CrossRef Medline
44. Potreck A, Weyland CS, Seker F, et al. **Accuracy and prognostic role of NCCT-ASPECTS depend on time from acute stroke symptom-onset for both human and machine-learning based evaluation.** *Clin Neuroradiol* 2022;32:133–40 CrossRef Medline

IV Flat Detector CT Angiography in Flat Detector CT Image-Guided Minimally Invasive Surgery for the Treatment of Intracerebral Hypertensive Hemorrhage

Zhang Shu, Wei Wang, Yufa Qiu, Lihong Zhang, Yu Zheng, Jian Wang, Wenyi Li,  Jiajia Ge, Ying Yu,  Nan Lv, and Chi Wang

ABSTRACT

BACKGROUND AND PURPOSE: Spontaneous intracerebral hemorrhage is a serious stroke subtype with high mortality and morbidity. Minimally invasive surgery plus thrombolysis is a promising treatment option, but it requires accurate catheter placement and real-time monitoring. The authors introduced IV flat detector CT angiography (ivFDCTA) into the minimally invasive surgery procedure for the first time, to provide vascular information and guidance for hematoma evacuation.

MATERIALS AND METHODS: Thirty-six patients with hypertensive intracerebral hemorrhage were treated with minimally invasive surgery under the guidance of ivFDCTA and flat detector CT (FDCT) in the angiography suite. The needle path and puncture depth were planned and calculated using software on the DSA workstation. The hematoma volume reduction, operation time, complications, and clinical outcomes were recorded and evaluated.

RESULTS: The mean preoperative hematoma volume of 36 patients was 35 (SD, 12) mL, the mean intraoperative volume reduction was 19 (SD, 11) mL, and the mean postoperative residual hematoma volume was 15 (SD, 8) mL. The average operation time was 59 (SD, 22) minutes. One patient had an intraoperative epidural hematoma, which improved after conservative treatment. The mean Glasgow Outcome Scale score at discharge was 4.3 (SD, 0.8), and the mean mRS score at 90 days was 2.4 (SD, 1.1).

CONCLUSIONS: The use of ivFDCTA in the evacuation of an intracerebral hemorrhage hematoma could improve the safety and efficiency of minimally invasive surgery and has shown great potential in hemorrhagic stroke management in selected patients.

ABBREVIATIONS: FDCT = flat detector CT; HICH = hypertensive ICH; ICH = intracerebral hemorrhage; ivFDCTA = IV FDCT angiography; MIS = minimally invasive surgery

Spontaneous nontraumatic intracerebral hemorrhage (ICH) stroke is associated with high mortality and morbidity across the world, and hypertensive ICH (HICH) accounts for about 60%, which has become a great burden to society.^{1,2} Rapid expansion of the ICH and secondary bleeding are always associated with poor clinical outcome. Timely bleeding control and necessary hematoma evacuation to prevent further deterioration are the keys to critical care management of ICH. Several recent randomized studies have investigated the safety and efficacy of minimally invasive surgery (MIS) plus rtPA in patients with ICH

and compared this strategy with standard medical care.³⁻⁵ Although no differences were found in the primary outcome of the comparative study, a reduction in clot size to ≤ 15 mL was associated with better functional outcomes, suggesting the importance of effective initial hematoma removal in improved prognosis.⁶

Accurate catheter placement and intraoperative real-time monitoring are necessary for substantial ICH evacuation. Currently, most MIS for hematoma evacuation is guided by a stereotactic apparatus or a neurosurgical medical robot but requires additional equipment and time-consuming preparation. Recently developed mixed-reality holographic navigation technology has also demonstrated its potential in the treatment⁷ of ICH, but it is not widely used and has not received adequate clinical validation. Endoscopy-assisted evacuation allows hematoma evacuation under direct view; however, the puncture damage caused by craniotomy is relatively large, and the procedure needs a surgeon with greater experience and operating skills.⁸

Minimally invasive evacuation of ICH under the guidance of flat detector CT (FDCT) has been reported in recent years, and its safety and feasibility in intraoperative puncture guidance and

Received October 30, 2023; accepted after revision January 11, 2024.

From the Departments of Stroke Center (S.Z., W.W., Y.Q., L.Z., C.W.) and Intervention (Y.Z., J.W.), Taicang First People's Hospital, Suzhou, China; Advanced Therapies (W.L., J.G.), Siemens Healthineers, Shanghai, China; and Department of Neurosurgery (Y.Y., N.L.), Changhai Hospital, Second Military Medical University, Shanghai, China.

Z. Shu and W. Wang are co-first authors.

This work was supported by the Taicang First People's Hospital Specific Project Fund. TCYY2020YJKT07.

Please address correspondence to Chi Wang, MD, Department of Stroke Center, Taicang First People's Hospital, No. 58 Changsheng South Road, Taicang City, Suzhou, Jiang su Province, China 215413; e-mail: watch_2008@163.com

<http://dx.doi.org/10.3174/ajnr.A8186>

real-time hematoma-evacuation monitoring have been demonstrated.^{9,10} In this study, we attempted to introduce IV FDCT angiography (ivFDCTA) to the treatment of ICH for the first time. A new 6-second IV DSA procedure was used, compared with previously reported FDCT-guided ICH evacuation, to implement cerebrovascular information during puncture needle path planning and to localize the hematoma. ivFDCTA is an imaging technique that enables the acquisition of the whole cerebral vasculature with a single injection of contrast media intravenously. It has been used for the visualization of intracranial artery stenosis and occlusion,¹¹ the assessment of intracranial aneurysm,¹²⁻¹⁴ and the follow-up of endovascular procedures,¹⁵⁻¹⁷ showing its feasibility and therapeutic value in the neurology field. This study aimed to confirm the reliability of the vascular images provided by ivFDCTA for needle diameter planning and real-time guidance during ICH puncture.

MATERIALS AND METHODS

Patients

This study was approved by the ethics committee of Taicang First People's Hospital. Patient consent for treatment was obtained according to the hospital guidelines. Between November 2020 and May 2023, thirty-six patients diagnosed with hypertensive hemorrhage were included in this study. The inclusion criteria were the following: 1) ICH with related neurologic symptoms and signs, 2) absence of cerebral hernia, 3) supratentorial ICH with a Glasgow Coma Scale score of ≥ 9 within 72 hours of onset, and 4) a distance from the hematoma to the cortical surface of > 1 cm. The exclusion criteria were the following: 1) CTA diagnosis of secondary cerebral hemorrhage, such as aneurysm or vascular malformation, 2) mRS score of > 2 before onset, and 3) long-term use of aspirin or anticoagulant drugs.

All patients underwent cranial CT (Somatom go.Fit; Siemens) before the hematoma evacuation. The volumes of the hematoma and surrounding edema were calculated by 3 separate radiologists in a single-blind way, and the average value was adopted. The volume of the hematoma (milliliters) = Length of the Maximal Hematoma Layer \times Width of the Maximal Hematoma Layer \times Number of Hematoma Layers $\times \pi/6$.

ivFDCTA

Patients were placed in a supine position under local anesthesia. Images were acquired using a 16-bit Artis Q ceiling angiography system (Siemens) with the patient in a supine position. All patients received general anesthesia to ensure coordination and image quality. ivFDCTA was acquired by using a manually triggered 6-second DSA DynaCT Head program, which includes a native and contrast-enhanced sweep. The contrast-enhanced run was not started until contrast media was seen in the intracranial ICA C1-C2 during the bolus-watching phase. Seventy milliliters of iodinated contrast media (320 mg/mL, Yangtze River Pharmaceutical Group) was injected into a cubital vein at a pressure of 300 psi through a 20F angiocatheter (BD Intima II Plus; Becton, Dickinson and Company) at a flow rate of 5 mL/s using a power injector. The acquisition of a native image was started after the beginning of contrast injection. Data acquisition per run was performed with the following parameters: acquisition time, 6 seconds per run; tube

voltage, 70 kV; section matrix, 512×512 ; flat detector size, 30×40 cm; total rotation angle, 200° ; angulation step, 0.5° per frame; 397 frames per run; dose, $1.2 \mu\text{Gy}/\text{fr}$. Window center and width of the bolus check sequence were set at 130 and 2500, respectively. Contrast-enhanced images were viewed in cross-sectional MIP thin mode, with a section thickness of 2 mm.

Needle Path Planning and Puncture Guidance

Native and contrast-enhanced images acquired by ivFDCTA were viewed in DualVolume mode (Siemens). The opacity of each volume was adjusted to enable a clear display of both the intracranial hematoma and vessels. Needle path and puncture depth were planned and calculated using the software syngo Needle Guidance on the DSA workstation (syngo X-Workplace; Siemens). The target point was chosen by selecting a point within the hematoma 1 cm away from the boundaries of the hematoma. The entry point was chosen on either side of the temporal site that was close to the hematoma. The needle guidance software enables a preview of the puncture path from the entry point to the target from 3 cross-sectional perspectives (sagittal, coronal, and axial). To prevent unintentional bleeding, we could adjust the planning path if there is the potential for a large blood vessel to be punctured (Fig 1).

Hematoma Evacuation and Intraoperative Monitoring

Once the needle path was determined, a corresponding C-arm working angle in bull's eye view was sent to the C-arm, and a red laser crosshair was displayed on patient's head to indicate the puncture entry point.

Minimally invasive craniopuncture was performed using a YL-1 Needle (Beijing WanTeFu Medical Apparatus). The YL-1 needle, with a diameter of 3 mm, is an internal drilling needle that is enclosed by a casing with small holes at the end to facilitate fluid flow. Initially, an electric drill is used in conjunction with the YL-1 needle for puncturing purposes. The first FDCT scan is performed when the puncture needle is fixed to the skull and the dura is not punctured. According to the results of FDCT, the direction of puncture is adjusted and the dural puncture is continued. To reach the center of the hematoma, we removed the assembly comprising the internal drill needle. To minimize potential brain damage risks, we used plastic needles as substitutes for internal drilling needles. These plastic needles have a blunt end and are 2 mm longer than their internal drill counterparts. The puncture needle is drilled through the skull and into the hematoma before the cannula is fixed to the skull and the hematoma is aspirated. A 20-second DynaCT scan (Siemens) was performed as necessary to monitor the degree of aspiration.

For patients with a large hematoma volume, it is often difficult to achieve a satisfactory hematoma-removal effect with 1 puncture aspiration. FDCT in the operation enables the surgeon to monitor the situation in real-time and perform a second puncture under sterile conditions if necessary (Fig 2). Aspiration was stopped when the hematoma volume was reduced by two-thirds or was < 15 mL, shown in the FDCT image.

The whole procedure is summarized in a flow chart shown in Fig 3.

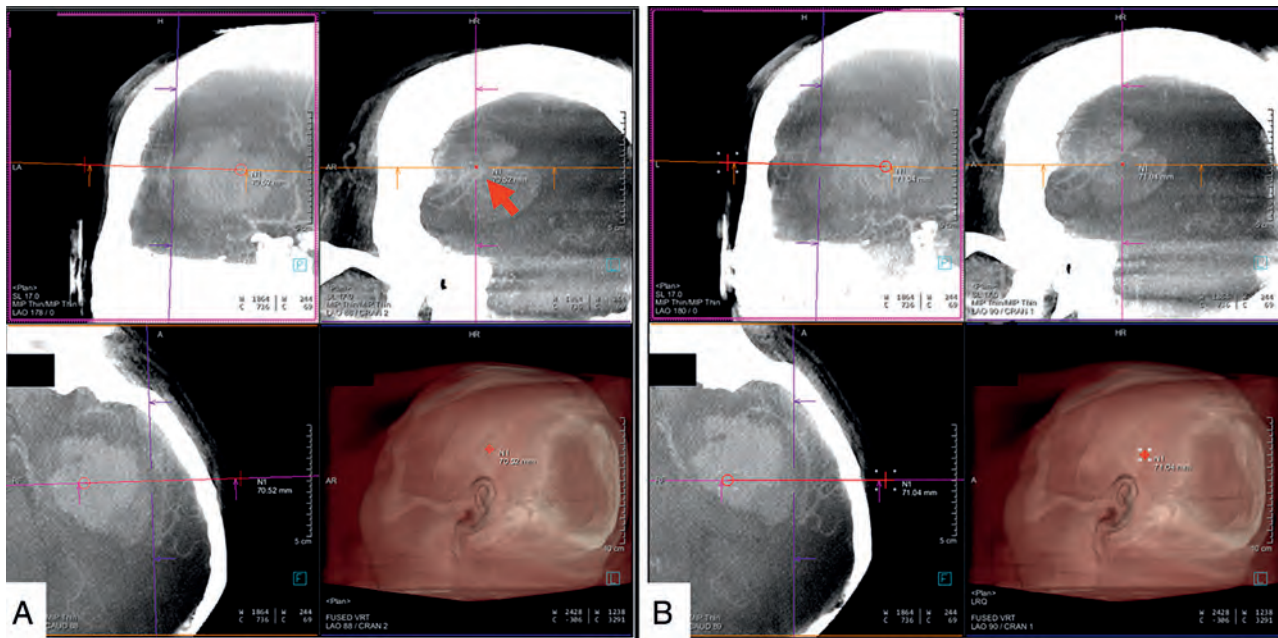


FIG 1. Needle path planning and puncture guidance on the ivFDCTA image using syngo Needle Guidance software. Hemorrhage in the left basal ganglia. A puncture needle path was planned by defining the skull entry point and hematoma target point. The final puncture entry point (B) was adjusted to 1 cm before the first planning (A) to avoid the intracranial vascular cluster at the temporal side (red arrow).

Surgery Evaluation

Following initial aspiration, a lysis fluid-containing urokinase is injected to facilitate further aspiration. The thrombolytic agent is reintroduced into the hematoma every 6–12 hours. A follow-up CT scan is performed 1–3 days after the initial drainage to measure the amount of blood remaining. The drainage needle remains in the brain for 3–5 days.

Common postoperative complications were recorded during hospitalization, including postoperative rebleeding, intracranial infection, and gastrointestinal bleeding.

Statistical Analysis

All data were analyzed by SPSS software, Version 16.0 (IBM). The data were presented as mean (SD).

RESULTS

Thirty-six patients were included in this study. The mean preoperative hematoma volume of 36 patients was 35 (SD, 12) mL, the mean intraoperative volume reduction was 19 (SD, 11) mL, and the mean postoperative residual hematoma volume was 15 (SD, 8) mL. The average operation time was 59 (SD, 22) minutes, there was an intraoperative epidural hematoma in 1 case, and the hematoma volume was 3 mL, which improved after conservative treatment. The maximum and minimum positioning errors were 3.5 and 0.3 mm. Patients' basic characteristics and postoperative evaluation are listed in the Table.

DISCUSSION

ICH accounts for 10%–40% of all strokes worldwide and is as high as 40% in Asia. The fatality and disability rate exceeds 60%,

and the incidence is increasing year by year. Possible treatments of ICH include¹ conservative medical treatment for hemostasis and coagulopathy or² surgical treatment to remove the hematoma. Whether surgery can improve the prognosis of patients with ICH remains controversial. The Surgical Treatment for Ischemic Heart Failure (STICH) and STICH II trials aimed to investigate the effectiveness of early surgery (mostly craniotomy) compared with initial medical treatment alone, and the results were neutral. However, the question about the performance of less invasive surgery to remove ICH was raised. The randomized controlled Minimally Invasive Surgery Plus Rt-PA for ICH Evacuation (MISTIE)⁴ II study demonstrated the safety and efficacy of alteplase in combination with MIS in ICH management. The MISTIE III trial compared the image-guided MISTIE treatment with standard medical care, but no improvement was found in the functional outcome at 365 days.⁵ However, in the subgroup study in which ICH volume was reduced to ≤ 15 mL or was $>70\%$, better mRS scores could be achieved. This finding indicates the importance of surgery efficiency in determining good functional outcome of MIS in ICH evacuation.⁶

The effectiveness of hematoma evacuation is heavily dependent on the decreased hematoma volume. According to our experience, the hematoma may contain a mixture of liquid, semisolid, and solid material throughout the evacuation procedure, making it impossible to reduce the volume equally. Accurate catheter placement with as much contact area as possible with the hematoma and intraoperative real-time monitoring are essential to ensure the safety and effectiveness of hematoma evacuation and avoid unintentional loss of brain tissue. The angiography system with intraoperative FDCT imaging of the brain parenchyma to assess the degree of ICH evacuation has been described before,

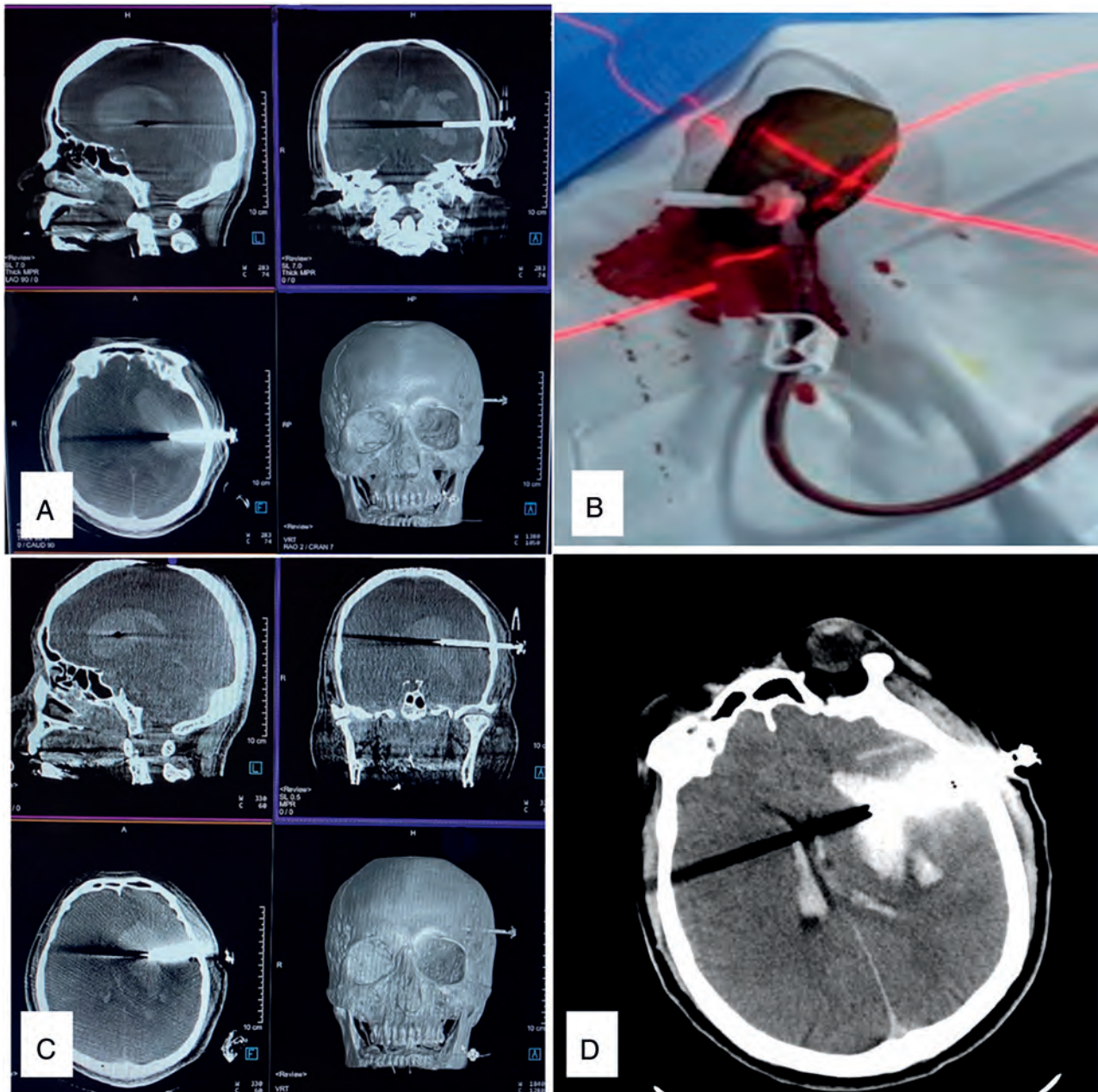


FIG 2. Monitoring of intraoperative hematoma evacuation under FDCT. The patient had an estimated hematoma volume of 45 mL. *A*, Discharge of 10 mL from the first hematoma. *B*, Laser crosshair indicated the second puncture entry point. *C*, A second puncture was performed, and the needle position was confirmed under FDCT. A total estimated volume of 25 mL of hematoma was aspirated. *D*, Postoperative CT shows a residual hematoma of 10 mL.

and the needle guidance software enables precise catheter placement and navigation accuracy, in which puncture path planning is realized on intraoperative FDCT 3D volume images by identifying the target hematoma and the entry point on the skull. A virtual flight along the needle path can be checked in 3 MPR (Multiplanar Reformation) segments to verify that the needle path does not injure any anatomic structure, and the laser positioner light is automatically on and indicates the entry point on the skull.^{9,10,18}

Minimally invasive craniopuncture using a YL-1 needle via a temporal approach has become a standard surgical method commonly used in China. It has shown the advantages of a small deviation, low cost, and low surgical difficulty with good functional

outcomes through multiple randomized clinical trials, making it a practical and promising technique for ICH clot removal, especially in primary hospitals with large patient populations.¹⁹⁻²² Compared with conventional CT-guided stereotactic aspiration, craniopuncture under the guidance of FDCT in an interventional operating room has become more suitable due to better environment hygiene and emergency event responses. However, it can be challenging to securely avoid the external carotid artery and major vessels of the lateral fissure when using a temporal approach. Prior research did not include cerebral vascular information in craniopuncture; the authors used noncontrast FDCT solely for planning and guidance.^{9,10,18}

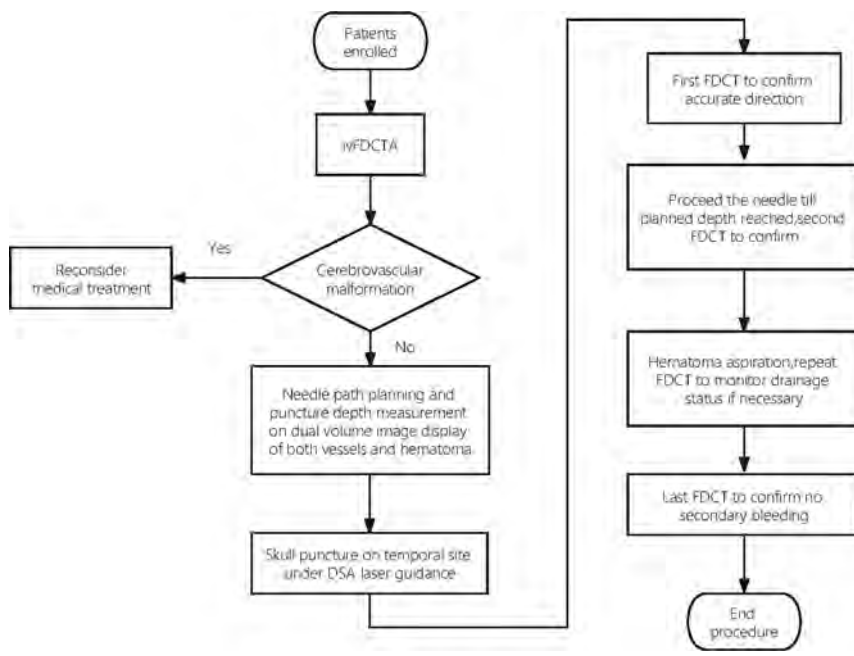


FIG 3. Flow chart of the ivFDCTA- and FDCT-guided HICH evacuation.

Basic characteristics and postoperative evaluation of all 36 patients

Characteristics	
Age (mean) (yr)	53 (SD, 12)
Sex (male) (%)	81%
NIHSS score on admission (median)	17 (SD, 6)
Preoperative GCS score (mean)	10 (SD, 2)
GOS	4.3 (SD, 0.8)
90-Day mRS	2.4 (SD, 1.1)
Complications	2.7%
Days to discharge	16.4 (SD, 5.3)

Note:—GCS indicates Glasgow Coma Scale; GOS, Glasgow Outcome Score.

In this study, we first introduced ivFDCTA into the hematoma-evacuation workflow. All the arteries of the brain can be seen due to the IV-injection acquisition protocol, which could be used for puncture needle path planning to prevent secondary bleeding. In previous studies, the rebleeding rate of minimally invasive brain puncture under CT was 8.8% to 10%.²³ Chen et al²⁴ reported a study of 48 patients with ICH treated with the YL-1 needle under CT guidance; 2 of these cases required repositioning the puncture needle due to inadequate initial placement. Three (6.3%) patients experienced early re-bleeding within the first 3 postoperative days, a rate higher than in our study. The 6-second ivFDCTA protocol is substantially faster than the 20-second previously reported protocol, but it provides adequate image quality for hematoma identification, reducing the radiation exposure and accelerating the preparation for the procedure. As shown in Fig 1, during puncture planning, both blood vessels and hematoma could be observed by displaying the ivFDCTA native and contrast-enhanced images, allowing the physician to plan the needle path safely and more accurately to avoid large vessels and reduce intraoperative bleeding and complications. In case of a large hematoma, it may be difficult to achieve the target of volume reduction with a single puncture, and multiple target points

may be needed.²⁵ Marquardt et al²⁶ demonstrated the safety and efficiency of multiple target aspiration techniques. Zhou et al²⁰ compared 80 patients with HICH who received CT-guided MIS and showed that the clearance rate of hematomas in patients with hematomas of >40 mL with a single puncture was less than in those with multiple punctures. With the ivFDCTA in ICH removal, the large vessels on the puncture tract can be accurately visualized and located, and intraoperative CT enables multiple punctures performed safely and sterilely in the interventional operating room (Fig 2).

Because it is reliable and convenient, minimally invasive puncture has been widely used in China to treat HICH. The 2 most commonly used puncture needles are the soft tube, also called the “soft channel” approach, and the YL-1 puncture needle, also known as the “hard-channel” technique. Comparisons

between the 2 methods are rare, yet available. In a study involving 150 patients, Xia et al²² found that there was no discernible difference in the amount of hematoma and perihematomal edema on day 7 between the 2 techniques. The benefits of the soft tube tend to be ease of direction adjustment and quick rinsing. We chose the hard channel because it allows us to fully use intraoperative FDCT while enabling safe adjustments outside the dura and accurate placement at the assigned position using the skull-fixation technique. If the first puncture volume reduction is not satisfactory, multiple punctures can be performed in a sterile state. On the contrary, due to the presence of the C-arm, the operating space directly above the head during soft-channel puncture will be affected. ivFDCTA is a technique to generate CTA-like images using DSA through noninvasive IV contrast media injection. In the field of neurology, this technique was first proposed as a non-invasive alternative for follow-up after placement of intracranial devices such as stents and flow diverters and enabled good visualization of both the device and vessel lumen.¹⁵⁻¹⁷ ivFDCTA also shows comparable image quality with 2D and 3D DSA in delineating and diagnosing vessel stenosis and aneurysms, and even better quality in visualizing complex aneurysms.¹²⁻¹⁴ In the ICH evacuation procedure, we also found that ivFDCTA has the potential to be used for a rapid screening of the cerebral vasculature malformations to avoid secondary bleeding during the evacuation procedure. According to the guideline for ICH management, CTA is recommended for detection of some structural causes of secondary ICH and signs of hematoma expansion.²⁷ However, patients with ICH, especially in those with a high NIHSS score, often have severe agitation and require sedation to undergo a CTA scan. Nevertheless, a standard anesthesia procedure and care management are not available due to limited space and equipment resources in the CT room. Most CT examination rooms lack sufficient first aid and patient-monitoring equipment to handle

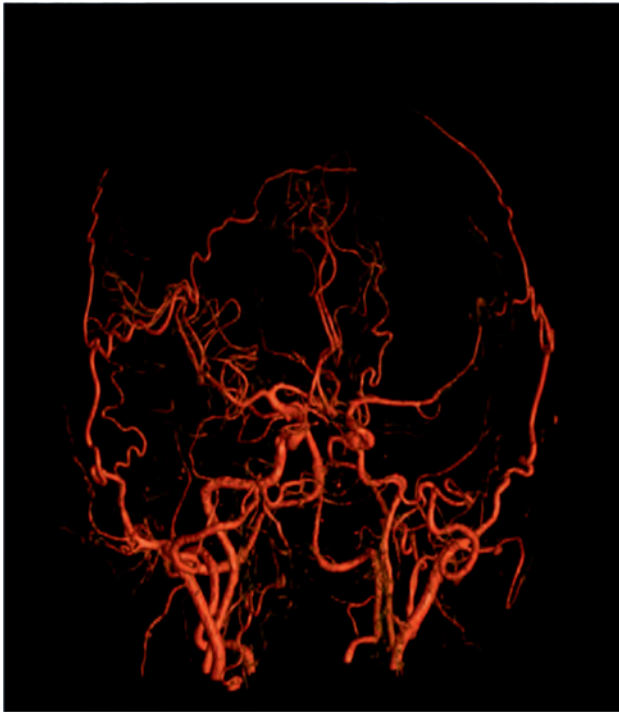


FIG 4. IV 3D DSA image.

emergencies, and patient risks may increase during suite transfers. Furthermore, bone artifacts and spatial resolution may restrict the precision of CTA-based vascular malformation diagnosis and geometric delineation. In addition to generating 2D cross-sectional images, the ivFDCTA methodology we describe in this article could also generate IV 3D DSA (Fig 4), which provides a volumetric view of the cerebral arteries and enables determination of the optimal C-arm working angle if intraoperative endovascular treatment is necessary. Therefore, with the use of ivFDCTA, clinical steps including screening for cerebrovascular disease, puncture needle path planning and navigation, hematoma evacuation, and endovascular treatment could all be performed in the angiography suite. This one-stop cerebral hemorrhage management workflow has the potential to eliminate the treatment delays and risks during transfer and increase the safety of the procedure and the efficiency of hematoma evacuation.

Our study has limitations. First, this is a retrospective single-center study. The amount of patient data collected is small and requires further research and the completion of statistical analyses of long-term neurologic outcomes. Second, there is no comparison group in this study. Comparison between FDCT and ivFDCTA guidance will be included to further explore the clinical value of ivFDCT in ICH management. Third, the initial calculation of the hematoma volume according to the Tada formula (Hematoma Amount = Long Diameter of the Largest Level of Hematoma × Short Diameter of the Largest Level of Hematoma × Number of Levels of Hematoma × $\pi/6$) is based on the principle that the bleeding focus is assumed to be an elliptic sphere, which has evolved from the formula for calculating the volume of an elliptic sphere. For the irregular shape of a hematoma, the calculation error is large and the calculated volume is often larger than the actual volume of the hematoma.

Another more accurate hematoma calculation method needs to be adopted.

CONCLUSIONS

Cerebral hemorrhage is still a fatal condition. It is necessary to continue improving the treatment of ICH for better clinical outcomes. In this study, for the first time, we introduced the application of ivFDCTA in the treatment of HICH MIS treatment and demonstrated its safety and feasibility. The use of ivFDCTA in ICH hematoma evacuation could improve the safety of MIS and has shown great potential in hemorrhagic stroke management in selected patients.

Disclosure forms provided by the authors are available with the full text and PDF of this article at www.ajnr.org.

REFERENCES

1. GBD 2019 Stroke Collaborators. **Global, regional, and national burden of stroke and its risk factors, 1990-2019: a systematic analysis for the Global Burden of Disease Study 2019.** *Lancet Neurol* 2021;20:795-820 CrossRef Medline
2. Tang Y, Yin F, Fu D, et al. **Efficacy and safety of minimal invasive surgery treatment in hypertensive intracerebral hemorrhage: a systematic review and meta-analysis.** *BMC Neurol* 2018;18:136 CrossRef Medline
3. Mould WA, Carhuapoma JR, Muschelli J, et al; MISTIE Investigators. **Minimally invasive surgery plus recombinant tissue-type plasminogen activator for intracerebral hemorrhage evacuation decreases perihematomal edema.** *Stroke* 2013;44:627-34 CrossRef Medline
4. Hanley DF, Thompson RE, Muschelli J, et al; MISTIE Investigators. **Safety and efficacy of Minimally Invasive Surgery Plus Alteplase in Intracerebral Haemorrhage Evacuation (MISTIE): a randomised, controlled, open-label, phase 2 trial.** *Lancet Neurol* 2016;15:1228-37 CrossRef Medline
5. Hanley DF, Thompson RE, Rosenblum M, et al; MISTIE III Investigators. **Efficacy and safety of Minimally Invasive Surgery with Thrombolysis in Intracerebral Haemorrhage Evacuation (MISTIE III): a randomised, controlled, open-label, blinded endpoint phase 3 trial.** *Lancet* 2019;393:1021-32 CrossRef Medline
6. Awad IA, Polster SP, Carrión-Penagos J, et al; MISTIE III Trial Investigators. **Surgical performance determines functional outcome benefit in the Minimally Invasive Surgery Plus Recombinant Tissue Plasminogen Activator for Intracerebral Hemorrhage Evacuation (MISTIE) Procedure.** *Neurosurgery* 2019;84:1157-68 CrossRef Medline
7. Peng C, Yang L, Yi W, et al. **Application of fused reality holographic image and navigation technology in the puncture treatment of hypertensive intracerebral hemorrhage.** *Front Neurosci* 2022;16:850179 CrossRef Medline
8. Zheng Z, Wang Q, Sun S, et al. **Minimally invasive surgery for intracerebral and intraventricular hemorrhage.** *Front Neurol* 2022;13:755501 CrossRef Medline
9. Yang Z, Hong B, Jia Z, et al. **Treatment of supratentorial spontaneous intracerebral hemorrhage using image-guided minimally invasive surgery: initial experiences of a flat detector CT-based puncture planning and navigation system in the angiographic suite.** *AJNR Am J Neuroradiol* 2014;35:2170-75 CrossRef Medline
10. Dornbos Iii D, Halabi C, DiNitto J, et al. **How to iGuide: flat panel detector, CT-assisted, minimally invasive evacuation of intracranial hematomas.** *J Neurointerv Surg* 2022;14:522-26 CrossRef Medline
11. Jeon JS, Sheen SH, Hwang GJ, et al. **Feasibility of intravenous flat panel detector CT angiography for intracranial arterial stenosis.** *AJNR Am J Neuroradiol* 2013;34:129-34 CrossRef Medline
12. Toyota S, Iwasako K, Takimoto H, et al. **Intravenous 3D digital subtraction angiography in the diagnosis of unruptured intracranial aneurysms.** *AJNR Am J Neuroradiol* 2008;29:107-09 CrossRef Medline

13. Göllitz P, Struffert T, Knossalla F, et al. **Angiographic CT with intravenous contrast injection compared with conventional rotational angiography in the diagnostic work-up of cerebral aneurysms.** *AJNR Am J Neuroradiol* 2012;33:982–87 CrossRef Medline
14. Lauric A, Heller RS, Schimansky S, et al. **Benefit of cone-beam CT angiography in visualizing aneurysm shape and identification of exact rupture site.** *J Neuroimaging* 2015;25:56–61 CrossRef Medline
15. Buhk JH, Lingor P, Knauth M. **Angiographic CT with intravenous administration of contrast medium is a noninvasive option for follow-up after intracranial stenting.** *Neuroradiology* 2008;50:349–54 CrossRef Medline
16. Struffert T, Kloska S, Engelhorn T, et al. **Optimized intravenous flat detector CT for non-invasive visualization of intracranial stents: first results.** *Eur Radiol* 2011;21:411–18 CrossRef Medline
17. Struffert T, Saake M, Ott S, et al. **Intravenous flat detector CT angiography for non-invasive visualisation of intracranial flow diverter: technical feasibility.** *Eur Radiol* 2011;21:1797–801 CrossRef Medline
18. Hecht N, Czabanka M, Kendlbacher P, et al. **Intraoperative CT and cone-beam CT imaging for minimally invasive evacuation of spontaneous intracerebral hemorrhage.** *Acta Neurochir (Wien)* 2020;162:3167–77 CrossRef Medline
19. Wang WZ, Jiang B, Liu HM, et al. **Minimally invasive craniopuncture therapy vs. conservative treatment for spontaneous intracerebral hemorrhage: results from a randomized clinical trial in China.** *Int J Stroke* 2009;4:11–16 CrossRef Medline
20. Zhou H, Zhang Y, Liu L, et al. **A prospective controlled study: minimally invasive stereotactic puncture therapy versus conventional craniotomy in the treatment of acute intracerebral hemorrhage.** *BMC Neurol* 2011;11:76 CrossRef Medline
21. Hersh EH, Gologorsky Y, Chartrain AG, et al. **Minimally invasive surgery for intracerebral hemorrhage.** *Curr Neurol Neurosci Rep* 2018;18:34 CrossRef Medline
22. Xia L, Han Q, Ni XY, et al. **Different techniques of minimally invasive craniopuncture for the treatment of hypertensive intracerebral hemorrhage.** *World Neurosurg* 2019;126:e888–94 CrossRef Medline
23. Hannah T, Kellner R, Kellner C. **Minimally invasive intracerebral hemorrhage evacuation techniques: a review.** *Diagnostics (Basel)* 2021;11:576 CrossRef
24. Chen X, Chen W, Ma A, et al. **Frameless stereotactic aspiration and subsequent fibrinolytic therapy for the treatment of spontaneous intracerebral haemorrhage.** *Br J Neurosurg* 2011;25:369–75 CrossRef Medline
25. Kim H, Edwards NJ, Choi HA, et al. **Treatment strategies to attenuate perihematomal edema in patients with intracerebral hemorrhage.** *World Neurosurg* 2016;94:32–41 CrossRef Medline
26. Marquardt G, Wolff R, Seifert V. **Multiple target aspiration technique for subacute stereotactic aspiration of hematomas within the basal ganglia.** *Surg Neurol* 2003;60:8–13; discussion 14 CrossRef Medline
27. Hemphill JC 3rd, Greenberg SM, Anderson CS, et al; Council on Clinical Cardiology. **Guidelines for the Management of Spontaneous Intracerebral Hemorrhage: A Guideline for Healthcare Professionals from the American Heart Association/American Stroke Association.** *Stroke* 2015;46:2032–60 CrossRef Medline

Mechanical Thrombectomy for Pediatric Arterial Ischemic Stroke from Acute M2 Occlusion

 Kartik D. Bhatia,  Elizabeth Pulcine, Ian Andrews, Sachin Gupta, Richard Webster, Christopher Troedson, Russell C. Dale, Michelle Lorentzos, Carmen Parra-Farinas, John Worthington, Kylie Tastula,  Timothy Ang,  Andrew Cheung,  Nathan Manning, and  Prakash Muthusami



ABSTRACT

SUMMARY: Pediatric large-vessel occlusion has a poor natural history. Recent retrospective studies have demonstrated the potential benefits, feasibility, and safety profile of mechanical thrombectomy in children. However, the role of thrombectomy in pediatric M2 occlusions remains uncertain. In this clinical report, we present a multicenter series of 6 pediatric patients with acute M2 occlusion (female = 1, male = 5; age range, 0.9–16.0 years, mean = 9.2). All 6 patients having undergone thrombectomy had excellent clinical outcomes (pediatric mRS = 0–1) at 3 months and final available follow-up (median, 12 months; range, 3–72 months). Factors relevant to treatment decision-making in pediatric M2 occlusions are discussed, including the important role of multidisciplinary team discussions during acute management.

ABBREVIATIONS: LVO = large-vessel occlusion; MeVO = medium-vessel occlusion; mTICI = modified treatment in cerebral ischemia; ped-mRS = pediatric mRS; Ped-NIHSS = pediatric NIHSS

Pediatric ischemic stroke due to large-vessel occlusion (LVO) has a poor natural history.¹ Approximately three-quarters of patients managed conservatively have moderate-to-severe disability or death at 3 months after stroke onset.¹ Given these poor outcomes and the clear benefit of mechanical thrombectomy in adults,² mechanical thrombectomy is increasingly used in pediatric LVO stroke despite a lack of randomized trial evidence in children.

A recent retrospective case-control study demonstrated improved clinical outcomes in 26 children who received mechanical thrombectomy (intracranial ICA = 10, M1 = 11, M2 = 3, basilar = 2) compared with 26 matched controls with acute LVO ischemic stroke.³ Favorable outcomes were also identified from the multicenter retrospective Save ChildS cohort study (median

mRS score = 1.0).⁴ These results suggest that mechanical thrombectomy is beneficial for selected pediatric patients with LVO.

In adults, there is increasing interest in the treatment of medium-vessel occlusion (MeVO) using mechanical thrombectomy, particularly for the second segment (M2) of the MCA.⁵ Subgroup analysis of a large prospective registry for mechanical thrombectomy in adults demonstrated favorable clinical outcomes (mRS = 0–2 at 90 days) in 72.5% of patients with M2 occlusion.⁶ There are multiple randomized trials underway comparing thrombectomy with the best medical management for MeVO in adults.

The role of mechanical thrombectomy for acute M2 occlusion in children is uncertain. Current clinical guidelines provide no recommendations regarding thrombectomy for pediatric MeVO.⁷ However, depending on patient-specific neurovascular anatomy and the location of the occlusion (dominant-versus-non-dominant hemisphere, perirolandic-versus-opercular branches), M2 segment occlusions can be as disabling as some M1 segment occlusions.^{5,8}

In this study, we present the clinical outcomes from 6 pediatric patients with M2 segment occlusion treated with mechanical thrombectomy, forming the largest published series in the literature, to the best of our knowledge.

Case Series

Institutional ethics approval was granted at each center. This was a retrospective, multicenter cohort study involving 3 tertiary pediatric hospitals and 1 adult hospital with the capability of providing mechanical thrombectomy for adolescents across New

Received October 6, 2023; accepted after revision January 8, 2024.

From the Department of Medical Imaging (K.D.B.), and Faculty of Medicine and Health (K.D.B., S.G., R.W., C.T., R.C.D., M.L.), Children's Hospital at Westmead Clinical School, University of Sydney, New South Wales, Australia; Division of Neurology (E.P.), Department of Paediatrics and Division of Image-Guided Therapy (C.P.F., P.M.), Department of Radiology, Hospital for Sick Children, Toronto, Ontario, Canada; Department of Neurology (I.A.), and Interventional Neuroradiology (A.C., N.M.), Sydney Children's Hospital, Randwick, New South Wales, Australia; T.Y. Nelson Department of Neurology and Neurosurgery (S.G., R.W., C.T., R.C.D., M.L.), Children's Hospital at Westmead, Westmead, New South Wales, Australia; and Department of Neurology (J.W., K.T., T.A.), Royal Prince Alfred Hospital, Camperdown, New South Wales, Australia.

Please address correspondence to Kartik D. Bhatia, FRANZCR, Department of Medical Imaging, Children's Hospital at Westmead, Corner of Hainsworth St and Hawkesbury Rd, Westmead, NSW, 2145, Australia; e-mail: Kartik.bhatia@health.nsw.gov.au



Indicates article with online supplemental data.

<http://dx.doi.org/10.3174/ajnr.A8182>

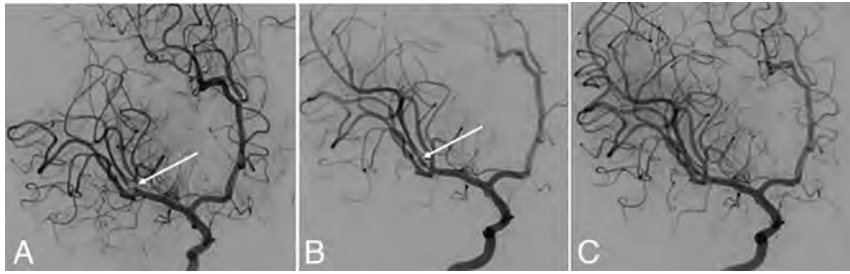


FIG 1. Oblique anterior-posterior-projection DSA images with a right ICA injection during a mechanical thrombectomy procedure. An 11-month-old infant (patient 4 in the Online Supplemental Data) with congenital cardiac disease had reduced movement of the left upper limb and face after waking from a nap. CTA demonstrated a right MCA proximal M2 occlusion. *A*, Subocclusive thrombus involving the proximal aspect of the right MCA superior M2 division (white arrow). *B*, Following a single-pass mechanical thrombectomy with a 3-mm-diameter stent retriever, angiographic vasospasm was present in the recanalized vessel segment (white arrow). *C*, Vasospasm resolution was noted after intra-arterial infusion of verapamil (1.5 mg) via the right ICA 4F catheter. The ped-mRS score at 3 months was 1.

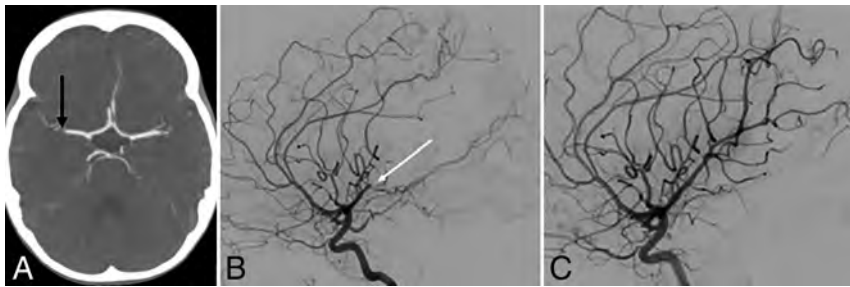


FIG 2. A 3-year-old patient (patient 3 in the Online Supplemental Data) developed fluctuating weakness of the left upper limb (Ped-NIHSS 3) after recent cardiac surgery for cor triatriatum. *A*, Axial CT angiogram demonstrates a filling defect in the right MCA distal M1 segment (black arrow). *B*, Lateral-projection DSA image with a right ICA injection demonstrates interval migration of the thrombus to the right MCA posterior (perirolandic) mid-M2 division (white arrow). After multidisciplinary discussion regarding the potential long-term disabling impact of a perirolandic infarct, it was agreed to proceed to the mechanical thrombectomy. *C*, After 2 passes with a 3-mm-diameter stent retriever, there was successful recanalization of the right perirolandic posterior M2 division. The ped-mRS score at 3 months was 0.

South Wales, Australia, and Ontario, Canada. Stroke registry databases were queried from January 2015 to August 2023 for all patients younger than 18 years of age with radiologically confirmed acute M2 occlusion (using CTA, MRA, or DSA) who were treated with mechanical thrombectomy. De-identified data were then pooled for analysis. Clinical outcomes were assessed using the pediatric modification of the mRS (ped-mRS)⁹ score at 3 months following stroke onset and at final available follow-up.

All available cases were included. Six consecutive pediatric patients with M2 occlusion who received mechanical thrombectomy were identified (female = 1, male = 5; age range, 0.9–16.0 years; mean = 9.2; SD = 6.60) (On-line Supplemental Data). Two patients also received bridging IV thrombolysis without clinical improvement before commencing thrombectomy. Three of the 6 patients having undergone thrombectomy were also included in our previously published case-control study.³ Four of the 6 patients had known congenital heart disease, and a fifth patient was found to have a patent foramen ovale with positive findings on a bubble test echocardiogram after the stroke episode. None of the patients had a prior history of stroke or recurrent stroke during

the follow-up period. None of the patients had diagnosed developmental delay before their stroke episodes.

The decision to offer mechanical thrombectomy was undertaken on a case-by-case basis following multidisciplinary discussions between pediatric neurology and pediatric interventional neuroradiology colleagues. None of the sites involved had specific guidelines for the treatment of M2 occlusion in pediatric patients due to the rarity of the condition and sparsity of data on the subject in the literature. Clinical and imaging factors considered relevant during treatment decision-making are detailed in the discussion.

All 6 patients had successful angiographic recanalization (modified treatment in cerebral ischemia [mTICI] = 2b–3) and no symptoms or functional disabilities (defined as excellent outcome; ped-mRS 0–1¹⁰) at 3 months poststroke as well as at the final available follow-up (mean = 14 months) (Online Supplemental Data). The mean pediatric NIHSS (Ped-NIHSS) score at baseline was 8.5 ([SD, 3.73]; range, 3–13), and 24 hours postprocedure, it was 1.7 ([SD, 1.4]; range, 0–3; mean reduction = 6.8 [SD, 2.7]; range, 3–10).

No patients developed symptomatic intracranial hemorrhage or required decompressive craniectomy. One patient who was on anticoagulation had an asymptomatic SAH in the ipsilateral Sylvian fissure on CT at

24 hours and developed a delayed femoral artery pseudoaneurysm successfully managed with percutaneous thrombin injection. Two patients having undergone thrombectomy had intraprocedural angiographic vasospasm following stent-retrieval use, successfully treated with intra-arterial verapamil injection in both cases (Fig 1).

Case Example. Patient 3 in our series (Online Supplemental Data) illustrates successful use of thrombectomy for a 3-year-old boy with a low and fluctuating Ped-NIHSS score. DSA demonstrated occlusion of the nondominant hemisphere perirolandic M2 division after initial CTA demonstrated a distal M1 occlusion (Fig 2). While it could be argued that this case should be managed conservatively, during the multidisciplinary discussion, the potential long-term impact of a perirolandic infarct was considered highly detrimental compared with the risks of proceeding with the intervention.^{5,8} Mechanical thrombectomy was successfully performed using stent retrieval combined with distal aspiration, achieving an mTICI 3 recanalization. The patient was completely asymptomatic at 3- and 12-month follow-ups (ped-mRS = 0).

DISCUSSION

In this case series, we demonstrated successful use of mechanical thrombectomy in 6 pediatric patients with M2 occlusion. All 6 patients had excellent clinical outcomes (ped-mRS = 0–1) at 3 months poststroke and final follow-up. While the sample sizes are too small for meaningful comparative statistical testing, the 5 pediatric patients with M2 occlusion managed with best medical treatment alone from our previously published case-control study all had mild-to-moderately severe disability at 3 months poststroke (ped-mRS = 2–4).³

No patients developed symptomatic intracranial hemorrhage or required decompressive craniectomy. The procedural complications (detailed above) were all minor with no long-term sequelae. In our view, postretrieval vasospasm in young children should be anticipated, and antispasmodic medications should be drawn up and ready for intra-arterial infusion. Overall, MeVO thrombectomy in this small pediatric sample appears relatively safe.

Close collaboration between pediatric neurology and interventional neuroradiology colleagues is essential for appropriate patient selection. During multidisciplinary team discussions for pediatric M2 occlusions, one should consider the following points:

- 1) Patient age and premorbid clinical status
- 2) Ped-NIHSS score
- 3) Probable stroke etiology
- 4) Nondominant-versus-dominant hemisphere involvement
- 5) Opercular-versus-perirolandic cortical involvement⁵
- 6) Presence of speech or dominant hand impairment
- 7) Overall risk profile of thrombectomy tailored to the individual patient
- 8) Availability of pediatric stroke and neurointerventional expertise.

Patients with suspected focal cerebral arteriopathy or possible Moyamoya syndrome should be considered carefully, with a bias toward medical therapy alone.⁷ The informed consent process undertaken with the patients' caregivers must be tailored on the basis of the above information, and the balance of risks versus benefits should be clearly communicated.

We would argue against using the Ped-NIHSS score in isolation for treatment decisions. Delayed deterioration of patients with LVO presenting with lower NIHSS scores is described in both pediatric¹¹ and adult settings.¹² Collateral blood flow within regions of the penumbra can fluctuate with time, and deterioration of such flow results in delayed infarct growth.¹³ Therefore, the condition of the child with a fluctuating Ped-NIHSS score may deteriorate during periods of relative hypotension (such as sleep), with a potential loss of treatment options. Interrater reliability of the Ped-NIHSS is lower when testing sensory/visual domains and is not validated in children younger than 2 years of age.¹⁴ Therefore, the Ped-NIHSS score should be considered in the wider context of clinical presentation, occlusion location, and potential long-term disability during a longer life span.

The role of perfusion imaging for the treatment decision-making in pediatric LVO stroke remains uncertain. Existing pediatric stroke guidelines make no recommendations regarding the

use of CT perfusion or MR perfusion imaging for patient selection.^{7,15} Quantitative parameters on CT perfusion imaging are known to vary with age during childhood, and this aspect must be considered during interpretation.¹⁶ Recent evidence suggests that performing perfusion imaging does not delay the time to recanalization in children treated with mechanical thrombectomy, that target mismatch criteria do not correlate with functional outcome, but a favorable hypoperfusion intensity ratio does correlate with clinical outcomes.¹⁷ In our experience, perfusion imaging can be helpful in borderline cases but is not sufficient to exclude a patient from being offered thrombectomy.

Our study has several limitations. First, the sample size is small but does form the largest published series of pediatric patients with M2 occlusion treated with thrombectomy. Second, there is probable underlying selection bias when selecting pediatric patients for thrombectomy in this context. This can be seen in the significantly greater delays in acquiring imaging in the control group from our previously published case-control study.³ Third, the role of thrombectomy for M2 occlusions in adults is still being assessed by at least 3 randomized trials. Fourth, 1 patient having undergone thrombectomy (case 4) was 11 months of age. The role of thrombectomy in infants remains controversial. Fifth, the main stroke etiologies in our study were cardioembolism and dissection. Pediatric stroke is heterogeneous, precluding generalization to the broader pediatric stroke population. Finally, the ped-mRS is potentially biased toward motor outcomes.

CONCLUSIONS

Mechanical thrombectomy for children with acute M2 occlusion is feasible, with a reasonable risk-benefit profile when appropriately selected by multidisciplinary care teams with expertise in pediatric stroke.

Disclosure forms provided by the authors are available with the full text and PDF of this article at www.ajnr.org.

REFERENCES

1. Bhatia KD, Briest R, Goetti R, et al. **Incidence and natural history of pediatric large vessel occlusion stroke: a population study.** *JAMA Neurol* 2022;79:488–97 CrossRef Medline
2. Goyal M, Menon BK, van Zwam WH, et al; HERMES Collaborators. **Endovascular thrombectomy after large-vessel ischaemic stroke: a meta-analysis of individual patient data from five randomised trials.** *Lancet* 2016;387:1723–31 CrossRef Medline
3. Bhatia KD, Chowdhury S, Andrews I, et al. **Association between thrombectomy and functional outcomes in pediatric patients with acute ischemic stroke from large vessel occlusion.** *JAMA Neurol* 2023;80:910–18 CrossRef Medline
4. Sporns PB, Sträter R, Minnerup J, et al. **Feasibility, safety, and outcome of endovascular recanalization in childhood stroke: the Save ChildS study.** *JAMA Neurol* 2020;77:25–34 CrossRef Medline
5. Saver JL, Chapot R, Agid R, et al; Distal Thrombectomy Summit Group. **Thrombectomy for distal, medium vessel occlusions: a consensus statement on present knowledge and promising directions.** *Stroke* 2020;51:2872–84 CrossRef Medline
6. Fifi JT, Yaeger K, Matsoukas S, et al. **Aspiration thrombectomy of M2 middle cerebral artery occlusion to treat acute ischemic stroke: a core lab-adjudicated subset analysis from the COMPLETE registry and literature review.** *Front Neurol* 2023;14:1076754 CrossRef Medline
7. Ferriero DM, Fullerton HJ, Bernard TJ, et al; American Heart Association Stroke Council and Council on Cardiovascular and

- Stroke Nursing. **Management of Stroke in Neonates and Children: A Scientific Statement From the American Heart Association/American Stroke Association.** *Stroke* 2019;50:e51–96 CrossRef Medline
8. Gong H, Zhao L, Tang G, et al. **The natural history and reperfusion therapy outcomes of acute ischemic stroke due to isolated M2 occlusions.** *Biomed Res Int* 2021;2021:6626604 CrossRef Medline
 9. Bigi S, Fischer U, Wehrli E, et al. **Acute ischemic stroke in children versus young adults.** *Ann Neurol* 2011;70:245–54 CrossRef Medline
 10. Saver JL, Chaisinanunkul N, Campbell BCV, et al; XIth Stroke Treatment Academic Industry Roundtable. **Standardized nomenclature for modified Rankin Scale Global disability outcomes: consensus recommendations from Stroke Therapy Academic Industry Roundtable XI.** *Stroke* 2021;52:3054–62 CrossRef Medline
 11. Xavier A, Kansara A, Majjhoo AQ, et al. **CT perfusion guided delayed recanalization with favorable outcome in pediatric stroke.** *J Neurointerv Surg* 2012;4:e33 CrossRef Medline
 12. Dargazanli C, Arquizan C, Gory B, et al; ETIS REGISTRY Investigators; **Mechanical thrombectomy for minor and mild stroke patients harboring large vessel occlusion in the anterior circulation: a multicenter cohort study.** *Stroke* 2017;48:3274–81 CrossRef Medline
 13. Campbell BC, Christensen S, Tress BM, et al; EPITHET Investigators. **Failure of collateral blood flow is associated with infarct growth in ischemic stroke.** *J Cereb Blood Flow Metab* 2013;33:1168–72 CrossRef Medline
 14. Ichord RN, Bastian R, Abraham L, et al. **Interrater reliability of the Pediatric National Institutes of Health Stroke Scale (PedNIHSS) in a multicenter study.** *Stroke* 2011;42:613–17 CrossRef Medline
 15. Medley TL, Miteff C, Andrews I, et al. **Australian Clinical Consensus Guideline: the diagnosis and acute management of childhood stroke.** *Int J Stroke* 2019;14:94–106 CrossRef Medline
 16. Wintermark M, Lepori D, Cotting J, et al. **Brain perfusion in children: evolution with age assessed by quantitative perfusion computed tomography.** *Pediatrics* 2004;113:1642–52 CrossRef Medline
 17. Lee S, Mlynash M, Christensen S, et al. **Hyperacute perfusion imaging before pediatric thrombectomy: analysis of the Save ChildS Study.** *Neurology* 2022;100:e1148–58 CrossRef Medline

Prasugrel Single Antiplatelet Therapy versus Aspirin and Clopidogrel Dual Antiplatelet Therapy for Flow Diverter Treatment for Cerebral Aneurysms: A Retrospective Multicenter Study

 Sophia Hohenstatt,  Işıl Saatci,  Jessica Jesser,  H. Saruhan Çekirge,  Naci Koçer,  Civan Islak,  Hannes Lücking,  Johannes DuPlessis,  Riitta Rautio,  Martin Bendszus,  Dominik F. Vollherbst, and  Markus A. Möhlenbruch



ABSTRACT

BACKGROUND AND PURPOSE: The optimal antiplatelet regimen after flow diverter treatment of cerebral aneurysms is still a matter of debate. A single antiplatelet therapy might be advantageous in determined clinical scenarios. This study evaluated the efficacy and safety of prasugrel single antiplatelet therapy versus aspirin and clopidogrel dual antiplatelet therapy.

MATERIALS AND METHODS: We performed a post hoc analysis of 4 retrospective multicenter studies including ruptured and unruptured aneurysms treated with flow diversion using either prasugrel single antiplatelet therapy or dual antiplatelet therapy. Primary end points were the occurrence of any kind of procedure- or device-related thromboembolic complications and complete aneurysm occlusion at the latest radiologic follow-up (mean, 18 months). Dichotomized comparisons of outcomes were performed between single antiplatelet therapy and dual antiplatelet therapy. Additionally, the influence of various patient- and aneurysm-related variables on the occurrence of thromboembolic complications was investigated using multivariable backward logistic regression.

RESULTS: A total of 222 patients with 251 aneurysms were included, 90 (40.5%) in the single antiplatelet therapy and 132 (59.5%) in the dual antiplatelet therapy group. The primary outcome—procedure- or device-related thromboembolic complications—occurred in 6 patients (6.6%) of the single antiplatelet therapy and in 12 patients (9.0%) of the dual antiplatelet therapy group ($P = .62$; OR, 0.712; 95% CI, 0.260–1.930). The primary treatment efficacy end point was reached in 82 patients (80.4%) of the single antiplatelet therapy and in 115 patients (78.2%) of the dual antiplatelet therapy group ($P = .752$; OR, 1.141; 95% CI, 0.599–2.101). Logistic regression showed that non-surface-modified flow diverters ($P = .014$) and fusiform aneurysm morphology ($P = .004$) significantly increased the probability of thromboembolic complications.

CONCLUSIONS: Prasugrel single antiplatelet therapy after flow diverter treatment may be as safe and effective as dual antiplatelet therapy and could, therefore, be a valid alternative in selected patients. Further prospective comparative studies are required to validate our findings.

ABBREVIATIONS: AIT = acute in-stent thrombosis; ASA = acetylsalicylic acid; DAPT = dual antiplatelet therapy; FD = flow diverter; PTA = percutaneous transluminal angioplasty; RROC = Raymond-Roy occlusion classification; SAPT = single antiplatelet therapy; TE = thromboembolic complications

Endovascular treatment of intracranial aneurysms still involves procedural complications. Despite multiple risk-reduction strategies, such as antiplatelet therapy and platelet reactivity testing,

Received October 27, 2023; accepted after revision January 7, 2024.

From the Department of Neuroradiology (S.H., J.J., M.B., D.F.V., M.A.M.), Heidelberg University Hospital, Heidelberg, Germany; Interventional Neuroradiology Section (I.S., H.S.C.), Koru and Bayindir Private Hospitals, Ankara, Turkey; Department of Neuroradiology (N.K., C.I.), Cerrahpasa Medical Faculty, Istanbul, Turkey; Department of Neuroradiology (H.L.), University of Erlangen-Nuremberg, Erlangen, Germany; Department of Clinical Neurosciences (J.D.), Royal Infirmary of Edinburgh, Edinburgh, United Kingdom; and Department of Interventional Radiology (R.R.), Turku University Hospital, Turku, Finland. D.F. Vollherbst and M.A. Möhlenbruch contributed equally to this work.

Please address correspondence to Markus A. Möhlenbruch, MD, Department of Neuroradiology, Heidelberg University Hospital, INF 400, 69120 Heidelberg, Germany; e-mail: markus.moehlenbruch@med.uni-heidelberg.de

 Indicates article with online supplemental data.

<http://dx.doi.org/10.3174/ajnr.A8163>

thromboembolic complications (TE) remain the leading cause of death and morbidity.¹ Especially, flow diverters (FDs) carry a relatively high risk of TE, and manufacturers usually recommend a dual antiplatelet therapy (DAPT).^{2,3} The most commonly used DAPT regimen is acetylsalicylic acid (ASA) in combination with clopidogrel; however, there is no standardized dose or duration.⁴ Recently, surface-modified FDs have been developed to reduce thrombogenicity, which could enable the use of single antiplatelet therapy (SAPT). Preliminary results of flow diversion with SAPT seem promising; however, it still remains unclear which drug is best suited for SAPT and whether it can be safely applied in conventional, non-surface-modified FDs.^{5–8} Resistance to ASA and clopidogrel has been described, which remarkably increases the risk of TE.⁹ Other potent P2Y₁₂ inhibitors with a high level of platelet inhibition and a less frequent drug resistance, such as prasugrel, can be an alternative antiplatelet therapy option for patients treated with FDs.^{10–12}

This retrospective multicentric study evaluated the efficacy and safety of prasugrel SAPT versus ASA and clopidogrel DAPT for aneurysm treatment with FDs. Both surface-modified and conventional FDs have been included.

MATERIALS AND METHODS

Patient Selection

We performed a post hoc analysis of 4 retrospective multicenter studies of flow diversion,¹³⁻¹⁶ including all patients who underwent FD treatment of ≥ 1 intracranial aneurysm between 2013 and 2021. Anterior and posterior circulation and ruptured and unruptured aneurysms were included. These studies evaluated both FDs with surface modification and non-surface-modified FDs. If prior implants were present in the target vessel (eg, intraluminal stent or FD), these patients were excluded. Of these patients, we further selected those treated with either SAPT with prasugrel or DAPT consisting of ASA and clopidogrel. Follow-up data had to be available for at least 3 months after the index procedure. If a patient receiving either prasugrel SAPT or ASA and clopidogrel DAPT died, he or she was included regardless of the duration of the follow-up.

The analysis was conducted in accordance with the Strengthening the Reporting of Observational Studies in Epidemiology (STROBE) reporting guideline for cohort studies (Online Supplemental Data).

Medication Protocols

We compared 2 different medication regimens: either SAPT with prasugrel or DAPT consisting of ASA and clopidogrel. Patients were assigned to the respective treatment arms according to the standard medication protocol of each participating site.

In the SAPT group, patients were loaded with prasugrel the day before the procedure with a standard loading dose of 30 mg, with possible adjustment according to the patient's weight (20 mg for patients weighting < 60 kg; 40 mg for overweight patients). The post-procedural medication included 5 mg (low dose in patients younger than 75 years of age or < 60 kg) or 10 mg of prasugrel once daily for 6–12 months, after which the patient either continued with reduced doses of prasugrel or was switched to 100 mg of ASA once daily for an additional 6 months or life-long based on a case-by-case decision.

Patients in the DAPT group were treated with 100 mg of ASA and 75 mg of clopidogrel (loading dose, 300 mg), starting no less than 5 days before the procedure, which was then maintained for a minimum of 3 months after the procedure. Thereafter, patients were switched to ASA-only according to the in-house protocols of each site.

Platelet inhibition was routinely tested before elective procedures and was managed according to the local standards of the respective institutions.

Patients with acutely ruptured aneurysms, who were treated in an emergency setting or if stent placement was unplanned, received an IV bolus of tirofiban immediately before stent deployment, followed by a maintenance dose for 6–24 hours (dosage adapted to the patient's weight according to the instructions for use), followed by either prasugrel or the above-described DAPT medication scheme.

In case of acute in-stent thrombosis (AIT) during the procedure, patients were also given an IV or intra-arterial bolus (depending on the respective institutional protocol) of a glycoprotein IIb/IIIa inhibitor (ie, tirofiban) as soon as possible. Likewise, the maintenance

dosage was given for 6–24 hours, followed by the intended oral antiplatelet drugs.

Data Collection

We performed a post hoc analysis of 4 retrospective multicenter studies.¹³⁻¹⁶ We reviewed data on patient demographics, clinical and aneurysm characteristics, procedure-related data, FD specifications, antiplatelet regimens according to the 2 options mentioned above, as well as follow-up data including the degree of aneurysm occlusion, the degree of intimal hyperplasia, and clinical outcome (Online Supplemental Data).

Aneurysmal occlusion rates were assessed using the O'Kelly Marotta Scale¹⁷ or the Raymond-Roy occlusion classification (RROC),¹⁸ respectively, for invasive catheter angiographies and contrast-enhanced MR imaging scans. To enhance clarity and comparability for the follow-up assessments of aneurysm occlusion, we referred to the RROC scale only.

The clinical evaluation was performed by a certified neurologist using the mRS before treatment in the immediate postoperative period (< 24 hours), at discharge, and then at subsequent clinical appointments scheduled for the same time as the respective imaging follow-up. Scores of 0 and 1 were assumed to indicate good functional outcome.

End Points

The primary safety end point was the occurrence of any kind of TE (symptomatic and asymptomatic documented by imaging alone). Secondary safety end points were the occurrence of permanently disabling TE, defined as those that led to a permanent shift of the preprocedural mRS score, hemorrhagic complications of any kind, the occurrence of intimal hyperplasia, and a good functional outcome at the latest clinical follow-up.

The primary efficacy end point was complete aneurysm occlusion (RROC I) at the latest radiologic follow-up according to the RROC. The secondary efficacy end point was adequate aneurysm occlusion (RROC I + II) at the latest radiologic follow-up according to the RROC. End point evaluation was site-assessed.

Statistics

SPSS Statistics, Version 25.0 (IBM) was used for statistical analysis. Quantitative data are presented as number (relative frequency) or mean (SD). Patients were divided into 2 groups according to periprocedural antiplatelet treatment (SAPT or DAPT). Between-group comparisons were performed with the Fisher exact test for categorical variables. To investigate the influence of patient- and procedure-related factors on the occurrence of TE, we analyzed all selected variables with clinical importance using univariate logistic regression models, with "thromboembolic complications" as the outcome variable. Subsequently, only the significant variables ($P < .05$) of these analyses were used in an interim multivariable logistic regression model. This model was adjusted with a variable selection on the basis of the P value with a backward stepwise approach based on the Wald test, resulting in the final multivariable logistic regression model. P values of .05 were defined as the threshold for statistical significance and were not adjusted for multiple testing due to the hypothesis-generating approach of the

Table 1: Main characteristics of the 2 medication groups including patients, aneurysms, and procedure-related characteristics^a

	SAPT	DAPT	P Value
Patient characteristics			
No. of patients	90	132	
Patient age (yr)	52 (SD, 11.8) (10–74)	56 (SD, 12.9) (14–92)	.555
Sex (female)	59 (65.6%)	101 (76.5%)	<.001 ^b
Aneurysm characteristics			
No. of aneurysms	102	149	
Aneurysm size	7.5 (SD, 6.1) (1–32)	6.7 (SD, 5.3) (1–28)	.099
SAH	13 (12.8%)	27 (18.1%)	.020 ^b
Saccular morphology	81 (81.4%)	109 (75.2%)	.021 ^b
Anterior circulation	91 (89.2%)	128 (85.9%)	.120 ^b
Procedural details			
No. of procedures	91	133	–
No. of implanted FD (total)	105	148	0.306
No. of implanted FD (with surface-modification)	29 (27.6%)	71 (47.9%)	<.001 ^b
Additional coiling	14 (13.7%)	29 (19.4%)	.016 ^b
PTA	–	14 (9.4%)	<.001 ^b
Previously treated aneurysms	20 (19.6%)	18 (12.1%)	.001 ^b

Note:—The en dash indicates 0 (0%).

^aData are mean (SD) (minimum–maximum) or absolute number of cases (relative frequency in percentages).

^bStatistically significant.

Table 2: Comparison of study end points between SAPT and DAPT^a

	SAPT (n = 90)	DAPT (n = 132)	P Value
Complications			
Thromboembolic (all)	6	12	.188
Thromboembolic (permanently disabling)	0	5	<.001 ^b
Hemorrhagic	0	3	.003 ^b
Intimal hyperplasia/asymptomatic parent artery occlusion	3 (2.9%) mild/3 (2.9%)	6 (4.0%) mild/2 (1.3%)	.768
Radiologic and clinical follow-up			
Follow-up duration	18 (SD, 12.3) (3–60)	18 (SD, 12.6) (6–74)	.553
Complete occlusion (RROC I) at latest follow-up	82 (80.4%)	115 (78.2%)	.367
Good clinical outcome at latest clinical follow-up (mRS 0–1)	90 (100%)	116 (87.8%)	<.001 ^b

^aData are mean (SD) (minimum–maximum) or absolute number of cases (relative frequency in percentages).

^bStatistically significant.

study. Hence, the *P* values should be interpreted descriptively. For ORs, 95% confidence intervals were calculated.

RESULTS

Patient and Aneurysm Characteristics and Procedural Details

A total of 222 consecutive patients (72.1% women; mean age, 54 [SD, 12.6] years) with 251 aneurysms who were treated in 224 procedures with FDs were included in this study. A flow chart (Online Supplemental Data) depicts how many patients were excluded from the respective studies and the reasons.

Forty patients had a history of SAH (18.0%); of these, 21 were treated in the acute stage within 3 days after aneurysm rupture. Thirty-eight aneurysms (15.1%) were secondarily treated due to residual aneurysm filling or regrowth after previous treatment with either coils or surgical clipping.

Most aneurysms (82.9%) were treated with flow diversion only, while 17.1% received adjunctive coiling. The rationale for adjunctive coiling was a maximum size of >10 mm, an irregular shape, or an acute aneurysm rupture. In-stent percutaneous transluminal angioplasty (PTA) to enhance vessel wall apposition of the FD was necessary in 14 cases (5.9%).

We used 4 different types of FDs with and without surface modification for the reduction of thrombogenicity: The Flow-

Redirection Endoluminal Device (FRED/FRED Jr; MicroVention) (*n* = 153, 56.9%) and its variant with an antithrombotic surface modification FRED X (MicroVention) (*n* = 49, 18.2%); and the Pipeline Vantage Embolization Device with Shield Technology (PED Vantage; Medtronic), which also has a surface modification (*n* = 67, 24.9%). The number of implanted FDs per treatment was 1 in 212 treatments (94.6%), 2 in 10 treatments (4.5%), and ≥3 in 2 treatments (0.9%).

The main patient and aneurysm characteristics as well as procedural details are summarized in the Online Supplemental Data.

Medication Subgroups

The SAPT group consisted of a total of 90 patients (40.5%) (65.6% women; mean age, 52 [SD, 11.8] years) with 102 aneurysms treated in 91 procedures with a total of 105 implanted devices. In this cohort, 13 patients (12.7%) had a history of SAH. Of these, 5 were treated in an acute setting within 3 days after the bleeding.

The DAPT group consisted of 132 patients (59.5%) (76.5% women; 56 [SD 12.9] years), who had 149 aneurysms treated in 133 interventions using 148 FDs. Twenty-seven patients (18.2%) had a history of SAH, and 16 of them were treated in an emergency setting.

More detailed data for both groups as well as between-group comparison results are reported in Table 1. Study end points are reported in Table 2.

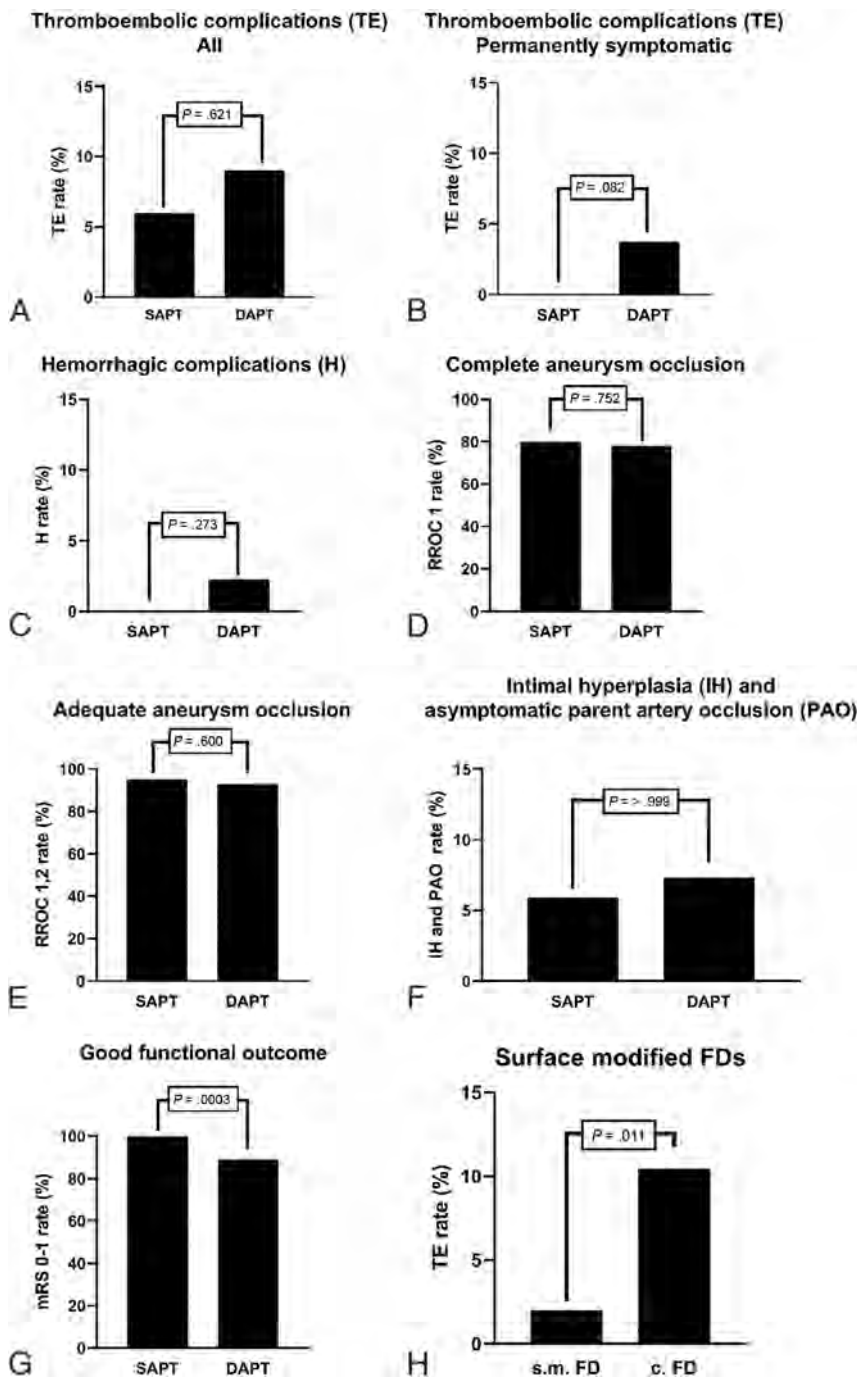


FIGURE. A, Rate of all observed thromboembolic procedure- or device-related complications in the SAPT with prasugrel and in the DAPT. B, Rate of permanently disabling thromboembolic procedure- or device-related complications in the SAPT and DAPT groups. C, Rate of hemorrhagic procedure-related complications in the SAPT and DAPT groups. D, Rate of complete aneurysm occlusion at latest follow-up in the SAPT and DAPT groups. E, Rate of adequate aneurysm occlusion at latest follow-up in the SAPT and DAPT groups. F, Rate of intimal hyperplasia and asymptomatic parent artery occlusion in the SAPT and DAPT groups. G, Rate of good functional outcome at the latest follow-up in the SAPT and DAPT groups. H, Thromboembolic complications in surface-modified or conventional FDs.

Procedural Complications

A total of 18 TE (8.1%) were observed in the peri- and postinterventional period. Twelve of these complications were observed in the DAPT group (66.7%), while the remaining 6 (33.3%) occurred in the SAPT group (Fig 1A). The medication regimen had no

significant effect on the occurrence of thromboembolic events in the Fisher exact test ($P = .621$; OR, 0.712; 95% CI, 0.260–1.930). We observed AIT in 8 cases, with the thrombus being detected either in the stent itself or in a covered side branch (5 in the DAPT group and 3 in the SAPT group); asymptomatic parent artery occlusion was noted in the follow-up of 5 cases (2 in the DAPT group and 3 in the SAPT group), and symptomatic peri- or postprocedural ischemic strokes led to a permanent mRS shift in 5 patients (all occurred in the DAPT group).

All cases of AIT were acutely treated with intraoperative administration of tirofiban. The thrombus dissolved in all instances, and the affected patients did not develop any clinical sequelae.

The permanently disabling TE ($n = 5$), all occurring in the DAPT group, are summarized in the Online Supplemental Data. The Fisher exact test showed only a trend without reaching statistical significance for the influence of the medication regimen on the occurrence of permanently disabling thromboembolic events ($P = .082$; OR, 0.000; 95% CI, 0.000–1.096) (Fig 1B).

Regarding the correlation of the FD type and the incidence of TE, regardless of the medication, we found a lower incidence of 2% in surface-modified FDs compared with 10.5% for conventional stents ($P = .011$; OR, 0.175; 95% CI, 0.039– 0.739) (Fig 1H). Considering the TE ($n = 6$) only in the SAPT group, they all occurred in the patients using the FRED Jr, a non-surface-modified FD, dedicated to small vessels.

The analysis of the influence of patient- and procedure-related factors on the occurrence of TE is reported in the Online Supplemental Data. The results of the final multivariable logistic regression model are presented in Table 3. FDs without surface modification ($P = .014$; OR, 7.119; 95% CI, 1.492– 33.960) and fusiform aneurysm morphology ($P = .004$; OR, 6.563; 95% CI, 1.835–23.472) were the 2 parameters that showed a significant relation to the occurrence of TE in the multivariable model.

A total of 3 hemorrhagic complications (1.3%), which were severe groin hematomas, occurred in the DAPT group, leading to a prolonged hospital stay. One necessitated a surgical intervention,

Table 3: Influence of patient and procedure-related factors on the occurrence of thromboembolic complications: final multi-variable logistic regression model

	P Value	OR (95% CI)
Non-surface-modified FD	.014	7.119 (1.492–33.960)
Fusiform morphology	.004	6.563 (1.835–23.472)

while the remaining 2 were managed conservatively. No severe hemorrhagic complications were observed in the SAPT group (Fig 1C).

Other procedure-related complications included 1 case of fatal hospital-acquired pneumonia, 3 cases of SAH sequelae (vasospasms and consequent infarctions), 1 case of anaphylaxis due to iodinated contrast media, and 1 case of worsening of a pre-existing stroke.

Radiologic and Clinical Follow-Up

The 251 aneurysms had a mean follow-up period of 18 (SD, 12.5) months (range, 3–74 months). Two patients, both of the DAPT group, had no follow-up due to periprocedural death. Both presented with acute SAH, and their conditions deteriorated during hospitalization with acquired pneumonia. One additionally had a postoperative in-stent thrombosis with progressive infarctions.

In the SAPT group, 82 aneurysms (80.4%) were completely occluded (RROC I), 15 aneurysms (14.7%) had a residual neck filling (RROC II), and 5 aneurysms (4.9%) had an aneurysmal filling at the last available follow-up. In the DAPT group, complete aneurysm occlusion (RROC I) was observed in 115 aneurysms (78.2%); residual neck filling (RROC II), in 23 (15.7%) aneurysms; and aneurysmal filling (RROC III), in 9 (6.1%) aneurysms. Therefore, the primary treatment efficacy end point was similarly reached in 80.4% of cases for the SAPT group ($n = 82$ aneurysms) and in 78.2% of cases in the DAPT group ($n = 115$ aneurysms) (Fig 1E). Adequate aneurysm occlusion, defined as RROC I and RROC II, was reached in 97 cases (95.1%) in the SAPT group and in 138 cases (92.6%) in the DAPT group (Fig 1F). The Fisher exact test showed no statistical significance of the influence of the medication regimen on the complete occlusion or on the adequate occlusion at latest follow-up ($P = .752$; OR, 1.141; 95% CI, 0.599–2.101 and $P = .600$; OR, 1.546; 95% CI, 0.508–4.109, respectively).

When we considered only aneurysms that were not additionally coiled, the primary treatment efficacy end point was reached in 79.6% ($n = 70$ aneurysms after excluding the $n = 14$ coiled aneurysms) in the SAPT group and in 76.5% ($n = 120$ aneurysms after excluding the $n = 29$ coiled aneurysms) in the DAPT group. Both groups had a mean follow-up of 18 months, in the SAPT group with an SD of 12.3 months (range, 3–60 months) and in the DAPT group with an SD of 12.6 months (range, 6–74 months) (Table 2).

Mild intimal hyperplasia (<50%) was observed in 3 (2.9%) parent arteries in the SAPT group and in 6 (4.0%) parent arteries in the DAPT group. There were no cases of moderate or severe intimal hyperplasia recorded. However, during follow-up, 5 cases of asymptomatic parent artery occlusion were assessed, 3 in the SAPT and 2 in the DAPT group (Fig 1D).

A good functional outcome, defined as an mRS of 0–1 at the latest clinical follow-up, was observed in all 90 patients (100%) in the SAPT group and in 116 patients (87.9%) in the DAPT group (Fig 1G). The influence of the medication regimen on the good functional outcome at the latest follow-up showed statistical significance in the Fisher exact test ($P = .001$; OR, +infinity; 95% CI, 3.275–+infinity). Because radiologic and clinical follow-ups occurred simultaneously, the latest clinical follow-up coincided with the latest radiologic follow-up.

DISCUSSION

In the present study, we demonstrated that SAPT with prasugrel is comparable with conventional DAPT with ASA and clopidogrel, both in terms of safety and efficacy. Thromboembolic and hemorrhagic events tended to be less frequent in terms of numeric values in the SAPT group, however, without reaching statistical significance. Occlusion rates at the latest available follow-up were similar in the 2 groups, while a good functional outcome was significantly better in the SAPT group.

The rate of symptomatic TE was 3.6% in our study, which is similar to that reported in the literature.³ The encountered TE are discussed in more detail in the respective publications.^{13–16} Prophylactic DAPT consisting of ASA and clopidogrel is commonly used to reduce the risk of TE after FD treatment for at least 3–6 months; however, there is no standardized antiplatelet treatment protocol.⁴ Despite this precaution, TE are still common and resistance to both ASA, and especially clopidogrel is thought to be among the main contributing factors to these adverse events. Emerging data suggest that ASA, which acts through inhibition of platelet cyclooxygenase leading to an irreversible inhibition of platelet-dependent thromboxane, may have an unpredictable antiplatelet response.^{19,20} Clopidogrel is a prodrug that is converted to its active form via an isoenzyme of cytochrome P450. Decreased plasma levels of the active clopidogrel metabolite can be influenced by genetic polymorphisms, diet, smoking, alcohol, and demographics,²¹ and clopidogrel resistance in the setting of neurointerventions has been reported to have a prevalence as high as 36.5%.⁹ Other potent antiplatelet agents, P2Y12 inhibitors, are becoming increasingly used in neurointerventional procedures, supported by evidence from the cardiac literature that showed a high level of platelet inhibition and less resistance.¹⁰

Prasugrel, a third-generation oral thienopyridine, has a similar mechanism of action to clopidogrel with the advantage of having a faster onset of action, more efficient platelet inhibition due to less variability in the patient response, and faster restoration of platelet activity after cessation.²¹ Prasugrel is a prodrug that is converted by liver enzymes into its active metabolite and binds irreversibly to P2Y12 receptors. Genetic polymorphisms do not (or only minimally) influence the metabolism of prasugrel, so there is no or little resistance to the drug. Prasugrel has been shown to be safe and effective in a broad variety of neurointerventions.^{21,22} Also in the setting of flow diversion, prasugrel is considered a safe alternative for clopidogrel-resistant patients because it seems to be associated with a lower incidence of thromboembolic and hemorrhagic complications, as well as mortality.^{13,23} Different meta-analyses of prospective and retrospective studies highlighted the potential benefits of alternative P2Y12

inhibitors such as prasugrel in reducing treatment-related complications.²⁴⁻²⁶ In the present study, we also observed a lower incidence of thromboembolic and hemorrhagic complication rates in the prasugrel-treated subgroup. Both in terms of absolute values and the severity of the complication, the prasugrel group was superior to the DAPT group, however without reaching statistical significance.

A type of TE that was observed homogeneously in both drug regimen groups was the occurrence of AIT. This observation suggests that AIT can occur independent of the medication used and could be best detected using an active surveillance strategy that enables fast counteracting.²⁷

In our study, we compared prasugrel, given as monotherapy, with a DAPT medication scheme. Which drug is most suitable for SAPT in the setting of flow diversion is still unclear. Different drugs have been used for SAPT, including ASA, prasugrel, or ticagrelor, another P2Y12 inhibitor.^{5-7,28} In 2 prospective trials investigating 2 different SAPT alternatives, in unruptured intracranial aneurysms using a surface-modified FD, ASA monotherapy was linked to a significantly higher incidence of ischemic complications (42.8%), while prasugrel monotherapy appeared to be safe in a comparable population.^{8,29}

Most data about SAPT in the setting of flow diversion rely on surface-modified FDs designed to have a less thrombogenic coating, allowing the use of SAPT. Indeed, the drawback of SAPT could be a potentially increased risk of TE, which, however, we did not observe in our study, as mentioned above. A small retrospective study found SAPT with ticagrelor to be safe after PED placement, a non-surface-modified FD.²⁸ In the present study, we included not only FDs with surface modification (FRED X and PED Vantage with Shield Technology) but also conventional FDs (FRED and FRED Jr). In the SAPT group, all TE ($n=6$) occurred with the FRED Jr, which is a non-surface-modified FD. This FD is designed to be specifically used for smaller, distal vessels. This design might bias this observation because thromboembolism is suspected to be higher in the distal vascular areas.³⁰ Nevertheless, non-surface-modified FDs were linked to an increased risk of the occurrence of TE in the multivariate logistic regression analysis. This link might justify a more cautious use of SAPT with this kind of FD; however, further dedicated studies are required. Fusiform aneurysm morphology was also unsurprisingly linked with an increased risk of the occurrence of TE. Prior studies have already demonstrated that fusiform aneurysms are at higher risk of TE.³¹

In terms of efficacy, the present study suggests comparable results between the 2 medication groups, with slightly higher RROC I occlusion rates at the latest available follow-up (80% versus 78%, respectively, in the SAPT versus DAPT group) and a similar incidence of in-stent stenosis (3% versus 4%, mild in all cases) and retreatment ($n=2$ versus $n=3$). The efficacy results were confirmed to be slightly higher in the SAPT group, also when considering only aneurysms that were not additionally coiled (80% versus 77%, respectively, in the SAPT versus DAPT group), because previous results are partially biased by the higher rate of adjunctive coiling in the DAPT group, which lightly augments the treatment efficacy in those patients.

The acceptance of prasugrel as the antiplatelet of choice for patients undergoing FD treatment does depend not only on the balance between thrombotic and bleeding events but also on the economic implications. Because the newer antiplatelet agents are more expensive than clopidogrel, prasugrel is likely to increase overall outpatient pharmacy expenditures. Nevertheless, data from the cardiology field suggest that prasugrel and ticagrelor are economically attractive treatment strategies as an alternative to clopidogrel because they might reduce other medical expenses.^{32,33} Yet, dedicated comparative studies about the cost-effectiveness of these therapies in neurointerventions are still lacking and required.

The main limitation of this study is its retrospective and observational design, with no randomization to the respective medication groups attributed to the site standard. Furthermore, the imaging and clinical data were not analyzed by an independent core lab, and end points were evaluated by the treating interventionalists themselves, possibly leading to an intrinsic reporting bias. Another important limitation is the inconsistency of the medication conversion both in terms of timing and in terms of the drug that was given according to in-house protocols at each site. The tests used for assessing antiplatelet reactivity differed among the participating centers and included VerifyNow (Werfen), light transmission aggregometry, and Multiplate (Roche Diagnostics). Moreover, there were discrepancies in the classification of what constituted normal levels in the platelet inhibition tests, which were based on different in-house standards. Furthermore, PTA rates were significantly higher in the DAPT group, which might eventually have biased the TE complication rates.

Larger studies are required to overcome the limitation of our small sample size, which might have prevented us from reaching statistical significance showing better outcomes for the prasugrel group. Nevertheless, to date, this is the largest study to directly compare the efficacy and safety of prasugrel SAPT with conventional ASA and clopidogrel DAPT in flow diversion.

CONCLUSIONS

When comparing prasugrel SAPT with ASA and clopidogrel DAPT after FD aneurysm treatment, we found no statistically significant difference regarding the occurrence of TE. Permanently disabling TE complications and hemorrhagic complications were more frequent in the DAPT group, however, without reaching statistical significance. TE were significantly more frequent in non-surface-modified FDs in distal, small vessels regardless of the medication. Occlusion rates at the latest available follow-up were comparable between groups. We conclude that the monotherapy with prasugrel may be at least as safe and effective as DAPT with ASA and clopidogrel and could, therefore, be a valid alternative in selected patients. Further prospective comparative studies are required to validate our findings and to better determine which patient subgroups would benefit the most from SAPT.

Disclosure forms provided by the authors are available with the full text and PDF of this article at www.ajnr.org.

REFERENCES

1. Fiehler J, Ries T. Prevention and treatment of thromboembolism during endovascular aneurysm therapy. *Klin Neuroradiol* 2009;19:73–81 CrossRef Medline
2. Zhou G, Su M, Yin YL, et al. Complications associated with the use of flow-diverting devices for cerebral aneurysms: a systematic review and meta-analysis. *Neurosurg Focus* 2017;42:E17 CrossRef Medline
3. Al-Mufti F, Cohen ER, Amuluru K, et al. Bailout strategies and complications associated with the use of flow-diverting stents for treating intracranial aneurysms. *Interv Neurol* 2020;8:38–54 CrossRef Medline
4. Tonetti DA, Jankowitz BT, Gross BA. Antiplatelet therapy in flow diversion. *Neurosurgery* 2020;86:S47–52 CrossRef Medline
5. Lobsien D, Clajus C, Behme D, et al. Aneurysm treatment in acute SAH with hydrophilic-coated flow diverters under single-antiplatelet therapy: a 3-center experience. *AJNR Am J Neuroradiol* 2021;42:508–15 CrossRef Medline
6. Hellstern V, Aguilar Perez M, Henkes E, et al. Use of a p64 MW flow diverter with hydrophilic polymer coating (HPC) and prasugrel single antiplatelet therapy for the treatment of unruptured anterior circulation aneurysms: safety data and short-term occlusion rates. *Cardiovasc Intervent Radiol* 2022;45:1364–74 CrossRef Medline
7. Bhogal P, Petrov A, Rentsenku G, et al. Early clinical experience with the p48MW HPC and p64MW HPC flow diverters in the anterior circulation aneurysm using single anti-platelet treatment. *Interv Neuroradiol* 2022;28:266–76 CrossRef Medline
8. de Castro-Afonso LH, Nakiri GS, Abud TG, et al. Treatment of distal unruptured intracranial aneurysms using a surface-modified flow diverter under prasugrel monotherapy: a pilot safety trial. *J Neurointerv Surg* 2021;13:647–51 CrossRef Medline
9. Fifi JT, Brockington C, Narang J, et al. Clopidogrel resistance is associated with thromboembolic complications in patients undergoing neurovascular stenting. *AJNR Am J Neuroradiol* 2013;34:716–20 CrossRef Medline
10. Warlo EM, Arnesen H, Seljeflot I. A brief review on resistance to P2Y₁₂ receptor antagonism in coronary artery disease. *Thromb J* 2019;17:11 CrossRef Medline
11. Pearce S, Maingard JT, Kuan Kok H, et al. Antiplatelet drugs for neurointerventions, Part 2: clinical applications. *Clin Neuroradiol* 2021;31:545–58 CrossRef Medline
12. Pearce S, Maingard JT, Li K, et al. Antiplatelet drugs for neurointerventions, Part 1: clinical pharmacology. *Clin Neuroradiol* 2020;30:425–33 CrossRef Medline
13. Jesser J, Alberalar ND, Kizilkilic O, et al. Safety and efficacy of the FRED Jr flow re-direction endoluminal device for intracranial aneurysms: retrospective multicenter experience with emphasis on midterm results. *Front Neurol* 2021;12:722183 CrossRef Medline
14. Vollherbst DF, Lucking H, DuPlessis J, et al. The FRESH study: treatment of intracranial aneurysms with the new FRED X flow diverter with antithrombotic surface treatment technology: first multicenter experience in 161 patients. *AJNR Am J Neuroradiol* 2023;44:474–80 CrossRef Medline
15. Vollherbst DF, Cekirge HS, Saatci I, et al. First clinical multicenter experience with the new Pipeline Vantage flow diverter. *J Neurointerv Surg* 2023;15:63–69 CrossRef Medline
16. Mohlenbruch MA, Seker F, Ozluk E, et al. Treatment of ruptured blister-like aneurysms with the FRED flow diverter: a multicenter experience. *AJNR Am J Neuroradiol* 2020;41:2280–84 CrossRef Medline
17. O'Kelly CJ, Krings T, Fiorella D, et al. A novel grading scale for the angiographic assessment of intracranial aneurysms treated using flow diverting stents. *Interv Neuroradiol* 2010;16:133–37 CrossRef Medline
18. Roy D, Milot G, Raymond J. Endovascular treatment of unruptured aneurysms. *Stroke* 2001;32:1998–2004 CrossRef Medline
19. Schror K. Aspirin and platelets: the antiplatelet action of aspirin and its role in thrombosis treatment and prophylaxis. *Semin Thromb Hemost* 1997;23:349–56 CrossRef
20. Ferreira M, Freitas-Silva M, Assis J, et al. The emergent phenomenon of aspirin resistance: insights from genetic association studies. *Pharmacogenomics* 2020;21:125–40 CrossRef Medline
21. Borchert RJ, Simonato D, Hickman CR, et al. P2Y₁₂ inhibitors for the neurointerventionalist. *Interv Neuroradiol* 2022;28:92–103 CrossRef Medline
22. Stetler WR, Chaudhary N, Thompson BG, et al. Prasugrel is effective and safe for neurointerventional procedures. *J Neurointerv Surg* 2013;5:332–36 CrossRef Medline
23. Atallah E, Saad H, Bekelis K, et al. The use of alternatives to clopidogrel in flow-diversion treatment with the Pipeline Embolization Device. *J Neurosurg* 2018;129:1130–35 CrossRef Medline
24. Podlasek A, Al Sultan AA, Assis Z, et al. Outcome of intracranial flow diversion according to the antiplatelet regimen used: a systematic review and meta-analysis. *J Neurointerv Surg* 2020;12:148–55 CrossRef Medline
25. Xia P, He C, Chen L, et al. Efficacy and safety of prasugrel therapy for intracranial aneurysms with endovascular treatment: a meta-analysis. *J Neurol Sci* 2019;397:174–78 CrossRef Medline
26. Cagnazzo F, Perrini P, Lefevre PH, et al. Comparison of prasugrel and clopidogrel used as antiplatelet medication for endovascular treatment of unruptured intracranial aneurysms: a meta-analysis. *AJNR Am J Neuroradiol* 2019;40:681–86 CrossRef Medline
27. Hohenstatt S, Ulfert C, Herweh C, et al. Acute intraprocedural thrombosis after flow diverter stent implantation: risk factors and relevance of standard observation time for early detection and management. *Clin Neuroradiol* 2022;33:343–51 CrossRef Medline
28. Mohammeden MH, English SW, Stapleton CJ, et al. Safety and efficacy of ticagrelor as single antiplatelet therapy in prevention of thromboembolic complications associated with the Pipeline Embolization Device (PED): multicenter experience. *J Neurointerv Surg* 2020;12:1113–16 CrossRef Medline
29. de Castro-Afonso LH, Nakiri GS, Abud TG, et al. Aspirin monotherapy in the treatment of distal intracranial aneurysms with a surface modified flow diverter: a pilot study. *J Neurointerv Surg* 2021;13:336–41 CrossRef Medline
30. Cagnazzo F, Perrini P, Dargazanli C, et al. Treatment of unruptured distal anterior circulation aneurysms with flow-diverter stents: a meta-analysis. *AJNR Am J Neuroradiol* 2019;40:687–93 CrossRef Medline
31. Brinjikji W, Lanzino G, Cloft HJ, et al. Risk factors for ischemic complications following Pipeline Embolization Device treatment of intracranial aneurysms: results from the IntrePED Study. *AJNR Am J Neuroradiol* 2016;37:1673–78 CrossRef Medline
32. Mahoney EM, Wang K, Arnold SV, et al. Cost-effectiveness of prasugrel versus clopidogrel in patients with acute coronary syndromes and planned percutaneous coronary intervention: results from the trial to assess improvement in therapeutic outcomes by optimizing platelet inhibition with Prasugrel-Thrombolysis in Myocardial Infarction TRITON-TIMI 38. *Circulation* 2010;121:71–79 CrossRef Medline
33. Kim K, Lee TA, Touchette DR, et al. Comparison of 6-month costs between oral antiplatelet agents following acute coronary syndrome. *J Manag Care Spec Pharm* 2018;24:800–12 CrossRef Medline

Wall Enhancement of Coiled Intracranial Aneurysms Is Associated with Aneurysm Recanalization: A Cross-Sectional Study

Stefan L. Leber, Eva M. Hassler, Manuela Michenthaler, Wilfried Renner, Hannes Deutschmann, and Gernot Reishofer



ABSTRACT

BACKGROUND AND PURPOSE: Wall enhancement of untreated intracranial aneurysms on MR imaging is thought to predict aneurysm instability. Wall enhancement or enhancement of the aneurysm cavity in coiled intracranial aneurysms is discussed controversially in the literature regarding potential healing mechanisms or adverse inflammatory reactions. Our aim was to compare the occurrence of aneurysm wall enhancement and cavity enhancement between completely occluded intracranial aneurysms and recanalized aneurysms after initially complete coil embolization.

MATERIALS AND METHODS: In this single-center cross-sectional study, we evaluated intracranial aneurysms after successful coil embolization for aneurysm recanalization, wall enhancement, and cavity enhancement with 3T MR imaging. We then compared the incidence of wall enhancement and cavity enhancement of completely occluded aneurysms with aneurysms with recanalization using the χ^2 test and performed a multivariate linear regression analysis with recanalization size as an independent variable.

RESULTS: We evaluated 59 patients (mean age, 54.7 [SD, 12.4] years; 48 women) with 60 intracranial aneurysms and found a significantly higher incidence of wall enhancement in coiled aneurysms with recanalization ($n=38$) compared with completely occluded aneurysms ($n = 22$, $P = .036$). In addition, there was a significantly higher incidence of wall enhancement in aneurysms with recanalization of >3 mm ($P = .003$). In a multivariate linear regression analysis, wall enhancement ($P = .010$) and an increase of overall aneurysm size after embolization ($P < .001$) were significant predictors of recanalization size (corrected $R^2 = 0.430$, CI 95%).

CONCLUSIONS: The incidence of aneurysm wall enhancement is increased in coiled intracranial aneurysms with recanalization and is associated with recanalization size.

ABBREVIATIONS: ACE = aneurysm cavity enhancement; AWE = aneurysm wall enhancement

Endovascular treatment is a first-line treatment for unruptured and ruptured intracranial aneurysms, but recurrence after coil embolization due to recanalization remains a challenge in the post-interventional management of intracranial aneurysms.¹ Therefore, identification and monitoring of factors potentially promoting the recurrence of treated intracranial aneurysms is of interest.

Healing or remodeling of intracranial aneurysms after embolization has been described as a progressive thrombus formation

together with a foreign body inflammatory reaction due to intraluminal coils. This process takes several months or even years, with initial formation of an unorganized thrombus and finally the formation of mature fibrocellular granulation tissue.²⁻⁴ Notably, unorganized fibrous tissue may persist for several years and might, therefore, be unstable.²

On MR imaging, enhancement of the aneurysm wall of untreated aneurysms has been the subject of intensive research during past years and might be associated with inflammation of the aneurysm wall and aneurysm disease progression.^{5,6} Recently, there is growing interest in the enhancement of the aneurysm wall (AWE) or of the aneurysm cavity (ACE) after coil embolization on MR imaging. However, data on these imaging features are conflicting, and their clinical significance remains unknown. Preliminary interpretations of AWE or ACE range from normal postinterventional phenomena^{4,7,8} to potential indicators of aneurysm healing⁹⁻¹¹ or indicators of an adverse course regarding aneurysm recurrence after treatment.^{10,12} In addition, recent data suggest that AWE of intracranial aneurysms before treatment

Received October 31, 2023; accepted after revision January 8, 2024.

From the Division of Neuroradiology, Vascular and Interventional Radiology (S.L.L., E.M.H., M.M., H.D., G.R.), Department of Radiology; and Clinical Institute of Medical and Chemical Laboratory Diagnostics (W.R.), Medical University of Graz, Graz, Austria.

Please address correspondence to Gernot Reishofer, PhD, Division of Neuroradiology, Vascular & Interventional Radiology, Department of Radiology, Medical University of Graz, Auenbruggerplatz 9, Graz, 8010, Austria; e-mail: gernot.reishofer@medunigraz.at

Indicates open access to non-subscribers at www.ajnr.org

Indicates article with online supplemental data.

<http://dx.doi.org/10.3174/ajnr.A8174>

might be an indicator of aneurysm recurrence after endovascular treatment.¹³

The aim of our study was to compare the incidence of AWE and ACE between groups of coiled intracranial aneurysms with and without recanalization, after initial complete occlusion.

MATERIALS AND METHODS

Patient Recruitment

We conducted this retrospective study according to the guidelines of the Declaration of Helsinki with approval of the local ethics committee of the Medical University of Graz (34-029 ex 21/22). We obtained written informed consent from all patients. During 16 months, we consecutively collected data from patients assigned to our department for routine follow-up of treated intracranial aneurysms. We excluded patients treated with alternative or additional treatment methods to coiling such as microsurgical clipping or flow diverters and those with insufficient image quality or known allergy to MR imaging contrast agents.

Imaging

We performed all imaging on a 3T Magnetom Prisma whole-body MR imaging system (Siemens). Patients underwent a standard protocol for aneurysm follow-up with fixed time points for contrast administration and postcontrast imaging (0.2 mmol/kg body weight of Dotarem; Guerbet). To assess any enhancement of aneurysms, we used a 2D T1WI black-blood TSE sequence (flip angle = 180°, TE/TR = 12/800 ms, FOV = 170 mm, voxel size = 0.5 × 0.5 × 2.5 mm) pre- and postcontrast. For assessment of aneurysm recanalization size, we used TOF angiography postcontrast.

Image Analysis

Two experienced neuroradiologists blinded to patient history or aneurysm status performed image analyses (S.L.L. and E.M.H.). A third experienced neuroradiologist resolved disagreements between the 2 raters (H.D.).

We defined recanalization as a recurrence of an initially completely coiled, occluded aneurysm (Raymond Roy I). We defined AWE as enhancement of the aneurysm wall compared with noncontrast T1WI and ACE as enhancement of the intraluminal parts of the aneurysm compared with noncontrast T1WI. AWE and ACE represent binary metrics (present or not present). We considered any signal increase on noncontrast T1WI compared with surroundings without further signal increase after contrast administration as rim artifacts.

The presence of SAH was confirmed on a CT scan followed by a CTA to confirm the presence of an intracranial aneurysm. Findings of unruptured intracranial aneurysms were incidental on CTA or MRA. The initial diameters of an aneurysm were determined on diagnostic DSA before coiling. To assess an increase of total aneurysm size after embolization, we compared the initial maximum aneurysm diameter before coiling with the current maximum aneurysm diameter on follow-up MR imaging to evaluate a potential difference in total aneurysm size. For recanalization size, we used the largest recanalization diameter on follow-up MRA.

For comparison of the incidence of AWE or ACE after coil embolization with regard to follow-up time after treatment, we

categorized coiled aneurysms into our standard follow-up intervals: up to 6 months, 7–12 months, 13–24 months, 25–48 months, 49–72 months, 73–96 months, and >96 months. For comparison of the incidence of AWE or ACE after coil embolization regarding aneurysm recanalization size, we compared those with aneurysms without recanalization with groups with aneurysm recanalization of 1–3 mm, 4–5 mm, and ≥6 mm.

Statistical Analysis

We performed all statistical analyses in SPSS Statistics, Version 27.0.1.0 (IBM) and presented continuous variables as mean (SD) and categorical variables as absolute numbers (percentage). For comparison of categorical variables, we used the Fisher exact test or χ^2 test if applicable. We tested continuous variables for normal distribution using the Shapiro-Wilk test and used the Mann-Whitney *U* test for non-normally distributed variables or the Student *t* test for normally distributed variables to assess group differences at a significance level of .05.

To assess interrater agreement for aneurysm enhancement patterns, we used the Cohen κ with κ values of 0 for no agreement, 0.10–0.20 for slight agreement, 0.21–0.40 for fair agreement, 0.41–0.60 for moderate agreement, 0.61–0.80 for substantial agreement, 0.81–0.99 for near-perfect agreement, and 1 for perfect agreement.

To analyze the potential effects on the recanalization size, we considered AWE, ACE, aneurysmal SAH, age, biologic sex, occurrence of aneurysm regarding the anterior or posterior circulation, and the difference in maximum aneurysm size before and after coil embolization as independent variables for a linear multivariate regression analysis. We excluded direct measurements of aneurysm size because of codependency. We were not able to determine the preinterventional maximum diameter of 3 aneurysms due to lack of data. In 1 case, we could not determine the ACE due to pulsation artifacts. We excluded these cases from the respective analyses. The authors S.L.L. and G.R. functioned as statistical guarantors.

RESULTS

Study Cohort

We included a total of 59 patients with 60 intracranial aneurysms in our study. The study cohort comprised 48 (81.4%) female patients. The mean age of our cohort at time of treatment was 54.7 years (range, 20–80 years). The mean follow-up time of all patients since their treatment was 43.5 months (range, 5–211 months). Aneurysm recanalization was present in 38 (63.3%) cases, 14 (23.3%) aneurysms were in the posterior circulation, and 27 (45.0%) aneurysms initially presented due to rupture (Table 1 and Fig 1).

Image Analysis

Interrater agreement according to the Cohen κ was substantial for AWE ($\kappa = 0.794$) and ACE ($\kappa = 0.797$). Figure 2 shows examples of coiled intracranial aneurysms with and without AWE or ACE (Fig 2A–D). Our study cohort comprised coiled intracranial aneurysms without any increase of signal intensity pre- and postcontrast (Fig 2A), aneurysms with increased signal intensity of the vessel wall precontrast without further increase

Table 1: Patient and aneurysm characteristics of our study cohort

	Recanalization (n= 38)	No Recanalization (n= 22)	P Value
Age (mean)	54.0 (SD, 12.9) yr	55.9 (SD, 11.4) yr	.583
Female	31 (81.6%)	17 (77.3%)	.688
aSAH	14 (23.7%)	13 (59.1%)	.095
Anterior circulation	29 (76.3%)	17 (77.3%)	.933
Posterior circulation	9 (13.2%)	5 (22.7%)	.933
AWE	21 (55.3%)	6 (27.3%)	.036
ACE	22 (59.5%)	12 (54.5%)	.712
Mean InitMaxDM	7.65 mm (SD, 2.81) mm	6.76 mm (SD, 2.51) mm	.2310
Mean CurrMaxDM	9.55 mm (SD, 3.58) mm	7.19 mm (SD, 2.46) mm	.005
Mean DiffMaxDM	1.89 mm (SD, 1.71) mm	0.45 mm (SD, 0.67) mm	.00004
Mean RecaMaxDM	3.71 mm (SD, 2.16) mm	0	n.d.

Note:—InitMaxDM indicates initial maximum diameter of aneurysm; CurrMaxDM, current maximum diameter of aneurysm; DiffMaxDM, difference of initial and current maximum diameters of aneurysm; RecaMaxDM, maximum diameter of aneurysm recanalization; aSAH, aneurysmal subarachnoid haemorrhage; n.d., not determined.

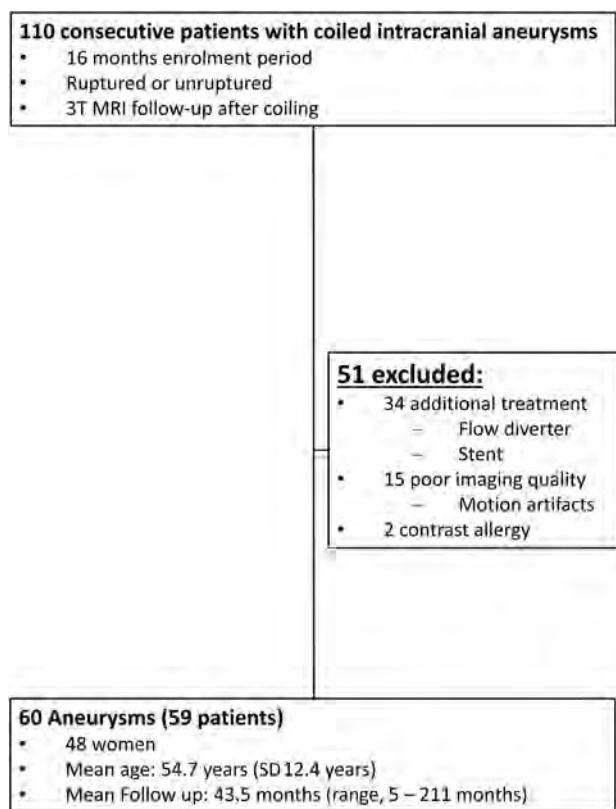


FIG 1. Flow chart displaying patient recruitment, exclusion criteria, and final study cohort.

of signal intensity postcontrast corresponding to rim artifacts (Fig 2B), and aneurysms with increased signal intensity of the vessel wall (AWE, Fig 2C) or the aneurysm cavity (ACE, Fig 2D) after contrast administration. Figure 2E, -F shows an MRA of the same aneurysms displayed in Fig 2C, -D, demonstrating that neither AWE nor ACE are necessarily collocated with aneurysm recanalization.

AWE and ACE Can Be Found in Short-Term and Long-Term Follow-Up of Coiled Intracranial Aneurysms

The median follow-up time of all aneurysms was 30 months. In the follow-up intervals of up to 30 months, AWE was present in 53.3% (16/30); and ACE, in 55.2% (16/29) respectively,

while in the follow-up intervals of >30 months, AWE was present in 36.7% (11/30); and ACE, in 60.0% (18/30), respectively. The portion of coiled aneurysms showing AWE decreased gradually from aneurysms investigated up to 6 months after treatment to aneurysms investigated between 25 and 48 months after treatment (Online Supplemental Data). Beyond 48 months, we did not observe a further decrease in the portion of AWE in coiled aneurysms. A detailed overview of the incidence of AWE and ACE regarding groups of different

follow-up intervals after coiling is provided in the Online Supplemental Data.

Increased Incidence of AWE in Coiled Intracranial Aneurysms with Recanalization

Of all previously coiled aneurysms, 27 (45%) had AWE on follow-up surveillance imaging (Table 1). AWE was significantly more frequent in coiled aneurysms with recanalization compared with coiled aneurysms without recanalization ($P = .036$). ACE was present in 34 (56.7%) of all evaluated aneurysms but showed no significant difference in the group comparison between aneurysms with and without recanalization ($P = .712$, Table 1).

Of 27 (45%) aneurysms treated before rupture, 15 had ACE and only 8 had AWE. In fact, AWE was significantly less frequent in aneurysms treated before rupture compared with unruptured treated aneurysms ($P = .03$, Online Supplemental Data).

AWE after Coil Embolization Is Associated with Aneurysm Recanalization Larger Than 3 mm

Both AWE and ACE appeared more frequently in aneurysms with recanalization of >3 mm (Online Supplemental Data and Fig 3). AWE was significantly more frequent in the group of aneurysms with recanalization of 4 or 5 mm ($P = .0033$) and the group of aneurysms with recanalization of ≥ 6 mm ($P = .0025$) compared with aneurysms without recanalization. We found no significant differences for ACE in this comparison (Online Supplemental Data and Fig 2A, -B).

In univariate linear regression analyses, AWE ($P < .001$, $R^2 = 0.2$, 95% CI) but not ACE ($P = .99$, $R^2 = 0.05$, 95% CI) was significantly associated with the size of the maximum diameter of aneurysm recanalization. In a multivariate regression analysis with recanalization size as a dependent variable, the overall regression model was statistically significant ($P < .001$) with a corrected R^2 of 0.43 (95% CI). The difference in the maximum aneurysm size before and after coil embolization ($P < .001$) as well as AWE ($P = .01$) was a statistically significant independent variable (Table 2).

DISCUSSION

Our analyses demonstrated a significantly higher incidence of AWE in coiled aneurysms with recanalization compared with completely occluded aneurysms as well as an association of AWE with recanalization size. Moreover, we show that aneurysm

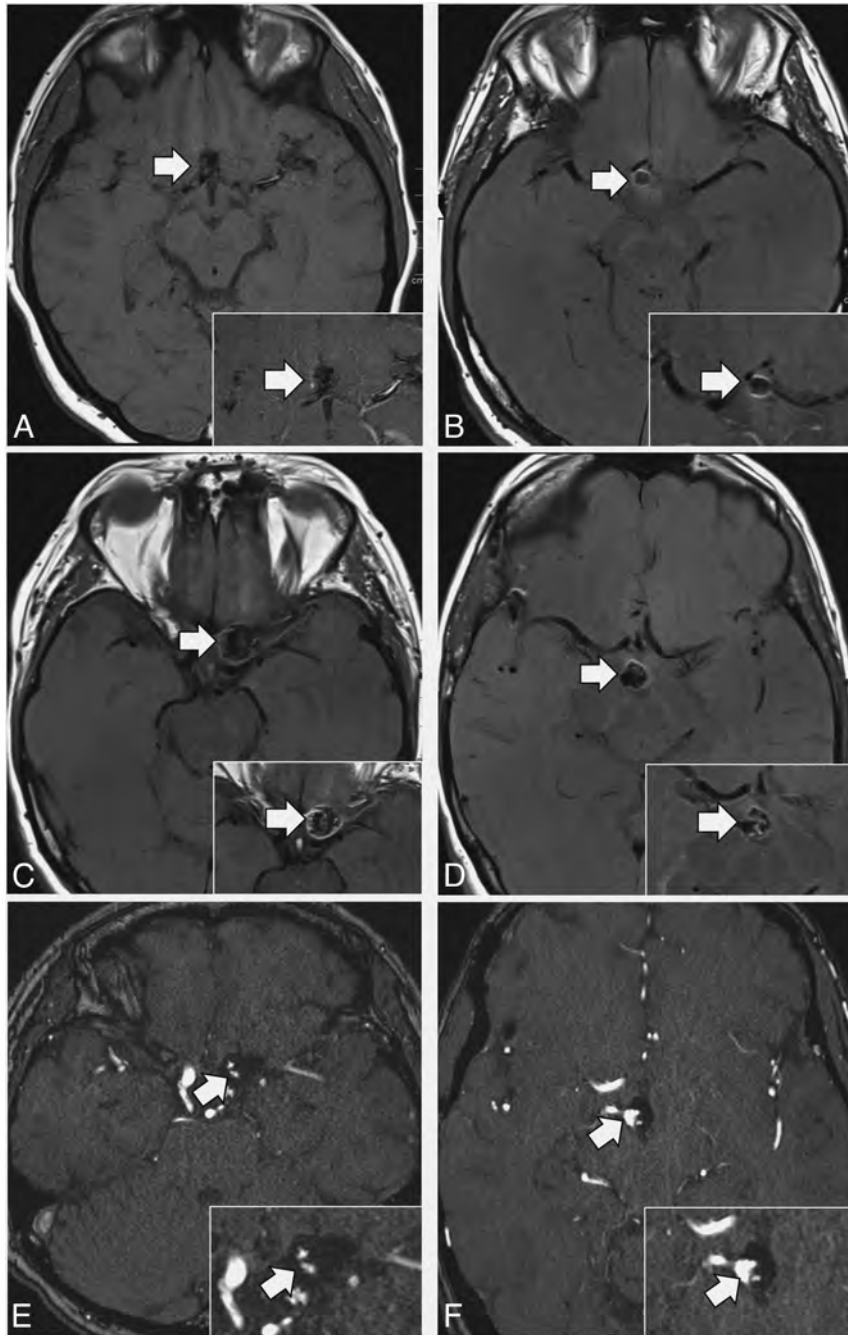


FIG 2. Examples of different enhancement patterns (AWE and ACE) of coiled intracranial aneurysms. *A–D*, MR imaging black-blood TSE images of coiled aneurysms (white arrows) precontrast with corresponding postcontrast images in the right lower corner. *E*, MRA of the aneurysm corresponding to *C* and *F* shows MRA of the aneurysm corresponding to *D* (white arrows). *A*, No enhancement in a coiled communicating anterior aneurysm. *B*, Rim artifacts in a treated communicating anterior aneurysm. *C*, ACE and AWE in a coiled left ICA aneurysm. *D*, Rim artifacts and ACE in a coiled basilar tip aneurysm. *E*, AWE and ACE are not necessarily at the same location as aneurysm recanalization. *F*, Aneurysm recanalization and ACE rather occur next to each other than at the same location in the aneurysm cavity.

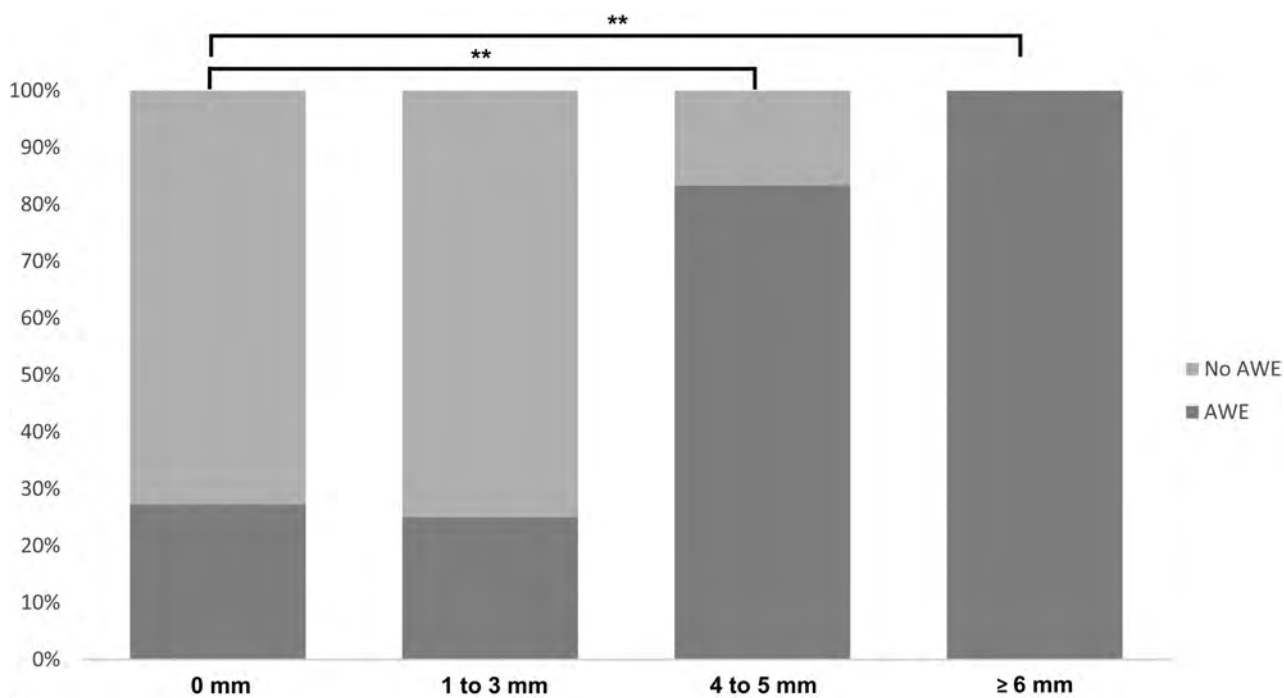
enhancement is not associated with aneurysmal SAH. These findings support the notion of AWE as an indicator of an adverse course after coiling rather than aneurysm healing alone.

Previous works have reported AWE in coiled intracranial aneurysms declining with time. Notably, the mean follow-up

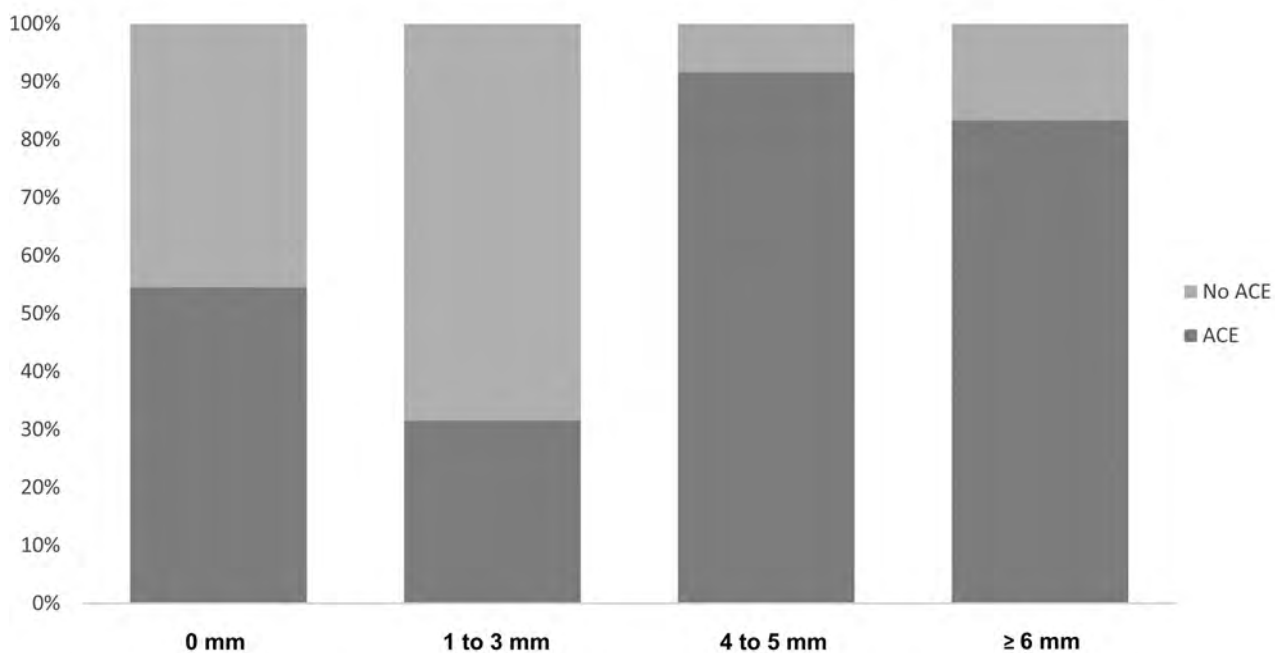
intervals in these studies were comparably shorter than ours.^{4,7–9,11} Our data are in line with a declining incidence of AWE in aneurysms up to 48 months after coiling. Beyond 48 months, AWE and ACE were still present in some cases, even in some aneurysms investigated >96 months after treatment. While previous works suggested aneurysm enhancement after coil embolization as a potential indicator of aneurysm healing,^{4,7–9} the presence of AWE or ACE in coiled aneurysms many years after treatment does not entirely fit this hypothesis. Indeed, some authors raised the possibility of an associated risk of aneurysm enhancement and aneurysm regrowth.^{9,10,12,14} Most interesting, all aneurysms displaying AWE without recanalization were investigated in a follow-up time of <30 months after embolization. Beyond the 30-month follow-up interval, AWE occurred exclusively together with aneurysm recanalization. This finding raises the question of whether aneurysm enhancement reflects beneficial but also detrimental properties of aneurysm remodeling after coil embolization, depending on the time point of observation.

Nikoubashman et al,¹⁰ reported ACE to most likely reflect contrast inflow in the recanalization of intracranial aneurysms after embolization and no association between ACE and aneurysm recurrence after treatment. Our data are not in line with this observation. ACE was not necessarily located at the same spot as blood inflow at the recanalization site when comparing pre- and postcontrast black-blood images with TOF-MRA. In addition, our work as well as that of others^{8,9} reports ACE in aneurysms without any recanalization at all. Another group suggested an association of ACE with a stable aneurysm state.⁹ In our analyses, ACE occurred more frequently in aneurysms with recanalization. However, this observation was not statistically significant, and different study designs hinder a direct comparison of results.

The occurrence of aneurysm recanalization after initially complete embolization is believed to be associated with ruptured status or the severity of SAH,¹⁵ and ruptured untreated intracranial aneurysms were demonstrated to show a high prevalence of AWE.¹⁶ Considering the pre- or postcontrast signal increase located at the



A



B

FIG 3. The incidence of AWE and ACE as percentages compared between groups of different recanalization sizes. A, AWE was significantly more frequent in aneurysms with recanalization of 4–5 mm and ≥ 6 mm but not in aneurysms with recanalization of 1–3 mm. B, ACE appeared more frequently in larger aneurysm recanalization without statistical significance (1–3 mm; 4–5 mm; ≥ 6 mm). Double asterisks indicate a *P*-value of .01 or lower.

aneurysm wall or in proximity to the aneurysm wall, it is tempting to assume that these imaging findings are related to inflammation or repair mechanisms due to aneurysmal SAH. Indeed, some previous studies on AWE in treated intracranial aneurysms excluded ruptured aneurysms from their analyses.^{4,7} Our data showed no increased prevalence of AWE or ACE in ruptured intracranial aneurysms compared with unruptured aneurysms after coiling.

This finding is comparable with data of other groups.^{8,10} Hence, aneurysmal SAH seems to have little impact on the presence of aneurysm enhancement after coil embolization.

Interpretation of our data is limited by a small sample size, a retrospective study design, and an inherent lack of histologic correlation. Validation of the presented data in independent patient cohorts and longitudinal study designs is needed.

Table 2: Parameters of independent variables of the multivariate regression analysis with the maximum recanalization diameter as a dependent variable

	B	β	T	Standard Error	CI (95%)	P Value
Age	0.021	0.109	0.997	0.022	-0.022–0.065	.324
AWE	1.565	0.317	2.668	0.586	0.386–2.743	.01
ACE	-0.088	-0.018	-0.151	0.581	-1.257–1.081	.881
aSAH	-0.363	-0.074	-0.666	0.545	-1.458–0.732	.509
Sex	1.167	0.195	1.875	0.622	-0.085–2.418	.067
Circulation	1.024	0.176	1.699	0.603	-0.188–2.235	.096
DiffMaxDM	0.793	0.517	4.743	0.167	0.457–1.129	<.001

Note:—DiffMaxDM indicates difference between initial maximum aneurysm diameter and current maximum diameter; B, regression coefficient; T, t-value; aSAH, aneurysmal subarachnoid haemorrhage.

CONCLUSIONS

Our data show that AWE and ACE may occur for several months or even years after coiling. The timepoint of observation regarding the follow-up interval after treatment but also recanalization size are relevant when observing enhancement of coiled intracranial aneurysms. Previous works contemplated a potential vulnerable phase during thrombus formation or delayed healing after coil embolization.^{9,10} An association of AWE with aneurysm recanalization size suggests implications for persisting AWE as a marker of aneurysm instability after initial complete coil occlusion due to persisting active remodeling or hemodynamic phenomena.¹⁴ Despite this evidence, it remains elusive whether AWE results from aneurysm recanalization or indicates a preceding trigger. In the future, longitudinal studies on the topic of enhancement of coiled intracranial aneurysms are of interest for a better understanding of the natural course of aneurysms with AWE or ACE. These studies should also address retreatment rates or the utility of diagnostic catheter angiograms in coiled intracranial aneurysms displaying AWE.

Disclosure forms provided by the authors are available with the full text and PDF of this article at www.ajnr.org.

REFERENCES

1. Etminan N, de Sousa DA, Tiseo C, et al. **European Stroke Organisation (ESO) guidelines on management of unruptured intracranial aneurysms.** *Eur Stroke J* 2022;7:V CrossRef Medline
2. Szikora I, Seifert P, Hanzely Z, et al. **Histopathologic evaluation of aneurysms treated with Guglielmi detachable coils or Matrix detachable microcoils.** *AJNR Am J Neuroradiol* 2006;27:283–88 Medline
3. Killer M, Arthur AS, Barr JD, et al. **Histomorphology of thrombus organization, neointima formation, and foreign body response in retrieved human aneurysms treated with hydrocoil devices.** *J Biomed Mater Res B Appl Biomater* 2010;94:4863–92 CrossRef Medline

4. Su IC, Willinsky RA, Fanning NF, et al. **Aneurysmal wall enhancement and perianeurysmal edema after endovascular treatment of unruptured cerebral aneurysms.** *Neuroradiology* 2014;56:4873–95 CrossRef Medline
5. Molenberg R, Aalbers MW, Appelman AP, et al. **Intracranial aneurysm wall enhancement as an indicator of instability: a systematic review and meta-analysis.** *Eur J Neurol* 2021;28:3837–48 CrossRef Medline
6. Zhong W, Su W, Li T, et al. **Aneurysm wall enhancement in unruptured intracranial aneurysms: a histopathological evaluation.** *J Am Heart Assoc* 2021;10:e018633 CrossRef Medline
7. Fanning NF, Willinsky RA, ter Brugge KG. **Wall enhancement, edema, and hydrocephalus after endovascular coil occlusion of intradural cerebral aneurysms.** *J Neurosurg* 2008;108:10743–86 CrossRef Medline
8. Zwarzany L, Owsiak M, Tyburski E, et al. **High-resolution vessel wall MRI of endovascularly treated intracranial aneurysms.** *Tomography* 2022;8:303–15 CrossRef Medline
9. Larsen N, Flüh C, Madjidyar J, et al. **Visualization of aneurysm healing: enhancement patterns and reperfusion in intracranial aneurysms after embolization on 3T vessel wall MRI.** *Clin Neuroradiol* 2020;30:8113–15 CrossRef Medline
10. Nikoubashman O, Tabrizi CM, Münstermann M, et al. **Findings and prognostic value of contrast-enhanced early magnetic resonance imaging after coil embolization of cerebral aneurysms.** *World Neurosurg* 2020;135:e3823–85 CrossRef Medline
11. Elsheikh S, Urbach H, Meckel S. **Contrast enhancement of intracranial aneurysms on 3T 3D black-blood MRI and its relationship to aneurysm recurrence following endovascular treatment.** *AJNR Am J Neuroradiol* 2020;41:4953–500 CrossRef Medline
12. Songsaeng D, Sakarunchai I, Harmontree S, et al. **Black-blood vessel wall magnetic resonance imaging: a new imaging biomarker for regrowth of coiled saccular aneurysms?** *Interdisciplinary Neurosurgery* 2021;23:100920 CrossRef
13. Hara T, Matsushige T, Yoshiyama M, et al. **Association of circumferential aneurysm wall enhancement with recurrence after coiling of unruptured intracranial aneurysms: a preliminary vessel wall imaging study.** *J Neurosurg* 2022;138:147–53 CrossRef Medline
14. Godi C, Destro F, Garofalo P, et al. **Hemodynamic nature of black-blood enhancement in long-term coiled cerebral aneurysms.** *Neuroradiology* 2023;65:1685–94 CrossRef Medline
15. Han Y, Liu J, Tian Z, et al. **Factors affecting recurrence and management of recurrent cerebral aneurysms after initial coiling.** *Interv Neuroradiol* 2020;26:300–08 CrossRef Medline
16. Santarosa C, Cord B, Koo A, et al. **Vessel wall magnetic resonance imaging in intracranial aneurysms: principles and emerging clinical applications.** *Interv Neuroradiol* 2020;26:135–46 CrossRef Medline

Large Single-Center Experience with Short-Term Follow-up of Neqstent-Assisted Coiling

 Fathallah Ismail Islam,  Nayyar Saleem, and Tufail Patankar



ABSTRACT

BACKGROUND AND PURPOSE: Endovascular treatment of wide-neck bifurcation aneurysms has historically proved difficult with variable outcomes. Different endovascular techniques such as balloon-assisted coiling, stent-assisted coiling, or intrasaccular devices provide a varied range of efficacy and safety. Neqstent-assisted coiling is a new device and technique that aim to provide a maximum of both. We analyzed the early clinical and radiologic outcomes after the use of this new technique and device in our practice.

MATERIALS AND METHODS: This study was a retrospective analysis of ruptured and unruptured intracranial aneurysms treated with the Neqstent. The primary radiologic outcomes were quantified on DSA, CTA, or MRA using the modified Raymond-Roy criteria. The outcomes were defined as immediate complete occlusion (modified Raymond-Roy criteria 1) and complete (modified Raymond-Roy criteria 1) and adequate occlusion (modified Raymond-Roy criteria 1 and modified Raymond-Roy criteria 2) at 6 months posttreatment. The primary safety outcome was the rate of device-related adverse events. Secondary safety outcomes included time to discharge and change in the mRS score at 6-month follow-up.

RESULTS: Twenty patients were treated with the Neqstent from November 2020 to January 2023. Nine had unruptured aneurysms, and 11 were patients with subarachnoid haemorrhage due to ruptured aneurysms. Eighteen of 20 aneurysms (90%) treated demonstrated complete occlusion (modified Raymond-Roy criteria 1) on immediate postembolization angiograms. Sixteen of 17 aneurysms treated (94.1%) remained adequately occluded on 6-month follow-up (modified Raymond-Roy criteria 1 and modified Raymond-Roy criteria 2). Immediate postoperative complications occurred in 2 patients; only 1 patient had residual neurologic deficits at 6 months (mRS = 2).

CONCLUSIONS: Management of large, wide-neck aneurysms remains difficult, with high rates of recurrence and complications. The use of the Neqstent shows promising short-term results for the treatment of complex wide-neck aneurysms. Initial complication rates for our cohort were relatively high. However, this result is likely related to the initial learning experience of device deployment and the use of antiplatelets.

ABBREVIATIONS: mRRC = modified Raymond-Roy criteria; WNBA = wide-neck bifurcation aneurysms

Since the International Subarachnoid Aneurysm Trial (ISAT) in 2002, coil embolization remains a safe and well-established technique for the treatment of ruptured and unruptured intracranial aneurysms.¹ Aneurysm recurrence following endovascular therapy has been an associated unfavorable outcome since its emergence. Although posttreatment rebleed risk remains low, the anxiety for patients remains an issue.²

Wide-neck bifurcation aneurysms (WNBAs) are defined as bifurcation intracranial aneurysms with an absolute neck diameter of 4.0 mm or a dome-to-neck ratio of <2.0.³ The incidence of aneurysm recurrence is a particular issue relating to complex wide-neck aneurysms. Subsequently, technologic advancements for endovascular treatment of ruptured and at-risk incidentally diagnosed aneurysms have rapidly expanded.⁴

Our study analyzed the use of the Neqstent (Stryker), a novel intrasaccular device designed to aid in the treatment of complex wide-neck bifurcation aneurysms. The aim of this study was to evaluate the efficacy and safety of a large single-center experience using the Neqstent. To the best of our knowledge, this is the largest real-life single-center experience published using this novel device.

Received October 26, 2023; accepted after revision January 11, 2024.

From the Department of Neuroradiology, Leeds General Infirmary, Leeds, UK.

Please address correspondence to Fathallah Ismail Islam, MBChB, Leeds General Infirmary, Department of Neuroradiology, Great George St, Leeds, LS1 3EX, United Kingdom of Great Britain and Northern Ireland; e-mail: fathallah.islim@nhs.net



Indicates article with online supplemental data.

<http://dx.doi.org/10.3174/ajnr.A8187>

Table 1: Sizing guide for Neqstent

Aneurysm Neck (mm)	Device Diameter (mm)	Microcatheter
3.0–5.0	7.0	0.021-inch
4.0–6.0	9.0	0.021-inch
5.0–8.0	11.0	0.021-inch
7.0–10.0	14.0	0.027-inch

MATERIALS AND METHODS

Study Design

The study is a retrospective, single-arm study. The patient eligibility criteria included patients with acute SAH with acutely ruptured intracranial aneurysms and elective patients with incidental intracranial aneurysms. The aneurysm treatment criterion was defined as bifurcation aneurysms with a neck of at least 4 mm or a dome-to-neck ratio of <2 . Patients were selected by the principal operators (T.P. and N.S.) without sponsor interference.

The primary efficacy end point was the successful occlusion of the aneurysm measured by the modified Raymond-Roy Classification (mRRC) at 6 months, proved by MRA, CTA, or DSA. Secondary efficacy outcomes included immediate postoperative angiographic occlusion rates and retreatment of aneurysm recurrences.

The primary safety end point was the rate of adverse events (any postprocedural neurologic deficit and a measure of the mRS score at 6 months). Secondary safety outcomes included time to patient discharge and the patient's functional outcome at that point.

Neqstent

The Neqstent is an adjunctive intrasaccular flow-diverter device that has been developed specifically for the treatment of complex wide-neck bifurcation aneurysms. It is a nitinol microbraided mesh with dual construction, containing a platinum core wire for visualization. It is compatible with 0.021- and 0.027-inch microcatheters, with sizes of 7, 9, 11, and 14 mm. The design allows a microcatheter to advance through the mesh for aneurysm dome coiling. The sizing of the device is dependent on the neck width as demonstrated in Table 1.

The similarity of the Neqstent to the Contour Neurovascular System (Stryker) is in the dual-mesh construction. The benefit of the Neqstent is that it contains 44% of the total number of wires (64 wires) in its construction compared with the Contour, which has 144 wires. The wire diameter is larger in the Neqstent; therefore, the actual surface area coverage of the device is 67% of what the Contour provides. This difference has the ability to pass a microcatheter through the construct for dome coiling while providing a similar level of neck protection and reconstruction in addition to flow diversion like the Contour. An example of Neqstent flow diversion with subsequent appearances post-coil deployment is demonstrated in the Online Supplemental Data.

Procedural Data

All procedures were performed with the patients under general anesthesia in biplane angiography suites. A common femoral approach was used under sonographic guidance. This series did

not prepare all patients with antiplatelets before the procedure. All patients received heparin intravenously after successful common femoral puncture with the aim of achieving an activated clotting time of 1.5–2 times the baseline. The use of triaxial or biaxial systems was decided before the procedure to ensure stable navigation and deployment of the microcatheters required and the Neqstent. This choice was dependent on the patient's vascular anatomy and the location of the aneurysm. On navigation into the target vessel, initial biplane and 3D rotational angiograms were obtained for planning and aneurysm measurement.

A 0.021-inch Headway (MicroVention) microcatheter for 7-, 9-, and 11-mm Neqstent devices and a 0.027-inch Headway microcatheter for the 14-mm Neqstent were required for navigation and deployment. A check angiogram would be performed on device deployment before detachment to ensure good aneurysm neck apposition. A 0.017-inch microcatheter (Echelon 10; Medtronic, or Headway 17) was adjunctively used for coil deployment into the aneurysm dome. In our cohort, we would always begin by jailing the microcatheter adjacent to the Neqstent. In cases of incomplete neck coiling of larger aneurysms, we would re-enter through the Neqstent using an 0.014-inch microwire and any 0.017-inch microcatheter such as the Headway or Echelon. The aim would be to coil the aneurysm to complete occlusion. Finally, angiography was performed to assess aneurysm occlusion.

Two patients received a bolus dose of IV Integridin (eptifibatid) and aspirin intraoperatively. Another 9 patients received IV aspirin intraoperatively. One patient was on warfarin before the procedure, which was continued immediately postoperatively with no other antiplatelet medications. Seven patients received short-term single-antiplatelet therapy (aspirin) for 3–6 weeks post treatment.

Aneurysm Occlusion

Immediate and 6-month posttreatment angiographic appearances were classified using the mRRC.⁵

RESULTS

A single regional interventional neuroradiology center enrolled patients from November 2020 to January 2023. Twenty patients with eligible aneurysms were treated with the Neqstent during the 27-month period.

The mean age of the population was 63 years (range, 44–78 years; 10 men, 10 women). Eleven patients presented with acute SAH due to aneurysm rupture. Nine patients had incidentally detected unruptured intracranial aneurysms for elective treatment. None of the aneurysms were previously treated.

The average aneurysm neck size was 5.6 mm (range, 2.89–10.8 mm). The average dome-to-neck ratio was 1.84 (range, 1.11–2.83). The aneurysm locations included 1 posterior communicating artery aneurysm, 2 ICA termination aneurysms, 6 anterior communicating artery aneurysms, and 5 basilar tip, and 6 MCA bifurcation aneurysms. Four basilar tip, 4 anterior communicating artery, 1 posterior communicating artery, and 2 MCA aneurysms were treated for rupture and consequent SAH. No patients have presented with postoperative bleeding from incidental aneurysms or rebleeding from ruptured aneurysms.

Table 2: Baseline aneurysm characteristics and occlusion outcomes

Characteristics		
Aneurysm location	Anterior communicating artery	6
	Basilar tip	5
	MCA	6
	ICA termination	2
	Posterior communicating artery	1
Presentation	Acute SAH	11
	Elective, incidental	9
	Average aneurysm dimensions (range)	
	Neck	5.6 mm (2.89–10.8 mm)
	Dome diameter	9.8 mm (5.0–17.0 mm)
	Dome height	8.5 mm (2.8–18.6 mm)
	DNR	1.84 (1.11–2.83)
Immediate occlusion (n = 20)	mRRC 1	18 (90%)
	mRRC 2	1 (5.0%)
	mRRC 3	1 (5.0%)
	6-Month occlusion (n = 17)	mRRC 1
	mRRC 2	1 (5.9%)
	mRRC 3	1 (5.9%)

Note:—DNR indicates dome-to-neck ratio.

The Neqstent device size was chosen according to the aneurysm neck sizes. Four 7-mm devices, five 9-mm devices, five 11-mm devices, and six 14-mm devices were used. Coils were deployed in 17 patients. A single patient's aneurysm thrombosed on device deployment without requiring any coils. All Neqstent devices were detached on completion of aneurysm dome coiling.

Balloon assistance was required in 1 case to prevent device protrusion. The Neqstent was protruding slightly into an M2 branch after device detachment but with no thrombus formation. A balloon was navigated into the branch and slightly inflated to push the edge of the device back into the aneurysm. This process resulted in no immediate angiographic complications. The patient awoke with no neurologic deficit.

Primary and Secondary Efficacy Outcomes

Table 2 demonstrates a summary of aneurysm characteristics and treatment efficacy. The Online Supplemental Data provide a breakdown of the clinical outcomes of the patient population. Eighteen aneurysms (90%) demonstrated complete occlusion (mRRC = 1) immediately postembolization. One aneurysm demonstrated contrast opacification within the coil interstices (mRRC = 3a), while another showed a small filling neck remnant (mRRC = 2).

Seventeen patients underwent 6-month radiologic follow-up (MRA = 15, CTA = 1, DSA = 1). Fifteen of 17 aneurysms (88.2%) demonstrated complete occlusion, and 16 aneurysms (94.1%) demonstrated adequate occlusion (mRRC = 1 and 2). Three patients did not undergo 6-month follow-up, 2 of whom due to ongoing rehabilitation from their initial SAH and subsequent neurologic insult. The remaining patient died from the initial SAH, which was not related to the treatment.

The only individual with an undertreated residual aneurysm in our series was patient 5, with a large very wide-neck aneurysm treated with a 14-mm Neqstent. The aneurysm dimensions were 12 × 10.8 × 18.6 mm (width × neck × height). An initial attempt was made with the Neqstent to avoid placing a stent for such a wide-neck aneurysm. The 14-mm device occupied and protected

most of the aneurysm neck; however, there was a small, uncovered component of the neck “dog ear.” The majority of the aneurysm was occluded with coils, but the decision was made to abandon the procedure at that point. Follow-up DSA showed interval growth in the neck residue, which was subsequently treated with further coiling and flow diversion with a Silk Vista Baby (Balt). Further follow-up DSA showed a decrease in size of the neck residue.

One patient underwent further treatment with a flow diverter. Patient 12, with a maximum dome diameter of 17 mm and a neck of 6 mm, had a small residual neck (mRRC = 2) on the immediate postembolization angiogram at the coil and device interface.

The patient presented 6 weeks later with worsening headaches. MR imaging revealed worsening perilesional edema; however, the MR angiogram and subsequent DSA demonstrated a stable residual neck (mRRC = 2). A decision was made to treat with flow diversion, and a 6-month follow-up MRA demonstrated a stable residual neck, with pronounced reduction of the perilesional edema.

Primary and Secondary Safety Outcomes

Two of 20 patients developed focal neurologic deficits in the immediate postoperative period. One patient's symptoms resolved on discharge. A single patient had a persistent neurologic deficit at 6-month follow-up (patient 1, mRS = 2). The remaining patients did not have a change in the pretreatment mRS after treatment with the Neqstent at 6-month follow-up.

The overall average time to discharge was 13.5 days. The average time to discharge of patients with acute SAH was 23.8 days, while the average time to discharge for elective patients was 2 days (range, 1–5 days).

The patient with complete recovery had a ruptured anterior communicating artery aneurysm (patient 3), with nonocclusive thrombus of left A2 origin post device deployment. The patient was administered 500 mg of aspirin IV. The clot remained stable. The patient awoke postoperatively with some right-sided weakness, and a postoperative CT demonstrated mild perirolandic ischemia. The patient continued on aspirin, 75 mg once a day, for 6 weeks and made a complete recovery, with no neurologic deficits.

The patient with persistent neurologic deficits was our first patient treated with the Neqstent (patient 1). This was an elective right MCA bifurcation aneurysm with a 4-mm neck. The device chosen was an 11-mm Neqstent. The patient initially presented with a stroke and was found to have a premorbid proximal stenosis involving the distal M1 segment. During the procedure, the device in combination with the microcatheter in situ through the stenosis likely caused compromise of the upper M2 branch. Subsequently, a small-volume thrombus was noted involving the upper M2 branch origin on the immediate postdeployment

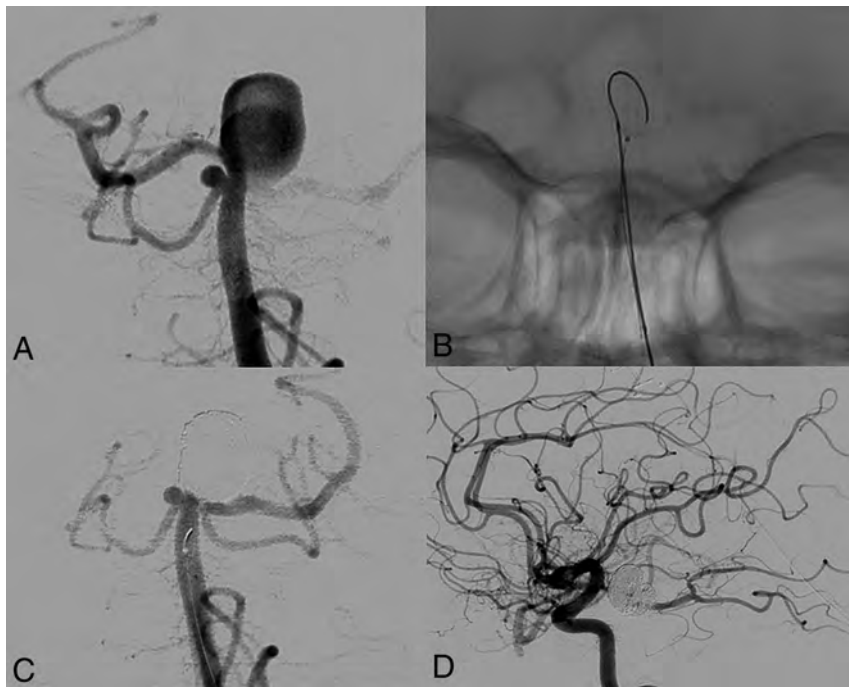


FIG 1. Sample case of the treatment of a ruptured basilar tip aneurysm. *A*, Selective angiography demonstrates a 5-mm wide neck and 9-mm maximum dome width. *B*, Deployed 11-mm Neqstent device with a jailed adjacent microcatheter and deployment of the first coil. *C*, Final angiographic result after detachment of the Neqstent device and complete aneurysm dome coiling. Reduced flow of the right P1 segment. *D*, Right posterior cerebral artery flow uptake by a large-caliber posterior communicating artery.

angiogram. An IV bolus of Integrilin and 500 mg of aspirin were administered, which cleared a significant volume of clot, with minor residual clot but no flow restriction. The patient developed a left-sided hemiparesis postoperatively. A postoperative CT demonstrated a left MCA infarct. The patient made a partial recovery and was mobilizing independently with a stick at 6-month follow-up (mRS = 2).

DISCUSSION

Wide-neck aneurysms are often technically challenging to treat due to the difficulty in stabilizing the coils inside the aneurysm. The difficulty is increased in wide-neck bifurcation aneurysms because branches often arise from the aneurysm neck. This scenario leads the operator to compromise on neck coverage with endovascular treatment, which can lead to high recurrence rates of wide-neck bifurcation aneurysms.⁶

A 2016 meta-analysis of endovascular coiling of wide-neck aneurysms, including bifurcation aneurysms, demonstrated long-term near-complete occlusion rates of 70%–75%, with recanalization rates of up to 10%.⁷

Several other endovascular techniques have been developed in the past 20 years, such as stent-assisted coiling and flow-diverter stents. A recent multicenter North American trial in 2020 of the use of stents in wide-neck anterior circulation aneurysms showed 84.7% complete aneurysm occlusion.⁸ However, the stroke risk and morbidity relating to stent-assisted coiling and flow-diverter stents are higher than in standard coiling and can be as high as 5%–8%.⁹ Additionally, the thromboembolic risk limits the use of

these techniques in ruptured intracranial aneurysms, due to the requirement of dual-antiplatelet treatment and the subsequent difficult balance of thromboembolic stroke versus worsening hemorrhage due to the primary bleed or possible neurosurgical instrumentation.

Subsequently, the concept of intrasaccular devices has come about, with the aim of creating a barrier at the level of the neck but no implant into the parent artery, therefore reducing the thromboembolic risk and the need for long-term dual antiplatelets. Such pure intrasaccular devices include the Woven EndoBridge (WEB; MicroVention) and the Contour Neurovascular System. The WEB and Contour retrospective and prospective studies have demonstrated good long-term outcomes and relatively low morbidity, with long-term complete occlusion rates of 54% and 73%, respectively, with both showing adequate occlusion rates of up to 85%.^{10,11} The concept of aneurysm neck reconstruction has been targeted through devices such as the pCONus (phenox) and the PulseRider (Pulsar Vascular).

These devices are deployed in the parent vessel to cover the aneurysm neck, which differs from the Neqstent, which is deployed in the aneurysm. The pCONus and PulseRider have demonstrated 60% and 64.2% short-term complete occlusion rates, respectively.^{12,13}

Our study looked at the short-term efficacy and safety outcomes with the use of the novel Neqstent device. A recent publication by Diana et al¹⁴ reviewed outcomes of adjunctive coil treatment with the Neqstent and Contour, with some cases of 6-month follow-up. The recent Coil-Assisted Flow Diversion Safety and Performance (CAFI) trial published results of 6 centers in Europe, which demonstrated a complete occlusion rate of 80% at 6-month follow-up, with a device-related morbidity rate of 10.5%. Our study is the largest single-center series to date with 6-month follow-up.¹⁵

Our early experience shows good outcomes relative to the recently published Woven EndoBridge Intrasaccular Therapy (WEB-IT) and Contour trials, with a complete occlusion rate of 88.2% and adequate occlusion of 94.1%. Only 1 patient had long-term treatment-related morbidity at 6 months. There is a notable chronologic decline of complications with increased technical experience and a better perioperative antiplatelet regimen. An example of successful embolization of a complex wide-neck bifurcation aneurysm is demonstrated in Fig 1.

Our experience shows that as with any pure intrasaccular device, accurate sizing is essential. The sizing of the device is simple and based purely on aneurysm neck width as demonstrated in Table 1. There are circumstances in which we would consider upsizing or downsizing. In cases of shallow wide-neck aneurysms,

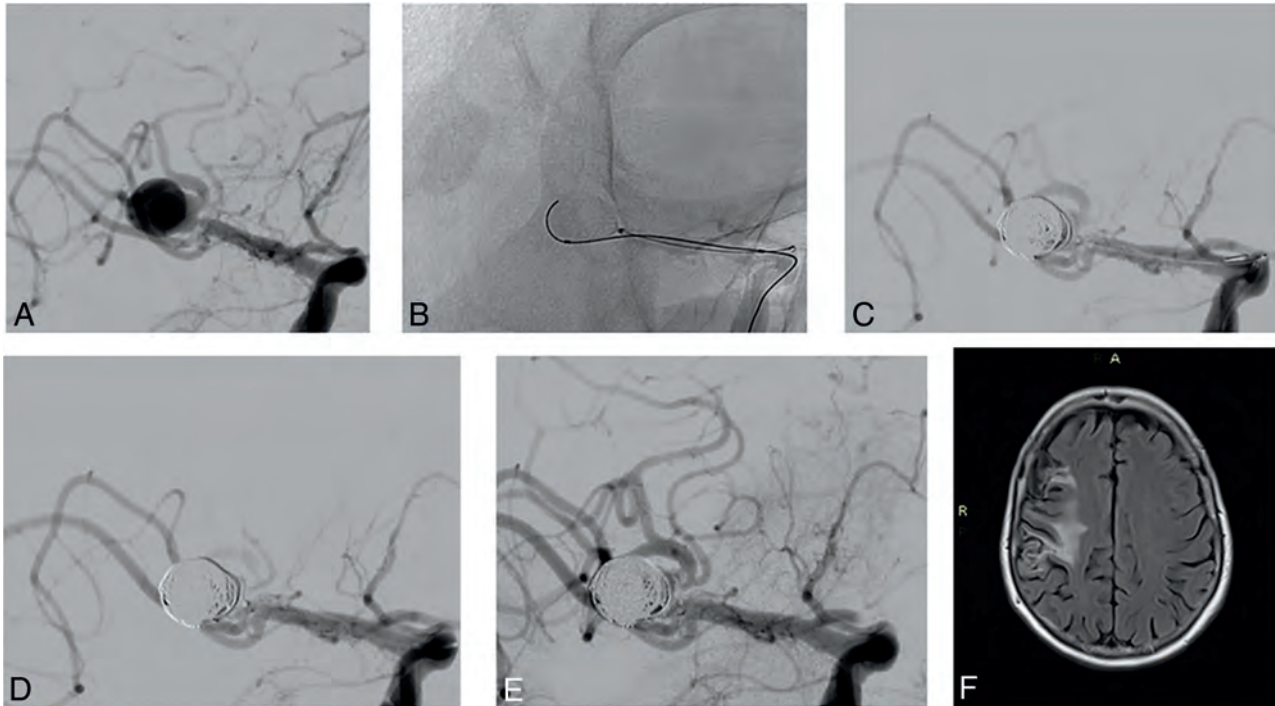


FIG 2. Sample case of a treated right MCA aneurysm. *A*, Working-projection angiogram with a superior M2 branch arising from the aneurysm neck. *B*, An 11-mm Neqstent device deployed with an adjacent jailed microcatheter and initial deployment of the first coil. *C*, Final angiographic result after detachment of the final coil and the Neqstent device. *D*, Compromise of the superior M2 branch due to device encroachment, with thrombus formation and reduced flow. *E*, Administration of IV aspirin and Integrilin, which reduced the clot volume and improved flow through the M2 branch. This result remained stable on 20- and 30-minute check angiograms. *F*, A 6-month follow-up FLAIR sequence demonstrates a sizable right-MCA cortical infarct.

the operator would consider a smaller Neqstent, if suitable, to ensure opening of the device. In cases of an irregularly shaped aneurysm with multiple lobules close to the aneurysm neck, the operator might decide to increase the size to ensure inclusion of the all the aneurysm neck components in the treatment.

The navigation and deployment of the device is similar to that in Contour and, in our experience, is easier than the WEB in large, complex aneurysms.

The WEB device sizing can be challenging, particularly in complex irregular aneurysms.¹⁶ The VIA catheter (MicroVention) used for navigation and deployment of WEB devices is stiffer and more difficult to navigate through tortuous anatomy. In cases of treatment of larger aneurysms, distal aneurysms, or through tortuous anatomy, we have found that navigating a smaller-profile Neqstent through a standard 0.021- or 0.027-inch microcatheter in addition to an 0.017-inch microcatheter for adjunctive coiling is easier than navigating a stiffer VIA catheter for WEB deployment. In cases of difficult anatomy or smaller vessels that would not allow 2 adjacent microcatheters, the Neqstent can be deployed and detached with a standard 0.021- or 0.027-inch microcatheter according to the size, removing the delivery system once deployed, then navigating a coiling microcatheter through the Neqstent to complete the coiling. Additionally, the WEB requires a larger shelf inventory for treatment of different-sized aneurysms, while the Neqstent offers easier sizing and can treat aneurysms with neck diameters up to 10 mm, with a requirement of only 4 different device sizes. Hence, the Neqstent allows

coiling larger aneurysms as long as the neck is ≤ 10 mm and the device can be well-apposed to the wall of the neck. If the device is not well-apposed or undersized, the aneurysm will invariably recur as seen in patient 1.

Accurate 3D sizing of the aneurysm neck is particularly important because oversized devices might risk compromise of adjacent vessels in wide-neck bifurcation aneurysms, particularly if the vessels arise from the aneurysm neck. Such a difficulty was observed in our first regional case of an MCA bifurcation aneurysm, in which there was slight compromise on an M2 branch with subsequent small clot formation as can be seen in Fig 2. Retrospectively, it was probably not the best case because there was proximal stenosis that would compromise the flow to the M2 branches. On the other hand, it shows the possibility of treating these complex aneurysms with proximal underlying stenosis safely with the Neqstent devices. After deployment, the operator withdrew the catheter proximal to the detachment marker and navigated the coiling catheter into the aneurysm. Therefore, at any 1 stage, only 1 catheter was across the stenosis. This scenario allowed treating the aneurysm but certainly led to compromise of the flow, but was managed with antiplatelets.

Despite the minimal device contact with the parent artery, the small flow-diverting component of the braided device increases the thromboembolic risk. The risk of adverse events relating to the technique and device in our study was in 2 of 20 patients (10%). This number is lower than the authors' review of WEB-related adverse events at 15.6%.¹⁷ Our current population size is

small, with early operator experience and an improving learning curve.

The thromboembolic risk can be tackled with intraoperative IV antiplatelet therapy if early angiographic thromboembolism is identified, or another option would be to load patients suspected of warranting treatment with the Neqstent with a short course of antiplatelets before the procedure. During our initial and early experience, we had not yet made the decision to routinely preload with an antiplatelet regimen. We currently do not give antiplatelets routinely. The decision to give prophylactic antiplatelets is based on device location across the aneurysm neck and whether there is any compromise of the parent or bifurcation vessels. The exact regimen is also heterogeneous and subjective, ranging from a single IV dose of aspirin to a possible short term (4–8 weeks) of single antiplatelets. The authors have extensive experience in intrasaccular devices including the WEB and Contour and recommend, if possible, giving perioperative antiplatelets. The Neqstent offers an advantage of avoiding preoperative antiplatelets because the device appears certainly less thrombogenic than the Contour or WEB in WNBA. Additionally, the small thromboembolic risk can be offset by a short-term postoperative course of single or dual antiplatelets. Studies of the antiplatelets have shown them to be relatively safe in patients with SAH, as was demonstrated in both our elective and acute series populations.¹⁸

The presence of coils for dome protection offers favorable immediate occlusion of the treated aneurysms, as demonstrated by the immediate occlusion rate of 90% in our study. This situation compares more favorably with other intrasaccular devices such as the Contour,¹⁹ which can be more attractive to operators who prefer coiling aneurysms. Although markedly similar to the Contour device, the adjunctive nature of the Neqstent with the use of coils to occlude the aneurysm dome offers immediate protection, hence the ability to use it in acutely ruptured intracranial aneurysms, while some operators may still have reservations about using the Contour for treatment of acutely ruptured aneurysms.

The Neqstent offers the best of both worlds. The easy-to-size device is used in conjunction with coils, which provide the ability to use the Neqstent for treatment of both ruptured and unruptured aneurysms. The flow-diverting property of the device reduces the risk of coil compaction and aneurysm recurrence. In the event of recurrence, the construct of the Neqstent allows re-entry for further coil deployment, offering easier re-treatment options than standard flow diverters or traditional pure intrasaccular devices.

Limitations

There are several limitations to this study. This was a retrospective, single-arm, single-center study for carefully selected WNBA aneurysms based on the suitability of the aneurysm location and morphology. Despite our center being a large-volume one treating approximately 300 aneurysms per year, the cohort size is relatively small, due to the initial learning experience required for this technique and careful aneurysm selection. However, with increased experience, our cohort of Neqstent-treated aneurysms has nearly doubled. The current cohort has a short-term

follow-up of only 6 months. The next interval follow-up for our patients will be in 2 years from treatment, which will be published.

CONCLUSIONS

The novel technique of Neqstent-assisted coiling shows promising early results in the treatment of complex wide-neck bifurcation intracranial aneurysms. Our results show favorable occlusion rates compared with other studies relating to stent-assisted coiling and flow diversion, with less morbidity and the ability to use them in ruptured intracranial aneurysms. It also shows favorable outcomes compared with recent studies involving intrasaccular devices such as the WEB and Contour.

Perioperative antiplatelets could be beneficial and warrant further research.

Future larger studies into the Neqstent with longer follow-up data as well as comparative clinical trials could be considered to identify the best treatments for wide-neck and wide-neck bifurcation aneurysms.

Disclosure forms provided by the authors are available with the full text and PDF of this article at www.ajnr.org.

REFERENCES

1. Molyneux AJ, Kerr RS, Yu LM, et al; International Subarachnoid Aneurysm Trial (ISAT) Collaborative Group. **International Subarachnoid Aneurysm Trial (ISAT) Collaborative Group. International subarachnoid aneurysm trial (ISAT) of neurosurgical clipping versus endovascular coiling in 2143 patients with ruptured intracranial aneurysms: a randomised comparison of effects on survival, dependency, seizures, rebleeding, subgroups, and aneurysm occlusion.** *Lancet* 2005;366:809–17 CrossRef Medline
2. Ferns SP, Nieuwkerk PT, van Rooij WJ, et al. **Long-term MRA follow-up after coiling of intracranial aneurysms: impact on mood and anxiety.** *Neuroradiology* 2011;53:343–48 CrossRef Medline
3. Mascitelli JR, Lawton MT, Hendricks BK, et al. **Analysis of wide-neck aneurysms in the Barrow Ruptured Aneurysm Trial.** *Neurosurgery* 2019;85:622–31 CrossRef Medline
4. Fatania K, Patankar DT. **Comprehensive review of the recent advances in devices for endovascular treatment of complex brain aneurysms.** *Br J Radiol* 2022;95:20210538 CrossRef Medline
5. Mendenhall SK, Sahlein DH, Wilson CD, et al. **The natural history of coiled cerebral aneurysms stratified by Modified Raymond-Roy Occlusion Classification.** *World Neurosurg* 2019;128:e417–46 CrossRef Medline
6. Pierot L, Spelle L, Cognard C, et al. **Wide neck bifurcation aneurysms: what is the optimal endovascular treatment?** *J Neurointerv Surg* 2021;13:e9 CrossRef Medline
7. Zhao B, Yin R, Lanzino G, et al. **Endovascular coiling of wide-neck and wide-neck bifurcation aneurysms: a systematic review and meta-analysis.** *AJNR Am J Neuroradiol* 2016;37:1700–05 CrossRef Medline
8. Zaidat OO, Hanel RA, Sauvageau EA, et al; ATLAS Investigators. **Pivotal trial of the Neuroform Atlas Stent for treatment of anterior circulation aneurysms: one-year outcomes.** *Stroke* 2020;51:2087–94 CrossRef Medline
9. Kabbasch C, Goertz L, Siebert E, et al. **WEB embolization versus stent-assisted coiling: comparison of complication rates and angiographic outcomes.** *J Neurointerv Surg* 2019;11:812–16 CrossRef Medline
10. Arthur AS, Molyneux A, Coon AL, et al; WEB-IT Study investigators. **The safety and effectiveness of the Woven EndoBridge (WEB) system for the treatment of wide-necked bifurcation aneurysms: final**

- 12-month results of the pivotal WEB Intrasaccular Therapy (WEB-IT) study.** *J Neurointerv Surg* 2019;11:924–30 CrossRef Medline
11. Liebig T, Killer-Oberpfalzer M, Gal G, et al. **The Safety and effectiveness of the Contour Neurovascular System (Contour) for the treatment of bifurcation aneurysms: the CERUS study.** *Neurosurgery* 2021;90:270–77 CrossRef Medline
 12. Sorenson TJ, Iacobucci M, Murad MH, et al. **The pCONUS bifurcation aneurysm implants for endovascular treatment of adults with intracranial aneurysms: a systematic review and meta-analysis.** *Surg Neurol Int* 2019;10:24 CrossRef Medline
 13. Srinivasan VM, Srivatsan A, Spiotta AM, et al. **Early postmarket results with PulseRider for treatment of wide-necked intracranial aneurysms: a multicenter experience.** *J Neurosurg* 2019;133:1756–65 CrossRef Medline
 14. Diana F, de Dios Lascuevas M, Peschillo S, et al. **Intrasaccular flow disruptor-assisted coiling of intracranial aneurysms using the novel Contour Neurovascular Systems and Neqstent: a single-center safety and feasibility study.** *Brain Sci* 2022;12:991 CrossRef Medline
 15. Liebig T, Gal G, O'Kelly C, et al. **Neqstent coil-assisted flow diverter (NQS) for the treatment of bifurcation aneurysms: the Coil-Assisted Flow Diversion Safety and Performance Study (CAFI).** *J Neurointerv Surg* 2023 Jul 7. [Epub ahead print] CrossRef Medline
 16. Goyal N, Hoit D, DiNitto J, et al. **How to WEB: a practical review of methodology for the use of the Woven EndoBridge.** *J Neurointerv Surg* 2020;12:512–20 CrossRef Medline
 17. Lawson A, Molyneux A, Sellar R, et al. **Safety results from the treatment of 109 cerebral aneurysms using the Woven EndoBridge technique: preliminary results in the United Kingdom.** *J Neurosurg* 2018;128:144–53 CrossRef Medline
 18. Hop JW, Rinkel GJ, Algra A, et al. **Randomized pilot trial of postoperative aspirin in subarachnoid hemorrhage.** *Neurology* 2000;54:872–78 CrossRef Medline
 19. Asnafi S, Rouchaud A, Pierot L, et al. **Efficacy and safety of the Woven EndoBridge (WEB) Device for the treatment of intracranial aneurysms: a systematic review and meta-analysis.** *AJNR Am J Neuroradiol* 2016;37:2287–92 CrossRef Medline

Brain Arteriovenous Malformation In Vitro Model for Transvenous Embolization Using 3D Printing and Real Patient Data

Rodrigo Rivera, Alvaro Cespedes, Juan Pablo Cruz, Aymeric Rouchaud, and Charbel Mounayer

ABSTRACT

BACKGROUND AND PURPOSE: Transvenous embolization has emerged as a novel technique for treating selected brain AVMs with high reported occlusion rates. However, it requires anatomic and technical skills to be successful and to ensure patient safety. Therefore, training and testing are essential for preparing clinicians to perform these procedures. Our aim was to develop and test a novel, patient-specific brain AVM in vitro model for transvenous embolization by using 3D printing technology.

MATERIALS AND METHODS: We developed a brain AVM in vitro model based on real patient data by using stereolithography resin 3D printing. We created a closed pulsed circuit with flow passing from the arterial side to the venous side, and we tested the effect of mean arterial pressure on retrograde nidus filling with contrast injections. Transvenous embolization simulations were conducted for each of the 12 identical models divided into 2 groups (2×6). This involved the use of an ethylene-vinyl alcohol liquid embolic agent injected through microcatheters either without or with a coil in the vein (groups 1 and 2, respectively).

RESULTS: Retrograde contrast advance to nidus was directly related to lower mean arterial pressure. Transvenous embolization tests with a liquid embolic agent adequately reproduced the usual embolization plug and push technique. We found no differences between the 2 group conditions, and additional venous coil neither increased nidus penetration nor reduced injection time in the model (57.6 versus 61.2% nidus occlusion rate, respectively).

CONCLUSIONS: We were able to develop and test a functional in vitro brain AVM model for transvenous embolization by using 3D printing to emulate its conditions and characteristics. Better contrast penetration was achieved with less mean arterial pressure, and no embolization advantage was found by adding coil to the vein in this model.

ABBREVIATIONS: CAD = computer-aided design; EVOH = ethylene-vinyl alcohol; LEA = liquid embolic agents; MAP = mean arterial pressure; SLA = stereolithography; TVA = transvenous approach; TVE = transvenous embolization

Endovascular embolization is a well-accepted treatment strategy for brain AVMs as either a standalone therapy or a part of multimodal management together with microsurgery or radiosurgery.¹

The classical and more commonly used endovascular treatment is the transarterial approach of using microcatheters to inject liquid embolic agents (LEA) to fill the nidus and exclude it either partially or completely from the circulation.¹⁻⁴

Since the early stages of brain AVM treatment, it has been a dogma to avoid occluding the vein until complete arterial or nidus

control is achieved. An abrupt or unintended venous occlusion could result in an increase of intranidal pressure, which could potentially lead to secondary catastrophic bleeding.^{3,5} Despite these considerations, some theoretic conceptualizations, animal experiments, and clinical series showed that transvenous embolization (TVE) for brain AVM was feasible as a potential route for endovascular treatment.^{6,7} More recent series have shown TVE to be a transformative strategy for the curative endovascular treatment of selected cases, demonstrating much higher occlusion rates than those of the classic arterial route.^{8,9}

The venous approach is technically demanding, and it requires thorough anatomic knowledge and highly developed endovascular skills. Endovascular training, material testing, and simulations for this access strategy have become an important need for achieving technical success and ensuring patient safety in recent years. Recently, Vollherbst et al,¹⁰ presented the first TVE in vivo model by using a swine rete mirabile. No other transvenous animal or in vitro model has been described thus far,

Received October 17, 2023; accepted after revision January 11, 2024.

From the Neuroradiology Department (R.R., J.P.C.), Instituto de Neurocirugia Dr. Asenjo, Santiago, Chile; CNRS XLIM UMLR 7252 (R.R., A.R., C.M.), Université de Limoges, Limoges, France; Department of Design and Manufacturing (A.C.), Universidad Tecnica Federico Santa Maria, Chile; Neuroradiology Department (A.R., C.M.), CHU Limoges, France.

Please address correspondence to Rodrigo Rivera, MD, PhD, Neuroradiology Department, Instituto de Neurocirugia Dr. Asenjo, Jose Manuel Infante 553, Providencia, Santiago, Chile, PO Box 7500691; e-mail: rodrigorivera@me.com; @neurofoxx

<http://dx.doi.org/10.3174/ajnr.A8188>

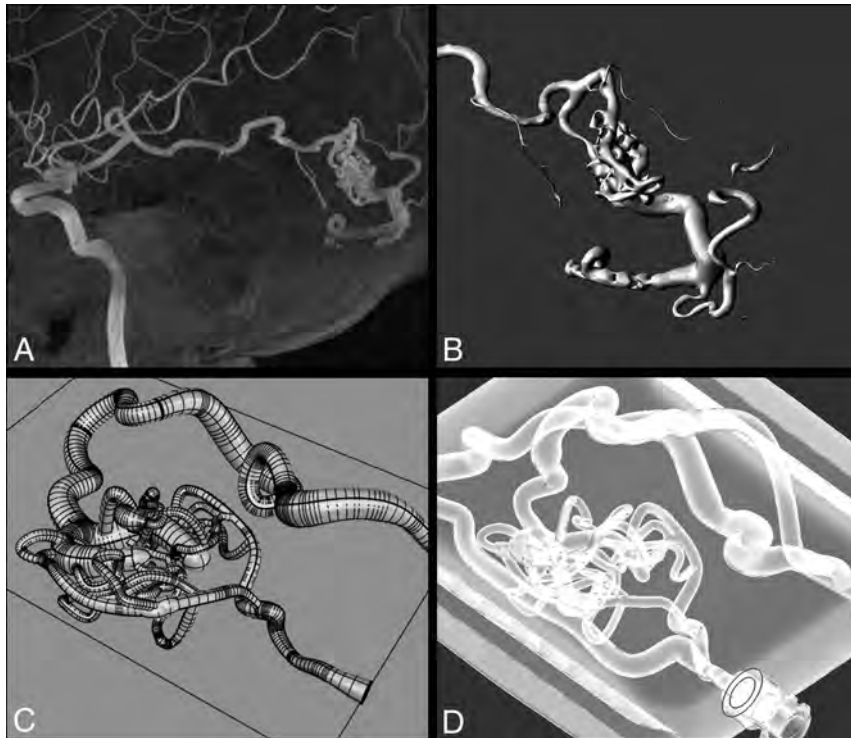


FIG 1. The process from the DICOM image to the model. A, MIP 3D reconstruction of the left temporal BAVM. Spetzler-Martin I. B, 3D image of the segmentation manual process by using the region growing technique with 3D Slicer Software. C, CAD representation of the BAVM model design after the main characteristics of the original disease. D, Final in vitro model inside the container, with transparent material and an external “normal” channel. BAVM indicates brain arteriovenous malformation.

though the latter have been widely used for other brain AVM endovascular treatment simulations.^{11–18}

The purpose of this study was to present the development and testing of a novel in vitro brain AVM in vitro model for TVE by using stereolithography (SLA) 3D printing and real patient data.

MATERIALS AND METHODS

This research was approved by the local Institutional Review Board. An in vitro brain AVM model was designed based on real patient data. We selected a left temporal brain AVM that was under 3 cm in diameter with single superficial venous drainage (grade I, according to the Spetzler–Martin classification).¹⁹ A 3D rotational acquisition was performed by using an Icono biplane angiography system (Siemens Healthineers). The brain AVM vessel information was exported in DICOM format, and a manual segmentation process (region growing technique) was done by using 3D Slicer (<https://www.slicer.org>). The brain AVM structure with the nidus was defined and transformed to Standard Triangle Language. We created a container or “chip” where the brain AVM model was fitted via computer-aided design (CAD) software (Fusion 360, Autodesk and Rhinoceros 3D, Robert McNeel & Associates). For the brain AVM tubing designs, we used the nonuniform rational B-spline methodology, which allows the formation of an endoskeleton via a sweep of isogeometric hexahedral control meshes. These meshes are compatible with

hemodynamic analyses and 3D rapid prototyping processes, which enables greater accuracy and efficiency in the design and simulation of the model. We simplified the model by removing the small structures that could not be adequately segmented, with the remaining smaller channels being between 0.5–1 mm. We added an external bypass channel that represented normal flow and luer lock connectors to the arterial input and venous output of the model.

The final CAD model was exported for 3D printing. We used a commercial Form 3B printer (FormLabs) with transparent resin (Clear V4) to create the model by using stereolithography (Fig 1).

We created a closed circuit setting of tubes and connectors with a pulsatile pump (FlowTek 125, United Biologics) that we used for all tests. The pump could modify the pulse and flow percentage, and the circulation was always from the arterial side to the venous side.

Transvenous Approach Injection Test

We aimed to determine the ideal pressure regimen of the system to allow counterflow to advance through the transvenous approach (TVA). The pulsatile pump was programmed with 60 cycles per minute, and 10 different flow percentages were tested: 70, 65, 60, 55, 50, 45, 40, 35, 30, and 25%. The circuit used NaCl 0.9% at 36°C. Pressure was measured using a transducer (TruWave, Edwards Lifesciences Services) in a 3-way connector at the entrance of the arterial part of the model and registered as the mean arterial pressure (MAP). We placed an Excelsior 1018 microcatheter (Stryker Neurovascular) at the venous collector, and iodinated contrast was manually injected (Visipaque 270, GE) under biplane fluoroscopy by using an Azurion 7 biplane (Philips Healthcare). We graded the contrast filling pattern by dividing the model into 4 different sections and assigning a score from 0–3 (with 0 representing no nidus filling and 3 representing the maximum retrograde contrast advance). The filling grade was compared with different MAP values by using the Pearson correlation test. The threshold for statistical significance was defined as $P \leq .05$.

Transvenous Embolization Test

We aimed to recreate the conditions of TVE by using LEA in 2 different settings, and we evaluated the impact of venous coiling on the nidus occlusion rate, total embolization time, and number of stops after reflux. For this purpose, we used the brain AVM model connected to the pulsatile pump. Normal saline at 36°C was used to fill the system. All embolizations were done with a

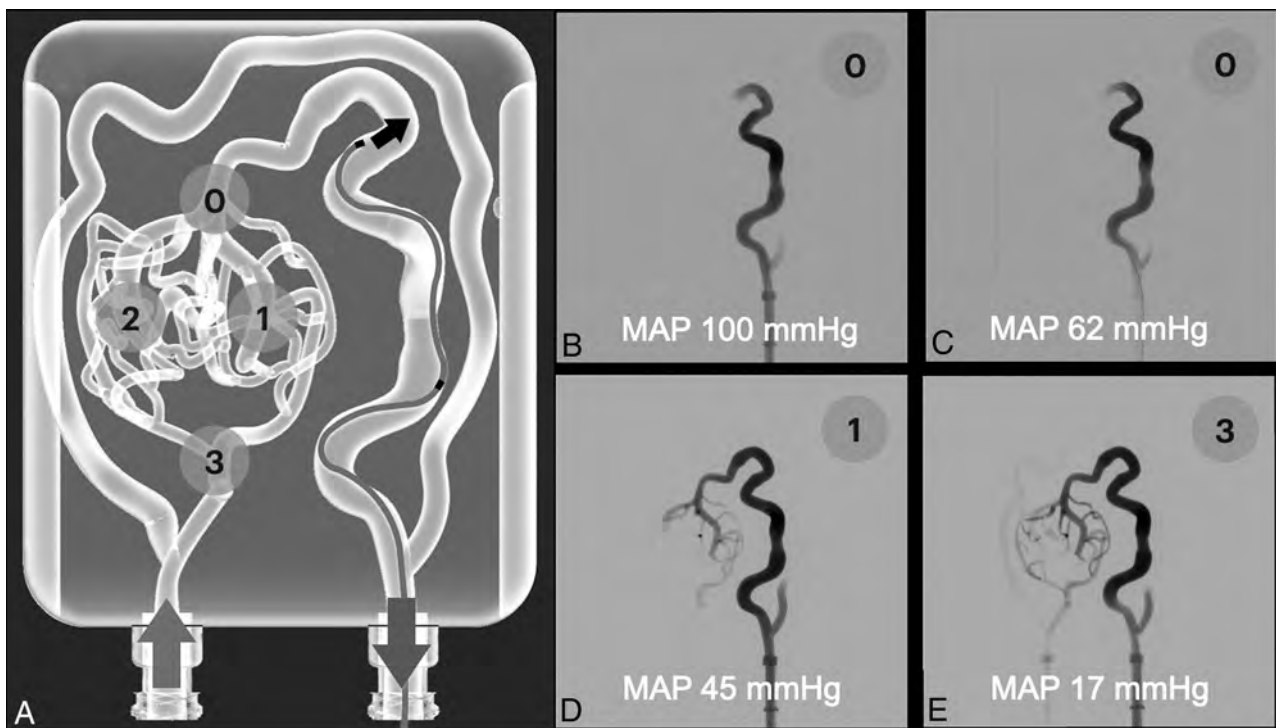


FIG 2. Contrast media retrograde test. Injections were done by using an Echelon 10 microcatheter and iodinated contrast. **A**, We tested 10 different input pressures from 10 different flow percentages, and we graded the retrograde advance from 0–3 as follows: 0 = no significant advance; 1 = 1 venous limb complete filling; 2 = 2 venous limbs complete filling; 3 = complete venous filling plus proximal arterial filling. **B–E**, Retrograde contrast injections with different MAP values. An increase in nidal contrast penetration was seen with lower MAP values, with a statistically significant correlation ($P = .001$).

pulse of 60 cycles per minute and a flow rate of 30%, which resulted in a MAP of 21 mmHg and a systolic pressure of 74 mmHg. Under these settings, the flow of the model was 42 mL/min. Under biplane fluoroscopy, we performed retrograde LEA embolizations with an ethylene-vinyl alcohol (EVOH) copolymer (Squid 18, Balt). Two experienced (>10 years) interventional neuroradiologists performed the embolizations. We embolized 12 identical in vitro models that were separated into 2 groups:

- Group 1. This group consisted of 6 models. A 1.5 F microcatheter (Apollo 1.5 30 mm, Medtronic) was navigated and positioned at the origin of the main vein over a 0.008" microguidewire (Hybrid, Balt). The dead space of the microcatheter was flushed with dimethyl sulfoxide. LEA was injected through the microcatheter manually via the usual manner, taking 30-second pauses when reflux over the microcatheter was seen or when filling the arterial feeder up to the main arterial side. The procedure was stopped when the reflux was greater than the venous drainage or when no more nidus filling was seen after several injection and pause cycles.
- Group 2. This group consisted of 6 models. A 1.5 F microcatheter was navigated and positioned in the same position as in group 1. A second microcatheter (Vasco 10+, Balt) was placed in a proximal position on the venous side, approximately 40 mm back from the first microcatheter tip. One bare platinum coil (Barricade 10×34 Frame complex coil; Balt) was deployed at this point using the "porcelain vein technique" as described by Mounayer's group,⁹ in which EVOH is deposited in a centripetal and circumferential manner along the vessel wall

during reflux to progressively reduce the inner diameter without immediately blocking the venous output. The LEA was then injected through the Apollo microcatheter using the same technique and injection/pause cycles as in group 1.

We measured the total injection time, number of pauses, and total injected LEA volume in both groups. We also determined the occlusion percentage of the nidus by using a 3D rotational acquisition without contrast at the end of the embolization procedure. The LEA of the model was segmented using the 3D Section software package, and the total filling volume was calculated using the PreForm software package (FormLabs). The percentage of nidal occlusion was calculated by using the total nidal volume from the CAD model minus the calculated nidal LEA volume from the 3D rotational images.

We used the Mann-Whitney U test to evaluate the differences between the 2 groups. The threshold for statistical significance was defined as $P \leq .05$.

RESULTS

TVA Injection Test

We found a statistically significant correlation between the MAP and contrast media retrograde filling through the brain AVM model ($P = .001$) (Fig 2). With lower MAP values, greater contrast nidal penetration and higher filling scores were found.

Transvenous Embolization Test

LEA was injected retrogradely to the model by using EVOH in 2 groups with the described techniques (Fig 3). No differences were

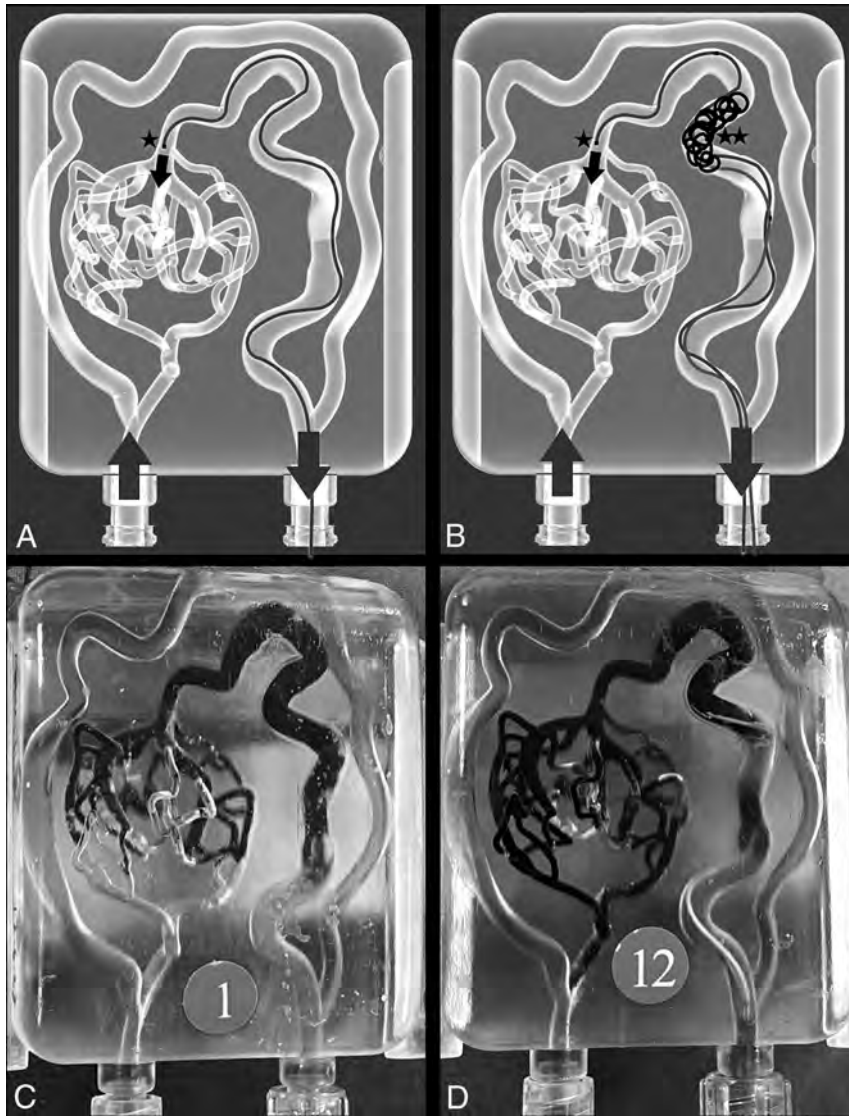


FIG 3. Transvenous embolization tests. TVE techniques were performed on 12 identical AVM models, divided into 2 groups (2 × 6). A, Group 1, where retrograde embolization was done by using an Apollo 1.5 30 mm microcatheter (★). B, Group 2, with the same position of the Apollo 1.5 30 mm (★) and a venous coil deployed with a Vasco+ microcatheter in a proximal vein position (★★). C, Real photograph after the EVOH embolization of a group 1 case. D, Real photograph after the EVOH embolization of a group 2 case.

Transvenous embolization results^a

Group	Group 1	Group 2	Significance
Total time (min:sec)	14:40	18:29	NS
Number of stops	13	15.5	NS
Total LEA (mL)	1.3 mL	1.75 mL	NS
Nidal LEA volume (mL)	0.46 mL	0.49 mL	NS
Nidal occlusion (%)	57.6	61.95	NS

^a Nonparametric test for different variables between groups by using the Mann-Whitney test. NS = nonsignificant.

found between group 1 (no coil on the venous side) and group 2 (bare platinum coil on venous collector) in any of the different measured variables (Table).

Embolizations were done by using the usual plug and push technique. Transparent resin material allowed a direct and easy

visualization of the embolization process. Digital subtraction angiography controls performed at the end of the embolization session showed no nidal contrast filling in any treated model.

DISCUSSION

Transvenous embolization has been described and increasingly used in recent years, and it has been demonstrated to be an outstanding approach by which to achieve a brain AVM cure in highly selected patients. Large series have showed high nidal occlusion rates and similar safety profiles compared with the usual endovascular trans-arterial approaches.^{9,20} This evolving technique requires the proper training and teaching of physicians, development of specific devices, and testing of new materials. Various models have been used for decades for these purposes, with the swine rete mirabile being the model of choice for endovascular training and testing.²¹⁻²³ In vitro models have been less explored to simulate brain AVM embolizations due to several limitations, including difficulties in defining the real nidal anatomy by using the currently available imaging modalities, complicated segmentation processes, and the complexity of building small hollow channels. Several in vitro models have been described since late 1970s for endovascular use by using different materials and structures that could resemble a brain AVM or nidus, from straight tubes to honeycomb-like structures as well as passing through tubes filled with beads, scouring pads, sponges, blood filters, or springs.^{13-17,24,25} A search for more realistic features has been done in the

last years. Kaneko et al¹² described an in vitro brain AVM model with realistic features and hollow channels by using 3D printing techniques in combination with solid printing and silicon coverage ready for LEA embolizations after the dissolution of inner solid compounds. Our group recently described a new, different technology process by using SLA 3D printing and millifluidic techniques that allow us to create an in vitro brain AVM model with small hollow channels that can be used for training and endovascular simulations.¹⁸ These in vitro models have been used to replicate arterial embolization treatments, but no TVE approaches have been performed. As previously stated, the only TVE model described thus far in the literature has been a swine rete mirabile in vivo model.¹⁰ In vivo models are of great importance and utility for endovascular training, but the management,

care facilities, transportation, costs, and ethical aspects regarding the use of animals for training, testing, or education present great barriers for their massive use.

In this study, we were able to present a novel in vitro brain AVM model for TVE. We were able to use the AVM data of a real patient and translate it to a 3D-printed SLA container. This process is an evolution of our earlier described SLA model, in which we created a simulated nidus anatomy.¹⁸ This is a first step, and we are aware that many challenges remain in adequately reproducing true nidus structures, but the current model opens many possibilities for training, rehearsal, and material testing, as has previously been done for brain aneurysms.²⁶⁻²⁹ Our new in vitro model has smaller hollow channels and more realistic structures and vessels. We expect more advances in the near future as acquisition imaging techniques and 3D printing technologies continue to improve and will eventually allow for the creation of smaller hollow or tubular structures.

Counterflow contrast injection proved to be in direct relation to MAP. Our model allowed us to define different pressure settings, and nidus retrograde filling was larger as systemic pressure was lower, with a statistically significant correlation. This concept was first described by Massoud et al⁶ with their transvenous retrograde nidus sclerotherapy under controlled hypotension technique of injecting contrast in a retrograde manner in a swine rete mirabile model. Contrast retrograde penetration was greater with lower MAP pressure values.⁶ The same concept has been applied in real TVE cases to create local or systemic hypotension for fast and complete nidus penetration, such as with proximal arterial balloon inflation, cardiac rapid ventricular pacing, and systemic induced hypotension.^{9,20,30}

The TVE in our model behaved similar to that in real cases. As expected, the navigation of the microcatheters was realistic and plausible with some extra friction in the in vitro model.²⁶ The injection of LEA began with some reflux to the vein, after which it began to advance through the nidus in the plug and push fashion. A plug rapidly was created, and fast and initial filling of the nidus was possible. Secondary reflux began and was controlled as much as possible with 30-second stops until our limit reflux was reached. We expected to have different occlusion results between our 2 experimental groups, with faster and greater nidus penetration in the second group, in which we used coil in the venous side. Nevertheless, we found no statistically significant difference between the two groups. We hypothesize that the absence of clot formation within the coil (because of the use of NaCl 0.9% to replace blood) and the limited number of coils used (1 long coil) may explain these results, as these are factors that contribute to stronger and better vein flow control. Our aim was to standardize the procedure and test the porcelain vein technique, so no other materials were used as glue, as described for the venous pressure cooker.²⁰ The nidus occlusion percentage was near 60%, though we expected to observe greater penetration and filling. However, we did see complete angiographic exclusion at the end of the procedure in all cases.

Our model presents other limitations. It is a solid in vitro model, so there were no elastic features as real vessels, and the model could not simulate procedure-related rupture as with an in vivo brain AVM. Friction inside the model felt higher than that

of human vessels, but microcatheter navigation was still adequately possible. Although we created a model based on a real brain AVM, there are still anatomic limitations of the reproducibility, and we could not replicate some smaller vessels because of actual image resolution, segmentation, and hollow vessel printing. The number of tested models was limited, and we did not test other flow control techniques at the venous side that could have contributed toward better nidus occlusion penetration, nor did we control proximal arterial flow with balloons.

However, despite some intrinsic limitations, we believe that our model presents several advantages as the model size, reproducibility, and easy transportation facilitate setup in any place or angiographic suite. The model is transparent, and though we did not actively test this feature, embolization is feasible and could be controlled without the use of X-rays. The procedure could be well-tested under direct vision or enhanced using a camera or video magnification.

Finally, we have successfully created a functional in vitro brain AVM model for TVE by using 3D printing to simulate its conditions and characteristics. This model can be used for training, educational purposes, and testing novel techniques and materials.

ACKNOWLEDGMENTS

We would like to thank Balt (Montmorency, France) for donating some of the materials that were used during the embolization tests as Squid 18 and Barricade coils.

Disclosure forms provided by the authors are available with the full text and PDF of this article at www.ajnr.org.

REFERENCES

1. van Beijnum J, van der Worp H, Buis DR, et al. **Treatment of brain arteriovenous malformations a systematic review and meta-analysis.** *JAMA* 2011;306:2011-19 CrossRef Medline
2. Saatci I, Geyik S, Yavuz K, et al. **Endovascular treatment of brain arteriovenous malformations with prolonged intranidal Onyx injection technique: Long-term results in 350 consecutive patients with completed endovascular treatment course - clinical article.** *J Neurosurg* 2011;115:78-88 CrossRef Medline
3. Valavanis A, Pangalu A, Tanaka M. **Endovascular treatment of cerebral arteriovenous malformations with emphasis on the curative role of embolisation.** *Interv Neuroradiol* 2005;11:37-43 CrossRef Medline
4. Loh Y, Duckwiler GR, Onyx Trial Investigators. **A prospective, multicenter, randomized trial of the Onyx liquid embolic system and N-butyl cyanoacrylate embolization of cerebral arteriovenous malformations: Clinical article.** *J Neurosurg* 2010;113:733-41 CrossRef Medline
5. Houdart E, Gobin YP, Casasco A, et al. **A proposed angiographic classification of intracranial arteriovenous fistulae and malformations.** *Neuroradiology* 1993;35:381-85 CrossRef Medline
6. Massoud TF, Hademenos GJ. **Transvenous retrograde nidus sclerotherapy under controlled hypotension (TRENTH): A newly proposed treatment for brain arteriovenous malformations - Concepts and rationale.** *Neurosurgery* 1999;45:351-65 CrossRef Medline
7. Nguyen TN, Chin LS, Souza R, et al. **Transvenous embolization of a ruptured cerebral arteriovenous malformation with en-passage arterial supply: Initial case report.** *J Neurointerv Surg* 2010;2:150-52 CrossRef Medline
8. Chapot R, Stracke P, Velasco A, et al. **The pressure cooker technique for the treatment of brain AVMs.** *J Neuroradiol* 2014;41:87-91 CrossRef Medline

9. Mendes GAC, Kalani MYS, Iosif C, et al. **Transvenous curative embolization of cerebral arteriovenous malformations: A prospective cohort study.** *Clin Neurosurg* 2018;83:957–64 CrossRef Medline
10. Vollherbst DF, Hantz M, Schmitt N, et al. **Experimental investigation of transvenous embolization of arteriovenous malformations using different in vivo models.** *J Neurointerv Surg* 2022;15:712–16 CrossRef Medline
11. Vollherbst DF, Sommer CM, Ulfert C, et al. **Liquid embolic agents for endovascular embolization: Evaluation of an established (Onyx) and a novel (PHIL) embolic agent in an in vitro AVM model.** *AJNR Am J Neuroradiol* 2017;38:1377–82 CrossRef Medline
12. Kaneko N, Ullman H, Ali F, et al. **In vitro modeling of human brain arteriovenous malformation for endovascular simulation and flow analysis.** *World Neurosurg* 2020;141:e873–9 CrossRef Medline
13. Ishikawa M, Horikawa M, Yamagami T, et al. **Embolization of arteriovenous malformations: Effect of flow control and composition of n-butyl-2 cyanoacrylate and iodized oil mixtures with and without ethanol in an in vitro model.** *Radiology* 2016;279:910–16 CrossRef Medline
14. Inagawa S, Isoda H, Kougo H, et al. **In-vitro simulation of NBCA embolization for arteriovenous malformation.** *Interv Neuroradiol* 2003;9:351–58 CrossRef Medline
15. Debrun GM, Vinuela FV, Fox AJ, et al. **Two different calibrated-leak balloons: Experimental work and application in humans.** *AJNR Am J Neuroradiol* 1982;3:407–14
16. Kerber CW, Bank WO, Cromwell LD. **Calibrated leak balloon microcatheter: A device for arterial exploration and occlusive therapy.** *AJR Am J Roentgenol* 1979;132:207–12 CrossRef Medline
17. Park S, Yoon H, Suh DC, et al. **An arteriovenous malformation model for testing liquid embolic materials.** *AJNR Am J Neuroradiol* 1997;18:1892–96
18. Rivera R, Cespedes A, Cruz JP, et al. **Endovascular treatment simulations using a novel in vitro brain arteriovenous malformation model based on three-dimensional printing millifluidic technology.** *Interv Neuroradiol* 2023 Jun 22:15910199231184605 CrossRef Medline
19. Spetzler RF, Martin NA. **A proposed grading system for arteriovenous malformations.** *J Neurosurg* 1986;65:476–83 CrossRef Medline
20. Koyanagi M, Mosimann PJ, Nordmeyer H, et al. **The transvenous retrograde pressure cooker technique for the curative embolization of high-grade brain arteriovenous malformations.** *J Neurointerv Surg* 2021;13:637–41 CrossRef Medline
21. Massoud TF, Ji C, Vinuela F, et al. **An experimental arteriovenous malformation model in swine: Anatomic basis and construction technique.** *AJNR Am J Neuroradiol* 1994;15:1537–45 Medline
22. Samaniego EA, Derdeyn CP, Hayakawa M, et al. **In vivo evaluation of the new PHIL low viscosity in a swine rete mirabile model.** *Interv Neuroradiol* 2018;24:706–12 CrossRef Medline
23. Murayama Y, Viñuela F, Ulhoa A, et al. **Nonadhesive liquid embolic agent for cerebral arteriovenous malformations: Preliminary histopathological studies in swine rete mirabile.** *Neurosurgery* 1998;43:1164–75 CrossRef Medline
24. Bartyński WS, O'Reilly GV, Forrest MD. **High-flow-rate arteriovenous malformation model for simulated therapeutic embolization.** *Radiology* 1988;167:419–21 CrossRef Medline
25. Kerber CW, Hecht ST, Knox K. **Arteriovenous malformation model for training and research.** *AJNR Am J Neuroradiol* 1997;18:1229–32 Medline
26. Paramasivam S, Baltsavias G, Psatha E, et al. **Silicone models as basic training and research aid in endovascular neurointervention - A single-center experience and review of the literature.** *Neurosurg Rev* 2014;37:331–37; discussion 337 CrossRef Medline
27. Nawka MT, Spallek J, Kuhl J, et al. **Evaluation of a modular in vitro neurovascular procedure simulation for intracranial aneurysm embolization.** *J Neurointerv Surg* 2020;12:214–19 CrossRef Medline
28. Pravdivtseva MS, Peschke E, Lindner T, et al. **3D-printed, patient-specific intracranial aneurysm models: From clinical data to flow experiments with endovascular devices.** *Med Phys* 2021;48:1469–84 CrossRef Medline
29. Yamaki VN, Cancelliere NM, Nicholson P, et al. **Biomodex patient-specific brain aneurysm models: The value of simulation for first in-human experiences using new devices and robotics.** *J Neurointerv Surg* 2021;13:272–77 CrossRef Medline
30. Waqas M, Dossani RH, Vakharia K, et al. **Complete flow control using transient concurrent rapid ventricular pacing or intravenous adenosine and afferent arterial balloon occlusion during transvenous embolization of cerebral arteriovenous malformations: Case series.** *J Neurointerv Surg* 2021;13:324–30 CrossRef Medline

Tumor Embolization via the Meningohypophyseal and Inferolateral Trunk in Patients with Skull Base Tumors Using the Distal Balloon Protection Technique

Kei Yamashiro, Motoharu Hayakawa, Kazuhide Adachi, Mitsuhiro Hasegawa, and Yuichi Hirose



ABSTRACT

BACKGROUND AND PURPOSE: Tumor embolization through the meningohypophyseal trunk and inferolateral trunk is known to be effective in skull base tumors; however, microcatheter cannulation into these arteries is difficult, and the number of cases that can be safely embolized is limited. In this study, we present a novel embolization procedure for the meningohypophyseal trunk and inferolateral trunk using the distal balloon protection technique and detail its clinical efficacy and complication risks. We developed this procedure to allow safe embolization in patients who cannot be adequately cannulated with microcatheters into these arteries.

MATERIALS AND METHODS: Patients who underwent meningohypophyseal trunk or inferolateral trunk embolization using the distal balloon protection technique for skull base tumors at our institution between 2010 and 2023 were included. In this procedure, the ICA was temporarily occluded with a balloon at the ophthalmic artery bifurcation, the microcatheter was guided to the meningohypophyseal trunk or inferolateral trunk vicinity, and embolic particles were injected into the arteries. The balloon was deflated after the embolic particles that had refluxed into the ICA were aspirated.

RESULTS: A total of 25 meningohypophyseal trunks and inferolateral trunks were embolized during 21 operations. Of these 25 arteries, only 9 (36.0%) were successfully cannulated with microcatheters. Nevertheless, effective embolization was achieved in all cases. Permanent complications occurred in only 1 case (4.8%) in which the central retinal artery was occluded during inferolateral trunk embolization, resulting in a visual field defect. No permanent complications resulting from the embolic cerebral infarction were observed. Of 16 cases that underwent MR imaging within a week after embolization, however, 11 (68.8%) demonstrated embolic cerebral infarctions.

CONCLUSIONS: In patients with skull base tumors with meningohypophyseal trunk or inferolateral trunk feeders that cannot be catheterized directly, embolization using the distal balloon protection technique for tumor supply can be considered as a salvage technique.

ABBREVIATIONS: AC = aspiration catheter; FR = flow reverse; GC = guide catheter; ILT = inferolateral trunk; MHT = meningohypophyseal trunk

Preoperative embolization is known to be effective against extra-axial tumors and is a widely accepted procedure.¹⁻¹¹ It is known that preoperative tumor embolization is particularly effective for skull base tumors because tumor-feeding arteries are located at the deepest part of the surgical field, making devascularization of feeding arteries difficult until the tumor has been removed.^{2,7,8,12}

However, preoperative embolization of skull base tumors presents several challenges.¹³ In particular, when embolizing the meningohypophyseal trunk (MHT) and inferolateral trunk (ILT), reflux of embolic particles into the ICA has been reported.^{2,4,7,10} This is because the MHT and ILT are usually very tortuous, making microcatheter cannulation into these arteries difficult.^{2,8} When the MHT and ILT are aggressively embolized, neurologic complications are reported to occur in 22.1% and 13.3% of cases, respectively.⁹ On the other hand, MHT and ILT embolization is safe provided that cannulation is performed reliably,^{4,7,8,10} though the number of patients who can be adequately catheterized into the MHT and ILT is limited. In a report of skull base meningioma embolization with safety being the highest priority, only 9 of 28 MHTs (32.1%) and 1 of 5 ILTs (20.0%) were embolized,¹⁰ indicating that safe tumor embolization via these arteries can be performed in only a limited number of cases.

Received November 23, 2023; accepted after revision January 13, 2024.

From the Department of Neurosurgery (K.Y., M. Hayakawa), Fujita Health University Okazaki Medical Center, Okazaki, Aichi, Japan; Department of Neurosurgery (K.Y., M. Hayakawa, K.A., Y.H.), Fujita Health University, Toyoake, Aichi, Japan; and Tokyo D-tower Hospital (M. Hasegawa), Tokyo, Japan.

Please address correspondence to Kei Yamashiro, MD, PhD, Department of Neurosurgery, Fujita Health University Okazaki Medical Center, 1, Gotanda, Harisaki-cho, Okazaki City, Aichi 4440827; e-mail: keiyamashiro1577@gmail.com; @YamashiroKei



Indicates article with online supplemental data.

<http://dx.doi.org/10.3174/ajnr.A8169>

To solve this problem, we developed a novel embolization procedure that combines a distal balloon protection technique.² In this procedure, the MHT and ILT are embolized while occluding the ICA with a balloon, and embolic particles that have refluxed into the ICA are aspirated and removed. This technique allows embolization of the MHT and ILT, even if they are difficult to cannulate using microcatheters. Our current report explores the efficacy and safety of MHT and ILT embolization using the distal balloon protection technique.

MATERIALS AND METHODS

Study Design and Population

We retrospectively analyzed all patients who underwent tumor embolization via the MHT and/or ILT for extra-axial skull base tumors using the distal balloon protection technique at our institution between February 2010 and March 2023. Extra-axial skull base tumors were defined as those attached to the dura mater located in the anterior fossa, cavernous sinus, sphenoid ridge, middle fossa, petroclival region, cerebellopontine angle, foramen magnum, or tentorium.

Data Collection. Patient information such as age, sex, tumor location, and pathology, as well as postembolization complications, was collected using medical records and pre- and postoperative CT and/or MR imaging. Neurologic findings immediately after tumor embolization, head CT performed immediately after tumor embolization, and MR imaging performed within 1 week of embolization were used to ascertain the occurrence of complications. The extent of tumor resection was determined using MR images obtained within 3 months after surgery and was divided into 3 grades: gross total resection, complete resection of the tumor mass; subtotal resection, complete resection of the tumor mass except for a part of the tumor adjacent to critical structures and a tumor invasion part into the dural sinuses; and partial resection, other than gross total resection and subtotal resection. In addition, angiograms and embolization operative records were reviewed to determine the surgical instrument used, artery embolized, and embolization efficacy. The latter was determined by 2 endovascular surgeons on the basis of postoperative ICA angiography findings of complete, partial, or no disappearance of tumor staining from the embolized artery. Finally, the operative records of tumor resection were reviewed to determine blood loss.

Evaluation of Postoperative Cerebral Infarction. The presence of postoperative cerebral infarction was evaluated through an MR imaging performed within 1 week following embolization. Cerebral infarction was diagnosed on the basis of the presence of high-intensity areas observed on DWI. The number and size of the cerebral infarction were evaluated using the DWI grading scale, as outlined in previous reports: grade A, no high-intensity areas; grade B, minor high-intensity areas (≤ 5 spots, with each spot ≤ 10 mm); grade C, some small high-intensity areas (> 6 spots, with each spot ≤ 10 mm); grade D, large high-intensity areas (at least 1 spot of > 10 mm).¹⁴

Surgical Procedure of Embolization Using Distal Balloon Protection. The indication for tumor embolization was determined by a discussion between the neurosurgeon performing the

tumor resection and the endovascular surgeon on the basis of tumor angiographic findings. Tumor embolization was performed primarily for tumors that were large and rich in blood flow; it was expected that it would be difficult to devascularize the feeding artery during tumor resection.

Tumor embolization was performed 1 day before tumor resection. All embolization procedures were performed with 7F- or 8F-equivalent guide catheters (GCs). Initially, the GC was guided via the right femoral artery into the ICA, and a balloon was guided near the ophthalmic artery bifurcation. Next, microcatheter cannulation was attempted into the MHT or ILT. If cannulation was difficult, the microcatheter was guided as closely as possible to the orifice of the MHT or ILT. After the ICA was occluded with a balloon at the bifurcation of the ophthalmic artery, the embolic particles were injected through a microcatheter into the MHT or ILT (Fig 1). During ICA occlusion, care was taken to ensure that the orifice of the ophthalmic artery was occluded to prevent the migration of embolic particles into the ophthalmic artery. The temporary occlusion of the ICA during embolization was limited to 10 minutes. After we confirmed that a sufficient embolic effect had been achieved, the embolic particles that had refluxed into the ICA were aspirated and removed using 3 methods.

The first method involved aspirating and removing the embolic particles from only the GC (GC method) (Fig 2A). In this method, the embolic particles were aspirated and removed using the GC after embolization. In the GC method, aspiration from the GC was performed at least 3 times, even if no embolic particles were identified; if embolic particles were identified, aspiration was repeated until no embolic particles were present.

The second method involved aspiration and removal of embolic particles using an aspiration catheter (AC) (AC method) (Fig 2B). In this method, apart from the GC used for embolization, a 6F- or 7F-equivalent GC was guided via the left femoral artery into the common carotid artery, and an AC was guided to the vicinity of the balloon to aspirate and remove the embolic particles that had refluxed into the ICA. Notably, when the ICA was occluded by using a PercuSurge Guidewire (Medtronic), no additional GC was inserted. In the AC method, similar to the GC method, aspiration from the AC was performed at least 3 times even if no embolic particles were identified; if embolic particles were identified, aspiration was repeated until no embolic particles were present.

In the third method, after the embolic particles were aspirated and removed by the AC method, the cervical ICA was further occluded with a balloon GC, the balloon on the distal side was deflated to allow the ICA to flow back, and the embolic particles were drained from the ICA via the balloon GC (AC and flow reverse [FR] method) (Figs 2C and 3). In the AC and FR method, aspiration from the balloon GC was completed once if no embolic particles were identified; however, if embolic particles were identified, aspiration was repeated until no embolic particles were present.

In all 3 methods, aspiration was performed after embolization using a 20-mL syringe, and continuous aspiration during embolization was not performed.

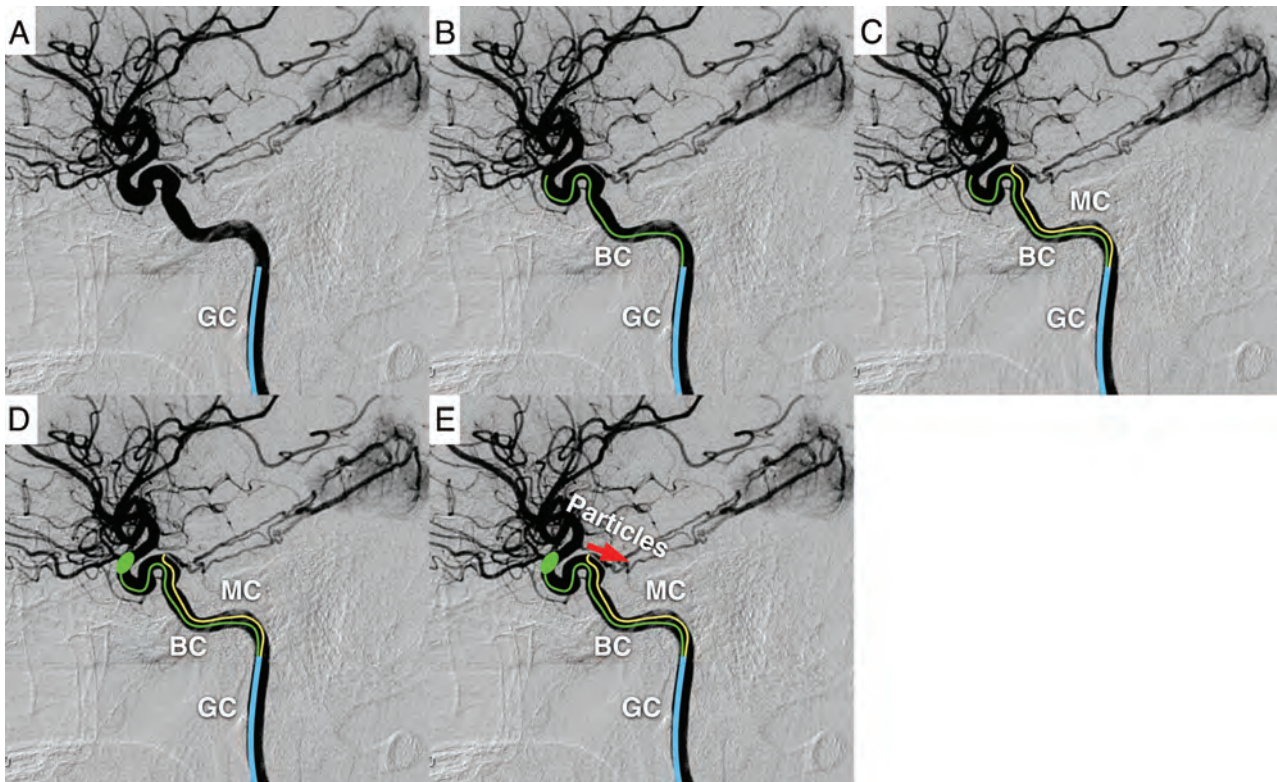


FIG 1. Schematic representation of tumor embolization using the distal balloon protection technique. First, a GC is placed in the ICA (A). Then, the balloon catheter is guided to the proximity of the bifurcation of the ophthalmic artery (B). Next, a microcatheter is inserted into the MHT or ILT (C). If cannulation is difficult, the microcatheter is guided near the orifice of the MHT or ILT. The balloon is then inflated to occlude the internal carotid and ophthalmic arteries (D). The embolic particles are injected from the microcatheter into the MHT or ILT (E). BC indicates balloon catheter; MC, microcatheter.

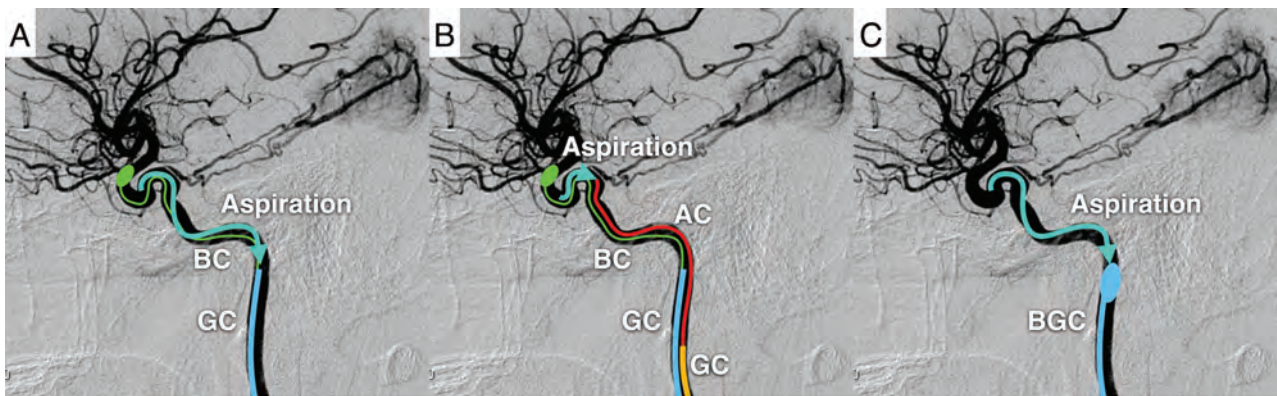


FIG 2. Schematic representation of aspiration and removal of embolic particle reflux into the internal carotid artery. In the GC method, embolic particles are aspirated and removed using the GC, while the ICA is occluded with a balloon (A). In the AC method, a GC different from the one used for embolization is placed in the common carotid artery (for convenience, the GC is depicted in the ICA), and the AC is guided to the vicinity of the meningohipophyseal or inferolateral trunk to aspirate and remove embolic particles (B). In the AC and FR method, after aspiration and removal of embolic particles by the aspiration method, the balloon GC is inflated to reverse blood flow in the ICA to remove embolic particles more reliably (C). BC indicates balloon catheter; BGC, balloon guide catheter.

Ethical Consideration. This retrospective study was approved by our institutional review board (Fujita Health University, protocol No.: HM23-123). All patients provided written informed consent for treatment, and we offered an opt-out approach for participation.

In this study, 3 different embolic particles were used (Embosphere [trisacryl gelatin microspheres], Merit Medical Systems); Ivalon

[polyvinyl alcohol], Ivalon; and Avitene [microfibrillar collagen], Zeria Pharmaceutical). Before the introduction of Embosphere, there were no approved embolic particles for tumor embolization in our country. Consequently, before the availability of Embosphere, Ivalon or Avitene were used as off-label embolic particles following the acquisition of written informed consent from the patient.

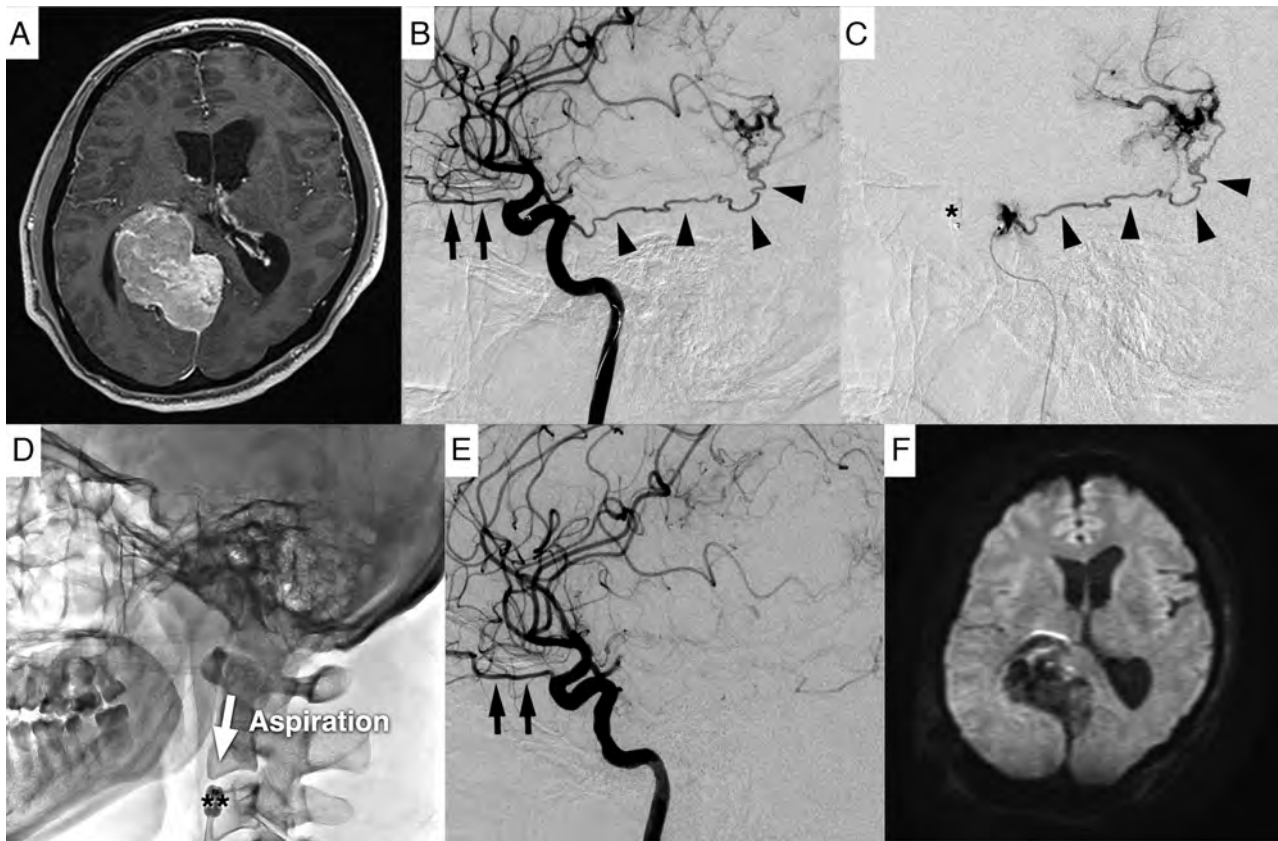


FIG 3. A case of tumor embolization via the MHT using the distal balloon protection technique. Preoperative tumor embolization was performed for a right falcotentorial meningioma through the right MHT (A and B). In this case, the microcatheter was guided to the vicinity of the orifice of the MHT because cannulation of the microcatheter into the MHT was not possible (C). Next, the ICA and ophthalmic artery were occluded with a balloon (C), and the MHT was embolized with embolic particles. After embolization, the AC was guided to the vicinity of the MHT to aspirate and remove the embolic particles. This step was followed by inflating the balloon GC and deflating the balloon catheter to reverse blood flow in the ICA to remove the embolic particles (D). Finally, complete embolization of the MHT was confirmed (E). Postoperative MR imaging showed no embolic cerebral infarction (F). The *black arrow* indicates the ophthalmic artery; *black arrowhead*, MHT; *single asterisk*, balloon catheter; *double asterisk*, balloon GC.

RESULTS

Patient Characteristics and Surgical Procedures

A total of 21 tumor embolization procedures via the MHT and/or ILT with the distal balloon protection technique were performed in 19 patients with extra-axial skull base tumors during this study. Two of the 19 patients underwent tumor embolization twice. The median age at surgery was 47 years (range, 21–68 years), with 13 women and 6 men. Of the 19 patients, 17 had meningiomas and 2 had solitary fibrous tumors. The meningioma subtypes were meningothelial in 8, angiomatous in 5, secretory in 2, chordoid in 1, and difficult to classify (diagnosed as World Health Organization grade 1 equivalent) in 1 patient. The tumor attachment sites were the petroclival in 13, falcotentorial in 3, sphenoid ridge in 2, and cerebellopontine angle in 1 patient.

A total of 19 MHTs and 6 ILTs were embolized using 21 embolization procedures. Of these embolized arteries, 8 MHTs (42.1%) and 1 ILT (16.7%) were successfully cannulated using microcatheters. Particles were used as the embolic material in all surgeries; Embosphere (100–300 μm or 300–500 μm) was used in 12 embolization procedures, Ivalon was used in 5, and Avitene was used in 4. Avitene used in this study was supplied in powder form, and a pinch of Avitene was dissolved in 20 mL of contrast

medium for the embolization procedure. As for the method of aspiration and removal of embolic particles, the GC method was used in 3 embolization procedures; the AC method, in 6; and the AC and FR method, in 12 (Online Supplemental Data).

Efficacy and Complications of Embolization

Regarding the efficacy of tumor embolization, complete disappearance of tumor stain was achieved in 14 of 19 MHTs (73.7%); and partial disappearance, in the remaining 5 (26.3%). Complete disappearance of the tumor stain was observed in 4 of 6 ILTs (66.7%); and partial disappearance, in the remaining 2 (33.3%). An embolic effect was observed in all cases. When the embolization effect was examined on the basis of whether the microcatheter could be cannulated into the ILT or MHT, the complete disappearance of the tumor stain was confirmed in 6 of the 9 arteries (66.7%) that could be cannulated and in 12 of the 16 arteries (75.0%) that could not (Online Supplemental Data).

Two of the 21 embolization procedures (9.5%) exhibited symptomatic complications associated with embolization of the ILT: transient hemiparesis associated with embolic cerebral infarction in one case and visual field disturbance due to central retinal artery occlusion in the other. Permanent sequelae were

observed in only 1 case (4.8%) of the above-mentioned visual field disturbance (Online Supplemental Data).

Regarding the postoperative imaging evaluation, all patients underwent CT immediately after embolization, and 16 of the 21 patients underwent MR imaging within 1 week after embolization. Postoperative MR imaging was performed in 1 of 3 cases using the GC method, in 4 of 6 cases using the AC method, and in 11 of 12 cases using the AC and FR method. Postoperative CT revealed no complications in any of the patients. However, MR imaging confirmed embolic cerebral infarction in 11 of 16 patients (68.8%): in 1 patient (100%) using the GC method, in 2 of 3 (50.0%) using the AC method, and in 8 of 11 (72.7%) using the AC and FR method. The details of the DWI grading scale were the following: grade A in 5 patients (31.3%), grade B in 2 (12.5%), grade C in 8 (50.0%), and grade D in 1 (6.3%). Of these 11 cerebral infarctions, 1 patient with the GC method had transient hemiparesis as described above, whereas 10 patients with the AC and AC and FR method were asymptomatic. According to the DWI grading scale, the patient with a grade D experienced transient paralysis, whereas 10 patients with grades B and C were asymptomatic. No cranial nerve ischemia occurred in any patient.

In 1 of the 12 patients with the AC and FR method in which the ILT was embolized, occlusion of the central retinal artery occurred, and the embolic particles were thought to have migrated into the central retinal artery through the anastomosis between the ILT and ophthalmic artery or the remaining embolic particles in the ICA migrated directly into the central retinal artery.

Tumor Resection

Tumor resection was successfully performed in all cases. Gross total resection was achieved in 2 cases; subtotal resection, in 9 cases; and partial resection, in 10 cases. The median blood loss during surgical resection was 212 mL (range, 30–848 mL). There were no cases in which tumor resection was interrupted due to difficulty in hemostasis. No major surgery-related complications or deaths occurred.

Representative Case (Surgical No. 10)

A man in his 30s presented with symptoms including headache, visual field disturbance, and cognitive dysfunction. MR imaging revealed an extra-axial skull base tumor with an attachment from the falx to the right cerebellar tent (Fig 3A). Preoperative ICA angiography showed a prominent tumor stain from the right MHT (Fig 3B), and tumor embolization from the MHT with the AC and FR method was performed 1 day before tumor resection (Online Supplemental Data).

To begin the embolization procedure, we initially guided a 7F balloon GC (OPTIMO EPD; Tokai Medical Products) into the right ICA via the right femoral artery. Next, a sheathless 5F GC (ASAHI FUBUKI Dilator kit; Asahi Intecc) was guided via the left femoral artery to the right common carotid artery for particle aspiration.

Efforts were made to cannulate the microcatheter (Excelsior 1018; Stryker) and microguidewire (Glidewire GT, 0.016-inch double angle; Terumo Interventional Systems) into the MHT via a 7F balloon GC, but these attempts were unsuccessful.

Therefore, the apex of the microcatheter was redirected to the orifice of the MHT, and the embolic particles (Embosphere 300–500 μ m) were injected toward the orifice after the temporal occlusion of the ICA at the origin of the ophthalmic artery was achieved using a microballoon catheter (Magic B1; Balt) through the 7F balloon GC (Fig 3C).

Immediately following embolization, the AC (Thrombuster; Kaneka Medix) was guided through a sheathless 5F GC to the vicinity of the balloon to aspirate and remove the remaining embolic particles in the ICA. In addition, the balloon GC was inflated to obstruct blood flow at the cervical ICA, and the distal microballoon catheter was deflated to reverse the blood flow in the ICA and drain the remaining embolic particles out of the body through the balloon GC (Fig 3D). Finally, the complete disappearance of tumor stain from the MHT was confirmed (Fig 3E). There were no new neurologic symptoms following embolization, and postoperative MR imaging revealed no evidence of embolic infarction (Fig 3F).

The tumor was resected using a posterior interhemispheric approach (operation time: 949 minutes, blood loss: 498 mL), and the patient was discharged without any postoperative complications. The pathologic diagnosis confirmed the presence of a solitary fibrous tumor.

DISCUSSION

To our knowledge, this is the first study to evaluate the efficacy and safety of tumor embolization via the MHT and ILT using the distal balloon protection technique. The distal balloon protection technique presented in this study can embolize essentially all MHTs and ILTs because cannulation into these arteries is not required and the incidence of permanent complications was 4.8%. Only 32.1% of MHTs and 20% of ILTs can be embolized when catheter cannulation is prioritized in conventional surgery, whereas complications occur in 22.1% of MHT embolizations and 13.3% of ILT embolizations when aggressive embolization is performed.^{9,10} The embolization of the MHT and ILT using the distal balloon protection technique greatly expanded the surgical target compared with conventional methods.

Embolization Efficacy

The results of this study showed that tumor embolization effects were observed after all operations. Even when microcatheter cannulation into the MHT or ILT was difficult, tumor stains completely disappeared in 75% of the cases, suggesting that even without cannulation, injecting embolic particles toward the target artery provides a sufficient tumor embolization effect. We have named the tumor embolization technique with distal balloon protection the “para-para method” (from the Japanese word “para-para,” which means sprinkle) because of sprinkling the embolic particles into the tumor. Although safety issues remain, the para-para method presented here allows tumor embolization via all MHTs and ILTs; this result is expected to significantly expand the indications for tumor embolization via MHT and ILT. Surgical instruments developed in recent years may facilitate the selection of these arteries. Arterial embolization after selecting these arteries is the first choice; however,

tumor embolization using the para-para method is useful as a second option when these arteries cannot be selected.

In the present study, gross total resection was achieved in only 2 cases. Because tumor embolization in this study was performed on tumors with large and abundant blood flow, the tumor part adjacent to the brainstem, eloquent cerebral cortex, cranial nerves, and critical arteries and veins, and invading the dural sinuses tended to be unresectable. Conversely, these results indicate that tumors with a high risk of complications were primarily included in the present study. Because tumor resection rates are determined by various factors, it is difficult to evaluate the efficacy of tumor embolization solely on the basis of tumor resection rates. On the other hand, the fact that there were no cases in which hemostasis was difficult to achieve during resection may reflect the effectiveness of tumor embolization.

Methods for Aspiration and Removal of Embolic Particles and Risk of Embolic Cerebral Infarction

Three methods were used to remove the embolic particles in this study; however, only the GC method caused symptomatic embolic cerebral infarction (grade D on the DWI grading scale). This result is presumably because the GC method can only aspirate blood around the GC and thus cannot sufficiently aspirate embolic particles. In contrast, the AC and AC and FR methods did not cause symptomatic cerebral infarction. While we used these methods, only minor cerebral infarctions of grade B or C on the DWI grading scale were observed. This issue may be because the aspiration of blood in the vicinity of the orifice of the MHT and ILT allowed sufficient aspiration and removal of embolic particles that refluxed into the ICA. However, a high frequency of postoperative embolic cerebral infarction has been observed even when the AC or AC and FR method was used. Embolization using the para-para method should be considered as an alternative when direct catheterization into the MHT and ILT is difficult. Compared with the AC method, the AC and FR method is presumed to be more reliable for aspirating and removing embolic particles, given the nature of the procedure. Because embolic infarction was confirmed in more than one-half of the cases in the present study, it would be preferable to use the AC and FR method, which more reliably removes embolic particles. In addition, distal access catheters having the same capability as aspiration catheters have been developed recently. Although the present study did not include a case with a distal access catheter, it is likely that a coaxial system with a distal access catheter could be used to aspirate embolic particles in a similar manner through a single access route.

Risk of Complications Other Than Cerebral Infarction

In addition to the aforementioned embolic cerebral infarction, other complications of the MHT and ILT have been reported, including occlusion of the vasa nervorum of the cranial nerves and the risk of migration of embolic particles into normal arteries via dangerous anastomoses.^{4,7,8,10}

Although no occlusion of the vasa nervorum occurred in this study, the choice of embolic material is known to be important for avoiding occlusion.^{4,5,7,8,10} The vasa nervorum diameter is usually less than 100–150 μm ,^{5,15} and avoiding the use of liquid embolic material while using embolic particles of $>100 \mu\text{m}$ is important to

avoid its occlusion.^{5,8} Conversely, tumor embolization is more effective when smaller-diameter embolic particles are used, which can reach the tumor more easily.⁷ Considering that tumor embolization is only an adjunctive therapy for tumor removal, it is necessary to avoid complications as much as possible. Although the extent of tumor stain and the location of tumor-feeding arteries can vary, it seemed reasonable to select embolic particles at least larger than the Embosphere 100–300 μm to balance the benefits obtained and the risk of complications, given that no cranial nerve disturbance occurred in this study.

In addition to the vasa nervorum, dangerous anastomosis should also be noted during embolization of the MHT and ILT.⁸ Particular attention should be paid to the anastomosis with the ophthalmic artery via the deep recurrent ophthalmic artery during embolization of the ILT.⁸ In the present study, occlusion of the central retinal artery occurred in 1 patient. Although it is conceivable that the remaining embolic particles in the ICA migrated directly to the central retinal artery, this dangerous anastomosis could have been the cause. In the aforementioned case, the microcatheter could not be cannulated into the ILT; therefore, the ILT could not be fully evaluated. Given the magnitude of the impact of visual field defects, it may be appropriate to avoid embolization from the ILT if the dangerous anastomosis cannot be adequately evaluated. Furthermore, because dangerous anastomoses that were not initially identified may be found after embolization,⁷ it is necessary to carefully consider the surgical indications for ILT embolization, especially considering the risk of blindness and the benefits of embolization. In the present study, the balloon was inflated at the ophthalmic artery bifurcation to prevent the embolic particles from migrating into the ICA via the ophthalmic artery if they flowed back into the external carotid artery; however, because the ICA cavernous portion has various dangerous anastomosis, inflating the balloon immediately distal to the artery to be embolized may further reduce the risk of the embolic particles migrating into the dangerous anastomosis.

Appropriateness of MHT and ILT Embolization

It is difficult to rigorously evaluate the clinical efficacy of tumor embolization because evaluating individual tumors identically is challenging and studies on tumor embolization are usually strongly influenced by neurosurgeon and endovascular surgeon biases.¹⁰ Therefore, tumor embolization, especially from arteries posing a risk for complications, should be decided carefully. The decision to perform tumor embolization in this study was ultimately made through discussion between the neurosurgeon and the endovascular surgeon; however, the basic selection was focused on tumors with large, abundant blood flow and difficulty in feeding artery devascularization. Consequently, tumors with rich blood flow, such as angiomatous meningiomas, chordoid meningiomas, and solitary fibrous tumors, were frequently embolized in this study. Although these hemorrhagic tumors accounted for approximately one-half of the cases in the present study, the median amount of bleeding was only 212 mL, which is less than that in previous reports,⁷ suggesting that tumor embolization was sufficiently effective.

There may be some controversy regarding the 4.8% permanent complication rate and the high frequency of postoperative embolic infarction shown in this study. Preoperative embolization is only

an adjunctive procedure to tumor resection, and a lower complication rate will be required. On the other hand, given the difficulty of resecting skull base tumors, the para-para method may be viewed favorably by neurosurgeons performing tumor resections because it may reduce the risk of surgical complications,¹³ increase the resection rate,¹⁶ and improve the progression-free survival.¹⁷ Even today, surgical complications and postoperative neurologic deficits related to tumor resection are common, particularly in petroclival meningiomas, which often have feeders branching from the MHT and ILT.¹⁸ The worsening of cranial nerve deficits after tumor resection has been reported to occur in 23% to 76% of patients,¹⁸⁻²⁵ and the worsening of extremity weakness occurs in approximately 10%.^{18,26} Furthermore, even in a series in which the gross total resection rate was kept as low as 15.4% via combination with postoperative radiation therapy, as many as 16.9% of patients had severe complications due to stroke or intracranial hematoma after tumor resection.¹⁸ These reports indicate that the removal of a petroclival meningioma, which is often the subject of the para-para method, is still challenging. Tumor embolization using the para-para method should be considered as a salvage technique when direct catheterization to the MHT or ILT is difficult, after weighing the complications of tumor resection against those of the para-para method.

Limitations

This study was conducted at a single institution, and the number of cases was small. In addition, several types of surgical instruments and embolic particles were used, and the procedure was not strictly standardized because it included 3 different methods of aspiration and removal of embolic particles. Furthermore, postoperative MR images were obtained after tumor removal in many cases, raising the issue of accuracy in assessing cerebral infarction after tumor embolization. A more accurate assessment of the efficacy and risk of complications of the para-para method would require the evaluation of a larger number of patients undergoing embolization using a uniform procedure. In addition, a comparison with patients who underwent tumor removal and did not undergo embolization would be warranted for future studies to determine the efficacy of tumor embolization.

CONCLUSIONS

Tumor embolization from the MHT and ILT remains challenging and should be performed in selected cases. However, the use of the para-para method is expected to expand the indications.

ACKNOWLEDGMENTS

The authors would like to thank Editage (www.editage.com) for the English language editing.

Disclosure forms provided by the authors are available with the full text and PDF of this article at www.ajnr.org.

REFERENCES

- Adachi K, Hasegawa M, Hayakawa M, et al. **Susceptibility-weighted imaging of deep venous congestion in petroclival meningioma.** *World Neurosurg* 2019;122:e20–31 CrossRef Medline
- Adachi K, Hayakawa M, Sadato A, et al. **Modified balloon protection technique for preoperative embolization of feeder arteries from internal carotid artery branches to skull-base tumor: technical note.** *J Neurol Surg A Cent Eur Neurosurg* 2016;77:161–66 CrossRef Medline
- Akimoto T, Ohtake M, Miyake S, et al. **Preoperative tumor embolization prolongs time to recurrence of meningiomas: a retrospective propensity-matched analysis.** *J Neurointerv Surg* 2023;15:814–20 CrossRef Medline
- Hirohata M, Abe T, Morimitsu H, et al. **Preoperative selective internal carotid artery dural branch embolisation for petroclival meningiomas.** *Neuroradiology* 2003;45:656–60 CrossRef Medline
- Manelfe C, Lasjaunias P, Ruscalleda J. **Preoperative embolization of intracranial meningiomas.** *AJNR Am J Neuroradiol* 1986;7:963–72 Medline
- Okada H, Hashimoto T, Tanaka Y, et al. **Embolization of skull base meningiomas with embosphere microspheres: factors predicting treatment response and evaluation of complications.** *World Neurosurg* 2022;162:e178–86 CrossRef Medline
- Raz E, Cavalcanti DD, Sen C, et al. **Tumor embolization through meningohypophyseal and inferolateral trunks is safe and effective.** *AJNR Am J Neuroradiol* 2022;43:1142–47 CrossRef Medline
- Robinson DH, Song JK, Eskridge JM. **Embolization of meningohypophyseal and inferolateral branches of the cavernous internal carotid artery.** *AJNR Am J Neuroradiol* 1999;20:1061–67 Medline
- Rosen CL, Ammerman JM, Sekhar LN, et al. **Outcome analysis of preoperative embolization in cranial base surgery.** *Acta Neurochir (Wien)* 2002;144:1157–64 CrossRef Medline
- Waldron JS, Sughrue ME, Hetts SW, et al. **Embolization of skull base meningiomas and feeding vessels arising from the internal carotid circulation.** *Neurosurgery* 2011;68:162–69; discussion 169 CrossRef Medline
- Yoon N, Shah A, Couldwell WT, et al. **Preoperative embolization of skull base meningiomas: current indications, techniques, and pearls for complication avoidance.** *Neurosurg Focus* 2018;44:E5 CrossRef Medline
- Chen L, Li DH, Lu YH, et al. **Preoperative embolization versus direct surgery of meningiomas: a meta-analysis.** *World Neurosurg* 2019;128:62–68 CrossRef Medline
- Ilyas A, Przybylowski C, Chen CJ, et al. **Preoperative embolization of skull base meningiomas: a systematic review.** *J Clin Neurosci* 2019;59:259–64 CrossRef Medline
- Higashiguchi S, Sadato A, Nakahara I, et al. **Reduction of thromboembolic complications during the endovascular treatment of unruptured aneurysms by employing a tailored dual antiplatelet regimen using aspirin and prasugrel.** *J Neurointerv Surg* 2021;13:1044–48 CrossRef Medline
- Latchaw RE. **Preoperative intracranial meningioma embolization: technical considerations affecting the risk-to-benefit ratio.** *AJNR Am J Neuroradiol* 1993;14:583–86 Medline
- Teasdale E, Patterson J, McLellan D, et al. **Subselective preoperative embolization for meningiomas: a radiological and pathological assessment.** *J Neurosurg* 1984;60:506–11 CrossRef Medline
- Macpherson P. **The value of pre-operative embolisation of meningioma estimated subjectively and objectively.** *Neuroradiology* 1991;33:334–37 CrossRef Medline
- Nguyen MP, Morshed RA, Cheung SW, et al. **Postoperative complications and neurological deficits after petroclival region meningioma resection: a case series.** *Oper Neurosurg (Hagerstown)* 2023;25:251–59 CrossRef Medline
- Almefty R, Dunn IF, Pravdenkova S, et al. **True petroclival meningiomas: results of surgical management.** *J Neurosurg* 2014;120:40–51 CrossRef Medline
- Little KM, Friedman AH, Sampson JH, et al. **Surgical management of petroclival meningiomas: defining resection goals based on risk of neurological morbidity and tumor recurrence rates in 137 patients.** *Neurosurgery* 2005;56:546–59 CrossRef Medline

21. Lang DA, Neil-Dwyer G, Garfield J. **Outcome after complex neurosurgery: the caregiver's burden is forgotten.** *J Neurosurg* 1999;91:359–63 CrossRef Medline
22. Nanda A, Javalkar V, Banerjee AD. **Petroclival meningiomas: study on outcomes, complications and recurrence rates.** *J Neurosurg* 2011;114:1268–77 CrossRef Medline
23. Wagner A, Alraun M, Kahlig V, et al. **Surgical and functional outcome after resection of 64 petroclival meningiomas.** *Cancers (Basel)* 2022;14:4517 CrossRef Medline
24. Xu F, Karamelas I, Megerian CA, et al. **Petroclival meningiomas: an update on surgical approaches, decision making, and treatment results.** *Neurosurg Focus* 2013;35:E11 CrossRef Medline
25. Erkmen K, Pravdenkova S, Al-Mefty O. **Surgical management of petroclival meningiomas: factors determining the choice of approach.** *Neurosurg Focus* 2005;19:E7 CrossRef Medline
26. Diluna ML, Bulsara KR. **Surgery for petroclival meningiomas: a comprehensive review of outcomes in the skull base surgery era.** *Skull Base* 2010;20:337–42 CrossRef Medline

Imaging Features of Primary Intracranial Sarcoma with *DICER1* Mutation: A Multicenter Case Series

 Rami W. Eldaya,  Richard J. Fagan,  Samir A. Dagher, Angshumoy Roy,  Sonika Dahyia,  Gregory N. Fuller,  Max Wintermark,  Matthew S. Parsons, and  Thierry A.G.M. Huisman



ABSTRACT

SUMMARY: Primary intracranial sarcoma, *DICER1*-mutant, is a rare, recently described entity in the fifth edition of the WHO Classification of CNS Tumors. Given the entity's rarity and recent description, imaging data on primary intracranial sarcoma, *DICER1*-mutant, remains scarce. In this multicenter case series, we present detailed multimodality imaging features of primary intracranial sarcoma, *DICER1*-mutant, with emphasis on the appearance of the entity on MR imaging. In total, 8 patients were included. In all 8 patients, the lesion demonstrated blood products on T1WI. In 7 patients, susceptibility-weighted imaging was obtained and demonstrated blood products. Primary intracranial sarcoma, *DICER1*-mutant, is a CNS neoplasm that primarily affects pediatric and young adult patients. In the present case series, we explore potential imaging findings that are helpful in suggesting this diagnosis. In younger patients, the presence of a cortical lesion with intralesional blood products on SWI and T1-weighted MR imaging, with or without extra-axial blood products, should prompt the inclusion of this entity in the differential diagnosis.

ABBREVIATIONS: ASL = arterial spin-labeling; DCE = dynamic contrast enhancement; SDH = subdural hematoma

The WHO Classification of CNS Tumors continues to evolve with the ever-expanding discovery of tumor molecular markers that have a direct impact on our understanding of tumor biology, precise classification, treatment options, prognosis, and outcome. The fifth edition of the WHO Classification of CNS Tumors, published in 2021, reflects new advances in the molecular diagnosis of CNS neoplasms and further builds on the updates of the revised fourth edition, published in 2016, and the recommendations of the Consortium to Inform Molecular and Practical Approaches to CNS Tumor Taxonomy (cIMPACT-NOW).¹⁻⁹

The fifth edition of the WHO Classification introduces 22 new tumor types.¹ One of these entities, under the umbrella of mesenchymal nonmeningothelial tumors, is primary intracranial sarcoma, *DICER1*-mutant,¹ which is a rare highly malignant entity that can be associated with familial *DICER1* syndrome and neurofibromatosis type 1.¹⁰⁻¹² Given the entity's rarity and recent

description, imaging data on primary intracranial sarcoma, *DICER1*-mutant, remain scarce. The few published case reports and series describing the entity have alluded to its imaging features; however, detailed imaging descriptions that include larger patient series remain lacking, and the emphasis of the literature has been on molecular diagnosis and treatment options.¹²⁻¹⁶

In this multicenter case series, we aim to present detailed multimodality imaging features, including both anatomic and advanced imaging characteristics of primary intracranial sarcoma, *DICER1*-mutant, with emphasis on the appearance of the entity on MR imaging with an attempt to elucidate imaging characteristics that can help in suggesting the diagnosis.

CASE SERIES

Methods

This retrospective study was approved by the Institutional Review Board at The University of Texas MD Anderson Cancer Center as a collaborative, multi-institutional study.

Patient Selection and Clinical Data. From January 2015 to October 2023, a total of 8 consecutive patients with a diagnosis of primary intracranial sarcoma with *DICER1* mutation were identified (Table 1), as follows: 3 patients diagnosed at the MD Anderson Cancer Center, 3 patients diagnosed at the Texas Children's Hospital, and 2 patients diagnosed at the Washington University School of Medicine in St Louis. Assessments of the pathology, clinical, and imaging data were then performed to assess

Received November 16, 2023; accepted after revision January 12, 2024.

From the Departments of Neuroradiology (R.W.E., S.A.D., G.N.F., M.W.), and Anatomical Pathology (G.N.F.), The University of Texas MD Anderson Cancer Center, Houston, Texas; Departments of Radiology (R.J.F., T.A.G.M.H.), and Pathology & Immunology (A.R.), Baylor College of Medicine, Houston, Texas; Department of Pathology (A.R.), and Edward B. Singleton Department of Radiology (T.A.G.M.H.), Texas Children's Hospital, Houston, Texas; Department of Pathology and Immunology (S.D.), and Mallinckrodt Institute of Radiology (M.S.P.), Washington University School of Medicine, St Louis, Missouri.

Please address correspondence to Rami Eldaya, MD, MBA, Assistant Professor, Neuroradiology, Diagnostic Imaging, MD Anderson Cancer Center, 1400 Pressler St, Unit 1482, FCT16.5072, Houston, Texas; e-mail: reldaya@mdanderson.org

<http://dx.doi.org/10.3174/ajnr.A8192>

Table 1: Demographic characteristics of patients with primary intracranial sarcoma, *DICER1*-mutant, included in this case series

Demographic Characteristic (Number Assessed)	Finding
Age (8)	Mean: 16 years Standard deviation: 11.57 years Range: 4–33
Presenting symptoms (7)	Headaches: 5 Extremity weakness: 2 Nausea: 2 Numbness: 2 Language deficit: 1 Blurry vision: 1 Unsteady gait: 1
Duration of symptoms (5)	Average: 7 days Range: 1–14 days
<i>DICER1</i> mutation (8)	Yes
Additional mutations	<i>ATRX</i> 5/5 patients <i>TP53</i> 7/7 patients
Other <i>DICER1</i> -related tumors (7)	None

the following inclusion criteria: all patients have tissue-based diagnosis confirmation at the above study institutions per described guidelines, including DNA methylation profiling and/or sequencing; all patients have clinical and demographic data available for extraction via each institution’s electronic medical record system; and all patients have, at a minimum, multisequence pretreatment MR imaging available for assessment.

Clinical and Pathologic Data Review. The following clinical data were collected from each patient’s electronic medical record: age, sex, presenting symptoms, duration of symptoms, and, when available, the presence of any hereditary cancer syndrome associated with additional extracranial malignancies, such as neurofibromatosis or *DICER1* syndrome.

The following data were extracted from each patient’s Pathology Report: confirmation of *DICER1* mutation and the presence of any other clinically relevant molecular alterations, such as a *TP53* mutation.

Imaging Data Review. All imaging characteristics were collected as a consensus, and scans were assessed by either a neuroradiology fellowship-trained radiologist (R.W.E., with 5 years of neuroradiology experience, reviewed the MD Anderson Cancer Center cases; M.S.P., with 17 years of neuroradiology experience, reviewed the Washington University School of Medicine in St Louis cases) or a pediatric neuroradiology fellowship-trained radiologist (T.A.G.M.H., with 32 years of neuroradiology experience, reviewed the Texas Children’s Hospital cases).

Patient imaging was reviewed on the participating institutions’ PACS. If a CT was available, the following features were assessed: presence of blood products within the tumor and presence of extra-axial blood products, including subdural hematoma (SDH) and SAH. The patients’ MR imaging was assessed for the following features: size of tumor in 3 dimensions; location of the tumor, including side and distribution as well as deep versus superficial; appearance on blood-sensitive sequences (T2* or SWI); appearance on DWI; presence of tumoral blood products on

T1WI; and presence of SDH or SAH. In addition, the tumor was characterized based on its macroscopic imaging morphology as either solid/mostly solid (if more than 90% solid), cystic (if more than 90% cystic), or mixed (if in between a solid/cystic mixture). Tumor enhancement was recorded as present or absent and then further assessed, if present, for pattern type (solid homogeneous, peripheral, patchy/ill-defined, or mixed) and extent (>75%, <25%, or in between). If advanced imaging was performed, an analysis of PWI and ¹H-MR spectroscopy was conducted, and the results were recorded. The type of perfusion technique was noted as DSC, dynamic contrast enhancement (DCE), and/or arterial spin-labeling (ASL), and perfusion maps were generated, thereby allowing for the determination of whether perfusion was altered relative to a normal-appearing brain (eg, elevated). If ¹H-MR spectroscopy was performed, a note was made of the type (single versus multi voxel tissue sampling), and a peak analysis was performed, including an assessment of the absolute peak values and ratios. Finally, a general pattern of imaging was extracted and summarized for an assessment of potentially helpful imaging markers in suggesting the diagnosis.

Results

Patient Characteristics. Table 1 summarizes the demographics and clinical characteristics. The average age at diagnosis was 16 years (range, 4–33 years). Five patients were 10 years or younger at diagnosis. Seven patients had presenting symptoms available for assessment, with headaches being the most common presenting symptom. In 5 patients, the duration of symptoms was known. Two patients had a subacute duration of symptoms for 2 weeks. Three patients presented acutely with durations of symptoms ranging from 1 day (2 patients) to 5 days (1 patient).

Pathology Characteristics. All 8 patients had a surgical resection or biopsy with the sequencing of the sampled tissue demonstrating a *DICER1* mutation. Additional commonly identified mutated genes included *ATRX* and *TP53* (Table 1).

Imaging Characteristics. Table 2 summarizes the imaging characteristics.

Seven patients had cortical/subcortical lesions, and 1 patient had a hypothalamic mass. Four patients had a right hemisphere cortical lesion. The parietal lobe was the most involved lobe, with 4 patients. One patient had multifocal disease isolated to the right frontal lobe. The average anteroposterior dimension of the lesions was 4.25 cm (SD, 2.76). The average transverse dimension was 3.79 cm (SD, 2.08). The average craniocaudal dimension was 4.37 cm (SD, 2.51). Five lesions were solid or mostly solid (>90% solid), and 3 lesions were mixed solid and cystic.

NCCT Imaging Findings. Three patients presented acutely and had NCCT that demonstrated hyperattenuated blood products within the lesion, which is suggestive of an acute/recent bleeding episode (Fig 1). One patient had an associated hyperattenuated subdural hematoma, and another patient had a hyperattenuated subarachnoid hemorrhage. The third patient had subarachnoid blood products diagnosed on MR imaging.

Table 2: MR imaging characteristics of patients with primary intracranial sarcoma, *DICER1*-mutant

MR Imaging Characteristic	Finding
Size (cm)	Anteroposterior dimension, 4.25 cm (SD, 2.76) Transverse dimension, 3.79 cm (SD, 2.08) Craniocaudal dimension, 4.37 cm (SD, 2.5)
Location	
Side	4 right, 3 left
Cortical/deep	7 cortical/subcortical, 1 hypothalamic
Cortical lobe	4 parietal, 2 frontal, 1 temporal/insula
Hemorrhage	
Tumor	7/7 hemorrhage on SWI 8/8 hemorrhage of T1WI
Extra-axial	2 SDH 2 SAH
Diffusion restriction	3 patients
Enhancement	
Presence	8/8 present
Pattern	5 solid homogeneous, 2 heterogeneous, 1 peripheral
Extent	5 > 75% enhancement; 2, 25%–75%; 1 < 25%



FIG 1. A 28-year-old patient presenting acutely with headaches over a 1-day period. Axial NCCT demonstrates acute hemorrhage within the right frontal lobe lesion (*black arrow*) with overlying right frontal convexity subdural hematoma (*white arrows*). CT also shows secondary leftward midline shift and regional mass effect.

MR Imaging Findings. Seven patients had a SWI sequence available for assessment. In all 7 patients, the lesion demonstrated susceptibility-related signal loss secondary to blood products. All 8 patients had T1WI available for assessment, and in all 8 patients, the lesion demonstrated blood products on T1WI. Three patients had an ADC value of less than $1 \times 10^{-3} \text{ mm}^2/\text{s}$. Diffusion restriction was in part explained by the blood products but was also

noted in the solid enhancing component and the solid nonenhancing component (Figs 2 and 5). The remaining patients did not demonstrate diffusion restriction. The solid component of the lesions demonstrated enhancement in all 8 patients. In 5 patients, the solid component demonstrated homogeneous enhancement; in 2 patients, the solid component enhancement was heterogeneous; and in 1 patient there was peripheral enhancement and central hemorrhage. In 5 patients, more than 75% of the solid component enhanced; in 2 patients, 25%–75% of the solid component enhanced; and only 1 patient had less than 25% enhancement of the solid component.

Four patients presented with accompanying extra-axial hemorrhage on initial MR imaging. Two patients had a subdural hematoma, and 2 patients had subarachnoid hemorrhage (Figs 2–5).

Advanced imaging was not frequently present on preoperative MR imaging examinations. One patient had ^1H -MR at both short TE (35 ms) and intermediate TE (135 ms), with elevated choline, decreased *N*-acetylaspartate, and the presence of a lactate peak on both echo times. One patient had PWI on preoperative MR imaging that demonstrated elevated relative cerebral blood volume.

In summary, imaging demonstrated cortical/subcortical lesions in most patients, with the lesions demonstrating blood products on both SWI and T1WI sequences. Accompanying extra-axial blood products were present in 50% of cases.

DISCUSSION

Intracranial sarcomas are rare, with less than 0.5% of sarcomas occurring in the CNS, making their diagnosis challenging.^{16,17} Furthermore, intracranial sarcomas typically occur in older populations and rarely affect children, with primary intracranial sarcoma, *DICER1*-mutant, being an exception.^{18,19} In addition, the tissue diagnosis of primary intracranial sarcoma, *DICER1*-mutant, based exclusively on the microscopic evaluation of H&E and immunostained sections, can be challenging, given the morphologic overlap with those of the more frequently occurring high-grade primary CNS tumors, such as gliosarcoma. However, the identification of *DICER1*-mutant CNS sarcoma-associated distinctive features, such as prominent eosinophilic cytoplasmic globules, florid microvascular proliferation in a checkerboard pattern at the tumor/brain interface, focal cartilage nodules, patchy expression of muscle differentiation immunophenotypic markers (desmin, myogenin), loss of the H3 K28 (K27) trimethylation mark (H3 K28me3), and stabilized overexpression of the nuclear p53 protein, greatly increase the index of suspicion.^{11,12,20} Definitive diagnosis is provided via next generation sequencing or tumor genetic profiling.^{11,13,16} A combination of these factors often results in the misdiagnosis or delayed diagnosis of primary intracranial sarcoma, *DICER1*-mutant. Imaging data are scarce and mostly limited to case reports and small series; thus the role of imaging in the initial diagnosis of the entity at the time of clinical presentation remains challenging, and further investigation is needed.²¹

In this case series, we detail the imaging findings of 8 patients with tissue analysis-confirmed primary intracranial sarcoma, *DICER1*-mutant. First, all tumors presented as supratentorial/cortical lesions. This observation comports with reported data indicating a strong predilection for supratentorial sites, which has been documented in 92% of reported cases.^{16,20–22} The cortical/subcortical

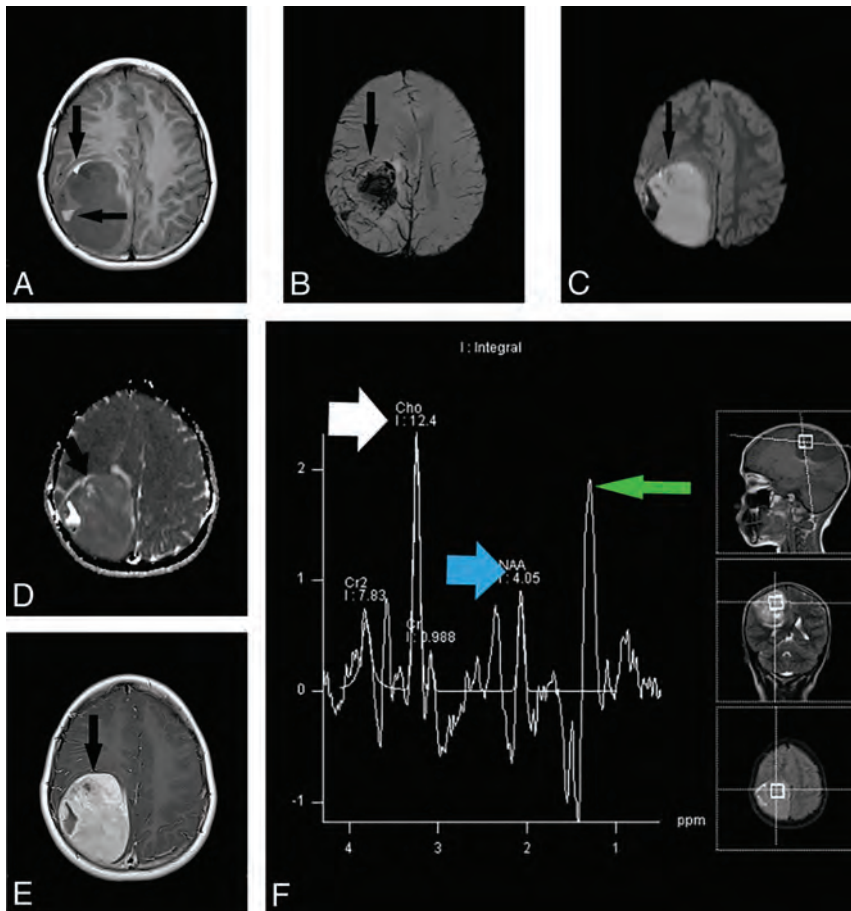


FIG 2. A 10-year-old patient presenting with headaches for 14 days. *A*, Axial precontrast T1 3D MPRAGE demonstrates right superior parietal lobe cortical/subcortical lesion with intrinsic T1 hyperintensity reflective of internal blood products along its anterior and lateral aspects (arrows). *B*, SWI sequence demonstrates loss of signal within the lesion, reflective of lesion blood products (arrow). *C* and *D*, DWI and ADC sequences demonstrate diffusion restriction within the lesion that is corresponding to both the solid enhancing component and blood products noted on postcontrast and SWI sequences. *E*, Axial postcontrast T1 MPRAGE demonstrates homogeneous enhancement of the non hemorrhagic component (arrow). *F*, Single voxel short TE (35 ms) ¹H-MRS demonstrates an elevated choline peak (white arrow), decreased N-acetyl aspartate peak (blue arrow), and elevated lactate peak (green arrow).

location noted in the present case series is consistent with reported data of cortical predilection.^{16,21} In 1 patient in the present series, the tumor arose in the hypothalamus, which, to our knowledge, has not been previously reported. There have been reports of cases arising in the pineal and infratentorial regions, which, together with our case, document the rare occurrence of primary intracranial sarcoma, *DICER1*-mutant, in noncortical locations.^{16,23}

An interesting observation noted in all patients in our case series was the presence of blood products within the lesion on multiple sequences; in all patients, blood products were noted on both SWI and T1WI. The presence of blood products on T1WI suggested frank hemorrhage within the lesions. This finding serves as a potential imaging phenotypical marker for raising the possibility of primary intracranial sarcoma, *DICER1* mutant, in the imaging differential diagnosis. In addition, 50% of patients presented with associated extra-axial blood products (2 patients with SDH, and 2 with SAH), further suggesting the vascular/hemorrhagic nature of these tumors with their increased propensity to bleed and present urgently with acute neurologic symptoms. This was further supported by the fact that 3 patients presented acutely with NCCT demonstrating acute lesion hemorrhage with/without associated acute extra-axial blood products. This possibly explains the relatively short period of symptoms noted

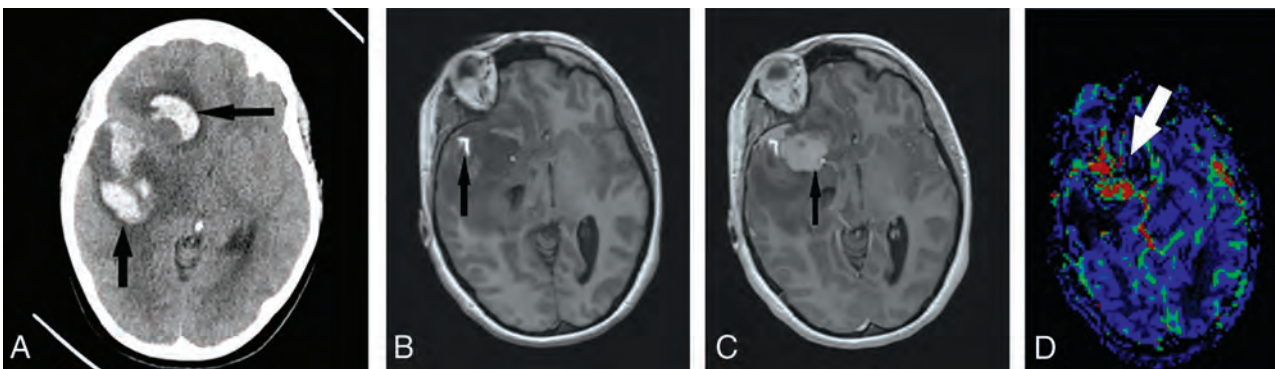


FIG 3. A 33-year-old patient presenting with 5-day history of worsening headaches with a rapid decrease in mentation. *A*, NCCT at the time of presentation demonstrates a large parenchymal hemorrhage involving the right frontal and temporal lobes with associated regional mass effect, leftward midline shift, and right ventricle effacement. *B*, Axial pre contrast T1 MPRAGE demonstrates areas of intrinsic T1 hyperintensity within the right temporal/insular lesion reflective of internal blood products (arrow). *C*, Axial postcontrast T1 MPRAGE demonstrates the homogeneous enhancement of the solid component (arrow). *D*, Dynamic susceptibility contrast relative cerebral blood volume color map demonstrating elevated relative cerebral blood volume within the enhancing component (arrow).

in all 5 patients with a known symptomatic duration of an average of 7 days from onset to presentation. The hemorrhagic nature of the lesion has been described in the pathologic assessment of tumor samples and in a few case reports and case series.^{10,12,13,16,21} However, the associated extra-axial hemorrhages have not been described before, and the relative frequency of hemorrhage of the lesion has not been assessed. The combination of these 2 imaging characteristics can serve as a potential clue for suggesting the diagnosis in pediatric patients and young adults.

Finally, the tumors demonstrate a variable degree of solid and cystic components as well as corresponding patterns of enhancement

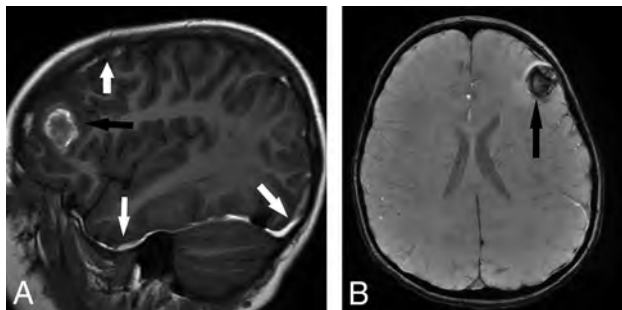


FIG 4. A 5-year-old presenting with headaches for 14 days. A, Sagittal precontrast T1 3D MPRAGE demonstrates a left frontal cortical/subcortical T1 intrinsically hyperintense mass that is reflective of internal blood products within the lesion (black arrow). Patient also has a left hemispheric thin subdural hematoma (white arrows). B, SWI sequence demonstrates a loss of signal within the lesion that is reflective of blood products (black arrow).

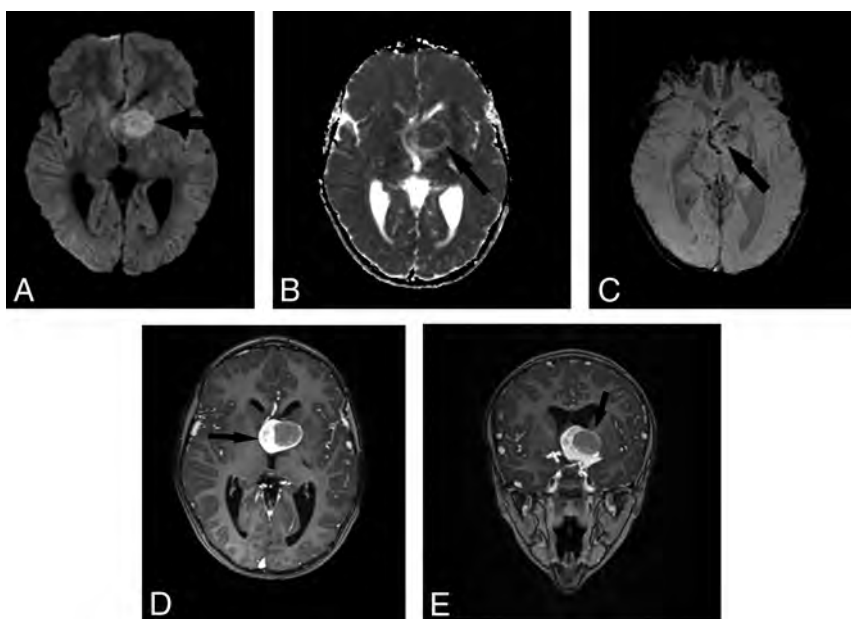


FIG 5. An 8-year-old patient with hypothalamic primary intracranial sarcoma, *DICER1*-mutant. A and B, DWI and ADC map demonstrating diffusion restriction of the left hypothalamic lesion nonenhancing component. This is partially explained by the blood products noted on SWI and the cellularity of the nonenhancing component. C, SWI sequence demonstrates a loss of signal within the lesion that is suggestive of blood products (arrow). D, Axial postcontrast T1 MPRAGE demonstrates a mixed enhancing and nonenhancing lesion with homogeneous enhancement of the solid component (arrow). E, Coronal postcontrast T1 MPRAGE demonstrates a mixed enhancing and nonenhancing lesion with homogeneous enhancement of the solid component (arrow).

and diffusion restriction. However, in most cases, most of the solid component showed solid homogeneous enhancement.

In summary, primary intracranial sarcoma, *DICER1*-mutant, typically presents as a cortical/subcortical lesion with tumoral blood products and occasionally with extra-axial blood products in younger patients. The presence of these imaging findings should suggest the entity as a possible diagnosis.

Limitations include the retrospective nature of the study as well as the small sample size. However, relative to prior reports, this is the largest dedicated study assessing the imaging features of primary intracranial sarcoma, *DICER1*-mutant. Given the rarity of primary intracranial sarcoma, *DICER1*-mutant, a large data set is difficult to achieve. Last, few patients have had an advanced tumor imaging assessment, with only 1 patient having MR spectroscopy data and 1 patient having perfusion data. However, the findings of this case series serve as a promising tool for larger, multicenter studies in the future that specifically aim to assess the imaging findings of primary intracranial sarcoma, *DICER1*-mutant. Furthermore, these imaging findings can serve as extractable features for machine learning models to aid in the diagnosis and prognosis of this entity.

CONCLUSIONS

Primary intracranial sarcoma, *DICER1*-mutant, is a rare, recently described CNS neoplasm that primarily affects pediatric and young adult patients. Detailed, dedicated imaging characterization of the entity is currently lacking in the radiology literature, and the few data that are available are primarily drawn from single case reports.

In the present case series, we explore potential imaging findings that are helpful in suggesting this diagnosis. The presence of a cortical lesion with intraleisional blood products on SWI and T1-weighted MR imaging, with or without extra-axial blood products, in younger patients should prompt the inclusion of this entity in the differential diagnosis.

Disclosure forms provided by the authors are available with the full text and PDF of this article at www.ajnr.org.

REFERENCES

1. WHO Classification of Tumours Editorial Board. *Central Nervous System Tumors*. 5th ed. International Agency for Research on Cancer 2022 (beta online version).
2. WHO Classification of Tumours Editorial Board. *Genetic Tumour Syndromes*. 5th ed. International Agency for Research on Cancer 2021.
3. Louis DN, Aldape K, Brat DJ, et al. **cIMPACT-NOW (the Consortium to Inform Molecular and Practical Approaches to CNS Tumor Taxonomy): A new initiative in advancing nervous system tumor classification.** *Brain Pathol* 2017;27:851–52 CrossRef Medline

4. Louis DN, Aldape K, Brat DJ, et al. **Announcing cIMPACT-NOW: the Consortium to Inform Molecular and Practical Approaches to CNS Tumor Taxonomy.** *Acta Neuropathol* 2017;133:1–3 CrossRef Medline
5. Louis DN, Giannini C, Capper D, et al. **cIMPACT-NOW update 2: Diagnostic clarifications for diffuse midline glioma, H3 K27M-mutant and diffuse astrocytoma/anaplastic astrocytoma, IDH-mutant.** *Acta Neuropathol* 2018;135:639–42 CrossRef Medline
6. Ellison DW, Hawkins C, Jones DTW, et al. **cIMPACT-NOW update 4: Diffuse gliomas characterized by MYB, MYBL1, or FGFR1 alterations or BRAFV600E mutation.** *Acta Neuropathol* 2019;137:683–87 CrossRef Medline
7. Brat DJ, Aldape K, Colman H, et al. **cIMPACT-NOW update 3: Recommended diagnostic criteria for “Diffuse astrocytic glioma, IDH-wildtype, with molecular features of glioblastoma, WHO grade IV”.** *Acta Neuropathol* 2018;136:805–10 CrossRef Medline
8. Louis DN, Ellison DW, Brat DJ, et al. **cIMPACT-NOW: A practical summary of diagnostic points from Round 1 updates.** *Brain Pathol* 2019;29:469–72 CrossRef Medline
9. Louis DN, Wesseling P, Aldape K, et al. **cIMPACT-NOW update 6: New entity and diagnostic principle recommendations of the cIMPACT-Utrecht meeting on future CNS tumor classification and grading.** *Brain Pathol* 2020;30:844–56 CrossRef Medline
10. Rigsby RK, Brahmabhatt P, Desai AB, et al. **Newly recognized CNS tumors in the 2021 World Health Organization Classification: Imaging overview with histopathologic and genetic correlation.** *AJNR Am J Neuroradiol* 2023;44:367–80 CrossRef Medline
11. Kamihara J, Paulson V, Breen MA, et al. **DICER1-associated central nervous system sarcoma in children: comprehensive clinicopathologic and genetic analysis of a newly described rare tumor.** *Mod Pathol* 2020;33:1910–21 CrossRef Medline
12. Lee JC, Villanueva-Meyer JE, Ferris SP, et al. **Primary intracranial sarcomas with DICER1 mutation often contain prominent eosinophilic cytoplasmic globules and can occur in the setting of neurofibromatosis type 1.** *Acta Neuropathol* 2019;137:521–25 CrossRef Medline
13. Marinelli A, Cuomo M, Franca RA, et al. **A rare adult primary intracranial sarcoma, DICER1-mutant identified by epigenomic profiling: A case report.** *Brain Sci* 2023;13:235 CrossRef
14. Sakaguchi M, Nakano Y, Honda-Kitahara M, et al. **Two cases of primary supratentorial intracranial rhabdomyosarcoma with DICER1 mutation which may belong to a “spindle cell sarcoma with rhabdomyosarcoma-like feature, DICER1 mutant.** *Brain Tumor Pathol* 2021;4:174–182
15. Nejo T, Takayanagi S, Tanaka S, et al. **Primary intracranial spindle cell sarcoma, DICER1-mutant, with MDM2 amplification diagnosed on the basis of extensive molecular profiling.** *Clin Med Insights Case Rep* 2022;15: CrossRef Medline
16. Diaz Coronado RY, Mynarek M, Koelsche C, et al. **Primary central nervous system sarcoma with DICER1 mutation-treatment results of a novel molecular entity in pediatric Peruvian patients.** *Cancer* 2022;128:697–707 CrossRef Medline
17. Merimsky O, Lepechoux C, Terrier P, et al. **Primary sarcomas of the central nervous system.** *Oncology* 2000;58:210–14 CrossRef Medline
18. Zhang G, Xiao B, Huang H, et al. **Intracranial synovial sarcoma: a clinical, radiological and pathological study of 16 cases.** *Eur J Surg Oncol* 2019;45:2379–85 CrossRef Medline
19. Ripperger T, Bielack SS, Borkhardt A, et al. **Childhood cancer predisposition syndromes-A concise review and recommendations by the Cancer Predisposition Working Group of the Society for Pediatric Oncology and Hematology.** *Am J Med Genet A* 2017;173:1017–37 CrossRef Medline
20. Alexandrescu S, Meredith DM, Lidov HG, et al. **Loss of histone H3 trimethylation on lysine 27 and nuclear expression of transducin-like enhancer 1 in primary intracranial sarcoma, DICER1-mutant.** *Histopathology* 2021;78:265–75 CrossRef Medline
21. Tauziède-Espariat A, Hasty L, Métais A, et al. **Mesenchymal non-meningothelial tumors of the central nervous system: a literature review and diagnostic update of novelties and emerging entities.** *Acta Neuropathol Commun* 2023;11:22 CrossRef Medline
22. Cardona AF, Chamorro Ortiz DF, Ruíz-Patiño A, et al. **DICER1-associated central nervous system sarcoma: A comprehensive clinical and genomic characterization of case series of young adult patients.** *Neurooncol Pract* 2023;10:381–90 CrossRef Medline
23. Wolf T, Coca AH, Weingertner N, et al. **All pineal tumors expressing germ cell tumor markers are not necessarily germ cell tumors: histopathological and molecular study of a midline primary intracranial sarcoma DICER1-mutant.** *Virchows Arch* 2023;482:431–35 CrossRef Medline

Clinical Arterial Spin-Labeling MR Imaging to Screen for Typical and Atypical Neurodegenerative Disease in the New Era of Alzheimer Treatment

Kevin Lee, Meem Mahmud, Darby Marx, Weiye Yasen, Omna Sharma, Jana Ivanidze, Elcin Zan, Liangdong Zhou, Yi Li, Mony J. de Leon, Anna S. Nordvig, and Gloria C. Chiang



ABSTRACT

SUMMARY: The clinical standard of care in the diagnosis of neurodegenerative diseases relies on [¹⁸F] FDG-PET/CT or PET MR imaging. Limitations of FDG-PET include cost, the need for IV access, radiation exposure, and availability. Arterial spin-labeling MR imaging has been shown in research settings to be useful as a proxy for FDG-PET in differentiating Alzheimer disease from fronto-temporal dementia. However, it is not yet widely used in clinical practice, except in cerebrovascular disease. Here, we present 7 patients, imaged with our routine clinical protocol with diverse presentations of Alzheimer disease and other neurodegenerative diseases, in whom arterial spin-labeling–derived reduced CBF correlated with hypometabolism or amyloid/tau deposition on PET. Our case series illustrates the clinical diagnostic utility of arterial spin-labeling MR imaging as a fast, accessible, and noncontrast screening tool for neurodegenerative disease. Arterial spin-labeling MR imaging can guide patient selection for subsequent PET or fluid biomarker work-up, as well as for possible therapy with anti-amyloid monoclonal antibodies.

ABBREVIATIONS: AD = Alzheimer disease; ADLs = activities of daily living; ASL = arterial spin-labeling; CI = cognitive impairment; COVID-19 = coronavirus 2019; IvPPA = logopenic variant progressive aphasia; MCI = mild cognitive impairment; MoCA = Montreal Cognitive Assessment; PCA = posterior cortical atrophy

Neurodegenerative disease, of which Alzheimer disease (AD) is the most common, is the leading cause of dementia and manifests as progressive cognitive impairment (CI) along with a variety of other neurologic symptoms.¹ Standard-of-care MR imaging can exclude potentially treatable, structural causes of CI and can identify atrophy but lacks sensitivity and specificity. In the era of anti-amyloid monoclonal antibody therapy for AD, identifying reliable and easily accessible diagnostic tools for neurodegenerative disease is of paramount importance.

FDG-PET is routinely used clinically to differentiate AD from other neurodegenerative diseases.¹ Recently, the Centers for Medicare and Medicaid Services decreased the restrictions on the

coverage of amyloid PET, providing more access to patients seeking anti-amyloid therapies.² However, both FDG and amyloid PET scans are costly, requiring IV access for radiotracer administration, radiation exposure, and proximity to a PET facility.

Arterial spin-labeling MR imaging (ASL-MR) is a noncontrast MR imaging technique that uses endogenous water in arterial blood for a qualitative and quantitative assessment of CBF.³ Its utility as a surrogate measure of neuronal activity and metabolism on FDG-PET has been described in AD research settings, particularly at the group level;⁴ however, it has thus far not been demonstrated in clinical practice.

We present 7 cases of neurodegenerative disease (6 with forms of AD) in which a clinical MR imaging protocol to evaluate cognitive impairment that included a 4.5-minute ASL MR image was effective at predicting findings on subsequent PET, even when structural imaging was not revealing. Full informed consent was obtained from all patients. We propose that ASL-MR could be a cost-effective AD screening and longitudinal follow-up tool.

CASE SERIES

Case 1: Early-Onset AD with Presenilin Mutation

A 57-year-old postmenopausal woman with a history of thyroid cancer and hyperlipidemia presented with slowly progressive short-term memory loss for 10–15 years, as well as anxiety and fatigue for 1–2 years. She was independent in activities of daily living (ADLs). Her father and 3 paternal siblings had onset of dementia at ages 50–60

Received November 8, 2023; accepted after revision January 3, 2024.

From the Weill Cornell Medical College (K.L., D.M., W.Y.), New York, New York; Department of Radiology (L.Z., Y.L., M.J.d.L., G.C.C.), Brain Health Imaging Institute, Department of Molecular Imaging and Therapeutics (J.I., E.Z.), and Department of Neurology (M.M., A.S.N.), Alzheimer's Disease and Memory Disorders Program, Weill Cornell Medicine, New York-Presbyterian Hospital, New York, New York; and Weill Cornell Medicine (O.S.), Qatar Foundation, Education City, Doha, Qatar.

G.C. Chiang and A.S. Nordvig contributed equally to this article.

This work was supported by National Institute of Neurological Disorders and Stroke NeuroNEXT Fellowship Award 5U24NS107168, National Institutes of Health/National Institute on Aging R01 AG068398, National Institutes of Health/National Institute on Aging R01 AG080011.

Please address correspondence to Kevin Lee, BS, c/o Gloria Chiang 525 E 68th St, Box 141, Starr 6 New York, NY 10065; e-mail: kel4009@med.cornell.edu; @GloriaChiangMD; @AnnaNordvig; @Kevin_Lee097



Indicates article with online supplemental data.

<http://dx.doi.org/10.3174/ajnr.A8164>

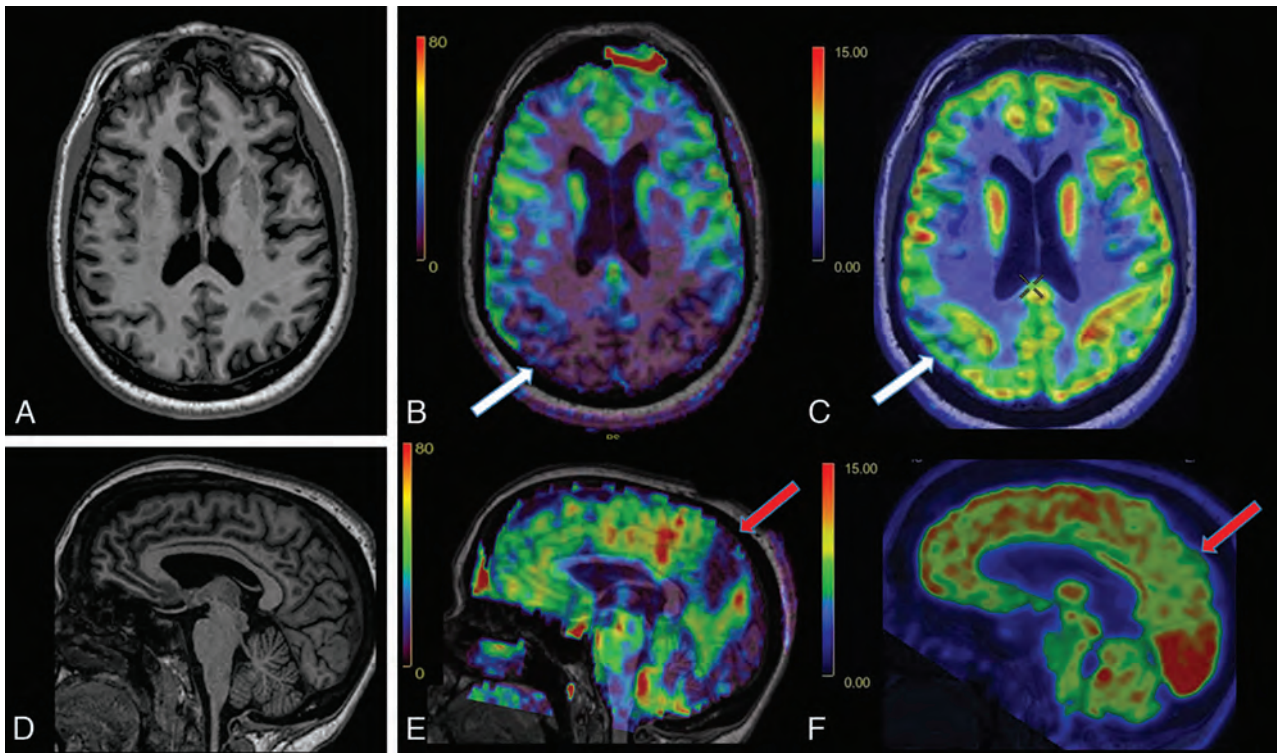


FIG 1. Early-onset AD with *presenilin* mutation. *A*, Axial 3D T1 MPRAGE image shows mild generalized volume loss. Axial CBF image (*B*) and axial FDG-PET image (*C*) show more pronounced decreased CBF than FDG avidity in the bilateral parietal lobes, particularly on the right (*white arrow*), and temporal lobes (not pictured), suggestive of AD. *D*, Sagittal 3D T1 MPRAGE image shows nonspecific volume loss. Sagittal CBF image (*E*) and sagittal FDG-PET image (*F*) show decreased CBF and FDG avidity in the precuneus (*red arrow*).

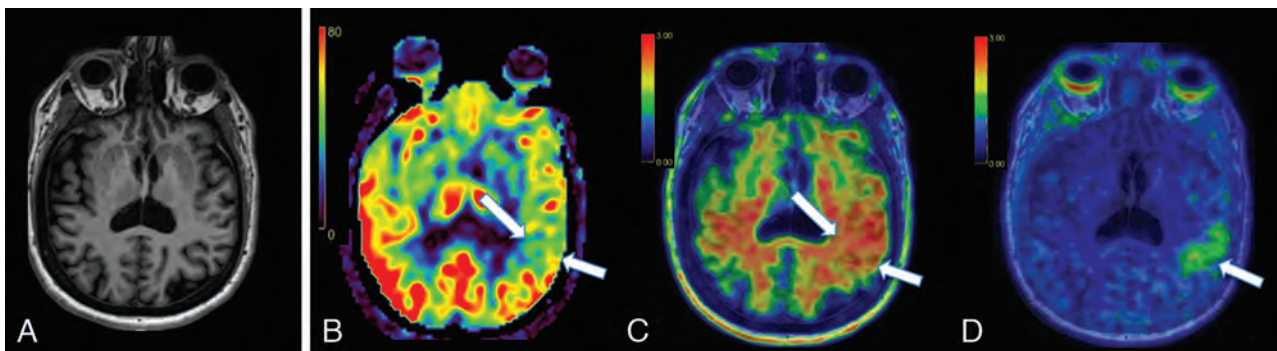


FIG 2. Early-onset AD and post-COVID brain fog. *A*, Axial 3D T1 MPRAGE image shows mild volume loss, more prominent in the left hemisphere. *B*, Axial CBF image shows asymmetrically decreased CBF in the left temporoparietal junction (*white arrows*). *C*, Axial [¹⁸F] florbetaben PET image shows asymmetric cortical deposition of β -amyloid (*white arrows*). *D*, Axial [¹⁸F]-MK6240 tau PET shows focal cortical deposition of tau (*white arrows*), corresponding to the area of lowest CBF noted in *B* and β -amyloid deposition in *C*.

years. Two siblings were cognitively healthy. Neurologic assessment showed mild cognitive impairment (MCI), a Montreal Cognitive Assessment (MoCA) score of 16/30, and mild parietal drift. Serum labs were noncontributory. Structural MR imaging showed nonspecific mild volume loss. ASL-MR showed decreased bilateral temporoparietal CBF, including in the precuneus (Fig 1 and Online Supplemental Data); FDG-PET corresponded to these findings (Fig 1 and Online Supplemental Data). Amyloid PET revealed diffuse cortical amyloid deposition (Online Supplemental Data). Genetic testing revealed a heterozygous *PSEN1* mutation (c.617G>C hereditary autosomal dominant AD). The patient has been prescribed lecanemab.

Case 2: Early-Onset AD and Long COVID Brain Fog

A 53-year-old woman with pre-existing hypertension and seronegative presumed rheumatologic disease presented with “brain fog,” insomnia, orthostasis, and headaches after mild coronavirus 2019 (COVID-19) infection. Following a COVID-19 vaccination, she developed Bell palsy and peripheral herpes simplex virus reactivation. She had previously worked full-time in a cognitively demanding position. Maternal family history was positive for AD onset around the age of 60. She had a MoCA score of 29/30, a Mini-Mental State Examination score of 30/30, and facial nerve findings of Bell palsy. The initial clinical diagnosis was post-COVID MCI, with worsened rheumatologic disease. However,

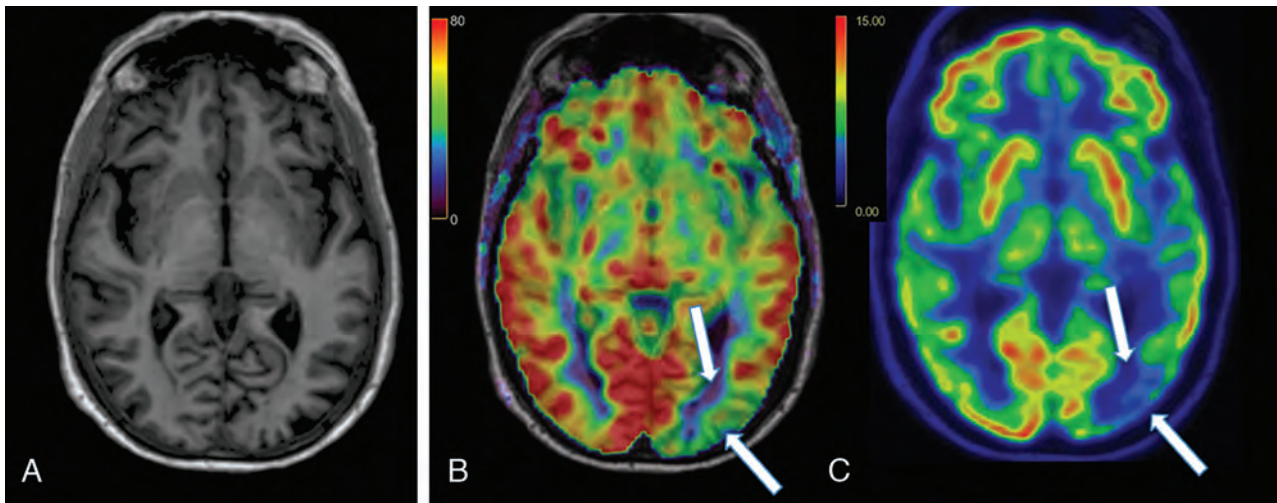


FIG 3. PCA, the “visual variant” of AD. *A*, Axial 3D T1 MPRAGE image demonstrates mild left occipital lobe atrophy. *B*, Axial CBF image shows asymmetrically decreased CBF in the left occipital lobe (*white arrows*), with corresponding decreased avidity on the axial FDG-PET image (*C*).

subsequent ASL-MR demonstrated asymmetrically decreased left temporoparietal CBF (Fig 2 and Online Supplemental Data), with confirmed β -amyloid deposition on [^{18}F] florbetaben PET and tau deposition on [^{18}F] MK-6240 PET, consistent with a diagnosis of AD (Fig 2 and Online Supplemental Data). There was also evidence of β -amyloid deposition in the parietal lobes bilaterally, but no other areas of tau deposition (Online Supplemental Data). The patient was prescribed lecanemab.

Case 3: Posterior Cortical Atrophy—the “Visual Variant” of AD

A 74-year-old woman with pre-existing hyperlipidemia, depression/anxiety, and insomnia presented with progressive forgetfulness for 2 years, as well as disorientation, worsened anxiety, and orthostasis for 4–7 years. She continued to work full-time. Examination revealed a MoCA score of 28/30, abnormal findings on bilateral Humphrey visual field testing, a left parietal drift, proprioceptive deficit and paratonia, and postural instability. MR imaging showed subtle left occipital lobe atrophy, with associated decreased CBF (Fig 3 and Online Supplemental Data). FDG-PET demonstrated corresponding decreased avidity, compatible with posterior cortical atrophy (PCA) (Fig 3 and Online Supplemental Data). The patient is considering lecanemab.

Case 4: Early-Onset PCA

A 55-year-old man with a history of hypertension and prior alcoholism, complicated by an episode of withdrawal seizures, presented with 1 year of “long COVID brain fog.” The onset of symptoms was subacute after mild COVID-19 infection. Deficits included worsening dysgraphia, spatial disorientation, visual scanning deficit, simultagnosia, finger agnosia, apraxia, short-term memory lapses, and depression/anxiety, all causing disability; ADLs were preserved. His MoCA score was 7/30, complicated by severe test anxiety. CSF was borderline for AD (amyloid β 42 = 385 pg/mL, phosphorylated tau = 62.1 pg/mL, amyloid-to-tau index = 0.61). MR imaging showed moderate generalized atrophy, with decreased CBF corresponding to areas of cortical tau deposition on subsequent tau PET (Online Supplemental Data). Involvement of the left occipital lobe and

visual symptoms were consistent with the clinical diagnosis of PCA, the visual variant of AD.

Case 5: Early-Onset Logopenic Variant Primary Progressive Aphasia, the “Language” Variant of AD

A 54-year-old woman presented with progressive short-term memory loss, word-finding difficulty, difficulty navigating streets, and trouble separating languages for the past several years. She remained working as a home nurse attendant. She had prediabetes, hyperlipidemia, and anxiety on sertraline. Her mother and maternal aunt had dementia in their 60s. She had occasional orientation deficits but full ADLs, a MoCA score of 15/30, trouble understanding complex commands, bradyphrenia, mild paratonia, and mild optic ataxia. Findings of a genetic dementia panel were negative. ASL-MR demonstrated decreased bilateral parietal and left temporal CBF (Online Supplemental Data), correlating to areas of decreased FDG-PET avidity, compatible with logopenic variant progressive aphasia (lvPPA) (Online Supplemental Data). This patient is a lecanemab candidate and is awaiting insurance coverage for an amyloid PET scan.

Case 6: lvPPA

A 76-year-old man presented with a progressive expressive language deficit, short-term memory loss, visual scanning difficulty, executive dysfunction, and difficulty with higher-level thinking for 4 years. He had hypertension, hyperlipidemia, and 2 maternal aunts with dementia in their 80s. He required reminders for some ADLs but could still follow current events. While his MoCA score was 4/30, he expressed complex concepts despite bradyphrenia, read with some hesitation, wrote, and repeated back risks of therapies. He had a mild postural tremor and ataxic gait. ASL-MR demonstrated decreased bilateral parietal, left-frontal and left-temporal CBF (Online Supplemental Data), more pronounced in extent than the degree of hypometabolism on FDG-PET (Online Supplemental Data). The asymmetric pattern and language deficit were compatible with lvPPA. Amyloid PET revealed diffuse cortical amyloid deposition (Online Supplemental Data).

Case 7: Progressive Supranuclear Palsy

A 59-year-old woman presented with progressive speech difficulty, short-term memory loss, apraxia, anxiety, and falls, progressing for 3 years and now needing reminders for ADLs. Her MoCA score was 15/30; she had prominent perseveration, dysarthria, phonemic paraphasia, terseness, and Parkinsonism with limited upgaze and postural instability. CSF protein and myelin basic protein were slightly elevated. MR imaging showed midbrain atrophy, suggestive of the “hummingbird” sign of progressive supranuclear palsy. This diagnosis was supported by decreased CBF and FDG avidity in the frontal lobes and [¹²³I] loflupane SPECT (DaTscan; GE Healthcare) findings indicating reduced radiotracer activity in the left caudate and left putamina greater than the right (Online Supplemental Data).

DISCUSSION

Our case series, which includes early and late onset of amnesic, visual, and language variants of AD and atypical parkinsonism, illustrates the clinical utility of ASL-MR in the management of individual patients with MCI or mild dementia. Most of the patients presented here had only mild, nonspecific volume loss on the volumetric T1-weighted sequence. However, ASL-MR was abnormal in all patients, with specific areas of decreased CBF corresponding to hypometabolism (cases 1, 3, 5, 6, and 7) or amyloid and tau deposition (cases 1, 2, 4, and 6) on PET. These findings lend strong support for an add-on, 4.5-minute, clinical noncontrast ASL-MR image to increase the sensitivity and utility of a routine clinical standard-of-care MR imaging for cognitive impairment.

The utility of ASL-MR as a proxy for FDG-PET in neurodegenerative disease has previously been described primarily in research settings. The concept that decreased CBF should approximate hypometabolism on FDG-PET arose from the observation that perfusion and metabolism in the brain are tightly coupled.⁵ Indeed, studies in patients with AD that used both ASL-MR and FDG-PET found a high degree of overlap between the abnormalities found on the 2 modalities.^{4,6} Additionally, studies in small AD cohorts have reported similar diagnostic accuracies between ASL-MR and FDG-PET.^{7,8} However, ASL-MR is still not yet widely used in the clinical realm for this indication. One reason may be that MR imaging in neurodegenerative disease has traditionally been used largely to exclude treatable causes of dementia, because the sensitivity and specificity of structural MR imaging alone for diagnosing AD is modest and no previous disease-modifying AD treatments existed. Furthermore, ASL-MR relies on arterial blood water as an endogenous tracer, which results in a low SNR, initially limiting radiologists' confidence. However, image quality has improved substantially, supporting the clinical use, as shown in our case series.

An added novelty of our case series compared with the existing literature is that we included atypical variants of neurodegenerative disease. Thus, we demonstrate the diagnostic utility of different patterns of decreased CBF and their correlation with subsequent PET findings to illustrate the clinical utility of ASL-MR beyond the typical Alzheimer pattern. Our findings are concordant with the previously demonstrated advantage of ASL-MR

in its ability to identify hypoperfusion before substantial volume loss, often exhibiting greater degrees of CBF reductions than grey matter tissue loss in affected regions (Online Supplemental Data).⁹ In some cases, CBF changes were more pronounced than their subtle FDG-PET hypometabolic correlates; this finding also suggests the high sensitivity of ASL-MR. Furthermore, we provide evidence for spatial overlap of CBF abnormalities and PET amyloid and tau deposition, suggesting that CBF can reflect underlying disease pathology.

The utility of FDG-PET in the diagnosis of atypical parkinsonism syndromes has been described, but ASL-MR has been described less.¹⁰ One study described CBF differences in Parkinson disease versus Parkinson-Plus syndrome but did not differentiate among the Parkinson-Plus syndromes.¹¹ Case 7 in our series exemplifies the utility of ASL-MR in identifying frontal hypoperfusion, which corresponds to FDG-PET findings of frontal hypometabolism in progressive supranuclear palsy. While the hummingbird sign on structural MR imaging is specific for a diagnosis of progressive supranuclear palsy, frontal hypometabolism seen on FDG-PET has been shown to correlate with disease duration and cognition, adding prognostic value beyond structural MR imaging.¹²

In summary, our case series is a small representation of our growing patient cohort that has received a standardized, clinical MR imaging protocol including ASL-MR and has demonstrated a spectrum of clinical severity of underlying Alzheimer disease and other neurodegenerative pathologies, from subjective impairment to MCI to dementia. We have found that ASL-MR is a highly sensitive screening tool for these pathologies. We have used CBF abnormalities to guide us toward further work-up, either via FDG-PET, amyloid/tau PET, and/or CSF sampling. In our case series, there was limited cerebrovascular burden (Online Supplementary Data), but future work can consider the impact of comorbid severe vascular disease on CBF.¹³ Additionally, CBF is only a surrogate measure of neuronal activity based on neurovascular coupling,¹⁴ so future work will evaluate instances of discordance between CBF and FDG and underlying pathophysiologic mechanisms for this discordance. Nevertheless, incorporation of this cost-effective technology into cognitive screening in the primary care or neurology clinical setting could translate into a profound population health impact, especially at a time when disease-modifying treatment is available, including the anti-amyloid monoclonal antibody therapies, such as lecanemab.^{15,16} These interventions are possibly most effective when initiated early, even presymptomatically, strengthening our case for the need to identify effective screening modalities.¹⁶

CONCLUSIONS

Our case series is concordant with prior knowledge that functional changes typically precede structural changes in patients with neurodegenerative disease. In each case of neurodegenerative disease presented, ASL-MR was an appropriate proxy for FDG-PET findings and, in some cases, amyloid and tau deposition. These patients are a small sample of our larger cohort of patients with CBF correlates to neurodegenerative disease with a wide spectrum of presentations. With standardization in clinical practice and technologic advancements in ASL-MR, CBF has

become a useful screening tool. Further investigations are necessary to support the widespread systematic deployment of this efficient and cost-effective cognitive screening tool in the race to identify, treat, and perhaps even monitor longitudinal change and treatment response in neurodegenerative disease from its earliest stages.

Disclosure forms provided by the authors are available with the full text and PDF of this article at www.ajnr.org.

REFERENCES

1. Bloudek LM, Spackman DE, Blankenburg M, et al. **Review and meta-analysis of biomarkers and diagnostic imaging in Alzheimer's disease.** *J Alzheimers Dis* 2011;26:627–45 CrossRef Medline
2. **CMS expands access to beta amyloid PET for medicare beneficiaries.** [https://www.acr.org/Advocacy-and-Economics/Advocacy-News/Advocacy-News-Issues/In-the-Oct-14-2023-Issue/CMS-Expands-Access-to-Beta-Amyloid-PET-for-Medicare-Beneficiaries#:~:text=CMS%20Expands%20Access%20to%20Beta%20Amyloid%20PET%20for%20Medicare%20Beneficiaries,-Share&text=The%20Centers%20for%20Medicare%20and,\(PET\)%20dementia%20care%20use](https://www.acr.org/Advocacy-and-Economics/Advocacy-News/Advocacy-News-Issues/In-the-Oct-14-2023-Issue/CMS-Expands-Access-to-Beta-Amyloid-PET-for-Medicare-Beneficiaries#:~:text=CMS%20Expands%20Access%20to%20Beta%20Amyloid%20PET%20for%20Medicare%20Beneficiaries,-Share&text=The%20Centers%20for%20Medicare%20and,(PET)%20dementia%20care%20use)
3. Wolk DA, Detre JA. **Arterial spin labeling MRI: an emerging biomarker for Alzheimer's disease and other neurodegenerative conditions.** *Curr Opin Neurol* 2012;25:421–28 CrossRef Medline
4. Riederer I, Bohn KP, Preibisch C, et al. **Alzheimer disease and mild cognitive impairment: integrated pulsed arterial spin-labeling MRI and 18F-FDG PET.** *Radiology* 2018;288:198–206 CrossRef Medline
5. Buxton RB, Frank LR. **A model for the coupling between cerebral blood flow and oxygen metabolism during neural stimulation.** *J Cereb Blood Flow Metab* 1997;17:64–72 CrossRef Medline
6. Chen Y, Wolk DA, Reddin JS, et al. **Voxel-level comparison of arterial spin-labeled perfusion MRI and FDG-PET in Alzheimer disease.** *Neurology* 2011;77:1977–85 CrossRef Medline
7. Musiek ES, Chen Y, Korczykowski M, et al. **Direct comparison of fluorodeoxyglucose positron emission tomography and arterial spin labeling magnetic resonance imaging in Alzheimer's disease.** *Alzheimers Dement* 2012;8:51–59 CrossRef Medline
8. Ceccarini J, Bourgeois S, Van Weehaeghe D, et al. **Direct prospective comparison of 18F-FDG PET and arterial spin labelling MR using simultaneous PET/MR in patients referred for diagnosis of dementia.** *Eur J Nucl Med Mol Imaging* 2020;47:2142–54 CrossRef Medline
9. Johnson NA, Jahng GH, Weiner MW, et al. **Pattern of cerebral hypoperfusion in Alzheimer disease and mild cognitive impairment measured with arterial spin-labeling MR imaging: initial experience.** *Radiology* 2005;234:851–59 CrossRef Medline
10. Zhao P, Zhang B, Gao S. **18[F]-FDG PET study on the idiopathic Parkinson's disease from several parkinsonian-plus syndromes.** *Parkinsonism Relat Disord* 2012;18(Suppl 1):S60–22 CrossRef Medline
11. Cheng L, Wu X, Guo R, et al. **Discriminative pattern of reduced cerebral blood flow in Parkinson's disease and Parkinsonism-Plus syndrome: an ASL-MRI study.** *BMC Med Imaging* 2020;20:78 CrossRef Medline
12. Blin J, Baron JC, Dubois B, et al. **Positron emission tomography study in progressive supranuclear palsy.** *Arch Neurol* 1990;47:747–52 CrossRef Medline
13. Telischak NA, Detre JA, Zaharchuk G. **Arterial spin-labeling MRI: clinical applications in the brain.** *J Magn Reson Imaging* 2015;41:1165–80 CrossRef Medline
14. Zhu WM, Neuhaus A, Beard DJ, et al. **Neurovascular coupling mechanisms in health and neurovascular uncoupling in Alzheimer's disease.** *Brain* 2022;145:2276–92 CrossRef Medline
15. van Dyck CH, Swanson CJ, Aisen P, et al. **Lecanemab in early Alzheimer's disease.** *N Engl J Med* 2023;388:9–21 CrossRef Medline
16. Sims JR, Zimmer JA, Evans CD, et al. TRAILBLAZER-ALZ 2 Investigators. **Donanemab in early symptomatic Alzheimer disease.** *JAMA* 2023;330:512–27 CrossRef Medline

A Comprehensive and Broad Approach to Resting-State Functional Connectivity in Adult Patients with Mild Traumatic Brain Injury

 Soroush Arabshahi,  Sohae Chung,  Alaleh Alivar,  Prin X. Amorapanth,  Steven R. Flanagan,  Farnq-Yang A. Foo,  Andrew F. Laine, and  Yvonne W. Lui



ABSTRACT

BACKGROUND AND PURPOSE: Several recent works using resting-state fMRI suggest possible alterations of resting-state functional connectivity after mild traumatic brain injury. However, the literature is plagued by various analysis approaches and small study cohorts, resulting in an inconsistent array of reported findings. In this study, we aimed to investigate differences in whole-brain resting-state functional connectivity between adult patients with mild traumatic brain injury within 1 month of injury and healthy control subjects using several comprehensive resting-state functional connectivity measurement methods and analyses.

MATERIALS AND METHODS: A total of 123 subjects (72 patients with mild traumatic brain injury and 51 healthy controls) were included. A standard fMRI preprocessing pipeline was used. ROI/seed-based analyses were conducted using 4 standard brain parcellation methods, and the independent component analysis method was applied to measure resting-state functional connectivity. The fractional amplitude of low-frequency fluctuations was also measured. Group comparisons were performed on all measurements with appropriate whole-brain multilevel statistical analysis and correction.

RESULTS: There were no significant differences in age, sex, education, and hand preference between groups as well as no significant correlation between all measurements and these potential confounders. We found that each resting-state functional connectivity measurement revealed various regions or connections that were different between groups. However, after we corrected for multiple comparisons, the results showed no statistically significant differences between groups in terms of resting-state functional connectivity across methods and analyses.

CONCLUSIONS: Although previous studies point to multiple regions and networks as possible mild traumatic brain injury biomarkers, this study shows that the effect of mild injury on brain resting-state functional connectivity has not survived after rigorous statistical correction. A further study using subject-level connectivity analyses may be necessary due to both subtle and variable effects of mild traumatic brain injury on brain functional connectivity across individuals.

ABBREVIATIONS: BOLD = blood oxygen level-dependent; fALFF = fractional amplitude of low-frequency fluctuations; FDR = false discovery rate; ICA = independent component analysis; IFCN = intrinsic functional connectivity networks; mTBI = mild traumatic brain injury; NBS = network-based statistics; rs-FC = resting-state functional connectivity; rs-fMRI = resting-state fMRI; SCAT3 = Sport Concussion Assessment Tool, 3rd edition; Spatial-GICs = Spatial Group Independent Components; Temporal-GICs = Temporal Group Independent Components; TFCE = threshold-free cluster enhancement

Traumatic brain injury is a significant cause of death and disability worldwide,¹ with up to 50–60 million new cases a year globally² and 2.5 million in the United States.³ Most of these cases are caused by mild head impacts, known as mild TBI (mTBI) or concussion.⁴ According to the committee of the Head Injury

Interdisciplinary Special Interest Group of American Congress of Rehabilitation Medicine, a person with an mTBI is identified by a trauma-induced disruption of brain function, evidenced by ≥ 1 of the following: a period of loss of consciousness, memory loss for events around the accident, altered mental state at the time of the accident (like feeling dazed or confused), and possible focal neurologic deficits. However, this condition is considered mild if the

Received October 2, 2023; accepted after revision January 12, 2024.

From Biomedical Engineering Department (S.A., A.F.L.), Columbia University, New York, New York; and Departments of Radiology (S.C., A.A., Y.W.L.), Rehabilitation Medicine (P.X.A., S.R.F.), and Neurology (F.-Y.A.F.), NYU Grossman School of Medicine, New York, New York.

The presented study was supported, in part, by grant funding from the National Institutes of Health (NIH): R01 NS119767-01A1, R01 NS039135-11, R01 NS119767. This work was also performed under the rubric of the Center for Advanced Imaging Innovation and Research (CAI2R), a National Center for Biomedical Imaging and Bioengineering supported by the National Institute of Biomedical Imaging and Bioengineering (NIBIB) (NIH P41 EB017183).

Please address correspondence to Soroush Arabshahi, MD, Columbia University, Biomedical Engineering, 500 West 120th St, Mudd Building, 373 Engineering Terrace, New York, NY 10027; e-mail: sa3617@columbia.edu; @soroush361

 Indicates open access to non-subscribers at www.ajnr.org

 Indicates article with online supplemental data.

<http://dx.doi.org/10.3174/ajnr.A8193>

loss of consciousness is <30 minutes, the initial Glasgow Coma Scale score is between 13 and 15, and posttraumatic amnesia lasts no more than 24 hours. This definition encompasses situations such as the head being struck, the head hitting an object, and the brain experiencing whiplash-like acceleration/deceleration movements, even when there is no direct external trauma to the head.⁵ Annually, >1 million emergency department visits in the United States are related to mTBI,⁶ resulting in a more than \$22.5 billion economic burden on the health care system and society.⁷ Moreover, up to 15% of patients have prolonged postconcussive symptoms,⁸ which include a broad range of somatic, behavioral, and emotional issues⁹ and can significantly impact the quality of life.¹⁰ Attempting to unpack the underlying pathophysiology of mTBI remains central to a better understanding of this injury. Specifically, relating structural injuries to functional deficits remains a challenge. It is known that WM injury can occur after mTBI,¹¹ thus, fMRI has naturally been used to investigate potential related disruption of coordinated neural activity.¹²

Several recent works using resting-state fMRI (rs-fMRI) suggest that there may be some alterations of resting-state functional connectivity (rs-FC) after mTBI. However, a variety of differing rs-fMRI analysis approaches, differences across the patient population, and small study cohorts add variance to results and contribute to a broad and somewhat confusing array of reported findings that range across many different functional networks and regions. For example, using a seed-based method, Mayer et al¹³ reported a decreased rs-FC within the default mode network and increased connectivity between the default mode network and lateral prefrontal cortex in mTBI participants (mTBI, 27; control, 26; mean time since injury = 11.5 days). However, their later study showed no significant differences using an independent component analysis (ICA) approach in a larger cohort (mTBI, 51; controls, 51; mean time since injury = 14 days).¹⁴ Similarly, Amir et al¹⁵ found decreased connectivity between the right lateral parietal and precuneus region of the default mode network using a seed-to-voxel method, while their ROI-to-ROI analysis failed to reveal significant group differences in the default mode, task-positive, or salience network (mTBI, 27; controls, 26; mean time since injury = 3 months). Many different regions (eg, dorsolateral prefrontal cortex, hippocampus, precuneus, thalamus) and different functional networks (eg, default mode, dorsal attention, frontoparietal, salience, visual) have all been implicated previously.¹⁶⁻²⁴ Many individual studies have limited cohort sizes (sometimes as few as 13 subjects). In addition, the characteristics of the cohorts vary (eg, time since injury, civilian versus sport-related) as well as the steps and parameters used in data preprocessing, and the methods to measure rs-FC vary.

In this study, an unbiased, broad, and comprehensive approach was used to investigate rs-FC changes for individuals with mTBI compared to healthy normals using a sizable prospective study cohort, refraining from any a priori assumptions, and using rigorous, multilevel statistical analyses. Standard fMRI preprocessing pipelines were performed using 3 popular analysis approaches, including ROI/seed-based analyses, ICA, and fractional amplitude of low-frequency fluctuations (fALFF). These techniques are among prominent choices in the field, each with its unique interpretation and limitations, yet they offer complementary perspectives in rs-FC

analysis.²⁵ Our aim was to integrate these methods in a singular study, providing a benchmark for evaluating both past and forthcoming research, with a focus on uncovering consistent findings and reliable rs-fMRI biomarkers through a comparative approach.

MATERIALS AND METHODS

Study Population

This prospective study was approved by our institutional review board at New York University Langone Health, and subjects provided written, informed consent before participation. Adult subjects (18–65 years of age) within 1 month of documented mTBI by the American Congress of Rehabilitation Medicine criteria²⁶ were included in this cohort. Participants with a history of prior TBI or other neurologic disorders, a history of participation in organized contact sports, and imaging contraindications were excluded. The cohort included 82 individuals with mTBI and 53 age- and sex-matched healthy controls. Five with mTBI did not complete imaging, and 7 other subjects (5 with mTBI and 2 controls) had fMRI quality issues. A total of 72 individuals with mTBI (mean age, 30 [SD, 11.66] years, time since injury = 18 [SD, 7.7] days; 47 women) and 51 controls (31 [SD, 12.09] years; 30 women) were finally included in this study (Table and Online Supplemental Data). Age, sex, educational background (as measured by years of education beyond high school), and time since injury for the mTBI group were included in a generalized linear model to investigate any correlation between measurements and these covariates. This investigation was conducted separately for each covariate and then combined as independent variables. Fifty-one patients with mTBI completed the Sport Concussion Assessment Tool, 3rd edition (SCAT3) questionnaire²⁷ to measure symptom severity. The number of symptoms (total of 22 symptoms) and a total symptom severity score (maximum possible score, 132)²⁸ were collected (Table). Individuals with mTBI who had SCAT3 symptom severity scores exceeding 39 (the median score) were categorized as in the more-severe subgroup, resulting in 26 subjects being identified as high SCAT3 subjects.

MR Imaging Acquisition

Imaging was performed on 3T MR imaging scanners (Magnetom Skyra/Prisma; Siemens, 60/63 subjects) using a 64-channel head coil. Closed-eye resting-state blood oxygen level-dependent (BOLD) images were acquired using an EPI sequence with the following imaging parameters: FOV = 220 × 220 mm, matrix = 74 × 74 × 38, in-plane resolution = 3 × 3 mm², slice thickness = 3 mm, TR/TE = 2000/25 ms, number of volumes = 153 (5.1 minutes), flip angle = 70°, generalized autocalibrating partially parallel acquisition factor = 2, bandwidth/pixel = 1826 Hz. For coregistration and segmentation, the MPRAGE sequence (TR/TE = 2100/3.19 ms, flip angle = 8°, image resolution = 1 × 1 × 1 mm³, matrix = 256 × 256 × 192) was also performed.

Image-Preprocessing Pipeline

We used a standard preprocessing pipeline implemented in the CONN toolbox (www.nitrc.org/projects/conn, Version 21.a).²⁹ Specifically, the pipeline included the following: motion correction using rigid registration on the first volume, slice-time

Demographics and injury characteristics of studied participants

Variables	mTBI	Control	Statistics
Initial recruitment (No.)	82	53	NA
Excluded (No.)			
Incomplete session	5	0	NA
Image quality issues	5	2	NA
Final inclusion (No.)	72	51	NA
Age (range) (mean) (yr)	18–65 (30 [SD, 11.66])	19–65 (31 [SD, 12.09])	$t = -0.82, P = .41$
Sex, M/F	25:47	21:30	$\chi^2 = 0.017, P = .89$
Education (range) (mean) (yr)	11–20 (16.08 [SD, 1.67])	12–20 (16.46 [SD, 1.81])	$t = -1.10, P = .27$
Hand preference, right (No.) (%)	44 (86.27%)	51 (70.33%)	$\chi^2 = 0.017, P = .89$
Cause of injury (No.) (%)			
Fall	21 (29.16%)	NA	NA
Hit by object	27 (37.5%)	NA	NA
Motor-vehicle accident	9 (12.5%)	NA	NA
Assault	4 (5.56%)	NA	NA
Sport-related	4 (5.56%)	NA	NA
Other	7 (9.72%)	NA	NA
Time since injury (range) (mean) (day)	3–31 (18 [SD, 7.7])	NA	NA
SCAT3			
No. of symptoms (range) (mean)	0–22 (14.25 [SD, 6.30])	NA	NA
Symptom severity score (range) (mean)	0–103 (43.53 [SD, 29.98])	NA	NA

Note:—NA indicates not applicable.

correction using the Siemens interleaved slice-timing pattern, unwrapping using a unified segmentation and normalization procedure to register the functional scan on the standard space (Montreal Neurological Institute 152_2mm),³⁰ and spatial smoothing with an 8-mm Gaussian full width at half maximum kernel. Outlier frames were identified and scrubbed using motion parameters (in-plane motion of >0.5 mm) and global mean intensity (SD, >3). Structural scans were also normalized and segmented into WM, GM, and CSF using direct nonlinear registration to the atlas (Montreal Neurological Institute 152_1 mm). The anatomic component correction denoising method³¹ was applied to decrease the effect of biologic noise. The hyperparameters (the number of principal components) were set to maintain a global mean BOLD signal of zero and a voxel-to-voxel correlation distribution with a zero mean. The motion-related, scrubbing, and rest-confounding regressors were also included in the anatomic component correction method. Then, a temporal bandpass filter with a frequency range of 0.008 to 0.09 Hz, linear detrending, and despiking were used to remove the remaining potential confounders.

Functional Connectivity Measures

Functional connectivity, characterized by synchronized low-frequency fluctuations of the BOLD signal across distinct brain regions, was measured to investigate group differences in rs-FC using 2 methods: 1) a model-based approach to measure the correlation of the signal between ROIs or seeds, and 2) a data-driven method, ICA, which eliminates the need for defining ROIs. These methods were selected on the basis of their general popularity, the established application of these techniques in mTBI rs-FC studies, and the complementary perspectives on rs-FC.

ROI/Seed-Based Connectivity. In this study, we used a total of 4 popular parcellation methods: 1) 8 functional networks (32 ROIs, available in the CONN toolbox), 2) 7 functional networks (7 ROIs),³² 3) 14 functional networks (264 seeds),³³ and 4) 22 functional networks (132 anatomic ROIs, available in the CONN

toolbox). The first and second parcellations are created on the basis of rs-fMRI data (using ICA and surface-level clustering methods, respectively). The third was based on a combination of task-mediated and rs-fMRI data, and the last was based on an anatomic atlas using a combination of supratentorial cortical and subcortical ROIs from the Harvard-Oxford atlas³⁴ and cerebellar parcellation from the automated anatomic labelling atlas³⁵ (Online Supplemental Data). The selection of ROI/seed locations influences the ROI/seed-based connectivity analysis.²⁵ Therefore, we opted for these specific parcellations to gain a comprehensive understanding and enable comparison with results from other studies.

Temporal Pearson correlation coefficients between each pair of ROIs were calculated as the rs-FC measure. Fisher z transformation was applied to account for the normality assumption in statistical analysis methods. Accordingly, corresponding connectivity matrices were generated for both groups. The Pearson correlation coefficient between group-level connectivity matrices was calculated as a measure of similarity. We applied 2 group-level comparisons: 1) a binary comparison between significantly connected ROIs uniquely present in mTBI and control groups as well as those present in both groups or neither group, and 2) correlation coefficient distributions examined over all connections to investigate differences in the amplitude of connectivity between groups.

We also calculated ROI-to-voxel correlations, which measured the connectivity between the ROI and all voxels in the brain. The outcome was a whole-brain correlational contrast map for each ROI. This method limits prior assumptions of connectivity among specific brain regions.

The impact of spatial smoothing on global and regional rs-FC measurements has been debated.³⁶ To address this concern, similar ROI-based comparisons were conducted using unsmoothed data (before applying the Gaussian full width at half maximum kernel). Furthermore, assuming that an rs-FC alteration may be seen only in patients with more severe symptoms, subsequent analyses were

conducted solely between the high SCAT3 mTBI subset and the control group.

Group ICA. A group ICA was applied, avoiding all a priori assumptions dependent on the selection of ROIs. The parameters were set to the default generally used in many ICA rs-FC studies including G1/tanh Fast ICA and group ICA 3 back-projection methods, dimensionality reduction of 64, and 40 total independent components. The correlational spatial match technique was used, and major intrinsic functional connectivity networks (IFCN) were identified according to the standard functional parcellation used in the ROI/seed-based method. For group-level analysis, subject-level activation maps, known as the β map for each spatial component, were compiled to extract statistically significant differences between groups (spatial-GICs analysis). Additionally, subject-level temporal components were cross-correlated to create a connectivity matrix between IFCNs (temporal-GICs analysis), and similar connectivity matrices, such as the ROI/seed-based method, were generated.

Fractional Amplitude of Low-Frequency Fluctuations. Voxelwise fractional amplitude of low-frequency fluctuations (fALFF)³⁷ was used to calculate the power ratio of band-passed (range, 0.008–0.09 Hz) frequencies to the full BOLD signal frequency spectrum (range, 0–0.25 Hz). Groups were compared with respect to BOLD power ratios to identify any potential ROIs of interest.

Statistical Analysis

Here, we strove for a high level of statistical rigor. First, we applied the Shapiro-Wilk test to assess the normality assumption over the group-level distribution of correlation coefficients ($P > .05$). Following this step, significantly connected ROIs/seeds/temporal-GICs within groups was determined using a 1-sample t test or Wilcoxon signed-rank test, depending on whether the normality assumption held for that specific connection. We then performed between-group comparisons using the Welch t test if both the mTBI and control groups' correlation coefficients were found to be normally distributed; otherwise, the Mann-Whitney U test was used. The significance level was set at $P < .05$ for both within-group and between-group comparisons; then, per each analysis, we corrected P values ($p_{corrected}$) for false discoveries using the Benjamini-Hochberg false discovery rate correction (FDR, $\alpha = 5\%$) method of multiple comparisons at the whole-brain level, rather than the ROI/network level. To account for the high number of hypothesis tests associated with the number of ROIs for a given parcellation, we used the method of network-based statistics³⁸ (NBS; <https://www.nitrc.org/projects/nbs/>) as an alternative to whole-brain multiple comparisons (t -statistic threshold = 1.6, with 10,000 permutations and a significance level of $P < .05$). A linear regression analysis was performed to investigate the relationship between symptom-severity scores within the mTBI group and the connectivity amplitude, focusing on connections identified as different before multiple comparison correction. For between-group comparisons on spatial contrasts such as the outcomes of ROI-to-voxel, spatial-GICs,

and fALFF, the nonparametric method of threshold-free cluster enhancement (TFCE)³⁹ was applied to correct cluster size in addition to the FDR correction. Due to many contrasts, the TFCE was used on between-source contrasts using any effect test (F -test). The power analysis for this study revealed that with the sample size used, it is feasible to achieve a statistical power of 80% at an .05 significance level, assuming an approximate effect size of 0.5 before multiple comparison correction. The statistical analyses were performed by the CONN toolbox and in-house scripts written in Python (using SciPy [<https://scipy.org/>] and Statsmodels [<https://pypi.org/project/statsmodels/>] libraries).

RESULTS

Demographics

We found no differences between subject cohorts in terms of demographics: age, sex, educational background, and hand preference (Table). There were no associations determined between covariates and connectivity measures for both separated and combined schemes ($P_{corrected} > .05$).

ROI/Seed-Based Connectivity

The 1-sample t test (or Wilcoxon signed-rank test) for within-group analysis revealed 164 positively and 115 negatively correlated ROIs of 496 investigated connections in the control group ($P_{corrected} < .05$, Fig 1A), whereas 164 positively and 129 negatively connected ROIs were found in the mTBI group (Fig 1B). The Pearson correlation coefficient of connectivity matrices between controls and the mTBI groups (Fig 1A, -B) is 0.97 ($P < .001$). We identified 239 statistically significant connections common to the mTBI and control groups, 40 unique to the control group and 54 unique to the mTBI group (Fig 1C). While group comparisons of connectivity distributions revealed no statistically significant connections between pairs of ROIs after multiple comparison correction (Fig 1E), there were 19 connections between pairs of ROIs that showed hyperconnectivity (mTBI $>$ control), and 20 showed hypoconnectivity (mTBI $<$ control), with the cerebellar network being most affected (10 hyperconnected links to ROIs in visual, sensorimotor, and dorsal attention networks; and 6 hypoconnected links to ROIs in the language and frontoparietal networks) ($P_{uncorrected} < .05$; Fig 1D). Among the 39 identified connections, 3 specific pathways—linking the posterior cerebellum to the left visual lateral region, the anterior cerebellum to the left inferior frontal gyrus associated with language, and the anterior cerebellum to the left posterior superior temporal gyrus related to language—demonstrated significant predictive capability for the SCAT3 symptom-severity scores (Online Supplemental Data). Use of the NBS approach for multiple comparison correction did not yield a consistent network showing a statistically significant difference ($P > .05$). No significant difference in connectivity amplitude was found using the other 3 brain-parcellations after multiple comparison correction. The detailed results are summarized in the Online Supplemental Data. Similar results emerged without smoothing, albeit with fewer connected ROIs within each group due to, possibly, the increased noise effect (Online Supplemental Data).

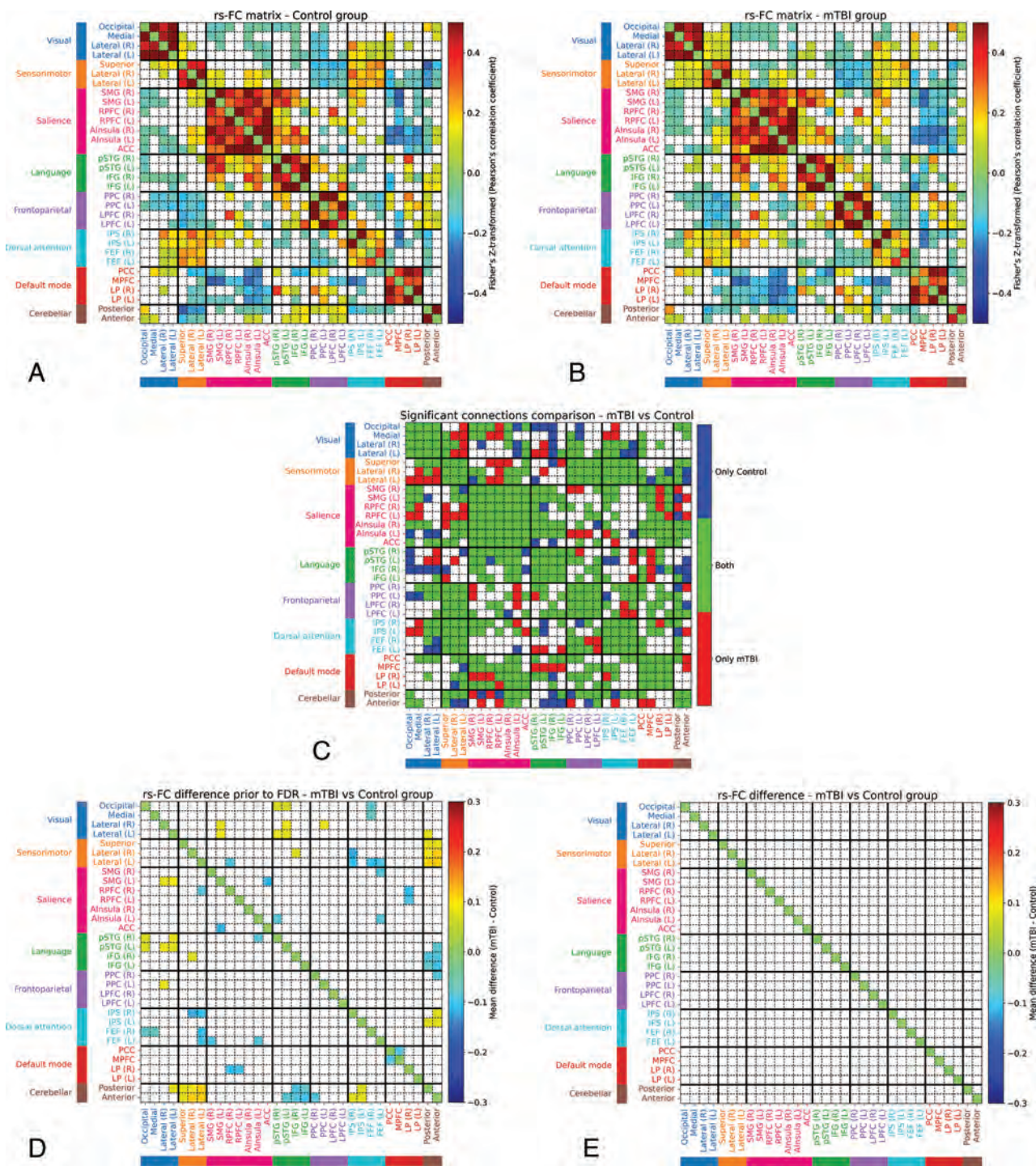


FIG 1. ROI-based analysis results using the CONN toolbox standard functional parcellation. A and B, The connectivity matrix for control and mTBI groups. The color for each pair of ROIs reflects statistically significant connectivity after FDR correction ($p_{corrected} < .05$) measured by the average Fisher z-transformation of the Pearson correlation coefficient. C, Matrix of significant connections, comparing A and B: Red indicates a significant connection unique to the mTBI group; blue indicates significant connections unique to the control group; and green indicates significance in both mTBI and control groups. D, Matrix of the mean difference (mTBI versus controls) for the connections that satisfy $P_{uncorrected} < .05$ using the Welch t test when comparing mTBI with controls. Highlighted connections involve all networks and nearly all ROIs, and the magnitude of differences is small. E, After multiple comparison correction (FDR) to account for the number of connections examined, no difference remains significant. Note that diagonal values (self-connection) are set to zero. A full list of ROIs is provided in the Online Supplemental Data. Results from other parcellation methods yield analogous results, whose matrices are presented in the Online Supplemental Data. L indicates left; R, right; SMG, Supramarginal gyrus; RPF, Rostral prefrontal cortex; pSTG, Posterior superior temporal gyrus; MPFC, Medial prefrontal cortex; IFG, Inferior frontal gyrus; LP, Lateral parietal; PPC, Posterior cingulate cortex; LPFC, Lateral prefrontal cortex; FEF, Frontal eye fields; IPS, Intraparietal sulcus.

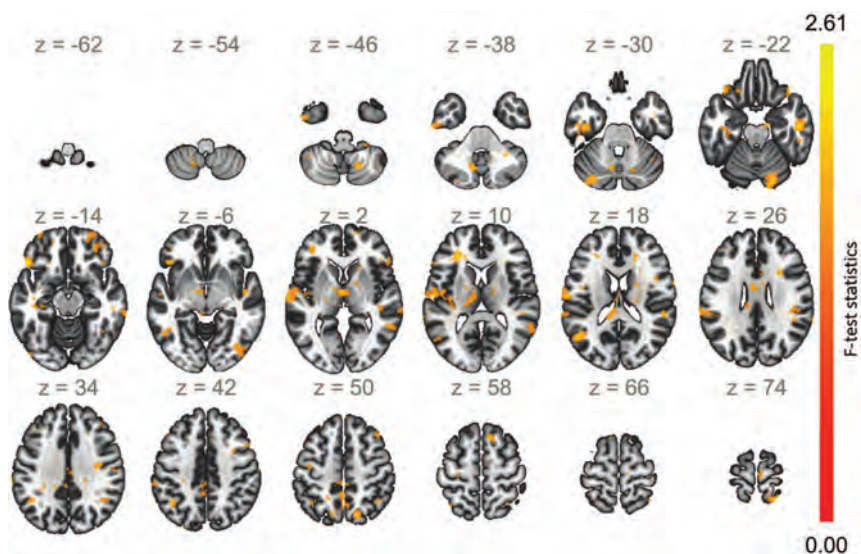


FIG 2. ROI-to-voxel results showing voxels with $P_{uncorrected} < .05$ based on any effect F -test statistics. All 32 ROIs from the standard functional parcellation of CONN are included here to highlight possible areas of connectivity difference between mTBI and control groups. The highlighted voxels are seen to be scattered across the brain, and no cluster survives after FDR and TFCE correction.

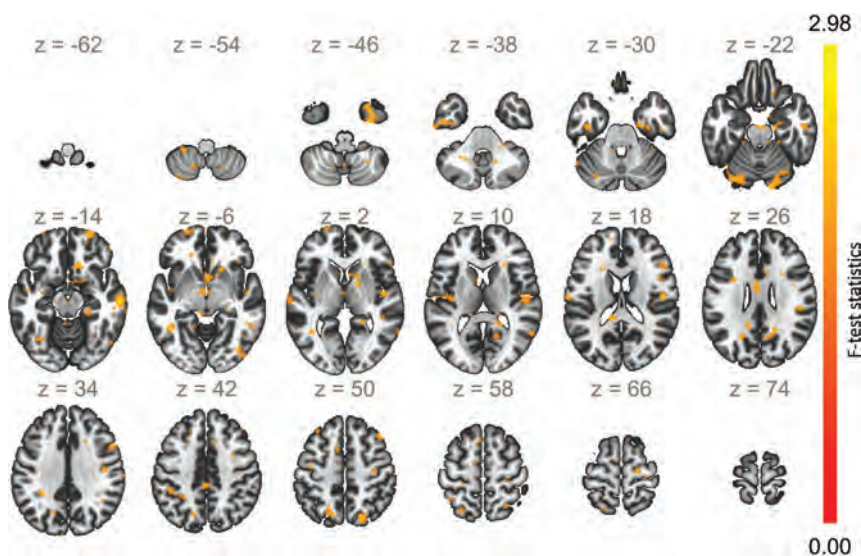


FIG 3. Similar to ROI-to-voxel analysis, this figure illustrates voxels with $P_{uncorrected} < .05$ according to any effect F -test on all 20 spatial-GICs. As in the analysis in Fig 2, no regions survive FDR and TFCE.

In the high SCAT3 mTBI subset, neither whole-brain analyses nor NBS multiple comparison procedures were able to identify statistically significant variations in connection or a consistent network. Before multiple comparisons, 27 connections (17 hyperconnectivity and 10 hypoconnectivity) scattered in all 8 functional networks were observed, while the only within-network difference was between the cerebellum anterior and the posterior ROIs (Online Supplemental Data).

Figure 2 shows the result of any effect (F -test) among sources for all 32 ROI-to-voxel contrast maps. The 3 largest clusters were found in the cerebellum, left temporal lobe, and left angular gyrus. Nonetheless, no cluster remained significant after applying the FDR

and TFCE. Because spatial smoothing reduces the sensitivity of TFCE,³⁹ the analysis was also executed on unsmoothed data, showing no statistically significant clusters of difference (differences before correcting for multiple comparison are depicted in the Online Supplemental Data).

Group ICA

Forty spatially independent components were produced from which we identified 20 components (spatial-GICs) to represent 9 IFCNs: auditory (1 component), cerebellar (2), default mode (2), dorsal attention (3), frontoparietal (2), language (2), sensorimotor (3), salience (1), and visual (4) (Online Supplemental Data). Evaluation of the spatial-GICs revealed no significant clusters after using FDR and TFCE. The results using the F -test before FDR and TFCE on all 20 spatial-GICs are depicted in Fig 3. The 3 largest clusters overlie the right accumbens, right central and parietal operculum cortex, and left cerebellum based on the standard anatomic atlas.

Among a total of 190 investigated connections, the subject-level temporal components (temporal-GICs) of the 20 spatial-GICs revealed 54 positively and 43 negatively connected components in the control group ($P_{corrected} < .05$, Fig 4A). In the mTBI group, 63 positively and 44 negatively correlated components were found ($P_{corrected} < .05$, Fig 4B). Connectivity matrices between the control and mTBI groups were significantly correlated ($r = 0.94$, $P < .001$). The binary comparison between connected or disconnected components (positively or negatively) is depicted in Fig 4C. Before correction for multiple comparisons, there were 1 hyperconnectivity and 1 hypoconnectivity for components within the visual network, 2 hyperconnectivities for components of visual-auditory and salience-language, as well as 2 hypoconnectivities for components of visual-cerebellar, and salience-default mode networks (Fig 4D). None survived FDR correction (Fig 4E).

fALFF

The voxelwise t test showed significant fALFF differences in the lateral occipital cortex (inferior and superior divisions), right cerebellum, left superior and medial frontal gyri, and precuneus anatomic regions ($P < .05$, Fig 5). However, no clusters remained significant after applying FDR and TFCE corrections.

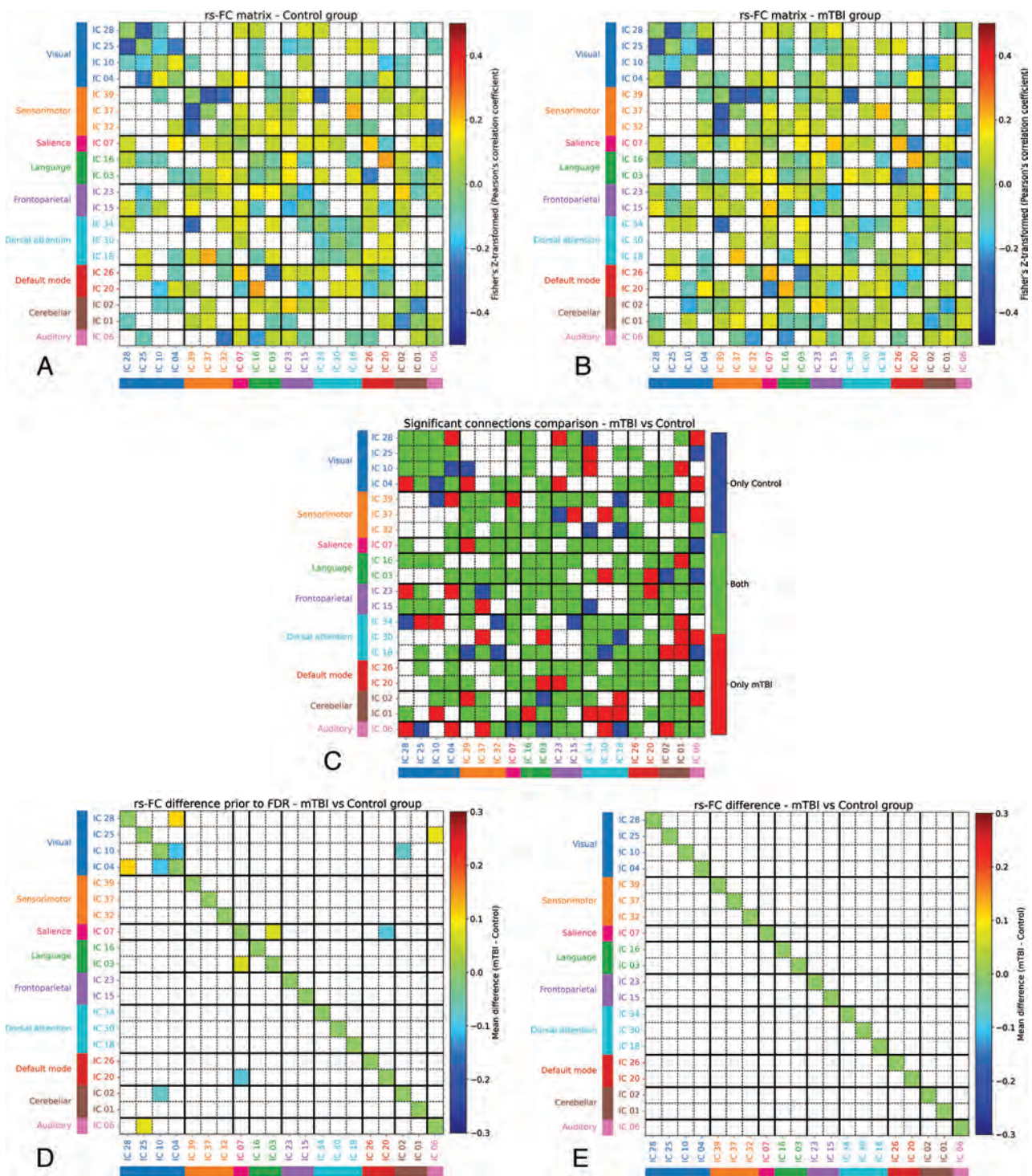


FIG 4. Temporal-GICs analysis results. *A* and *B*, The connectivity matrix for control and mTBI groups. The color for each pair of temporal-GICs reflects statistically significant connectivity after FDR correction ($P_{corrected} < .05$) measured by average Fisher z-transformation of the Pearson correlation coefficient. *C*, Matrix of significant connections, comparing *A* and *B*: Red indicates significant connections unique to the mTBI group; blue indicates significant connections unique to the control group; and green indicates significance in both the mTBI and control groups. *D*, Matrix of mean difference (mTBI and controls) for the temporal-GICs connections that satisfy $P_{uncorrected} < .05$ using the Welch *t* test comparing those with mTBI with controls. Highlighted connections involve temporal-GICs of 6 IFCNs, excepting sensorimotor, frontoparietal, and dorsal attention; however, the magnitude of differences is small. *E*, After multiple comparison correction (FDR) to account for the number of connections examined, no difference remains significant. IC indicates independent component.

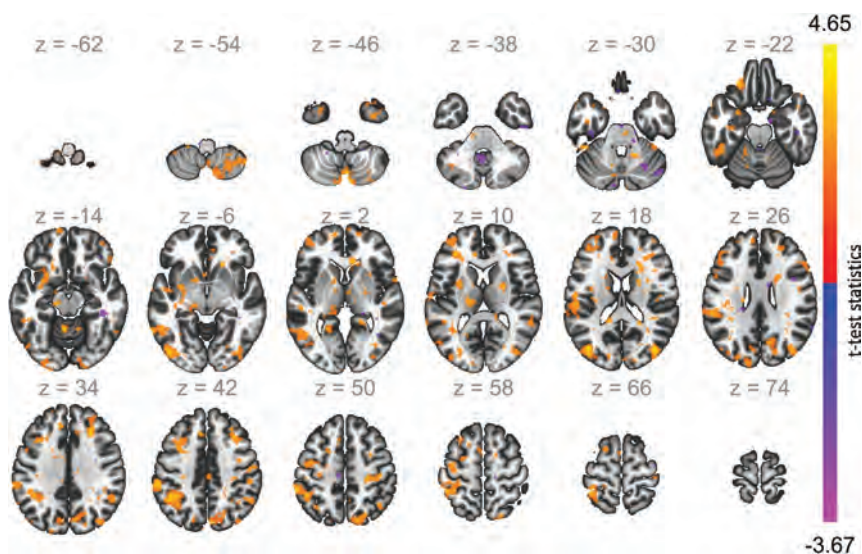


FIG 5. Voxelwise *t* test on fALFF measures comparing mTBI with healthy control groups with $P_{\text{uncorrected}} < .05$. Because fALFF is a voxelwise scalar measure, any effect *F*-test was not used, and the contrast shows *t*-values. No clusters survive FDR and TFCE correction.

DISCUSSION

By means of a broad approach using several popular and generally used methods, the results of this study show no statistically significant differences between subjects with mTBI and matched healthy controls measured by whole-brain rs-FC after multiple comparison corrections. The findings are consistent across multiple functional connectivity measures and methods applied to our well-characterized cohort of subjects with mTBI using rigorous statistical analysis. A few differences could be seen before correction for multiple comparisons, though these are only variably aligned with what has been previously reported in the literature.

During the past 2 decades, many studies have investigated connectivity differences between those with mTBI and control subjects using a whole family of measurements collectively referred to as rs-FC, reporting various ranges of results. Here, we focus on the explicit study of rs-FC without extending to other analysis methods such as dynamic rs-FC, graph theory measures, regional homogeneity, or other acquisition methods such as task-mediated fMRI and structural connectivity. These other methods are not explored here though they do represent additional and valid approaches that may shed light on brain connectivity in individuals with mTBI.^{14,19,40-47} Furthermore, though we explore the popular primary methods of investigating rs-FC, we recognize that no study can be genuinely exhaustive because there are innumerable ways to combine optimization of parameters, pre-processing methods, and brain parcellations. In this study, we have taken a conservative statistical approach in applying multiple-step corrections for multiple comparisons. This level of statistical rigor would not necessarily be required for research focusing on only a very limited number of regions rather than taking a whole-brain survey approach; this methodologic difference may contribute to some of the differences between the results of the current study and those of prior works. Despite using NBS as an alternative to whole-brain multiple comparison methods to mitigate the elevated risk of false-negatives due to numerous hypothesis

tests, the results were inconclusive and failed to identify any subnetwork of differences. This finding leads us to acknowledge that hypothesis-driven methodologies, similar to those reported in earlier studies, may yield more robust and replicable rs-FC biomarkers in mTBI populations. However, the objective of the current study was to discern stable whole-brain differences, a goal that was not achieved by applying stringent-yet-rigorous statistical correction.

This study raises a critical issue regarding the statistical power of its analysis. The small effect sizes derived from the measurements lead to under-powered conclusions, a problem that is exacerbated when considering the multiple comparison issue, which significantly lowers the threshold for statistical significance.⁴⁸ For instance, the largest effect size observed was 0.5723 for the ACC-

SMG (L) connection within the salience network, using the ROI/seed-based method and the 8 functional networks parcellation. A sample size of 49 is required, which is marginally met by our current cohort, to confirm this finding with a pre-multiple comparison framework. However, this requirement applies only to the finding with the largest effect size; confirming that other connection differences would require a much larger sample size. The need for increased sample sizes becomes even more pronounced when accounting for multiple comparisons. This reliance on conventional statistical methods introduces a degree of uncertainty in establishing consistent and reproducible biomarkers for rs-FC differences in the literature regarding patients with mTBI. To overcome this challenge, we propose 3 potential solutions: 1) increasing the participant count, 2) using hypothesis-driven and prior-based investigations, and 3) developing new rs-FC measurements and statistical analyses that are less sensitive to these parameters. Each of these options has its advantages and drawbacks. For instance, acquiring a large sample size may not be practical, and hypothesis-driven studies risk confirmation bias. Consequently, the existence of rs-FC differences in subjects with mTBI remains a complex and somewhat unresolved question. Nonetheless, our study strives to address this issue as thoroughly as possible by using rigorous and standard methodologies, setting a benchmark for future research in this field.

Before multiple comparison correction, the findings point to the cerebellum as an area of interest in rs-FC after injury. Specifically, there is some reduced connectivity between cerebellar ROIs and language networks and increased connectivity between the cerebellum and sensorimotor regions, as well as the cerebellum and intraparietal sulcus ROIs of the dorsal attention network. This observation is supported by knowing that only connections to and from the cerebellum can predict the symptom-severity score. In addition, on the basis of ROI-to-voxel analysis, >50% of the largest differences cluster overlaps with 20% of the right cerebellum. Spatial-GICs and fALFF analyses also

highlight sizable clusters within the right cerebellum. Although there is limited evidence in the literature discussing cerebellar rs-FC in mTBI,^{40,41,49,50} further studies are warranted to investigate changes in this region after injury. Our findings also show that several clusters of differences throughout the entire supratentorial brain are peripherally located (Figs 2, 3, and 5). Nonetheless, all these observations are made before using rigorous correction for multiple comparisons, making it overall difficult to speculate very much. Additionally, a common assumption is a lower rs-FC in patients with severe mTBI, but our analysis of participants with high SCAT3 and mTBI demonstrated a smaller number of potential injured connections compared with the analysis including all participants with mTBI (27 < 39); this unusual observation signals that the rs-FC differences without multiple comparisons are possibly false discoveries.

This study has several limitations. First, the increased number of hypothesis tests involved in whole-brain statistical correction could impede the true discoveries, potentially leading to the oversight of significant results,⁵¹ a challenge stemming principally from the currently predominant strategies used for multiple comparisons. We endeavored to temper this issue by leveraging NBS and undertaking preliminary analysis before applying corrections; however, we identified only a restricted set of conclusive biomarkers, localized mainly in cerebellum regions, which have been underexplored in the existing literature. Furthermore, while FDR-based multiple comparison correction methods do not necessitate independent test statistics, their effectiveness is greatly influenced by the correlations among these statistics.⁵² This issue is a significant consideration because test statistics in practical scenarios are often not completely independent. Second, the effect of mTBI on human brain connectivity manifests with a considerable degree of heterogeneity, requiring a more detailed stratification that accounts for the variable nature of symptoms, both acute and persistent, alongside correlations with neuropsychological evaluations and the diverse kinematics of the injuries sustained. This nuanced approach is imperative in developing reliable imaging biomarkers through rs-FC. Last, the potential influence of chronic diffuse axonal injury on prolonged postconcussion symptoms⁵³ suggests that studying only the acute stages of injury, as pursued in this research, might not reveal significant distinctions. Future research, adopting a longitudinal approach with follow-up assessments, stands to better facilitate more pronounced discoveries, enhancing our comprehension of the complexities involved.

CONCLUSIONS

By using group-level statistical analyses after applying a range of standard, state-of-the-art methods to study rs-FC, we did not observe statistically significant group-level rs-FC differences between patients with mTBI within 1 month of injury and healthy controls after multiple comparison correction. It is likely that due to the kinematic properties of mTBI and other subject-specific features, functional injuries are challenging to probe using group-based analyses such as those used here. Current conventional rs-FC methods and whole-brain statistical analysis frameworks may be insufficient for amplifying subtle changes in neural activity as may occur in patients with mTBI, and overall variance may be

high. There is a need to examine all sensitive features of the BOLD signal, develop subject-level rs-FC measurements to consider injury individually, and explore new ways to study rs-FC in this population.

Disclosure forms provided by the authors are available with the full text and PDF of this article at www.ajnr.org.

REFERENCES

1. Fleming S, Ponsford J. **Long term outcome after traumatic brain injury.** *BMJ Publishing Group* 2005;331:1419 CrossRef Medline
2. Hyder AA, Wunderlich CA, Puvanachandra P, et al. **The impact of traumatic brain injuries: a global perspective.** *NeuroRehabilitation* 2007;22:341–53 CrossRef Medline
3. Coronado VG, McGuire LC, Sarmiento K, et al. **Trends in traumatic brain injury in the US and the public health response: 1995–2009.** *J Safety Res* 2012;43:299–307 CrossRef Medline
4. Maas AI, Menon DK, Adelson PD, et al; InTBIR Participants and Investigators. **Traumatic brain injury: integrated approaches to improve prevention, clinical care, and research.** *Lancet Neurol* 2017;16:987–1048 CrossRef Medline
5. Kay T, Harrington DE, Adams R, et al. **Definition of mild traumatic brain injury.** *J Head Trauma Rehabil* 1993;8:86–87
6. Bazarian J, McClung J, Cheng Y, et al. **Emergency department management of mild traumatic brain injury in the USA.** *Emerg Med J* 2005;22:473–77 CrossRef Medline
7. Miller GF, DePadilla L, Xu L. **Costs of nonfatal traumatic brain injury in the United States, 2016.** *Med Care* 2021;59:451–55 CrossRef Medline
8. Røe C, Sveen U, Alvsåker K, et al. **Post-concussion symptoms after mild traumatic brain injury: influence of demographic factors and injury severity in a 1-year cohort study.** *Disabil Rehabil* 2009;31:1235–43 CrossRef Medline
9. Centers for Disease Control and Prevention. *International Statistical Classification of Diseases and Related Health Problems: Alphabetical index.* U.S. Department of Health and Human Services; 2004
10. Zhou Y, Milham MP, Lui YW, et al. **Default-mode network disruption in mild traumatic brain injury.** *Radiology* 2012;265:882–92 CrossRef Medline
11. Chung S, Fieremans E, Wang X, et al. **White matter tract integrity: an indicator of axonal pathology after mild traumatic brain injury.** *J Neurotrauma* 2018;35:1015–20 CrossRef Medline
12. Yuh EL, Hawryluk GW, Manley GT. **Imaging concussion: a review.** *Neurosurgery* 2014;75(Suppl 4):S50–63 CrossRef Medline
13. Mayer AR, Mannell MV, Ling J, et al. **Functional connectivity in mild traumatic brain injury.** *Hum Brain Mapp* 2011;32:1825–35 CrossRef Medline
14. Mayer AR, Ling JM, Allen EA, et al. **Static and dynamic intrinsic connectivity following mild traumatic brain injury.** *J Neurotrauma* 2015;32:1046–55 CrossRef Medline
15. Amir J, Nair JK, Del Carpio-O'Donovan R, et al. **Atypical resting state functional connectivity in mild traumatic brain injury.** *Brain Behav* 2021;11:e2261 CrossRef Medline
16. Johnson B, Zhang K, Gay M, et al. **Alteration of brain default network in subacute phase of injury in concussed individuals: resting-state fMRI study.** *Neuroimage* 2012;59:511–18 CrossRef Medline
17. Zhang K, Johnson B, Gay M, et al. **Default mode network in concussed individuals in response to the YMCA physical stress test.** *J Neurotrauma* 2012;29:756–65 CrossRef Medline
18. Sours C, George EO, Zhuo J, et al. **Hyper-connectivity of the thalamus during early stages following mild traumatic brain injury.** *Brain imaging Behav* 2015;9:550–63 CrossRef Medline
19. Lu L, Zhang J, Li F, et al. **Aberrant static and dynamic functional network connectivity in acute mild traumatic brain injury with cognitive impairment.** *Clin Neuroradiol* 2022;32:205–14 CrossRef Medline
20. Irimia A, Maher AS, Chaudhari NN, et al; Alzheimer's Disease Neuroimaging Initiative. **Acute cognitive deficits after traumatic brain**

- injury predict Alzheimer's disease-like degradation of the human default mode network. *Geroscience* 2020;42:1411–29 CrossRef Medline
21. Banks SD, Coronado RA, Clemons LR, et al. **Thalamic functional connectivity in mild traumatic brain injury: longitudinal associations with patient-reported outcomes and neuropsychological tests.** *Arch Phys Med Rehabil* 2016;97:1254–61 CrossRef Medline
 22. Slobounov S, Gay M, Zhang K, et al. **Alteration of brain functional network at rest and in response to YMCA physical stress test in concussed athletes: rs-fMRI study.** *Neuroimage* 2011;55:1716–27 CrossRef Medline
 23. Xiong K, Zhang J, Zhang Y, et al. **Brain functional connectivity and cognition in mild traumatic brain injury.** *Neuroradiology* 2016;58:733–39 CrossRef Medline
 24. Li F, Lu L, Shang S, et al. **Disrupted functional network connectivity predicts cognitive impairment after acute mild traumatic brain injury.** *CNS Neurosci Ther* 2020;26:1083–91 CrossRef Medline
 25. Lv H, Wang Z, Tong E, et al. **Resting-state functional MRI: everything that nonexperts have always wanted to know.** *AJNR Am J Neuroradiol* 2018;39:1390–99 CrossRef Medline
 26. Carroll L, Cassidy J, Holm L, et al; WHO Collaborating Centre Task Force on Mild Traumatic Brain Injury. **Methodological issues and research recommendations for mild traumatic brain injury: the WHO Collaborating Centre Task Force on Mild Traumatic Brain Injury.** *J Rehabil Med* 2004;43:113–25 CrossRef Medline
 27. McCrory P, Meeuwisse WH, Aubry M, et al. **Consensus statement on concussion in sport: the 4th International Conference on Concussion in Sport, Zurich, November 2012.** *J Athl Train* 2013;48:554–75 CrossRef Medline
 28. Guskiewicz KM, Register-Mihalik J, McCrory P, et al. **Evidence-based approach to revising the SCAT2: introducing the SCAT3.** *Br J Sports Med* 2013;47:289–93 CrossRef Medline
 29. Whitfield-Gabrieli S, Nieto-Castanon A. **CONN: a functional connectivity toolbox for correlated and anticorrelated brain networks.** *Brain Connect* 2012;2:125–41 CrossRef Medline
 30. Fonov V, Evans AC, Botteron K, et al; Brain Development Cooperative Group. **Unbiased average age-appropriate atlases for pediatric studies.** *Neuroimage* 2011;54:313–27 CrossRef Medline
 31. Behzadi Y, Restom K, Liu J, et al. **A component based noise correction method (CompCor) for BOLD and perfusion based fMRI.** *Neuroimage* 2007;37:90–101 CrossRef Medline
 32. Yeo BT, Krienen FM, Sepulcre J, et al. **The organization of the human cerebral cortex estimated by intrinsic functional connectivity.** *J Neurophysiol* 2011;106:1125–65 CrossRef Medline
 33. Power JD, Cohen AL, Nelson SM, et al. **Functional network organization of the human brain.** *Neuron* 2011;72:665–78 CrossRef Medline
 34. Desikan RS, Ségonne F, Fischl B, et al. **An automated labeling system for subdividing the human cerebral cortex on MRI scans into gyral based regions of interest.** *Neuroimage* 2006;31:968–80 CrossRef Medline
 35. Tzourio-Mazoyer N, Landeau B, Papathanassiou D, et al. **Automated anatomical labeling of activations in SPM using a macroscopic anatomical parcellation of the MNI MRI single-subject brain.** *Neuroimage* 2002;15:273–89 CrossRef Medline
 36. Alahmadi AA. **Effects of different smoothing on global and regional resting functional connectivity.** *Neuroradiology* 2021;63:99–109 CrossRef Medline
 37. Zou QH, Zhu CZ, Yang Y, et al. **An improved approach to detection of amplitude of low-frequency fluctuation (ALFF) for resting-state fMRI: fractional ALFF.** *J Neurosci Methods* 2008;172:137–41 CrossRef Medline
 38. Zalesky A, Fornito A, Bullmore ET. **Network-based statistic: identifying differences in brain networks.** *Neuroimage* 2010;53:1197–207 CrossRef Medline
 39. Smith SM, Nichols TE. **Threshold-free cluster enhancement: addressing problems of smoothing, threshold dependence and localisation in cluster inference.** *Neuroimage* 2009;44:83–98 CrossRef Medline
 40. Shi J, Teng J, Du X, et al. **Multi-modal analysis of resting-state fMRI data in mTBI patients and association with neuropsychological outcomes.** *Front Neurol* 2021;12:639760 CrossRef Medline
 41. Vergara VM, Mayer AR, Kiehl KA, et al. **Dynamic functional network connectivity discriminates mild traumatic brain injury through machine learning.** *Neuroimage Clin* 2018;19:30–37 CrossRef Medline
 42. Zhan J, Gao L, Zhou F, et al. **Decreased regional homogeneity in patients with acute mild traumatic brain injury: a resting-state fMRI study.** *J Nerv Ment Dis* 2015;203:786–91 CrossRef Medline
 43. van der Horn HJ, Liemburg EJ, Scheenen ME, et al. **Graph analysis of functional brain networks in patients with mild traumatic brain injury.** *PLoS One* 2017;12:e0171031 CrossRef Medline
 44. Hou W, Sours Rhodes C, Jiang L, et al. **Dynamic functional network analysis in mild traumatic brain injury.** *Brain Connect* 2019;9:475–87 CrossRef Medline
 45. Boroda E, Armstrong M, Gilmore CS, et al. **Network topology changes in chronic mild traumatic brain injury (mTBI).** *Neuroimage Clin* 2021;31:102691 CrossRef Medline
 46. Nathan DE, Bellgowan JF, Oakes TR, et al. **Assessing quantitative changes in intrinsic thalamic networks in blast and nonblast mild traumatic brain injury: implications for mechanisms of injury.** *Brain Connect* 2016;6:389–402 CrossRef Medline
 47. Arciniega H, Shires J, Furlong S, et al. **Impaired visual working memory and reduced connectivity in undergraduates with a history of mild traumatic brain injury.** *Sci Rep* 2021;11:2789–13 CrossRef Medline
 48. Marek S, Tervo-Clemmens B, Calabro FJ, et al. **Reproducible brain-wide association studies require thousands of individuals.** *Nature* 2022;603:654–60 CrossRef Medline
 49. Vergara VM, Mayer AR, Damaraju E, et al. **Detection of mild traumatic brain injury by machine learning classification using resting state functional network connectivity and fractional anisotropy.** *J Neurotrauma* 2017;34:1045–53 CrossRef Medline
 50. Vergara VM, Damaraju E, Mayer AB, et al. **The impact of data pre-processing in traumatic brain injury detection using functional magnetic resonance imaging.** *Annu Int Conf IEEE Eng Med Biol Soc* 2015;2015:5432–35 CrossRef Medline
 51. Storey JD, Tibshirani R. **Statistical significance for genomewide studies.** *Proc Natl Acad Sci U S A* 2003;100:9440–45 CrossRef Medline
 52. Efron B. **Correlation and large-scale simultaneous significance testing.** *J Am Stat Assoc* 2007;102:93–103 CrossRef
 53. Frati A, Cerretani D, Fiaschi AI, et al. **Diffuse axonal injury and oxidative stress: a comprehensive review.** *Int J Mol Sci* 2017;18:2600 CrossRef Medline

Reduced Cortical Thickness Correlates of Cognitive Dysfunction in Post-COVID-19 Condition: Insights from a Long-Term Follow-up

Rosalía Dacosta-Aguayo,  Josep Puig, Noemi Lamonja-Vicente, Meritxell Carmona-Cervelló, Brenda Biaani León-Gómez, Gemma Monté-Rubio, Victor M. López-Linfante, Valeria Zamora-Putin, Pilar Montero-Alia, Carla Chacon, Jofre Bielsa,  Eduard Moreno-Gabriel,  Rosa Garcia-Sierra, Alba Pachón, Anna Costa, Maria Mataró, Julia G. Prado, Eva Martínez-Cáceres, Lourdes Mateu, Marta Massanella, Concepción Violán, and Pere Torán-Monserrat for the Aliança ProHEpiC-19 CognitIU (The APC Collaborative Group)



ABSTRACT

BACKGROUND AND PURPOSE: There is a paucity of data on long-term neuroimaging findings from individuals who have developed the post-coronavirus 2019 (COVID-19) condition. Only 2 studies have investigated the correlations between cognitive assessment results and structural MR imaging in this population. This study aimed to elucidate the long-term cognitive outcomes of participants with the post-COVID-19 condition and to correlate these cognitive findings with structural MR imaging data in the post-COVID-19 condition.

MATERIALS AND METHODS: A cohort of 53 participants with the post-COVID-19 condition underwent 3T brain MR imaging with T1 and FLAIR sequences obtained a median of 1.8 years after Severe Acute Respiratory Syndrome coronavirus 2 (SARS-CoV-2) infection. A comprehensive neuropsychological battery was used to assess several cognitive domains in the same individuals. Correlations between cognitive domains and whole-brain voxel-based morphometry were performed. Different ROIs from FreeSurfer were used to perform the same correlations with other neuroimaging features.

RESULTS: According to the Frascati criteria, more than one-half of the participants had deficits in the attentional (55%, $n = 29$) and executive (59%, $n = 31$) domains, while 40% ($n = 21$) had impairment in the memory domain. Only 1 participant (1.89%) showed problems in the visuospatial and visuoconstructive domains. We observed that reduced cortical thickness in the left parahippocampal region ($t(48) = 2.28, P = .03$) and the right caudal-middle-frontal region ($t(48) = 2.20, P = .03$) was positively correlated with the memory domain.

CONCLUSIONS: Our findings suggest that cognitive impairment in individuals with the post-COVID-19 condition is associated with long-term alterations in the structure of the brain. These macrostructural changes may provide insight into the nature of cognitive symptoms.

ABBREVIATIONS: BMI = body mass index; COVID-19 = coronavirus disease 2019; PCC = post-COVID-19 condition; reproa = Reproducibility Analysis; SARS-CoV-2 = Severe Acute Respiratory Syndrome coronavirus 2; WAIS = Wechsler Adult Intelligence Scale; WHO = World Health Organization

Post-COVID-19 condition (PCC) refers to the persistent and multisystemic symptoms that some individuals develop after infection with Severe Acute Respiratory Syndrome coronavirus 2 (SARS-CoV-2), even if they experienced an asymptomatic or

mild coronavirus 2019 (COVID-19). Recent studies indicate that 5% and 30% of COVID-19 survivors of the first, second, and third waves and about 65% of those hospitalized due to the disease may have the PCC.¹⁻³ According to the World Health

Received September 19, 2023; accepted after revision January 3, 2024.

From the Institut Universitari d'Investigació en Atenció Primària Jordi Gol (IDIAP Jordi Gol) (R.D.-A., N.L.-V., M.C.-C., B.B.L.-G., V.M.L.-L., V.Z.-P., P.M.-A., C.C., J.B., E.M.-G., R.G.-S., A.P., A.C., C.V., P.T.-M.), Unitat de Suport a la Recerca Metropolitana Nord, Mataró, Spain; Department of Clinical Psychology and Psychobiology (R.D.-A., M.M.), University of Barcelona, Barcelona, Spain. Institut de Neurociències, University of Barcelona, Barcelona, Spain. Institut de Recerca Sant Joan de Déu, Esplugues de Llobregat, Spain; Comparative Medicine and Bioimaging Center (J.P., G.M.-R.), Germans Trias i Pujol Research Institute, Badalona, Spain; Department of Radiology (IDI) (J.P.), IDIBGI Hospital Universitari de Girona Doctor Josep Trueta, Girona, Spain; Multidisciplinary Research Group in Health and Society (N.L.-V., V.M.L.-L., P.M.-A., E.M.-G., R.G.-S., P.T.-M.), Institut Universitari d'Investigació en Atenció Primària Jordi Gol, Barcelona, Spain; Palau-Solità Healthcare Centre (V.M.L.-L., V.Z.-P.), Palau-Solità Plegamans Institut Català de la Salut, Barcelona, Spain; Department of Medicine (V.M.L.-L., E.M.-C.), Universitat Autònoma de Barcelona, Cerdanyola de Vallès, Bellaterra, Spain; Grup de Recerca en Impacte de les Malalties Cròniques i les seves Trajectòries (C.C., C.V.), Institut Universitari d'Investigació en Atenció Primària Jordi Gol, Barcelona, Spain. Germans Trias i Pujol Research Institute, Badalona, Spain; Department of Social Psychology (E.M.-G.), Universitat Autònoma de Barcelona, Cerdanyola de Vallès, Bellaterra, Spain; Nursing Department, Faculty of

Medicine (R.G.-S.), Universitat Autònoma de Barcelona, Barcelona, Spain; IrsiCaixa-AIDS Research Institute and Germans Trias i Pujol Health Research Institute (J.G.P., M.M.), Can Ruti Campus, Badalona, Spain; Centro de Investigación Biomédica en Red de Enfermedades Infecciosas (J.G.P., L.M., M.M.), Instituto de Salud Carlos III, Madrid, Spain; Germans Trias i Pujol Research Institute (J.G.P., E.M.-C., L.M., M.M., C.V., P.T.-M.), Can Ruti Campus, Badalona, Spain; Immunology Department (E.M.-C.), FOCIS Center of Excellence, Universitat Autònoma de Barcelona, Cerdanyola del Vallès, Spain; Immunology Division, Laboratori Clinic Metropolitana Nord (E.M.-C.), Hospital Universitari Germans Trias i Pujol, Badalona, Spain; Infectious Diseases Department (L.M.), Fight against AIDS Foundation (FLS), Germans Trias i Pujol Hospital, Can Ruti Campus, Badalona, Spain; Red Española de Investigación en Covid Persistente (L.M., M.M.), European Innovation and Collaboration Programme, Badalona, Spain; Red de Investigación en Cronicidad (C.V.), Atención Primaria y Prevención y Promoción de la Salud (RICAPPS), Instituto de Salud Carlos III, Madrid, Spain; Universitat Autònoma de Barcelona (C.V.), Bellaterra, Spain; and Department of Medicine (P.T.-M.), Faculty of Medicine, Universitat de Girona, Girona, Spain.

This research was funded by grant No. SLT0020/6_14 and in the call for grants corresponding to the year 2021 of the Strategic Plan for Research and Innovation in Health 2016-2020, modality research projects oriented to primary care, with file code

Organization (WHO) criteria, the PCC occurs in individuals with a history of probable or confirmed SARS CoV-2 infection, usually 3 months after the onset of COVID-19 with symptoms that last for at least 2 months and cannot be explained by an alternative diagnosis.⁴ Common symptoms include fatigue, shortness of breath, and cognitive dysfunction, all of which negatively impact daily functioning. After initial recovery from an acute COVID-19 episode, symptoms may manifest for the first time or persist from the initial illness. In addition, symptoms may fluctuate or relapse across time.⁵

According to a recent study, previous COVID-19 infection might have caused at least 1 incident condition in 20% of the survivors 18–64 years of age and in 25% of the survivors 65 years of age or older.⁶ This finding significantly impacts their quality of life. Various mechanisms have been speculated to contribute to the impairment of the CNS. Different pathophysiologic mechanisms have been proposed to explain these changes.^{6,7}

Several studies have documented the cognitive impact of SARS-CoV-2 infection, but the underlying brain changes are still unclear.⁸ Few studies have performed a comprehensive neuropsychologic assessment in patients recovered from COVID-19 with objective cognitive symptoms; this assessment could provide valuable insight into the cognitive impact of the infection. The most common cognitive impairments objectified by COVID-19 with the PCC are in attention, memory, and executive functions.^{8,10-14}

Few studies have performed associations between brain alterations and cognitive deficits.^{8,15-16} Furthermore, there is a paucity of data on the long-term neuroimaging findings related to cognitive function in individuals who develop the PCC; this information could shed light on the pathophysiology and prognosis of these patients. The structural changes in GM volume, which may explain these cognitive deficits, are inconsistent across studies. Some studies have reported reduced GM volume in the hippocampus after a mean of 11 months postinfection compared with noninfected controls.^{8,15} The hippocampus is involved in memory formation and consolidation.¹⁷⁻²⁰ Another study found that patients with the PCC with fatigue had lower GM volume in the left thalamus, putamen, and pallidum, which is related to attention and short-term memory.²¹ On the other hand, 1 study observed an increased GM volume in the thalamus and the hippocampus, but a decrease in the cortical regions in patients with the PCC.²² None of these studies evaluated associations between MR imaging findings and the cognitive assessment outcomes. Other studies found no significant difference in GM volume between patients having acquired COVID-19 and noninfected controls having acquired SARS-CoV-2. Those studies were conducted between 2 and 11 months after SARS-CoV-2 infection.^{8,23-26} No studies have been conducted nearly 2 years after the first

SARS-CoV-2 infection in patients with persistent cognitive symptoms.

The aim of the present study was to elucidate the long-term cognitive outcomes of participants with the PCC.

MATERIALS AND METHODS

Standard Protocol Approvals, Registrations, and Patient Consents

The research project followed the ethics standards and guidelines of the ethics committee of the Foundation University Institute for Primary Health Care Research Jordi Gol i Gurina, which approved the study protocol (reference 21/220-P). The participants were informed of the objectives, procedures, risks, and benefits of the study, and they provided written consent to participate and share their data for research purposes. The data were pseudonymized using a numeric coding system and stored securely in a REDcap database (<https://www.project-redcap.org/>). All procedures were conducted according to good clinical practices and the General Data Protection Regulation 2016/679 on data protection and privacy for all individuals within the European Union.

Study Population

The Aliança ProHEpiC Cognitiu study (The APC Study) aims to investigate the cognitive and neural effects of COVID-19 infection in different groups of individuals. The study includes participants who have persistent symptoms after recovering from COVID-19 with and without cognitive symptoms, as well as participants who were infected but did not develop the PCC and uninfected participants.²⁷ In this report, we present the structural MR imaging data of a subsample that underwent brain imaging and cognitive assessment as part of the study.

This cross-sectional study involved 53 participants who had the PCC with cognitive symptoms after recovering from COVID-19. They were recruited from primary health centers and hospitals in Northern Barcelona (Spain) between August 1, 2020, and March 2023. The study followed the WHO criteria for confirming the PCC diagnosis.⁴ The participants also had to be at least 12 weeks postinfection and between 20 and 70 years of age. The study excluded those with pre-existing psychiatric, neurologic, or neurodevelopmental disorders that could cause cognitive deficits, those with a history of drug or alcohol abuse or a life expectancy of <6 months, and those who could not undergo MR imaging due to medical contraindication or claustrophobia.

Study Procedure

The study collected data from the participants in 2 sessions. In the first session, participants provided sociodemographic information: sex (male, female), age (in years), education level (elementary, secondary, high school, university degree, specialist or master, doctorate), job field (doctor, nurse, health services, health assistants, other), weight (kilograms), height (centimeters), body mass index (BMI) (according to the WHO standards):²⁸ underweight, normal weight, overweight, obesity class I, obesity class II, obesity class III, high blood pressure (Yes, No), cholesterol (Yes, No), diabetes (Yes, No), tobacco (never, smoker, ex-smoker), and alcohol consumption (Yes, No). During this first session, all

SLT002/000055 of the Departament de Salut. Generalitat de Catalunya. This study is also supported, in part, by grants from National Health Institute Carlos III COV20/00660 to J.G.P. and by the CIBER–Consorcio Centro de Investigación Biomédica en Red (CB 2021), Instituto de Salud Carlos III, Ministerio de Ciencia e Innovación and Unión Europea, Next Generation EU. M. Mataró is supported by ICREA Academia program. M. Mataró acknowledge research funding by a “Ramón y Cajal” contract (RYC2020-028934-I/AEI/10.13039/501100011033) from the Spanish Ministry of Science and Innovation.

The funder had no role in the study design, data collection, data analysis, data interpretation, or writing of this work.

Please address correspondence to Concepción Violán, MD, CAP La Llàntia, Mare de Déu de Guadalupe, 2-planta 1, Mataró, Barcelona, Spain; e-mail: cviolanf.mnics@gencat.cat

 Indicates article with online supplemental data.

<http://dx.doi.org/10.3174/ajnr.A8167>

participants completed a comprehensive neuropsychological assessment (see below). They also reported their COVID-19 experience (date and method of diagnosis, clinical spectrum including symptoms and treatment). In the second session, individuals with a PCC underwent a brain MR imaging within 6 months from the cognitive assessment. To protect the privacy of our participants, we used cryptographic hashtags to anonymize the project database. We also used the same 10-digit numeric encoding system hosted by REDCap, Version 12.4.22, Vanderbilt University, for the MR imaging study.

Cognitive Assessment

The cognitive domains of executive function, attention and processing speed, memory, language, and visuospatial and visuoconstructive functions were evaluated by a comprehensive neuropsychological battery administered by a trained, qualified clinical neuropsychologist with >5 years of experience in the assessment of neurologic disorders and a psychologist carefully trained and supervised by the same clinical neuropsychologist. The cognitive tests used for each domain were as follows: for executive functions, the Digit Span Backward subtest from the Wechsler Adult Intelligence Scale 3rd edition (WAIS-III),^{29,30} (a difference score [B-A] that removed the speed element from the test evaluation was calculated);³¹ the phonetic (letters beginning with P, M, and R, 1 minute each) and semantic verbal fluency tests (“animals” in 1 minute);^{32,33} and the interference score of the Color-Word Stroop Test;³⁴ for attention and velocity, the Digit Span Forward subtest,^{29,30} the Symbol Search from the WAIS-III,³⁵ the Trail-Making Test-A,^{29,30} and the Symbol Digit Technique Test (WAIS-III),³² for memory, the total learning and delayed recall from the Rey Auditory Verbal Learning Test³⁶ and the delayed recall from the Rey Osterrieth complex figure (ROCF);^{37,38} for language, the short version of the Boston Naming Test³⁹ and the vocabulary test from the WAIS-III;³⁵ and for visuospatial and visuoconstructive functions, the copy accuracy of the ROCF.^{37,38} Fatigue was assessed with the Modified Impact Fatigue Scale. This scale includes 3 subscales: cognitive, physical, and psychosocial. In this scale, participants are asked to rate the extent of fatigue in their life in the past 4 weeks, with 0 indicating no problem and 4 indicating extreme problem. There are a total of 21 items, 10 cognitive items, 9 physical items, and 2 psychosocial items. The maximum score is 76, forty for the cognitive subscale, 28 for the physical subscale, and 8 for the psychosocial scale, with a score higher than 38 meaning significant fatigue.⁴⁰

Criteria for Cognitive Impairment

We used the Frascati criteria⁴¹ to assess cognitive impairment in participants with the PCC because there is no widely accepted standard for this population. According to these criteria, patients have cognitive impairment if they score below -1.5 SD on any subtest within a cognitive domain or below -1 SD on 2 subtests of the same cognitive domain.

Neuroimaging

Neuroradiologic Assessment of the Structural MRIs. The assessment was conducted by the neuroradiologist, who has 21 years of expertise, primarily aimed at excluding the presence of brain

lesions. This exclusion was achieved through the examination of T1-weighted, FLAIR, and diffusion sequences, with a specific focus on identifying regions of encephalomalacia due to trauma or previous surgical interventions, territorial vascular infarctions, lacunes, or brain tumors. No incidental findings were identified that needed specific medical attention or further secondary testing in our cohort.

A total of 5 individuals had isolated and nonspecific hyperintensity in the supratentorial, subcortical WM. These hyperintensities did not correspond to lacunar infarcts and were not considered for the analysis of cerebral cortical thickness.

A clinical neuroradiologist performed an initial assessment to ensure that none of the 53 participants showed ischemic pathology or other macrostructural injuries.

MR Imaging Acquisition Protocol. All images were acquired on a Vantage Galan 3T MR imaging (Canon Medical Systems) at the Center for Comparative Medicine and Bioimage Image (Germans Trias i Pujol Research Institute, Badalona, Spain) using a 32-channel head SPEEDER coil (AcanMed) with foam padding and headphones to limit head movement and suppress scanner noise. The MR imaging protocol included a 3D MPRAGE T1-weighted sequence acquired in the sagittal plane (TR = 2000 ms; TE = 2.7 ms; 158 slices; section thickness = 1 mm; no gap; matrix = 256×256 ; in-plane resolution = 1×1 ; TI = 900 ms; flip angle = 15° ; FOV = 256×256 mm; and voxel size = $1 \times 1 \times 1$ mm³; seven minutes and 50 seconds), and a FLAIR image, also in the sagittal plane (TR = 5000 ms; TE = 504 ms; 72 slices; section thickness = 1 mm; no gap; matrix = 256×256 ; in-plane resolution = 1×1 ; TI = 1500 ms; flip angle = 15° ; FOV = 256×256 mm; voxel size = $1 \times 1 \times 1$ mm³; five minutes and 15 seconds).

MR Imaging Analysis

FreeSurfer Analysis. We used FreeSurfer, Version 7.3.2 (<http://surfer.nmr.mgh.harvard.edu>) to analyze MR imaging data. This software reconstructs gray/white matter and pial surfaces and measures cortical thickness based on intensity and continuity information from MR imaging volumes. It also segments the whole brain and measures subcortical volumes.⁴² We used T1 and FLAIR images for FreeSurfer parcellation, which improve its reliability and robustness. We still had issues with the skull-stripping for some participants, which has been amended using `mri_gcut` (https://surfer.nmr.mgh.harvard.edu/fswiki/mri_gcut) in FreeSurfer. We also visually inspected the final parcellations for all participants and found no error or artifactual parcellation. We focused our analyses on 46 anatomic ROIs (Online Supplemental Data).

GM and WM Preprocessing Protocol. We used Reproducibility Analysis (reproa, <https://github.com/reprostat/reproanalysis>), a neuroimaging pipeline written in Matlab (MathWorks) to process MR imaging data, which commands SPM12 (Statistical Parametric Mapping; <https://www.fil.ion.ucl.ac.uk/spm/>) functions. We first aligned the 3D T1 image to the Montreal Neurological Institute template and then aligned the FLAIR image to the previously registered 3D T1 image using a 6 *df* linear transformation. We applied multichannel segmentation (SPM12,

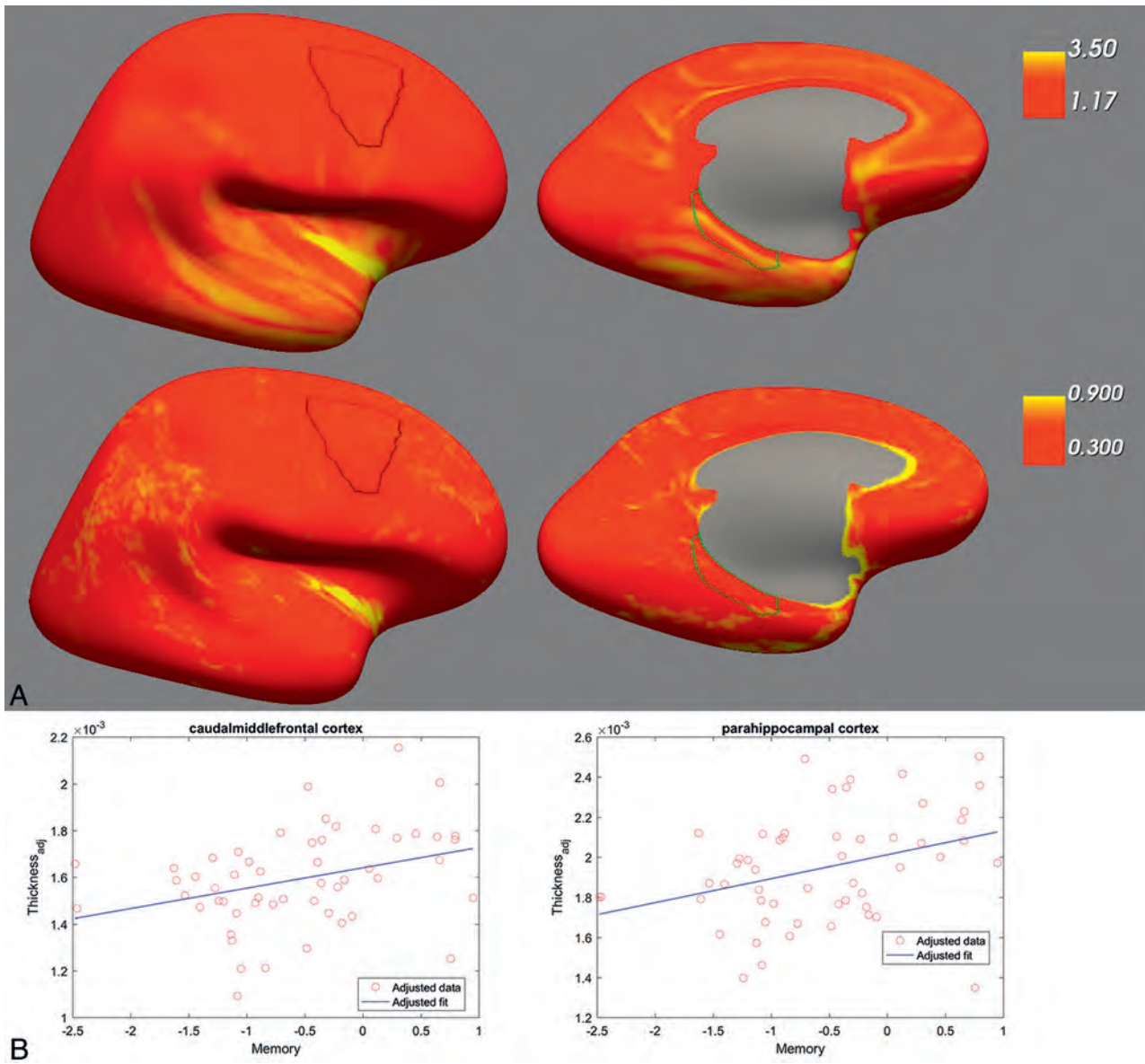


FIGURE A, FreeSurfer view of the cortical thickness estimates averaged across the whole sample of 53 participants. The *left image* shows the right caudal-middle frontal region, and the *right image* shows the left parahippocampal region. The *upper row* shows the mean estimates, and the *lower row* shows the SD. **B**, Relationship between the (adjusted) cortical thickness (in millimeters) and the performance in the memory domain (in z scores) as estimated by the linear regression model.

“Unified Segmentation and Normalization”) to the aligned 3D T1 and FLAIR images to obtain 6 tissue classes: GM volume, WM volume, CSF, bone, soft tissue, and residual noise. We used Diffeomorphic Anatomical Registration Through Exponentiated Lie Algebra Toolbox (DARTEL, part of SPM) to register the GM and WM images from native space to a custom standard space. We then normalized the group template to the Montreal Neurological Institute template using an affine transformation and applied the combined normalization parameters to each participant’s GM and WM images, preserving density estimates. For voxel-based morphometry analysis, we scaled the normalized GM and WM images by the total tissue volume and smoothed them with an 8-mm full width at half maximum Gaussian kernel. The estimated GM and WM templates were further corrected for intracranial volume.

Statistical Analysis. Statistical analyses on demographic data were performed with the Statistical Package for the Social Sciences, Version 17.0 for Windows (SPSS; IBM). The distributions of demographic variables were tested for normality using the Shapiro-Wilk test. Continuous variables were expressed as mean (SD) or median and interquartile range. Categorical variables were defined as frequencies and percentages. Cognitive tests were z scored before the analysis, considering age and years of education for the main tests. We used the model comparison to test whether a linear model including the BMI could explain individual variation in global GM.

We extracted the volumes and cortical thickness of 46 regions from the FreeSurfer output (Online Supplemental Data), and we normalized them by total intracranial volume. We then performed multiple linear regression analyses to test the relationship between

the normalized volumes and the cognitive performance for each cognitive domain. We controlled for sex, age, and years of education. We also tested whether including the BMI improved the model. We corrected for multiple testing using a false discovery rate at a threshold of $q = 0.05$, corresponding to a significance level of $P = .033$.

To examine the association between GM volume and WM volume and cognitive domains, we used the Randomize tool (Version 2.1; www.fmrib.ox.ac.uk/fsl/randomize/index.html) from the FMRIB Software Library (FSL; <http://www.fmrib.ox.ac.uk/fsl>), which performs permutation tests on voxel-based morphometry data.⁴³ We set the permutations to 10,000 and applied the tool to the GM and WM templates generated by *reproa*.⁴⁴ We constructed a general linear model to identify the brain regions in which GM and WM volumes were significantly related to the cognitive domains. We applied threshold-free cluster enhancement to correct for multiple comparisons. We also included age, sex, and years of education as covariates in the model.

RESULTS

Demographic and Clinical Characteristics

The results of the demographic and clinical characteristics are summarized in the Online Supplemental Data. The sample consisted of 53 individuals mainly with a history of mild COVID-19 infection, with a mean age of 48.23 (SD, 9.2) years and a mean education level of 14.04 (SD, 2.6) years. Most participants were women (88.7%) and had a mild-moderate clinical spectrum of COVID-19 (81.1%). Only 17% of the participants required hospitalization in the acute phase due to COVID-19. The most common vascular risk factors of the sample were smoking (current or former, 44.2%) and alcohol consumption (40.4%). According to the WHO standards, 34% of the participants were overweight (BMI = 25–29.9), 13.2% were obese (BMI 30–34.9), and 13.2% were extremely obese (BMI ≥ 35). The mean time since the diagnosis of COVID-19 was 1.8 years.

The Online Supplemental Data summarize the self-reported symptoms experienced by participants with the PCC at the time of evaluation. The most common symptoms were weakness (92.5%), discomfort, and fatigue (83%), followed by nonspecific insomnia (80%), muscle pain (71.9%), vertigo and dizziness (71.2%), and tingling sensations (66.7%). The most common cognitive symptoms were difficulty with concentration and memory (96.2%), followed by brain fog (84.9%); 92.5% of the sample scored > 38 points on the Modified Impact Fatigue Scale, which measures fatigue, indicating significant fatigue.

Cognitive Characteristics

The results of the neuropsychological tests are summarized in the Online Supplemental Data. We found that cognitive tests showing the most impairment, with scores below -1.5 SD, were semantic verbal fluency (41.5%), phonologic verbal fluency (32.1%), and digit span forward (33%). When we considered cognitive domains and following the Frascati criteria, the cognitive domains showing the most impairment were executive function (58.5%), attention and processing speed (54.7%), and memory (39.6%). Only 1 participant showed problems in the visuospatial and visuoconstructive functions (1.9%). None had difficulty in the language domain.

GM and WM Voxel-Based Morphometry Results (*Reproa*)

We did not find any significant corrected result in the correlations between GM or WM volume and cognitive symptoms.

Adding the BMI to the regression model led to a nonsignificant increase in the log likelihood ($\chi^2(1) = 1.6569$, $P = .198$), indicating that the BMI does not account for the additional variance of the global GM. Thus, BMI was omitted as a covariate from the general linear model. Also, according to the Akaike and Bayesian information criteria, the model without the BMI was a better fit (Akaike Information Criterion: 1455.55 versus 1455.89 and Bayesian Information Criterion: 1463.43 versus 1465.74 for the model without and with BMI, respectively).

Cortical Thickness (*FreeSurfer*)

The regression analysis showed that lower memory performance was significantly associated with a decrease of the cortical thickness of 2 brain regions after adjusting for total intracranial volumes, sex and age, ROIs, and the number of cognitive domains tested. The results indicate that 1 SD decrease in memory performance is associated with 0.20- μm and 0.09- μm reductions in the left parahippocampal (adjusted $r^2 = 0.3$, $b = 1.20 \times 10^{-4}$; $CI_b = 0.14 \times 10^{-4}$; 2.25×10^{-4} , $t(48) = 2.28$, $P = .03$) and the right caudal-middle-frontal (adjusted $r^2 = 0.27$, $b = 0.87 \times 10^{-4}$; $CI_b = 0.08 \times 10^{-4}$; 1.67×10^{-4} , $t(48) = 2.20$, $P = .033$) regions, respectively (Figure).

DISCUSSION

The current study examined the brain structural changes in 53 participants with the PCC who reported cognitive symptoms nearly 2 years after infection, with an average age of 48.23 years and a predominance of women.

We found that the most common symptoms were weakness, discomfort, and fatigue, followed by nonspecific insomnia, muscle pain, vertigo and dizziness, and tingling sensations. The participants' cognitive symptoms were consistent with those in previously published studies.^{8,10-14} The cognitive tests showing the most impairment were semantic verbal fluency, phonologic verbal fluency, and digit span forward. The cognitive domains showing the most impairment were executive function, attention and processing speed, and memory.

We found that decreased cortical thickness of the left parahippocampal region and the right caudal-middle-frontal region was positively associated with the impairment of the memory domain. Lower scores in this domain were associated with less cortical thickness in these anatomic regions. The parahippocampal part is the medial temporal lobe, and it has been linked to subjective memory symptoms and very early Alzheimer disease.^{45,46} Only 4 studies have investigated the long-term effects of COVID-19 on cortical thickness, with conflicting results. Douaud et al¹⁵ found that reduced GM thickness in the orbitofrontal cortex and the parahippocampal gyrus was associated with cognitive impairment. Sanabria-Díaz et al⁴⁷ reported lower cortical volume in the orbitofrontal, frontal, and cingulate regions but did not assess cognitive function. Petersen et al⁴⁸ found no difference in cortical thickness between patients recovered from COVID-19 versus uninfected matched controls or any association with cognition. Finally, Rothstein²² observed reduced GM thickness in several cortical regions but did not relate this to any cognitive test. It is necessary to investigate the cognitive and brain structural changes

associated with the PCC to gain a better understanding of its nature and to develop cognitive therapies to improve patients' neurocognitive symptoms.

As far as we know, this is the first study to identify macrostructural alterations in a cohort of young and middle-aged individuals almost 2 years after experiencing the PCC, along with cognitive symptoms that persisted and were objectively measured. When we compared these results with the those in the published literature, only 2 studies, conducted by Douaud et al¹⁵ and Díez-Cirarda et al,¹⁶ identified similar findings in the parahippocampal and hippocampal regions, but in an elderly population (51–81 years of age) in the first one and in 1 young middle-aged cohort (50.89 [SD, 11.25] years) in the second one. We also found statistically significant cortical thickness reduction in the right caudal-middle-frontal region. This region involves age-related memory impairment.⁴⁹ Douaud et al¹⁵ found reduced GM thickness in the orbitofrontal cortex. As in our case, it was linked to memory impairment. On the other hand, other studies found reduced cortical thickness in the orbitofrontal and cingulate regions, but its relationship with cognitive function needed clarification because no associations between the MR imaging findings and cognition were conducted.^{22,47}

The fact that we did not find any significant gray or white matter volume alterations does not rule out the possibility of brain changes, as occurs frequently in patients with early-stage Alzheimer disease.⁵⁰ The link between SARS-CoV-2 infection and new-onset autoimmune diseases is strong and covers a wide range of disorders,⁵¹ including myalgic encephalitis and chronic fatigue syndrome.⁵² More specifically, patients with chronic fatigue syndrome and myalgic encephalitis have been reported to experience memory and concentration problems and difficulties in processing complex information.⁵³ Consistently, Thapaliya et al⁵⁴ found cortical thickness reduction in the caudal-middle-frontal region in patients with chronic fatigue syndrome and myalgic encephalitis. Multiple sclerosis has been proposed as a model to study the effects of SARS-CoV-2⁵⁵ as well. In a study conducted by Fujimori et al, in 2021,⁵⁶ the authors found that cortical thickness reduction patterns in MS are mostly characterized by the degree of temporal lobe cortical atrophy, which may start in the relapsing-remitting phase.

Furthermore, the persistent cognitive problems, such as memory loss, confusion, and difficulty concentrating shown in individuals who have the PCC are similar to those experienced by some patients with cancer after undergoing chemotherapy or radiation therapy, a condition known as cancer-related cognitive impairment or “chemo brain,” which targets the hippocampus as well.⁵⁷ Unfortunately, the prognosis for those diseases is often poor.⁵⁸ Last, neurodegenerative diseases with cognitive impairment have been linked to those anatomic regions as well.⁴⁶

We think that the gray and white matter voxel-based morphometry is hampered by the lack of an uninfected SARS-CoV-2 or recovered COVID-19 matched control group, as well as the small sample size.

In addition, we are confident that there must be functional alterations in the brain, because these usually occur before a structural region is affected and account for structural changes.⁵⁹

Our study is strengthened because we are assessing participants with the PCC and cognitive symptoms 1.8 years after the SARS-CoV-2 infection in a relatively young population, and we found brain structural abnormalities associated with objective cognitive symptoms. These abnormalities could not have been detected with conventional MR imaging within the health care system because we used an exhaustive research-oriented MR imaging protocol.

Although this study is one of the most complete, including neuroimaging and cognitive evaluation of patients with the PCC available to date, it also has several limitations. Larger samples should replicate these findings to generalize them to this population type and to include control groups. Future research should address 3 different lines of research: First, this type of MR imaging analysis should be repeated in individuals with the PCC with cognitive symptoms and should compare them with control groups; second, these same studies should be repeated for longer periods to determine whether these structural changes are sustained across time, evolve, or reverse. Finally, cognitive interventions should be tested to assess whether they have a significant impact on cognition and its neural correlates.

CONCLUSIONS

The present study used a comprehensive neuropsychologic battery and a highly specialized MR imaging protocol to investigate brain volumes and cortical thickness and their associations with cognitive function in 53 relatively young participants. Our results showed that the cognitive deficits were associated with changes in brain macrostructure, especially in the left parahippocampal region and the right caudal-middle-frontal region, possibly explaining the cognitive symptoms described by these participants.

ACKNOWLEDGMENTS

The authors would like to sincerely thank the participants for their effort and selfless involvement in the study. In addition, they want to thank the Management Department, Primary Care Directorate, and the Directorate of the Clinical Laboratory of the Metropolitan North for the facilities they have given for the project.

Disclosure forms provided by the authors are available with the full text and PDF of this article at www.ajnr.org.

REFERENCES

1. Ballering AV, van Zon SK, Olde Hartman TC, et al; Lifelines Corona Research Initiative. **Persistence of somatic symptoms after COVID-19 in the Netherlands: an observational cohort study.** *Lancet* 2022; 400:452–61 CrossRef Medline
2. Perlis RH, Santillana M, Ognyanova K, et al. **Prevalence and correlates of long COVID symptoms among US adults.** *JAMA Netw Open* 2022;5:e2238804 CrossRef Medline
3. Bowe B, Xie Y, Al-Aly Z. **Postacute sequelae of COVID-19 at 2 years.** *Nat Med* 2023;29:2347–57 CrossRef Medline
4. Soriano JB, Murthy S, Marshall JC, et al; WHO Clinical Case Definition Working Group on Post-COVID-19 Condition. **A clinical case definition of post-COVID-19 condition by a Delphi consensus.** *Lancet Infect Dis* 2021;22:e102–07 CrossRef Medline
5. Davis HE, Assaf GS, McCorkell L, et al. **Characterizing long COVID in an international cohort: 7 months of symptoms and their impact.** *EClinicalMedicine* 2021;38:101019 CrossRef Medline

6. Bull-Otterson L, Baca S, Saydah S, et al. **Post-COVID conditions among adult COVID-19 survivors aged 18–64 and ≥65 years—United States, March 2020–November 2021.** *MMWR Morb Mortal Wkly Rep* 2022;71:713–17 CrossRef Medline
7. Castanares-Zapatero D, Chalón P, Kohn L, et al. **Pathophysiology and mechanism of long COVID: a comprehensive review.** *Ann Med* 2022;54:1473–87 CrossRef Medline
8. Díez-Cirarda M, Yus M, Gómez-Ruiz N, et al. **Multimodal neuroimaging in post-COVID syndrome and correlation with cognition.** *Brain* 2023;146:2142–52 CrossRef Medline
9. Davis HE, McCorkell L, Vogel JM, et al. **Long COVID: major findings, mechanisms and recommendations.** *Nat Rev Microbiol* 2023;21:133–46 CrossRef Medline
10. Delgado-Alonso C, Valles-Salgado M, Delgado-Álvarez A, et al. **Cognitive dysfunction associated with COVID-19: a comprehensive neuropsychological study.** *J Psychiatr Res* 2022;150:40–46 CrossRef Medline
11. García-Sánchez C, Calabria M, Gruden N, et al. **Neuropsychological deficits in patients with cognitive complaints after COVID-19.** *Brain Behav* 2022;12:e508 CrossRef Medline
12. Voruz P, Allali G, Benzakour L, et al. **Long COVID neuropsychological deficits after severe, moderate, or mild infection.** *Clinical and Translational Neuroscience* 2022;6:9 CrossRef Medline
13. Hadad R, Khoury J, Stanger C, et al. **Cognitive dysfunction following COVID-19 infection.** *J Neurovirol* 2022;28:430–37 CrossRef Medline
14. Ariza M, Cano N, Segura B, et al; NAUTILUS Project Collaborative Group. **COVID-19 severity is related to poor executive function in people with post-COVID conditions.** *J Neurol* 2023;270:2392–408 CrossRef Medline
15. Douaud G, Lee S, Alfaro-Almagro F, et al. **SARS-CoV-2 is associated with changes in brain structure in UK Biobank.** *Nature* 2022;604:697–707 CrossRef Medline
16. Díez-Cirarda M, Yus-Fuertes M, Sanchez-Sanchez R, et al. **Hippocampal subfield abnormalities and biomarkers of pathologic brain changes: from SARS-CoV-2 acute infection to post-COVID syndrome.** *eBioMedicine* 2023;94:104711 CrossRef Medline
17. Lu Y, Li X, Geng D, et al. **Cerebral micro-structural changes in COVID-19 patients: an MRI-based 3-month follow-up study.** *EClinicalMedicine* 2020;25:100484 CrossRef Medline
18. Hafiz R, Gandhi TK, Mishra S, et al. **Higher limbic and basal ganglia volumes in surviving COVID-negative patients and the relations to fatigue.** *Neuroimage Rep* 2022;2:100095 CrossRef Medline
19. Qin Y, Wu J, Chen T, et al. **Long-term microstructure and cerebral blood flow changes in patients recovered from COVID-19 without neurological manifestations.** *J Clin. Invest* 2021;131:147329 CrossRef Medline
20. Tu Y, Zhang Y, Li Y, et al. **Post-traumatic stress symptoms in COVID-19 survivors: a self-report and brain imaging follow-up study.** *Mol Psychiatry* 2021;26:7475–80 CrossRef Medline
21. Heine J, Schwichtenberg K, Hartung TJ, et al. **Structural brain changes in patients with post-COVID fatigue: a prospective observational study.** *EClinicalMedicine* 2023;58:101874 CrossRef Medline
22. Rothstein TL. **Cortical grey matter volume depletion links to neurological sequelae in post COVID-19 “long haulers.”** *BMC Neurol* 2023;23:22 CrossRef Medline
23. Voruz P, Cionca A, Alcántara IJ, et al. **Functional connectivity underlying cognitive and psychiatric symptoms in post-COVID-19 syndrome: is anosognosia a key determinant?** *Brain Commun* 2022;4:fcac057 CrossRef Medline
24. Cecchetti G, Agosta F, Canu E, et al. **Cognitive, EEG, and MRI features of COVID-19 survivors: a 10-month study.** *J Neurol* 2022;269:3400–12 CrossRef Medline
25. Bungenberg J, Humkamp C, Hohenfeld C, et al. **Long COVID-19: objectifying most self-reported neurological symptoms.** *Ann Clin Transl Neurol* 2022;9:141–54 CrossRef Medline
26. Hosp JA, Dressing A, Blazhenets G, et al. **Cognitive impairment and altered cerebral glucose metabolism in the subacute stage of COVID-19.** *Brain* 2021;144:1263–76 CrossRef Medline
27. Dacosta-Aguayo R, Lamonja-Vicente N, Chacón C, et al. **Neurocognitive profile of the post-COVID condition in adults in Catalonia: a mixed method prospective cohort and nested case-control study: study protocol.** *Vaccines (Basel)* 2022;10:849 CrossRef Medline
28. World Health Organization. **“A healthy lifestyle: WHO recommendations,” 06-May-2010.** Available: <https://www.who.int/europe/news-room/fact-sheets/item/a-healthy-lifestyle—who-recommendations>. Accessed June 24, 2023
29. Pena-Casanova J, Quinones-Ubeda S, Quintana-Aparicio M, et al; for the NEURONORMA Study Team. **Spanish Multicenter Normative Studies (NEURONORMA Project): Norms for Verbal Span, Visuospatial Span, Letter and Number Sequencing, Trail Making Test, and Symbol Digit Modalities Test.** *Arch Clin Neuropsychol* 2009;24:321–41 CrossRef Medline
30. Tamayo F, Casals-Coll M, Sánchez-Benavides G, et al. **Estudios normativos españoles en población adulta joven (Proyecto NEURONORMA jóvenes): normas para las pruebas span verbal, span visuoespacial, Letter-Number Sequencing, Trail Making Test y Symbol Digit Modalities Test.** *Neurología* 2012;27:319–29 CrossRef Medline
31. Lezak MD, Howieson DB, Bigler ED, et al. *Neuropsychological Assessment.* 5th ed. Oxford University Press; 2012
32. Pena-Casanova J, Quinones-Ubeda S, Gramunt-Fombuena N, et al; for the NEURONORMA Study Team. **Spanish multicenter normative studies (NEURONORMA Project): norms for verbal fluency tests.** *Arch. Clin. Neuropsychol* 2009;24:395–411 CrossRef
33. Casals-Coll M, Sánchez-Benavides G, Quintana M, et al. **Estudios normativos españoles en población adulta joven (proyecto NEURONORMA jóvenes): normas para los test de fluencia verbal.** *Neurología* 2013;28:33–40 CrossRef Medline
34. Strauss E, Sherman E, Spreen O. *A Compendium of Neuropsychological Tests: Administration, Norms, and Commentary.* Oxford University Press; 2006
35. Wechsler D. **Wechsler Adult Intelligence Scale.** WAIS-III. Pearson. 1997
36. Schmidt M. *Rey Auditory Verbal Learning Test: A Handbook.* Los Angeles (CA): Western Psychological Services; 1996
37. Pena-Casanova J, Gramunt-Fombuena N, Quinones-Ubeda S, et al; for the NEURONORMA Study Team. **Spanish Multicenter Normative Studies (NEURONORMA Project): norms for the Rey-Osterrieth Complex Figure (copy and memory), and Free and Cued Selective Reminding Test** *Arch Clin Neuropsychol* 2009;24:371–93 CrossRef Medline
38. Palomo R, Casals-Coll M, Sánchez-Benavides G, et al. **Spanish normative studies in young adults (NEURONORMA young adults project): norms for the Rey-Osterrieth Complex Figure (copy and memory) and Free and Cued Selective Reminding Test** *Neurología* 2013;28:226–35 CrossRef Medline
39. Kaplan E, Goodglass H, Weintraub S. *Boston Naming Test.* Philadelphia: Lea & Febiger; 1983
40. Strober LB, Bruce JM, Arnett PA, et al. **Tired of not knowing what that fatigue score means? Normative data of the Modified Fatigue Impact Scale (MFIS).** *Mult Scler Relat Disord* 2020;46:102576 CrossRef Medline
41. Gates TM, Cysique LA. **The chronicity of HIV infection should drive the research strategy of NeuroHIV treatment studies: a critical review.** *CNS Drugs* 2016;30:53–69 CrossRef Medline
42. Fischl B. **FreeSurfer.** *Neuroimage* 2012;62:774–81 CrossRef Medline
43. Winkler AM, Ridgway GR, Webster MA, et al. **Permutation inference for the general linear model.** *Neuroimage* 2014;92:381–97 CrossRef Medline
44. Taylor JR, Williams N, Cusack R, et al. **The Cambridge Centre for Ageing and Neuroscience (Cam-CAN) data repository: structural and functional MRI, MEG, and cognitive data from a cross-sectional adult lifespan sample.** *Neuroimage* 2017;144:262–69 CrossRef Medline

45. Meiberth D, Scheef L, Wolfsgruber S, et al. **Cortical thinning in individuals with subjective memory impairment.** *J Alzheimers Dis* 2015;45:139–46 CrossRef Medline
46. Krumm S, Kivisaari SL, Probst A, et al. **Cortical thinning of parahippocampal subregions in very early Alzheimer's disease.** *Neurobiol Aging* 2016;38:188–96 CrossRef Medline
47. Sanabria-Diaz G, Etter MM, Melie-Garcia L, et al. **Brain cortical alterations in COVID-19 patients with neurological symptoms.** *Front Neurosci* 2022;16:992165 CrossRef Medline
48. Petersen M, Nägele FL, Mayer C, et al. **Brain imaging and neuropsychological assessment of individuals recovered from a mild to moderate SARS-CoV-2 infection.** *Proc Natl Acad Sci U S A* 2023;120:e221732120 CrossRef Medline
49. Ferreira D, Molina Y, Machado A, et al. **Cognitive decline is mediated by gray matter changes during middle age.** *Neurobiol Aging* 2014;35:1086–94 CrossRef Medline
50. Josephs KA, Whitwell JL, Ahmed Z, et al. **β -amyloid burden is not associated with rates of brain atrophy.** *Ann Neurol* 2008;63:204–12 CrossRef Medline
51. Sharma C, Bayry J. **High risk of autoimmune diseases after COVID-19.** *Nat Rev Rheumatol* 2023;19:399–400 CrossRef Medline
52. Komaroff AL, Lipkin WI. **Insights from myalgic encephalomyelitis/chronic fatigue syndrome may help unravel the pathogenesis of postacute COVID-19 syndrome.** *Trends Mol Med* 2021;27:895–906 CrossRef Medline
53. Jason LA, Richman JA, Rademaker AW, et al. **A community-based study of chronic fatigue syndrome.** *Arch Intern Med* 1999;159:2129–37 CrossRef Medline
54. Thapaliya K, Marshall-Gradisnik S, Staines D, et al. **Alteration of cortical volume and thickness in myalgic encephalomyelitis/chronic fatigue syndrome.** *Front Neurosci* 2022;16:848730 CrossRef Medline
55. Rebsamen M, Friedli C, Radojewski P, et al. **Multiple sclerosis as a model to investigate SARS-CoV effect on brain atrophy.** *CNS Neurosci Ther* 2023;29:538–43 CrossRef Medline
56. Fujimori J, Fujihara K, Wattjes M, et al. **Patterns of cortical grey matter thickness reduction in multiple sclerosis.** *Brain Behav* 2021;11:e02050 CrossRef Medline
57. Fernández-Castañeda A, Lu P, Geraghty AC, et al. **Mild respiratory COVID can cause multi-lineage neural cell and myelin dysregulation.** *Cell* 2022;185:2452–68.e1668 CrossRef Medline
58. Ghali A, Lacout C, Fortrat J-O, et al. **Factors influencing the prognosis of patients with myalgic encephalomyelitis/chronic fatigue syndrome.** *Diagnostics* 2022;12:2540 CrossRef Medline
59. Cauda F, Nani A, Manuello J, et al. **Brain structural alterations are distributed following functional, anatomic and genetic connectivity.** *Brain* 2018;141:3211–32 CrossRef Medline

Optic Nerve Sheath MR Imaging Measurements in Patients with Orthostatic Headaches and Normal Findings on Conventional Imaging Predict the Presence of an Underlying CSF-Venous Fistula

Wouter I. Schievink, Marcel M. Maya, Angelique Sao-Mai S. Tay, Peyton L. Nisson, Jay Acharya, Rachelle B. Taché, and Miriam Nuño



ABSTRACT

BACKGROUND AND PURPOSE: Spontaneous spinal CSF leaks typically cause orthostatic headache, but their detection may require specialized and invasive spinal imaging. We undertook a study to determine the value of simple optic nerve sheath MR imaging measurements in predicting the likelihood of finding a CSF-venous fistula, a type of leak that cannot be detected with routine spine MR imaging or CT myelography, among patients with orthostatic headache and normal conventional brain and spine imaging findings.

MATERIALS AND METHODS: This cohort study included a consecutive group of patients with orthostatic headache and normal conventional brain and spine imaging findings who underwent digital subtraction myelography under general anesthesia to look for spinal CSF-venous fistulas.

RESULTS: The study group consisted of 93 patients (71 women and 22 men; mean age, 47.5 years; range, 17–84 years). Digital subtraction myelography demonstrated a CSF-venous fistula in 15 patients. The mean age of these 8 women and 7 men was 56 years (range, 23–83 years). The mean optic nerve sheath diameter was 4.0 mm, and the mean perioptic subarachnoid space was 0.5 mm in patients with a CSF-venous fistula compared with 4.9 and 1.2 mm, respectively, in patients without a fistula ($P < .001$). Optimal cutoff values were found at 4.4 mm for optic nerve sheath diameter and 1.0 mm for the perioptic subarachnoid space. Fistulas were detected in about 50% of patients with optic nerve sheath diameter or perioptic subarachnoid space measurements below these cutoff values compared with <2% of patients with optic nerve sheath diameter or perioptic subarachnoid space measurements above these cutoff values. Following surgical ligation of the fistula, optic nerve sheath diameter increased from 4.0 to 5.3 mm and the perioptic subarachnoid space increased from 0.5 to 1.2 mm ($P < .001$).

CONCLUSIONS: Concerns about a spinal CSF leak should not be dismissed in patients with orthostatic headache when conventional imaging findings are normal, and simple optic nerve sheath MR imaging measurements can help decide if more imaging needs to be performed in this patient population.

ABBREVIATIONS: BMI = body mass index; DSM = digital subtraction myelography; ONS = optic nerve sheath; ONSD = optic nerve sheath diameter; OP = opening pressure; SAS = subarachnoid space; SIHDAS = SIH Disability Assessment Score; SIH = spontaneous intracranial hypotension

Orthostatic headaches, ie, headaches that worsen after assuming the upright position and that are least noticeable on awakening in the morning before getting out of bed, are the hallmark of spontaneous intracranial hypotension (SIH).^{1,2} CSF leaks

at the level of the spine are responsible for causing SIH in most patients.¹

The diagnosis of SIH can be made with confidence under the following circumstances: 1) brain MR imaging shows a combination of ≥ 1 of the typical reversible findings of SIH, ie, subdural fluid collections, enhancement of the pachymeninges, engorgement of venous structures, pituitary enlargement, and sagging of the brain (mnemonic, SEEPS); or 2) if spine imaging shows the presence of an extradural CSF collection, indicating a dural tear and CSF leak.^{1,3} An estimated one-fifth of patients with spinal CSF leaks have normal findings on brain imaging.⁴ However, a common type of spontaneous spinal CSF leak, the CSF-venous fistula, is not associated with an extradural spinal CSF collection

Received October 17, 2023; accepted after revision January 4, 2024.

From the Departments of Neurosurgery (W.I.S., A.S.-M.S.T., P.L.N., R.B.T.) and Imaging (M.M.M., J.A.), Cedars-Sinai Medical Center, Los Angeles, California; and Department of Public Health Sciences (M.N.), University of California, Davis, Davis, California.

Please address correspondence to Wouter I. Schievink, MD, Department of Neurosurgery, Cedars-Sinai Medical Center, 127 South San Vicente Blvd, Los Angeles, CA 90048; e-mail: schievinkw@cshs.org; @WouterSchievink

Indicates article with online supplemental data.

<http://dx.doi.org/10.3174/ajnr.A8165>

and thus is not detectable on routine CT myelography or spine MR imaging.¹ These spinal CSF-venous fistulas require specialized imaging with digital subtraction myelography (DSM)^{5,6} or dynamic CT myelography^{6,7} for their detection. In a prior study using DSM, we found that approximately 10% of patients with orthostatic headaches and normal conventional brain and spine imaging findings have an underlying spinal CSF-venous fistula.⁸ Since the completion of that study, we have added MR imaging sequences to our SIH protocol that allow precise measurements of the optic nerve sheath (ONS). The ONS diameter (ONSD) is correlated with CSF pressure and is known to be significantly altered in not only intracranial hypertension but also SIH.⁹⁻¹⁴ However, to our knowledge, the ONSD has not been studied in patients with orthostatic headaches and normal findings on routine brain and spine imaging. The hypothesis of the current study is that ONSD could be affected by the presence of a CSF-venous fistula causing loss of CSF in the setting of otherwise normal brain MR imaging findings.

MATERIALS AND METHODS

This cohort study was approved by the Cedars-Sinai Medical Center institutional review board, who waived the requirement for written informed consent.

The patient population consisted of a consecutive group of patients with orthostatic headaches, normal findings on brain MR imaging, and no evidence of extradural CSF on spine MR imaging with MR myelography,¹⁵ who underwent DSM in the lateral decubitus position between June 2020 and May 2022. The goal of DSM was to identify a spontaneous spinal CSF-venous fistula. Patients who had a history of any prior brain MR imaging or spinal imaging consistent with SIH or spinal CSF leak and patients who did not have a brain MR imaging performed at our institution with the SIH protocol before DSM were excluded from the analysis.

SIH Disability Assessment Score

All patients completed a modified Migraine Disability Assessment Test 5-item questionnaire to assess the severity of the symptoms before and after treatment.¹⁶ This questionnaire measures disability in 3 domains of activity (employment, household work, and nonwork activities), capturing the number of days affected during a 3-month period, with the score ranging from 0 to 270 (3 [domains] × 3 [months] × 30 [days]).¹⁶ The modification consists of substituting “symptoms of SIH” for “headaches.” We refer to this modified questionnaire as the SIH Disability Assessment Score questionnaire. (SIHDAS).¹⁷ A score of 0–5 (grade I) equates to little or no disability, a score of 6–10 (grade II) is mild disability, a score of 11–20 (grade III) is moderate disability, and a score of 21–270 (grade IV) is severe disability.

Brain MR Imaging Protocol

MR imaging was performed on 1.5 or 3T scanners. The SIH brain MR imaging protocol is shown in the Online Supplemental Data. The MR imaging sequences allowing precise measurements of the ONS consisted of coronal fat-suppressed T2-weighted sequences through the orbit (TR = 5750 ms, TE = 99 ms, flip angle = 150°, section thickness = 3.0 mm, section gap = 0%, FOV = 230 mm²).

Definition of Normal Brain MR Imaging Findings

The findings of a normal brain MR imaging were based on the report of 1 of 4 board-certified neuroradiologists, all with a special interest in SIH. For this study, findings of all brain MR imaging designated as normal were re-reviewed by 1 board-certified neuroradiologist who was not involved in the initial interpretation of the brain MR imaging and 1 board-certified neurosurgeon to confirm the absence of the reversible findings of SIH, ie, subdural fluid collections; enhancement and/or thickening of the pachymeninges; venous engorgement using the venous distention sign;¹⁸ pituitary enlargement using the measurements of maximal pituitary height;¹⁹ and brain sagging using a cutoff of 5.5 mm for the pontomammillary distance,²⁰ a cutoff of 45° for the pontomesencephalic angle,²¹ and a cutoff of 5 mm for cerebellar tonsillar herniation. In addition, the absence of infratentorial superficial siderosis²² and calvarial hyperostosis,²³ the 2 mostly irreversible brain MR imaging findings that may be observed in patients with chronic SIH, was confirmed. Any discrepancies were adjudicated by a second board-certified neuroradiologist.

Brain MR Imaging Assessments

The ONSD and perioptic subarachnoid space (Fig 1) were measured by 2 board-certified neuroradiologists and 1 senior neurosurgery resident blinded to the outcome of the DSM. On the basis of prior measurements of ONSD and perioptic subarachnoid space as reported by Rohr et al,²⁴ who found significant variability of these measurements within the first 10 mm of the optic nerve, measurements were made 10–12 mm posterior to the globe. In addition, a previously published and validated probabilistic score for the presence of SIH, known as the Bern score,²⁵ was calculated by the same 2 board-certified neuroradiologists and a senior neurosurgery resident blinded to the outcome of the DSM. Measurements by an individual physician of the ONSD, perioptic subarachnoid space, and Bern score were averaged for the final measurement.

DSM Technique

In all patients, the DSM technique as described by Hoxworth et al²⁶ was used with some minor modifications.^{5,27} Briefly, DSM is performed with the patient under general endotracheal anesthesia with deep paralysis and suspended respiration for maximal detail and temporal resolution. Patients are positioned in the lateral decubitus position in a biplane angiography suite, with tilt table capability. Pillows or foam padding are placed to optimize cervicothoracic alignment. Under fluoroscopic guidance, a 22-ga needle is placed midline, usually at the L2–3 level, being careful to avoid tenting and subdural injection. An opening pressure is obtained at this time. Then, an accurate needle position is confirmed with an injection of 0.5 mL of contrast (Omnipaque 240 or 300 mg/mL; GE Healthcare). Patients are then further positioned on the basis of the area of interest, with the table tilted to achieve contrast flow to the cervicothoracic spine. Finally, contrast is injected manually 1 mL per second, with suspended respiration for 60–75 seconds while acquiring biplane subtraction images at 1–2 frames per second.

Statistical Analysis

Continuous variables are presented as means (SDs) in addition to medians and interquartile ranges. Categorical variables are presented

as absolute numbers and percentages. Comparison of demographic and disease characteristics between groups by fistula status are performed using a *t* test or Mann-Whitney Wilcoxon test for continuous variables, and χ^2 and Fisher exact tests are performed to compare categorical variables. Logistic regression analysis was used to calculate the predicted probability of a fistula. Receiver operating

characteristic curves were used to determine optimal thresholds for perioptic subarachnoid space and the ONSD for the outcome of a fistula. We computed agreement (κ) of the perioptic subarachnoid space, ONSD, and Bern scores among multiple raters implementing the Magree macro (<https://www.agreestat.com/books/sas2/chap3/chap3sas.pdf>) in the subarachnoid space (SAS). Pearson

correlation coefficients were calculated among body mass index (BMI), opening pressure (OP), ONSD, and the perioptic subarachnoid space. All statistical analyses were performed using SAS, Version 9.4 (SAS Institute).

RESULTS

Clinical and Radiographic Characteristics

The mean age of the 93 patients with orthostatic headache was 47.5 (SD, 15.7) years. There were 71 women (76.3%) and 22 men (23.7%). The mean duration of orthostatic headache was 51.2 months (median, 32 months). An occipital or suboccipital headache was the most common, occurring in 43 patients (46.2%). At the onset of symptoms, orthostatic worsening of the headache occurred within 10 minutes in 35 patients (37.6%), between 11 and 60 minutes in 32 patients (34.4%), and after 60 minutes in 26 patients (31.2%).

Lateral decubitus DSM demonstrated a CSF-venous fistula in 15 (16.1%) of the 93 patients. The mean age of the 7 men and 8 women was 56 (14.4 SD) years. There was a less pronounced female preponderance among the patients with

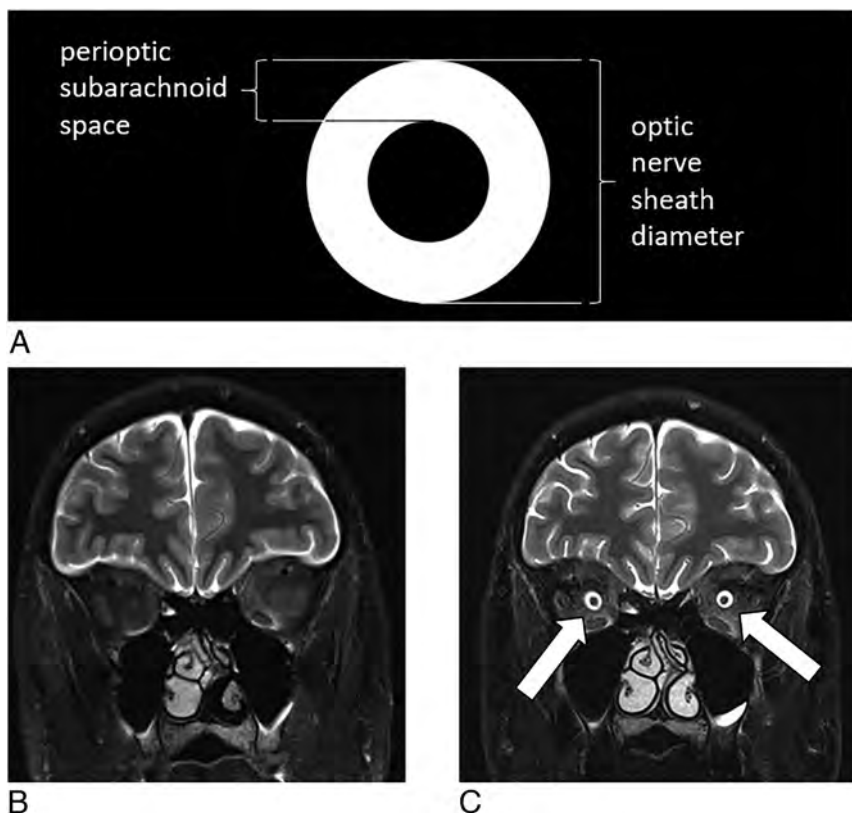


FIG 1. How to measure the ONSD and perioptic subarachnoid space. Illustration (A) depicting the measurements for the ONSD and the perioptic subarachnoid space. Pre- (B) and post- (C) operative coronal fat-suppressed T2-weighted MR imaging shows restoration of the perioptic subarachnoid space (arrows) following ligation of a spinal CSF-venous fistula.

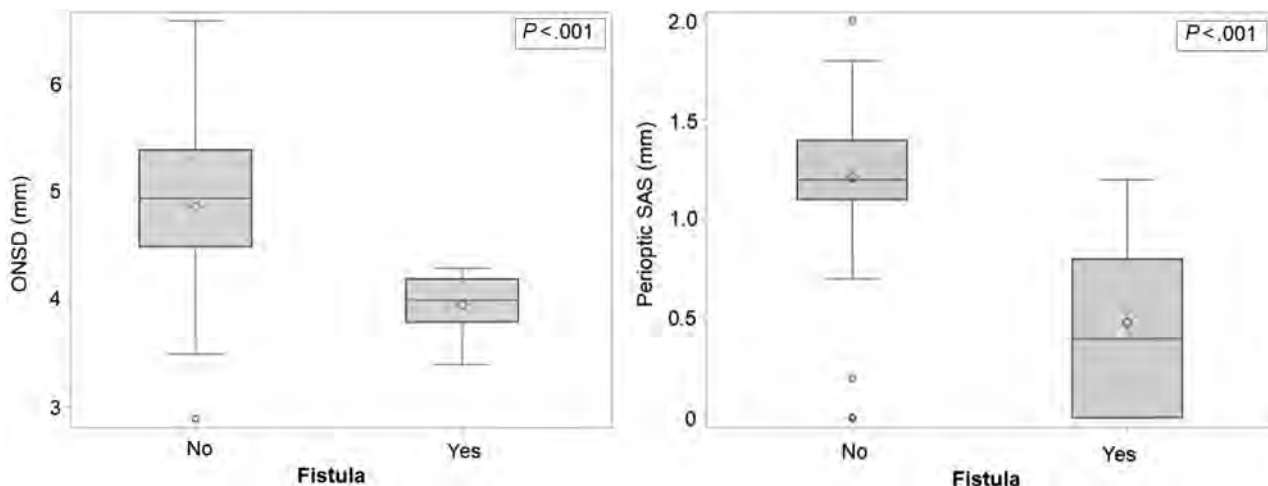


FIG 2. ONSD and perioptic subarachnoid space measurements in patients with and without spinal CSF-venous fistulas. Box and whisker plots of the ONSD and perioptic SAS in patients without and with a spinal CSF-venous fistula. The box represents the upper and lower quartiles with the line splitting the box representing the median. The diamond represents the mean. The whiskers represent the upper and lower values of the data, up to 1.5 times the interquartile range. The single points represent the outliers.

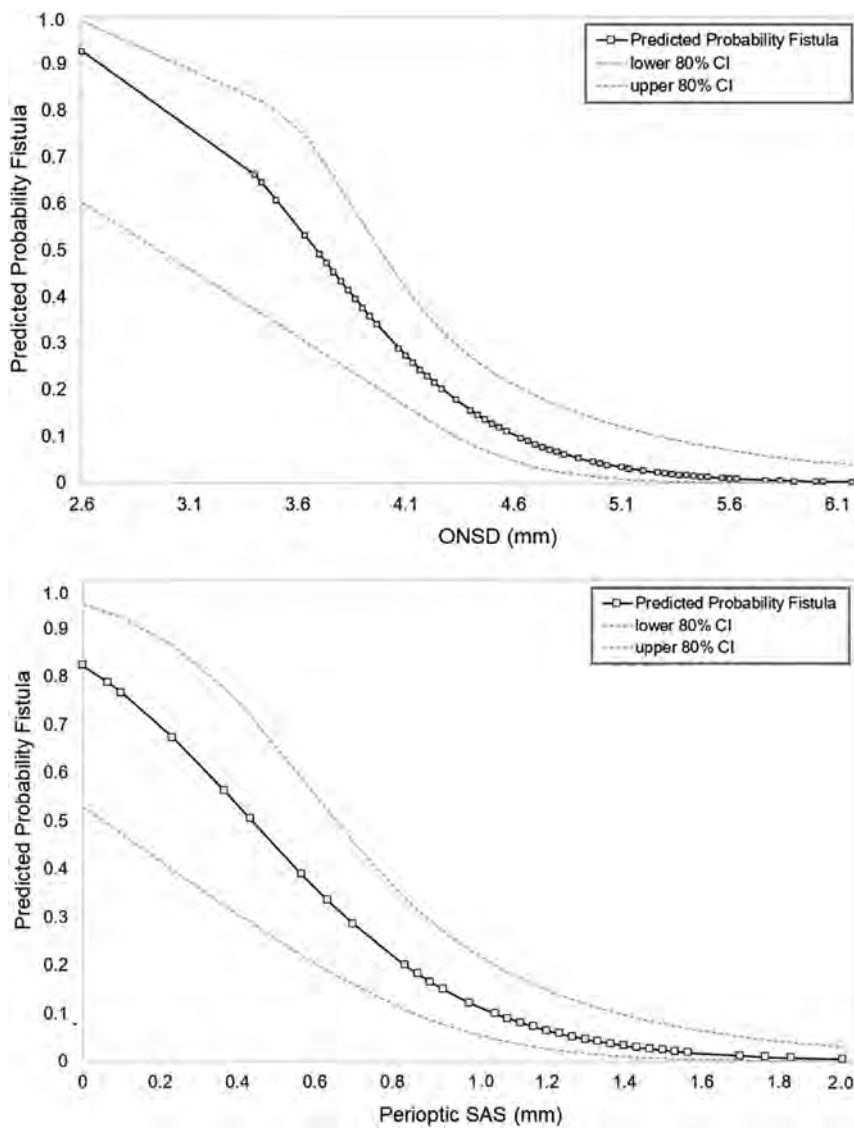


FIG 3. Predicted probability of finding a spinal CSF-venous fistula based on the ONSD and perioptic subarachnoid space measurements. The graphs depict the predicted probability (and 80% confidence intervals) of identifying a CSF-venous fistula according to ONSD and perioptic SAS.

a CSF-venous fistula ($P = .022$), and these patients were about a decade older than patients without a CSF-venous fistula ($P = .015$), but there were no significant differences in the duration of symptoms, location of the headache, time to orthostatic worsening of the headache, BMI, results of prior epidural blood patching, time interval between the onset of symptoms and the first brain MR imaging, or time interval between the brain MR imaging with the SIH protocol and DSM (Online Supplemental Data). Although CSF opening pressure was normal in all patients (reference range, 6–25 cm CSF), it was lower in those who were found to have a CSF-venous fistula (13.3 versus 16.1 cm CSF; $P < .016$). A CSF-venous fistula was found in 19.4% of patients with a spinal meningeal diverticulum and in 4.8% of those without such a diverticulum ($P = .177$). The SIHDAS was II in 1 patient, III in 1 patient, and IV in 13 patients. All 15 patients had a single CSF-venous fistula, and all fistulas were located in the thoracic spine. The CSF-venous fistula was on the right side in 9 patients and on the left side in 6 patients.

Findings among Those with and without a Spinal CSF-Venous Fistula

The mean ONSD was significantly decreased in patients with a CSF-venous fistula (4.0 mm), compared with patients without a CSF-venous fistula (4.9 mm) ($P < .001$) (Fig 2). This difference in the ONSD was mostly due to the reduction of the perioptic subarachnoid space, a component of the ONSD. The mean perioptic subarachnoid space measured 0.5 mm among the patients with a CSF-venous fistula and 1.2 mm in the patients without a CSF-venous fistula ($P < .001$) (Fig 2). By means of the Youden index analysis, optimal cut-off values were found at 4.4 mm for ONSD and 1.0 mm for the perioptic subarachnoid space. Using these cutoff values, we detected fistulas in 47% and 54% of patients, respectively, with the ONSD or perioptic subarachnoid space measurements below these cutoff values compared with 0% and 2% of patients with ONSD or perioptic subarachnoid space measurements above these cutoff values. The predicted probability of identifying a CSF-venous fistula increased <1% at a perioptic subarachnoid space of 1.8 mm to 82% at a perioptic subarachnoid space of 0 mm, and from <1% at an ONSD of 5.7 mm to 93% at an ONSD of 2.6 mm (Fig 3).

Receiver operating characteristic curve analysis revealed an area under the curve of 0.883 (95% CI, 0.816–0.950) for ONSD and 0.932 (95% CI, 0.877–0.987) for the perioptic subarachnoid space. By means of the ONSD cutoff point of 4.4 mm for identifying a CSF-venous fistula, specificity was 79.5% and sensitivity was 100%. With the perioptic subarachnoid space cutoff point of 1.0 mm for identifying a CSF-venous fistula, specificity was 85.9% and sensitivity was 93.3%.

There was no significant difference in the mean Bern score between patients with a CSF-venous fistula (0.58) compared with those without a CSF-venous fistula (0.64) ($P = .78$). Interrater agreement was substantial for all measurements, including the Bern score ($\kappa = 0.73$), perioptic subarachnoid space ($\kappa = 0.79$), and the ONSD ($\kappa = 0.87$). Significant linear correlations were found between the ONSD and the perioptic subarachnoid space with CSF opening pressure and BMI (Fig 4).

Treatment of a Spinal CSF-Venous Fistula and the Postoperative Course

All 15 patients with a CSF-venous fistula underwent an uneventful laminoforaminotomy for clip ligation of the fistula. Postoperative brain MR imaging with the same SIH protocol was performed in

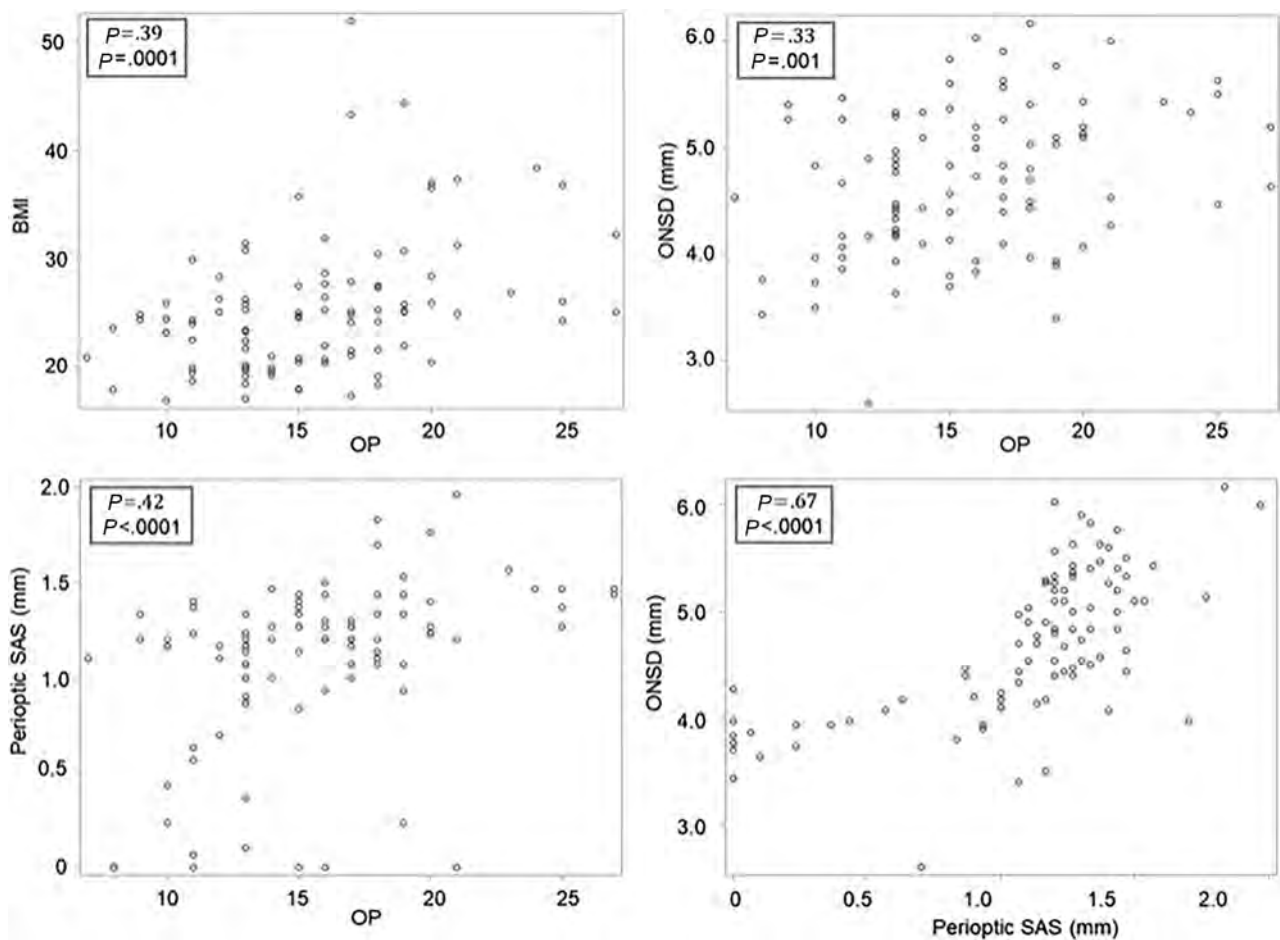


FIG 4. The relationship among the BMI, CSF opening pressure, ONSD, and perioptic subarachnoid space. Scatterplots depict the relationships among BMI, CSF OP (in centimeters CSF), ONSD, and the perioptic SAS. By ranking from the weakest to the strongest correlation, positive correlations are found between the ONSD and OP, BMI and OP, perioptic SAS and OP, and ONSD and perioptic SAS.

14 of the 15 patients between 18 and 52 hours (mean, 40 hours) following surgical ligation of the CSF-venous fistula. Postoperatively, the ONSD increased from 4.0 to 5.3 mm, and the perioptic subarachnoid space increased from 0.5 to 1.2 mm ($P < .001$) (Fig 5). There was no change in the Bern score (0.58 to 0.42). During a mean clinical postoperative follow-up of 10 months (range, 3–26 months), 12 patients (80%) reported complete or near-complete and sustained resolution of SIH symptoms (SIHDAS grade II, III, or IV to grade I), 1 patient (6.7%) reported incomplete resolution of SIH symptoms (SIHDAS grade IV to III), and 2 patients (13.3%) reported no change in SIH symptoms (SIHDAS grade IV). The mean SIHDAS for all 15 patients improved from 139.9 to 21.5 ($P < .001$).

DISCUSSION

In this study, we found that among patients with orthostatic headache and normal findings on conventional brain and spine imaging, the ONSD and perioptic subarachnoid space were significantly decreased in patients with a CSF-venous fistula compared with patients without a CSF-venous fistula. In this patient population, we found CSF-venous fistulas in about one-half of patients with a perioptic subarachnoid space measuring ≤ 1.0 mm or with an ONSD measuring ≤ 4.4 mm (measured 10–12 mm posterior to the globe) compared with $< 2\%$ of patients with measurements above these cutoff values.

The perioptic subarachnoid space is a continuation of the intracranial subarachnoid space, and unlike the intracranial subarachnoid space that is enveloped by the dura mater, it is surrounded by the soft tissues of the orbit, allowing unrestricted expansion or collapse depending on the amount of CSF volume.^{28,29} We hypothesize that in the presently reported patients with CSF-venous fistulas and normal findings on conventional brain MR imaging, the CSF loss was sufficient to cause a decrease in the perioptic subarachnoid space volume but not sufficient to cause the other brain MR imaging features of SIH. Rapid restoration of the normal perioptic subarachnoid space was seen within about 24–48 hours after surgical ligation of the CSF-venous fistula. In a series of experiments, Hansen and Helmke³⁰ have shown a prompt response of the ONSD to changes in spinal CSF volume and pressure.

In our prior study, we found CSF-venous fistulas in 10% of patients with orthostatic headache but normal conventional brain and spine imaging findings; fistulas were present in 20% of patients with meningeal diverticula and in none of the patients without diverticula.⁸ Although we found similar results in the current study, the number of patients without meningeal diverticula was relatively small and the difference did not reach statistical significance. Prior studies have shown a relationship between the ONSD and BMI and between the ONSD and CSF pressure. The ONSD is weakly correlated with BMI and strongly

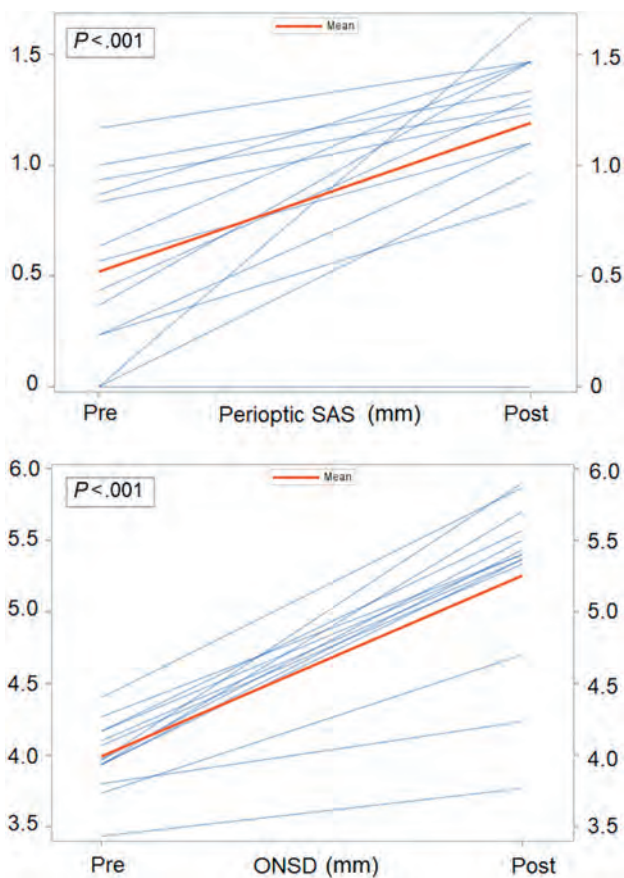


FIG 5. Normalization of the ONSD and perioptic subarachnoid space following ligation of spinal CSF-venous fistulas. Individual measurements of the pre- and postoperative ONSD and perioptic SAS following ligation of the spinal CSF-venous fistula.

correlated with CSF opening pressure and with intracranial pressure. We were able to replicate these findings for BMI, ONSD, and CSF opening pressure, providing internal validation of the data.

The Bern score is based on a summation of several of the well-established features of SIH on brain MR imaging and was established and validated to predict the presence of spinal extradural CSF and specifically excluded CSF-venous fistulas,²⁵ but subsequently, this score has also been used in the evaluation and follow-up of patients with SIH due to CSF-venous fistulas.³¹ In the present study of patients with orthostatic headaches and normal conventional brain and spine imaging findings, the Bern score was not able to differentiate patients with a CSF-venous fistula from those without such a fistula, and there was no change in the Bern score following surgical ligation of the CSF-venous fistula.

The MR imaging sequence used in the present study adds 4 minutes of MR imaging time. This MR imaging sequence allows precise and reproducible measurements, and in our study, interrater agreement was substantial for both the peri-optic subarachnoid space and the ONSD. Ultrasonography also has been used extensively for the evaluation of the ONS and has the advantage of obtaining measurements in different body positions, but the technology is very user-dependent, limiting its use.^{12,14}

The burden of SIH is high among patients seeking medical care,³²⁻³⁴ and this was reflected in the SIHDAS in the present study, showing severe disability in almost all patients. Following treatment of the CSF-venous fistula, the SIHDAS was significantly improved with complete or near-complete resolution of the symptoms of SIH in 80% of patients.

It has been known since the 1990s that CSF opening pressure may be normal in patients with SIH,³⁵ and this finding has now been confirmed in several SIH patient populations, including in patients with CSF-venous fistulas.^{5,8,36} In the current study, all patients had a normal CSF opening pressure, but CSF opening pressure was lower in those with a CSF-venous fistula.

Spontaneous spinal CSF-venous fistulas were first described in 2014.³⁷ These abnormal communications between the spinal subarachnoid space and epidural veins were initially believed to be rare but are now known to be a common cause of SIH. The radiographic studies necessary for the reliable detection of CSF-venous fistulas currently require a lumbar puncture and use an iodine-based contrast agent and ionizing radiation, are expensive and time-consuming, and, in our institution, are performed with the patient under general endotracheal anesthesia. The current study shows that measurements of the ONSD and perioptic subarachnoid space will be of use in making decisions regarding increasing imaging for patients with orthostatic headache but otherwise normal conventional brain and spine imaging findings.

This study had some limitations. First, the current study mostly represents a highly selected group of patients referred to a quaternary referral center for SIH, and the generalizability of our findings is unknown. However, the radiographic techniques capable of reliably demonstrating spinal CSF-venous fistulas are not widely available and are mainly used in high-volume SIH referral centers. Second, this study was undertaken during the coronavirus 2019 (COVID-19) pandemic, and this timing may have introduced referral and other biases favoring a patient population with higher disability. However, the overall detection rate of finding a CSF-venous fistula was very similar to that in a prior study performed before the COVID-19 pandemic. Third, brain MR imaging findings of SIH may spontaneously resolve with time despite persistent symptoms, and the timing of MR imaging in our study could not be standardized. However, the time interval between the onset of symptoms and the first MR imaging did not differ between those with and without a CSF-venous fistula. Finally, this was a single-center study, and the relatively small number of patients resulted in our calculations having relatively wide confidence intervals.

CONCLUSIONS

ONS MR imaging measurements showing a reduced ONS diameter and perioptic subarachnoid space predict the presence of an underlying spinal CSF-venous fistula in patients with orthostatic headaches and normal conventional brain and spine imaging findings. In addition, ONS measurements normalized promptly after ligation of the fistula.

Disclosure forms provided by the authors are available with the full text and PDF of this article at www.ajnr.org.

REFERENCES

1. Schievink WI. **Spontaneous intracranial hypotension.** *N Engl J Med* 2021;385:2173–78 CrossRef Medline
2. Mehta D, Cheema S, Davagnanam I, et al. **Diagnosis and treatment evaluation in patients with spontaneous intracranial hypotension.** *Front Neurol* 2023;14:1145949 CrossRef Medline
3. Schievink WI. **Spontaneous spinal cerebrospinal fluid leaks and intracranial hypotension.** *JAMA* 2006;295:2286–96 CrossRef Medline
4. D'Antona L, Jaime Merchan MA, Vassiliou A, et al. **Clinical presentation, investigation findings, and treatment outcomes of spontaneous intracranial hypotension syndrome: a systematic review and meta-analysis.** *JAMA Neurol* 2021;78:329–37 CrossRef Medline
5. Schievink WI, Maya MM, Moser FG, et al. **Lateral decubitus digital subtraction myelography to identify spinal CSF-venous fistulas in spontaneous intracranial hypotension.** *J Neurosurg Spine* 2019;31:1–4 CrossRef Medline
6. Kranz PG, Gray L, Malinzak MD, et al. **CSF-venous fistulas: anatomy and diagnostic imaging.** *AJR Am J Roentgenol* 2021;217:1418–29 CrossRef Medline
7. Mamlouk MD, Ochi RP, Jun P, et al. **Decubitus CT myelography for CSF-venous fistulas: a procedural approach.** *AJNR Am J Neuroradiol* 2021;42:32–36 CrossRef Medline
8. Schievink WI, Maya M, Prasad RS, et al. **Spontaneous spinal cerebrospinal fluid-venous fistulas in patients with orthostatic headaches and normal conventional brain and spine imaging.** *Headache* 2021;61:387–91 CrossRef Medline
9. Watanabe A, Horikoshi T, Uchida M, et al. **Decreased diameter of the optic nerve sheath associated with CSF hypovolemia.** *AJNR Am J Neuroradiol* 2008;29:863–64 CrossRef Medline
10. Rohr A, Jensen U, Riedel C, et al. **MR imaging of the optic nerve sheath in patients with craniocervical hypotension.** *AJNR Am J Neuroradiol* 2010;31:1752–57 CrossRef Medline
11. Takeuchi N, Horikoshi T, Kinouchi H, et al. **Diagnostic value of the optic nerve sheath subarachnoid space in patients with intracranial hypotension syndrome.** *J Neurosurg* 2012;117:372–77 CrossRef Medline
12. Fichtner J, Ulrich CT, Fung C, et al. **Management of spontaneous intracranial hypotension: transorbital ultrasound as discriminator.** *J Neurol Neurosurg Psychiatry* 2016;87:650–55 CrossRef Medline
13. Holbrook JF, Hudgins PA, Bruce BB, et al. **Novel orbital findings of intracranial hypotension.** *Clin Imaging* 2017;41:125–31 CrossRef Medline
14. Wang L-J, Zhang Y, Li C, et al. **Ultrasonographic optic nerve sheath diameter as a noninvasive marker for intracranial hypotension.** *Ther Adv Neurol Disord* 2022;15:17562864211069744 CrossRef Medline
15. Tay ASS, Maya M, Moser FG, et al. **Computed tomography vs heavily T2-weighted magnetic resonance myelography for the initial evaluation of patients with spontaneous intracranial hypotension.** *JAMA Neurol* 2021;78:1275–76 CrossRef Medline
16. Stewart WF, Lipton RB, Whyte J, et al. **An international study to assess reliability of the Migraine Disability Assessment (MIDAS) score.** *Neurology* 1999;53:988–94 CrossRef Medline
17. Schievink WI, Maya MM, Barnard ZR, et al. **Behavioral variant frontotemporal dementia as a serious complication of spontaneous intracranial hypotension.** *Oper Neurosurg (Hagerstown)* 2018;15:505–15 CrossRef Medline
18. Farb RI, Forghani R, Lee SK, et al. **The venous distension sign: a diagnostic sign of intracranial hypotension at MR imaging of the brain.** *AJNR Am J Neuroradiol* 2007;28:1489–93 CrossRef Medline
19. Forghani R, Farb RI. **Diagnosis and temporal evolution of signs of intracranial hypotension on MRI of the brain.** *Neuroradiology* 2008;50:1025–34 CrossRef Medline
20. Shah LM, McLean LA, Heilbrun ME, et al. **Intracranial hypotension: improved MRI detection with diagnostic intracranial angles.** *AJR Am J Roentgenol* 2013;200:400–07 CrossRef Medline
21. Houk JL, Amrhein TJ, Gray L, et al. **Differentiation of Chiari malformation type I and spontaneous intracranial hypotension using objective measurements of midbrain sagging.** *J Neurosurg* 2021;136:1796–803 CrossRef Medline
22. Schievink WI, Maya MM, Harris J, et al. **Infratentorial superficial siderosis and spontaneous intracranial hypotension.** *Ann Neurol* 2023;93:64–75 CrossRef Medline
23. Johnson DR, Carr CM, Luetmer PH, et al. **Diffuse calvarial hyperostosis in patients with spontaneous intracranial hypotension.** *World Neurosurg* 2021;146:e848–53 CrossRef Medline
24. Rohr A, Riedel C, Reimann G, et al. **Pseudotumor cerebri: quantitative normalwerte anatomischer kennstrukturen im kraniellen MRT.** *RoFo* 2008;180:884–90 CrossRef Medline
25. Dobrocky T, Grunder L, Breiding PS, et al. **Assessing spinal cerebrospinal fluid leaks in spontaneous intracranial hypotension with a scoring system based on brain magnetic resonance imaging findings.** *JAMA Neurol* 2019;76:580–87 CrossRef Medline
26. Hoxworth JM, Patel AC, Bosch EP, et al. **Localization of a rapid CSF leak with digital subtraction myelography.** *AJNR Am J Neuroradiol* 2009;30:516–19 CrossRef Medline
27. Galvan J, Maya M, Prasad RS, et al. **Spinal cerebrospinal fluid leak localization with digital subtraction myelography: tips, tricks, and pitfalls.** *Radiol Clin* 2024;62:321–32 CrossRef Medline
28. Anderson DR. **Ultrastructure of meningeal sheaths: normal human and monkey optic nerves.** *Arch Ophthalmol* 1969;82:659–74 CrossRef Medline
29. Hayreh SS. **The sheath of the optic nerve.** *Ophthalmologica* 1984;189:54–63 CrossRef Medline
30. Hansen HC, Helmke K. **Validation of the optic nerve sheath response to changing cerebrospinal fluid pressure: ultrasound findings during intrathecal infusion tests.** *J Neurosurg* 1997;87:34–40 CrossRef Medline
31. Brinjikji W, Garza I, Whealy M, et al. **Clinical and imaging outcomes of cerebrospinal fluid-venous fistula embolization.** *J Neurointerv Surg* 2022;14:953–56 CrossRef Medline
32. Cheema S, Joy C, Pople J, et al. **Patient experience of diagnosis and management of spontaneous intracranial hypotension: a cross-sectional online survey.** *BMJ Open* 2022;12:e057438 CrossRef Medline
33. Jesse CM, Häni L, Fung C, et al. **The impact of spontaneous intracranial hypotension on social life and health-related quality of life.** *J Neurol* 2022;269:5466–73 CrossRef Medline
34. Liaw V, McCreary M, Friedman DI. **Quality of life in patients with confirmed and suspected spinal CSF leaks.** *Neurology* 2023;101:e2411–22 CrossRef Medline
35. Mokri B, Hunter SF, Atkinson JLD, et al. **Orthostatic headaches caused by CSF leak but with normal CSF pressures.** *Neurology* 1998;51:786–90 CrossRef Medline
36. Kranz PG, Tanpitukpongse TP, Choudhury KR, et al. **How common is normal cerebrospinal fluid pressure in spontaneous intracranial hypotension?** *Cephalalgia* 2016;36:1209–17 CrossRef Medline
37. Schievink WI, Moser FG, Maya MM. **CSF-venous fistula in spontaneous intracranial hypotension.** *Neurology* 2014;83:472–73 CrossRef Medline

Evaluation of MR Elastography as a Noninvasive Diagnostic Test for Spontaneous Intracranial Hypotension

Ian T. Mark, Pragalv Karki, Jeremy Cutsforth-Gregory, Waleed Brinjikji, Ajay A. Madhavan, Steven A. Messina, Petrice M. Cogswell, John J. Chen, Richard L. Ehman, John Huston, and Matthew C. Murphy



ABSTRACT

BACKGROUND AND PURPOSE: Spontaneous intracranial hypotension is a condition resulting from a leak of CSF from the spinal canal arising independent of a medical procedure. Spontaneous intracranial hypotension can present with normal brain MR imaging findings and nonspecific symptoms, leading to the underdiagnosis in some patients and unnecessary invasive myelography in others who are found not to have the condition. Given the likelihood that spontaneous intracranial hypotension alters intracranial biomechanics, the goal of this study was to evaluate MR elastography as a potential noninvasive test to diagnose the condition.

MATERIALS AND METHODS: We performed MR elastography in 15 patients with confirmed spontaneous intracranial hypotension from September 2022 to April 2023. Age, sex, symptom duration, and brain MR imaging Bern score were collected. MR elastography data were used to compute stiffness and damping ratio maps, and voxelwise modeling was performed to detect clusters of significant differences in mechanical properties between patients with spontaneous intracranial hypotension and healthy control participants. To evaluate diagnostic accuracy, we summarized each examination by 2 spatial pattern scores (one each for stiffness and damping ratio) and evaluated group-wise discrimination by receiver operating characteristic curve analysis.

RESULTS: Patients with spontaneous intracranial hypotension exhibited significant differences in both stiffness and damping ratio (false discovery rate–corrected, $Q < 0.05$). Pattern analysis discriminated patients with spontaneous intracranial hypotension from healthy controls with an area under the curve of 0.97 overall, and the area under the curve was 0.97 in those without MR imaging findings of spontaneous intracranial hypotension.

CONCLUSIONS: Results from this pilot study demonstrate MR elastography as a potential imaging biomarker and a noninvasive method for diagnosing spontaneous intracranial hypotension, including patients with normal brain MR imaging findings.

ABBREVIATIONS: AUC = area under the curve; CVF = CSF-venous fistula; FDR = false discovery rate; MCALT = Mayo Clinic Adult Life span Template; MRE = MR elastography; nm = normal; SIH = spontaneous intracranial hypotension; SVM = support vector machine

Spontaneous intracranial hypotension (SIH) can present with debilitating symptoms and is caused by spontaneous CSF leakage from the spine. Identified leaks can be subtyped into dural tears (ventral type 1a, posterolateral type 1b), ruptured meningeal diverticula (type 2), or CSF-venous fistula (CVF) (type 3), the last of which is only diagnosed with a myelogram requiring lumbar

puncture.¹ While patients with SIH most frequently present with orthostatic headaches, they can also present with other nonspecific symptoms such as nausea, neck pain, hearing changes, dizziness, or even behavioral changes mimicking dementia.² As part of the diagnostic work-up of SIH, brain MR imaging can show diffuse dural thickening and enhancement, subdural fluid collections, venous distension, and morphologic changes of brain sag.³ Up to 20% of patients with SIH, however, have normal findings on brain MR imaging.² Additionally, CSF pressures can be misleading, because most patients with SIH have a normal opening CSF pressure.⁴ Patients with a delay in diagnosis can have increased morbidity.⁵ Thus, the search for additional noninvasive tests to diagnose SIH and accurately triage patients to undergo myelography is critical in the treatment of these patients.

MR elastography (MRE) is a noninvasive technique to measure tissue mechanical properties.⁶ During the application of external vibration, a phase-contrast MR imaging pulse sequence

Received November 3, 2023; accepted after revision January 3, 2024.

From the Departments of Radiology (I.T.M., P.K., W.B., A.A.M., S.A.M., P.M.C., R.L.E., J.H., M.C.M.), Neurology (J.C.-G., J.J.C.), and Ophthalmology (J.J.C.), Mayo Clinic, Rochester, Minnesota.

This work was supported by the National Institutes of Health (R37 EB001981 and R01 AG076636).

Please address correspondence to Ian Mark, MD, Department of Radiology, Mayo Building, 3-72W, 200 1st Street SW, Rochester, MN 55905; e-mail: Mark.Ian@mayo.edu; @iantmark

Indicates open access to non-subscribers at www.ajnr.org

Indicates article with online supplemental data.

<http://dx.doi.org/10.3174/ajnr.A8162>

is used to measure the resulting displacement field. Tissue mechanical properties are then estimated from the displacement field with an inversion algorithm, which can include measures of elasticity and viscosity. MRE has been used to evaluate brain shear stiffness (or simply stiffness) in many other conditions including brain tumors, Alzheimer disease, demyelinating and neuroinflammatory disorders, amyotrophic lateral sclerosis, and traumatic brain injury.^{7,8} The purpose of this study was to use MRE to measure brain stiffness and damping ratio in patients with known SIH and compare them with controls. We hypothesized that there will be stiffness changes at the vertex in addition to the brainstem from the effects of brain sag.

MATERIALS AND METHODS

Patient Selection

After we obtained institutional review board approval and written informed consent, brain MRE examinations were performed on 15 patients with SIH who were diagnosed with a CVF from September 2022 to April 2023. Dynamic myelogram images diagnosing the CVF were obtained and interpreted by one of our board-certified neuroradiologists who specializes in CSF leaks. The CVF was subsequently verified by an additional neuroradiologist (I.T.M.). All patients met The International Classification of Headache Disorders-3 criteria for SIH. The number of days between diagnostic myelography and MRE was recorded. MRE was performed before catheter embolization treatment. Patient age, sex, and symptom duration were recorded. Brain MRIs were reviewed for the Bern score.⁹

Image Acquisition

MRE data and T1-weighted anatomic images were collected on 3T MR imaging scanners (GE Healthcare). All MRE examinations were performed at 60 Hz with 3-mm resolution.

Data from 44 control participants (age range, 56–89 years) were included from a previously published study.¹⁰ This cohort was scanned on a 3T GE Healthcare scanner and confirmed to be negative for amyloid-PET and cognitive impairment. In this cohort, an inversion recovery echo-spoiled gradient echo (the pulse sequence was used for anatomic imaging with parameters including an imaging matrix of 256 by 256 pixels, TR/TE of 6.3/2.8 ms, flip angle of 11°, inversion time of 400 ms, FOV of 27 cm, and bandwidth of 31.25 kHz). The MRE data were acquired using a spin-echo echo-planar imaging technique at 60-Hz vibration. The acquisition parameters were the following: TR/TE of 3600/62 ms, FOV of 24 cm, imaging matrix of 72 × 72 reconstructed to 80 × 80, 48 contiguous 3-mm-thick axial slices, one 18.2-ms motion-encoding gradient on each side of the refocusing radiofrequency pulse, motion-encoding in x, y, and z directions, and 8 phase offsets spaced evenly during a period corresponding to 60-Hz motion.

The remaining 21 control participants (range, 19–53 years of age) and 15 patients with SIH (range, 35–70 years of age) were scanned on a compact GE Healthcare 3T system.^{11,12} The controls in this cohort did not have any neurologic conditions or increased intracranial pressure. Anatomic images were obtained using a T1-weighted MPRAGE acquisition with parameters of TR/TE of 6.1/2.5 ms, inversion time of 600 ms, flip angle of 8°,

FOV of 160 × 160 mm, image matrix of 256 × 256, section thickness of 1.2 mm, and acquisition time of 4 minutes 18 seconds. MRE acquisition was performed using a flow-compensated spin-echo echo-planar imaging method, and vibrations were applied by a pneumatic actuator with a frequency of 60 Hz. The acquisition parameters were TR/TE of 4000/59 ms, FOV of 24 × 24 cm, image matrix of 80 × 80, 48 contiguous 3-mm-thick axial slices, one 16.7-ms 8-G/cm motion-encoding gradient on each side of the refocusing pulse, motion-encoding in x, y, and z directions, and 8 phase offsets spaced evenly over 1 period corresponding to a motion of 60 Hz.¹³

Viscoelastic Property Map Estimation

Stiffness and damping ratio maps were computed by neural network inversion.¹⁴ The shear modulus of a viscoelastic material at a given frequency is given by the complex valued quantity $G = G' + iG''$. From this modulus, stiffness is computed as $2|G|^2/(G' + |G|)$, and the damping ratio is defined as $G''/2G'$.^{15,16} Training data were generated with a finite difference model of the wave equations, assuming harmonic motion in linear viscoelastic materials using a random distribution of shear moduli (stiffness range, 1–5 kPa; damping ratio range, 0–0.5), which was described in detail in previous studies.^{14,17} The true mechanical properties were spatially varied to relax the tissue homogeneity assumption. From the training set, random patches were selected and randomized by the application of phase cycling, noise, and masking. Separate neural networks were trained to estimate the stiffness and damping ratio using Keras and TensorFlow backend.^{18,19} Training was performed with an Adam optimizer using a batch size of 100 and 1000 batches per epoch.²⁰ Two learning rates were used (0.001 and 0.0001), and learning was stopped at each rate when the mean squared error did not improve for 3 consecutive epochs.

To apply the Neural Network Intelligence (NNIs) in vivo, first, we computed tissue probability maps for each participant using the unified segmentation algorithm in SPM12 software (<http://www.fil.ion.ucl.ac.uk/spm/software/spm12>) and tissue priors from the Mayo Clinic Adult Life span Template (MCALT).^{21,22} T1-weighted images were registered and resliced to the MRE magnitude image (T2-weighted), and segmentation was performed according to both channels to obtain tissue probability maps in MRE space. A brain mask was computed to indicate voxels with a combined probability of white and gray matter tissues greater than the probability of CSF. The inverse deformation field was applied to the MCALT lobar atlas to obtain these region assignments in MRE space.

Displacement data were filtered to reduce interslice phase discontinuities,²³ unwrapped by using a graph cuts algorithm,²⁴ and an adaptive curl operator was applied to reduce the effects of longitudinal waves on shear property estimation. Each examination was processed in 3 subregions to avoid processing across the major dural folds, which act as shear wave sources. These subregions, defined as the intersection of relevant lobar atlas assignments and the brain mask, were the left cerebrum plus the corpus callosum, right cerebrum plus the corpus callosum, and the cerebellum plus the brainstem. Because the corpus callosum is included in 2 subregions, final estimates were computed as the

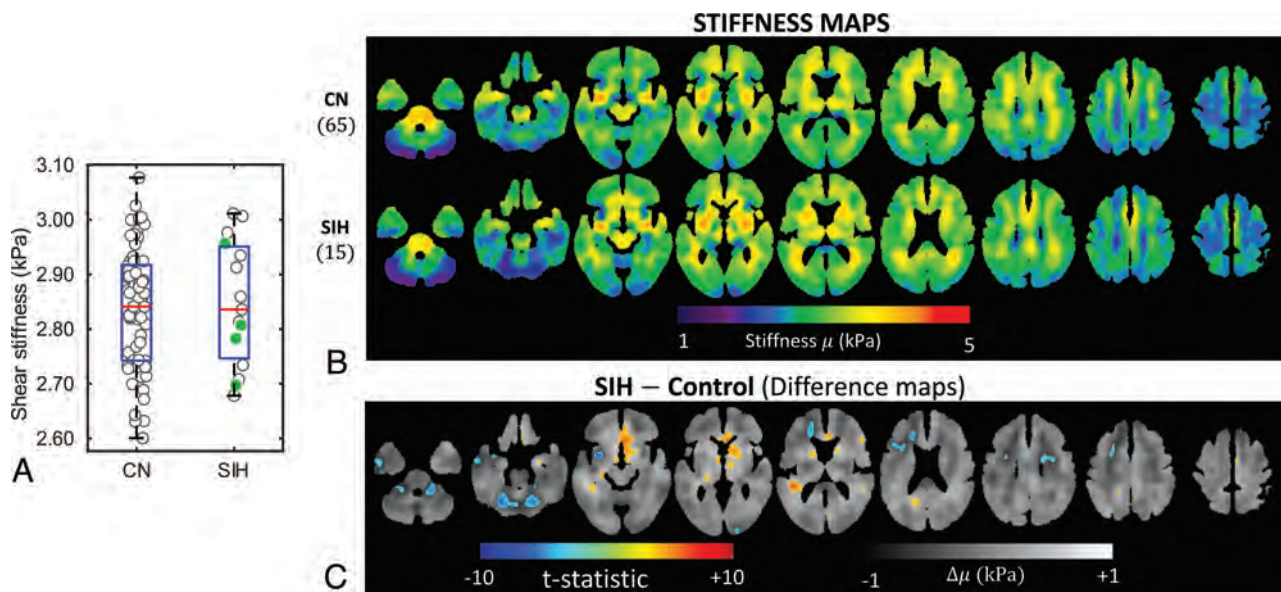


FIG 1. A, Group-wise boxplot and mean stiffnesses of individuals shown with a jitter plot. The solid (green) markers are cases of SIH-nm. B, Averaged stiffness maps of the controls and patients with SIH (upper row) and a difference map between the 2 groups (lower row). The SIH group has increased stiffness around the ventricles compared with the controls as seen in the difference plots (C) around the frontal horns and atria of the lateral ventricles. There is also softening around the frontal horn of the right lateral ventricle in the SIH group. A gray-scale map in the difference maps shows the plain difference between the groups, and the colormap shows the positive false discovery thresholded ($Q < 0.05$, t-statistics map); 9037 voxels reach the positive false discovery threshold for the stiffness difference maps. CN indicates control.

average of the 2 subregion estimates. This procedure was repeated for the stiffness and damping ratio separately.

Voxelwise Mapping

Using the previously computed deformation field, we warped mechanical property maps into the MCALT space using nearest-neighbor interpolation. Then at each voxel, a linear model was fit to stiffness estimates at each voxel with predictors, including a constant, age, age², sex, and a categorical variable for the diagnosis of SIH. These predictors were included because the brain stiffness has been shown to be associated with age and sex,¹⁰ and these effects could obscure the SIH effect. A quadratic term for age was included because of the wide age range of study participants, resulting in a significant nonlinear age effect on both mechanical properties, as shown in the Online Supplemental Data. A *t* test was performed on the SIH predictor, and false discovery rate (FDR) correction was applied according to the method of Storey, with $Q < 0.05$ considered significant. An additional categorical predictor for the scanner was evaluated, but the scanner predictor was excluded because none of the voxels were found to have a significant effect after the FDR correction.

Pattern Analysis

We used a previously described pattern analysis to summarize each participant's MRE findings.²⁵ For computing an individual's pattern scores with leave-one-out cross-validation, first their viscoelastic map was held aside and voxelwise modeling was performed in the remaining participants (with the same predictors as above). The map of the held-out individual was corrected for age, sex, and the mean viscoelastic property on the basis of the modeling result. Then a correlation coefficient was calculated between the corrected viscoelastic property map and a map of the

expected SIH effect and converted to a *z* score via the Fisher transformation. For each participant, the *z* scores were calculated separately for the stiffness and damping ratio maps and used as features in a support vector machine (SVM) classifier with a linear kernel and box constraint of 1. Using leave-one-out cross-validation, we evaluated the SVM model for its ability to distinguish the SIH group from the control group as measured by accuracy and the area under the receiver operating characteristic curve. Including the scanner effect slightly improved the estimated area under the receiver operating characteristic curve and accuracy, but the scanner effect was not statistically significant. Therefore, we excluded it and opted to report the more conservative result.

RESULTS

Fifteen patients with confirmed CVF were enrolled and imaged with brain MRE. Eleven patients had a CVF diagnosed with digital subtraction myelography,^{26,27} and 4 patients were diagnosed with dynamic photon-counting CT myelography (CTM).²⁸ Nine patients (60%) were women. The mean age was 53.2 years (range, 35–70 years). The mean Bern score was 4.7 (range, 0–9). Four patients had a Bern score of 0. Symptom duration ranged from 1 month to 6 years. All 15 patients reported headache. Thirteen (86.7%) had orthostatic headache, while the remaining 2 (13.3%) had headaches that worsened with exertion. Five patients (33.3%) had photophobia, and 10 (66.7%) patients reported tinnitus. MRE was performed at least 1 day after myelography (mean, 10.7 days; range, 1–77 days).

Global stiffness (Fig 1A) and damping ratio (Fig 2A) estimates did not significantly differ between control participants and patients with SIH, but significant clusters were detected for each measure by voxelwise modeling. Mean stiffness maps for each

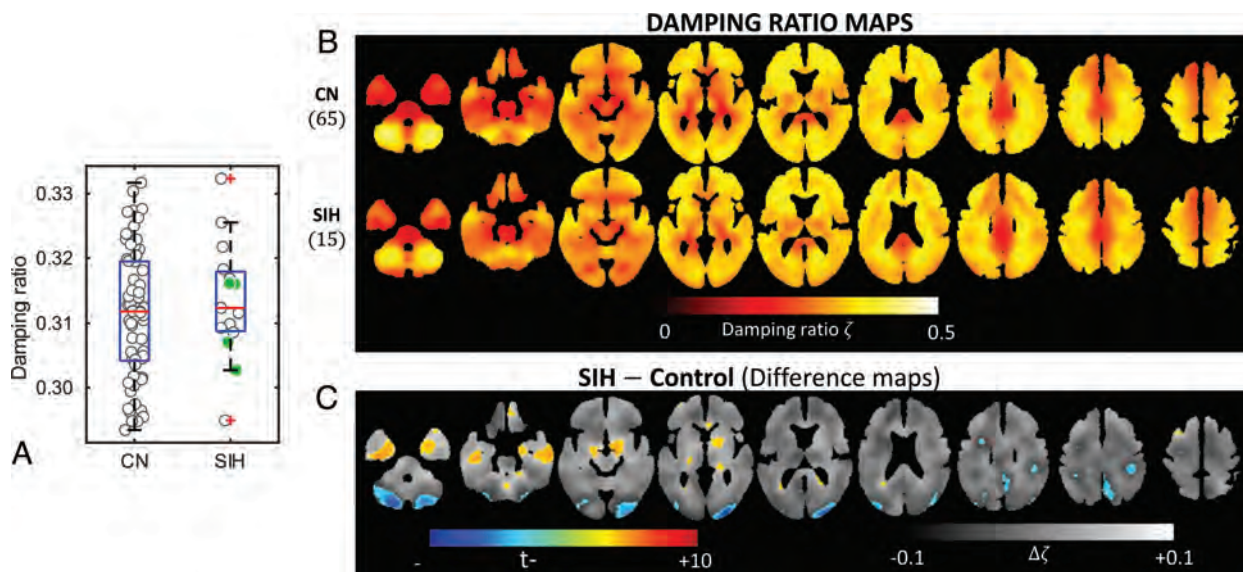


FIG 2. A, Group-wise boxplot and mean damping ratios of individuals shown with a jitter plot. The solid (green) markers are SIH-nm cases. B, Averaged damping ratio maps of the controls and patients with SIH (upper row) and a difference map between the 2 groups (lower row). There is an increased damping ratio around the lateral ventricles and inferior temporal lobes in patients with SIH as seen in the difference maps (C). There are additional areas of decreased damping ratio in the occipital poles and posterior cerebellum compared with decreased stiffness around those areas. CN indicates control.

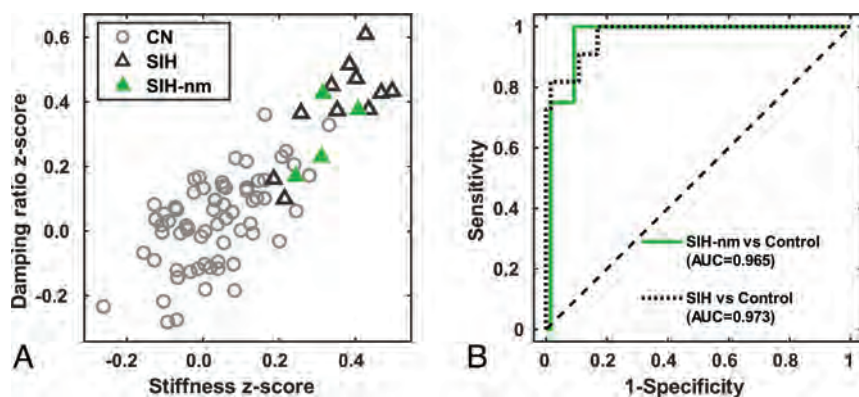


FIG 3. Leave-one-out pattern analysis correlation z score plot (A) and the receiver operating characteristic curve (B) from a cross-validated SVM model using the z scores as predictors for distinguishing patients with SIH from controls. Patients with SIH are shown with triangular markers separated into distinct clusters in the pattern analysis plot. The solid (green) triangular markers are patients with SIH with Bern 0 brain MR imaging, labeled as SIH-nm, compared with the open triangular markers that show some degree of sag on MR imaging. The SVM model has an AUC of 0.97, overall distinguishing SIH from controls, and 0.96 for distinguishing SIH-nm from controls. CN indicates control.

group are shown in Fig 1B, while differences are shown in Fig 1C. Patients with SIH had increased brain stiffness in the periventricular structures, including the medial basal forebrain, right periauricular white matter, and anterior corpus callosum and decreased stiffness toward the cerebellum and the frontal lobe around the ventricle (t test, $Q < 0.05$, 9037 significant voxels detected). The findings were more pronounced when evaluating the damping ratio (Fig 2B, -C), with patients with SIH having additional voxels of a decreased damping ratio in the occipital poles and posterior cerebellum. The inferior temporal lobes also demonstrated an increased damping ratio in patients with SIH (19,103 significant voxels detected).

Results from the pattern analysis are summarized in Fig 3. Patients with SIH clustered distinctly from controls (Fig 3A). Overall, patients with SIH had an area under the curve (AUC) of 0.97 compared with controls. Four patients with normal brain MR imaging findings (Bern score 0 and labeled as SIH-nm) also had high stiffness and damping ratio z scores compared to controls. The SVM classifier had an AUC of 0.97 and an accuracy of 94% for distinguishing those with SIH-nm from controls as shown in Fig 3B. The cases with MR imaging features of SIH had an AUC of 0.97 and accuracy of 92%.

DISCUSSION

In this study, we demonstrated that patients with SIH have distinct brain stiffness and damping ratio patterns relative to controls and can be distinguished by using a machine learning classifier. This finding potentially has clinical significance because patients with SIH can present with nonspecific symptoms and normal findings on brain MR imaging. An efficient work-up and diagnosis of SIH is paramount, because a delay in SIH diagnosis can lead to increased patient morbidity. Thus, MRE merits further investigation as a potential noninvasive imaging biomarker for SIH.

Previous studies have reported on both qualitative and quantitative brain MR imaging findings that suggest SIH.^{9,29-31} A systematic review and meta-analysis revealed that 19% of patients with SIH have normal findings on brain MR imaging.² Schievink et al³²

later studied 60 patients with orthostatic headache and normal brain and spine imaging findings and found that 10% of those patients had a CVF. This cohort of patients with SIH and normal findings on brain MR imaging presents 2 problems: First, the presumed exclusion of SIH based on normal findings on brain MR imaging leads to underdiagnosis. Second, many patients who do not have SIH end up undergoing an invasive myelogram, driven by high clinical concern and the lack of objective data with high sensitivity that can exclude SIH. Our study, while only including a small number of patients as pilot data, is the first step in working toward a quantifiable approach that can help address these problems.

Multiple prior studies have used brain MRE to evaluate stiffness changes with increased intracranial pressure. Using a porcine model, Arani et al³³ demonstrated that MRE brain stiffness measurements changed with acute intracranial pressure increases. Kolipaka et al³⁴ found increased global brain stiffness in patients with idiopathic intracranial hypertension compared with healthy controls. Later, Cogswell et al¹³ found increased brain stiffness pattern scores in patients with idiopathic intracranial hypertension, which were reversible after continuing treatment. No prior work has been performed with MRE to measure brain stiffness in patients with SIH. We found clusters of voxels with increased stiffness and damping ratio along the inferior temporal lobes, medial basal forebrain, anterior corpus callosum, and periaxial white matter and decreased stiffness and damping ratio toward the occipital lobe, cerebellum, and posterior parietal lobe. When designing this study, we hypothesized that changes in brain stiffness would occur at the vertex as well as in the brainstem, due to morphologic changes of brain sag. Our study found that this hypothesis was not the case. The exact etiology that preferentially alters stiffness in the central and inferior structures is unclear, but perhaps is due to downward pressure on the brain from the loss of spinal CSF. Alternatively, brain stiffness changes related to altered venous outflow or glymphatic flow could contribute to these findings but would need further exploration.

Most interesting in our study, 4 of the 15 patients had a Bern score of 0 but still exhibited the characteristic brain stiffness and damping ratio patterns similar to those in the cases with SIH with higher Bern scores. While SIH symptomatology is frequently orthostatic, it is unknown whether imaging findings of brain sag and venous distension can normalize in the supine position. Our findings could be explained by 2 potential phenomena: Supine positioning could alleviate brain sag and venous distension while brain stiffness changes persist, or brain stiffness changes could occur before the patient develops brain sag and venous engorgement. This is an area for future investigation.

The main limitation of this study is the small number of patients with SIH, particularly the cases with normal MR imaging findings. A larger sample will first enable lower-variance validation designs to provide more stable estimates of out-of-sample accuracy and also allow analysis of subgroups, particularly those stratified by brain MR imaging findings or symptoms. This pilot study serves as a starting point that warrants further investigation to determine the potential value of MRE in diagnosing SIH and providing a new window into its etiology.

CONCLUSIONS

This study used MRE to evaluate patients with SIH and found distinct stiffness and damping ratio patterns in patients with SIH relative to controls, including patients with normal findings on brain MR imaging. This pilot study introduces MRE as a new potential imaging biomarker and diagnostic test for SIH.

Disclosure forms provided by the authors are available with the full text and PDF of this article at www.ajnr.org.

REFERENCES

1. Schievink WI, Maya MM, Jean-Pierre S, et al. **A classification system of spontaneous spinal CSF leaks.** *Neurology* 2016;87:673–79 CrossRef Medline
2. D'Antona L, Jaime Merchan MA, Vassiliou A, et al. **Clinical presentation, investigation findings, and treatment outcomes of spontaneous intracranial hypotension syndrome: a systematic review and meta-analysis.** *JAMA Neurol* 2021;78:329–37 CrossRef Medline
3. Schievink WI. **Spontaneous intracranial hypotension.** *N Engl J Med* 2021;385:2173–78 CrossRef Medline
4. Kranz PG, Gray L, Amrhein TJ. **Spontaneous intracranial hypotension: 10 myths and misperceptions.** *Headache* 2018;58:948–59 CrossRef Medline
5. Schievink WI, Maya MM, Harris J, et al. **Infratentorial superficial siderosis and spontaneous intracranial hypotension.** *Ann Neurol* 2023;93:64–75 CrossRef Medline
6. Murphy MC, Huston J, 3rd, Ehman RL. **MR elastography of the brain and its application in neurological diseases.** *Neuroimage* 2019;187:176–83 CrossRef Medline
7. Yin Z, Romano AJ, Manduca A, et al. **Stiffness and beyond: What MR elastography can tell us about brain structure and function under physiologic and pathologic conditions.** *Top Magn Reson Imaging* 2018;27:305–18 CrossRef Medline
8. Hiscox LV, Johnson CL, Barnhill E, et al. **Magnetic resonance elastography (MRE) of the human brain: technique, findings and clinical applications.** *Phys Med Biol* 2016;61:R401–37 CrossRef Medline
9. Dobrocky T, Grunder L, Breiding PS, et al. **Assessing spinal cerebrospinal fluid leaks in spontaneous intracranial hypotension with a scoring system based on brain magnetic resonance imaging findings.** *JAMA Neurol* 2019;76:580–87 CrossRef Medline
10. Arani A, Murphy MC, Glaser KJ, et al. **Measuring the effects of aging and sex on regional brain stiffness with MR elastography in healthy older adults.** *Neuroimage* 2015;111:59–64 CrossRef Medline
11. Foo TK, Laskaris E, Vermilyea M, et al. **Lightweight, compact, and high-performance 3T MR system for imaging the brain and extremities.** *Magn Reson Med* 2018;80:2232–45 CrossRef Medline
12. Foo TFK, Laskaris E, Vermilyea M, et al. **Lightweight, compact, and high-performance 3T MR system for imaging the brain and extremities.** *Magn Reson Med* 2018;80:2232–45 CrossRef Medline
13. Cogswell PM, Murphy MC, Madhavan AA, et al. **Features of idiopathic intracranial hypertension on MRI with MR elastography: prospective comparison with control individuals and assessment of postintervention changes.** *AJR Am J Roentgenol* 2022;219:940–51 CrossRef Medline
14. Scott JM, Arani A, Manduca A, et al. **Artificial neural networks for magnetic resonance elastography stiffness estimation in inhomogeneous materials.** *Med Image Anal* 2020;63:101710 CrossRef Medline
15. Manduca A, Oliphant TE, Dresner MA, et al. **Magnetic resonance elastography: non-invasive mapping of tissue elasticity.** *Med Image Anal* 2001;5:237–54 CrossRef Medline
16. Manduca A, Bayly PJ, Ehman RL, et al. **MR elastography: principles, guidelines, and terminology.** *Magn Reson Med* 2021;85:2377–90 CrossRef Medline
17. Scott JM, Pavuluri K, Trzasko JD, et al. **Impact of material homogeneity assumption on cortical stiffness estimates by MR elastography.** *Magn Reson Med* 2022;88:916–29 CrossRef Medline

18. Abadi M, Agarwal A, Barham P, et al. **Tensorflow: a system for large-scale machine learning.** *arXiv: CS 1605.08695v2*. May 31, 2016. <https://arxiv.org/abs/1605.08695v2>. Accessed December 15, 2023
19. Chollet F. **Keras.** <https://keras.io>. Accessed December 15, 2023
20. Kingma DP, Ba J. **Adam: a method for stochastic optimization.** *arXiv CS1412.6980*. January 30, 2017. <https://arxiv.org/abs/1412.6980>. Accessed December 15, 2023
21. Ashburner J, Friston KJ. **Unified segmentation.** *Neuroimage* 2005;26:839–51 CrossRef Medline
22. Schwarz CG, Gunter JL, Ward CP, et al. **[P2–415]: the Mayo Clinic adult lifespan template: better quantification across the lifespan.** *Alzheimer's & Dementia* 2017;13:P792 CrossRef
23. Murphy MC, Huston J, 3rd, Jack CR, Jr, et al. **Measuring the characteristic topography of brain stiffness with magnetic resonance elastography.** *PLoS One* 2013;8:e81668 CrossRef Medline
24. Bioucas-Dias JM, Valadão G. **Phase unwrapping via graph cuts.** *IEEE Trans Image Process* 2007;16:698–709 CrossRef Medline
25. Murphy MC, Cogswell PM, Trzasko JD, et al. **Identification of normal pressure hydrocephalus by disease-specific patterns of brain stiffness and damping ratio.** *Invest Radiol* 2020;55:200–08 CrossRef Medline
26. Mark I, Madhavan A, Oien M, et al. **Temporal characteristics of CSF-venous fistulas on digital subtraction myelography.** *AJNR Am J Neuroradiol* 2023;44:492–95 CrossRef Medline
27. Kim DK, Brinjikji W, Morris PP, et al. **Lateral decubitus digital subtraction myelography: tips, tricks, and pitfalls.** *AJNR Am J Neuroradiol* 2020;41:21–28 CrossRef Medline
28. Madhavan AA, Cutsforth-Gregory JK, Brinjikji W, et al. **Diagnostic performance of decubitus photon-counting detector CT myelography for the detection of CSF-venous fistulas.** *AJNR Am J Neuroradiol* 2023;44:1445–50 CrossRef Medline
29. Shah LM, McLean LA, Heilbrun ME, et al. **Intracranial hypotension: improved MRI detection with diagnostic intracranial angles.** *AJR Am J Roentgenol* 2013;200:400–07 CrossRef Medline
30. Farb RI, Forghani R, Lee SK, et al. **The venous distension sign: a diagnostic sign of intracranial hypotension at MR imaging of the brain.** *AJNR Am J Neuroradiol* 2007;28:1489–93 CrossRef Medline
31. Kranz PG, Tanpitukpongse TP, Choudhury KR, et al. **Imaging signs in spontaneous intracranial hypotension: prevalence and relationship to CSF pressure.** *AJNR Am J Neuroradiol* 2016;37:1374–78 CrossRef Medline
32. Schievink WI, Maya M, Prasad RS, et al. **Spontaneous spinal cerebrospinal fluid-venous fistulas in patients with orthostatic headaches and normal conventional brain and spine imaging.** *Headache* 2021;61:387–91 CrossRef Medline
33. Arani A, Min HK, Fattahi N, et al. **Acute pressure changes in the brain are correlated with MR elastography stiffness measurements: initial feasibility in an in vivo large animal model.** *Magn Reson Med* 2018;79:1043–51 CrossRef Medline
34. Kolipaka A, Wassenaar PA, Cha S, et al. **Magnetic resonance elastography to estimate brain stiffness: measurement reproducibility and its estimate in pseudotumor cerebri patients.** *Clin Imaging* 2018;51:114–22 CrossRef Medline

Benefits of Photon-Counting CT Myelography for Localization of Dural Tears in Spontaneous Intracranial Hypotension

 Ajay A. Madhavan,  Jeremy K. Cutsforth-Gregory,  Waleed Brinjikji,  John C. Benson, Ben A. Johnson-Tesch,  Greta B. Liebo,  Ian T. Mark,  Michael P. Oien,  Darya P. Shlapak,  Lifeng Yu, and  Jared T. Verdoorn



ABSTRACT

SUMMARY: Photon-counting CT is an increasingly used technology with numerous advantages over conventional energy-integrating detector CT. These include superior spatial resolution, high temporal resolution, and inherent spectral imaging capabilities. Recently, photon-counting CT myelography was described as an effective technique for the detection of CSF-venous fistulas, a common cause of spontaneous intracranial hypotension. It is likely that photon-counting CT myelography will also have advantages for the localization of dural tears, a separate type of spontaneous spinal CSF leak that requires different myelographic techniques for accurate localization. To our knowledge, prior studies on photon-counting CT myelography have been limited to techniques for detecting CSF-venous fistulas. In this technical report, we describe our technique and early experience with photon-counting CT myelography for the localization of dural tears.

ABBREVIATIONS: CTM = CT myelography; DSM = digital subtraction myelography; EID = energy-integrating detector; PCCT = photon-counting CT; PC-CTM = photon-counting CT myelography; SIH = spontaneous intracranial hypotension; SR = standard resolution; UHR = ultra-high-resolution; VMI = virtual monoenergetic image

Spontaneous intracranial hypotension (SIH) is caused by a spinal CSF leak, which, in turn, may be secondary to a dural tear (type 1), a leaking meningeal diverticulum (type 2), or a CSF-venous fistula (type 3).¹ Clinical manifestations of SIH are frequently debilitating and occasionally life-threatening. SIH is often reversible when treated, but this procedure requires identification of the site and type of CSF leak present. Brain MR imaging is an effective means of corroborating a diagnosis of SIH but findings can be normal in a subset of patients.² Spine MR imaging and/or conventional CT myelography is helpful to determine the type of CSF leak present; those with dural tears almost universally have extradural CSF, while those with leaking diverticula or CSF-venous fistulas are typically negative for extradural CSF collections.³ After these initial tests, advanced myelography is almost always needed to precisely localize a spinal CSF leak.

Recently, decubitus myelography using photon-counting CT (PCCT) was described as an effective technique for the detection of CSF-venous fistulas.⁴ PCCT uses a different type of x-ray

detector than traditional energy-integrating detector (EID) CT. The detector used in PCCT permits direct conversion of x-rays into an electrical pulse with energy proportional to the incident photon. In contrast, EID CT detectors require a 2-step conversion process that results in summation of photon energies and loss of individual photon energy information. Furthermore, PCCT detectors do not require septa between detector elements, reducing limitations on spatial resolution.⁴ PCCT myelography (PC-CTM) was shown to identify CSF-venous fistulas that were missed on decubitus digital subtraction myelography (DSM) and decubitus EID CT myelography (EID CTM). This finding was largely related to several technologic advantages conferred by PCCT, including improved spatial resolution, higher temporal resolution, and inherent spectral sensitivity, all of which can be useful to detect subtle CSF leaks.⁵ PCCT has also been shown to confer dose reduction compared with EID CT in spine imaging, with 1 study showing a >50% dose reduction in CT of the lumbar spine.⁶

To our knowledge, PC-CTM has not been previously used for the localization of dural tears. Although dural tears are not typically as elusive on imaging as CSF-venous fistulas, they can, nonetheless, be challenging to precisely localize. PC-CTM likely provides advantages compared with typical techniques currently used such as DSM and dynamic EID CTM. Here, we describe a technique for dynamic PC-CTM used to localize dural tears in patients with SIH with spine MR imaging demonstrating extradural CSF collections.

Received December 3, 2023; accepted after revision January 8, 2024.

From the Division of Neuroradiology (A.A.M., W.B., J.C.B., B.A.J.-T., G.B.L., I.T.M., M.P.O., D.P.S., L.Y., J.T.V.), Department of Radiology, and Department of Neurology (J.K.C.-G.), Mayo Clinic, Rochester, Minnesota.

Please address correspondence to Ajay Madhavan, MD, Division of Neuroradiology, Department of Radiology, Mayo Clinic, 200 First St SW, Rochester, MN 55905; e-mail: madhavan.ajay@mayo.edu



Indicates article with online supplemental data.

<http://dx.doi.org/10.3174/ajnr.A8179>

TECHNICAL REPORT

Previous Myelographic Techniques

In recent years, the 2 main techniques used for localization of dural tears have included DSM and dynamic EID CTM.⁷ These procedures are performed with the patient positioned prone when a ventral dural tear is suspected and decubitus when a lateral dural tear is anticipated.⁸ DSM provides higher spatial and temporal resolution and typically has a lower radiation dose compared with dynamic CTM on EID scanners.⁹ By contrast, the main advantage of dynamic EID CTM is that it provides cross-sectional detail, which often allows one to determine not only the level but also the precise laterality of a dural tear (for example, left/right ventrolateral versus midline ventral). Furthermore, dynamic CTM can reveal osseous spicules or osteophytes that frequently cause ventral dural leaks, while such lesions are usually occult on DSM.¹⁰ Dynamic CTM was initially described in 2003 by Luetmer and Mokri.¹¹ Since that time, the technique has been improved with newer-generation CT technology.¹²⁻¹⁴ To date, all described techniques for dynamic CTM have used EID CT scanners, most recently including modern dual-energy CT scanners with fast scan speeds.^{12,13} PCCT represents a fundamental shift in CT technology, using a novel detector mechanism that permits a wide variety of the aforementioned improvements.

Dynamic PC-CTM Technique

In our practice, all patients with suspected SIH undergo non-contrast MR imaging of the entire spine. If this demonstrates extradural CSF, a dural tear is assumed to be present.¹⁵ If the extradural CSF collection is largely ventral, a ventral dural tear is suspected. If the extradural collection is predominantly dorso-lateral or if there is a large or irregular meningeal diverticulum, greater consideration is given to the possibility of a lateral leak site. On the basis of these factors, prone-versus-decubitus positioning for subsequent myelography is chosen. The decision among DSM, dynamic EID CTM, and dynamic PC-CTM is currently based on the radiologist's preference and/or equipment availability.

For dynamic PC-CTM, patients are placed prone or decubitus on the PCCT scanner table (NAEOTOM Alpha; Siemens), using a custom cushion to elevate the pelvis. Lumbar puncture is performed under CT guidance at L2-L3 or below using a 22-ga Quincke spinal needle. Intrathecal needle positioning is confirmed with a tiny (~0.2 mL) injection of Omnipaque 300 (GE Healthcare). A low-dose monitoring scan is set up approximately 2 spinal levels below the lowest level at which extradural CSF is present. Next, 2 mL of contrast is injected while the monitoring scan is continuously repeated every 5 seconds. As soon as intrathecal contrast is visible on the monitoring scan, 2-4 scans of the spine are initiated, with the exact number of scans depending on patient-specific factors (for example, more scans may be obtained if the patient has undergone previously unrevealing myelograms). The scan range may be limited to the spinal levels at which extradural CSF is present or may include the entire spine, largely depending on proceduralist's preference. An additional 1-2 mL of contrast is injected immediately before every scan. The scans are obtained as quickly as allowed by the scanner, with usually only 2-3 seconds of delay between scans.

Each scan is obtained in standard resolution mode (SR, 144 × 0.4 mm detector collimation), except for the final scan, which is obtained in the ultra-high-resolution mode (UHR, 120 × 0.2 mm detector collimation). The SR mode provides greater temporal resolution due to a shorter scan time, though the resulting section thickness is limited to 0.4 mm. The UHR mode usually has approximately double the scan time but can provide a section thickness as low as 0.2 mm. The rationale for performing a UHR scan at only the final acquisition is to provide at least 1 high-resolution scan without impairing the temporal resolution during the most time-sensitive portion of the examination. Both scan modes confer spectral sensitivity even when a single x-ray source is used, meaning that images can be reconstructed at any desired virtual monoenergetic level. All scans use a rotation time of 0.5 seconds and a CARE keV IQ level of 200. The pitch is 1.2 (SR) or 1.0 (UHR). Automatic exposure control is used, with a manual tube potential of 140 kV.

In our protocol, all scans are reconstructed with the lowest section thickness allowed by the scan mode (0.4 mm for SR and 0.2 mm for UHR). A low-energy threshold (referred to as T3D by the manufacturer and including all photon energies from 25 to 140 keV) is applied to all series. Separately, we reconstruct 40-keV virtual monoenergetic images (VMIs) to maximize iodine conspicuity (thus, 2 series are created for each scan performed). We use a Br48 kernel (quantum iterative reconstruction setting of 3) for the 40-keV VMIs and a Br56 kernel (quantum iterative reconstruction setting of 4) for T3D reconstructions. These are both relatively sharp kernels that provide high spatial resolution while maintaining an acceptable noise level. As with previously described techniques, the site of the dural tear is determined by direct visualization of a contrast column leaking into the epidural space (Fig 1). The approximate leak site can also be inferred by the lowest spinal level at which epidural contrast is seen, though this is a less definitive finding, and direct visualization of the exact level is strongly preferred.

DISCUSSION

We have described a technique for dynamic PC-CTM that can be used for the precise localization of dural tears. Fundamentally, this technique is similar to those previously described for EID CT. However, there are several nuances unique to PCCT, and radiologists considering PC-CTM for this purpose should become familiar with the different scan modes, reconstructions, and benefits of PCCT.

Our early experience has demonstrated several advantages of dynamic PC-CTM specific to the localization of dural leaks. First, the high temporal resolution conferred by the SR scan mode allows rapid imaging of the spine as the intrathecal contrast bolus ascends. This is crucial because dural tears usually result in fast CSF leaks, and high temporal resolution maximizes the chance of observing the precise location where contrast leaks into the epidural space (Fig 1). The difference in temporal resolution between dynamic PC-CTM and dynamic EID CTM varies depending on the specific EID scanner used. We have observed that both the time between scans and the time per scan are approximately 50% longer on dynamic EID CT performed on our dual-energy scanner (Definition Flash; Siemens) compared

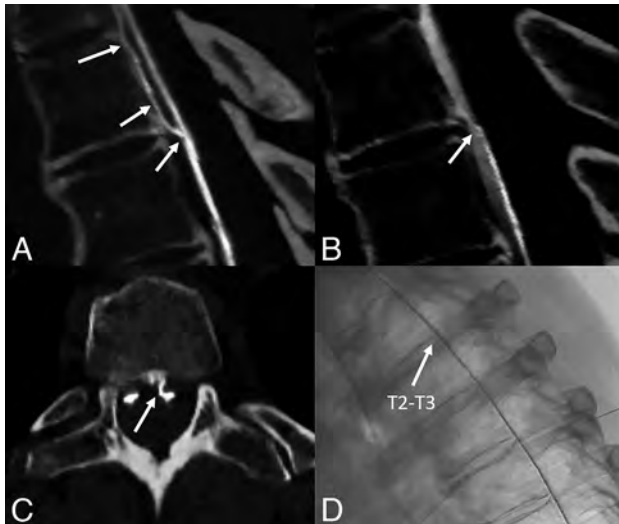


FIG 1. Ventral dural tear localized on PC-CTM after negative prone DSM and negative prone dynamic EID CTM. Sagittal low-energy threshold (T3D) reconstructions from the first scan during dynamic PC-CTM demonstrate a ventral leak at T2–T3 (A, arrow). The leak remained visible on the second scan obtained 4 seconds later (not shown) but was barely visible on the third scan obtained after another 4 seconds (B, arrow), largely because of dense contrast that had already leaked into the epidural space. An axial 0.4-mm image from the first scan (C) clearly shows the precise site of the dural tear, which is slightly to the left of midline (C, arrow). This leak was occult on prone DSM (unsubtracted image D, arrow), as well as on prone dynamic EID CTM (not shown), both of which were performed before the PC-CTM.

with PCCT. Second, PC-CTM offers very high spatial resolution. This has a variety of benefits for localization of dural tears, including more precise anatomic discrimination of the leak site, greater confidence in localization of subtle leaks, and exquisite characterization of tiny osseous spicules that often cause these leaks (Figs 1–2).¹⁰ Third, PC-CTM has inherent spectral sensitivity, meaning that VMIs can be reconstructed without the need for dual-energy or dual-source techniques. We have found that 40-keV VMIs are useful to increase the conspicuity of subtle CSF leaks (Online Supplemental Data). Although dual-energy CT can provide VMIs as well, they come at the cost of slower scan speeds. Finally, PC-CTM has a lower radiation dose compared with EID CT.⁶ A reduced-dose EID CT–based technique was recently described by Mamlouk et al,¹⁴ and dynamic PC-CTM has the potential to even further reduce the radiation dose to these patients.

Our technical report has limitations, the most important of which is the small number of patients on which this examination has been performed ($n=6$). The site of the dural tear was precisely localized in all 6 of these patients, including 5 ventral leaks and 1 lateral leak. Three patients had previously unrevealing findings on myelograms. Specifically, 1 underwent an initially negative prone DSM, 1 underwent an initially negative dynamic EID CTM, and 1 underwent both an initially negative DSM and negative dynamic EID CTM (Fig 1). For the 2 patients who underwent both a dynamic EID CTM and dynamic PC-CTM, we observed a dose reduction per scan of 20% and 25%, respectively (measured in dose-length product). Future studies on larger patient populations will be needed to determine how frequently PC-CTM adds

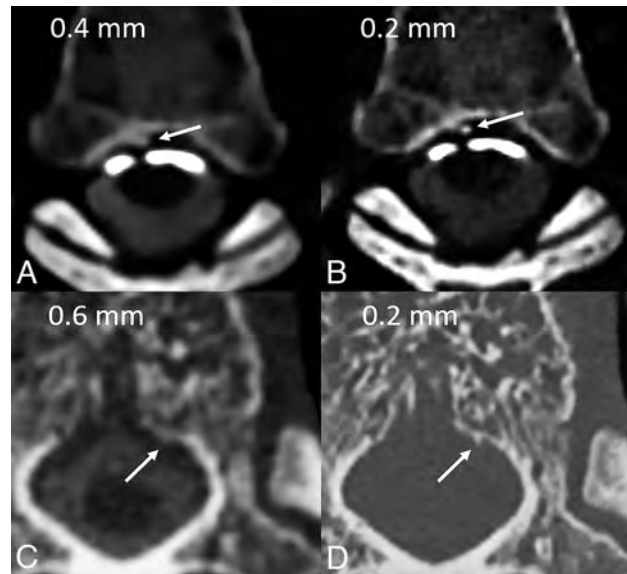


FIG 2. Benefits of high spatial resolution in 2 patients with ventral dural tears. In the first patient (A and B), axial low-energy threshold (T3D) images from a prone dynamic PC-CTM demonstrate a thin column of epidural contrast that had leaked ventrally at T5–T6 (A and B, arrows). The contrast column is more exquisitely delineated from the vertebral body cortex when the same image is reconstructed at 0.2 mm compared with 0.4 mm. In the second patient, a ventral leak at T11 was diagnosed on prone DSM. A postmyelographic EID CT image at 0.6 mm (C) shows a questionable osseous excrescence at the level of the leak (C, arrow) without a definite spicule. Subsequent PCCT image at 0.2 mm (D) shows that this lesion is, in fact, a sharp osseous spicule arising from the vertebral cortex (D, arrow), confirming the presumed cause of the leak, which was later identified and repaired at surgery.

true diagnostic value and how much dose reduction is typically achieved, but our preliminary experience with this application of PC-CTM has been promising. It will be particularly important to compare DSM, dynamic EID CTM, and dynamic PC-CTM in a randomized fashion, because varying results between modalities could theoretically be due to uncontrolled factors such as spontaneous opening or closure of leaks. Another limitation of this study is that PCCT is not available at all institutions. However, it is likely that this technology will become more prevalent in the near future, underpinning the need for continued investigation of its role in patients with SIH.

Disclosure forms provided by the authors are available with the full text and PDF of this article at www.ajnr.org.

REFERENCES

- Schievink WI, Maya MM, Jean-Pierre S, et al. A classification system of spontaneous spinal CSF leaks. *Neurology* 2016;87:673–79 CrossRef Medline
- Schievink WI, Maya M, Prasad RS, et al. Spontaneous spinal cerebrospinal fluid-venous fistulas in patients with orthostatic headaches and normal conventional brain and spine imaging. *Headache* 2021;61:387–91 CrossRef Medline
- Kranz PG, Gray L, Malinzak MD, et al. Spontaneous intracranial hypotension: pathogenesis, diagnosis, and treatment. *Neuroimaging Clin N Am* 2019;29:581–94 CrossRef Medline
- Madhavan AA, Yu L, Brinjikji W, et al. Utility of photon-counting detector CT myelography for the detection of CSF-venous

- fistulas. *AJNR Am J Neuroradiol* 2023;44:740–44 CrossRef Medline
5. Madhavan AA, Cutsforth-Gregory JK, Brinjikji W, et al. **Diagnostic performance of decubitus photon-counting detector CT myelography for the detection of CSF-venous fistulas.** *AJNR Am J Neuroradiol* 2023;44:1445–50 CrossRef Medline
 6. Marth AA, Marcus RP, Feuerriegel GC, et al. **Photon-counting detector CT versus energy-integrating detector CT of the lumbar spine: comparison of radiation dose and image quality.** *AJR Am J Roentgenol* 2024;222:e23.29950 CrossRef Medline
 7. Hoxworth JM, Trentman TL, Kotsenas AL, et al. **The role of digital subtraction myelography in the diagnosis and localization of spontaneous spinal CSF leaks.** *AJR Am J Roentgenol* 2012;199:649–53 CrossRef Medline
 8. Madhavan AA, Verdoorn JT, Shlapak DP, et al. **Lateral decubitus dynamic CT myelography for fast cerebrospinal fluid leak localization.** *Neuroradiology* 2022;64:1897–903 CrossRef Medline
 9. Nicholson PJ, Guest WC, van Prooijen M, et al. **Digital subtraction myelography is associated with less radiation dose than CT-based techniques.** *Clin Neuroradiol* 2021;31:627–31 CrossRef Medline
 10. Rosebrock RE, Diehn FE, Luetmer PH, et al. **Penetrating osseous spicules causing high-flow ventral CSF leaks in the setting of relatively low BMI: a preliminary study.** *Clin Neuroradiol* 2018;28:539–43 CrossRef Medline
 11. Luetmer PH, Mokri B. **Dynamic CT myelography: a technique for localizing high-flow spinal cerebrospinal fluid leaks.** *AJNR Am J Neuroradiol* 2003;24:1711–14 Medline
 12. Mark IT, Madhavan AA, Benson JC, et al. **Updated ultrafast dynamic computed tomography myelography technique for cerebrospinal fluid leaks.** *Interv Neuroradiol* 2023 Aug 20 [Epub ahead of print] CrossRef Medline
 13. Thielen KR, Sillery JC, Morris JM, et al. **Ultrafast dynamic computed tomography myelography for the precise identification of high-flow cerebrospinal fluid leaks caused by spiculated spinal osteophytes.** *J Neurosurg Spine* 2015;22:324–31 CrossRef Medline
 14. Mamlouk MD, Shen PY, Dahlin BC. **Modified dynamic CT myelography for type 1 and 2 CSF leaks: a procedural approach.** *AJNR Am J Neuroradiol* 2023;44:341–46 CrossRef Medline
 15. Callen AL, Timpone VM, Schwertner A, et al. **Algorithmic multi-modality approach to diagnosis and treatment of spinal CSF leak and venous fistula in patients with spontaneous intracranial hypotension.** *AJR Am J Roentgenol* 2022;219:292–301 CrossRef Medline

Anton N. Hasso

It is with profound sadness that we share the news of Dr Anton (Tony) N. Hasso, MD, Emeritus Professor and former Chair of Radiology at the University of California, Irvine (UCI), who peacefully departed on March 6, 2024, at the age of 83.

Dr Hasso became an integral part of the UCI family in 1996, leaving an indelible mark as Chair of Radiological Sciences, following a distinguished career at Loma Linda. His legacy is one of philanthropy, leadership, and profound influence on the growth of the Radiological Sciences Department.

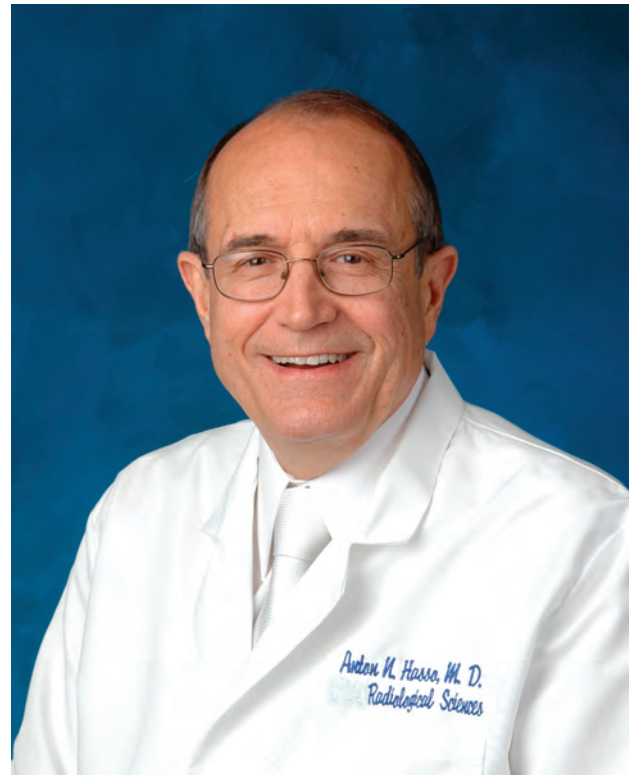
Throughout his illustrious career, Dr Hasso held esteemed positions, including serving as President of the American Society of Neuroradiology, the American Society of Head and Neck Radiology, and the Western Neuroradiological Society. He was a founding member of the World Federation of Neuroradiological Societies and its inaugural treasurer. Additionally, he contributed significantly to the American Roentgen Ray Society and held the presidency of the California Radiological Society.

A pioneer in neuroradiology, Dr Hasso's influence extended beyond academic achievements. His expertise in head and neck and MR imaging is evident in 6 authored textbooks, more than 140 peer-reviewed publications, and contributions to more than 70 book chapters. He served on the Diagnostic Imaging Study Section at the National Institutes of Health and represented the Council of Medical Education of the American Medical Association on the Diagnostic Radiology Residency Review Committee. Later in his career and into retirement, Dr Hasso took a keen interest in vascular lesions, contributing significantly to the Vascular Birthmark Foundation.

Dr Hasso was not only a distinguished professional but also a cherished mentor and educator. A reflection from a former trainee and now faculty member captures Dr Hasso's teaching style: "As a third-year medical student looking for any project, Dr Hasso gave me a book chapter to write. I had asked for a case report, of course. As I spent three months in a small office next to his, he guided me through this project that I was sure was beyond me. Every meeting was a smile and a laugh and a point toward a reference to fix my mistakes. That is how he taught. A smile, a laugh, and advice."

Beyond his professional achievements, Dr Hasso was a warm and compassionate individual, always willing to share his wealth of information and time generously. His untimely departure leaves a void in our community, and he will be dearly missed by all who had the privilege of knowing him.

Dr Hasso received his BSc degree from La Sierra University and his MD from Loma Linda University School of Medicine in



California. His academic journey included an internship at the University of Southern California Medical Center, a radiology residency at the White Memorial Medical Center in Los Angeles, and a cardiovascular radiology fellowship at Loma Linda University. Notably, he furthered his expertise through a National Institute of Neurological Diseases and Stroke Special Fellowship in Neuroradiology at the University of California Los Angeles Center for Health Sciences and a postdoctoral fellowship in orbital and ear, nose, and throat radiology at the Foundation A. De Rothschild in Paris, France.

Dr. Hasso was preceded in death by his wife, Peggy Fritzsche, also a visionary and leader in radiology and mammography, in 2009. Together, they raised 2 sons. Dr Hasso is survived by his significant other, Jean Tonn.

Our community will remember this extraordinary, courageous, and remarkable human being.

Daniel Chow
University of California, Irvine

<http://dx.doi.org/10.3174/ajnr.A8266>

Spaceflight-Associated Neuro-Ocular Syndrome and Idiopathic Intracranial Hypertension: Can Anemia and Hyperemia Underlie Both?

We read with interest the article in the *AJNR* by Tidwell et al¹ which describes a head-down tilt study with increased inspired carbon dioxide (CO₂) levels, which was undertaken as an analog to long-duration spaceflight. The purpose of this study was to investigate the alterations occurring in brain physiology in long-term spaceflight. This study may shed some light on the spaceflight-associated neuro-ocular syndrome (SANS). SANS affects the vision of individuals undergoing spaceflight.² The authors found that there was a decrease in CBF of 18%, an increase in ventricular size of 7%, and an increase in perivascular space size of 20% in their study.¹ They acknowledged that although their study replicated some of the physiology of spaceflight, the CBF may actually be increased in long-term spaceflight rather than decreased as they found, and they referenced our review on the subject.² In our review article, the literature indicated that there was evidence of a 41%–56% increase in cardiac output, an 83% increase in straight sinus blood flow velocity, and an 84% increase in the middle cerebral vein flow velocity in long-term spaceflight.² We wish to discuss the relevance of blood flow and SANS in light of our own most recent findings in idiopathic intracranial hypertension (IIH).

The ocular findings in SANS and IIH are similar.² While it has long been thought that IIH is associated with either a normal or reduced CBF, it has recently been shown that there is a subset of patients with IIH who have an increased CBF, ie, cerebral hyperemia.³ Approximately 20% of patients with IIH are anemic.³ A review of the hemoglobin concentration in a previously published cohort of children being investigated for IIH showed that 17% were anemic, with these individuals' hemoglobin concentrations being 16% below the mean reference levels.³ These anemic children had their average CBF increased by 60% compared with controls. Cerebral hyperemia is an expected result of anemia, and elevated blood flow can increase the venous pressure, which is the presumed underlying cause of IIH.³ Most interesting, chronic he-

molytic anemia and a reduction in the hemoglobin concentration of about 10% are found in long-term spaceflight.⁴ Thus, anemia in both IIH and spaceflight would be expected to be associated with cerebral hyperemia and not a reduced blood flow. Perhaps the head-down-tilt experiment could be supplemented with hypoxia as well as an increased inspired CO₂ level to increase the CBF and better match the effects of spaceflight.

Disclosure forms provided by the authors are available with the full text and PDF of this article at www.ajnr.org.

REFERENCES

1. Tidwell JB, Taylor JA, Collins HR, et al. **Longitudinal changes in cerebral perfusion, perivascular space volume, and ventricular volume in a healthy cohort undergoing a spaceflight analog.** *AJNR Am J Neuroradiol* 2023;44:1026–31 CrossRef Medline
2. Bateman GA, Bateman AR. **A perspective on spaceflight associated neuro-ocular syndrome causation secondary to elevated venous sinus pressure.** *NPJ Microgravity* 2022;8:3 CrossRef Medline
3. Bateman GA. **A scoping review of the discrepancies in the measurement of cerebral blood flow in idiopathic intracranial hypertension: oligemia, euvoemia or hyperemia?** *Fluids Barriers CNS* 2023;20:63 CrossRef Medline
4. Waisberg E, Ong J, Masalkhi M, et al. **Anemia and spaceflight associated neuro-ocular syndrome (SANS).** *Prehosp Disaster Med* 2023 July 31. [Epub ahead of print] CrossRef Medline

✉ G.A. Bateman

Department of Medical Imaging
John Hunter Hospital
Newcastle, New South Wales, Australia
Newcastle University Faculty of Health
Callaghan Campus
Newcastle, New South Wales, Australia

✉ A.R. Bateman

School of Mechanical Engineering
University of New South Wales
Sydney, New South Wales, Australia

<http://dx.doi.org/10.3174/ajnr.A8025>

REPLY:

We thank Drs Bateman and Bateman for their comments. In their letter¹ and in their review,² Bateman and Bateman highlight the limitations of the head-down tilt bedrest model as an analog for cerebrovascular changes that may occur during spaceflight. In this regard, we stress the importance for space agencies and commercial spaceflight providers to prioritize studies of cerebral perfusion in astronauts.

In addition to the limitations inherent in the head-down tilt bedrest model, it is important to keep in mind the difficulties of measuring perfusion during spaceflight and the limitations of the various methods used for measuring cerebral perfusion. Due to the constraints of the human spaceflight setting, conventional imaging techniques for measuring cerebral perfusion such as xenon-enhanced CT, SPECT, PET, dynamic perfusion CT, and MR imaging perfusion³ may be used only on the ground before and after spaceflight. In this situation, without inflight data, it is unclear whether measurements made after spaceflight reflect inflight physiology or, alternatively, an adaptive response to returning to one gravity on Earth.

Furthermore, each of these methods has limitations concerning the quantification of CBF.³ In particular, arterial spin-labeling (ASL) MR imaging, as used by Tidwell et al,⁴ requires adjustment for individual hematocrit levels to avoid overestimation of perfusion. This is important to take into account when evaluating longitudinal changes in perfusion by ASL MR imaging in individuals who may develop anemia such as patients with idiopathic intracranial hypertension or astronauts undergoing long-term spaceflight as pointed out by Bateman and Bateman.¹

Ideally, CBF would be measured on-orbit during spaceflight. Several investigators have used Doppler ultrasound inflight; however, as Bateman and Bateman² point out in their review, mixed results have been obtained using Doppler ultrasound, which indirectly infers CBF based on CBF velocity.

Another method that may be suitable for on-orbit use is near-infrared spectroscopy. In a study performed as part of a private astronaut mission to the International Space Station sponsored by Axiom Space in 2023, the Axiom Mission 2 crew used near-

infrared spectroscopy to measure CBF during spaceflight.⁵ We are awaiting, with interest, the results of this study.

Given the complexity of factors that may contribute to altered cerebral perfusion and spaceflight-associated neuro-ocular syndrome (SANS) development, ultimately a multimodal approach, using both inflight and ground-based methods for measuring cerebral perfusion in astronauts, will be needed to gain a better understanding of the impact of spaceflight on cerebrovascular physiology. In addition, these studies would provide essential data for developing evidence-based protocols to reduce the risk of the occurrence of an inflight neurovascular emergency, such as stroke, among future space travelers.

REFERENCES

1. Bateman GA, Bateman AR. **Spaceflight-Associated Neuro-Ocular Syndrome and Idiopathic Intracranial Hypertension: Can Anemia and Hyperemia Underlie Both?** *AJNR Am J Neuroradiol* 2024;45:E4 CrossRef
2. Bateman GA, Bateman AR. **A perspective on spaceflight associated neuro-ocular syndrome causation secondary to elevated venous sinus pressure.** *NPJ Microgravity* 2022;8:3 CrossRef Medline
3. Wintermark M, Sesay M, Barbier E, et al. **Comparative overview of brain perfusion imaging techniques.** *J Neuroradiol* 2005;32:294–314 CrossRef Medline
4. Tidwell JB, Taylor JA, Collins HR, et al. **Longitudinal changes in cerebral perfusion, perivascular space volume, and ventricular volume in a healthy cohort undergoing a spaceflight analog.** *AJNR Am J Neuroradiol* 2023;44:1026–31 CrossRef Medline
5. AXIOM SPACE. **Ax-2 mission bolsters opportunities for innovation and scientific research in space.** <https://www.axiomspace.com/missions/ax2/research>. Accessed March 19, 2024

Donna R. Roberts

Department of Radiology and Radiological Science
Medical University of South Carolina
Charleston, South Carolina

International Space Station National Laboratory
Melbourne, Florida

Joe Tidwell

J. Andrew Taylor
Department of Radiology and Radiological Science
Medical University of South Carolina
Charleston, South Carolina

<http://dx.doi.org/10.3174/ajnr.A8278>

Enlargement of Perivascular Spaces as a Downstream Consequence of Spaceflight Analog-Induced Alterations in Cerebral Venous Hemodynamics

We read with great interest the article by Tidwell and colleagues¹ entitled “Longitudinal Changes in Cerebral Perfusion, Perivascular Space Volume, and Ventricular Volume in a Healthy Cohort Undergoing a Spaceflight Analog” published recently in the *American Journal of Neuroradiology*. We would like to congratulate the authors for performing this MR imaging study in a spaceflight analog with findings of great importance for future human space missions, and would appreciate the opportunity to make a comment.

The authors evaluated the relationship among changes in cerebral perfusion, ventricular volume, and perivascular space (PVS) volume in healthy participants before, during, and after a spaceflight analog comprising 30 days of 6° head-down tilt (HDT) bed rest combined with 0.5% atmospheric CO₂.¹ Global perfusion decreased during the analog period, whereas ventricular volume and PVS volume increased. This was followed by a reversal of these patterns during the 2-week recovery period. The authors correctly state that an increase in PVS volume may reflect obstruction or inefficiency in the exchange of CSF and interstitial fluid (ISF) that occurs in the perivascular channels. Given the negative correlation between cerebral perfusion and PVS volume seen in their study and given that CSF is driven through PVS by arterial pulsations, they propose that decreased perfusion could reduce the ability to circulate CSF, causing the observed PVS dilation.

Here, we propose an additional alternate mechanism to explain how altered hemodynamics in real and simulated microgravity may contribute to PVS dilation. In a recent article, we speculated that altered venous hemodynamics during spaceflight may cause disruption of the glymphatic system.² Microgravity has been demonstrated to cause stagnation and even reversal of the cerebral venous outflow in the internal jugular veins of a long-duration International Space Station crew.³ This finding suggests that spaceflight may cause venous congestion and even some degree of retrograde blood flow from the central veins through the internal jugular vein into the brain. Signs of cerebral venous congestion have also been demonstrated in an HDT microgravity analog setting.⁴ Cerebral vein distention could then increase the hydraulic resistance of perivenous spaces, given that increased blood volume in the cerebral veins may result in closure of the

perivenous spaces.² This outcome could compromise the glymphatic outflow and drainage, resulting in CSF-ISF stagnation. As a consequence, the CSF may stagnate and accumulate at the periarterial site, with resultant periarterial dilation.² We propose that this could provide an additional alternate explanation for the observed PVS enlargement during the analog period.

Disclosure forms provided by the authors are available with the full text and PDF of this article at www.ajnr.org.

REFERENCES

1. Tidwell JB, Taylor JA, Collins HR, et al. **Longitudinal changes in cerebral perfusion, perivascular space volume, and ventricular volume in a healthy cohort undergoing a spaceflight analog.** *AJNR Am J Neuroradiol* 2023;44:1026–31 CrossRef Medline
2. Wostyn P, Mader TH, Gibson CR, et al. **Does long-duration exposure to microgravity lead to dysregulation of the brain and ocular glymphatic systems?** *Eye Brain* 2022;14:49–58 CrossRef Medline
3. Marshall-Goebel K, Laurie SS, Alferova IV, et al. **Assessment of jugular venous blood flow stasis and thrombosis during spaceflight.** *JAMA Netw Open* 2019;2:e1915011 CrossRef Medline
4. Marshall-Goebel K, Ambarki K, Eklund A, et al. **Effects of short-term exposure to head-down tilt on cerebral hemodynamics: a prospective evaluation of a spaceflight analog using phase-contrast MRI.** *J Appl Physiol (1985)* 2016;120:1466–73 CrossRef Medline

● Peter Wostyn

Department of Psychiatry
PC Sint-Amandus
Beernem, Belgium

● Thomas H. Mader

NASA Ophthalmology Consultant
Moab, Utah

● C. Robert Gibson

South Shore Eye Center
League City, Texas
KBR
Houston, Texas

● Maiken Nedergaard

Faculty of Health and Medical Sciences
Center for Translational Neuromedicine
University of Copenhagen
Copenhagen, Denmark
Center for Translational Neuromedicine
University of Rochester Medical Center
Rochester, New York

<http://dx.doi.org/10.3174/ajnr.A8062>

REPLY:

We thank Wostyn et al¹ for their comments and for the alternative explanation, based on venous congestion, that they provide for the perivascular space (PVS) volume increase observed in the bed rest subjects in our study.² Indeed, altered cerebral venous hemodynamics have been documented in astronauts,^{3,4} and we have shown an increase in PVS volumes in astronauts and cosmonauts after spaceflight.⁵ Although altered venous outflow would be expected to have occurred in the bed rest subjects participating in our study, it was not measured. Taken together, these results suggest that an altered cerebrovascular physiology occurs both in the ground-based spaceflight analog of head-down tilt bed rest and during long-term spaceflight. The relative contributions that altered arterial or venous flow may have made individually or collectively to increase the PVS volume are unclear, suggesting further studies are needed to disentangle the underlying mechanisms involved. In that regard, advanced MR imaging techniques including MRA, MRV, and SWI sequences (which enhance the visualization of small venous structures) should be included in future MR imaging protocols used in head-down tilt bed rest studies and for pre- and postflight astronaut brain MR imaging.⁶

REFERENCES

1. Wostyn P, Mader TH, Gibson CR, et al. **Enlargement of perivascular spaces as a downstream consequence of spaceflight analog-induced alterations in cerebral venous hemodynamics.** *AJNR Am J Neuroradiol* 2024;45:E6 CrossRef

2. Tidwell JB, Taylor JA, Collins HR, et al. **Longitudinal changes in cerebral perfusion, perivascular space volume, and ventricular volume in a healthy cohort undergoing a spaceflight analog.** *AJNR Am J Neuroradiol* 2023;44:1026–31 CrossRef Medline

3. Marshall-Goebel K, Laurie SS, Alferova IV, et al. **Assessment of jugular venous blood flow stasis and thrombosis during spaceflight.** *JAMA Netw Open* 2019;2:e1915011 CrossRef Medline

4. Rosenberg M, Coker MA, Taylor JA, et al. **Post-flight dural venous sinus congestion in astronauts with spaceflight-associated neuro-ocular syndrome.** *JAMA Netw Open* 2021;4:e2131465 CrossRef Medline

5. Barisano G, Seppehrband F, Collins HR, et al. **The effect of prolonged spaceflight on cerebrospinal fluid and perivascular spaces of astronauts and cosmonauts.** *Proc Natl Acad Sci U S A* 2022;119:e2120439119 CrossRef

6. Roberts DR, Stahn AC, Seidler RD, et al. **Towards understanding the effects of spaceflight on the brain.** *Lancet Neurol* 2020;19:808 CrossRef Medline

Donna R. Roberts

Department of Radiology and Radiological Science
Medical University of South Carolina
Charleston, South Carolina

International Space Station National Laboratory
Melbourne, Florida

Joe Tidwell

J. Andrew Taylor

Department of Radiology and Radiological Science
Medical University of South Carolina
Charleston, South Carolina

<http://dx.doi.org/10.3174/ajnr.A8279>



Simplify the MOC Process



Manage your CME Credits Online

CMEgateway.org

Available to Members of Participating Societies

American Board of Radiology (ABR)
American College of Radiology (ACR)
American Roentgen Ray Society (ARRS)
American Society of Neuroradiology (ASNR)
Commission on Accreditation of Medical
Physics Educational Programs, Inc. (CAMPEP)
Radiological Society of North America (RSNA)
Society of Interventional Radiology (SIR)
SNM
The Society for Pediatric Radiology (SPR)

It's Easy and Free!

Log on to CME Gateway to:

- View or print reports of your CME credits from multiple societies from a single access point.
- Print an aggregated report or certificate from each participating organization.
- Link to SAMs and other tools to help with maintenance of certification.

American Board of Radiology (ABR) participation!

By activating ABR in your organizational profile, your MOC-fulfilling CME and SAM credits can be transferred to your own personalized database on the ABR Web site.

Sign Up Today!

go to CMEgateway.org

AJNR *go green*

***AJNR* urges American Society of Neuroradiology members to reduce their environmental footprint by voluntarily suspending their print subscription.**

The savings in paper, printing, transportation, and postage directly fund new electronic enhancements and expanded content.

The digital edition of *AJNR* presents the print version in its entirety, along with extra features including:

- Publication Preview
- Case Collection
- Podcasts
- The *AJNR* News Digest
- The *AJNR* Blog

It also reaches subscribers much faster than print. An electronic table of contents will be sent directly to your mailbox to notify you as soon as it publishes.

Readers can search, reference, and bookmark current and archived content 24 hours a day on www.ajnr.org.

ASNR members who wish to opt out of print can do so by using the *AJNR* Go Green link on the *AJNR* Website (<http://www.ajnr.org/content/subscriber-help-and-services>). Just type your name in the email form to stop print and spare our ecosystem.



AJNR

Dear *AJNR* Subscriber:

I hope this message finds you well. We've made significant enhancements to *AJNR*, including an expanded Editorial Board, an Academy of Reviewers, and a Junior Editorial Board. Now, I'm excited to share a crucial update about the *AJNR*'s future.

Towards the end of the year, *AJNR* will undergo a major transformation, transitioning to a fully electronic format and bidding farewell to traditional paper publication. This shift is driven by the need to manage rising costs associated with printing, shipping, and storage. Our goal is to achieve fiscal balance without imposing substantial increases in article processing charges.

The move to an electronic format brings numerous benefits. It opens the door to more personalized content, allowing readers to tailor their *AJNR* experience. The electronic format also enhances visual elements with more images and various media types, including videos and scrollable image stacks, especially valuable in neuroradiology.

Additionally, the electronic format allows for supplementary content, enriching the reader's experience with easy access to materials, commentaries, and related resources. We're committed to implementing enhanced searchability, catering to the diverse needs of neuroradiologists, researchers, trainees, and students.

While I have been a dedicated collector of *AJNR*'s physical copies for over two decades, recognizing the sadness in parting with this tradition, financial pragmatism compels us to embrace technological advancements. Despite this transition, we aim to maintain a sense of optimism and adaptability.

To involve our community in this journey, *AJNR* plans sessions to gather feedback, concerns, and innovative ideas. By fostering an open dialogue, we aim to shape our electronic platform in line with our audience's evolving expectations.

Please participate in these sessions that will be advertised on the *AJNR* website or please feel free to reach out directly to me (mw.ajnr.eic@gmail.com) with any concern or suggestion.

Also, please immediately activate your individual subscription account and also consider registering for Publish Ahead of Print (including Preprint) and electronic Table of Contents, Case of the Week, and Keyword/Author Alerts. These links as well as additional information including upcoming Zoom sessions can be found at the *AJNR* website using the QR code below.

<https://www.ajnr.org/content/ajnr-update>

Thank you in advance for your engagement.

Sincerely,

Max Wintermark
Editor-in-Chief



Moving to a fully Electronic Format by 2025

Read the important announcement from Editor-in-Chief Dr. Max Wintermark in this month's editorial.

Feedback and innovative ideas are encouraged through:	• Online sessions • AJNR booth at ASNR24 • Email mw.ajnr.eic@gmail.com
---	---

